frontiers | Research Topics

Unconventional resources: provenance analysis, sediment transport, reservoir evaluation, geo-energy

Edited by
Wenguang Wang, Xixin Wang, Chao Liu,
Yongqiang Chen and Yihuai Zhang

Published in
Frontiers in Earth Science

FRONTIERS EBOOK COPYRIGHT STATEMENT

The copyright in the text of individual articles in this ebook is the property of their respective authors or their respective institutions or funders. The copyright in graphics and images within each article may be subject to copyright of other parties. In both cases this is subject to a license granted to Frontiers.

The compilation of articles constituting this ebook is the property of Frontiers.

Each article within this ebook, and the ebook itself, are published under the most recent version of the Creative Commons CC-BY licence. The version current at the date of publication of this ebook is CC-BY 4.0. If the CC-BY licence is updated, the licence granted by Frontiers is automatically updated to the new version.

When exercising any right under the CC-BY licence, Frontiers must be attributed as the original publisher of the article or ebook, as applicable.

Authors have the responsibility of ensuring that any graphics or other materials which are the property of others may be included in the CC-BY licence, but this should be checked before relying on the CC-BY licence to reproduce those materials. Any copyright notices relating to those materials must be complied with.

Copyright and source acknowledgement notices may not be removed and must be displayed in any copy, derivative work or partial copy which includes the elements in question.

All copyright, and all rights therein, are protected by national and international copyright laws. The above represents a summary only. For further information please read Frontiers' Conditions for Website Use and Copyright Statement, and the applicable CC-BY licence.

ISSN 1664-8714
ISBN 978-2-8325-5837-9
DOI 10.3389/978-2-8325-5837-9

About Frontiers

Frontiers is more than just an open access publisher of scholarly articles: it is a pioneering approach to the world of academia, radically improving the way scholarly research is managed. The grand vision of Frontiers is a world where all people have an equal opportunity to seek, share and generate knowledge. Frontiers provides immediate and permanent online open access to all its publications, but this alone is not enough to realize our grand goals.

Frontiers journal series

The Frontiers journal series is a multi-tier and interdisciplinary set of open-access, online journals, promising a paradigm shift from the current review, selection and dissemination processes in academic publishing. All Frontiers journals are driven by researchers for researchers; therefore, they constitute a service to the scholarly community. At the same time, the *Frontiers journal series* operates on a revolutionary invention, the tiered publishing system, initially addressing specific communities of scholars, and gradually climbing up to broader public understanding, thus serving the interests of the lay society, too.

Dedication to quality

Each Frontiers article is a landmark of the highest quality, thanks to genuinely collaborative interactions between authors and review editors, who include some of the world's best academicians. Research must be certified by peers before entering a stream of knowledge that may eventually reach the public - and shape society; therefore, Frontiers only applies the most rigorous and unbiased reviews. Frontiers revolutionizes research publishing by freely delivering the most outstanding research, evaluated with no bias from both the academic and social point of view. By applying the most advanced information technologies, Frontiers is catapulting scholarly publishing into a new generation.

What are Frontiers Research Topics?

Frontiers Research Topics are very popular trademarks of the *Frontiers journals series*: they are collections of at least ten articles, all centered on a particular subject. With their unique mix of varied contributions from Original Research to Review Articles, Frontiers Research Topics unify the most influential researchers, the latest key findings and historical advances in a hot research area.

Find out more on how to host your own Frontiers Research Topic or contribute to one as an author by contacting the Frontiers editorial office: frontiersin.org/about/contact

Unconventional resources: provenance analysis, sediment transport, reservoir evaluation, geo-energy

This ebook is split into several files; this is part one of the ebook, please see the overview text of the Research Topic page to access the second part of the ebook.

Topic editors

Wenguang Wang — Northeast Petroleum University, China
Xixin Wang — Yangtze University, China
Chao Liu — Northeast Petroleum University, China
Yongqiang Chen — Commonwealth Scientific and Industrial Research Organisation (CSIRO), Australia
Yihuai Zhang — University of Glasgow, United Kingdom

Citation

Wang, W., Wang, X., Liu, C., Chen, Y., Zhang, Y., eds. (2025). *Unconventional resources: provenance analysis, sediment transport, reservoir evaluation, geo-energy*. Lausanne: Frontiers Media SA. doi: 10.3389/978-2-8325-5837-9

Table of contents

05 Editorial: Unconventional resources: provenance analysis, sediment transport, reservoir evaluation, geo-energy
Wenguang Wang, Xixin Wang, Yongqiang Chen, Chao Liu and Yihuai Zhang

09 A fracture modeling method for ultra-deep reservoirs based on geologic information fusion: an application to a low porosity sandstone reservoirs in X gas field of a basin in western China
Rujun Wang, Yongliang Tang, Fenglai Yang, Jiaofeng She, Xiaorui Li, Naidong Chen, Ce Ji and Yingzheng He

21 Fracture-vuggy carbonate reservoir characterization based on multiple geological information fusion
Yan Wang, Pengfei Xie, Huitao Zhang, Yuming Liu and Aiying Yang

36 Formation mechanism of the upper Paleozoic tight sandstone gas reservoir in the Daniudi gas field, Ordos Basin, China
Fan Song, Qingyuan Kong, Nina Su, Guohua Jiao and Miaomiao Xu

51 Diagenetic alterations and deep high-quality reservoirs within deltaic distributary channel facies: a case study from the Permian Shihezi formation in the Hongde area, southwestern Ordos basin, China
Xiaoming Wu, Zhicheng Shen, Yanxin Bao, Weilin Wang, Zhandong Yan, Bo Wang, Xiaoyin Zheng, Luxing Dou and Zhigang Wen

63 Sedimentary characteristics and model of seasonal deltaic sandstone: a case study on the continental red bed from the Cretaceous Baxigai Formation, Tarim Basin, NW China
Tong Wang, Yong Hu, Bin Li, Wenxiang He, Xiaoyang Gao, Luxing Dou and Jian Wang

81 Prediction of permeability in a tight sandstone reservoir using a gated network stacking model driven by data and physical models
Pengyu Shi, Pengda Shi, Kang Bie, Chuang Han, Xiaowei Ni, Zhiqiang Mao and Peiqiang Zhao

94 Clarifying the contribution of multiscale pores to physical properties of Chang 7 tight sandstones: insight from full-scale pore structure and fractal characteristics
Zhen Li, Yilin Ren, Rui Chang, Yuanli Zhang, Xuze Zhang and Weichao Tian

109 Research on the data-driven inter-well fracture channeling identification method for shale gas reservoirs
Feng He, Ming Yue, Yibo Zhou, Huaiying He, Wei Jiang, Long Liu, Chao Qian and Pinghua Shu

118 Characterization of reservoir quality in tight sandstones from the Benxi Formation, eastern Ordos Basin, China
Guoyong Li, Cong Li, Boming Zhang, Lei Zhang, Zhuang Liang and Qi Chen

137 Source and geological significance of Jurassic asphalt in the Ruoqiang Sag of Southeast Depression, Tarim Basin, Northwestern China
Xiaodong Lan, Zhongkai Bai, Youxing Yang, Zhenglong Jiang and Jile Zhang

153 Research on loss rules of oil and gas in preserved shale cores after open air exposure
Jinyou Zhang, Min Wang, Jinbu Li, Zhao Liu and Liang Xu

165 Quantitative characterization of the carbonate rock microstructure considering topological features: a case study from the Gaoshiti–Moxi block of the Sichuan Basin
Huaimin Dong, Bin Luo, Chenyue Dang, Shuang Xu, Feng Wang and Peng Chi

183 Key factors controlling the accumulation of oil reservoir in the Gaosheng area of Western Depression, Liaohe Basin, Northeastern China
Guangjie Zhao, Fujie Jiang, Qiang Zhang, Hong Pang, Xingzhou Liu and Di Chen

frontiers | Frontiers in Earth Science

TYPE Editorial
PUBLISHED 11 December 2024
DOI 10.3389/feart.2024.1530200

Check for updates

OPEN ACCESS

EDITED AND REVIEWED BY
Martyn Tranter,
Aarhus University, Denmark

*CORRESPONDENCE
Wenguang Wang,
wangwenguang.0@163.com,
wangwg@nepu.edu.cn

RECEIVED 18 November 2024
ACCEPTED 04 December 2024
PUBLISHED 11 December 2024

CITATION
Wang W, Wang X, Chen Y, Liu C and Zhang Y (2024) Editorial: Unconventional resources: provenance analysis, sediment transport, reservoir evaluation, geo-energy.
Front. Earth Sci. 12:1530200.
doi: 10.3389/feart.2024.1530200

COPYRIGHT
© 2024 Wang, Wang, Chen, Liu and Zhang. This is an open-access article distributed under the terms of the Creative Commons Attribution License (CC BY). The use, distribution or reproduction in other forums is permitted, provided the original author(s) and the copyright owner(s) are credited and that the original publication in this journal is cited, in accordance with accepted academic practice. No use, distribution or reproduction is permitted which does not comply with these terms.

Editorial: Unconventional resources: provenance analysis, sediment transport, reservoir evaluation, geo-energy

Wenguang Wang[1]*, Xixin Wang[2], Yongqiang Chen[3], Chao Liu[1] and Yihuai Zhang[4]

[1]Institute of Unconventional Oil & Gas, Northeast Petroleum University, Daqing, Heilongjiang, China, [2]Development Geology, Yangtze University, Wuhan, Hubei, China, [3]Energy RU/Permanent Carbon Locking Future Science Platform, CSIRO, Kensington, WA, Australia, [4]James Watt School of Engineering, University of Glasgow, Glasgow, United Kingdom

KEYWORDS

unconventional resource, provenance analysis, sediment transport, reservoir evaluation, geo-energy

Editorial on the Research Topic
Unconventional resources: provenance analysis, sediment transport, reservoir evaluation, geo-energy

With the progress of theoretical understanding, exploration, and development techniques, the community has made significant efforts in unconventional oil and gas resources. Global unconventional oil and gas production is proliferating, and its role in global energy supply is increasingly prominent. Given the rich unconventional oil and gas resources, it is necessary to conduct in-depth research on provenance analysis, sediment transport, reservoir evaluation, and geo-energy. This Research Topic aims to provide operational evaluation ideas for unconventional resource prediction through reservoir provenance analysis, sediment transport, reservoir evaluation, and geo-energy, and ultimately improve oil and gas exploration practice. This Research Topic contains 28 papers related to the provenance analysis, sediment transport, reservoir evaluation, and geo-energy of unconventional resources. These 28 papers are as follows:

The modelling of unconventional reservoirs is mainly aimed at reservoirs, which are originally tight reservoirs and generally have no profitable output and demand artificial stimulations. A large number of horizontal wells, branch wells, and other technologies are targeted at enhancing production. Wang et al. proposed a fracture-vuggy carbonate reservoir modeling method based on multiple geological information fusion. Different from the traditional method, the four kinds of reservoirs are characterized in a fusion model. More reservoir development factors, for example, fault factor, depth factor, and wells interpretation are taken into consideration. The model result is closer to the real data. Wang et al. proposed a fracture grading modeling method based on geological information fusion. This method utilizes fracture development control factors and seismic attribute information as constraints for fracture modeling to establish a discrete fracture network model. This approach enhances the accuracy of fracture prediction and provides a basis for the exploration of ultra-deep low-porosity sandstone reservoirs. Song et al. carried

out experiments including fluid inclusion tests, and C–O isotope tests, which revealed the densify mechanism of the Upper Paleozoic sandstone reservoirs in the Daniudi gas field, and divided the tight gas reservoirs into two types: self-sourced and near-source accumulations. The study provided a new understanding of the formation process of tight sandstone gas reservoirs and a reference for the exploration and development of the same type of gas reservoirs. Li et al. reveal that micropores (<7 nm) do not contribute to the storage and percolation but contribute significantly to contrasting specific surface area, that mesopores only contribute to total porosity but not to permeability. The macropores (>300 nm) contribute to both porosity and permeability, which demonstrate that the content and heterogeneity of macropores are key indicators for the quality of the Chang 7 tight sandstones.

Wu et al. studied the diagenetic alterations and distribution of high-quality reservoirs within deltaic distributary channel facies. A concept model about favorable lithofacies with high reservoir quality was proposed. This model revealed favorable lithofacies in deltaic sand bodies could form lithologic traps, which have important exploration and development value for lithologic hydrocarbon reservoirs.

Shi et al. proposed an improved stacked model with a gate network module to predict the permeability of tight sandstone reservoirs. The GNS model can automatically evaluate the impact of various logging parameters and significantly improve the prediction accuracy, which helps to enhance the reliability of tight reservoir evaluation parameters.

He et al. established a data-driven fracture propagation model and fracture channeling identification method, successfully explains the reason for cross-well fracture channeling, and its conclusion aligns with the actual monitoring results.

Shi et al. proposed a method to characterize the regional distribution of complex multi-layer migration pathways for oil and gas in the paleo-slope zone outside petroliferous basins' source kitchens. This study established a method creatively for determining the threshold for oil and gas migration along sandbodies and faults, and it improves the exploration efficiency of petroleum in areas with similar geological conditions like eastern basins in China.

Zhang et al. study the dynamic loss process and the molecular changes of hydrocarbons in preserved shale samples exposed in open air for different time, and reveal that there is a large amount of oil loss of about 42%–78% for samples with maturity %Ro between 1.01 and 1.53. The oil loss is mainly contributed by free oil, while adsorbed oil remains unchanged. NMR T1–T2 mapping can be an important method to estimate *in situ* fluid saturation without sample crushing.

Dong et al. employed nuclear magnetic resonance (NMR), X-ray micro-computed tomography (micro-CT), and mercury injection capillary pressure (MICP) to analyze the descriptive topological and geometric features of carbonate samples from the Gaoshiti-Moxi area of the Sichuan Basin, compared the corresponding experimental results, and developed a novel comprehensive characterization approach for its parameters, which is conducive to characterizing the pore structure of carbonate rock.

Zhao et al. characterized the source rocks and the structural evolution history is restored by using 2D-Move software. The characteristics of reservoirs and caps are clarified, and the controlling factors of reservoir formation are summarized. The sandstone reservoir has fracture and dissolution porosity, which provide storage space for oil accumulation. Faults and unconformities provide pathways for oil migration. The dense basalt is a good cap layer to preserve the reservoir. The research results are of great significance to guide future oil and gas exploration in the Liaohe Basin.

Li et al. revealed the main controlling factors of reservoir heterogeneity in the Jiaxian area through thin rock sections, scanning electron microscopy, high-pressure mercury intrusion, and conventional property analysis. The multi-stage metamorphic hydrocarbon expulsion process in coal seams enriched the organic-inorganic interactions in coal-bearing strata, adding some reservoir capacity.

Zhang et al. proposed a new method for dynamic monitoring of hydraulic fracturing of shale gas by borehole-to-surface Transient Electromagnetic Methods (BSTEM). By combining field-based shale gas fracturing monitoring models, the response patterns of the borehole-to-surface transient electromagnetic field under different fracturing stages are analyzed, which can guide importance for the application of borehole-to-surface transient electromagnetic methods in monitoring hydraulic fracturing of shale gas.

Wang et al. constructed a three-dimensional model using hydraulic fracturing software based on the discrete lattice theory and synthetic rock mass method. The effect of a relatively short cluster spacing (5 m or less) on fracture propagation behavior was investigated through a series of case studies, considering operational parameters (injection rate, the number of fractures) and reservoir parameters (reservoir Young's modulus, stress anisotropy, principal stress direction).

Wang et al. employed a well-seismic fusion method, incorporating RGB seismic attribute fusion technology, to classify and detail the sedimentary architecture of thin-layer beach-bar sand bodies in Niger's G oilfield. By integrating seismic attributes and well-logging data, it identifies the spatial distribution and connectivity of sand bodies, presenting a comprehensive architecture classification. These findings enhance the fine characterization of thin-layer beach-bar reservoirs, supporting efficient reservoir development and offering an important methodological reference for similar geological settings.

He et al. explored the necessity of switching from water injection to natural gas injection in the fault-controlled fracture-cavity reservoir in Shunbei. They studied the optimization of natural gas injection parameters and methods, analyzed the natural gas displacement mechanism, optimized well pattern layout and injection-production parameters, and constructed an evaluation system for natural gas injection. This improves reservoir development efficiency and oil production rate, reduces the risk of gas channeling, and provides technical support for oil and gas field development.

Li et al. based on a systematic study of the noble gas and stable isotope characteristics of normally-pressured shale gas samples, revealed the origin of noble gas from normally-pressured shale gas reservoirs and discussed the accumulation and expulsion mechanisms of normally-pressured shale gas in the tectonically complex margin of the southeastern Sichuan Basin. The result can provide insights into the enrichment mechanism of shale gas reservoirs and the prediction of shale gas production capacity in other structurally complex regions of the world.

Wang et al. analyzed the Carboniferous Dawuba and Cambrian Niutitang shales in the Upper Yangtze Platform, South China, revealing their paleoenvironmental conditions and gas potential. Dawuba shales formed in warm, arid, reducing conditions, while Niutitang shales experienced cooler, arid climates. Both have high gas generation

potential, with Dawuba featuring Type II2 kerogens and Niutitang Type I. Despite low gas content, promising exploration areas include the Qiannan Depression's Shangyuan and Zongdi regions.

Fu et al. investigated the influence of extensional strike-slip fault systems on hydrocarbon accumulation in the Bohai Bay Basin's Huanghekoudong and Miaoxi'nan sub-sags. Utilizing three-dimensional seismic data, new sequence stratigraphic frameworks, and advanced analysis techniques, they develop a model detailing how these systems shape sub-sag evolution and trap formation. This research enhances understanding of structural trapping dynamics, providing crucial insights for exploration strategies in similar geological settings globally.

Yuan et al. proposed a method for the identification of complex lithology of tight marl reservoir based on logging data. Lithological identification of 2D and 3D plots is established using sensitive GR, DEN, and RT. Corresponding identification standards are built in two hierarchies. The lithological characteristics of vertical, horizontal, and plane are discussed in the research area, which may aid in understanding the complex marl reservoir in the Leikoupo Formation 32 Submember of the Sichuan Basin, China.

Meng et al. found that the factors that influence the CO_2 injectivity are CO_2 injection rate, reservoir pressure, formation water saturation, and permeability, respectively. The oil recovery is mainly influenced by CO_2 injection rate and formation permeability, and the influences of reservoir pressure and water saturation on oil recovery are smaller. To improve the CO_2 injectivity, the threshold values for radial perforation and fracture half-length are 25 m and 50 m.

The different provenance controls the distribution of sedimentary facies in the vertical and lateral directions, which in turn controls the spatial distribution of the grain size and clastic composition. The study of provenance analysis and sediment transport can integrate tectonics, climate, provenance lithotypes, transport dynamics, and burial diagenesis, which can provide a comprehensive understanding of unconventional reservoirs. Wang et al. studied the seasonal deltaic deposits in the Cretaceous red bed of the Tarim Basin. As seasonal deltaic deposits were still not well studied in previous research, a concept depositional model about seasonal deltaic deposits was proposed in this research. This model revealed different types of distributary channels in Cretaceous arid paleoclimate, which have important value for both delta sedimentology and deltaic hydrocarbon reservoir exploration. Lan et al. used the Jurassic asphalt found in the QD1 well, combined with the source rocks of drilling cores and outcrops, and explored the possible hydrocarbon source and forming process in the Ruoqiang Sag using oil-source correlation and hydrocarbon accumulation geochronology methods. Peng et al. analyzed beach-bar reservoirs in Qinghai Lake, NW China, linked to unconventional hydrocarbon reservoirs. It highlights the influence of lake-level fluctuations, wind wave dynamics, sediment provenance, and terrain gradient on beach bar formation and morphology. Large-scale fluctuations set initial conditions, while small-scale ones refine features. Wind dynamics define depth zones, affecting morphology. Beach bars are categorized by sediment provenance: bedrock, alluvial fan, and braided river systems. Terrain gradients under 0.7° favor formation, aiding hydrocarbon exploration and sedimentary geology. Wang et al. spectral analysis and wavelet transform are used to study the high frequency Milankovitch sedimentary cycle in Fengcheng Formation. A high resolution astronomical age scale is established, and the 2-stage sedimentary cycle and 8-layer sweet spot are identified. Qi et al. take the Chang 6 lobate delta in the Wuliwan area of the Jing'an Oilfield in the Yishan Slope of the Ordos Basin as an example, this study sets parameters including sediment grain size, hydraulic conditions, and slope gradient similar to those underground to simulate the evolution of the shallow-water delta in the research area through flume experiments, dissect its internal configuration characteristics, establish a sedimentary model, and provide guidance for water flooding adjustments in the oilfield. Dong et al. based on the observation and description of drilling cores, carbon and oxygen isotope tests, inclusion analysis, logging data analysis, and seismic data interpretation, they depict the filling architecture, analyze the stages of collapse–filling, and discuss the differential evolution process and associated filling mechanism of typical paleounderground rivers.

Machine learning and artificial intelligence are of great value to the research of unconventional reservoirs. Wei et al. presented a hybrid feature selection method that integrates hyperspectral data with machine learning for precise estimation of dolomite content in carbonate rocks. This non-destructive approach improves the accuracy of field-based mineral identification and facilitates more detailed geological surveys, offering practical significance for oil resource assessment and exploration.

Author contributions

WW: Supervision, Validation, Visualization, Writing–original draft, Writing–review and editing. XW: Writing–original draft, Writing–review and editing. YC: Writing–original draft, Writing–review and editing. CL: Writing–original draft, Writing–review and editing. YZ: Writing–original draft, Writing–review and editing.

Funding

The author(s) declare that financial support was received for the research, authorship, and/or publication of this article. This study was co-funded by the National Natural Science Foundation of China (grant number: 42202144), the Innovative Research Groups of the National Natural Science Foundation of China (grant number: U19B2006), and the Natural Science Foundation of Shandong Province (grant number: ZR2022QD048).

Conflict of interest

The authors declare that the research was conducted in the absence of any commercial or financial relationships that could be construed as a potential conflict of interest.

Generative AI statement

The author(s) declare that no Generative AI was used in the creation of this manuscript.

Publisher's note

All claims expressed in this article are solely those of the authors and do not necessarily represent those of their affiliated organizations, or those of the publisher, the editors and the reviewers. Any product that may be evaluated in this article, or claim that may be made by its manufacturer, is not guaranteed or endorsed by the publisher.

frontiers | Frontiers in Earth Science

TYPE Methods
PUBLISHED 11 January 2024
DOI 10.3389/feart.2023.1351264

Check for updates

OPEN ACCESS

EDITED BY
Xixin Wang,
Yangtze University, China

REVIEWED BY
Nina Su,
China University of Petroleum (East China), China
Luxing Dou,
Yangtze University, China
Yin Yanshu,
Yangtze University, China

*CORRESPONDENCE
Jiaofeng She,
yujf_tlm@163.com

RECEIVED 06 December 2023
ACCEPTED 29 December 2023
PUBLISHED 11 January 2024

CITATION
Wang R, Tang Y, Yang F, She J, Li X, Chen N, Ji C and He Y (2024), A fracture modeling method for ultra-deep reservoirs based on geologic information fusion: an application to a low porosity sandstone reservoirs in X gas field of a basin in western China.
Front. Earth Sci. 11:1351264.
doi: 10.3389/feart.2023.1351264

COPYRIGHT
© 2024 Wang, Tang, Yang, She, Li, Chen, Ji and He. This is an open-access article distributed under the terms of the Creative Commons Attribution License (CC BY). The use, distribution or reproduction in other forums is permitted, provided the original author(s) and the copyright owner(s) are credited and that the original publication in this journal is cited, in accordance with accepted academic practice. No use, distribution or reproduction is permitted which does not comply with these terms.

A fracture modeling method for ultra-deep reservoirs based on geologic information fusion: an application to a low porosity sandstone reservoirs in X gas field of a basin in western China

Rujun Wang[1], Yongliang Tang[1], Fenglai Yang[1], Jiaofeng She[1]*, Xiaorui Li[1], Naidong Chen[1], Ce Ji[2,3] and Yingzheng He[2,3]

[1]Tarim Oilfield Company, PetroChina, Korla, China, [2]State Key Laboratory of Petroleum Resources and Prospecting, China University of Petroleum (Beijing), Beijing, China, [3]College of Geoscience, China University of Petroleum (Beijing), Beijing, China

The reservoirs of ultra-deep and low-permeability sandstones typically exhibit characteristics of lithological tightness and poor physical properties. Fractures control the oil and gas content as well as the productivity of such reservoirs. However, the distribution of fractures is complex, exhibiting strong heterogeneity. Therefore, a systematic study on reservoir fracture modeling can provide geological foundations for the development of such reservoirs. Due to the considerable burial depth of these reservoirs, conventional methods relying solely on seismic information have limited reliability, and the established discrete network models of fractures are often less dependable. In this paper, taking the X gas reservoir in a basin in western China as an example, we discuss a fracture modeling method based on the integration of geological information to enhance the efficiency and accuracy of fracture modeling. The modeling method primarily involves the use of deterministic methods to obtain large-scale fractures, while random simulation is employed for small and medium-scale fractures. The fracture development control factors and seismic attribute information are integrated using permanence of ratios (PR) model to establish a fracture development probability field model. Subsequently, the geometric parameters of fractures and the fracture density model are used as input parameters to generate a discrete network model of small and medium-scale fractures using a object-based modeling method. Finally, based on the fracture equivalent property model and verified through geological understanding, analysis of production dynamics, and numerical simulation of the gas reservoir, it is demonstrated that the fracture model established using the proposed method aligns with geological understanding and exhibits high reliability.

KEYWORDS

ultra-deep sandstone reservoirs, fracture modeling, seismic attribute, probability fusion, PR model

1 Introduction

With the maturity of deep exploration and development technologies and equipment, global oil and gas exploration and development has gradually entered the ultra-deep layer (Sun et al., 2013; Lei et al., 2021; Jia, 2023) (>6,000 m). China possesses abundant ultra-deep oil and gas resources, and in the past 20 years, large oil and gas reservoirs have been discovered in ultra-deep formations, such as the Changxing Formation in the Yuanba Gas Field in the Sichuan Basin, the Yanchang Formation in the Upper Triassic of the Ordos Basin, the Fuman-Shunbei Or-do-vician and the Kubuqi-Dabeikeleisu structural zone in the Tarim Basin (Guo et al., 2023; Chengzao et al., 2012; Qi and Li, 2014; Zhang et al., 2014). These sand-stone reservoirs, due to their high burial depth, experience strong compaction and cementation effects, resulting in poor matrix properties. However, compared with the fracture porosity, matrix porosity is still one to three orders of magnitude higher, making porosity the primary space for oil and gas accumulation and controlling steady production (Olson et al., 2009; Zeng and Xiang-Yang, 2009; Liu, 2010; Li et al., 2012; Liu et al., 2016; Li et al., 2017). Structural fractures serve as the main pathways for oil and gas migration, providing predominantly permeability (Wang et al., 2020a; Wang et al., 2020b; Wang et al., 2021; Wang et al., 2022a).

Fractures in low-permeability sandstone reservoirs are composed of fractures of different scales (Zeng et al., 2020; Lu et al., 2021). Fractures of different scales have different controlling effects on wells. Large-scale fractures typically extend in the range of hundreds of meters to kilometers in planar extent, and wells encountering large-scale fractures have high production capacity (Xue et al., 2014; Dong et al., 2020), but they often encounter water quickly. Medium and small-scale fractures, on the other hand, are typically within the range of hundreds of meters and can alter the permeability of the surrounding rock formations (Xue et al., 2014; Dong et al., 2020). Wells encountering these fractures have higher production capacity and experience more uniform water invasion along the fractures. Therefore, a fracture grading modeling approach is often used (Dong et al., 2020). However, due to the strong randomness and complex distribution patterns of fractures, it is challenging to establish fracture models that accurately represent the actual conditions. Currently, there are mainly two approaches for reservoir fracture modeling: the equivalent continuous model (Hennings et al., 2000; Huang et al., 2017) and the discrete fracture network model (DFN) (Wang and Hu, 2012; Dong et al., 2018; Yu et al., 2023). The equivalent continuous model divides the reservoir into a finite number of grids and assigns a certain average fracture attribute value to each grid (Lang and Guo, 2013). The DFN model uses discrete surface elements with specific directions, lengths, and areas to represent the distribution of fractures, and predicts fluid flow characteristics based on the geometric shape and conductivity of the fractures (Dershowitz and Wei, 2000). Compared to the equivalent continuous model, DFN can better capture the heterogeneity and multiscale nature of fractures. It also has the advantages of multi-disciplinary collaboration and utilization of multiple data sources. Therefore, DFN is currently the most widely used and rapidly developing model for fracture modeling (Shang et al., 2023). For multiscale fracture modeling, a combination of deterministic and stochastic modeling approaches is generally employed. Large-scale fractures can be determined through the interpretation of 3D seismic data and thus deterministic modeling methods can be used (Dershowitz and Wei, 2000; Hou et al., 2012; Liu et al., 2017). These methods have higher credibility. Medium and small-scale fractures, on the other hand, are often modeled using stochastic methods (Sun et al., 2019; Giuffrida et al., 2020; Wang et al., 2022b; Dan et al., 2022), with 3D seismic attributes used to constrain inter-well predictions. However, these models are of-ten limited by the accuracy of seismic data, and relying solely on them can lead to discrepancies between the models and the actual conditions, which hinders the efficient development of tight sandstone reservoirs (Ding et al., 2015; Gao et al., 2018; Lu et al., 2021).

This study takes the X gas reservoirs in a basin in western China as an example. The core samples and imaging data in the study area are relatively complete. On the basis of fully considering the controlling factors of fracture development, a fracture grading modeling approach is conducted by combining geological and seismic information. The large-scale fracture model is determined through deterministic modeling, while the medium and small-scale fracture model is developed using a probability fusion method based on the PR probability. The geological and seismic information are fully integrated to establish a fracture development probability field, which is used to constrain the construction of the discrete fracture network model. The aim of this study is to provide geological basis for the efficient development of this type of oil and gas reservoirs and to provide references for the fracture modeling of other ultra-deep low-permeability sandstone reservoirs.

2 Geological overview

The X gas reservoirs is located in a basin in western China and is a recently discovered trillion cubic meter-level giant gas field. The natural gas in the reservoirs mainly comes from coal-bearing formations and lacustrine mudstones in the Middle-Lower Jurassic and Middle-Upper Triassic strata. It has laid a solid resource foundation for China's "West-East Gas Transmission" project (Wang, 2014; Wang et al., 2018; Yang et al., 2021). The X gas reservoirs is a billion-cubic-meter-scale large natural gas reservoirs discovered under the guidance of salt-related structural modeling theory.

The X gas reservoirs was formed during the Mesozoic Yanshan movement and the Cenozoic Himalayan movement. It is a regional northeast-trending elongated anticline, with a near east-west thrust fault developed in the northern and southern parts (Figure 1). The stratigraphy encountered in the study area from top to bottom includes the Quaternary (Q) series, the Neogene Kuqa Formation (N_2k), the Kangcun Formation ($N_{1\text{-}2}k$), the Jidike Formation (N_1j), the Paleogene Suweiyi Formation ($E_{2\text{-}3}s$), the Kumugeli Formation ($E_{1\text{-}2}km$), the Cretaceous Baskichik Formation (K_1bs), and the Basai Formation (K_1bx). The target reservoirs is the Baskichik Formation, which is a red-brown fine sandstone and interbedded thin mudstone in a braided river delta-front depositional system (Gao et al., 2014; Lai et al., 2018; Wang et al., 2023). The cap rock is composed of gypsum and salt rocks of the Kumugeli Formation. Due to Late Cretaceous tectonic uplift and erosion, the baskichik Formation is unconformably overlain by the overlying strata and conformably

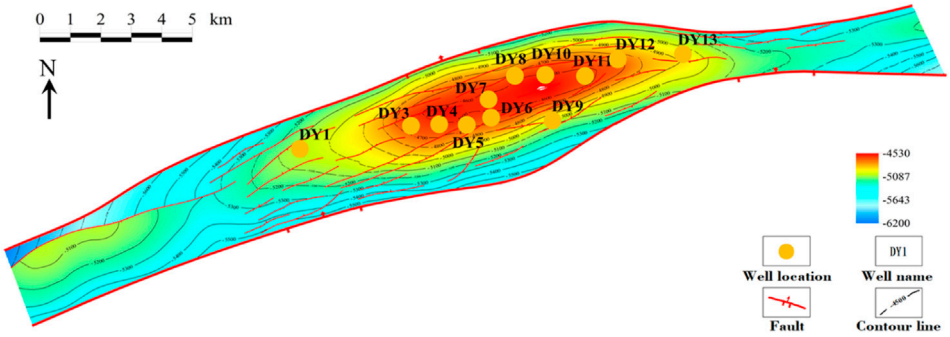

FIGURE 1
Structure map of Baskichik Formation in the study area.

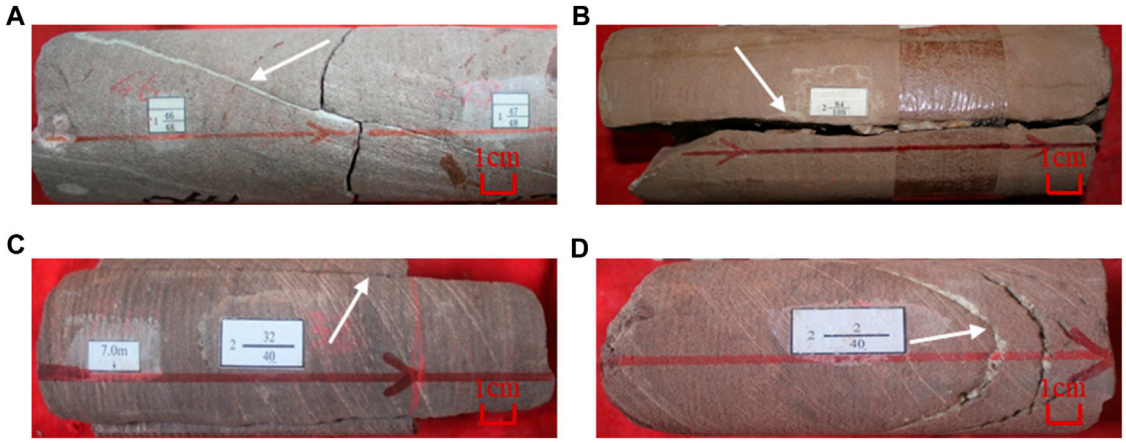

FIGURE 2
Structural fractures in the study area. **(A)** Filling structural fractures; **(B)** Filling structural fractures; **(C)** Unfilled structural fractures; **(D)** Filling structural fractures.

contacts the underlying Basai Formation (Deng et al., 2009; Wang et al., 2016). The measured matrix porosity of the target formation is an average of 5.4%, and the matrix permeability is an average of 0.055mD. Core observations and imaging logging interpretations show that structural fractures are highly developed in the study area (Figure 2). The well test permeability is much higher than the matrix permeability, indicating that the presence of fractures greatly improves the reservoir's fluid flow capacity and is an important controlling factor for high gas production.

3 Materials and methods

The development of reservoir fractures is complex and is controlled by multiple fac-tors such as sedimentation and tectonics (Sun et al., 2019; Giuffrida et al., 2020; Dan et al., 2022). In this study, we fully utilized core samples, thin sections, imaging well logs, and seismic data to investigate the controlling fac-tors of fracture development. Based on this, a fracture grading modeling approach was conducted, with deterministic modeling used for the large-scale fracture model and stochastic modeling used for the medium and small-scale fracture model. In the process of modeling the medium and small-scale fractures, a probability field of fracture development controlled by a single factor was first constructed. Then, a probability fusion method based on PR probability was used to establish a probability field of fracture development controlled by multiple factors. This was used to constrain the construction of the discrete fracture network model, providing guidance for subsequent well placement deployment.

4 Results

4.1 Control factors of fracture development

4.1.1 Different positions of anticline

Based on the interpretation of imaging well logs, the fracture parameters of wells at different locations in the anticline of the X gas reservoirs were statistically analyzed to analyze their spatial distribution characteristics. The results show that in conventional anticline-type oil and gas reservoirs, the core of

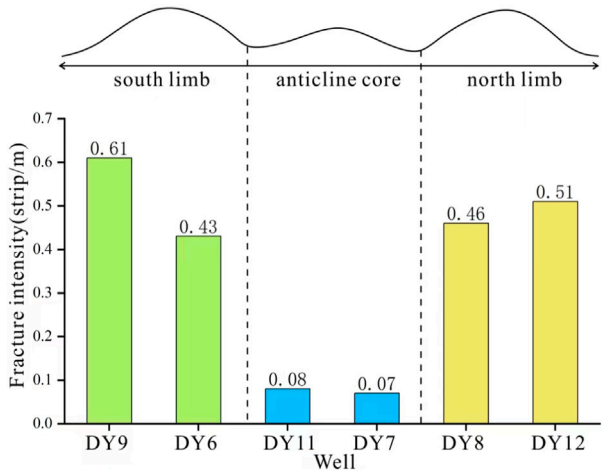

FIGURE 3
Fracture line density distribution map in different structural positions.

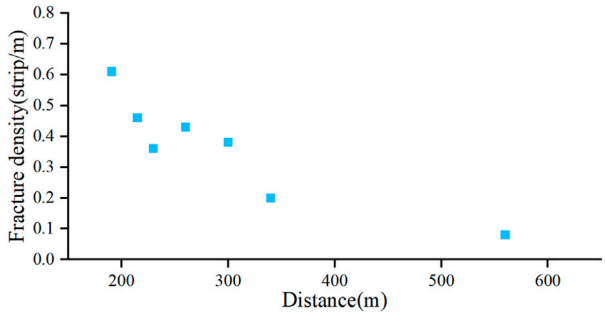

FIGURE 4
Fracture line density distribution map in different structural positions.

the anticline exhibits the strongest curvature deformation and the highest density of structural fractures. However, in the X gas reservoirs, the wells located in the flank of the anticline show a higher density of fracture development compared to those in the core of the anticline (Figure 3). This is due to the characteristic of low stress in the core and high stress in the flank of the X gas reservoirs, which is a result of its reverse thrust-style overthrust anticline structure.

4.1.2 To the fracture distance

The X gas reservoirs is characterized by the development of 23 major faults with a nearly east-west orientation. Based on the interpretation of core fractures and imaging well log fractures, the relationship between fault proximity and the degree of fracture development in adjacent wells was analyzed, and the distribution pattern was summarized. It was observed that as the distance from the fault increases, the line density of fractures gradually decreases (Figure 4), indicating that fault development is conducive to reservoir fracture development.

4.1.3 Lithofacies

Based on the analysis of core samples and laboratory data, different lithologies exhibit distinct micro-pore structure characteristics, resulting in variations in petrophysical parameters. Therefore, based on the lithology, petrophysical properties, and micro-pore structure characteristics of reservoir rocks, the distributary channel and sheet-like sand deposition microfacies were further classified into three lithofacies types: Type 1, Type 2, and Type 3 sandstone facies. The interdistributary bay mudstone was classified as the fourth lithofacies type. Type 1 lithofacies mainly occur in the middle of distributary channels, while Type 2 and Type 3 lithofacies are primarily found at the edges of the channels. Due to the limited core data, conventional well logging curves are used to determine lithofacies types. By analyzing the relationship between different lithofacies types and conventional well logging responses, a well logging-based lithofacies identification criteria (Table 1) is established and used for lithofacies classification at individual wells.

Based on the previous classification of different lithofacies types, the fracture line density of different lithofacies at each well point was analyzed, with emphasis on imaging well logging interpretation. The statistical results showed that the fracture line density was highest in the second lithofacies type, followed by the first and third lithofacies types, while the fourth lithofacies type exhibited the lowest fracture line density (Figure 5). This can be attributed to the fact that the second lithofacies type is mainly composed of fine sandstone, with high content of brittle minerals such as feldspar and quartz. As a result, the rock is more prone to fracture and release stress through brittle deformation, leading to increased fracture development. On the other hand, the fourth lithofacies is predominantly composed of mudstone. Under similar stress conditions, mudstone can absorb more stress, resulting in a lower degree of fracture development.

4.2 Large-scale fracture modeling

Large-scale fractures are interpreted directly from conventional 3D seismic data as faults using deterministic methods. The process involves initially interpreting the faults on seismic sections based on their seismic signatures and fault combinations. This enables the determination of parameters such as fault location and orientation. Subsequently, a deterministic modeling approach is employed to directly establish a discrete network model of large-scale fractures that matches the interpreted faults (Figure 6).

4.3 Small and medium scale fracture modeling

In this study, we employed seismic attributes and geological information that are sensitive to fracture information as the fundamental constraints for modeling small and medium-scale fractures. Based on the fracture identification results from imaging well logging, fracture development intervals were delineated, and the probability of fracture development was calculated for each well. The fracture development probability is defined as the ratio of the thickness of the fracture development

TABLE 1 Quantitative division standard of reservoir lithofacies of baskichik formation.

Lithofacies	Lithology	Sedimentary micro	Capillary curve type	Matrix Φ(%)	Matrix K(mD)	Logging response characteristics
First kind	medium sandstone	River channel, river flank	II,III	>7	>1	GR<60 DEN<2.55
Second kind	fine sandstone	River channel, river flank	II,III	7–4	1–0.5	60<GR<80 2.55<DEN<2.6
Third kind	Siltstone, muddy siltstone	River flank, sheet sand	III,IV	>4	0.5–0.035	60<GR<80 2.6<DEN
Fourth kind	mudstone	Interdistributary Bay				80<GR

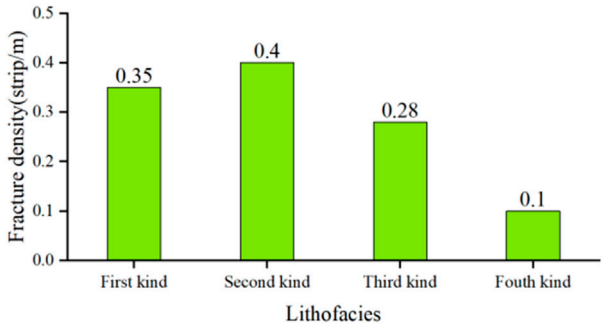

FIGURE 5
Relationship between fracture development density and fault distance.

interval to the thickness of the formation. A higher value indicates a more developed fracture system.

4.3.1 Seismic attribute fusion body

Due to limitations in the accuracy of seismic data acquisition technology, it is not possible to directly identify small to medium-scale fractures in seismic attributes. However, these attributes can provide information on the relative development of fractures, allowing for inter-well prediction. Seismic attributes extracted from post-stack seismic data can serve as important indicators for predicting fractures between wells. Through analysis of these extracted seismic attributes, it is observed that the maximum curvature and maximum likelihood attributes exhibit a good response to fracture development. Regions with high curvature and maximum likelihood values align well with the distribution of faults in the study area. Therefore, these two seismic attributes can be used as secondary data constraints for fracture modeling.

To facilitate the calculation of probabilities, the maximum curvature and maximum likelihood attributes undergo normalization. The formula Eq. 1 for normalization is as follows:

$$CD_i = \frac{D_i - D_{min}}{D_{max} - D_{min}} \quad (1)$$

In the formula, D_i is the attribute value of a grid node, D_i is the attribute maximum value of all grid nodes, D_{max} is the attribute maximum value of all grid nodes, D_{min} is the attribute minimum value of all grid nodes, CD_i value is between 0 and 1, the more developed the fracture, the greater the value.

The normalized seismic attribute fusion body can reflect the degree of fracture development. The larger the value is, the more developed the fracture is, but it cannot directly reflect the probability of fracture development. Therefore, according to the correlation analysis (Figure 7) between the fracture development probability and the seismic attributes of each well, the absolute value of the correlation coefficient between the seismic attributes and the fracture development probability is taken as the weight coefficient of each seismic attribute, and the calculation formula Eq. 2 of the seismic attribute fusion body is obtained by using the weighted average method as follows:

$$S_i = \frac{0.62 \times CCur_i + 0.51 \times CLik_i}{0.62 + 0.51} \quad (2)$$

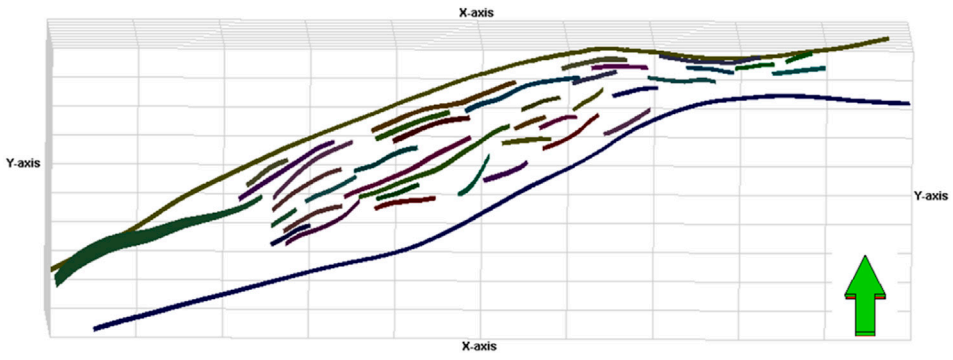

FIGURE 6
Large-scale fracture model of Baskichik Formation reservoir in the study area.

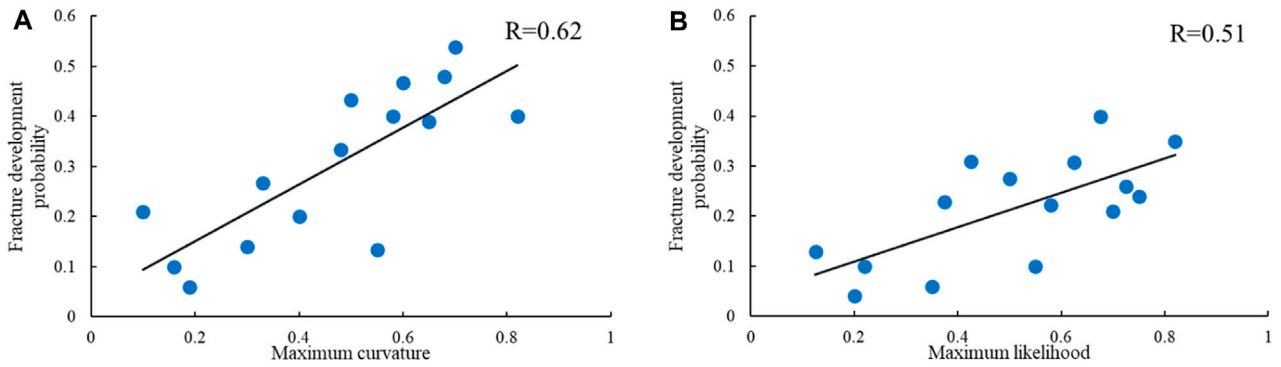

FIGURE 7
The correlation between fracture development probability and seismic attributes. **(A)** Correlation diagram of fracture development probability and maximum curvature attribute; **(B)** Correlation diagram of fracture development probability and maximum likelihood attribute.

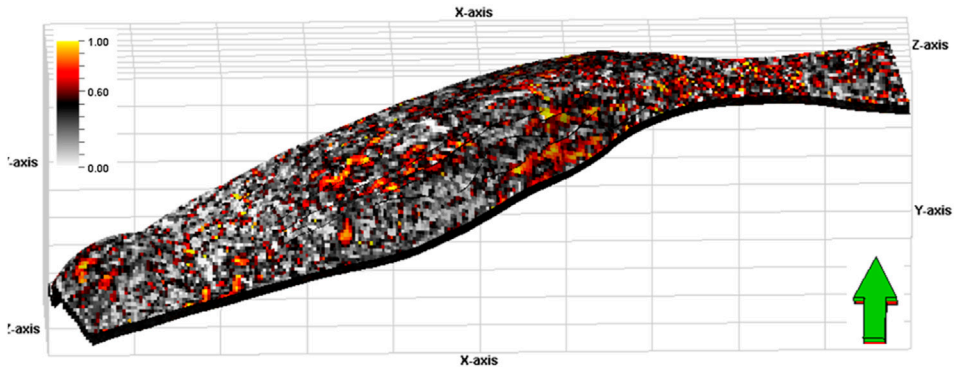

FIGURE 8
Maximum curvature and maximum likelihood seismic attribute fusion body.

In the formula, S_i is the normalized seismic fusion attribute of a grid node, and the value of S_i is between 0 and 1. The more developed the fracture is, the larger the value is. $CCur_i$ is the normalized curvature value of a grid node, and $CLike_i$ is the normalized likelihood value of a grid node.

Finally, using the formula, the seismic attributes are transformed into a seismic attribute fusion volume that controls the probability of fracture development. From Figure 8, it can be observed that the seismic attribute fusion volume highlights the regions where the fracture prediction results across different seismic attribute volumes are consistent. This enhances the visibility of the fracture development areas and improves prediction accuracy while reducing inter-well uncertainty.

4.3.2 Geological information attribute body

Due to the inherent uncertainty in seismic information, relying solely on seismic data for inter-well predictions often leads to discrepancies with actual production and development understanding. Therefore, in this study, we have introduced the aforementioned factors controlling fracture development as constraints to obtain more realistic fracture models. This will provide stronger evidence for subsequent oil and gas field development. Based on the structural position, distance to fault, and spatial distribution of lithofacies, corresponding attribute volumes were constructed, and these results were utilized as supplementary constraints in fracture modeling.

4.3.2.1 The probability distribution of fracture development controlled by fault distance

We conducted a statistical analysis on the relationship between the probability of fracture development in individual wells and the distance to the fault, and found that the probability of fracture development decreases exponentially as the distance to the fault increases (Figure 9A). Then, we used the formula Eq. 3 relating the probability of fracture development to the distance to the fault to calculate the probability distribution of fracture development controlled by fault distance (Figure 9B).

$$P\left(\frac{F}{Fd}\right) = 87.829x^{-0.971}, R^2 = 0.69 \quad (3)$$

4.3.2.2 The probability body of fracture development controlled by lithofacies

Through statistical analysis on the relationship between the probability of fracture development in a single well and lithofacies, for ease of calculation, the lithofacies types were

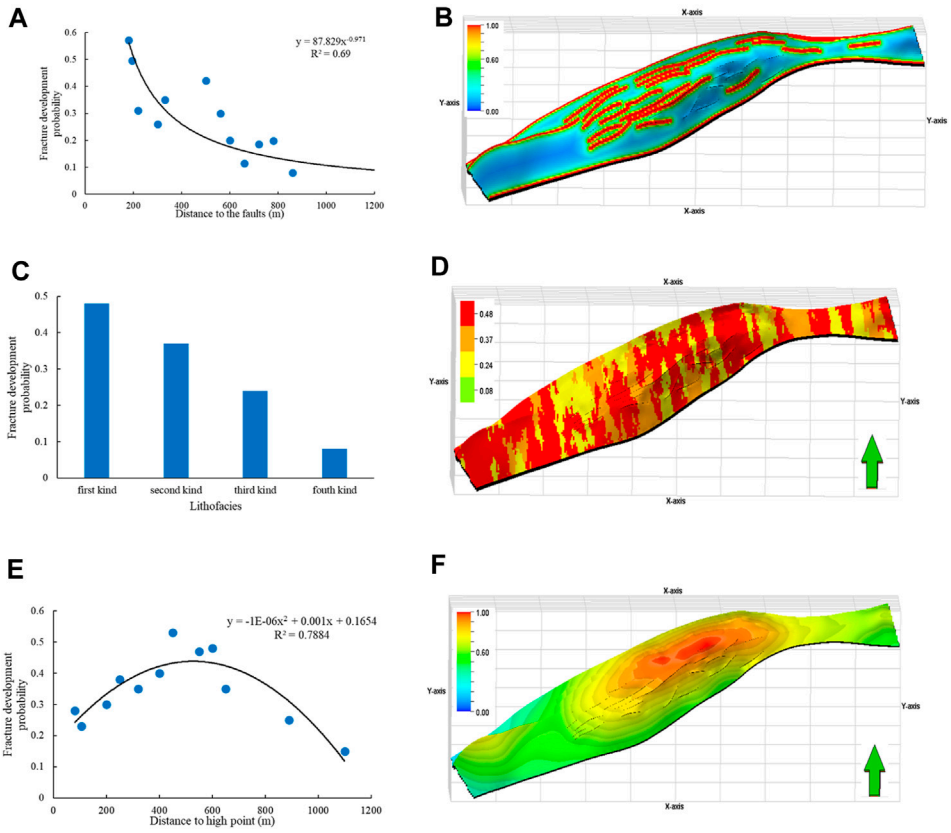

FIGURE 9
Fracture development probability body controlled by correlation analysis and geological information. **(A)** Distance from fault; **(B)** The distance from the fault controls the probability of fracture development;**(C)** lithofacies; **(D)** Lithofacies control fracture development probability body; **(E)** Structural position controls fracture development probability body; **(F)** Structural position controls fracture development probability body.

renamed according to the descending order of fracture development probability, and the average probability values for different types were taken (Figure 9C). Based on this, the probability body of fracture development conditions was calculated (Figure 9D).

4.3.2.3 The probability volume of fracture development condition in different positions of the anticline

Based on the statistical analysis of the relationship between the fracture development probability of a single well and the distance to the high point of the anticline, the relationship between the fracture development probability and the distance to the high point of the anticline is established(Figure 9E). Based on this formula, the fracture development condition probability body controlled by different positions of the anticline is calculated from the model of the distance to the high point of the anticline (Figure 9F).

4.3.3 PR multivariate probability fusion

The PR model refers to the constant updating ratio theory in engineering approximation learning, which assumes that "the ratio of probability updates does not change with the introduction of a variable." This assumption requires the variables to be in some form of independence and lack of correlation. This independence is neither complete nor conditional independence, but rather a weak assumption that approximates reality and minimizes the calculation error of the model. Journel provided a detailed derivation of the PR model (Jo and urnel, 2002) and demonstrated that the model satisfies all the theorems of probability theory. The computational formula (Eq. 4 and Eq. 5) for the PR model is as follows:

$$P(A|D_i, i = 1, \ldots, n) = \frac{1}{1+x} \tag{4}$$

Of which

$$x = \frac{\prod_{i=1}^{n} d_i}{\alpha^{n-1}} \geq 0, \alpha = \frac{1-P(A)}{P(A)}, d_i = \frac{1-P(A|D_i)}{P(A|D_i)}, i = 1, \ldots, n \tag{5}$$

In the formula, A represents the main variable (such as fracture development), D_i denotes the i-th secondary variable., n represents the number of secondary variables, P($A|\ D_i$) represents the conditional probability of the main variable (such as fracture development) when the secondary variable takes a certain value, and P(A) represents the main variable (such as fracture development) prior probability, P($A|D_i$,i=1,. . .,n) represents when all the secondary variables(i=1,. . .,n). The comprehensive conditional probability of the main variable (such as fracture development) when taking a set of fixed values.

Due to the multiple controlling factors of fracture development event (A), in this study, a seismic attribute fusion body (D1), distance to fault (D2), distance to the highest point of the anticline (D3), and lithology (D4) were selected as four factors to

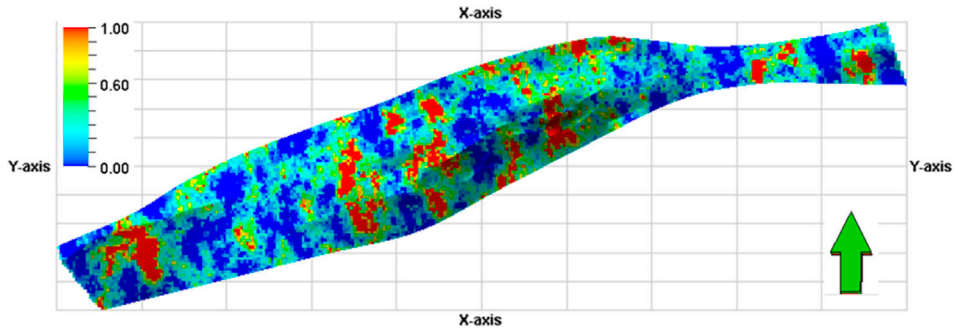

FIGURE 10
Medium and small scale fracture development probability body.

comprehensively evaluate the probability of fracture development in the study area. The probability of fracture development for each factor can be calculated individually, but when considering the interdependence of the four events, it becomes challenging to recombine these four conditional probabilities as P(A|D1, D2, D3, D4). The PR method satisfies the requirements of ensuring all limiting conditions, even in the presence of complex interdependencies among data. Therefore, this method is chosen to construct the comprehensive probability of fracture development.

The seismic attribute fusion volume, distance to faults, distance to the crest of the anticline, and lithofacies-controlled fracture development conditional probability volume were incorporated into the above formula to calculate the comprehensive fracture development conditional probability volume (Figure 10). The model reveals that high probability zones of fracture development are mainly distributed near faults or in certain lithofacies regions. This indicates that fracture development is primarily influenced by structural factors and lithology, which aligns with geological understanding and demonstrates the reliability of the fracture probability volume model.

4.3.4 Fracture density model

The establishment of a fracture density model is crucial in fracture modeling. Firstly, based on imaging well logs for fracture interpretation, individual well fracture density curves were plotted. Fracture density is defined as the number of fractures per unit formation thickness, and it has a strong positive correlation with fracture development probability. Higher fracture development probability corresponds to higher fracture density. Therefore, in this study, individual well fracture density curves were used as hard data for modeling, while a fracture probability volume model was utilized as soft data. The sequential Gaussian co-simulation method was employed to establish a fracture development density volume (Figure 11). The model reveals that areas with high fracture density are distributed near faults and the first type of lithofacies, which is consistent with geological expectations.

4.3.5 Fracture discrete network model

Based on the statistical data of the occurrence and orientation of small-scale fractures in the study area, parameters for modeling small-scale fractures were defined. The object-based marked point processes simulation was employed to generate fracture slices stochastically. At the same time, combined with annealing simulation, the fracture density model is taken as the objective function, so that the generated fracture slices meet the fracture density requirements in the model. Reasonable termination conditions can make the model closer to the real fracture network system. In this paper, the number of fractures in the study area is selected as the termination condition of the simulation. According to the fracture density of the geological understanding in the study area, the total number of fractures in the study area is calculated. When the number of fractures in the model reaches the calculated total for the study area, the simulation is terminated. Finally, a discrete network model of small and medium-sized fractures in the study area is established(Figure 12).

4.4 Fracture properties model

The fracture equivalent porosity of the grid node is equal to the ratio of the sum of the fracture volume in the grid to the grid volume. The formula Eq. 6 is as follows:

$$\phi_f = \frac{\sum A_{fi} \times \omega_{fi}}{V_{cell}} \times 100\% \quad (6)$$

In the formula, ϕ_f is the fracture equivalent porosity of the grid, %; A_{fi} is the fracture area in the grid, m^2; ω_{fi} is the fracture opening in the grid, m; V_{cell} is the mesh volume, m^3.

Based on the discrete fracture network model of X gas reservoirs, the equivalent porosity of each grid is calculated using a formula, which is coarsened into the matrix reservoir model to obtain the equivalent porosity model of the fractures (Figure 13A). The modeling results indicate that the fracture porosity value is around 0.06%.

Using the Oda method, the equivalent permeability of fractures in different directions for each grid was calculated. This equivalent permeability model was subsequently upscaled to the matrix reservoir model, yielding equivalent permeability models in the i, j, and k directions (Figures 13B–D). The model shows that the fracture permeability is mainly in the range of 10 mD to 100 mD, which is significantly higher than the matrix permeability. This indicates that fractures can greatly enhance the permeability of tight sandstone reservoirs. High-value areas with permeability greater than 75 mD were identified in the DY12, DY4, and DY5 well areas.

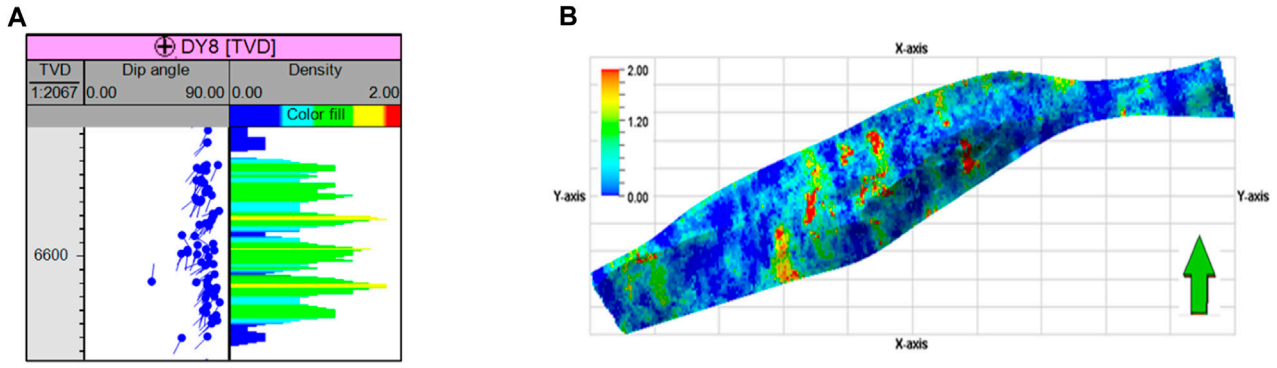

FIGURE 11
Medium and small scale fracture density model.**(A)** Imaging logging interpretation of fracture density curve; **(B)** Fracture density model.

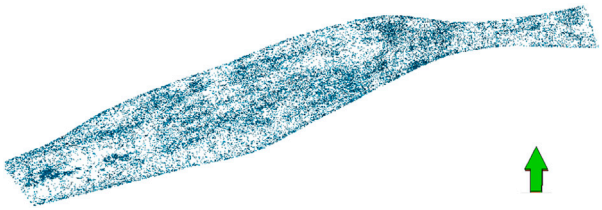

FIGURE 12
Fracture discrete network model of Baskichik Formation in the study area.

Through comparing with individual well productivity, a correlation between individual well productivity and fractures is discovered: under the assumption of similar reservoir thickness, wells with higher fracture density exhibit larger effective permeability around the wellbore, resulting in higher daily gas production. Conversely, wells with lower fracture density yield smaller daily gas production, indicating that fractures can enhance individual well productivity by controlling reservoir flow capacity.

4.5 Model verification

The effectiveness of the established fracture model was validated through three aspects, ensuring that it can accurately reflect the current geological understanding, align with production practices, and be used for numerical simulations and fitting.

(1) Geological understanding: The distribution of fractures in each layer and the total number of fractures in the model obtained by this modeling are in line with the existing geological understanding.
(2) Dynamic analysis: Based on the equivalent fracture property model, the DY12, DY4, and DY5 well areas were identified as high-permeability zones. By comparing them with the initial unrestricted flow rates, the unrestricted flow rate of DY12 well was 386.6×10^4 m^3/d, DY4 well was 195.4×10^4 m^3/d, and DY5 well was 171.7×10^4 m^3/d. These values indicate that the modeled fracture network corresponds well with the actual development and testing data, demonstrating a high level of model accuracy.
(3) Numerical simulation of the reservoir was conducted using the established fracture model as the underlying geological model. The historical fitting of daily gas and water production rates for the X reservoir is illustrated in Figure 14, showing a high level of accuracy with a conformity rate of over 90%. This indicates that the developed model of the basement fractures effectively captures the actual geological characteristics of the target reservoir.

5 Discussion

In low-permeability sandstone reservoirs, fractures have a direct impact on the productivity of oil and gas wells. Currently, fracture modeling typically combines deterministic and stochastic approaches. The construction of a small to medium-scale fracture development density model is a current and challenging research focus. Numerous scholars have conducted extensive work on predicting small to medium-scale fractures based on numerical simulation of structural stress fields, pre-stack and post-stack seismic information, and other methods. However, there are still several issues that warrant further consideration: (1) When predicting fractures in ultra-deep fracture-prone reservoirs, the resolution of seismic data is often low, leading to significant discrepancies between the constructed models and the actual fractures present; (2) The primary controlling factors for fracture development can vary across different regions. Therefore, the preferred conditions established by previous researchers may not necessarily be applicable until the main controlling factors for fractures are explicitly identified; (3) Fracture orientations can vary within the same region, making it challenging to integrate fracture density models and fracture orientation attribute information. As a result, the spatial distribution prediction of fracture geometry exhibits poor performance.

The future trend in fracture modeling involves the integration of multiple disciplines and methods. In-depth research can be conducted in the following areas: (1) Currently, multi-scale fracture modeling is commonly employed, and there exists a certain correlation between

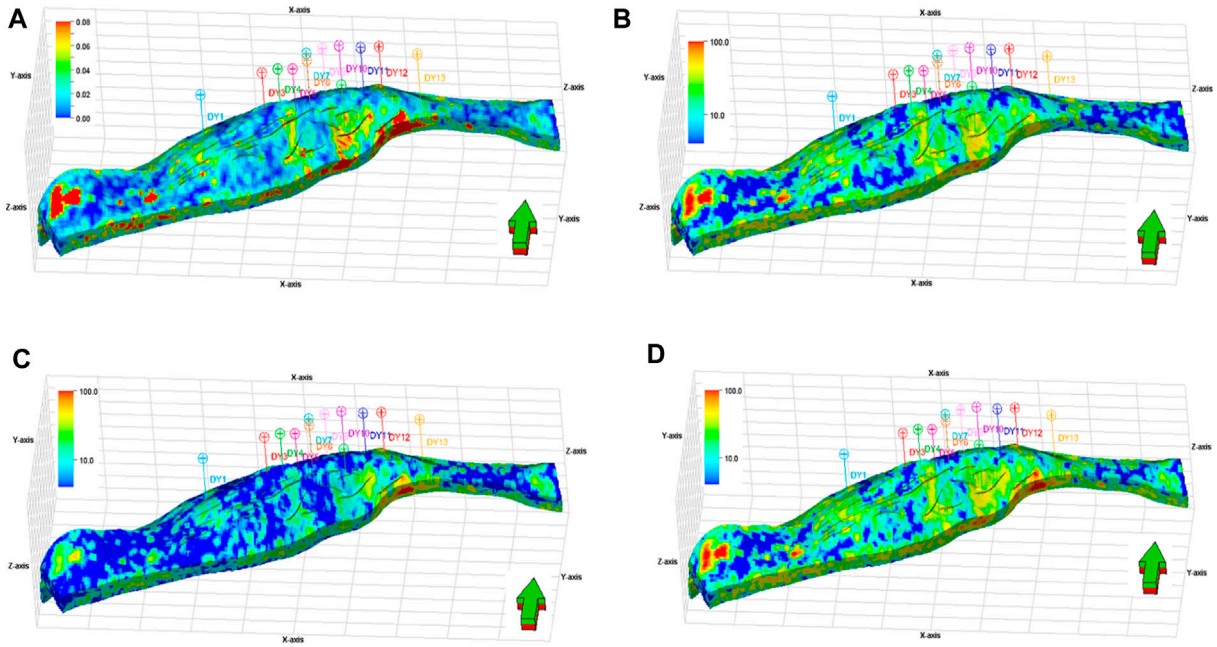

FIGURE 13
Fracture equivalent attribute model. **(A)** equivalent porosity model; **(B)** i direction equivalent permeability model; **(C)** j direction equivalent permeability model; **(D)** k direction equivalent permeability model.

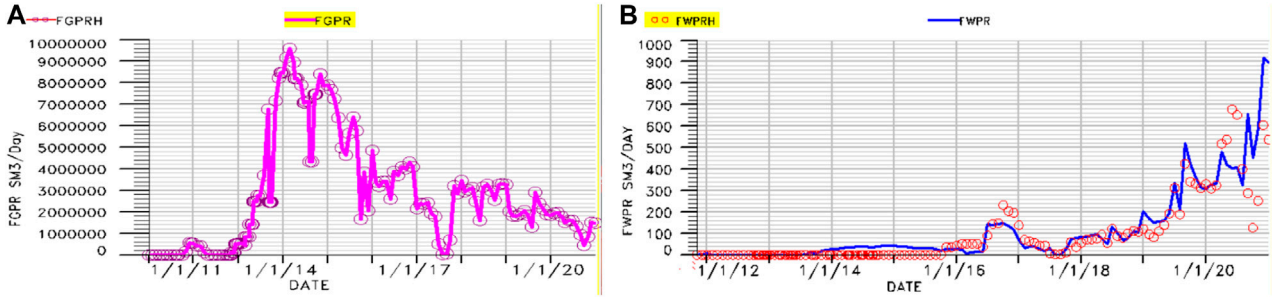

FIGURE 14
Actual production history matching diagram. **(A)** Nissan gas history matching diagram; **(B)** Daily water production history matching map.

fractures at different scales. It is important to establish a quantitative model that utilizes large-scale fractures as constraints for modeling small-scale fractures; (2) Strengthening physical simulation experiments can contribute to the study of fracture patterns in different rock types under varying stress conditions, providing guidance for modeling; (3) Multiple methods such as outcrop observations, seismic analysis, reservoir geomechanics, and far-field acoustic investigations can be used to study the three-dimensional distribution characteristics of fracture orientations. It is essential to establish a trend-constrained model for fracture orientations.

6 Conclusion

(1) Fractures in X gas reservoir are primarily controlled by structural position, distance to faults, and lithofacies. The highest fracture line density is observed in the crestal flank and near fault zones, whereas the fracture density is relatively lower in the crestal core region. Among lithofacies types, the second lithofacies exhibits the highest fracture development line density, followed by the first lithofacies.

(2) A fracture model for the X gas reservoir was established based on the integration of probability ranking (PR) and geological information, leading to a fracture modeling technique that incorporates multiple data sources, including core analysis, well logging, production dynamics, and seismic data. This integration enhances the accuracy and reliability of the constructed fracture model.

(3) At the core of this method is the construction of fracture development probabilities for different segments based on the development of fractures. By integrating these probabilities using PR analysis, a comprehensive fracture development

probability volume is established, thereby improving the accuracy of inter-well fracture development predictions.

(4) To assess the applicability of the discrete fracture model, three aspects were considered: geological understanding, dynamic characteristics of the reservoir production, and numerical simulations. The distribution of fractures was found to align with the current geological understanding. Analysis of the production dynamics of the reservoir indicated that wells with high initial unimpeded flow rates were predominantly located in areas with high values of equivalent permeability, which corresponds to real-world observations. The credibility of the discrete fracture model was further validated through numerical simulations, which yielded a comprehensive historical fitting of actual daily gas and water production rates.

Data availability statement

The original contributions presented in the study are included in the article/Supplementary Material, further inquiries can be directed to the corresponding author.

Author contributions

RW: Methodology, Writing–original draft, Data curation. YT: Methodology, Writing–review and editing. FY: Investigation, Writing–original draft. JS: Conceptualization, Writing–review and editing. XL: Formal Analysis, Writing–review and editing. NC: Investigation, Writing–original draft. CJ: Writing–review and editing. YH: Writing–original draft.

Funding

The author(s) declare financial support was received for the research, authorship, and/or publication of this article. This work was supported by National Natural Science Foundation of China (No. 42172154).

Conflict of interest

Authors RW, YT, FY, JS, XL, and NC were employed by PetroChina Tarim Oilfield Company.

The remaining authors declare that the research was conducted in the absence of any commercial or financial relationships that could be construed as a potential conflict of interest.

Publisher's note

All claims expressed in this article are solely those of the authors and do not necessarily represent those of their affiliated organizations, or those of the publisher, the editors and the reviewers. Any product that may be evaluated in this article, or claim that may be made by its manufacturer, is not guaranteed or endorsed by the publisher.

References

Chengzao, J., Zheng, M., and Zhang, Y. (2012). Unconventional hydrocarbon resources in China and the prospect of exploration and development. *Petroleum Explor. Dev.* 39 (2), 139–146. doi:10.1016/s1876-3804(12)60026-3

Dan, L., Shi, C., Wen, J., Wei, L., Zhang, X., and Zhang, J. (2022). Application of multi-information fusion modeling technology for fractures in dual-medium carbonate reservoir. *Petroleum Geol. Recovery Effic.* 29 (1), 46–52. doi:10.13673/j.cnki.cn37-1359/te.2022.01.006

Deng, H., Xin, Z., Hai, Y., Lei, G., and Ma, Y. (2009). Geological structure and its controls on giant oil and gas fields in Kuqa depression, Tarim Basin: a clue from new shot seismic data. *Geotect. Metallogenia* 33 (1), 19–32. doi:10.1016/S1874-8651(10)60080-4

Dershowitz, B. P. T., and Wei, L. (2000). Integration of discrete feature network methods with conventional simulator approaches. *Spe Reserv. Eval. Eng.* 3 (2), 165–170. doi:10.2118/62498-pa

Ding, W., Yin, S., Wang, X., Zhang, N., Zhang, M., and Cao, X. (2015). Assessment method and characterization of tight sandstone gas reservoir fractures. *Earth Sci. Front.* 22 (4), 173–187. doi:10.13745/j.esf.2015.04.019

Dong, S., Lyu, W., Xia, D., Wang, S., Du, X., Wang, T., et al. (2020). An approach to 3D geological modeling of multi-scaled fractures in tight sandstone reservoirs. *Oil Gas Geol.* 41 (3), 627–637.

Dong, S., Zeng, L., Xu, C., Cao, H., Wang, S., and Lu, W. (2018). Some progress in reservoir fracture stochastic modeling research. *Oil Geophys. Prospect.* 53 (3), 625–641. doi:10.13810/j.cnki.issn.1000-7210.2018.03.023

Gao, J., Zhou, L., Feng, Q., and Mu, Z. (2018). Progress in reservoir structural fracture characterization and prediction. *Geol. Sci. Techology Inf.* 37 (4), 158–166. doi:10.19509/j.cnki.dzkq.2018.0421

Gao, Z., Feng, J., Zhou, C., Cui, J., Li, X., Zhao, X., et al. (2014). Arid climate seasonal rivers deposition: a case of lower cretaceous in kuche river outcrop. *Acta Sedimentol. Sin.* 32 (6), 1060–1071.

Giuffrida, A., Fabrizio, A., Andrea, R., Elisa, P., Vincenco, L., Martin, E., et al. (2020). Fracture stratigraphy and DFN modelling of tight carbonates, the case study of the Lower Cretaceous carbonates exposed at the Monte Alpi (Basilicata, Italy). *Mar. Petroleum Geol.* 112, 104045. doi:10.1016/j.marpetgeo.2019.104045

Guo, D., Wang, Y., and Ke, G. (2023). Key technologies for sustainable production of ultra-deep high-sulfur bioherm gas reservoirs with bottom water in the Changxing Formation, Yuanba Gas Field. *Nat. Gas. Ind.* 43 (09), 93–101. doi:10.3787/j.issn.1000-0976.2023.09.009

Hennings, P., Olson, J., and Thompson, L. (2000). Combining outcrop data and three-dimensional structural models to characterize fractured reservoirs: an example from Wyoming. *AAPG Bull.* 84 (6), 830–849. doi:10.1306/a967340a-1738-11d7-8645000102c1865d

Hou, J., Ma, X., Liu, Y., and Zhao, B. (2012). Modelling of carbonate fracture-vuggy reservoir: A case study of Ordovician reservoir of 4th block in Tahe Oilfield. *Earth Sci. Front.* 19 (2), 59–66.

Huang, X., Li, Z., Zhou, G., Liu, Q., Li, H., and Wang, H. (2017). Fracture porosity modeling of fractured tight sandstone reservoir:a case study of the reservoir in Member 2 of Xujiahe Formation, Pingluoba structure, Sichuan Basin. *Acta Pet. Sin.* 38 (5), 570–577. doi:10.7623/syxb201705010

Jia, C. (2023). Key scientific and technological problems of petroleum exploration and development in deep and ultra-deep formation. *J. China Univ. Petroleum (Edition Nat. Sci.* 47 (05), 1–12. doi:10.3969/j.issn.1673-5005.2023.05.001

Journel, A. G. (2002). Combining knowledge from diverse sources: an alternative to traditional data independence hypotheses. *Math. Geol.* 34 (5), 573–596. doi:10.1023/a:1016047012594

Lai, J., Han, N., Jia, Y., Ji, Y., Wang, G., Pang, X., et al. (2018). Detailed description of the sedimentary reservoir of a braided delta based on well logs. *Geol. China* 45 (2), 304–318. doi:10.12029/gc20180207

Lang, X., and Guo, Z. (2013). Fractured reservoir modeling method based on discrete fracture network model. *Acta Sci. Nat. Univ. Pekin.* 49 (6), 964–972. doi:10.13209/j.0479-8023.2013.128

Lei, Q., Xu, Y., Yang, Z., Cai, B., Wang, X., Zhou, L., et al. (2021). Progress and development directions of stimulation techniques for ultra-deep oil and gas reservoirs. *Petroleum Explor. Dev.* 48 (1), 221–231. doi:10.1016/s1876-3804(21)60018-6

Liu, C., Zhang, R., Zhang, H., Wang, J., Mo, T., Wang, K., et al. (2017). Genesis and reservoir significance of multi-scale natural fractures in Kuqa foreland thrust belt,

Tarim Basin, NW China. *Petroleum Explor. Dev.* 44 (3), 495–504. doi:10.1016/s1876-3804(17)30057-5

Liu, J., Wu, M., Song, R., Huang, L., and Dai, X. (2017). Study on simulation method of multi-scale fractures in low permeability reservoirs. *J. Southwest Petroleum Univ. Sci. Technol. Ed.* 39 (4), 90–103. doi:10.11885/j.issn.1674-5086.2016.06.25.03

Liu, W., Zhou, X., Li, S., and Zhang, S. (2016). A case study of the third member of Shahejie Formation in Dongpu Depression. *Nat. Gas. Geosci.* 27 (11), 1993–2004. doi:10.11764/j.issn.1672-1926.2016.11.1993

Liu, X. (2010). Simulation of fracture parameters in the 3~(rd) sand unit of the Paleogene Fu-2 member in the Qiaohekou oilfield. *Oil Gas Geol.* 31 (2), 250–254. doi:10.1016/S1876-3804(11)60008-6

Li, Y., Li, J., Yang, R., Wang, Y., and Fan, A. (2012). Relationship between gas bearing capacity and reservoir fractures of tight sand reservoirs in the eastern block 2 of the Sulige Gas Field. *Nat. Gas. Ind.* 32 (6), 28–30.

Lu, W., Zeng, L., Chen, S., Lu, P., Dong, S., et al. (2021). Characterization methods of multi-scale natural fractures in tight and low-permeability sandstone reservoirs. *Geol. Rev.* 67 (2), 543–556. doi:10.16509/j.georeview.2021.02.020

Olson, J., Laubach, S., and Lander, R. (2009). Natural fracture characterization in tight gas sandstones: integrating mechanics and diagenesis. *AAPG Bull.* 93 (11), 1535–1549. doi:10.1306/08110909100

Qi, L., and Li, X. (2014). Exploration practice and prospects of giant carbonate field in the Lower Paleozoic of Tarim Basin. *Oil Gas Geol.* 35 (6), 771–779. doi:10.11743/ogg20140604

Shang, X., Duan, T., Bao, H., Long, S., and Li, D. (2023). A new model of natural fractures in shale gas reservoirs based on fracture facies characterization:A case study from the Jiaoshiba Block of the Fuling Shale Gas Field. *Nat. Gas. Ind.* 43 (6), 44–56. doi:10.3787/j.issn.1000-0976.2023.06.004

Sun, L., Zou, C., Zhu, R., Zhang, Y., Zhang, S., Zhang, B., et al. (2013). Formation, distribution and potential of deep hydrocarbon resources in China. *Petroleum Explor. Dev.* 40 (6), 687–695. doi:10.1016/s1876-3804(13)60093-2

Sun, S., Zhao, S., Hou, J., Zhou, Y., Song, S., and He, Y. (2019). Hierarchical modeling of multi-scale fractures in tight sandstones: a case study of the eighth member of the Yanchang formation in wellblock 92 of the Honghe oilfield. *Petroleum Sci. Bull.* 4 (01), 11–26. doi:10.3969/j.issn.2096-1693.2019.01.002

Wang, H., and Hu, G. (2012). Realization and optimization of discrete fracture network model of buried hill fractured reservoir in C oilfield,Bohai Bay. *Lithol. Reserv.* 24 (1), 74–79. doi:10.3969/j.issn.1673-8926.2012.01.014

Wang, K., Zhang, H., Zhang, R., Wang, J., Dai, J., and Yang, X. (2016). Characteristics and influencing factors of ultra-deep tight sandstone reservoir structural fracture: a case study of Keshen-2 gas field, Tarim Basin. *Acta Pet. Sin.* 37 (6), 715–727. doi:10.7623/syxb201606003

Wang, K., Zhang, R., Fang, X., Wang, J., and Zhang, T. (2018). Characteristics and property modeling of ultra-deep fractured-porous tight sandstone reservoir: a case study on the Keshen 8 gas reservoir in Kuqa depression. *China Pet. Explor.* 23 (06), 87–96. doi:10.3969/j.issn.1672-7703.2018.06.010

Wang, R., Wang, S., Xian, B., Zhu, S., Fan, Q., Shan, C., et al. (2023). Sedimentary microfacies and configuration of skeleton sand bodies in the third member of Bashijiqike Formation in northern Kuqa Depression n, Tarim Basin. *Nat. Gas. Geosci.* 34 (10), 1681–1695. doi:10.11764/j.issn.1672-1926.2023.07.001

Wang, X., Hou, J., Li, S., Dou, L., Song, S., Kang, Q., et al. (2020a). Insight into the nanoscale pore structure of organic-rich shales in the Bakken Formation, USA. *J. Petroleum Sci. Eng.* 191, 107182. doi:10.1016/j.petrol.2020.107182

Wang, X., Liu, Y., Hou, J., Li, S., Kang, Q., Sun, S., et al. (2020b). The relationship between synsedimentary fault activity and reservoir quality — a case study of the Ek1 formation in the Wang Guantun area, China. *Interpretation-a J. Subsurf. Charact.* 8 (3), SM15–SM24. doi:10.1190/int-2019-0131.1

Wang, X., Yu, S., Li, S., and Zhang, N. (2022b). Two parameter optimization methods of multi-point geostatistics. *J. Petroleum Sci. Eng.* 208, 109724. doi:10.1016/j.petrol.2021.109724

Wang, X., Zhang, F., Li, S., Dou, L., Liu, Y., Ren, X., et al. (2021). The architectural surfaces characteristics of sandy braided river reservoirs, case study in gudong oil field, China. *China. Geofluids*. 2021, 1–12. doi:10.1155/2021/8821711

Wang, X., Zhou, X., Li, S., Zhang, N., Ji, L., and Lu, H. (2022a). Mechanism study of hydrocarbon differential distribution controlled by the activity of growing faults in faulted basins: case study of Paleogene in the Wang guantun area, bohai bay basin, China. *Lithosphere* 2021, 7115985. doi:10.2113/2022/7115985

Wang, Z. (2014). Formation mechanism and enrichment regularities of kelasu subsalt deep large gas field in Kuqa depression,Tarim Basin. *Nat. Gas. Geosci.* 25 (2), 153–166. doi:10.11764/j.issn.1672-1926.2014.02.0153

Xue, Y., Xia, D., Su, Z., Wu, X., and Ji, S. (2014). Fracture modeling at different scales based on convergent multi-source information. *J. Southwest Petroleum Univ. Sci. Technol. Ed.* 36 (2), 57–63. doi:10.11885/j.issn.1674-5086.2012.08.30.11

Yang, H., Li, Y., Tang, Y., Lei, G., Zhou, P., Zhou, L., et al. (2021). Accumulation conditions, key exploration and development technologies for Keshen gas field in Tarim Basin. *Acta Pet. Sin.* 42 (3), 399–414. doi:10.7623/syxb202103012

Yu, C., Wen, R., Zhang, X., Pang, F., Zhao, X., Chen, Z., et al. (2023). Research on reservoir fracture identification and modeling in M oilfield. *Petrochem. Ind. Appl.* 42 (06), 87–92. doi:10.3969/j.issn.1673-5285.2023.06.020

Zengxiang-Yang, L. L. (2009). Fractures in sandstone reservoirs with ultra-low permeability: a case study of the upper triassic Yanchang Formation in the Ordos Basin, China. *Aapg Bull.* 93 (4), 461–477. doi:10.1306/09240808047

Zeng, L., Lyu, P., Qu, X., and Fan, J. (2020). Multi-scale fractures in tight sandstone reservoirs with low permeability and geological conditions of their development. *Oil Gas Geol.* 41 (3), 449–454. doi:10.11743/ogg20200301

Zhang, R., Yang, H., Wang, J., Shou, J., Zeng, Q., and Liu, Q. (2014). The formation mechanism and exploration significance of ultra-deep, low-porosity and tight sandstone reservoirs in Kuqa depression, Tarim Basin. *Acta Pet. Sin.* 35 (6), 1057–1069. doi:10.7623/syxb201406003

frontiers | Frontiers in Earth Science

TYPE Original Research
PUBLISHED 11 January 2024
DOI 10.3389/feart.2023.1345028

Check for updates

OPEN ACCESS

EDITED BY
Wenguang Wang,
Northeast Petroleum University, China

REVIEWED BY
Muming Wang,
University of Calgary, Canada
Yuping Wu,
Xi'an Shiyou University, China
Bo Liao,
China University of Petroleum (East China), China

*CORRESPONDENCE
Pengfei Xie,
xie.pengfei@ucalagry.ca

RECEIVED 27 November 2023
ACCEPTED 21 December 2023
PUBLISHED 11 January 2024

CITATION
Wang Y, Xie P, Zhang H, Liu Y and Yang A (2024), Fracture-vuggy carbonate reservoir characterization based on multiple geological information fusion.
Front. Earth Sci. 11:1345028.
doi: 10.3389/feart.2023.1345028

COPYRIGHT
© 2024 Wang, Xie, Zhang, Liu and Yang. This is an open-access article distributed under the terms of the Creative Commons Attribution License (CC BY). The use, distribution or reproduction in other forums is permitted, provided the original author(s) and the copyright owner(s) are credited and that the original publication in this journal is cited, in accordance with accepted academic practice. No use, distribution or reproduction is permitted which does not comply with these terms.

Fracture-vuggy carbonate reservoir characterization based on multiple geological information fusion

Yan Wang[1,2], Pengfei Xie[3,4]*, Huitao Zhang[1,2], Yuming Liu[4] and Aiying Yang[5]

[1]Key Laboratory of Enhanced Oil Recovery of Carbonate Fractured-vuggy Reservoir, Sinopec, Urumqi, Xinjiang, China, [2]Exploration and Development Research Institute of Northwest Oilfield Branch of Sinopec, Urumqi, China, [3]School of Geosciences, Yangtze University, Wuhan, China, [4]State Key Laboratory of Oil and Gas Resources and Exploration, China University of Petroleum, Beijing, China, [5]Research Institute of Exploration and Development, Petro China Huabei Oilfield Company, Renqiu, China

The complexity and strong heterogeneity of carbonate reservoirs with fracture-vuggy structures present significant challenges in reservoir characterization. To address these challenges, we propose a novel multi-element information fusion modeling approach. This approach is designed to integrate multiple methods and incorporate multi-probability fusion at various facies and scales, thereby bridging the gap between geological information and reservoir modeling. Our methodology involves four key steps. First, the statistics between frequency of karst and geological information are acquired, and we quantify the statistics to regression equations. Second, these regression equations are transferred to probability bodies. The probability bodies can be applied in modeling as a soft control. But just one single body can be input in modeling process. Third, multiple probability bodies are fused into a fusion probability body by a probability fusion algorithm, which can keep the potential information of probability bodies. Finally, we apply the probability body in modeling workflow. By this way, the fusion method bridges the gap between geological information and modeling. The model established through our proposed method showed a significant level of consistency with reservoir re-evaluation, achieving an impressive 90% degree of alignment. Furthermore, the history match analysis revealed a high correlation, indicating the model's reliability. The method effectively integrates various scales and types of geological information, offering an accurate approach to complex carbonate reservoir modeling.

KEYWORDS

carbonate reservoir, Fractured-vuggy reservoir, geological modeling, probability fusion, fracture

1 Introduction

Fracture-vuggy carbonate reservoirs, which account for a large proportion of oil and gas reserves, are important targets of oil and gas exploration and development. However, fracture-vuggy carbonate reservoirs have undergone a serious late-stage transformation, with various reservoir types and complex development laws. Among them, the main reservoir is the ancient karst fracture-vuggy system, which

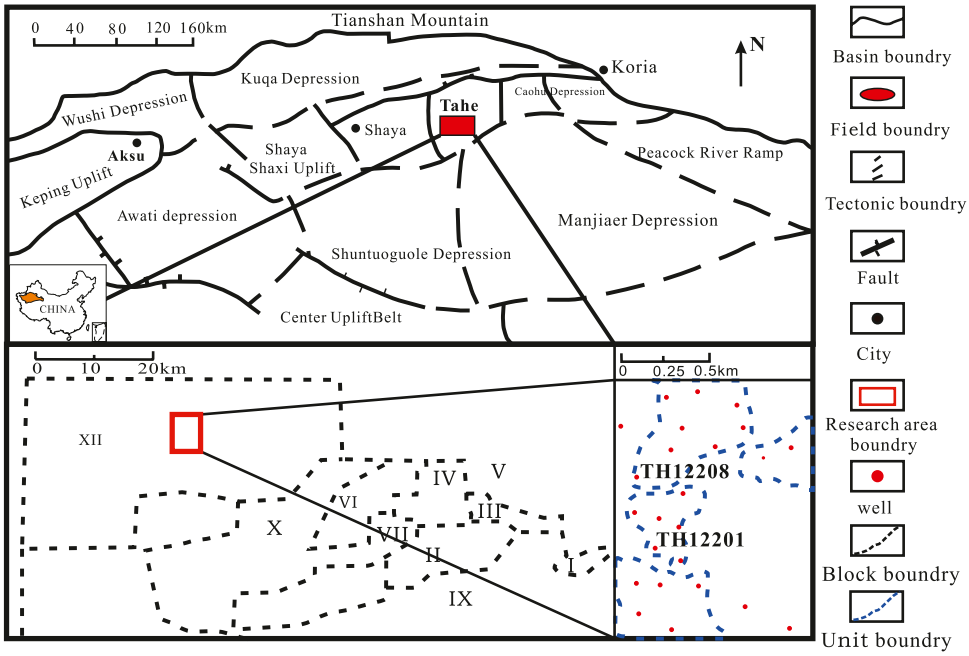

FIGURE 1
Geological location map of the study area.

is more difficult to characterize than pore-type and fracture-type carbonate reservoirs (Hou et al., 2012). Therefore, we have to improve the modeling method to combine with the geological knowledge in fracture-vuggy carbonate reservoir characterization (Yang et al., 2016; Li, 2013; Yang).

At present, a series of mature modeling ideas or methods have been proposed by researchers for fracture-vuggy carbonate reservoirs, which are hereby divided into three categories: deterministic modeling methods based on interpretation results (Zhang et al., 2020; Lu et al., 2021), stochastic modeling methods based on geostatistics (Xie et al., 2023), and modeling methods based on machine learning (Suihong et al., 2022). Among deterministic modeling methods, the seismic attribute-based geological body carving method is a commonly used fracture-vuggy characterization method. In geostatistical modeling methods, the sequential indicator simulation method, for example, expresses the correlation of two points in space through a variogram function, and interpolates the underground reservoir space. Multi-point geostatistics (MPS) randomly generates data events at unevaluated points by scanning the data events in training images (Deutsch, 2002; Mariethoz et al., 2010; He et al., 2014; Wang X. et al., 2022), which is capable of generating fracture-vuggy models. On this basis, geologists have added some constraints of geological and geophysical information, including constraints on the causes of formation of fractures and faults, and constraints on seismic attributes. In this way, the quality of the stochastic models has been greatly improved. The deep learning algorithm has also been applied to carbonate modeling thanks to the development of computer hardware and software. As the most advanced image generation algorithm, the generative adversarial network can learn from a large number of training images, and the trained network can reproduce the geological model and greatly accelerate the model generation speed (Xie et al., 2022). The above mentioned modeling methods still have limitations in practical application. Despite good modeling results achieved by advanced machine learning-based modeling methods, machine learning needs a large amount of training data (Song et al., 2021a), while fracture-vuggy carbonate reservoirs have few outcrops on the ground, so it is difficult to obtain a large amount of training data. Moreover, a lot of computing resources are needed in the training process, and suitable conditions are usually unavailable in practical work. In practice, the fracture-vuggy models are still established by combining deterministic modeling methods, the two-point statistics modeling method, and the MPS method. The existing information constraint methods can introduce geological prior knowledge into the modeling process, but the focus is always on the controlling effect of a single factor on a single reservoir, while reservoirs of the same type are generally related to various factors. For example, the development of karst caves is affected by faults, denudation surfaces, etc., accompanied by relatively stable seismic response characteristics. The single facies control or probabilistic volume can no longer meet the requirements of multi-information fusion.

With the Ordovician fracture-vuggy carbonate reservoir in Area 12 of Tahe Oilfield as an example, the geological situation of the study area was introduced in Section 2; the basic principle of the proposed method was presented in Section 3; in Section 4, the discrete models of different types of reservoirs in the study area were established based on their causes of formation by combining multiple modeling methods with the multi-information probabilistic volume fusion as the soft constraint on stochastic modeling, and then fused by conforming to geological and

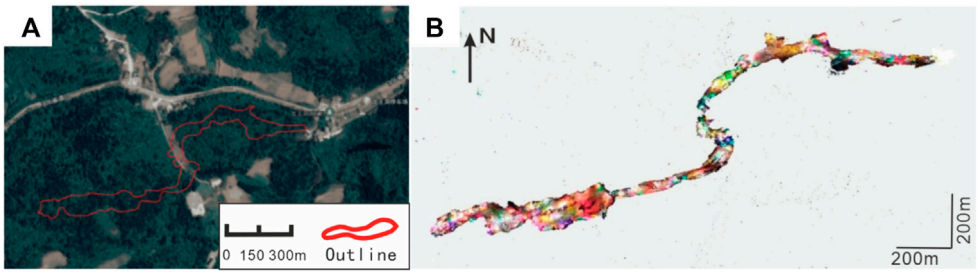

FIGURE 2
Modern underground river structure (Qinghua et al., 2019). **(A)** are the outline and location from the image. **(B)** is the laser scanning result.

statistical laws, thus establishing a refined geological model of this fracture-vuggy carbonate reservoir; In Section 5, the final model was subjected to oil reservoir model test.

2 Geological setting

Tahe Oilfield (Figure 1A), which is located in the south-central part of Akekule convex, Shaya uplift, Tarim Basin, adjoins Caohu depression in the east, Halahatang depression in the west, Mangar depression in the south, and Yakela-Luntai fault-convex in the north. The Ordovician carbonate formation in this oilfield is the main horizon with the development of paleokarsts and marine fracture-vuggy oil reservoirs (Zhang et al., 2004; Qiang and Fei, 2013; Liu YM. et al., 2018; Shang et al., 2020; Lu et al., 2021), being a rarely seen complex reservoir on a global scale. It has experienced multi-period tectonic movements and late karst reformation, resulting in uneven fracture-vuggy development and very strong heterogeneity. The main effective reservoir space is the ancient karst fracture-vuggy system (Qiang et al., 2015; Li et al., 2016; Liu Y. et al., 2018), which can be divided into three major classes of reservoirs according to the space size, morphology, and causes of formation, namely, underground rivers formed by fluctuating corrosion of groundwater systems (Yan-feng et al., 2021), fault-controlled karsts formed by corrosion along fault zones (Changcheng et al., 2016), and dissolution caves formed by weathering and leaching (Yang and Qiang, 2016). However, fractures contribute little to oil and gas accumulation and mainly act as seepage channels to transport oil and gas, and they can be divided into large-scale fractures, medium-scale fractures, and small-scale fractures according to their size. Among them, dissolution caves and small-scale fractures are strongly weathered and leached, which can be called weathered crust reservoirs. Underground rivers, fault-controlled karsts, and dissolution cave reservoirs store 95% of oil and gas production, thus being the focus of reservoir development.

This study area is the middle part of the Area 12 in Tahe Oilfield (Figure 1B), which is divided into four fracture-vuggy units, among which TH12208 and TH12201 are the main fracture-vuggy units (Figure 1C). There are a total of 24 development wells, including 22 vertical wells and 2 horizontal wells, with an accumulated oil production of 198×10^4 t. In addition, this area is rich in seismic data (dominant frequency: 28 Hz, sampling interval: 2 ms, group interval: 15 m) as well as well logging and drilling data, which lays a good foundation for modeling.

3 Multi-information fusion modeling method

The workflow of the multi-information fusion modeling method for fracture-vuggy carbonate reservoirs is described as follows: all the factors that affect reservoir development are considered and digitalized into probabilistic information, then multi-information is integrated by means of probabilistic fusion (Allard et al., 2012) as a constraint condition between wells in the modeling process, so that the established geological model conforms to geological information and geophysical information. According to the types and scales of reservoirs, discrete models of large-scale fractures, medium-scale fractures, underground rivers, fault-controlled karsts, dissolution caves, and small-scale fractures are established, among which dissolution caves and small-scale fractures constitute weathered crust reservoirs. Large-scale fractures are established deterministically by seismic fracture interpretation results, and medium-scale fractures are modeled deterministically based ant tracking and identification results. The underground rivers are subjected to geological body carving according to the seismic response characteristics and the geological mode of underground river outcrops. For fault-controlled karst reservoirs, faults control the developments of karsts, the control of karst by the distance from faults can be represented in a probability body. The seismic attributes indicate the distribution, we establish a probability body based on the seismic attribute. The outcrops show the geometry of the reservoir. This kind of reservoir can be modeling by object-based method to represent the geometry. The weak conditioning of object-based modeling method makes it difficult to meet the well data, and we apply it to establish a training image. Thus, the MPS method is used to combine the probability body and training image to generate the fault-controlled karst reservoirs. For dissolution caves, constraints between wells are applied according to the distance to the unconformity surface and seismic attributes, and a model is constructed through the sequential indicator method. Small-scale fractures are constrained according to the fracture development density (correlates with a seismic attribute), and simulated using the object-based method.

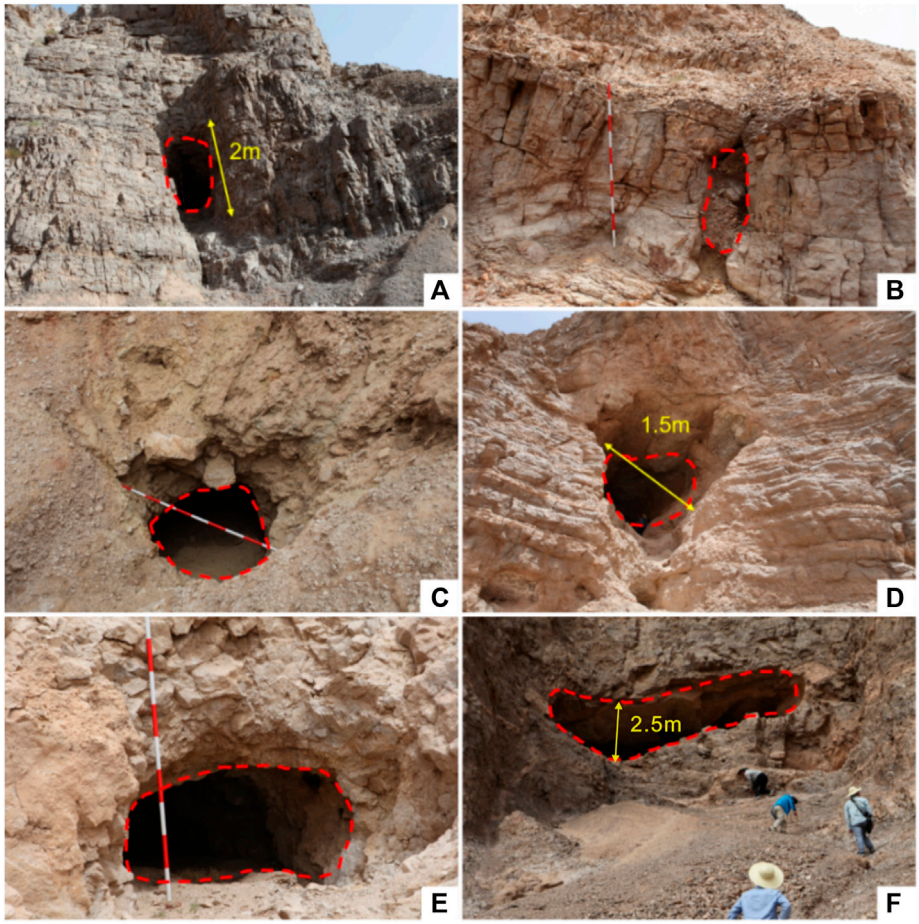

FIGURE 3
(A, B) are circular caves, **(C, D)** are rectangle caves and **(E, F)** are ellipse caves.

3.1 Large-medium fracture models

The fracture system in the study area is mainly controlled by the early Hercynian tectonic movement, along with the evident multi-level nature. Faults (large-scale fractures) constitute an important factor controlling the development of other reservoirs and also the first modeling step. Given the obvious controlling effect of the large-scale fracture on the medium-scale fracture, a large-scale fracture model was firstly established by following the principle of hierarchical modeling. Then, a medium-scale fracture model was established. Both of them were "discrete fracture network (DFN)" models, that is, the fracture distribution in the reservoir was characterized by a large number of discrete fracture pieces differing in the direction, length, shape, dip angle, and azimuth angle.

Large-scale fractures present strong seismic response and unique response laws, and reliable fracture interpretation results can be obtained through manual interpretation (Ma et al., 2014), while medium-scale fractures are controlled by large-scale fractures and have the system characteristics of large-scale fractures. The response characteristics of fractures are strengthened through coherent volume interpretation, and ant tracking technology is used to automatically identify fractures based on the attributes of seismic coherent volumes. The obtained ant body attributes can be matched, supplemented, and corrected according to the fracture system information of large-scale fractures, and the medium-scale fracture results can be acquired conforming to seismic data and geological cognition, so the discrete models of large-scale and medium-scale fractures are modeled by deterministic modeling methods.

3.2 Underground river reservoirs

An underground river system includes chamber caverns and main channel caverns, whose development, from the cause analysis, is controlled by multiple factors such as groundwater supply, fractures, water tables, and lithological differences (Popov et al., 2009; Fairchild, 2012; Li et al., 2020). Underground river karst caves show a unique development law, which is branched and banded on the plane, continuous or discontinuous, with an overall large scale, multi-layer or single-layer distribution on the cross section, and a complex structure, and filled with a large amount of collapsed breccia or

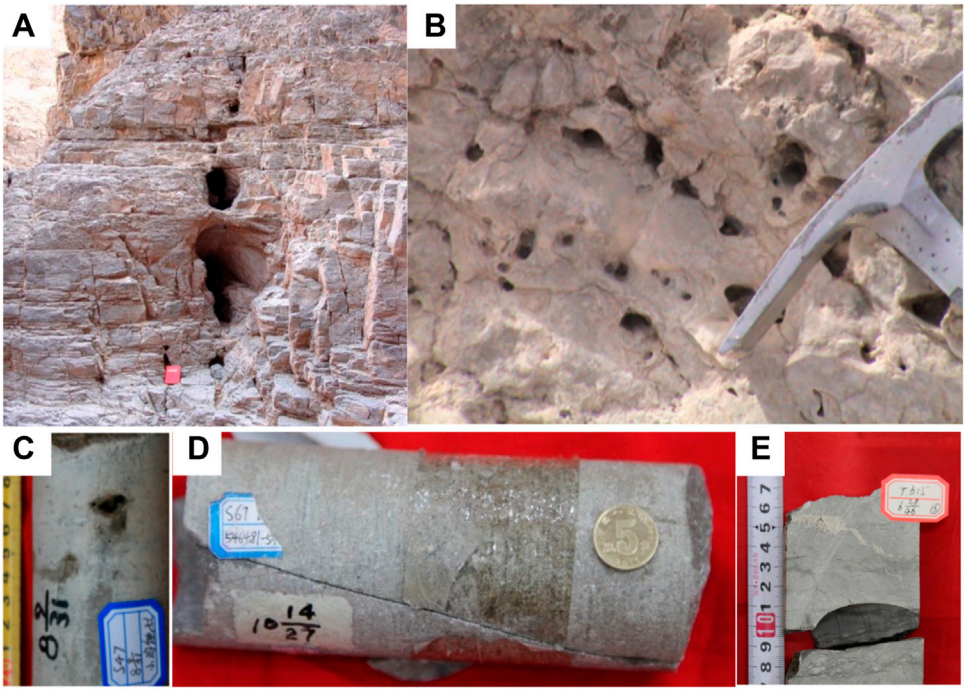

FIGURE 4
(A) shows that dissolved caves correlate the weather crusts horizon, **(B)** are small scale dissolved caves in a high dense, **(C, D and E)** are different caves in core.

sand mud. Due to the protection of cave walls, the fillings inside the caves are weakly mechanically compacted and remain good porosity (Qi and Lu, 2010), so they can be used as effective storage spaces. In the drilling process, emptying and leakage phenomena are common, the beaded seismic reflection characteristics, low resistivity, and extremely low density are manifested, and attenuation occurs frequently during imaging logging.

According to the laser scanning results (Figure 2B) of Longwang Cave (Figure 2A), Hunan Province, it is found that, different from the sand body overlapping and large-scale development of conventional rivers, underground rivers are isolated and developed on a small scale. Therefore, only a small number of wells have encountered underground river reservoirs during drilling in the study area, which leads to the scarcity of condition points, insufficient acquisition of cross-well rules, and it is difficult to obtain a convincing geological model by the stochastic modeling method. Despite the smaller scale of underground rivers than that of conventional river channels, underground rivers are different from the matrix and karst caves, and the resolution of their seismic data can meet the identification requirements. The main body of an underground river can be identified by seismic interpretation, and the identification results can be re-sampled into three-dimensional grids for deterministic modeling. Based on the principle of "well-seismic combination, geological constraint," human-machine interactive correction was performed considering the underground river characteristics exhibited by outcrops, and an underground river model was finally established.

3.3 Fault-controlled karst reservoirs

Fault-controlled karst reservoirs mostly develop near faults, which are formed by the vertical flow of surface water along faults. Different from underground river caves, they exist as isolated caves or cave groups in morphology, and their development is closely related to faults and fractures. On the whole, however, fault-controlled karsts are important effective reservoirs because of their strong development randomness, major changes in the scale difference, and a low filling degree. Moreover, their logging characteristics resemble those of underground rivers, but their seismic characteristics are different. Generally, the seismic characteristics of karsts extend on a small scale and exist in an isolated state.

From the cause analysis, the development of fault-controlled karst reservoirs is controlled by faults. The statistical fault-controlled karst caves in Bachu outcrop (Figure 3) can be divided into multiple types based on their morphologies, for example, circular, rectangle, ellipse, etc. The object-based modeling method is a stochastic simulation method applicable to target bodies with specific spatial forms and a modeling method suitable for fault-controlled karst reservoirs, but it fails to reflect the influence of faults on karst processes. The closer a fault-controlled karst is to the fault, the greater the karst development scale, and the higher the frequency, and different zones vary in frequency and scale constraint. Therefore, the training image was established through the multi-point geostatistics method and the object method, its spatial geometrical morphological characteristics were reserved, and the relationships of the cave height and development density of fault-controlled karsts with the distance to the fault were respectively determined. Then, multiple fault-controlled karst zones were

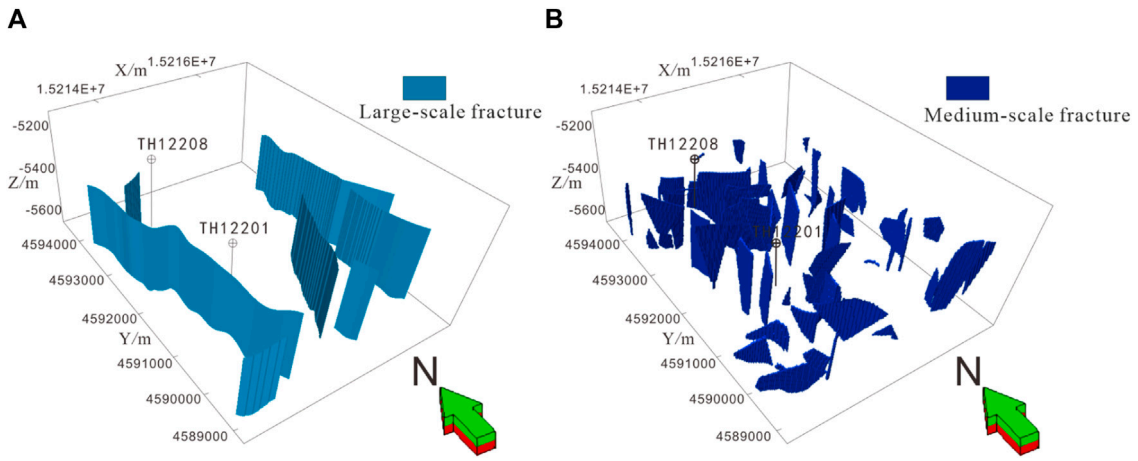

FIGURE 5
(A) is the large-scale fracture model of Area 12, **(B)** is the medium-scale fracture model of Area 12.

divided on the plane according to statistical laws. Next, different scales of fault-controlled karst training images were established based on different development scales of fault-controlled karsts in different zones. Moreover, the developmental probabilistic volume based on the distance to the fault was established in line with the relationship between the distance to the fault and the development frequency. Finally, the formation causes constraint was added to the multi-point statistical modeling process by combining multiple zones, multiple training images, and the probabilistic volume, thus realizing the modeling process constrained by double formation causes.

Among them, the probabilistic volume can not only integrate cause information but also other information. For example, fault-controlled karst reservoirs can also be characterized by geophysical information, and usually, fault-controlled karsts on a certain scale present "beaded" reflection characteristics as manifested in their seismic data (Xinbian et al., 2014; Shang et al., 2020). Hence, a good correlation is observed between seismic attributes and fault-controlled karst reservoirs. However, the modeling process can only be controlled by one probabilistic volume (such as Sneism (Mariethoz and Caers, 2014)and Simpat (Strebelle, 2002)), so it is necessary to fuse multiple probabilistic volumes through a fusion algorithm, so as to obtain the probabilistic volume of multi-information fusion and realize multi-information constraints.

For the probabilistic fusion method, the permanence of ratios (PR) model (Allard et al., 2012) is selected, which has weak preconditions, considering both the independence of different data sources and the redundancy of information. This model, which is improved from the conventional probabilistic multiplication method, has been widely used in the field of earth sciences. The PR model performs multiplication of multiple probabilities, with its formula as follows:

$$P\{C|F,S\} = \left((1-P\{C\})/(P\{C\})\right)/\left((1-P\{C\})/(P\{C\}) + (1-P\{C|F\})/(P\{C|F\}) \cdot (1-P\{C|S\})/(P\{C|S\})\right) \quad (1)$$

Where F is the distance to the fault, S represents the seismic attribute, C represents fault-controlled karst, $P\{C|F,S\}$ is the fusion probability of fault-controlled karst development under the multi-factor influence, $P\{C\}$ is the prior probability of fault-controlled karst development, $P\{C|S\}$ denotes the cave development probability under the condition of distance to the fault, and $P\{C|F\}$ stands for the cave development probability under the condition of the seismic attribute.

3.4 Weathered crust reservoirs

Weathered crusts are mainly stored in dissolution caves and small-scale cracks and formed mainly due to weathering and leaching actions. In the process of surface water flowing, undercutting channels, swallow holes, etc. are formed. When water flows into soluble karst, bedding dissolution pores, cracks, and so on (dissolution caves) are generated. High-angle dissolution fractures (small-scale fractures) develop at faults, tectonic fractures, and weathered fractures. From the aspect of logging, weathered crusts are characterized by slightly low density, increased acoustic time difference, and decreased gamma ray, and, from the perspective of imaging logging, they present the obvious characteristics of dark star points, which are often densely developed with large porosity and can be used as effective reservoirs.

According to the outcrop data, dissolution caves develop under the weathering front, and according to their development causes, they are irregular pores and caves formed by dissolution, so they are controlled by the weathering denudation surface. On the whole, the dissolution caves are widely distributed, and they are distributed in a plane shape under the unconformity surface (Figure 4A). Locally, such dissolution caves randomly develop in the reservoir space without fixed morphological characteristics (Figures 4B,C) and serve as good oil-bearing reservoir space and an important oil-gas migration channel. According to their characteristics of uniform random distribution and no fixed morphology, the dissolution caves are modeled using the sequential Gaussian method, which, however, is of uncertainties. By reference to the idea of fault-controlled karsts, therefore, the cause information and geophysical information were integrated into the probabilistic volume of reservoir development, specifically as follows: 1) The closer to the top weathered crust, the more obvious the weathering and dissolution, dissolution caves develop, the distance to the weathered crust and the development probability of

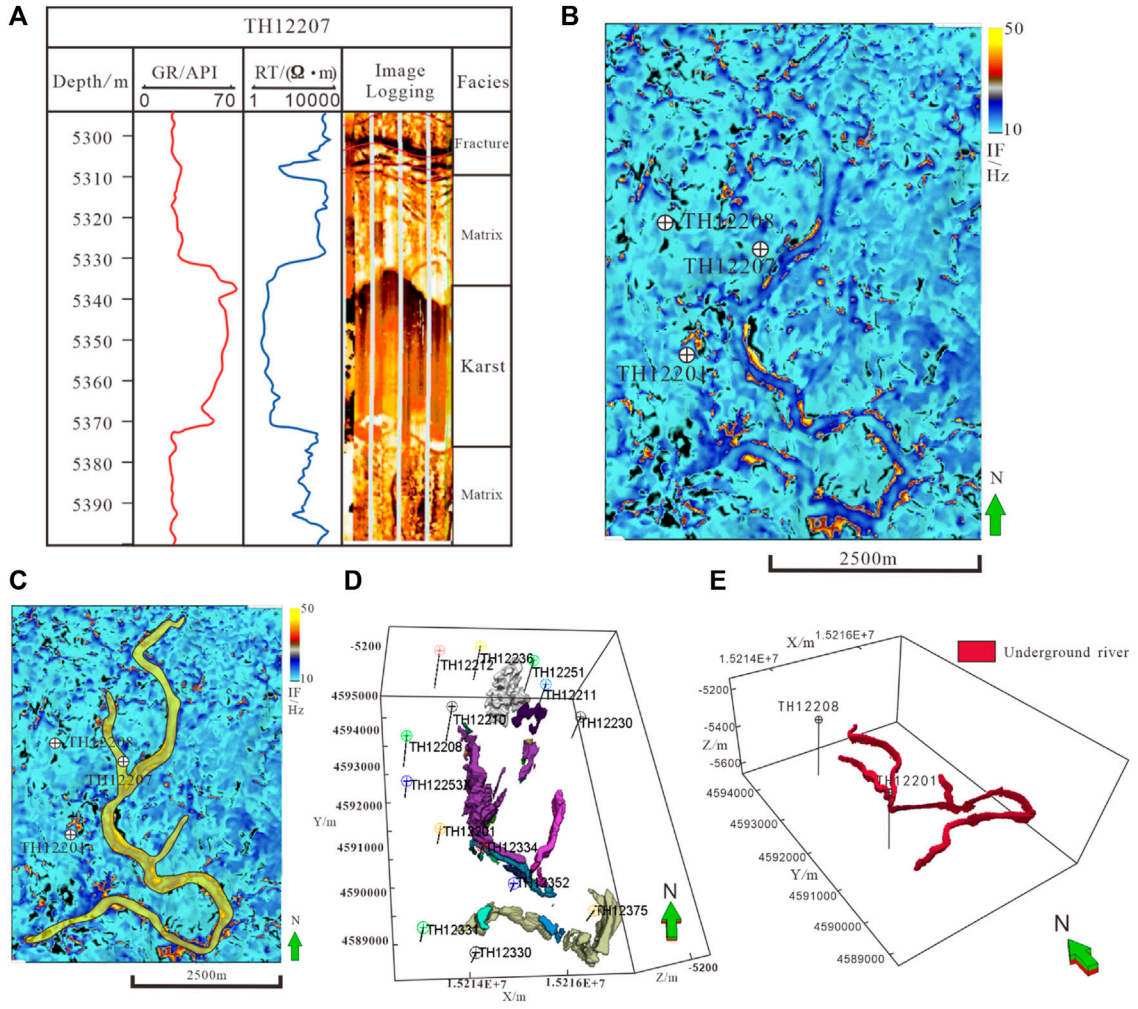

FIGURE 6
(A): the well log interpretation of Well TH12207. **(B)**: the IF attribute slice if Area 12. **(C)**: the boundry of IF attribute slice. **(D)**: the geobody is a prediction based on a cut-off value and the initial seismic attribute. **(E)**: a predicted model of underground river by manual revision.

dissolution caves are calculated, and a causes-controlled probabilistic volume is established; 2) the areas with dense development of dissolution pores and caves show event seismic attribute response characteristics, so seismic information is correlated with dissolution caves to some extent, and a probabilistic volume controlled by seismic information can be established. Here, the aforesaid PR probability fusion model was also adopted to finally obtain a probabilistic volume with multi-information fusion.

Small-scale fractures are composed of tectonic fractures and dissolution fractures. The original structural fractures (Figure 4D) are often corroded and enlarged to form dissolution fractures (Figure 4E) after being corroded by groundwater. In other words, affected by large-scale faults, the zoning and orientation of such fractures are controlled by the development characteristics of the original fractures. Moreover, they are randomly distributed in the whole reservoir, and can serve as channels connecting caves, with a small scale (usually 1–5 mm wide and 5–50 cm long) and extensive development. Since the resolution of seismic data interpretation is exceeded (main seismic frequency is 28 Hz), it is impossible to obtain deterministic results from seismic information, but sections with dense fracture distribution are apparently correlated with the coherent volume attribute. Therefore, the fracture characteristics, including the fracture type, dip angle, azimuth angle, fracture development density, and other parameters, were determined by rock core and logging data, and models were established using the object simulation method under coherent volume attribute constraints.

4 Modeling of different types of karst reservoirs

4.1 Large and medium-scale fracture modeling

Through artificial interpretation and identification of seismic data, there are 6 major faults in the study area, with a fault distance of about 5–30 m, a dip angle of about 80°, and an extension length of 500–3,000 m. The distribution model of a large-scale fracture (fault) was established by the deterministic modeling method (Figure 5A).

The information of fault formation systems (NE, NNW, and NS fault formation systems) could be obtained according to the interpretation results of large-scale fractures. Then, the artificially

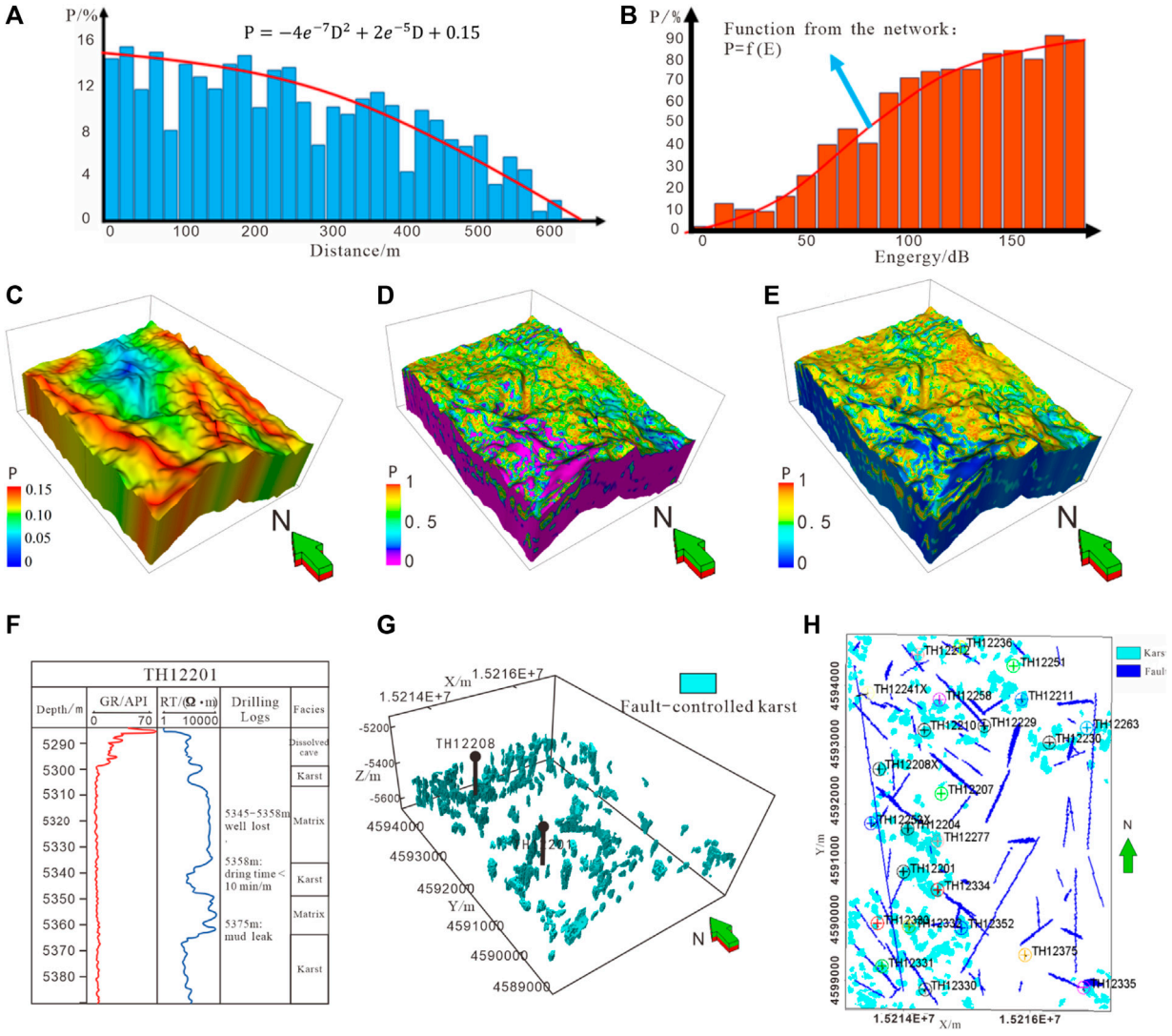

FIGURE 7
(A, B) represent the correlation analysis of developed probability-distance from fault and developed probability-energy seismic attribute. **(C, D)** are probability model from the correlation of fig 7A and 7B. The **(E)** is a fused model of fig 7C and 7D. The **(F)** is a interpretation result of fault-controlled karst in Well TH12201, based on this result, the karst model is simulated by geostatistical modeling method. the top-view map is shown as **(H)**.

interpreted earthquake faults were supplemented and corrected using automatically extracted fracture information by means of man-machine interaction, and 36 medium-scale fractures were automatically picked up by ant bodies in the study area. Finally, a deterministic discrete distribution model of medium-scale fractures was established according to the interpretation results of ant bod (Figure 5B).

4.2 Modeling of underground river reservoirs

According to the logging data of TH12207 well (Figure 6A), the target section exhibits the obvious characteristics of underground rivers, which present a high gamma (GR) value that changes suddenly and a low resistivity (RT) value in logging, indicating serious mud filling. Moreover, evident attenuation is observed through imaging logging. Based on the correlation analysis between the plane seismic attributes and the well logging interpretation results, the correlation between the instantaneous earthquake frequency is considered high. Therefore, the instantaneous earthquake frequency attribute (Figure 6B) of the river channel was tracked starting from the underground river encountered during TH12207 well drilling, so as to obtain the plane distribution pattern of this river channel (Figure 6C). Next, a 3D prediction model of the underground river (Figure 6D) was depicted through the Geobody seismic carving method in Petrel software on basis of the wave impedance attribute. The channel distribution characteristics of the predicted underground river were clear and coincided with the characteristics of the underground river reflected by outcrop data as a whole. Furthermore, the underground river structure was corrected with the mode dependence on outcrop characteristics (Figure 2).

Figure 6E shows the distribution model of underground rivers in TH12208 and TH12201 fracture-vuggy units after manual revision. The results show that the underground river develops from north to

10.3389/feart.2023.1345028

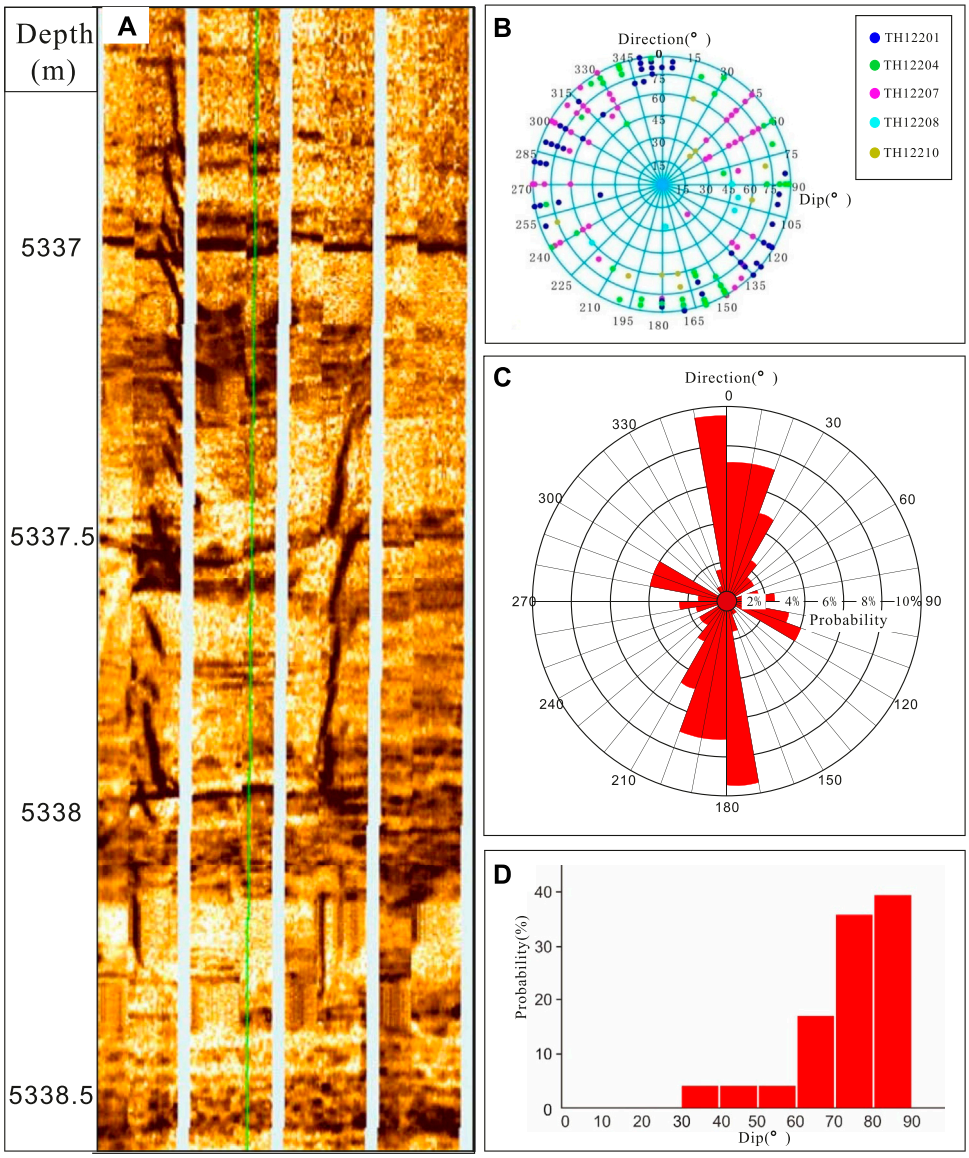

FIGURE 8
Small-scale fractures occurrence and density statistics. **(A)** is an example of image logging. Based on logging data, the statistics of fractures direction distribution and density are acquired in **(B, C, D)**.

south, with a total length of about 10 km. Two small underground river branches with an average thickness of about 30 m develop on both sides of the main underground river. Besides, the underground river is high in the south and low in the middle.

4.3 Modeling of fault-controlled karst reservoirs

According to the logging information and drilling leakage information, fault-controlled karsts can be identified, with a height of 2–16 m and a length and width of 2–10 m. Based on the outcrop shape, the target body was established, and three zones were established according to the distance to the fault and the frequency range of karst development: 0–80 m from the fault, 80–250 m from the fault, and more than 250 m from the fault. Next, three training images were stablished through the object method to characterize the scale and frequency of different karst bodies. Afterward, and formation cause mechanism of faults was integrated into the training images so that the modeling process could be simulated synchronously in different zones.

The corresponding training images were used for multi-point geostatistical simulation in different zones. However, the three training images could not reflect the gradual relationship between karst development and faults, earthquake constraint and fault distance constraint were required. The fault distance constraint was input in the form of probabilistic volumes. Among 26 karst reservoirs identified through well logging, those within 400 m range from the fault accounted for over 70%, while a few karst reservoirs were distant from the fault. Accordingly, the relationship between fault-controlled karsts and the distance to the fault could be acquired. Then, based on this, the probability formula between

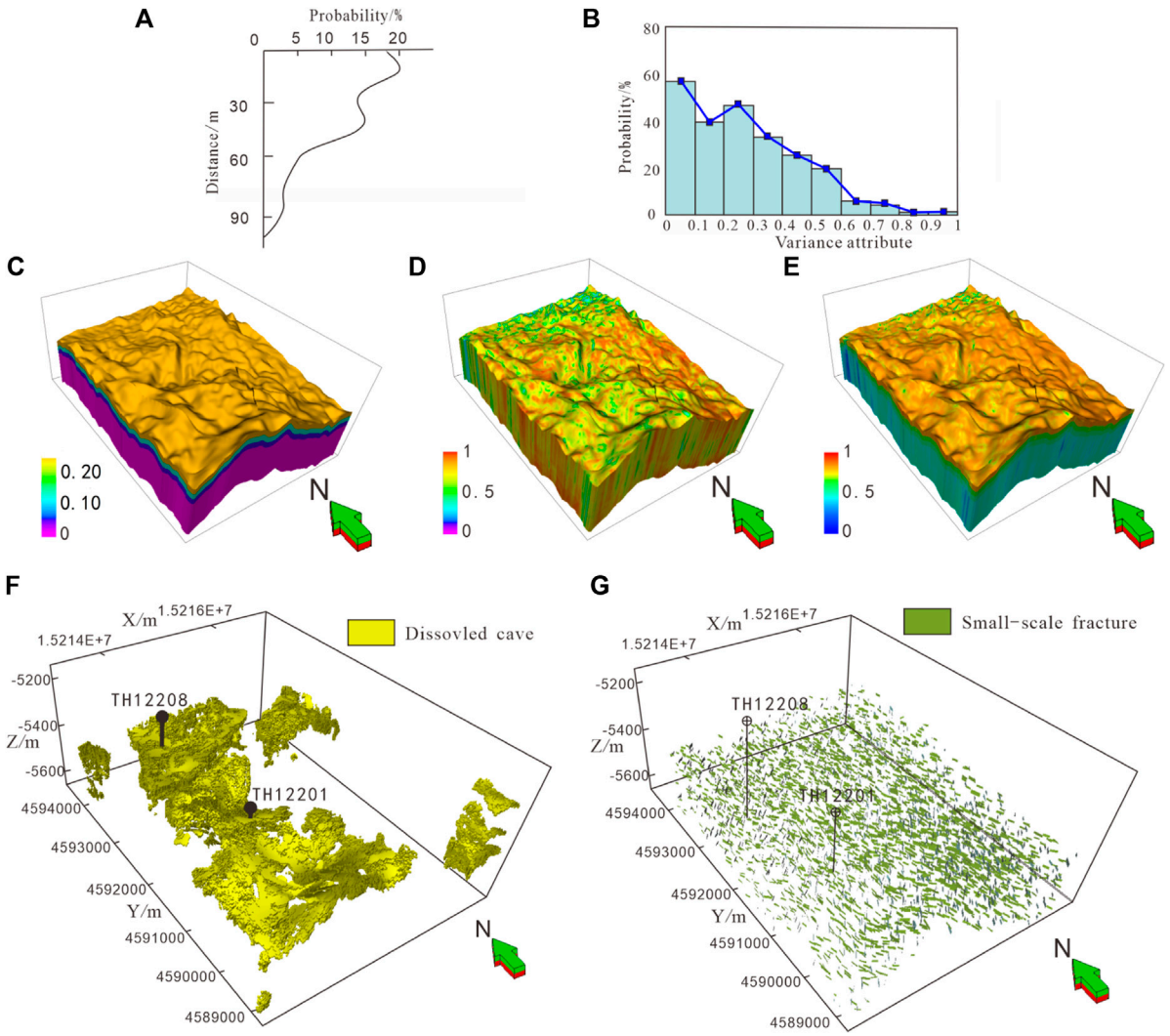

FIGURE 9
(A, B) are correlations of dissolved fracture probability-distance from the crust horizon and dissolved fracture probability-variance attribute, The probability model **(C, D)** are generated base on **A, B**. The figure 9C is a fused probability model by PR model. The **(F)** is a dissolved cave and **(G)** is a small-scale fracture model.

karst caves and the distance to the fault was solved (Figure 6A), and the probabilistic volume of karst development controlled by the corresponding fault was established (Figure 7A). The specific process of earthquake constraint was described as follows: after time-depth conversion of seismic data, the above-ground karst and seismic attributes were determined based on the drilling leakage results and the corresponding seismic attributes. The results show that the seismic spectrum energy in seismic attributes is favorably correlated with fault-controlled karsts. The functional relationship between seismic spectrum energy and fault-controlled karst development frequency was obtained through the neural network algorithm (Figure 7B), and the corresponding karst development probabilistic volumes were established on this basis (Figure 7D). Finally, the two probabilistic volumes were fused by the probabilistic multiplication method (Formula 1) to obtain a comprehensive probabilistic volume (Figure 7E).

Under the constraint of comprehensive probabilistic volume and training images and taking the well point interpretation results (Figure 7F) as the conditional data, the multi-point simulation scanning template was set to 15 × 15 × 3, the multi-grid level was set to 3, and the maximum number of known neighborhood nodes was 8. Three corresponding training images were input in three zones, and the fault-controlled karst model with formation cause mechanism and karst geometry (Figure 7G) was finally obtained by combining the boundary control of fracture-vuggy units. The results show that fault-controlled karst reservoirs were mainly distributed near the NNW major fault in the west of TH12208 and TH12201 fracture-vuggy units, with the cave size ranging from 8 m to 30 m, mainly being vertical and horizontal types, and the closer to the fault, the larger the cave size, and with the increase in the distance to the fault, the cave morphology gradually transits from the vertical type to the horizontal type. It is worth noting that according to the production dynamics data of the oilfield, the effective reservoirs do not develop outside the fracture-vuggy units. To conform to the actual production situation, the fracture-vuggy unit boundary was adopted for

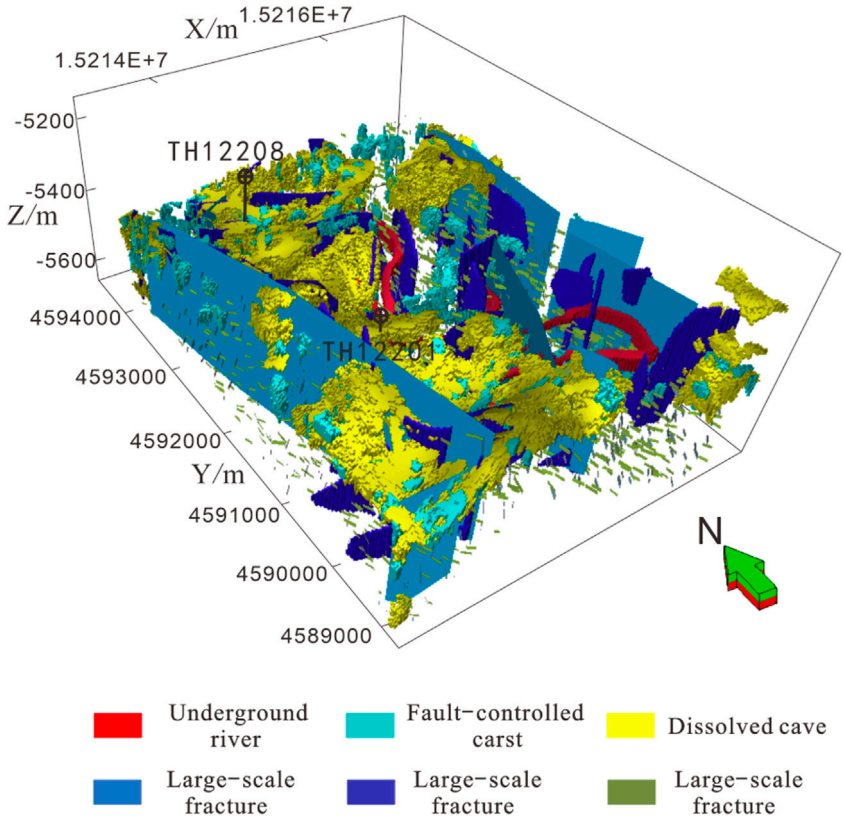

FIGURE 10
Fusion process and geological models.

control, so the reservoirs were mainly controlled by the large faults in the west (Figure 7H), while the northeastern faults generated a minor influence on the karst body, with a low karst development efficiency, which accorded with the actual situation of effective reservoirs not encountered during well drilling in this area.

4.4 Modeling of weathered crust reservoirs

Dissolution caves and small-scale fractures constitute the weathered crust reservoir, which is the communication channel between the caves. According to the core and imaging logging results (Figure 8A), the small-scale fractures are mainly high-angle tectonic shear fractures, with the extension length mainly distributed in 0.5–50 cm; based on the fracture occurrence statistics of imaging logging in the study area (Figure 8B), there are three fracture formation systems in the study area, including NE, NW, and NS. The fracture development density is established through the statistical dip angle and fracture development frequency (Figures 8C,D). Different well locations display different azimuth angles and development frequencies, and the dip angle of fractures in the study area is mainly 75°–90°. Based on the statistical parameters and development density of small-scale fractures, the discrete model of small-scale fractures was established by the object method under constraints of coherent volume attributes and probabilistic volumes (Figure 9G).

According to the well data, a total of 11 development sections of dissolution caves were identified in 7 wells of fracture-vuggy units TH12208 and TH12201, among which the development frequency of those within 30 m from the unconformity surface was 42% and that within 30 m from the unconformity surface was 58%. The development sections of dissolution caves mainly developed near 90 m range of the Ordovician unconformity surface. Based on the statistical results, the depth of the top unconformity surface and the vertical development probability of dissolution caves could be obtained (Figure 9A), and a development probabilistic volume was established accordingly (Figure 9C). The developmental probabilistic volume (9d) based on seismic attributes could be established given the high correlation between the coherent volume attribute in seismic attributes and the dissolution caves (9b). The above two probabilistic volumes were subjected to probabilistic fusion to obtain a comprehensive development probabilistic volume of dissolution caves (9e).

The relevant parameters in the sequential indicator simulation modeling were set as follows: the main variation direction of the variogram function was 330° with a variation range of 2,000 m, the secondary variation direction was 240° with a variation range of 1,500 m, and the vertical variation range was 10 m. An exponential model was used as the variogram function model. Then, simulation was performed using the sequential indicator simulation method with trends, and a dissolution cave reservoir model was acquired with the probabilistic volume of dissolution cave development between wells as the constraint data (Figure 9F). From the established dissolution cave reservoir model, dissolution cave

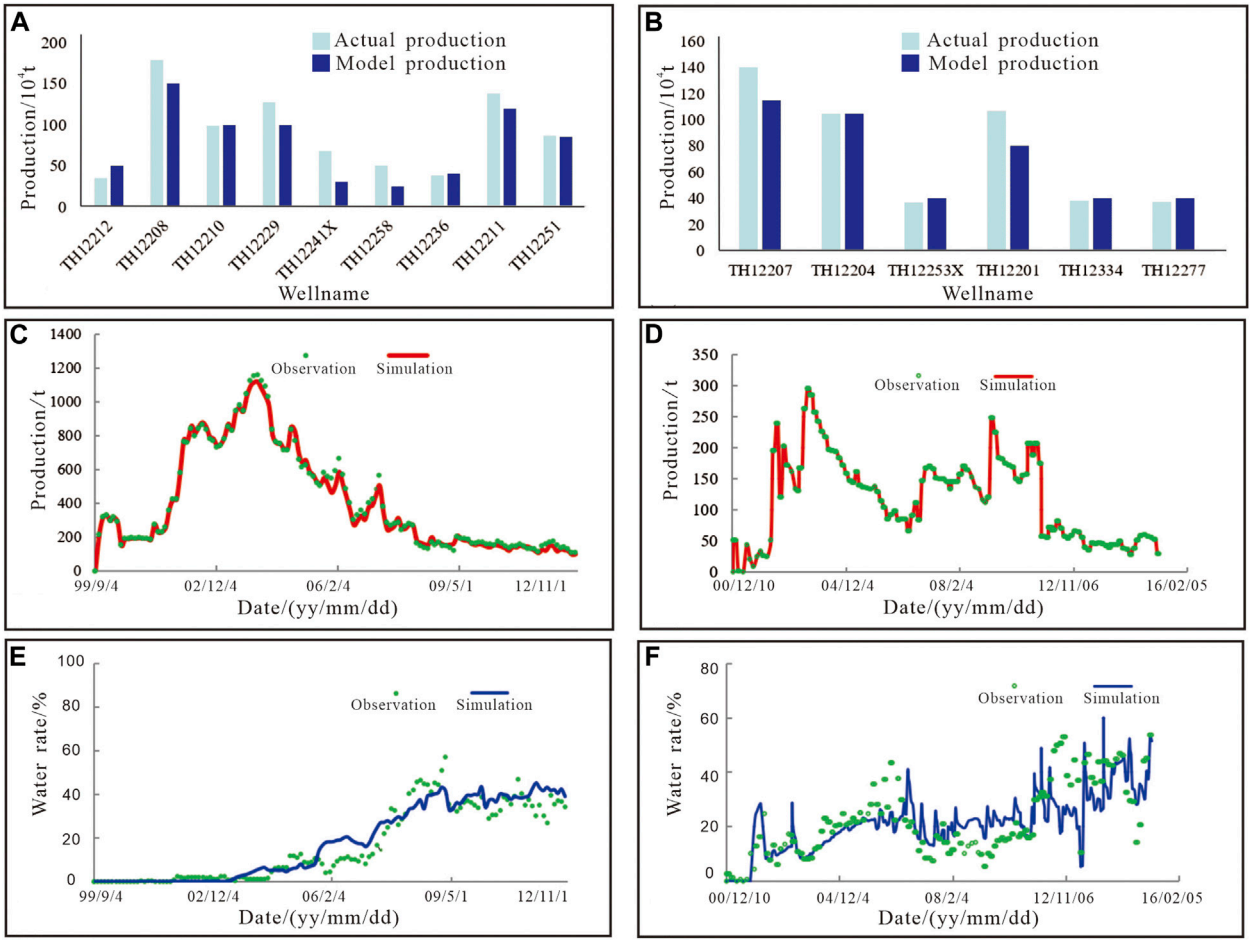

FIGURE 11
(A, B) are comparations of real production oil and model reserves in units TH12201, TH12208. **(C-F)** are correlation analysis of the simulated oil production and water cut in TH12201, TH12208 unit.

reservoirs presented a local flaky distribution and mainly developed within a certain depth range beneath the Ordovician unconformity surface.

Finally, the dissolution cave model and small-scale fracture model were superposed to acquire a weathered crust distribution model in the study area (Figure 9H).

4.5 Model fusion optimization

Because the discrete distribution models of underground rivers, fault-controlled karsts, and dissolution cave reservoirs and multi-scale fracture models were established independently, and the stochastic modeling method was used in both reservoir and small-scale fracture modeling, the same grid might be used as an effective grid in different models when all discrete distribution models were fused, but this was inconsistent with the actual geological conditions. To solve the conflict among reservoirs characterized by grids, a certain fusion principle was put forward.

(1) From a reservoir capacity and model uncertainty standpoint, underground rivers and fault-controlled karst reservoirs possess robust reservoir capacities, contributing significantly to cumulative output. However, underground rivers present greater uncertainty than fault-controlled karst reservoirs, warranting a higher prioritization. Conversely, weathered crust reservoirs, characterized by minute fractures and dissolution caves, exhibit the poorest physical properties and highest randomness among effective reservoirs, thus receiving the lowest priority. Regarding fractures, large-scale fractures (faults) are delineated through deterministic interpretation, medium-scale fractures via a blend of random extraction and human-computer interaction, and small-scale fractures through stochastic simulation. Consequently, the prioritization for integration is large-scale fractures first, followed by medium and small-scale fractures, respectively. In the final stage, small-scale fractures, medium-scale fractures, large-scale fractures, dissolution caves, fault-controlled karst, and underground rivers are sequentially incorporated into the study area's three-dimensional space. In overlapping zones, reservoirs assigned later will be preserved.

(2) The relationship between fractures and caves in reservoir configurations can generally be categorized into three types: karst cave-large fracture, karst cave-fracture-karst cave, and

dissolution cave-small fracture. Separate models for karst caves and fractures are developed based on their respective geological model constraints and statistical laws. However, during the fusion process, the specific fracture-karst cave configuration pattern is not taken into account, except for the statistical law constraint applied to the fracture model. To address this, the fracture-vuggy relationship is fine-tuned using the simulated annealing method (Xie et al., 2022). The simulated annealing method is a probabilistic technique used for finding an approximate solution to an optimization problem, particularly those involving a large search space. It's inspired by the process of annealing in metallurgy, a technique involving heating and controlled cooling of a material to increase the size of its crystals and reduce their defects. This adjustment involves altering the orientation and position of fractures (as illustrated in Figure 10A), which enhances reservoir connectivity in a manner that aligns with dynamic data. Ultimately, the fracture model that best conforms to the fracture-vuggy configuration relationship is preferentially selected.

(3) Probabilistic similarity, in the context of geological modeling, refers to ensuring that the final reservoir model accurately represents the statistical characteristics of the actual geological formations. After initial adjustments to models (as per steps 1 and 2), the original karst or dissolution cave reservoir model might be significantly altered when fused with other reservoir models, leading to substantial changes. This can result in the volume proportions of various reservoirs in the new model not aligning with the original statistical data.

After the above three operation steps are completed, the fusion model of karst, fracture, and cave reservoirs in the study area is finally obtained (Figure 10), in which underground rivers are continuously distributed, fault-controlled karsts mainly develop near faults, and dissolution caves and small-scale fractures (weathered crust) are widely developed as connecting channels. The development characteristics of fracture-vuggy units are well reflected by this fusion model.

5 Model test

Based on the final fusion geological model, the oil reservoir reserves in the study area are calculated as $1{,}507 \times 10^4$ t. Therein, the reserves of underground rivers, fault-controlled karsts, and weathered crusts are 417×10^4 t, 479×10^4 t, and 310×10^4 t, respectively, among which the reserves of dissolution caves, small-scale fractures, and large and medium-scale fracture models are 302×10^4 t, 8×10^4 t, and 1×10^4 t, respectively. By comparing the well-controlled reserves and production dynamic reserves of the model (Figures 11A,B), it can be seen that the calculation results of reserves of each well in TH12201 and TH12208 fracture-vuggy unit models basically accord with the actual recalculation results of single-well dynamic reserves, which indirectly verifies the effectiveness of the model.

On the basis of the three-dimensional geological model, the numerical simulation was carried out for the oil reservoirs in fracture-vuggy units TH12201 and TH12208 (Figures 11C–F), and the coincidence rate of both the simulated oil production and water cut was greater than 90%. The model simulation results showed a high degree of fitting with the actual production results, proving the high precision of the geological model and according with the actual underground situation, and the favorable position of the remaining oil distribution could be determined. Based on this model, an infill well has been implemented in the unit TH12201, the average daily oil production reaches 45 t, the cumulative oil production up to now is 7.167×10^4 t, and only 0.079 t of water is produced.

6 Discussion

In this paper, we introduced a fracture-vuggy modeling method that leverages multiple geological data points, treating these pieces of geological information as probability models within our modeling approach. Probability models enable us to mathematically constrain the modeling scope, reducing uncertainties in the geological modeling process. However, it's important to note that reservoir behavior is influenced by a multitude of factors. To address this complexity, our approach fuses these factors using a PR model, allowing us to overcome the limitations associated with models controlled by a single probability parameter. Undoubtedly, our method represents significant progress in improving model quality. Yet, challenges persist in its practical application. In this process, all information is utilized as soft data (probability models), and the accuracy of simulation is constrained by correlation relationships. When there are insufficient sample points to establish robust correlation coefficients, our method may introduce high uncertainty in the soft data. The reservoir is influenced by many geological factors, for example, the rock physical property decides the distribution karst, the stronger fragility of rock, the easier generation of karst or fracture. Thus, more and more information need to be added in limit factors. It makes difficult to keep the potential information of so many data. Maybe we need a better fusion algorithm to solve this problem. For example, neural network algorithms can get the optional solution by many times iteration. The solution can extract the non-linear relation between probability bodies and keep principal components of multiple factors, which may improve the quality of fusion.

The reservoir is influenced by numerous geological factors. For instance, the physical properties of the rock determine the distribution of karst; the more fragile the rock, the more susceptible it is to the formation of karst or fractures. Consequently, there is a growing need to include additional limiting factors, which poses challenges in preserving the potential information contained in this wealth of data. Perhaps a more effective fusion algorithm is required to address this issue. For example, neural network algorithms can iteratively generate an optimal solution (Dorrington and Link, 2004; Li et al., 2019). The solution have the capacity to extract nonlinear relationships among probability models and retain the principal components of multiple factors, potentially enhancing the quality of fusion.

Fracture-vuggy reservoirs exhibit pronounced heterogeneity and non-stationarity. In this context, we generate karst reservoirs using the MPS modeling method. MPS modeling involves pattern extraction from scanned data events, essentially reproducing

patterns by copying and pasting (Song et al., 2021b; Wang L. et al., 2022; Chen et al., 2022). Clearly, characterizing the non-stationarity of fracture-vuggy reservoirs through MPS modeling is challenging. To capture global information, we must explore methods for extracting potential data from the training image. Machine learning methods have proven to be at the forefront of pattern recognition, making machine learning algorithms a viable solution for uncovering abstract geological features. This approach represents a novel way to incorporate abstract geological knowledge into the modeling process. For instance, geologists (Mosser et al., 2018; Zhang et al., 2019; Song et al., 2022; Liao et al., 2023) have successfully applied generative adversarial networks (GANs), a generative model algorithm, to learn geological patterns and reproduce them in geological modeling. Researchers have used seismic data and sand fraction data to control channel geometry and the number of channels. By combining the strengths of seismic inversion and machine learning methods, we can harness abstract geological knowledge to characterize the structure of underground rivers and fault-controlled karst formations. When apply the machine learning method to modeling works, the challenges we may face include enough and convincing training data, the computing hardware and computer knowledge.

7 Conclusion

The modeling of carbonate reservoirs with fracture-vuggy structures, characterized by diverse storage types with varied origins, shapes, and sizes, requires a nuanced approach. Initially, the modeling process involves categorizing and classifying the different storage types. Based on the characteristics of each storage type, suitable methods are selected: object or multipoint statistical methods for storage bodies with specific forms and random distributions, sequential indicator simulation methods for those with non-specific forms and random distributions, and deterministic methods for specific geological bodies. The integration of geological and geophysical information through multi-probability body fusion maximizes the contributions of different data types to the model, enhancing multi-information driving, reducing uncertainty, and resulting in a refined 3D geological model. This model adheres to three fusion principles: isotope priority for hierarchical fusion based on causal relationships, fracture relationship configuration with iterative correction using simulated annealing, and probability similarity for volume adjustments to match statistical patterns. Validated through numerical simulation and drilling tests, this model effectively informs adjustments in development plans for such complex reservoirs.

Data availability statement

The original contributions presented in the study are included in the article/Supplementary material, further inquiries can be directed to the corresponding author.

Author contributions

YW: Writing–review and editing, Funding acquisition. PX: Writing–original draft, Writing–review and editing. HZ: Data curation, Formal Analysis, Writing–review and editing. YL: Funding acquisition, Writing–review and editing. AY: Visualization, Writing–review and editing.

Funding

The author(s) declare financial support was received for the research, authorship, and/or publication of this article. This research was funded by Sinopec Key Laboratory Open Fund Project for Enhancing Recovery in Fractured Reservoirs, grant number 34400000-22-ZC0607-0002. This research was supported by Key Laboratory for EOR of Fractured-Vuggy Carbonate Reservoir and National Natural Science Foundation of China (No. 42172154).

Conflict of interest

The authors YW and HZ were employed by the company Sinopec. The author AY was employed by the Petro China Huabei Oilfield Company.

The remaining authors declare that the research was conducted in the absence of any commercial or financial relationships that could be construed as a potential conflict of interest.

The study received funding from Sinopec Key Laboratory Open Fund Project for Enhancing Recovery in Fractured Reservoirs. The funder had the following involvement in the study: study design.

Publisher's note

All claims expressed in this article are solely those of the authors and do not necessarily represent those of their affiliated organizations, or those of the publisher, the editors and the reviewers. Any product that may be evaluated in this article, or claim that may be made by its manufacturer, is not guaranteed or endorsed by the publisher.

References

Allard, D., Comunian, A., and Renard, P. (2012). Probability aggregation methods in geoscience. *Math. Geosci.* 44 (5), 545–581. doi:10.1007/s11004-012-9396-3

Changcheng, H., Chengyan, L., Xinbian, L., Lihua, R., Ting, W., Xianguo, Z., et al. (2016). Characterization and genesis of fault-controlled karst reservoirs in ordovician carbonate karst slope of tahe oilfield, tarim basin. *Oil Gas Geol.* 37 (5), 644–652. doi:10.11743/ogg20160504

Chen, M., Wu, S., and Bedle, H. (2022). Modeling of subsurface sedimentary facies using self-attention generative adversarial networks (SAGANs). *J. Petroleum Sci. Eng.*, 214. doi:10.1016/j.petrol.2022.110470

Deutsch, C. (2002). *Geostatistical reservoir modeling*, 376.

Dorrington, K. P., and Link, C. A. (2004). Genetic-algorithm/neural-network approach to seismic attribute selection for well-log prediction. *GEOPHYSICS* 69 (1), 212–221. doi:10.1190/1.1649389

Fairchild, I. J., and Andy, B. (2012). *Carbonate and karst cave geology*, 28–72.

He, X. L., Sonnenborg, T. O., Jørgensen, F., and Jensen, K. H. (2014). The effect of training image and secondary data integration with multiple-point geostatistics in groundwater modelling. *Hydrology earth Syst. Sci.* 18 (8), 2943–2954. doi:10.5194/hess-18-2943-2014

Hou, J.-G., Jiang, X. M., and Yu, m. (2012). Modeling of carbonate fracture-vuggy reservoir, a case study of Ordovician reservoir of 4th Block in Tahe Oilfield. *Earth Sci. Front.* 19 (02), 59–66.

Li, S., Kang, Z., Feng, X. T., Pan, Z., Huang, X., and Zhang, D. (2020). Three dimensional hydrochemical model for dissolutional growth of fractures in karst aquifers. *Water Resour. Res.* 56 (3), e2019WR025631. doi:10.1029/2019wr025631

Li, W., Yue, D., Wang, W., Wang, W., Wu, S., Li, J., et al. (2019). Fusing multiple frequency-decomposed seismic attributes with machine learning for thickness prediction and sedimentary facies interpretation in fluvial reservoirs. *J. Petroleum Sci. Eng.* 177, 1087–1102. doi:10.1016/j.petrol.2019.03.017

Li, Y. (2013). The theory and method for development of carbonate fracture-cavity reservoir in Tahe oilfield. *Acta pet. Sin.* 34 (01), 115–121. doi:10.7623/syxb201301013

Li, Y., Hou, J., and Ma, X. (2016). Data integration in characterizing a fracture-cavity reservoir, Tahe oilfield, Tarim basin, China. *Arabian J. Geosciences* 9 (8), 532. doi:10.1007/s12517-016-2562-z

Liao, B., Wang, J., Sun, J., Lv, K., Liu, L., Wang, Q., et al. (2023). Microscopic insights into synergism effect of different hydrate inhibitors on methane hydrate formation: experiments and molecular dynamics simulations. *Fuel* 340, 127488. doi:10.1016/j.fuel.2023.127488

Liu, Y., Hou, J., Li, Y., Dong, Y., Ma, X., and Wang, X. (2018b). Characterization of architectural elements of ordovician fractured-cavernous carbonate reservoirs, Tahe oilfield, China. *J. Geol. Soc. India* 91 (3), 315–322. doi:10.1007/s12594-018-0856-3

Liu, Y. M., Hou, J. G., and Li, Y. Q. (2018a). A multi-constrained modeling method for paleokarst carbonate reservoirs: an application to the Ordovician reservoir in the Tahe Oilfield. *Petroleum Sci. Bull.* 3 (02), 125–133.

Lu, X. R., Sun, J. F., and Wu, X. W. (2021). Internal architecture characterization of fractured-vuggy carbonate reservoirs: a case study on the Ordovician reservoirs, Tahe Unit S67, Tarim Basin. *OIL GAS Geol.* 42 (03), 728–737.

Ma, L. J., Kong, Q. Y., and Liu, K. Y. (2014). Weak reflection characteristics and its formation mechanism of rdovician reservoir in Tahe Oilfield. *OPG* 49 (02), 338–343 222.

Mariethoz, G., and Caers, J. (2014). *Multiple-point geostatistics: stochastic modeling with training images*.

Mariethoz, G., Renard, P., and Straubhaar, J. (2010). The Direct Sampling method to perform multiple-point geostatistical simulations. *Water Resour. Res. - WATER RESOUR RES* 46 (11). doi:10.1029/2008wr007621

Mosser, L., Olivier, D., and Martin, J. B. (2018). Conditioning of three-dimensional generative adversarial networks for pore and reservoir-scale models. *80th EAGE Conference and Exhibition 2018*, 1–5. doi:10.3997/2214-4609.201800774

Popov, P., Qin, G., Bi, L., Enfendiev, Y., Kang, Z., Li, J., et al. (2009). Multiphysics and Multiscale Methods for Modeling Fluid Flow Through Naturally Fractured Carbonate Karst Reservoirs. *Spe Technical Conference and Exhibition* 12, 218–231. doi:10.2118/105378-MS

Qi, L., and Lu, Y. (2010). Development characteristics and main controlling factors of the Ordovician carbonate karst in Tahe oilfield. *Oil Gas Geol.* 31 (1), 1–12. doi:10.11743/ogg20100101

Qiang, J., and Fei, T. (2013). Investigation of fracture-cave constructions of karsted cabonate reservoirs of ordovician in Tahe oilfield, Tarim Basin. *J. China Univ. Petroleum Ed. Nat. Sci.* 37 (5), 15–21. doi:10.3969/j.issn.1673-5005.2013.05.003

Qiang, J., Fei, T., and Hongfang, Z. (2015). Comprehensive evaluation of fracture-cave units in karst carbonates in Tahe Oilfield, Tarim Basin. *Petroleum Geol. Exp.* 37 (3), 272–279. doi:10.7603/s40972-015-0042-2

Qinghua, C., Ming, C., and Du, H. (2019). Application of 3D digital outcrop characterization technology based on laser scanning in modern karst research. *Henan Sci.* 37 (3), 422–428. doi:10.3969/j.issn.1004-3918.2019.03.017

Shang, X. F., Duan, T. Z., and Zhang, W. B. (2020). Characterization of dissolution facies belt in fracture-cavity carbonate rocks mainly controlled by fault-controlling karst: a case study of Ordovician reservoirs in the Block 10 of Tahe oilfield. *ACTA PET. SIN.* 41 (03), 329–341. doi:10.7623/syxb202003007

Song, S., Mukerji, T., and Hou, J. (2021a). GANSim: conditional facies simulation using an improved progressive growing of generative adversarial networks (GANs). *Math. Geosci.* 53 (7), 1413–1444. doi:10.1007/s11004-021-09934-0

Song, S., Mukerji, T., and Hou, J. (2021b). Geological Facies modeling based on progressive growing of generative adversarial networks (GANs). *Comput. Geosci.* 25 (3), 1251–1273. doi:10.1007/s10596-021-10059-w

Song, S., Zhang, D., and Mukerji, T. (2022). GANSim-surrogate: an integrated framework for conditional geomodelling and uncertainty analysis. *J. Hydrology* 620B, 129493. doi:10.1016/j.jhydrol.2023.129493

Strebelle, S. (2002). Conditional simulation of complex geological structures using multiple-point statistics. *Math. Geol.* 34, 1–21. doi:10.1023/a:1014009426274

Suihong, S., Yanqing, S., and Jiagen, H. (2020). Review of a generative adversarial networks (GANs)-based geomodel-ling method. *Petroleum Sci. Bull.* 7 (1), 34–49. doi:10.3969/j.issn.2096-1693.2022.01.004

Wang, L., Yin, Y., Zhang, C., Feng, W., Li, G., Chen, Q., et al. (2022b). A MPS-based novel method of reconstructing 3D reservoir models from 2D images using seismic constraints. *J. Petroleum Sci. Eng.* 209, 109974. doi:10.1016/j.petrol.2021.109974

Wang, X., Yu, S., Li, S., and Zhang, N. (2022a). Two parameter optimization methods of multi-point geostatistics. *J. Petroleum Sci-ence Eng.* 208, 109724. doi:10.1016/j.petrol.2021.109724

Xie, P., Hou, J., Yin, Y., Chen, Z., Chen, M., and Wang, L. (2022). Seismic inverse modeling method based on generative adversarial networks. *J. Petroleum Sci. Eng.* 215, 110652. doi:10.1016/j.petrol.2022.110652

Xie, P. F., Hou, J. G., and Wang, Y. (2023). Application of multi-information fusion modeling of fracture-vuggy reservoir in Ordovician reservoir of 12th block in Tahe Oilfield. *J. China Univ. Petroleum Ed. Nat. Sci.* 47 (03), 1–14. doi:10.3969/j.issn.1673-5005.2023.03.001

Xinbian, L., Chengjiang, H., and Guangxiao, D. (2014). Development features of karst ancient river system in Ordovician reservoirs, Tahe Oil Field. *Petroleum Geol. Exp.* 3, 268–274. doi:10.11781/sysydz201403268

Yan-feng, L., Wen-biao, Z., Tai-zhong, D., and Hua-wei, Z. (2021). Numerical simulation method for the formation of fault-karst carbonate reservoir process based on cellular automaton. *Sci. Technol. Eng.* 21 (9), 3550–3555. doi:10.3969/j.issn.1671-1815.2021.09.017

Yang, L., and Qiang, J. (2016). Karst zonings and fracture-cave structure characteristics of Ordovician reservoirs in Tahe oilfieid, Tarim Basin. *Acta Pet. Sin.* 37 (3), 289–298. doi:10.7623/syxb201603001

Yang, L. I. (2012). Ordovician carbonate fracture-cavity reservoirs identification and quantitative characterization in Tahe Oilfield. *J. China Univ. Petroleum Ed. Nat. Sci.* 36 (1), 1–7. doi:10.3969/j.issn.1673-5005.2012.01.001

Yang, L. I., Jiagen, H., and Yongqiang, L. I. (2016). Features and hierarchical modeling of carbonate fracture-cavity reservoirs. *Petroleum Explor. Dev.* 43 (4), 600–606. doi:10.11698/PED.2016.04.12

Zhang, S., Jin, Q., and Cheng, F. Q. (2020). Genesis relation of surface and underground rivers and reservoir charac- teristics in paleokarst drainage systems:A case study of Ordovician karst in the Tahe oilfield. *CARSOLOGICA Sin.* 39 (06), 900–910. doi:10.11932/karst2020y37

Zhang, T. F., Peter, T., Dupont, E., Zhu, L. C., Liang, L., and Bailey, W. (2019). Generating geologically realistic 3D reservoir facies models using deep learning of sedimentary architecture with generative adversarial networks. *Petroleum Sci.* 16 (3), 541–549. doi:10.1007/s12182-019-0328-4

Zhang, X. M., Yang, J., and Yang, Q. L. (2004). Reservoir description and reserves estimation technique for fracture-cave type carbonate reservoir in Tahe Oilfield. *ACTA PET. SIN.* 25 (1), 13–18. doi:10.3321/j.issn:0253-2697.2004.01.003

frontiers | Frontiers in Earth Science

TYPE Methods
PUBLISHED 31 January 2024
DOI 10.3389/feart.2024.1355494

Check for updates

OPEN ACCESS

EDITED BY
Xixin Wang,
Yangtze University, China

REVIEWED BY
Zhen Zhang,
Chinese Academy of Geological Sciences, China
Hong Pang,
China University of Petroleum, China

*CORRESPONDENCE
Fan Song,
songfan@upc.edu.cn

RECEIVED 14 December 2023
ACCEPTED 16 January 2024
PUBLISHED 31 January 2024

CITATION
Song F, Kong Q, Su N, Jiao G and Xu M (2024), Formation mechanism of the upper Paleozoic tight sandstone gas reservoir in the Daniudi gas field, Ordos Basin, China.
Front. Earth Sci. 12:1355494.
doi: 10.3389/feart.2024.1355494

COPYRIGHT
© 2024 Song, Kong, Su, Jiao and Xu. This is an open-access article distributed under the terms of the Creative Commons Attribution License (CC BY). The use, distribution or reproduction in other forums is permitted, provided the original author(s) and the copyright owner(s) are credited and that the original publication in this journal is cited, in accordance with accepted academic practice. No use, distribution or reproduction is permitted which does not comply with these terms.

Formation mechanism of the upper Paleozoic tight sandstone gas reservoir in the Daniudi gas field, Ordos Basin, China

Fan Song[1,2]*, Qingyuan Kong[1,2], Nina Su[1,2], Guohua Jiao[3] and Miaomiao Xu[1,2]

[1]National Key Laboratory of Deep Oil and Gas, China University of Petroleum (East China), Qingdao, China, [2]School of Geosciences, China University of Petroleum (East China), Qingdao, China, [3]Xinchun Petroleum Development Limited Company, China Petroleum and Chemical Corporation, Dong Ying, China

The upper Paleozoic gas reservoir in the Daniudi gas field, Ordos Basin, is one of the typical tight sandstone gas reservoirs in China. Research into the sequential order of reservoir densification and gas accumulation is the key to revealing the formation mechanism of tight sandstone gas reservoirs. However, this scientific issue is still a subject of debate in the Daniudi gas field. Based on a series of reservoir experiments and in combination with stratigraphic burial and thermal maturity history, a comprehensive study is conducted on the formation and natural gas accumulation processes of the upper Paleozoic sandstone reservoir in the Daniudi gas field. Study results indicate that the main causes of sandstone reservoir densification of the study area include long-term compaction, multistage quartz cementation and carbonate cementation. In accordance with the time order of reservoir densification and gas accumulation, the formation of tight gas reservoirs can be divided into two types: self-sourced and near-source accumulations. In the former, before sandstone reservoir densification occurs, low-maturity natural gas generated from coal rocks and dark mudstones enter the reservoir quickly, migrate towards structural highs as driven by buoyancy, and then accumulate and form gas reservoir in favourable lithologic traps. In the latter, after tight sandstone reservoirs are formed, high-maturity gas migrates along fractures formed in the Late Cretaceous and accumulate in the nearby reservoir with micro-fractures. The study results provide a new understanding of the formation process of tight sandstone gas reservoirs and provides a reference for the exploration and development of the same type gas reservoirs.

KEYWORDS

tight sandstone reservoir, diagenesis, gas generating centre, gas accumulation, Daniudi gas field, Ordos Basin

1 Introduction

The Ordos Basin is located in the central north of China; it is the second largest sedimentary basin, with an area of ~25 × 10^4 km^2. Within the basin, the upper Paleozoic is a main area where tight sandstone gas accumulates, and it has great exploration prospects. At present, five large gas fields with natural gas reserves of >1,000 × 10^8 m^3, namely, Sulige, Daniudi, Uxiqi, Jingbian, and Yulin, have been discovered in the basin

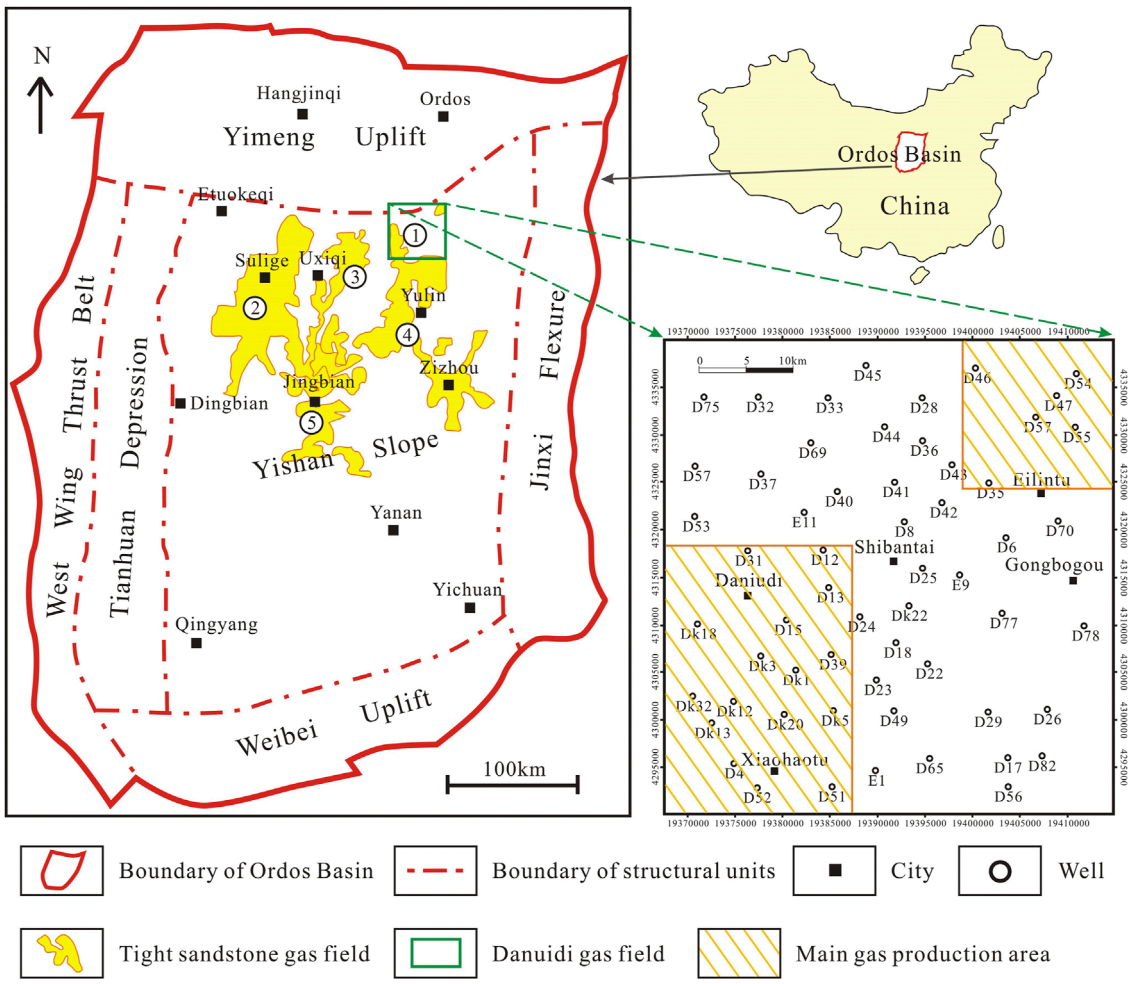

FIGURE 1
Structural location and the main well position of the Daniudi gas field, Ordos Basin. Note: 1: Daniudi gas field; 2: Sulige gas field; 3: Uxiqi gas field; 4: Yulin gas field; 5: Jingbian gas field. In the Daniudi gas field, the major gas pay zone includes Permian braided river reservoirs in the southwest and Carboniferous barrier bar reservoir in the northeast.

(Wang et al., 2015; Sun et al., 2019). Extensive research has been conducted on the natural gas accumulation of upper Paleozoic gas fields in the Ordos Basin, believing that this region is a continuous or quasi-continuous tight sandstone gas field. The gas reservoir is non-buoyancy driven and exhibits widespread gas generation, near-source accumulation and no obvious gas-bearing boundary (Zhang et al., 2000; Dai et al., 2005; Zhang et al., 2007; Zhao et al., 2012; Zou et al., 2013; Lan et al., 2016). With regard to the relationship between reservoir densification and gas accumulation, the general perception is that after tight sandstone reservoirs are formed, natural gas formed in source rocks migrates vertically through fracture systems under excessive pressure and enters reservoirs, gathering near hydrocarbon generation centres (Islam, 2009; Karim et al., 2010; Yang et al., 2012; Xi et al., 2015; Wu et al., 2017). However, a study on the tight sandstone gas reservoir in the Daniudi gas field in the northern basin shows great differences in terms of natural gas migration and accumulation characteristics in different stages of reservoir densification. Based on rock thin section identification, cathodoluminescence (CL), fluid inclusions, C–O isotope assay and source rock geochemical analysis in combination with stratigraphic burial and thermal maturity history, we found the sequence of diagenetic evolution and gas accumulation of the upper Paleozoic sandstone reservoir in the Daniudi gas field. We then propose a model of the formation of tight sandstone gas reservoirs. The findings can guide the research of similar gas reservoirs.

2 Geological setting

The Daniudi gas field lies in the northeast of the Yishan slope, Ordos Basin, and has an area of 2,000 km^2 (Figure 1). The area generally occurs as a flat, gentle, W-dipping monocline, with a dip angle of <1°. Faults are not developed, whereas strata are completely developed within the Daniudi gas field (Zou et al., 2009). In the Carboniferous Taiyuan Fm and Permian Shanxi Fm and Xiashihezi Fm, typical marine–continental transitional facies coal-bearing clastic rocks are developed, which constitute the major

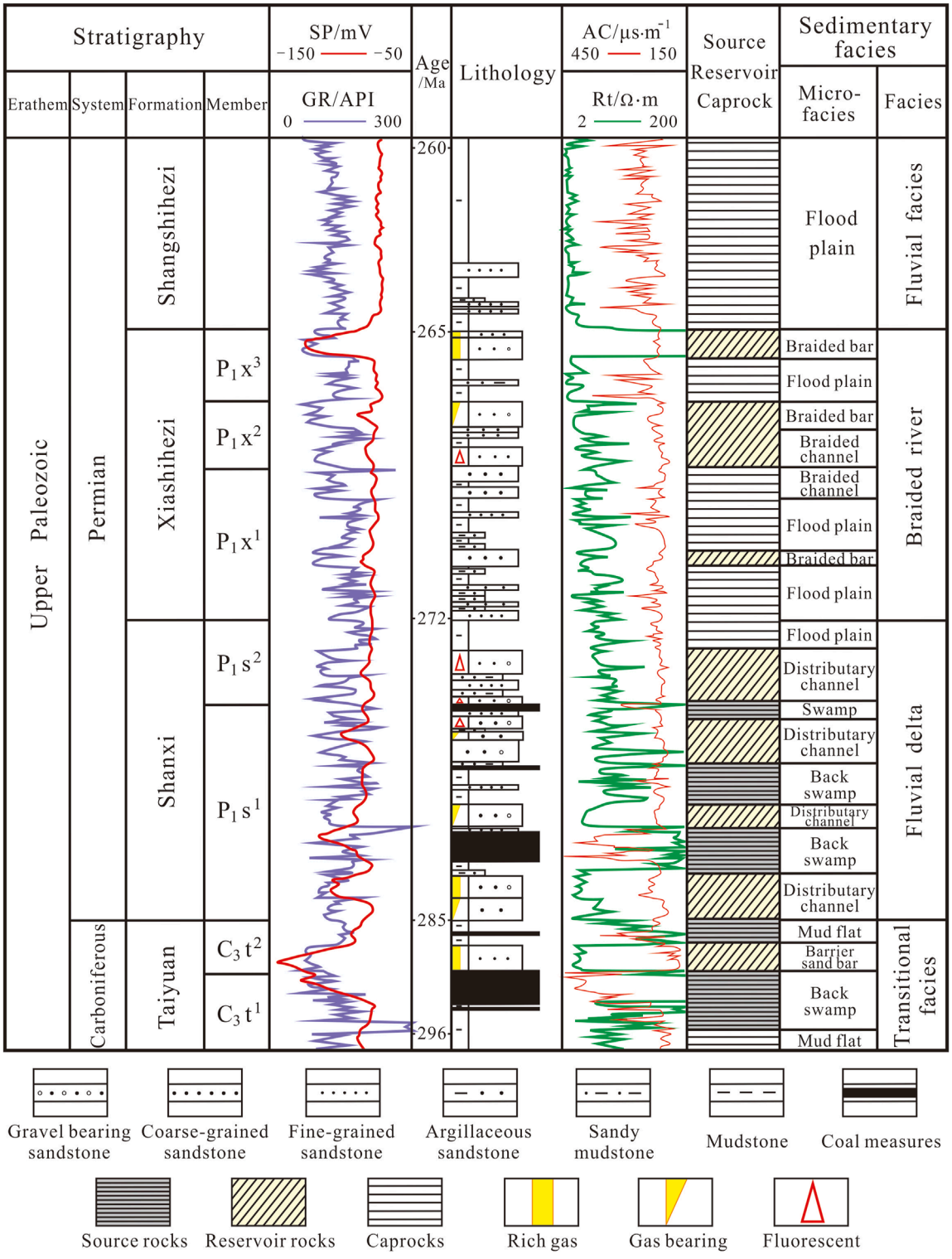

FIGURE 2
Generalized upper Paleozoic stratigraphy of the Daniudi gas field, showing major oil and gas combinations. There are seven gas-bearing formations of the upper Paleozoic in the study area.

horizon for natural gas development in the area. Coal seams and carbon mudstones of the Taiyuan and the Shanxi Fms are main source rocks of natural gas pools. Taiyuan Fm. barrier bars, Shanxi Fm delta front distributary channel sands and Xiashihezi Fm braided river sands are favourable reservoir. Shangshihezi Fm flooding plain lacustrine facies mudstones are the regional cover of upper Paleozoic

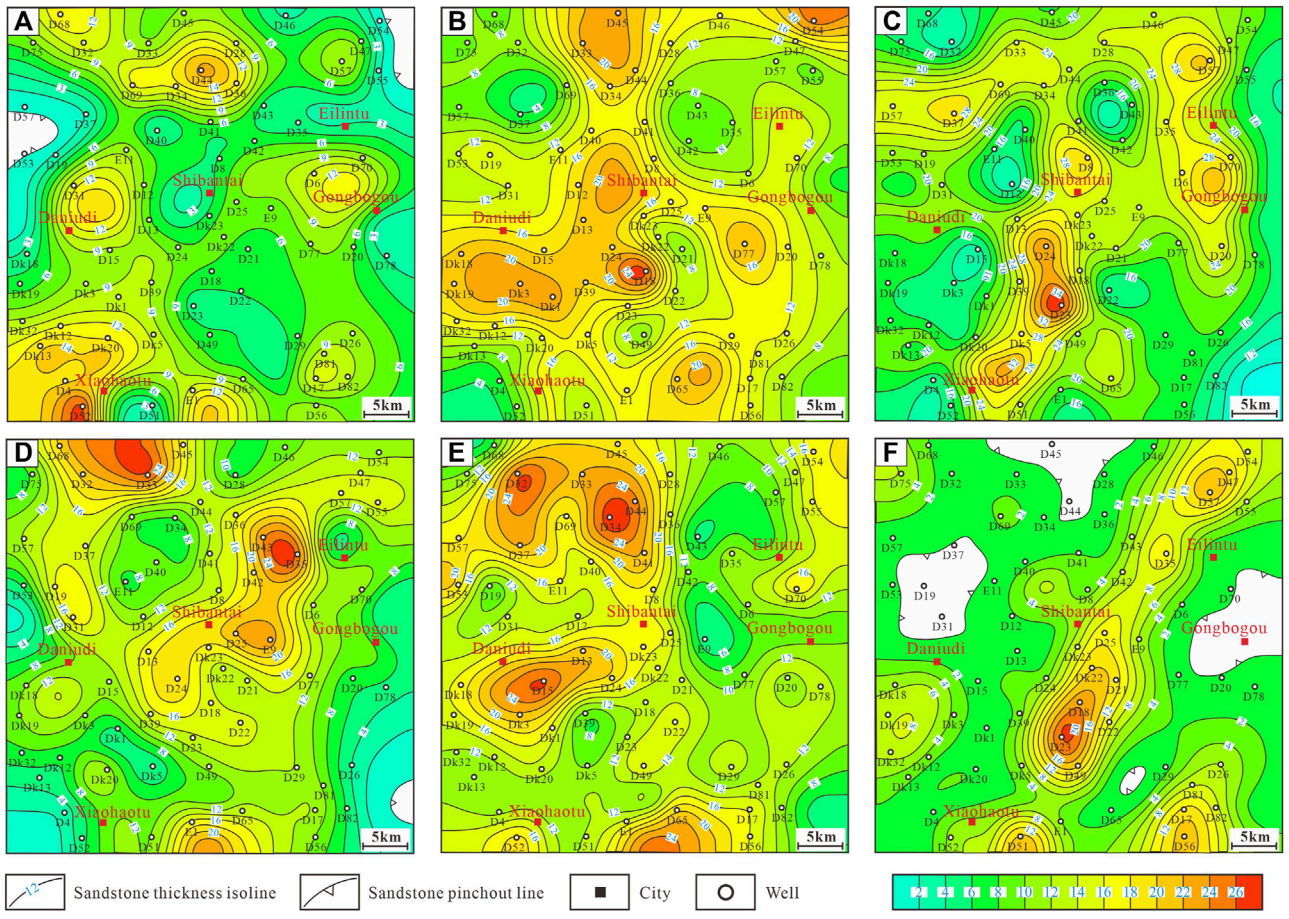

FIGURE 3
Sandstone thickness of the upper Paleozoic reservoir in the Daniudi gas field. Note: **(A)**, Mbr 3 of the Xiashihezi Fm; **(B)**, Mbr 2 of the Xiashihezi Fm; **(C)**, Mbr 1 of the Xiashihezi Fm; **(D)**, Mbr 2 of the Shanxi Fm; **(E)**, Mbr 1 of the Shanxi Fm; **(F)**, Mbr 2 of the Taiyuan Fm.

natural gas reservoirs within the basin (Cai et al., 2005; Fu et al., 2013; Su et al., 2016).

Gas exploration practice shows that the upper Paleozoic of the Daniudi gas field from lower upwards includes seven gas-bearing formations (Figure 2). The Mbr 1 and Mbr 2 of the Taiyuan Fm are in a marine–continental transitional facies sedimentary environment; the Mbr 1 and Mbr 2 of the Shanxi Fm are fluvial delta facies; the Mbr 1, Mbr 2, and Mbr 3 of the Xiashihezi Fm are mainly braided river facies. By the end of 2014, the Daniudi gas field achieved a production of 40×10^8 m^3 per year, with an accumulative gas yield of >20 billion m^3. The major gas pay zone includes braided river reservoirs of the Xiashihezi Fm in the southwest and barrier bar reservoir of the Taiyuan Fm in the northeast. Gas output of the two areas accounts for 90% of the entire gas field (Figure 1).

3 Methods

The Danudi gas field is the key area of natural gas development in the tight sandstone reservoir of upper Paleozoic in the Ordos Basin. Consequently, a large amount of the drilling for natural gas has taken place in this area, thereby providing core materials, well logs and many other exploration and development data for this study. The data used in this paper were derived from more than 50 wells in the Daniudi gas field. More than 600 rock composition data, 320 grading analysis data, 6,500 reservoir physical property data points and natural gas composition data were obtained from the Exploration and Production Research Institute of Huabei Company, SINOPEC.

A bulk of Upper Paleozoic core samples were selected from the Daniudi gas field and analysed. More than 150 thin sections were created to observe the pore structure and diagenetic phenomena. CL was conducted on 30 thin sections under standard operating conditions by using a Technosyn cathode luminoscope with an EPMA-1600 electron microprobe to determine the stages of cementation. Eighty polished thin sections were made for fluid inclusion petrographic observation and microthermometry analyses to determine the formation of authigenic minerals and diagenetic evolution sequence. In addition, 40 sandstone samples were selected from 18 wells in different formations for stable carbon and oxygen isotopic measurements. A bulk of mudstone samples were crushed for Rock-Eval pyrolysis to obtain the geochemical parameters of source rocks; these parameters mainly include total organic carbon content (TOC), residual soluble hydrocarbon (S_1), pyrolysed hydrocarbon (S_2), hydrogen index

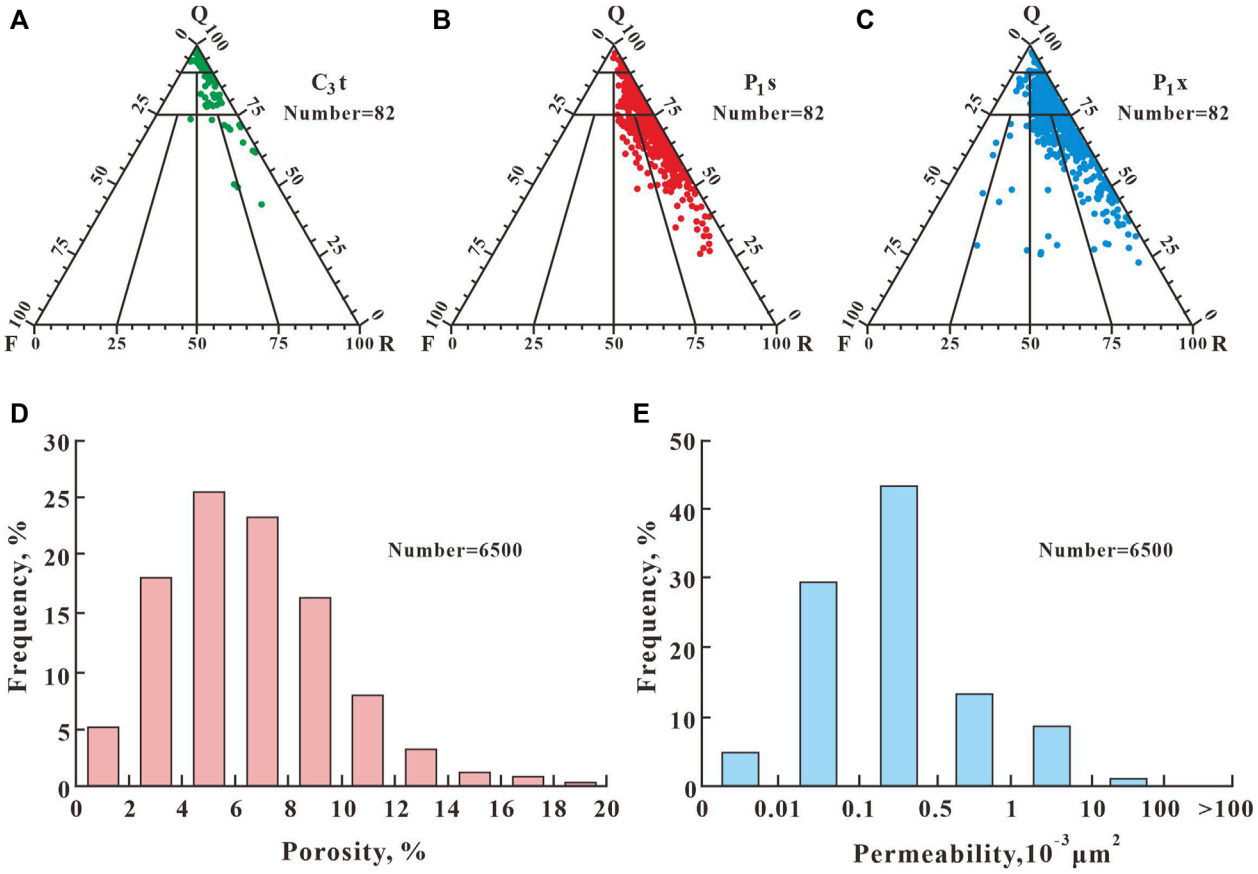

FIGURE 4
Rock composition and reservoir physical property of the Upper Paleozoic tight sandstone in the Daniudi gas field. Note: **(A–C)**, Classification of sandstone using Folk's (1974) classification, the Taiyuan Formation is dominated by quartz sandstone, and the Shanxi and Xiashihezi formations are dominated by lithic sandstone and lithic quartz sandstone; **(D,E)**, Reservoir porosity and permeability distribution, indicating a low-porosity and ultralow-permeability tight reservoir.

(HI; HI = S_2/TOC × 100) and temperature at which the maximum amount of pyrolytic hydrocarbon is produced (Tmax). S_1 + S_2 reflects the total hydrocarbon generation potential. In addition, the vitrinite reflectance (R_o) of the mudstone was measured by conventional microphotometric methods. All experiments related to this study were conducted in the State Key Laboratory of Petroleum Resource and Prospecting of the China University of Petroleum. The above experimental results can help define the formation of gas reservoir.

4 Result

4.1 Reservoir sands distribution

The Carboniferous Taiyuan Fm, the Permian Shanxi Fm and Xiashihezi Fm of the upper Paleozoic in the Daniudi gas field are a set of typical marine facies tidal flat–offshore delta–continental braided river sedimentary sequences (Fu et al., 2013; Yang and Liu, 2014), with thick reservoir sands and high lateral continuity (Figure 3). In the sedimentary period of Taiyuan Fm, the area was in an epicontinental sedimentary environment. Large-scale barrier bars formed in the study area, with an extension length of 50 km and a dominant sand thickness varying 6 m–20 m; these barrier bars served as effective pathways for gas migration. In the area with small sand thickness around barrier bars, the reservoir densification is more obvious due to the strong compaction. While the densification of thick sand reservoir is mainly related to the quartz overgrowth. In the period of the Mbr 1 of the Shanxi Fm, the study area was in a coastal plain environment, and shore–delta sedimentary systems were developed. Reservoir sands are mainly distributary channel–underwater distributary channel coarse sandstones, and the sandstone thickness is comparatively large in the western study area. Delta plain sediments were mainly developed in the period of the Mbr 2 of the Shanxi Fm; thick-bedded distributary channel sands are distributed in the centre and north. Similar to Taiyuan Formation, the area with thin sand and high shaliness has strong compaction and strong densification. In the sedimentary period of Xiashihezi Fm, the paleoclimate turned dry and multistage braided sands were superpositioned and mainly developed in the Daniudi gas field (Ren et al., 2007). River channels were thick and migrated frequently, and the reservoir sands were 30–80 m thick. In this period, the thickness of sandstone is large, and the reservoir has strong anti-compaction ability. The reservoir densification of

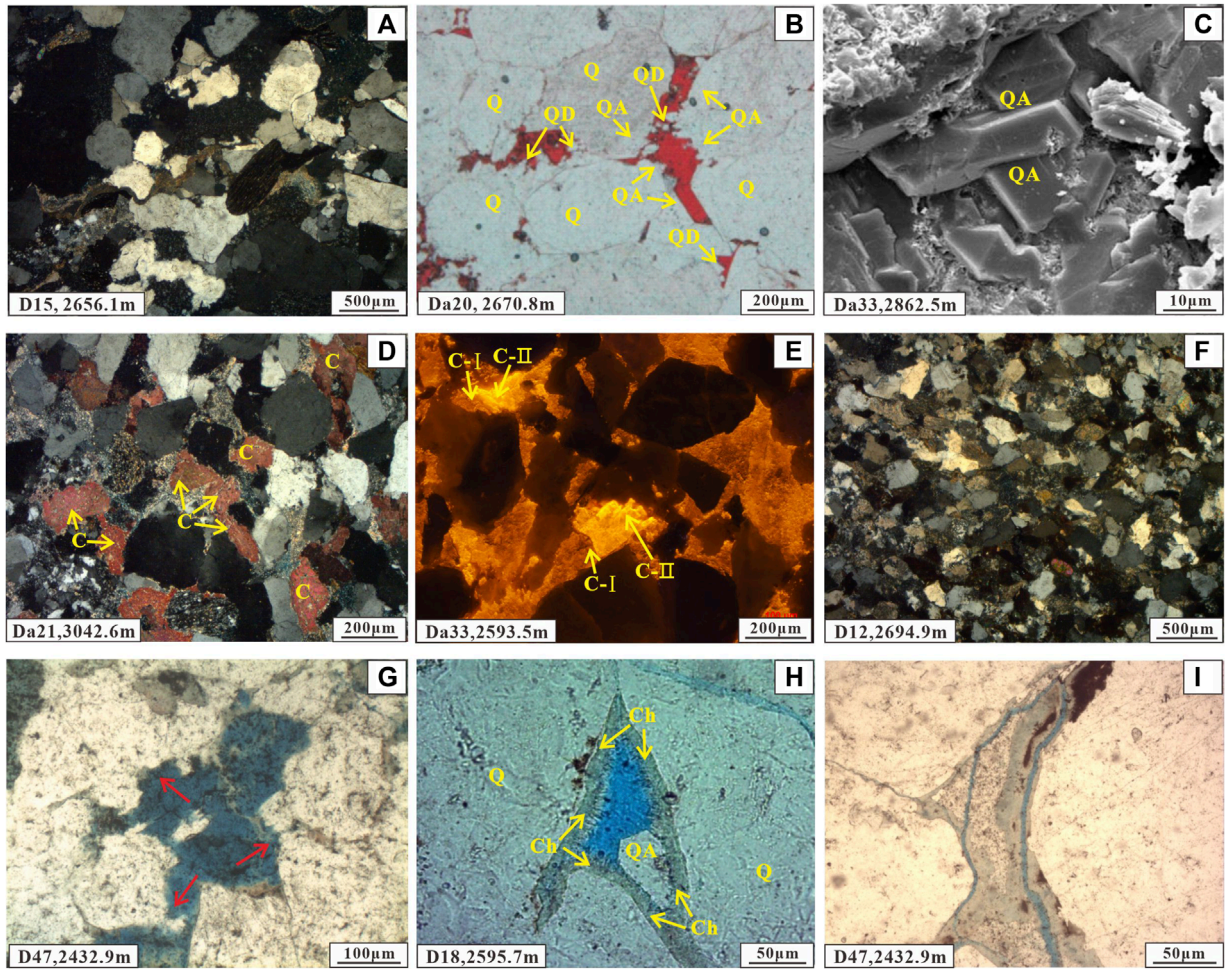

FIGURE 5
The characteristics of reservoir lithology and secondary pore in the Upper Paleozoic tight sandstone reservoir in the Daniudi gas field. Note: **(A)**, Fine-grained sandstone were subject to strong compaction and contacted closely, Crossed Nicol; **(B)**, Moderate-coarse-grained quartz sandstone with multistage quartz overgrowths, Single Nicol; **(C)**, Authigenic quartz occludes primary pores, SEM image; **(D)**, Calcite filled primary pores, Crossed Nicol; **(E)**, Two stages of carbonate cements, Cathodoluminescence image; **(F)**, Fine-medium-grained lithic quartz sandstone, clastic grains have close contact relations, Crossed Nicol; **(G)**, Intergranular dissolved pore and intragranular dissolved pore, Single Nicol; **(H)**, Quartz grains are encapsulated by chlorite film, Single Nicol; **(I)**, Granular boundary micro-fractures, Single Nicol. Q–quartz; QA–authigenic quartz; Ch–chlorite; C–calcite.

Xiashihezi Fm is mainly caused by multi-stage and multi-type cementation.

4.2 Reservoir lithology and physical property

The upper Paleozoic reservoir rocks of the Daniudi gas field are comprised by medium–coarse-grained lithic sandstone, lithic quartz sandstone and quartz sandstone. The Taiyuan Fm is comprised by quartz sandstone (Figure 4A), while the Shanxi Fm and Xiashihezi Fm are comprised by lithic sandstone and lithic quartz sandstone, with minor quartz sandstone and feldspar lithic sandstone (Figures 4B, C). Clastic quartz includes monocrystalline quartz and polycrystalline quartz; the lithic fragments are mainly epimetamorphic rocks, such as slate and phyllite, with secondary volcanic clasts. The lithic fragments are mostly plastic and underwent intense compaction and then deformation (Figure 5A). Fillings in the reservoirs are mainly matrix and various authigenic cements, with an average content of 10%–15%. The matrix includes argillaceous components, such as kaolinite and illite, with an average content of 8%; the cements mainly include multistage authigenic quartz, calcite and ferrocalcite (Figures 5B–E), with minor ankerite, siderite, chlorite and kaolinite. Microscopy shows that clastic grains have close contact relations, such as linear or concavo-convex, and moderate sorting, subangular and porous cementation (Figure 5F).

In accordance with the statistics of reservoir physical property data, the upper Paleozoic reservoir in the Daniudi gas field has a porosity of 2%–12% with an average of 6.9% and permeability of 0.01×10^{-3}–10×10^{-3} μm^2 with an average of 0.76×10^{-3} μm^2 (Figures 4D, E), indicating a low-porosity and ultralow-permeability tight reservoir. In various gas sets, reservoir properties are mostly favourable in the Mbr 2 and Mbr 3 of the Xiashihezi Fm (Table 1). The upper Paleozoic reservoir

TABLE 1 Porosity and permeability of the Upper Paleozoic sandstone reservoir in the Daniudi gas field, Ordos Basin.

Fm	Number of samples	Porosity (%)			Permeability ($\times10^{-3}\mu m^2$)		
		Minimum	Maximum	Average	Minimum	Maximum	Average
P_1x^3	1,280	0.75	19.52	8.58	0.008	23.01	1.351
P_1x^2	828	0.25	21.45	8.26	0.006	58.15	1.257
P_1x^1	863	0.20	16.31	6.06	0.001	13.60	0.395
P_1s^2	742	0.50	13.49	5.72	0.001	9.42	0.424
P_1s^1	1,490	0.20	15.58	5.65	0.001	10.27	0.394
C_3t^2	845	2.10	18.92	7.27	0.005	60.50	0.935
C_3t^1	452	0.50	17.58	6.82	0.002	15.74	0.581
Upper Paleozoic	6,500	0.20	21.45	6.90	0.001	60.50	0.762

underwent long-term diagenetic reworking; the reservoir space are predominantly secondary pores, including intergranular dissolved pores, intragranular dissolved pores and matrix dissolved pores, with secondary residual primary intergranular pores (Figures 5G, H). Secondary pores are mainly quartz-dissolved pores and secondarily feldspar and lithic-dissolved pores, thereby indicating the reservoirs of the study area have two diagenetic fluid environments, i.e., acidic and alkaline. In addition to pores, there are also some micro-fractures in the study area. The micro-fractures are mainly the granular boundary fractures, which are often curved shape and partially dissolved (Figure 5I).

4.3 Pore structure

Statistics of mercury-injection parameters imply that the sandstones in the study area have an average pore throat radius of 0.33 μm and a sorting coefficient of throats varying from 0.95 to 5.95 with an average of 3.54. This result suggests that most of the sandstones have poorly sorted pore throats and are dominated by combinations of micropores and microthroats (Table 2). The Carboniferous–Permian reservoir has a displacement pressure varying from 0.01 MPa to 40 MPa; the Xiashihezi Fm has minimum average displacement pressure, followed by the Shanxi Fm and then the Taiyuan Fm This variation tendency reflects that reservoir densification intensifies as the burial depth increases.

The Carboniferous–Permian reservoir of the Daniudi gas field has a median capillary pressure of 1.04–112.1 MPa. This capillary pressure averages 32.84 MPa in the Xiashihezi Fm, 36.8 MPa in the Shanxi Fm and 19.67 MPa in the Taiyuan Fm, generally displaying opposite characteristics to displacement pressure and decreasing as the burial depth increases. The median pore throat radius averages from 0.007 μm to 0.705 μm, which is 0.12 μm in the Xiashihezi Fm, 0.075 μm in the Shanxi Fm and 0.21 μm in the Taiyuan Fm. The maximum average pore throat radius is found in the Taiyuan Fm, and the minimum average pore throat radius is observed in the Shanxi Fm (Table 2). These findings suggest that the maximum pore throat radius has great influences on displacement pressure, and the median pore throat radius has great influences on reservoir properties.

4.4 Characteristics of source rocks and natural gas

The upper Paleozoic source rocks of the Daniudi gas field are mainly marine–continental transitional facies coal-measure source rocks, followed by dark mudstones. The organic matter types are mainly III–II type kerogens (Li et al., 2014; Liu et al., 2015; Wu et al., 2017). In accordance with various indexes (organic abundance) of coal rocks and dark mudstones (Figures 6, 7), the coal rocks have an average *w* (TOC) of 60.55%, average *w* (chloroform bitumen "A") of 0.8225%, average total hydrocarbon (HC) of 3,275 μg/g and potential of generating hydrocarbon S1 + S2 of 88.5 mg/g on average. Eighty percent of the samples have the potential to generate hydrocarbon of >50 mg/g; the indexes indicate that the coal rocks are of high quality as source rocks. Organic carbon is widely distributed in dark mudstones; about 75% of the samples have *w* (TOC)>0.5%, with an average of 1.77%, and about 30% of the samples have W (chloroform bitumen "A") > 0.05%, with an average of 0.0447%. About 27% of the samples have total hydrocarbon >200 μg/g, with an average of 170 μg/g; about 55% of the samples have the potential to generate hydrocarbon S1 + S2>0.5 mg/g, with an average of 1.5 mg/g. These indexes suggest that dark mudstones contribute to hydrocarbon generation and are of moderately–highly favourable source rocks.

The upper Paleozoic source rocks are unevenly distributed in the Daniudi gas field; thick-bedded source rocks are chiefly distributed in the southwest (Lu and Miao, 2018). Coal-measure source rocks are 18–30 m thick in the area, and dark mudstones are 35–55 m thick and are a main natural gas generating zone. A comparison of the organic abundance parameters of various Fms and Members of the upper Paleozoic in the Daniudi gas field (Table 3) indicates that the organic abundance indexes of the First Member coal rocks and dark

10.3389/feart.2024.1355494

TABLE 2 Parameters of mercury injection curves of the Upper Paleozoic sandstone reservoir in the Daniudi gas field, Ordos Basin.

Fm	Displacement pressure (Mpa)		Median capillary pressure ($\times10^{-3}\mu m^2$)		Median throat radius (μm)		Maximum throat radius (μm)		Throat sorting coefficient (μm)	
	Range	Average	Range	Average	Range	Average	Range	Average	Range	Average
Xiashihezi (P_1x)	0.01–10	0.85	1.04–106.27	32.84	0.007–0.705	0.12	0.41–74.24	6.43	0.95–5.86	3.42
Shanxi (P_1s)	0.08–40	0.95	1.89–112.1	36.8	0.007–0.57	0.075	0.57–12.03	3.53	1.23–5.95	3.7
Taiyuan (C_3t)	0.25–2.5	1.15	1.7–89.2	19.67	0.014–0.64	0.21	0.294–1.05	0.73	2.41–5.15	3.23

mudstones of the Taiyuan Fm suggest moderately–highly favourable source rocks. The dark mudstones and coals in the Second Member of the Taiyuan Fm have organic abundance indexes higher than those of the First Member and are also a better type. However, because coal rocks are distributed in a small area, their potential to generate hydrocarbon is lower than that of the First Member. The organic abundance of the dark mudstones in the Xiashihezi Fm is slightly higher than that of the Taiyuan Fm, while the organic abundance of coal in the Xiashihezi Fm is slightly lower than that of the Taiyuan Fm. In the plan view, the dark mudstones in the Shanxi Fm have a TOC that is generally higher in the west and lower in the east, and the coals have a TOC that is lower in the centre and higher in the periphery. The dark mudstones in the Shanxi Fm have slightly lower organic abundance indexes, and the strata almost no coal. The Xiashihezi Fm dark mudstones have a TOC that is mostly lower than 0.5% and its organic abundance obviously lower than those of the Taiyuan Fm and the Shanxi Fm, thereby reflecting that the main hydrocarbon-generating horizons of the upper Paleozoic in the Daniudi gas field are Taiyuan and Shanxi Fm source rocks.

The upper Paleozoic tight sandstone gas in the Daniudi gas field is composed of alkane and minor non-hydrocarbon gases (Table 4). The alkane content ranges from 82.5% to 95.8%, the C_{2-5} content ranges from 2.2% to 15.3%, and the non-hydrocarbon gases mainly include CO_2 and H_2, with a content of <5%. The methane content has a positive correlation to aridity coefficient, and the aridity coefficient (C1/C1-4) ranges from 0.845 to 0.977. Natural gas in the Xiashihezi Fm is dry gas, with an aridity coefficient of >0.95, while natural gas in the Taiyuan and Shanxi Fms are comparatively humid, with aridity coefficients of <0.95. The strata near source rocks in Shanxi Fm exhibit greatly increased wet content, thereby reflecting favourable fractionation effects and a high content of near-source heavy hydrocarbon gas. The C isotopic value of methane in the Upper Paleozoic tight sandstone gas varies mainly from −37‰ to −34‰, the C isotopic value of ethane ranges from −26.5‰ to −23.5‰ and the Ro value ranges from 0.5% to 1.5%. Compared with the tight gas in the Sulige and Jingbian gas fields, tight gas in the Daniudi gas field has an obviously lower aridity coefficient, and natural gas is mainly controlled by thermal maturity and not mixed with biogas (Zhao et al., 2014; Yang et al., 2016).

5 Discussion

5.1 Burial and thermal maturity history of source rocks

Since the Mesozoic, the Ordos Basin has tectonically undergone three periods, i.e., development of gentle, flat structures in the middle Triassic (Indosinian movement period), development of paleo-uplifts in the late Triassic–early Cretaceous (Yanshan movement period) and formation of present-day slopes (Xishan movement period) (Yang et al., 2005; Liu et al., 2016; He et al., 2019). In the late Triassic, the basin quickly subsided, which greatly increased the paleo-geothermal gradient to 33°C–48°C/km. In the late Early Cretaceous, after the strata reached maximum burial depth, they were uplifted, leading to decreased geothermal gradient and formation temperature.

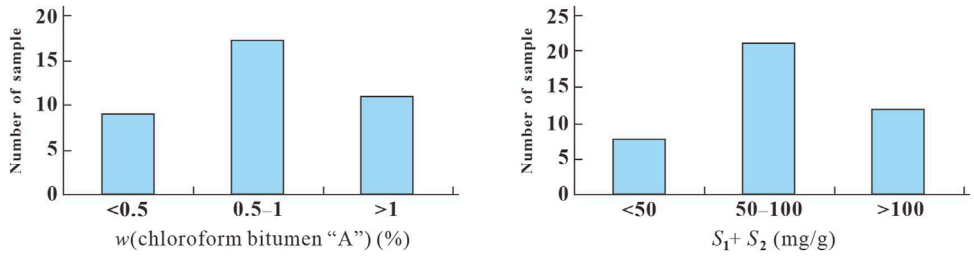

FIGURE 6
The distribution characteristics of organic matter richness index of the Upper Paleozoic coal rocks in the Daniudi gas field. The indexes indicate that the coal rocks are of high quality as source rocks.

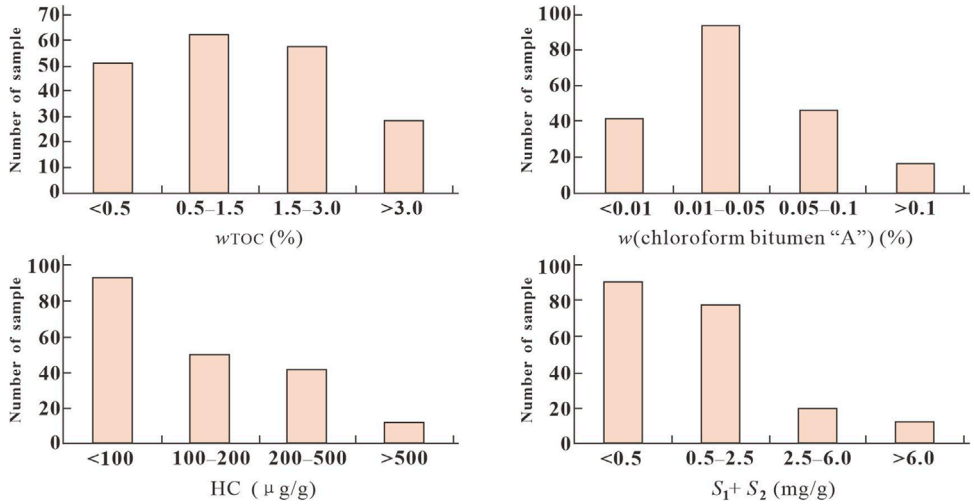

FIGURE 7
The distribution characteristics of organic matter richness index of the Upper Paleozoic dark mudstones in the Daniudi gas field. These indexes suggest that dark mudstones contribute to hydrocarbon generation and are of moderately–highly favourable source rocks.

TABLE 3 The organic matter richness of the Upper Paleozoic source rocks of various interval of the Daniudi gas field.

Fm	Lithology	*w* (TOC) (%)		*w* (chloroform bitumen "A") (%)		Total hydrocarbon (μg/g)		S_1+S_2 (mg/g)	
		Range	Average	Range	Average	Range	Average	Range	Average
P_1x^1	Dark mudstones	0.15–2.35	0.85	0.004–0.07	0.02	12–295	85	0.05–1.7	0.5
P_1s^2	Dark mudstones	0.075–8.45	1.25	0.004–0.18	0.03	15–1,490	130	0.01–10.4	0.85
P_1s^1	Dark mudstones	0.42–13.82	2.3	0.008–0.55	0.06	35–1995	207	0.12–27.4	2
	Coal rocks	18.85–84.5	58.5	0.25–1.95	0.8	615–7,287	3,327	11.1–208	82.5
C_3t^2	Dark mudstones	1.05–7.75	2.85	0.02–0.3	0.075	60–665	290	0.4–13.8	2.2
	Coal rocks	63–84.5	71	0.35–2.5	1.15	1,555–9,740	4,095	63.4–259	145
C_3t^1	Dark mudstones	0.25–10.1	1.75	0.006–0.15	0.035	15–720	165	0.04–4.5	0.6
	Coal rocks	20.5–76.5	63	0.38–1.25	0.77	1955–4,570	3,007	19.2–152	95.5

TABLE 4 Chemical and stable isotopic compositions of natural gas from the Upper Paleozoic reservoir in the Daniudi gas field.

Well	Fm	Chemical composition (%)								$\delta^{13}C$ (‰, PDB)				
		CH_4	C_2H_6	C_3H_8	iC_4H_{10}	nC_4H_{10}	H_2	CO_2	N_2	CH_4	C_2H_6	C_3H_8	iC_4H_{10}	nC_4H_{10}
D16	P_1x^3	95.7	3.5	0.1	0.07	0.09	0.01	0.37	1.2	−37.6	−28.8	−25.7	−23.7	−24.8
DK3	P_1x^3	92.7	4.9	0.6	0.13	0.18	0.01	0.42	0	−37.7	−27.3	−24.3	−25.6	−24.1
D66	P_1x^3	95.5	2.9	0.1	0.06	0.06	0.02	0.09	0	−38.8	−28.1	−23.8	−23.1	−23.2
D21	P_1x^2	92.3	4.6	0.6	0.13	0.17	0.02	0.41	0.2	−38.5	−28.6	−25.0	−24.7	−24.0
D29	P_1x^2	86.7	7.9	2.0	0.29	0.38	0.03	0.55	0.2	−37.7	−27.7	−22.8	−22.3	−21.8
DK3	P_1x^1	83.7	3.8	0.3	0.07	0.12	0.01	0.12	1.8	−37.3	−27.8	−24.3	−24.8	−24.2
D11	P_1x^1	89.3	7.2	1.4	0.27	0.35	0.02	0.65	0.1	−40.2	−27.9	−25.5	−25.4	−24.1
D66	P_1x^1	86.8	8.9	1.7	0.18	0.28	0.01	0.42	0	−40.5	−27.2	−23.2	−23.7	−22.7
D24	P_1s^2	85.8	7.2	1.6	0.39	0.59	0.01	0.33	1.5	−39.7	−27.7	−25.1	−23.5	−22.6
D12	P_1s^2	87.7	7.7	1.6	0.28	0.27	0.02	0.65	0	−38.8	−26.5	−23.5	−23.1	−21.7
DK2	P_1s^2	85.9	8.9	2.0	0.38	0.35	0.01	0.78	0	−39.1	−26.0	−24.1	−22.9	−22.0
D15	P_1s^2	87.3	6.4	2.1	0.37	0.37	0.03	0.65	0	−36.3	−26.8	−23.1	−22.3	−21.6
D22	P_1s^2	87.1	8.1	1.7	0.29	0.28	0.01	0.91	0	−38.6	−27.3	−24.7	−23.2	−22.7
D18	P_1s^2	86.9	7.9	2.0	0.38	0.39	0.02	0.82	0	−38.0	−27.1	−25.1	−22.4	−21.7
D14	P_1s^2	89.3	5.9	1.0	0.18	0.21	0.01	1.85	0	−36.1	−26.8	−24.2	−22.7	−21.3
D23	P_1s^1	88.7	6.7	0.7	0.11	0.17	0.01	2.35	0	−37.3	−26.7	−24.3	−22.6	−21.5
D11	P_1s^1	95.2	3.1	0.1	0.06	0.07	0.01	0.25	0	−37.8	−28.2	−23.7	−23.9	−22.1
D22	C_3t^2	88.7	6.6	1.0	0.18	0.17	0.05	2.11	0	−39.7	−27.3	−24.1	−21.9	−21.6
D35	C_3t^2	88.3	6.7	1.1	0.21	0.18	0.12	1.98	0	−39.3	−27.2	−25.4	−22.7	−21.5
D47	C_3t^2	88.8	6.0	1.3	0.27	0.27	0.04	0.73	0	−39.5	−28.1	−23.6	−23.5	−23.2

Stratigraphic and tectonic evolutions are comparatively consistent within the Daniudi gas field. According to the thermal maturity history analysis of typical wells (Figure 8), the upper Paleozoic source rocks within the gas field mainly underwent three stages of thermal evolution history, including late Triassic, late Jurassic and Cretaceous–late Paleocene. At the end of the Triassic, the bottom of the Taiyuan Fm had a burial depth of up to 2,500 m, and the source rocks in the bottom entered the maturity threshold, started hydrocarbon generating evolution and subsequently suffered from tectonic uplifting; however, the uplifted denudation volume was small. In Jurassic, source rocks entered the second stage of hydrocarbon generation evolution, evolving into a mature stage with the Ro value reaching up to 1.0%, and then starting to generate a massive amount of hydrocarbon. As a result of the continuous subsidence and sedimentation in the early Cretaceous, source rocks continued their hydrocarbon generation evolution and their Ro values evolved to 1.3% in Carboniferous. Under the fast subsidence and sedimentation during the Late Cretaceous–Paleocene, the source rocks evolved quickly, generated hydrocarbon and entered the third hydrocarbon generation evolution stage, having Ro values exceeding 1.5% and reaching a highly mature stage. Eocene tectonic uplifting terminates the source rock evolution even up to the present. The maximum burial depth of the reservoir was 3,800–4,000 m, and the formation temperature decreased from 170°C to 190°C to the present 80°C–90°C.

5.2 Diagenetic evolution and reservoir densification process

The upper Paleozoic coal-measure source rocks of the Daniudi gas field have high thermal maturities with Ro mainly varying from 1.2% to 1.5% and Tmax ranging from 460°C to 480°C. The primary pores in the reservoir are hardly exist, the reservoir spaces are minor

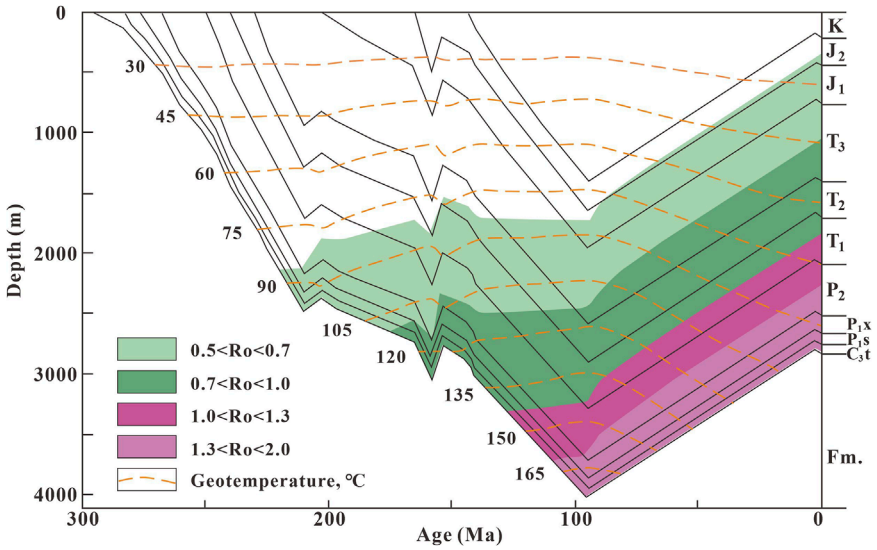

FIGURE 8
Burial history, geothermal history, and maturity history of the strata in the Daniudi Gas Field. The upper Paleozoic source rocks within the gas field mainly underwent three stages of thermal maturity history, including late Triassic, late Jurassic and Cretaceous–late Paleocene.

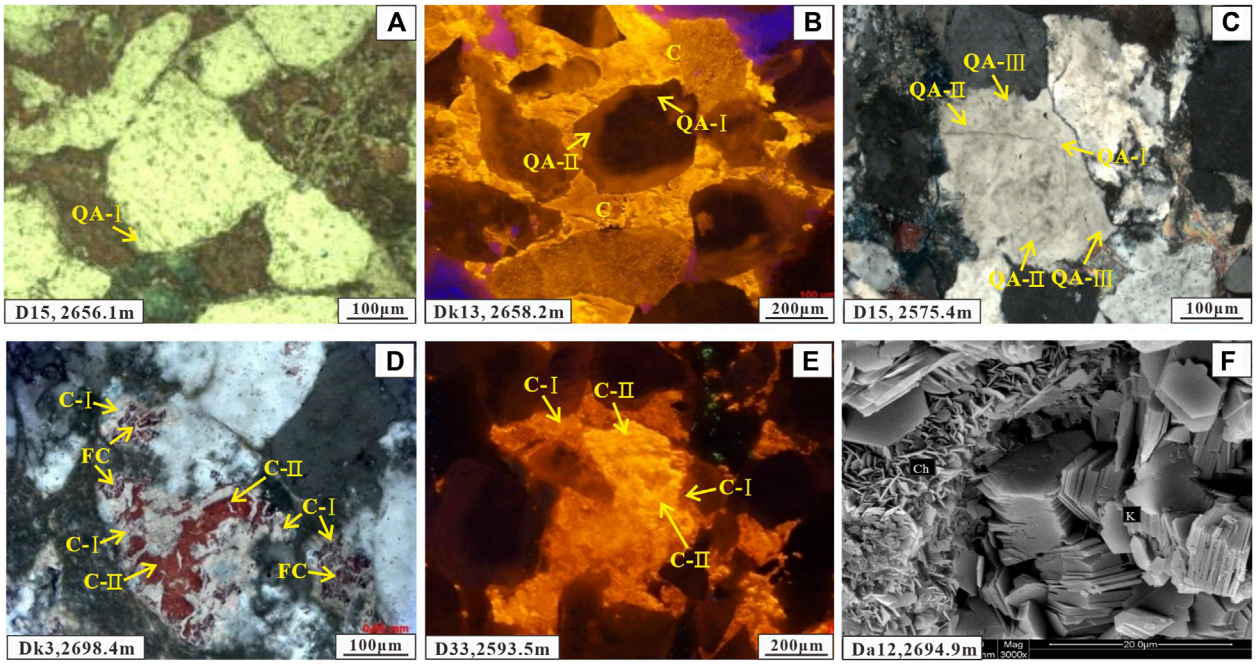

FIGURE 9
The characteristics of cements in the Upper Paleozoic tight sandstone reservoirs. Note: **(A)**, Stage I quartz overgrowth, Single Nicol; **(B)**, Stage II quartz overgrowth unevenly encircled quartz grains, Cathodoluminescence image; **(C)**, Three stages of quartz overgrowth, Crossed Nicol; **(D)**, Carbonate cements formed in two stages, Crossed Nicol; **(E)**, Two stages of carbonate cements, Cathodoluminescence image; **(F)**, kaolinite and chlorite occlude primary pores, SEM image. Q–quartz; QA–authigenic quartz; K–kaolinite; Ch–chlorite; C–calcite.

secondary dissolution pores and microfractures, and the porosities are less than 10%. Clay minerals of the reservoir are dominated by illite/smectite formation, with secondary kaolinite and chlorite; the degree of order of illite/smectite formation varies from 15% to 30%. According to China's criteria for classification of diagenetic stages of clastic rocks (SY/T 5477-2003), the reservoir is mainly in the middle diagenetic Stage B. The upper Paleozoic sandstone reservoir in the Daniudi gas field underwent complicated diagenetic evolution; the main causes of reservoir densification include long-term mechanical compaction and multistage of siliceous and calcite cementation.

FIGURE 10
Diagenetic evolution sequence of the Upper Paleozoic sandstone reservoirs in the Daniudi Gas Field. The upper Paleozoic tight sandstone reservoir in the Daniudi gas field underwent complicated diagenetic evolution, generally including fast burial compaction, diagenetic evolution in acid–alkaline fluid environments and strongly cemented densification stages.

The upper Paleozoic sandstone reservoir has a maximum burial depth of up to 4,000 m and underwent long-term intense compaction. This condition is mainly expressed by the elongated and bent epimetamorphic lithic fragments, the clastic grains orientated in linear or concavo-convex contacts and observable cracks on the surface of some rigid grains. Calculation indicates that the reservoir compaction rate varies from 22.2% to 97.5% and the loss ratio of pores varies from 7.56% to 33.15% with an average of 25.3%. The reservoir has multistage siliceous and calcareous cements as well as minor clay mineral cements, which further compact the reservoir. Microscopic observation indicates that quartz has typical three stages of overgrowth. Stage I quartz overgrowth occurs in one side of the quartz grains (Figure 9A) with small widths (<0.02 mm) and minor quantity; inclusions inside the overgrowth have a homogenisation temperature of 78°C. Stage II quartz overgrowth surrounds the quartz grains (Figure 9B), with large widths and automorphic crystal faces; inclusions inside the overgrowth have a homogenisation temperature of 91.6°C. Stage III quartz overgrowth is mostly in zigzag or sutured linear contacts, with two stages of dust line (Figure 9C); the overgrowth occupies almost all residual intergranular pores, with widths of >0.05 mm and basically no automorphic crystal faces; inclusions have homogenisation temperatures of 112.4°C. The calcareous cement types include early-stage carbonate cements, such as calcite and dolomite, and late-stage carbonate cements, such as ferrocalcite and ferrodolomite (Figure 9D). Microscopic observation indicates

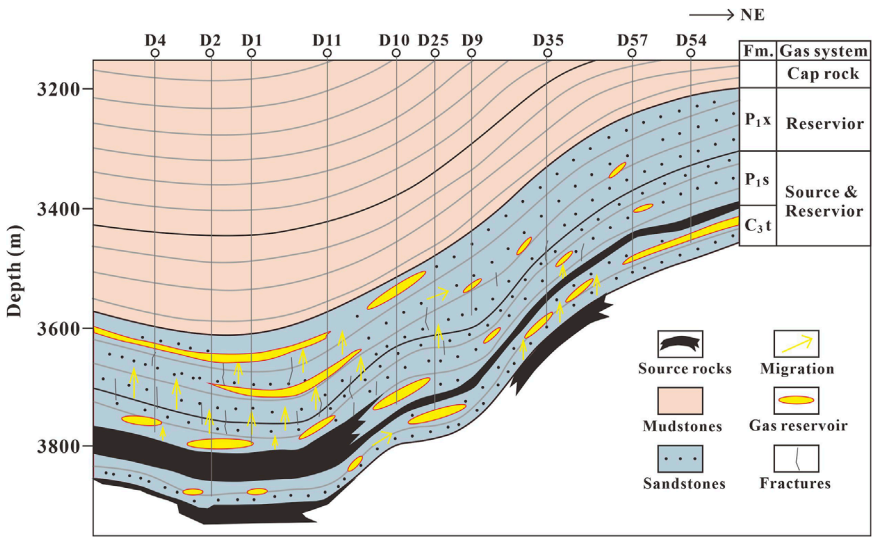

FIGURE 11
Gas accumulation model of the Upper Paleozoic tight sandstones in the Daniudi Gas Field, Ordos Basin.

that the reservoir has two obvious stages of calcareous cement: Stage I cements are mainly calcite in intergranular pores, which usually occur as thin films along pores and appear yellow in cathode luminescence; Stage II cements are mainly calcite and ferrocalcite in intergranular pores; as a result of the high Fe ion content, the cements show a bright colour (generally bright yellow) in CL, which are greatly different from early-stage cements (Figure 9E). In addition, intergranular pores are filled with argillaceous material and autogenic clay minerals, which is also an important factor for reservoir densification (Figure 9F).

The upper Paleozoic tight sandstone reservoir in the Daniudi gas field underwent complicated diagenetic evolution (Figure 10), including fast burial compaction, diagenetic evolution in acid–alkaline fluid environments and strongly cemented densification stages. Compaction in the early diagenetic B stage decreased the reservoir porosity by 15%–20%. Quartz overgrowth formed from the early diagenetic B stage to the middle diagenetic A_2 stage under formation temperatures of 80°C–130°C and an acid fluid environment, decreasing the porosity by 5%–10%. Carbonate cements usually occurred when the fluid environment turned alkaline after quartz enlargement rims were formed, which decreased the porosity by 3%–5%. The finalisation of reservoir densification is ~140 Ma BP (early Cretaceous), the formation temperature was ~130°C and Ro was 0.8%. Under intense diagenetic reworking, reservoir properties showed very strong anisotropism in space, and natural gas in the reservoir hardly migrated because of buoyancy.

5.3 Formation of gas reservoir

Natural gas that has been extracted from the upper Paleozoic in the Daniudi gas field is mostly high-maturity coal-generated gas and mainly composed of CH_4 (Yang et al., 2010; Li et al., 2016). According to the C isotope assay results of CH_4, the two major gas pay zones in the Daniudi gas field have greatly different CH_4 $\delta^{13}C$ values (Figure 10; Table 4). In the gas reservoirs of the Xiashihezi Fm in the southwest, methane has $\delta^{13}C$ ranging from −36.15‰ to −33.28‰, representing high-maturity natural gas; while in the gas reservoir of the Taiyuan Fm in the northeast, methane gas has low $\delta^{13}C$, ranging from −39.02‰ to −36.58‰, representing low-maturity natural gas. This phenomenon indicates that the two major gas pay zones in the Daniudi gas field have different natural gas accumulation processes. According to the natural gas generation–migration history of the upper Paleozoic in the study area, gas accumulation can be classified into two types, i.e., self-sourced and near-source accumulations.

Self-sourced accumulation mainly occurs in the Taiyuan and Shanxi Fms; in the sedimentary evolution system from barrier coast–tidal flat to delta, the reservoirs mainly include barrier bar sands and distributary channel sands (Liu et al., 2019), and the cap rock is the mudstone in the coal-measure strata, forming a self-generation and self-accumulation system with coal rocks within the interval and dark mudstones. Natural gas that was generated from gas generation centres in the Shanxi and Taiyuan Fm entered the reservoirs quickly. Barrier bar reservoirs have favourable physical properties; thus, continuous natural gas plumes can be formed, providing sufficient buoyancy for natural gas lateral migration. Natural gas migrated towards the northeastern Daniudi gas field and accumulated in favourable lithologic traps. Natural gas accumulation in this stage occurs earlier than the formation of tight reservoirs. Near-source accumulations Near-source accumulation mainly occurs in the Xiashihezi Fm. The source rocks are the underlying Taiyuan Fm and Shanxi Fm coal-measure source rocks; the reservoirs are mainly fluvial facies sands, and the overlying Shangshihezi Fm hugely thick mudstone and the mudstone adjoining reservoirs are the cap rock, forming a lower-generation, upper-accumulation combination. After tight

sandstone reservoirs were formed, massive high-maturity gases were generated. However, natural gas migration was difficult because of poor reservoir physical properties and high capillary force. Fractures that formed in the late Cretaceous stratigraphic uplifting provided access for natural gas migration. Natural gas migrated vertically through these fracture beds and accumulated in sandstones with developed fractures. In accordance with the geologic conditions, transportation system, natural gas accumulation tracer, migration force and generation–accumulation combination, the accumulation model of the upper Paleozoic tight sandstone gas reservoir was proposed (Figure 11). Generally, in the period of the Shanxi Fm and Taiyuan Fm, favourable lithologic traps near gas generation centres are the areas with the highest exploration potential.

6 Conclusion

The upper Paleozoic sandstone reservoir in the Daniudi gas field experienced long-term compaction, multistage quartz cementation and carbonate cementation, which caused the densification of the sandstones. The reservoir has porosity varying from 2% to 12%, with an average of 6.9%, and permeability varying from 0.01×10^{-3} μm^2 to 10×10^{-3} μm^2, with an average of 0.76×10^{-3} μm^2. In various gas layers, reservoirs in the Mbr 2 and Mbr 3 of the Xiashihezi Fm have comparatively favourable properties.

The upper Paleozoic source rocks of the Daniudi gas field are principally coal rocks and dark mudstones; the source rocks are mainly developed in the Taiyuan and Shanxi Fms, the organic type is dominated by III and the source rocks are basically in a highly mature stage. Source rocks of the study area mainly underwent the late Triassic, late Jurassic and Cretaceous–late Paleocene. Thick-bedded source rocks are chiefly distributed in the southwest of the study area, and the Taiyuan and Shanxi Fms source rocks have the maximum quantity of hydrocarbon generation.

In accordance with the coupling relationship between upper Paleozoic sandstone densification and gas generation–accumulation process in the Daniudi gas field, the formation of tight sandstone gas reservoirs can be classified into two types: self-sourced and near-source accumulations. In the period of the Shanxi Fm and Taiyuan Fm, before sandstone reservoir densification occurred, low-maturity natural gas generated from coal rocks and dark mudstones quickly entered the reservoir, migrated northeastwards along conducting sands driven by buoyancy and accumulated in favourable lithologic traps. In the period of Xiashihezi Fm, the tight sandstone reservoir formed; high-maturity natural gas migrated along late Cretaceous fractures and accumulated in the nearby reservoir with abundant microfractures.

Data availability statement

The original contributions presented in the study are included in the article/Supplementary material, further inquiries can be directed to the corresponding author.

Author contributions

FS: Conceptualization, Funding acquisition, Methodology, Supervision, Writing–original draft, Writing–review and editing. QK: Methodology, Writing–review and editing, Software. NS: Investigation, Project administration, Validation, Visualization, Writing–original draft, Conceptualization, Funding acquisition. GJ: Resources, Supervision, Visualization, Conceptualization, Funding acquisition, Methodology, Project administration, Writing–review and editing. MX: Methodology, Validation, Software, Writing–review and editing.

Funding

The author(s) declare financial support was received for the research, authorship, and/or publication of this article. This study was co-funded by the National Natural Science Foundation of China (41702158), the Natural Science Foundation of Shandong Province (ZR2022MD014) and the Fundamental Research Funds for the Central Universities (18CX02057A).

Conflict of interest

Author GJ was employed by Xinchun Petroleum Development Limited Company, SINOPEC.

The remaining authors declare that the research was conducted in the absence of any commercial or financial relationships that could be construed as a potential conflict of interest.

Publisher's note

All claims expressed in this article are solely those of the authors and do not necessarily represent those of their affiliated organizations, or those of the publisher, the editors and the reviewers. Any product that may be evaluated in this article, or claim that may be made by its manufacturer, is not guaranteed or endorsed by the publisher.

References

Cai, C. F., Hu, G. Y., He, H., Li, J., Li, J. F., and Wu, Y. S. (2005). Geochemical characteristics and origin of natural gas and thermochemical sulphate reduction in Ordovician carbonates in the Ordos Basin, China. *J. Petroleum Sci. Eng.* 48, 209–226. doi:10.1016/j.petrol.2005.06.007

Dai, J. X., Li, J., Ding, W. W., Hu, G. Y., Luo, X., Tao, S. Z., et al. (2005). Gas geochemical characteristics on the gas fields reserves of over one hundred billion cubic meters in China. *Petroleum Explor. Dev.* 32, 16–22.

Fu, J. H., Wei, X. S., and Nan, J. X. (2013). Characteristics and origin of reservoirs of gas fields in the Upper Paleozoic tight sandstone, Ordos Basin. *J. Palaeogeogr.* 15, 529–538. (in Chinese with English abstract). doi:10.7605/gdlxb.2013.04.042

He, C., Ji, L. M., Su, A., Wu, Y. D., Zhang, M. Z., Zhou, S. X., et al. (2019). Source-rock evaluation and depositional environment of black shales in the Triassic Yanchang Formation, southern Ordos Basin, north-central China. *J. Petroleum Sci. Eng.* 173, 899–911. doi:10.1016/j.petrol.2018.10.089

Islam, M. A. (2009). Diagenesis and reservoir quality of bhuban sandstones (neogene), titas gas field, bengal basin, Bangladesh. *J. Asian Earth Sci.* 35, 89–100. doi:10.1016/j.jseaes.2009.01.006

Karim, A., Piper, P. G., and Piper, J. W. D. (2010). Controls on diagenesis of lower cretaceous reservoir sandstones in the western sable subbasin, offshore nova scotia. *Sediment. Geol.* 224, 65–83. doi:10.1016/j.sedgeo.2009.12.010

Lan, C. L., Yang, M. H., and Zhang, Y. Z. (2016). Impact of sequence stratigraphy, depositional facies and diagenesis on reservoir quality: a case study on the Pennsylvanian Taiyuan sandstones, northeastern Ordos Basin, China. *Mar. Petroleum Geol.* 69, 216–230. doi:10.1016/j.marpetgeo.2015.09.009

Li, J., Li, J., Li, Z. S., Wang, D. L., Gong, S., Zhang, Y., et al. (2014). The hydrogen isotopic characteristics of the Upper Paleozoic natural gas in Ordos Basin. *Org. Geochem.* 74, 66–75. doi:10.1016/j.orggeochem.2014.01.020

Li, M., Hou, Y. D., Luo, J. L., Chen, J. P., Luo, X. R., and Jia, Y. N. (2016). Burial, diagenesis, hydrocarbon charging evolution process and quantitative analysis of porosity evolution: a case study from He 8 tight sand gas reservoir of the Upper Paleozoic in Eastern Ordos Basin. *Oil Gas Geol.* 37, 882–892. (in Chinese with English abstract). doi:10.11743/ogg20160610

Liu, D., Zhang, W. Z., Kong, Q. F., Feng, Z. Q., Fang, C. C., and Peng, W. L. (2016). Lower Paleozoic source rocks and natural gas origins in Ordos Basin, NW China. *Petroleum Explor. Dev.* 43, 591–601. doi:10.1016/s1876-3804(16)30069-6

Liu, D. K., Sun, W., Ren, D. Z., and Li, C. Z. (2019). Quartz cement origins and impact on storage performance in Permian Upper Shihezi Formation tight sandstone reservoirs in the northern Ordos Basin, China. *J. Petroleum Sci. Eng.* 178, 485–496. doi:10.1016/j.petrol.2019.03.061

Liu, Q. Y., Jin, Z. J., Meng, Q. Q., Wu, X. Q., and Jia, H. C. (2015). Genetic types of natural gas and filling patterns in Daniudi gas field, Ordos Basin, China. *J. Asian Earth Sci.* 107, 1–11. doi:10.1016/j.jseaes.2015.04.001

Lu, J. H., and Miao, J. J. Q. Q. (2018). Analysis of the hydrocarbon generation potential of Carboniferous-Permian source rocks of the Daniudi gas field. *J. Geol.* 42, 60–69. (in Chinese with English abstract). doi:10.3969/j.issn.1674-3636.2018.01.009

Ren, Z. L., Zhang, S., Gao, S. L., Cui, J. P., Xiao, Y. Y., and Xiao, H. (2007). Tectonic thermal evolution history of the Ordos basin and its hydrocarbon accumulation significance. *Sci. China. Ser. D.* 37, 23–32.

Su, N. N., Song, F., Qiu, L. W., Chen, S. Y., and Zhang, N. (2016). Diagenetic evolution of tight sandstone reservoir in lower Shihezi formation from Daniudi gas field. *J. Central South Univ.* 47, 3555–3561. (in Chinese with English abstract). doi:10.11817/j.issn.1672-7207.2016.10.036

Sun, L. D., Zou, C. N., Jia, A. L., Wei, Y. S., Zhu, R. K., Wu, S. T., et al. (2019). Development characteristics and orientation of tight oil and gas in China. *Petroleum Explor. Dev.* 46, 1073–1087. doi:10.1016/s1876-3804(19)60264-8

Wang, J. L., Feng, L. Y., Steve, M., Xu, T., Gail, T., and Mikael, H. (2015). China's unconventional oil: a review of its resources and outlook for long-term production. *Energy* 82, 31–42. doi:10.1016/j.energy.2014.12.042

Wu, X. Q., Liu, Q. Y., Zhu, J. H., Li, K., Liu, G. X., Chen, Y. B., et al. (2017). Geochemical characteristics of tight gas and gas-source correlation in the Daniudi gas field, the Ordos Basin, China. *Mar. Petroleum Geol.* 79, 412–425. doi:10.1016/j.marpetgeo.2016.10.022

Xi, K. L., Cao, Y. C., Jahren, J., Zhu, R. K., Bjørlykke, K., Haile, B. G., et al. (2015). Diagenesis and reservoir quality of the lower cretaceous quantou formation tight sandstones in the southern songliao basin, China. *Sediment. Geol.* 330, 90–107. doi:10.1016/j.sedgeo.2015.10.007

Yang, H., and Liu, X. S. (2014). Progress in paleozoic coal-derived gas exploration in the Ordos Basin, west China. *Petroleum Explor. Dev.* 41, 144–152. doi:10.1016/s1876-3804(14)60017-3

Yang, R. C., Fan, A. P., Han, Z. Z., and Wang, X. P. (2012). Diagenesis and porosity evolution of sandstone reservoirs in the East II part of Sulige gas field, Ordos Basin. *Int. J. Min. Sci. Technol.* 22, 311–316. doi:10.1016/j.ijmst.2012.04.005

Yang, Y. T., Li, W., and Ma, L. (2005). Tectonic and stratigraphic controls of hydrocarbon systems in the Ordos Basin: a multicycle cratonic basin in central China. *AAPG Bull.* 89, 255–269. doi:10.1306/10070404027

Yang, Z., He, S., Guo, X. W., Li, Q. Y., Chen, Z. Y., and Zhao, Y. C. (2016). Formation of low permeability reservoirs and gas accumulation process in the Daniudi gas field, northeast Ordos Basin, China. *Mar. Petroleum Geol.* 70, 222–236. doi:10.1016/j.marpetgeo.2015.10.021

Yang, Z., He, S., Zou, C. N., Li, Q. Y., and Chen, Z. Y. (2010). Coupling relationship between reservoir diagenesis and natural gas accumulation of Daniudi gas field in north Ordos Basin. *Acta Pet. Sin.* 31, 372–385. (in Chinese with English abstract).

Zhang, J. L., Chang, X. C., and Zhang, J. G. (2000). Deep basin gas reservoir research in Upper Paleozoic formation in Ordos basin. *Petroleum Explor. Dev.* 27, 30–35.

Zhang, L. P., Luo, X. R., Ma, X. H., Chen, M. J., and Wu, M. H. (2007). Diagenetic trap in deep basin gas: taking Yulin gas field in Ordos basin as an example. *Chin. Sci. Bull.* 52, 679–687.

Zhao, J. Z., Fu, J. H., Yao, J. L., Liu, X. S., Wang, H. E., Cao, Q., et al. (2012). Quasi-continuous accumulation model of large tight sandstone gas field in Ordos Basin. *Acta Pet. Sin.* 33, 37–52. (in Chinese with English abstract).

Zhao, J. Z., Zhang, W. Z., Li, J., Cao, Q., and Fan, Y. F. (2014). Genesis of tight sand gas in the Ordos Basin, China. *Org. Geochem.* 74, 76–84. doi:10.1016/j.orggeochem.2014.03.006

Zou, C. N., Tao, S. Z., and Fang, X. (2009). *Formation and distribution of large size oil and gas zone*. Beijing: Science Press.

Zou, C. N., Yang, Z., Tao, S. Z., Yuan, X. J., Zhu, R. K., Hou, L. H., et al. (2013). Continuous hydrocarbon accumulation over a large area as a distinguishing characteristic of unconventional petroleum: the Ordos Basin, North-Central China. *Earth-Science Rev.* 126, 358–369. doi:10.1016/j.earscirev.2013.08.006

frontiers | Frontiers in Earth Science

TYPE Original Research
PUBLISHED 06 February 2024
DOI 10.3389/feart.2024.1363309

Check for updates

OPEN ACCESS

EDITED BY
Wenguang Wang,
Northeast Petroleum University, China

REVIEWED BY
Yang Wang,
Chang'an University, China
Zaitian Dong,
Liaoning Technical University, China
Bingshan Ma,
Southwest Petroleum University, China

*CORRESPONDENCE
Luxing Dou,
luxingdou@yangtzeu.edu.cn
Zhigang Wen,
wzg728@sina.com

RECEIVED 30 December 2023
ACCEPTED 16 January 2024
PUBLISHED 06 February 2024

CITATION
Wu X, Shen Z, Bao Y, Wang W, Yan Z, Wang B, Zheng X, Dou L and Wen Z (2024), Diagenetic alterations and deep high-quality reservoirs within deltaic distributary channel facies: a case study from the Permian Shihezi formation in the Hongde area, southwestern Ordos basin, China.
Front. Earth Sci. 12:1363309.
doi: 10.3389/feart.2024.1363309

COPYRIGHT
© 2024 Wu, Shen, Bao, Wang, Yan, Wang, Zheng, Dou and Wen. This is an open-access article distributed under the terms of the Creative Commons Attribution License (CC BY). The use, distribution or reproduction in other forums is permitted, provided the original author(s) and the copyright owner(s) are credited and that the original publication in this journal is cited, in accordance with accepted academic practice. No use, distribution or reproduction is permitted which does not comply with these terms.

Diagenetic alterations and deep high-quality reservoirs within deltaic distributary channel facies: a case study from the Permian Shihezi formation in the Hongde area, southwestern Ordos basin, China

Xiaoming Wu[1,2,3], Zhicheng Shen[3], Yanxin Bao[3], Weilin Wang[3], Zhandong Yan[3], Bo Wang[3], Xiaoyin Zheng[4], Luxing Dou[1,2]* and Zhigang Wen[1,2]*

[1]College of Resources and Environment, Yangtze University, Wuhan, China, [2]Key Laboratory of Exploration Technologies for Oil and Gas Resources, Ministry of Education, Yangtze University, Wuhan, China, [3]No. 7 Oil Production Plant, PetroChina Changqing Oilfield Company, Xian, China, [4]Technology Development Department, XMotors.ai Inc., Santa Clara, CA, United States

Deep tight gas reservoirs are considered important hydrocarbon exploration targets. High-quality reservoir prediction is critical for successfully exploring and developing deeply buried tight sandstone gas. Previous research has found that the reservoir quality of deeply buried tight sandstones is controlled by diagenesis and sedimentary facies. However, the variation of diagenetic alterations in different facies is still poorly studied on deltaic tight gas sandstone. In this study, core analysis, wireline log data, and 3D seismic were studied for the characterization of diagenetic alterations and sedimentary facies. The tight sandstones were formed in braided river delta deposits. Gravel-bearing coarse-grained sandstone facies and cross-bedded sandstone facies developed in tight sandstones. The Gravel-bearing coarse-grained sandstone is formed in the mid-channel bar of deltaic distributary channels. The major diagenetic processes developed in the tight sandstone include compaction, cementation, and dissolution. Constructive diagenesis can generate secondary pores, mainly including dissolution and kaolinite metasomatism, which can effectively improve reservoir physical properties. Through the diagenesis alterations linked to different lithofacies in cored wells, there are obvious diagenesis variations in different lithofacies. Despite strong compaction, the reservoirs in coarse sandstone facies have developed internal dissolution. After compaction, cementation, and dissolution to increase porosity, the reservoir retains intergranular and secondary pores and forms relatively high-quality reservoirs. The fine sandstone facies with cross-bedding are strongly compacted, with internal ductile particles being compacted and deformed, and the particle orientation is clearly arranged. The reservoir is tight, and the development of dissolution in the reservoir is weak, resulting in poor reservoir quality. In addition, reservoirs located at the interface between sandstone and mudstone are often affected by diagenesis, resulting in the

development of calcareous cementation, leading to poor reservoir quality. Therefore, high-quality reservoirs are mostly distributed in coarse sand lithofacies, mainly distributed in the mid-channel bar of distributary channel deposits. Sedimentary facies control the original physical properties of the reservoir with different content and texture; the quality of the original reservoir is subject to diagenetic alteration in different ways. The points in this study could offer insights better to predict deep tight reservoir quality in continental basins.

KEYWORDS

sedimentary facies, reservoir quality, tight sandstone, Shihezi formation, Ordos basin

1 Introduction

Tight sandstone gas has become one of the world's most important unconventional oil and gas resources and has huge resource reserves and broad development prospects in continental basins. However, in continental basins, tight sandstone gas reservoirs are characterized by rapid sedimentary facies change, complex sand body distribution, and strong heterogeneity of reservoir quality. In the process of production and development, there are many problems, such as low single-well productivity, great differences in gas productivity in different exploration wells, and rapid production decline. Reservoir heterogeneity strongly affects the fluid flow and recovery factors of reservoirs (Wardlaw and Taylor, 1976; Wardlaw and Cassan, 1979; Weber, 1982; Wang, et al., 2023). Therefore, in recent years, the formation mechanism of tight sandstone reservoirs and the distribution of high-quality reservoirs have been important topics of continental hydrocarbon-bearing basin exploration. According to previous studies, diagenetic alterations in sandstones are important controlling factors of the reservoir quality. Sedimentary research of reservoirs is also important as the sedimentary facies could be related to sedimentary structure, grain size, and sorting of those hydrocarbon-bearing sandstones. The spatial distribution of diagenetic alternations in different sedimentary facies is also studied (Morad et al., 2000; El-ghali et al., 2006a; El-ghali et al., 2006b; Morad et al., 2010). In continental basins, reservoirs were well developed in the delta facies. Most of the high-quality reservoirs could be developed in deltaic distributary channel facies. However, the spatial distribution of diagenetic alternations and reservoir quality within deltaic distributary channel facies is still understudied in lacustrine basins.

The Ordos Basin is China's largest oil and gas-bearing continental basin and is rich in tight gas reservoirs (Yang et al., 2005; Yang et al., 2012; Xu et al., 2018). Tight sandstone gas reservoirs have been found in the Upper Paleozoic deposits of the basin. Most of the reservoirs developed among those deposits in the Taiyuan Formation, Shanxi Formation, and Lower Shihezi Formation. In recent years, natural gas exploration has had a great breakthrough in the southwest of the Yishan Slope structural belt, Ordos Basin. In 2018, the Qingyang gas field was discovered in the southwest of the basin. The gas reservoir is developed in the upper Paleozoic fluvial-delta sandstone deposit, which belongs to the typical ultra-low permeability tight reservoir (Fu et al., 2019; Zhu et al., 2021). Recent exploration indicates that the Upper Paleozoic natural gas resources have good development potential. The efficient development of those natural gas mainly depends on the distribution model of high-quality reservoirs about the deep buried tight gas reservoirs. Therefore, the Upper Paleozoic deposits could be an analog to analyze the distribution model of high-quality reservoirs in tight sandstone.

This study focuses on the distribution of diagenetic alterations and reservoir quality within deltaic distributary channel sandstone using 3D seismic, core, and wireline log curves data. Deltaic distributary channels of the Upper Paleozoic Shihezi Formation from the proximal to distal in the Hongde area, southwestern Ordos Basin were selected as targets. The study aims were listed as follows: 1) To describe and interpret the sedimentary facies of the deltaic distributary channel deposits and horizontal distribution; 2) To get diagenesis features and alternations in lithofacies of distributary channel deposits; 3) To discuss diagenetic alterations linked to depositional lithofacies, Then, high-quality reservoir quality distribution model within deltaic distributary channel was clarified in the Lower Shihezi Formation.

2 Geological setting

The Ordos Basin is surrounded by the Yinshan Mountains in the north, the Qinling Mountains in the south, the Luliang Mountains in the east, and the Tengger Desert in the west. The basin is sub-divided into six structural units, including the Yishan slope, the Weibei uplift, the Yimeng uplift, the Western Shanxi fold belt, the Western obduction zone, and the Tianhuan depression (Figure 1). The Hongde area is in the southwest of Ordos Basin. The tectonic unit is located on the western of the Yishan slope, south of the Tianhuan depression, with the Qingyang gas field in the southeast of the area, and the Upper Paleozoic tight sandstone has great potential for natural gas exploration (Wang et al., 2016; Fu et al., 2019). The Late Paleozoic stratigraphy in the Hongde area was a set of clastic rock from the marine-continental transitional facies, with a total sedimentary rock thickness of about 700 m (Zhu S. F. et al., 2021). The Benxi Formation, the Taiyuan Formation, the Shanxi Formation, the Lower Shihezi Formation, the Upper Shihezi Formation, and the Shiqianfeng Formation were developed sequentially from the bottom up, in which the coal measure source rocks of the Benxi Formation, the Taiyuan Formation, and the Shanxi Formations continuously supplied hydrocarbons to the overlying strata (Meng et al., 2021).

The target layer in this paper is the He 8 member of the Permian Shihezi Formation, which is the major oil and gas-producing layers in this area. Previous research concluded that the sedimentary

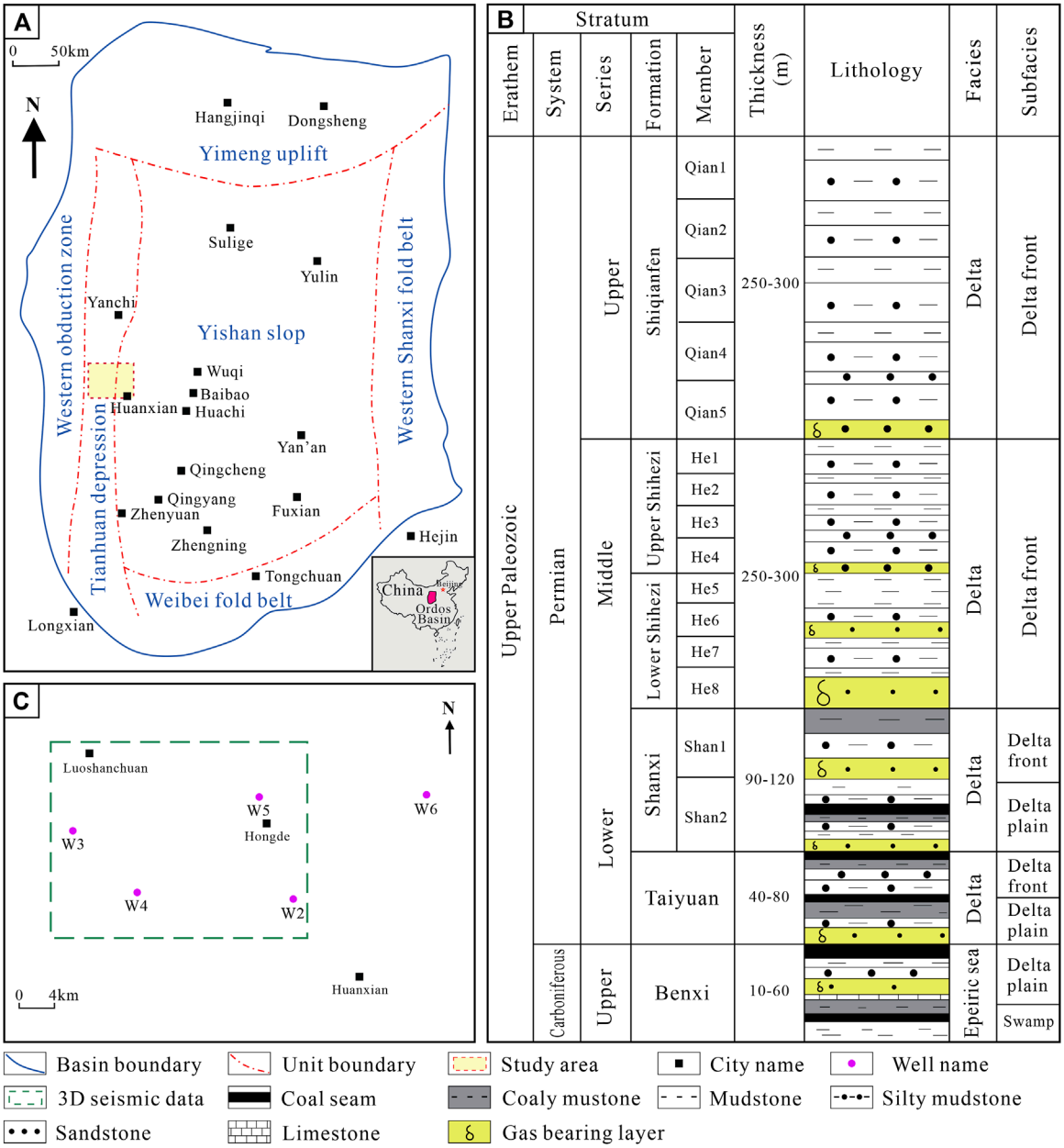

FIGURE 1
Location of the Hongde area, with tectonic setting of the Ordos Basin and the stratigraphy division. **(A)** Map showing the location and division of tectonic units of the Ordos Basin (modify from Liu et al. (2015)). **(B)** Stratigraphical section of the Upper Paleozoic strata. **(C)** Gas exploration wells and seismic data cover range in study area.

environment of the Permian in the Ordos Basin was relatively warm and humid, and the sedimentary water depth was around 20 m. The study area is characterized by relatively flat topographic slope, non-development of large-scale fault, tectonic stability, and strong hydrodynamic conditions that can carry a large number of sediments, which provide favorable conditions for shallow-water delta sedimentation (Xiao et al., 2008; Guo et al., 2020; Zhu et al., 2021; Xia et al., 2022).

The Upper Paleozoic tight sandstone reservoirs in the study area have deep burial depths (range from 3500–4500 m), tight reservoirs (average porosity <7%, average permeability $<0.5\times10^{-3}$ μm^2), complex microscopic pore-throat structures, and a variety of pore types (Cui et al., 2021; Qi et al., 2021). Recent oil and gas exploration and development studies show that the tight sandstone gas reservoir of the He 8 member of the Permian Shihezi Formation in the Hongde area is rich, and some exploration wells have already discovered natural gas reservoirs, which has an excellent prospect for natural gas exploration. It is urgent to research the reservoir quality of the He 8 member of the Permian Shihezi Formation, which is still in the initial period.

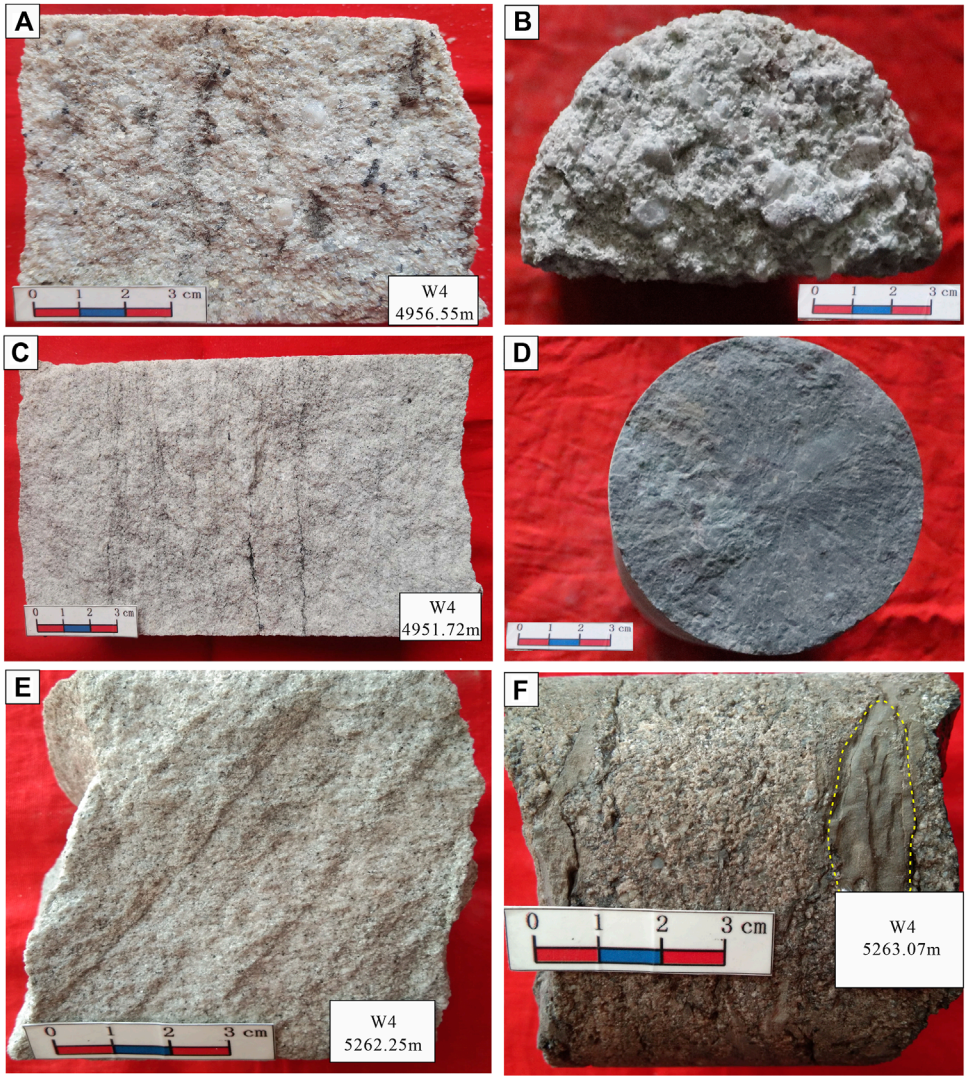

FIGURE 2
Typical lithofacies photographs from cores. **(A)** Massive gravel-bearing coarse sandstone (Sg), well W4, 4956.55 m. **(B)** Massive gravel-bearing coarse sandstone (Sg), well W5, 4459.8 m. **(C)** Sandy gravel-bearing lithic sandstone, well W4, 4951.72 m. **(D)** Black mudstone, well W5, 4462.3 m. **(E)** Cross-bedding coarse sandstone (Sp), well W3, 5262.25 m. **(F)** Massive coarse sandstone with black mud clasts (mark by yellow line) in well W3 (Sm), 5263.07 m.

3 Data and methods

This study used the cores, log curves, 3D seismic data, and reservoir physical property (porosity and permeability) data. The data used in this study are from the PetroChina Changqing Oilfield Company. Detailed descriptions, photographs, and sediment particle size analysis from 56 m of core records in 4 cored wells that penetrated the He 8 member were taken for identification of lithofacies. 3D seismic data that cover the central part of the study area (289 km^2). Porosity and permeability data come from 220 tight sandstone samples from 4 wells. Wireline log curve data was used to identify sedimentary facies in other wells without cores. Detailed descriptions of the tight sandstone core samples in the He 8 member of the Shihezi Formation were taken to identify and interpret lithofacies. The lithofacies and vertical association of the tight sandstone deposits are summarized based on color, grain size, and sedimentary structure. The characteristics of lithofacies from the different depositional sequences were interpreted after core description. The log curve characteristics of different sedimentary facies were studied in the Shihezi Formation.

Based on the study of lithofacies and log curves facies analysis of the He 8 member, sedimentary facies interpretation was conducted on the wells in the Hongde area. The sedimentary variation was revealed through a comparison of lithofacies from the deltaic distributary channels developed in the Shihezi Formation. The vertical sedimentary facies variation was studied through well-tied profiles from the proximal to the distal direction of the deltaic deposits of the He 8 member. The diagenesis features and alternations in different lithofacies were studied using thin sections. The high-quality reservoirs were identified using porosity and

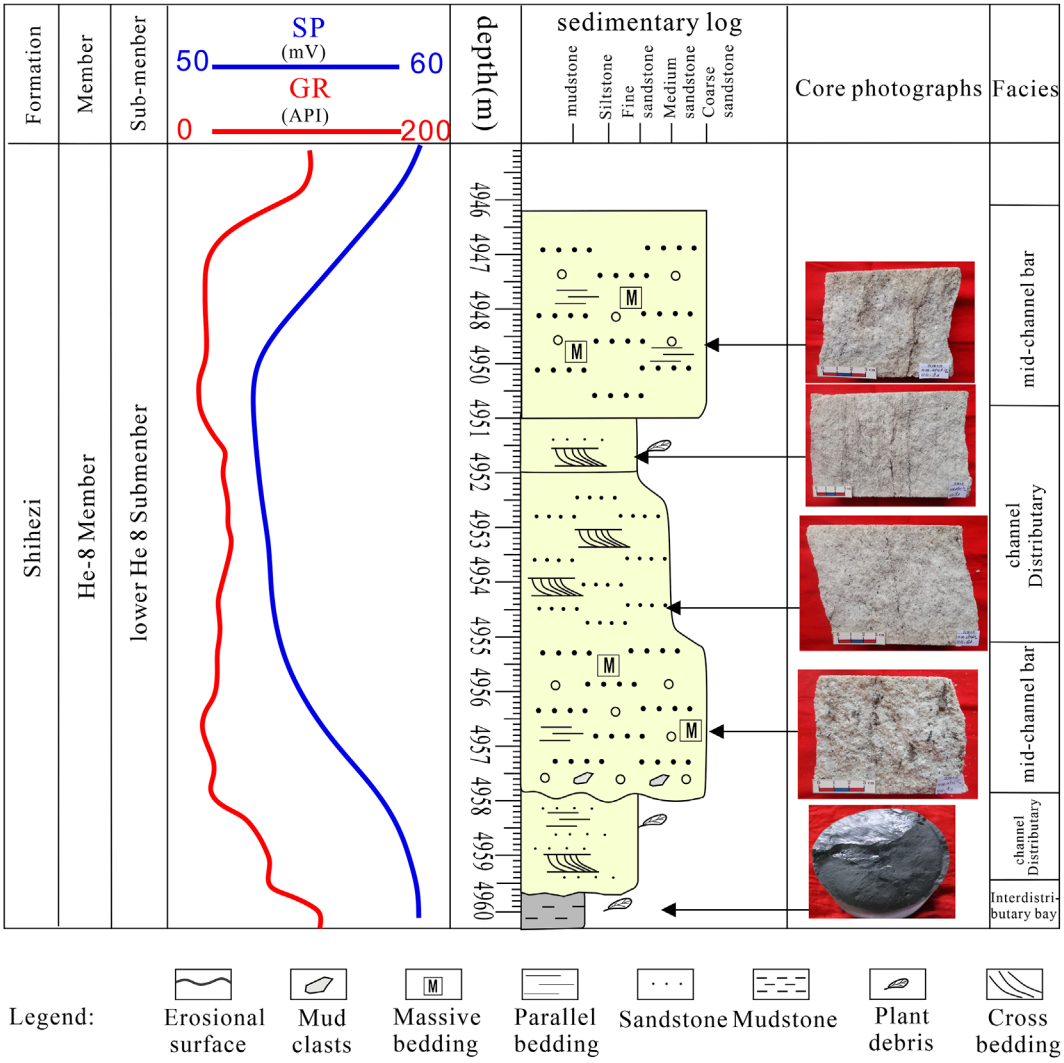

FIGURE 3
Sedimentary microfacies interpretation and lithofacies description of well W4, and typical lithofacies photographs.

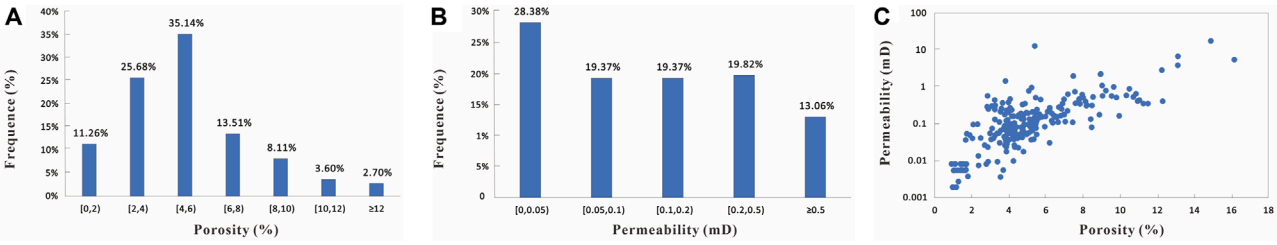

FIGURE 4
Reservoir quality of the sandstone from the He 8 member. **(A)** The distribution of reservoir porosity. **(B)** The distribution of reservoir permeability. **(C)** Plots of the relationship between porosity and permeability from the reservoir test data.

permeability in those wells. This study used wireline log curves from four exploration wells and 3D seismic data to predict the deltaic tight sandstones. Seismic amplitude attribute extraction and seismic inversion were used in this study for tight sandstone reservoir prediction. The horizontal distribution of the deltaic tight sandstone is predicted through sedimentary facies and sand body

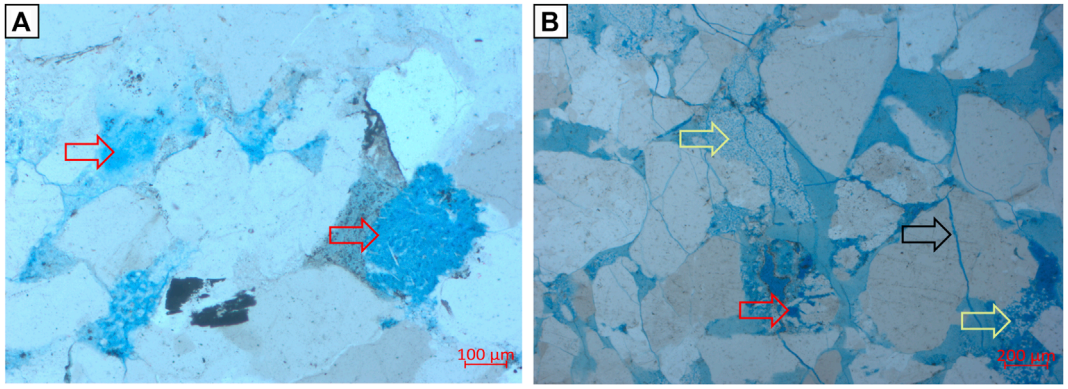

FIGURE 5
Photomicrographs showing the lithology and pores from thin section observations. **(A)** Intragranular dissolved pores, (mark by red arrow) W4 4950.8 m; **(B)** Intracrystalline pores (mark by yellow arrows) and intragranular pores (mark by red arrow), note the fractures in quartz grains, (mark by black arrow) W5 4457.1 m.

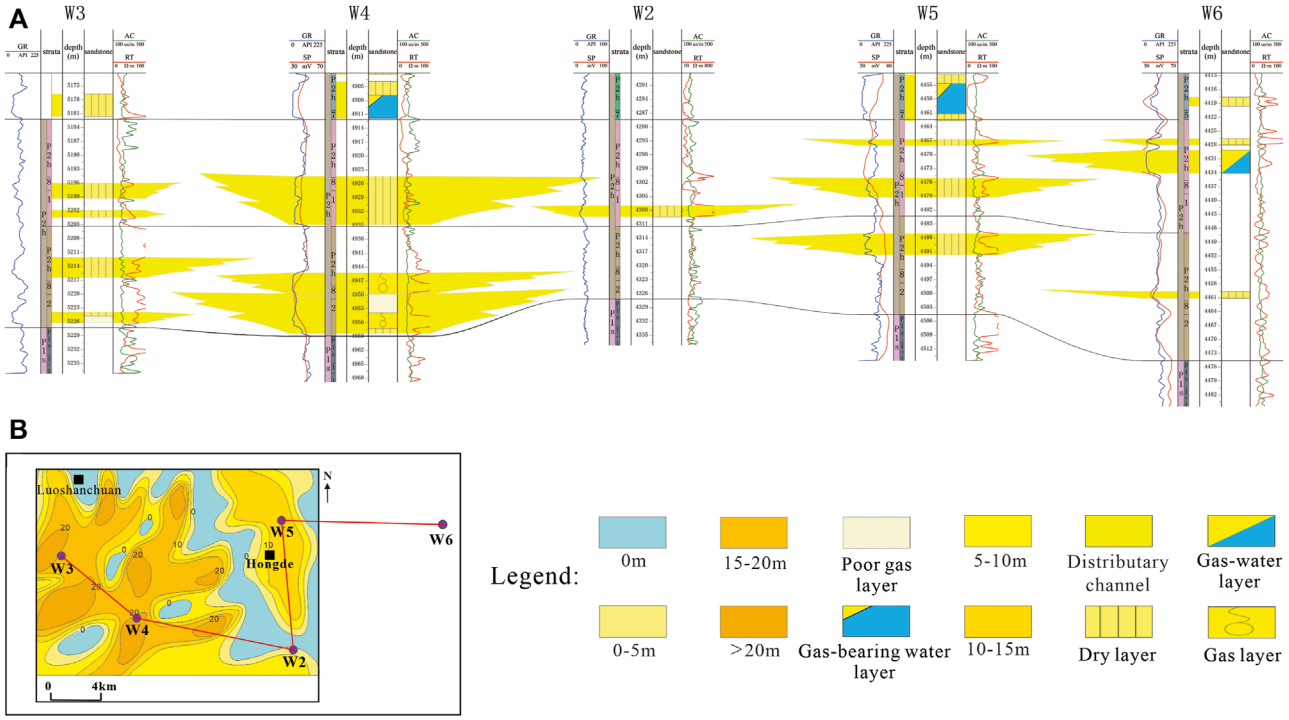

FIGURE 6
(A) Well-tie profile of sand bodies and distributary channel in the He 8 member. Note the position of the profile on the sand body thickness contour map **(B)**.

thickness contour map. With the assistance of wireline log curves and 3D seismic data, the vertical and horizontal distributions of high-quality reservoirs were investigated through sedimentary lithofacies and sand body thickness contour map. The relationship between diagenetic alterations and depositional lithofacies in deltaic distributary channels is analyzed for further discussion. Basis on horizontal and vertical analysis, the high-quality reservoir quality distribution model within the deltaic distributary channel is discussed in the discussion chapter.

4 Results

4.1 Lithofacies characteristics and interpretation

During the depositional period of the He 8 member, due to the rapid decrease in baseline, cold and dry climate, and increased stratigraphic slope, the sediment supply rate increased (Zhu S. F. et al., 2021). As a result, the shoreline continued to

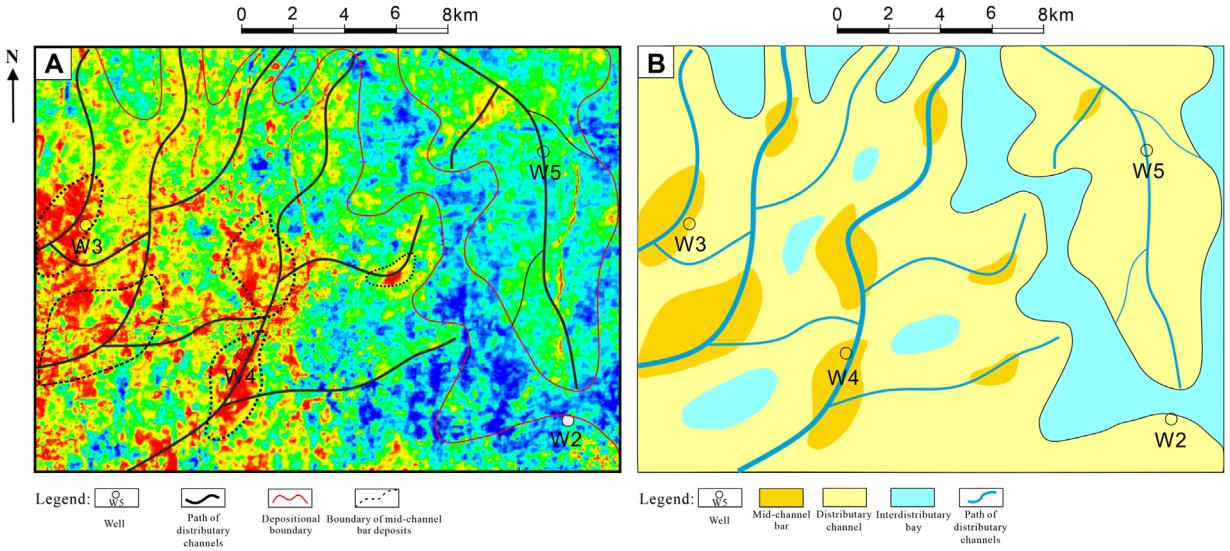

FIGURE 7
Sedimentary facies distribution of the He 8 member in the Hongde area. **(A)** RMS amplitude of the He 8 member. **(B)** Sedimentary facies of the He 8 member.

advance towards the edge of the delta front, and the branching and merging of channels were more frequent, mainly developing braided river deltas. The subaqueous distributary channel sand bodies are the major types of sand bodies, with gravel-bearing coarse-grained sandstone facies, cross-bedding coarse sandstone facies, and black mudstone facies commonly found in the He 8 member (Figure 2).

In the distributary channel microfacies, the lithology is relatively coarse, with the development of sandstone and gravel-bearing coarse sandstone. The overall sorting is medium to good, and the sedimentary structure is mainly composed of cross-bedding and parallel bedding. At the bottom, fine conglomerate and visible erosion surfaces are often developed, and the main thickness is 5–8 m. Vertically, there are mainly positive and compound positive rhythms. In terms of logging response characteristics, the microfacies of the distributary channel exhibit a bell-shaped or composite shape of gamma ray and resistivity curves, with generally higher amplitudes (Figure 3). The distributary channel can develop mid-channel bar deposits inside, and coarse-grained lithology is usually developed in the mid-channel bar, including conglomerate and gravel-bearing coarse sandstone. The sorting is generally medium to good, with visible massive bedding and parallel bedding. In terms of logging response characteristics, mid-channel bar deposits often exhibit a box-shaped gamma ray curve.

4.2 Physical properties

By analyzing the tight sandstone samples of the He 8 member in the study area. Porosity ranges between 0.8% and 16.3%, with a mean value of 5.1%, and the permeability ranges between 0.001 mD and 10 mD, with a mean value of 0.42 mD. The samples with porosity less than 10% and permeability less than 0.5 mD accounted for 87% of the total samples. Porosity and permeability distributions of different lithofacies vary greatly (Figure 4).

4.3 Diagenesis features and pores in the reservoirs

This study takes the microscopic features as the core and combines thin section analysis to analyze and conclude that the major diagenetic processes developed in the study area include compaction, pressure dissolution, cementation and metasomatism, and dissolution. According to the impact of diagenesis on reservoir properties, diagenesis can be divided into two categories: constructive diagenesis and destructive diagenesis. Constructive diagenesis can generate secondary pores, mainly including dissolution and kaolinite metasomatism, which can effectively improve reservoir physical properties. On the contrary, destructive diagenesis can reduce pores, mainly through mechanical compaction, pressure solution, and cementation, which significantly reduces reservoir physical properties. Although kaolinite cementation can fill pores and block throats, the intracrystalline pores formed by it do indeed constitute gas storage spaces in the study area. The pore types of the tight sandstone reservoir in the He 8 member of the study area are mainly intragranular dissolved pores, Intracrystalline pores, and intragranular pores followed by a certain amount of residual intergranular pores (Figure 5). The pore types between different layers are similar, but there are significant differences between different lithologies. In quartz sandstone, due to its strong compaction resistance, the content of intragranular pores and intragranular dissolved pores is relatively high.

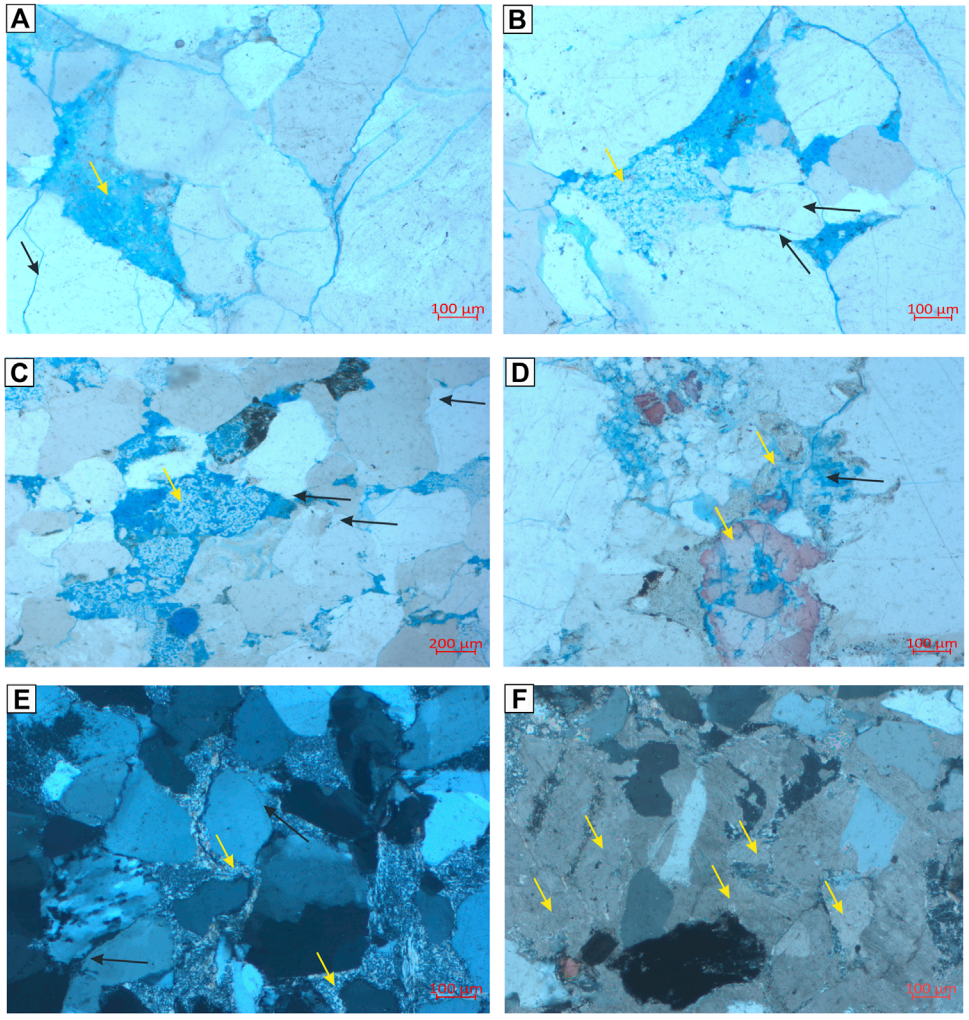

FIGURE 8
Photomicrographs showing the lithology, pore. **(A)** Intragranular dissolved pores, (mark by yellow line), note the fractures in quartz grains (mark by black line) W4, 4956.55 m. **(B)** Intragranular dissolved pores (mark by yellow line) and intergranular pores, (mark by black lines) W4, 4955.32 m. **(C)** Intragranular dissolved pores (mark by yellow lines) and intergranular pores, (mark by black lines) W4, 4947.03 m. **(D)** Intragranular dissolved pores (mark by yellow lines) and intergranular pores, (mark by black lines) W4, 4954.34 m. **(E)** Intragranular dissolved pores (mark by black lines) and intergranular pores, (mark by yellow lines) W4, 4952.24 m. **(F)** Intragranular dissolved pores, (mark by yellow lines) W4, 4958.11 m.

4.4 Distribution of facies prediction using 3D seismic

The single-well facies in the He 8 member are interpreted by sedimentary interpretation from cored wells. Draw the well-tie profile of sedimentary facies comparison through single-well facies (Figure 6A). Moreover, the plane distribution of sand body is predicted based on the RMS seismic attributes in the Hongde area. The distribution of thick sandstone is also consistent with the high-value area on the RMS seismic attribute map (Figure 7A). The distribution trend of sand bodies is described in plain view. Then, the sedimentary facies were predicted in the He 8 member. From the thickness contour map of the sandstone in the He 8 member, the delta lobe has a continuous distribution pattern (Figure 6B).

The He 8 member of the Upper Paleozoic sedimentary environment in the research area is delta deposits under shallow water gentle slope conditions, with distributary channels and mid-channel bar deposits. On the plane, the distributary channels are well developed on the delta lobe. The mid-channel bars are distributed in a long strip or lens shape in the middle of the distributary channel. The W4 well developed the mid-channel bars facies (Figure 7B).

5 Discussion

5.1 Diagenetic alterations linked to depositional lithofacies

By comparing the diagenesis of different lithofacies in typical core wells, it was found that there are apparent differences in the development of reservoir diagenesis of different lithofacies. Despite strong compaction, the gravel-bearing coarse-grained sandstone reservoirs in coarse sandstone lithofacies have developed internal dissolution. After compaction, cementation to reduce porosity, and

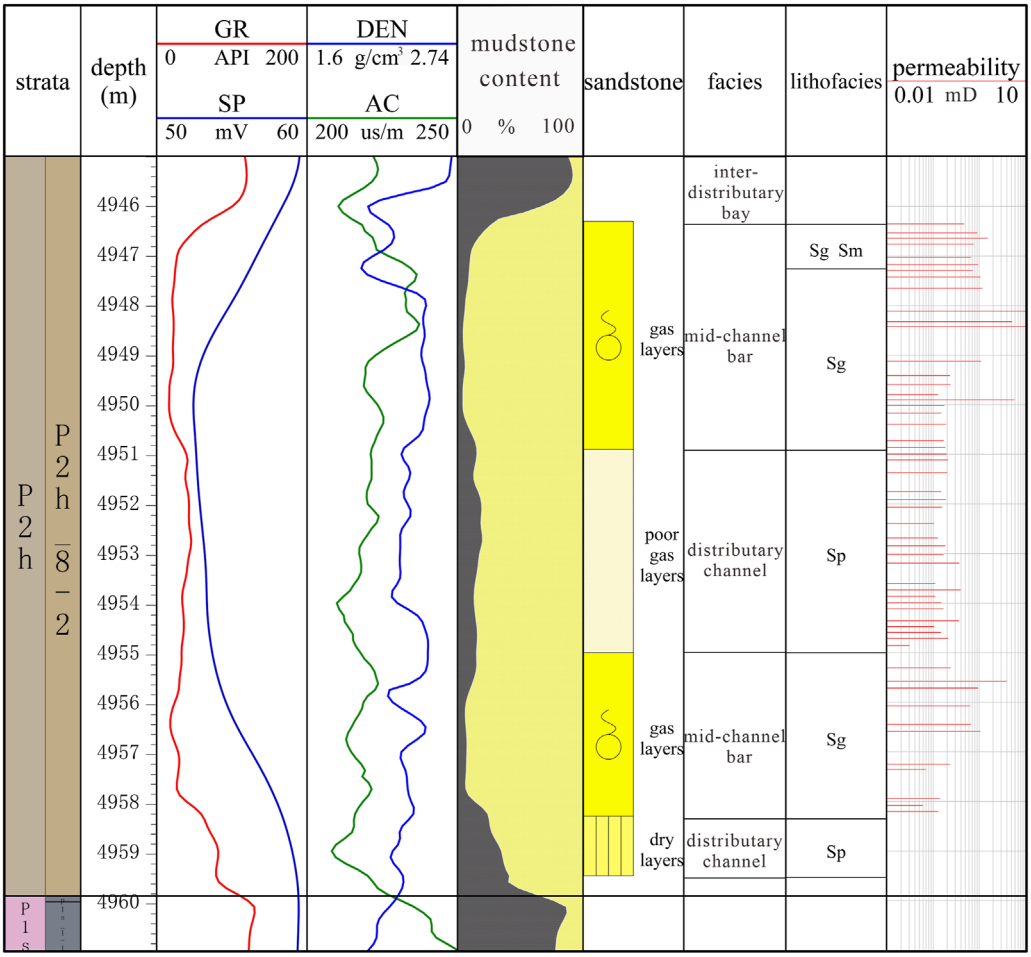

FIGURE 9
Comparison of vertical physical properties of different lithofacies.

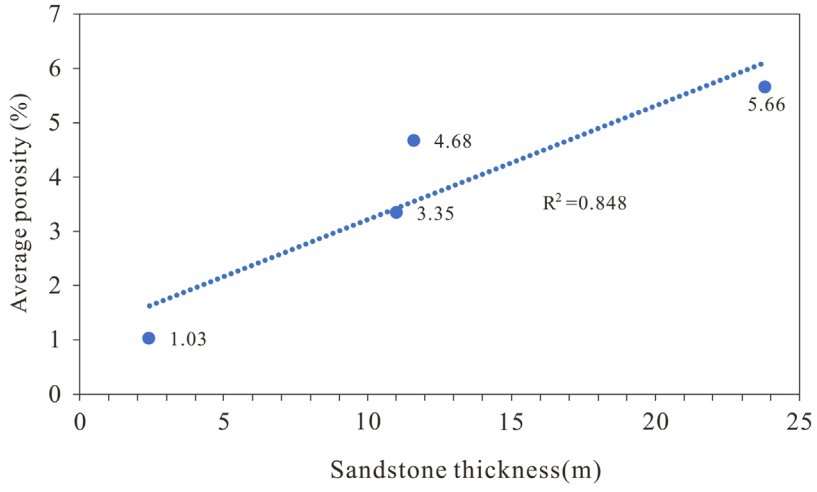

FIGURE 10
Cross plot between sandstone thickness and average porosity of the sandstone in He 8 member.

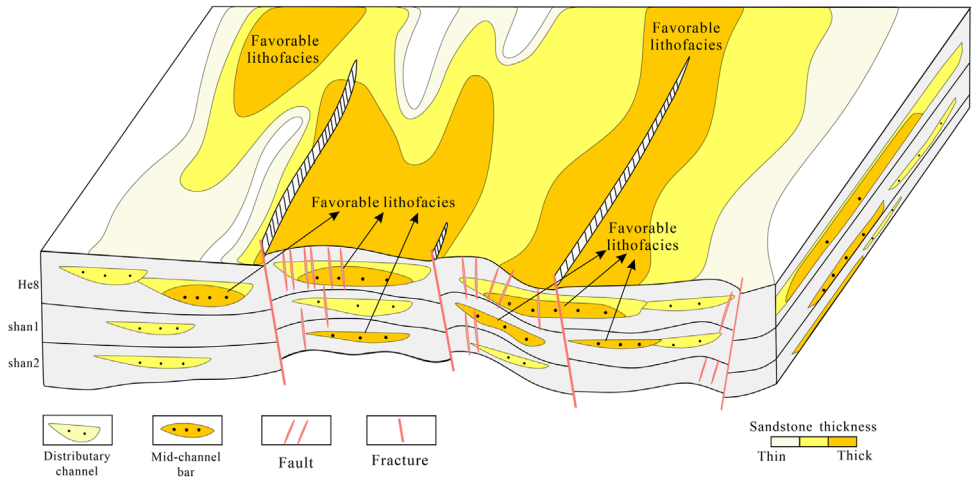

FIGURE 11
Development model of favorable lithofacies in the He 8 member of the study area.

dissolution to increase porosity, the secondary pores were preserved in the sandstone and formed relatively high-quality reservoirs (Figure 8). The cross-bedding fine sandstone lithofacies were strongly compacted, with internal ductile particles being compacted and deformed. The particle orientation is clearly observed in those lithofacies. The reservoir in those lithofacies is tight, and dissolution in the reservoirs is weak. This could be the major reasons for the formation of poor reservoir quality. In addition, diagenesis at the interface between sandstone and mudstone is often affected by geological fluid from the mudstone during compaction, resulting in the development of calcareous cementation. This leads to a poor reservoir quality near the mudstone. Therefore, the distribution characteristics of lithofacies are the major factors controlling reservoir quality. The high-quality reservoirs are mostly distributed in coarse sandstone lithofacies, mainly distributed in the mid-channel bar deposits (Figure 9).

5.2 High-quality reservoir quality distribution model within deltaic distributary channel

Deposition controls the original physical properties of the reservoir (Li et al., 2017), mainly reflected in the impact of differences in sedimentary fabric and components on the quality of the original reservoir. The coarse the particle size of the rock and the lower the shaliness content, the higher the quality of the original reservoir and the better the porosity and permeability. There are significant differences in sedimentary fabrics and components among different types of sandstone in the study area, resulting in significant differences in their original porosity and permeability. In the previous study of sedimentary facies, it was believed that the He 8 section developed braided river shallow water delta deposits. Through the thickness contour map of well controlled sand bodies and seismic data, it was found that thick sand is mainly distributed inside the mid-channel bar of the delta distributary channel. Through core observation and thin section analysis, it was found that the lithofacies types are mostly gravel-bearing coarse sandstone facies and gravel-bearing sandstone facies. Through microscopic analysis, it is believed that the gravel-bearing coarse sandstone facies and gravel-bearing sandstone facies developed in the core beach of the distributary channel are the main high-quality reservoir lithofacies. Dissolution is a critical diagenetic process in developing tight sandstone reservoirs in coal-bearing strata. The dissolution phenomenon is relatively common in the sandstone reservoirs of the Shihezi Formation in the research area, and there are two main types of dissolution: one is the dissolution of rock debris, and the other is the dissolution of intergranular cement. The medium-to-coarse sandstone and massive bedding pebbly medium-to-coarse sandstone are formed into high-quality reservoirs after compaction, cementation to reduce porosity, and dissolution to increase porosity. High-quality reservoirs are distributed in the middle of distributary channels. The intersection diagram of single well sand body thickness and porosity shows that high-quality reservoirs are developed in thick sand intervals, and there is a clear correlation between reservoir quality and sand body thickness (Figure 10). The logging curve of the thick sand intervals is box-shaped. Based on the formation and preservation mechanism of reservoirs and the development characteristics of gas reservoirs, a sweet spot development model of dominant rock facies in reservoirs has been established (Figure 11).

6 Conclusion

(1) Based on cores, well log curves and 3D seismic data, the He 8 member of the Permian Shihezi Formation in the Hongde area, western Ordos basin mainly developed braided river deltaic deposits. The He 8 member sandstone section develops thick sandstone in distributary channels. The deltaic sandstone gradually pinches out from southwest to northeast. The mid-channel bars were developed in distributary channels.

(2) The lithology of He 8 members of Upper Paleozoic in the study area is mainly lithic quartz sandstone, and quartz sandstone.

The main reservoir space of the tight sandstones in He 8 members is intergranular pores, intergranular solution and intracrystalline pores, with porosity of 5.14% and permeability of 0.42 mm D. The reservoir quality is mainly controlled by its pore radius.

(3) From the diagenesis features study of those tight reservoirs The Upper Paleozoic He 8 member in the study area experienced the diagenesis of rigid particle compaction and fracture, plastic particle compaction and deformation, quartz secondary enlargement, kaolinite and calcite cementation and metasomatism, grain dissolution. Diagenetic materials mainly come from the grain dissolution and transformation between clay minerals. Compaction and are destructive diagenesis and dissolution are main constructive diagenesis in the tight sandstones.

(4) Through microscopic analysis, the gravel-bearing coarse sandstone lithofacies developed in the mid-channel bar of the distributary channel are the main high-quality reservoir lithofacies. Although these lithofacies sandstones have undergone strong compaction, the quartz content in the sandstone components is relatively high, and some pores can still be preserved. The internal dissolution of the reservoir develops, forming tight gas reservoirs. High quality reservoirs exhibit characteristics of locally developed planar and vertically developed layers, and are likely to exhibit discontinuous and dispersed distribution within three-dimensional subsurface deltaic-lacustrine deposits.

(5) The favorable lithofacies in deltaic sand bodies in the He 8 member in the western Ordos basin could form lithologic traps, which have important exploration and development value for lithologic natural gas reservoirs. The high-quality reservoirs are pinched out as sweet spot in the sandstone deposits. forming a favorable zone of the lithologic traps.

Data availability statement

The original contributions presented in the study are included in the article/Supplementary material, further inquiries can be directed to the corresponding authors.

Author contributions

XW: Conceptualization, Methodology, Writing–original draft. ZS: Conceptualization, Methodology, Writing–original draft. YB: Conceptualization, Methodology, Writing–original draft. WW: Methodology, Writing–review and editing. ZY: Methodology, Writing–review and editing. BW: Formal Analysis, Writing–review and editing. XZ: Writing–review and editing, Formal Analysis. LD: Writing–review and editing, Project administration. ZW: Writing–review and editing, Project administration.

Funding

The author(s) declare that financial support was received for the research, authorship, and/or publication of this article. This research was supported by National Natural Science Foundation of China (No. 42202177)

Acknowledgments

The authors wish to thank the No. 7 Oil Production Plant, PetroChina Changqing Oilfield Company for providing various data for this study. We are also greatly appreciate reviewers and editors for their constructive comments for their precious advice.

Conflict of interest

Authors XW, ZS, YB, WW, ZY, and BW were employed by the PetroChina Changqing Oilfield Company. Author XZ was employed by the XMotors.ai Inc.

The remaining authors declare that the research was conducted in the absence of any commercial or financial relationships that could be construed as a potential conflict of interest.

Publisher's note

All claims expressed in this article are solely those of the authors and do not necessarily represent those of their affiliated organizations, or those of the publisher, the editors and the reviewers. Any product that may be evaluated in this article, or claim that may be made by its manufacturer, is not guaranteed or endorsed by the publisher.

References

Cui, G. X., Wei, Q. L., Xiao, L., Wang, S., Hu, R., and Wang, C. H. (2021). Reservoir characteristics of permian lower He 8 member in longdong area, Ordos Basin. *Geoscience* 35 (4), 1088–1097. doi:10.19657/j.geoscience.1000-8527.2021.04.028

El-ghali, M. A. K., Morad, S., Ai-Aasm, I., Ramseyer, K., and Mansurberg, H. (2006b). Distribution of diagenetic alterations in glaciogenic sandstones within a depositional facies and sequence stratigraphic framework: evidence from the Upper Ordovician of the Murzuq Basin, SW Libya. *Sediment. Geol.* 190, 299–327. doi:10.1016/j.sedgeo.2006.05.020

El-ghali, M. A. K., Tajori, K. G., Mangsurberg, H., Ogle, N., and Kalin, R. M. (2006a). Origin and timing of siderite cementation in Upper Ordovician glaciogenic sandstones from the Murzuq basin, SW Libya. *Mar. Pet. Geol.* 23, 459–471. doi:10.1016/j.marpetgeo.2006.02.002

Fu, J. H., Wei, X. S., Luo, S. S., Zuo, Z. F., Zhou, H., Liu, B. X., et al. (2019). Discovery and geological knowledge of the large deep coal-formed Qingyang gas field, Ordos Basin, NW China. *Petroleum Explor. Dev.* 46 (6), 1111–1126. doi:10.1016/s1876-3804(19)60267-3

Guo, Y. Q., Wang, M. X., Guo, B. C., Cai, Z. C., Hui, L., He, Z. Q., et al. (2020). Sedimentary system characteristics and paleographic evolution of Upper Paleozoic of northern west margin. Ordos Basin. *J. Northwest Univ. Nat. Sci. Ed.* 50 (1), 93–104. doi:10.16152/j.cnki.xdxbzr.2020-01-013

Li, Z., Wu, S. H., Xia, D. L., Zhang, X. F., and Huang, M. (2017). Diagenetic alterations and reservoir heterogeneity within the depositional facies: a case study from distributary-channel belt sandstone of Upper Triassic Yanchang Formation reservoirs (Ordos Basin, China). *Mar. Pet. Geol.* 86, 950–971. doi:10.1016/j.marpetgeo.2017.07.002

Liu, F., Zhu, X. M., Li, Z., Xu, L. M., Niu, X. B., Zhu, S. F., et al. (2015). Sedimentary characteristics and facies model of gravity flow deposits of Late Triassic Yanchang Formation in southwestern Ordos Basin, NW China. *Pet. Explor. Dev.* 42 (5), 633–645. doi:10.1016/S1876-3804(15)30058-6

Meng, X. L., Ai, Q. L., Wang, J. C., Bian, X. Y., Zhu, C. R., An, W. H., et al. (2021). Reservoir-forming conditions of deep tight sandstone gas reservoirs, Qingyang gasfield, Ordos Basin. *Nat. Gas Explor. Dev.* 44 (1), 104–110. doi:10.12055/gaskk.issn.1673-3177.2021.01.014

Morad, S., Al-Ramadan, K., Ketzer, J. M., and De Ros, L. F. (2010). The impact of diagenesis on the heterogeneity of sandstone reservoirs: a review of the role of depositional facies and sequence stratigraphy. *AAPG Bull.* 94 (8), 1267–1309. doi:10.1306/04211009178

Morad, S., Ketzer, J. M., and De Ros, L. F. (2000). Spatial and temporal distribution of diagenetic alterations in siliciclastic rocks: implications for mass transfer in sedimentary basins. *Sedimentology* 47, 95–120. doi:10.1046/j.1365-3091.2000.00007.x

Qi, R., He, F. Q., Wang, F. B., Jia, H. C., and Wang, W. (2021). Exploration breakthrough of upper paleozoic of well changtan 1 in southern Ordos Basin and its significance. *China Pet. Explor.* 26 (3), 68–78. doi:10.3969/j.issn.1672-7703.2021.03.006

Wang, Y., Cheng, H. F., Hu, Q. H., Jia, L. B., Wang, X. M., Gao, S. S., et al. (2023). Adsorption of methane onto mudstones under supercritical conditions: mechanisms, physical properties and thermodynamic parameters. *Petroleum Sci.* 20 (1), 34–47. doi:10.1016/j.petsci.2022.08.017

Wang, Z. L., Wei, L., Wang, X. Z., Wang, N. X., Fan, C. Y., Li, Y. J., et al. (2016). Accumulation process and mechanism of lower paleozoic gas reservoir in yan'an area, Ordos Basin. *Acta Pet. Sin.* 37 (1), 99–110. doi:10.7623/syxb2016S1010

Wardlaw, N. C., and Cassan, J. P. (1979). Oil recovery efficiency and the rock-pore properties of some sandstone reservoirs. *Bull. Can. Petrol. Geol.* 27, 117–138. doi:10.35767/gscpgbull.27.2.117

Wardlaw, N. C., and Taylor, R. P. (1976). Mercury capillary pressure curves and the interpretation of pore structure and capillary behavior in reservoir rocks. *Bull. Can. Petrol. Geol.* 24, 225–262. doi:10.35767/gscpgbull.24.2.225

Weber, K. J. (1982). Influence of common sedimentary structures on fluid flow in reservoir models. *J. Petrol. Technol.* 34, 665–672. doi:10.2118/9247-PA

Xia, H., Wang, L., Zhang, D. F., Wang, J. P., Fan, Q. Q., Feng, M., et al. (2022). Sequence architecture, sedimentary evolution and controlling factors of the Permian Shan-1 Member, Qingyang gas field, southwestern Ordos Basin. *Oil Gas Geol.* 43 (6), 1397–1488. doi:10.11743/ogg20220610

Xiao, J. X., Sun, F. J., He, N. X., Liu, R. E., Li, J., Xiao, H. P., et al. (2008). Permian Shanxi Formation and member 8 of xiashihezi Formation in Ordos Basin: palaeogeography and catchment area for sediments derived from north and south provenances. *J. Palaeogeogr.* 10 (4), 341–354. Available at: http://journal09.magtechjournal.com/gdlxb/CN/10.7605/gdlxb.2008.04.002.

Xu, Q. H., Shi, W. Z., Xie, X. Y., Busbey, A. B., Xu, L. T., Wu, R., et al. (2018). Inversion and propagation of the late paleozoic porjianghaizi fault (north Ordos Basin, China): controls on sedimentation and gas accumulations. *Mar. Petrol. Geol.* 91, 706–722. doi:10.1016/j.marpetgeo.2018.02.003

Yang, H., Fu, J., Liu, X., and Meng, P. (2012). Accumulation conditions and exploration and development of tight gas in the Upper Paleozoic of the Ordos Basin. *Petrol. explor. Dev.* 39 (3), 315–324. doi:10.1016/S1876-3804(12)60047-0

Yang, Y. T., Li, W., and Ma, L. (2005). Tectonic and stratigraphic controls of hydrocarbon systems in the Ordos basin: a multicycle cratonic basin in central China. *AAPG Bull.* 89, 255–269. doi:10.1306/10070404027

Zhu, R. J., Li, R. X., Liu, X. S., Yang, M. Y., Qin, X. L., Wu, X. L., et al. (2021). Characteristics of the diagenetic evolution of tight sandstone gas reservoir and its property in the upper paleozoic erathem in southwestern ordos basin. *J. Lanzhou Univ. Nat. Sci.* 57 (05), 637–649+658. doi:10.13885/j.issn.0455-2059.2021.05.009

Zhu, S. F., Cui, H., Chen, J. H., Luo, G. J., Wang, W. Y., Yang, Y., et al. (2021). Sedimentary system and sandstone reservoir petrology of a shallow water delta: case study of the Shan-1 and He-8 members in the western Ordos Basin. *Acta Sedimentol. Sin.* 39 (1), 126–139. doi:10.14027/j.issn.1000-0550.2020.115

frontiers | Frontiers in Earth Science

TYPE Original Research
PUBLISHED 13 February 2024
DOI 10.3389/feart.2024.1348336

Check for updates

OPEN ACCESS

EDITED BY
Wenguang Wang,
Northeast Petroleum University, China

REVIEWED BY
Shengli Li,
China University of Geosciences, China
Yang Wang,
Chang'an University, China
Mingyang Wei,
Southwest Petroleum University, China

*CORRESPONDENCE
Wenxiang He,
hwx@yangtzeu.edu.cn
Luxing Dou,
luxingdou@yangtzeu.edu.cn

RECEIVED 02 December 2023
ACCEPTED 18 January 2024
PUBLISHED 13 February 2024

CITATION
Wang T, Hu Y, Li B, He W, Gao X, Dou L and Wang J (2024), Sedimentary characteristics and model of seasonal deltaic sandstone: a case study on the continental red bed from the Cretaceous Baxigai Formation, Tarim Basin, NW China.
Front. Earth Sci. 12:1348336.
doi: 10.3389/feart.2024.1348336

COPYRIGHT
© 2024 Wang, Hu, Li, He, Gao, Dou and Wang. This is an open-access article distributed under the terms of the Creative Commons Attribution License (CC BY). The use, distribution or reproduction in other forums is permitted, provided the original author(s) and the copyright owner(s) are credited and that the original publication in this journal is cited, in accordance with accepted academic practice. No use, distribution or reproduction is permitted which does not comply with these terms.

Sedimentary characteristics and model of seasonal deltaic sandstone: a case study on the continental red bed from the Cretaceous Baxigai Formation, Tarim Basin, NW China

Tong Wang[1,2], Yong Hu[1,2], Bin Li[3], Wenxiang He[1,2]*, Xiaoyang Gao[1,2], Luxing Dou[1,2]* and Jian Wang[1,2]

[1]College of Resources and Environment, Yangtze University, Wuhan, China, [2]Key Laboratory of Exploration Technologies for Oil and Gas Resources, Ministry of Education, Yangtze University, Wuhan, China, [3]Research Institute of Petroleum Exploration and Development, PetroChina Tarim Oilfield Company, Korla, China

Seasonal delta is a sandy fan-shaped sedimentary system formed by seasonal river flooding in continental basins. Modern sedimentary finds that seasonal deltas mainly develop in an arid-semi-arid climate environment with gentle terrain. However, the study of seasonal deltas in ancient rock records is still insufficient, leading to misinterpretations as other sedimentary systems, which poses challenges to the correct understanding of the origin and spatial distribution of sand body deposits. In this study, the red bed deposits of the Cretaceous Baxigai Formation in the west of the Tabei Uplift were selected as the research object. Based on core observation and description, a comprehensive analysis of the sedimentary environment, sedimentary characteristics and sedimentary model of the Baxigai Formation was carried out using data such as well-logging and analytical testing, combined with modern depositional characteristics. Research shows that the sedimentary sequence of the Baxigai Formation red bed developed a seasonal delta sedimentary system in the arid climate. The seasonal delta deposits provide an opportunity to understand the influencing of river flow and total sedimentary loading vary greatly on the sedimentary model, sedimentary mechanism, and distribution of sand bodies in arid climates. The sedimentary process of the seasonal delta in the Baxigai Formation was controlled by the dual-stage sedimentation process in an arid paleoclimate. During the flood period, the supercritical flow sedimentary structures are widely developed in the major distributary channels, and the distributary channels migrate and bifurcate frequently. On the delta plain, crevasse channels are formed through the avulsion of major distributary channels. During the dry period, due to the consumption of water seepage and evaporation transfer, terminal distributary channels are abandoned, crevasse channels are not developed, and the sediment is exposed. The density of the distributary channels is reduced, and the total sedimentary loading is low. The distributary channels sand body is the skeleton sand body of the seasonal delta. This study is of great significance for accurately explaining the formation process of seasonal

deltas and provides a useful reference for further exploration and deployment of oil and gas reservoirs and paleogeographic reconstruction in the study area.

KEYWORDS

seasonal delta, sedimentary environment, sedimentary model, Baxigai Formation, Tarim Basin

1 Introduction

Seasonal deltas are formed by the seasonal river recharge, driven by ephemeral and high-energy flood events, and mainly develop in arid-semi-arid climate environments with gentle terrain (Liu B. B. et al., 2019; Gugliotta et al., 2016). Essential characteristics of seasonal delta: 1) The sediment are mainly red bed deposits, and there is no apparent foreset bed in the profile; 2) The river is controlled by seasonal precipitation, the river discharge and total sedimentary loading variation greatly and the supercritical flow sedimentary structure is widely developed in the deposits; 3) The delta is dominated by rivers action and the center of the basin lacks a large catchment area (Liu Y. F. et al., 2019; Zhang et al., 2018; Li et al., 2021). Although there are many examples of seasonal deltas deposition in an arid environment, in the continental basin sedimentology, the research on the sedimentary origin, distribution, and sedimentary model of seasonal deltas sand bodies in arid environments are not thorough enough, and many seasonal delta sedimentary systems in arid climate may not be correctly explained in ancient rock records. Delta reservoir formation theory has made significant achievements in guiding hydrocarbon exploration in continental basins (Yang et al., 2003; Fu et al., 2013). The Tabei Uplift is one of the Tarim Basin's most favorable oil and gas enrichment areas, rich in oil and gas resources (Liu B. B. et al., 2019; Huang et al., 2018). In recent years, with the discovery of low-amplitude structural oil and gas reservoirs such as YM463 and YM46, two lithological oil and gas reservoirs YD7 and YM467, the Baxigai Formation, as an essential reservoir system in the west of the Tabei Uplift, have gradually attracted attention and have become one of the critical exploration targets (Ma et al., 2022; Luo et al., 2021). However, the structural background of the Baxigai formation in the study area is complex. The characteristics of the sand body are deep burial, thin thickness, regionalization, and complex lateral changes; moreover, the region is affected by the climate, the depositional environment is complex, and the sand body depositional types are diverse. At present, the understanding of the depositional mechanism and depositional pattern of the sand body of the Baxigai formation is insufficient, and a single depositional mode cannot well explain the complex depositional mechanism of the sand body in the study area. In recent years, Many scholars have conducted in-depth research on the Cretaceous Baxigai Formation in the Kuqa Piedmont and Tabei Uplift, mainly analyzing the distribution of sedimentary facies in large areas. However, there are few studies on the Baxigai Formation in the west of the Tabei Uplift, and only the Kapushaliang group is studied as a whole group. Previous studies have not fully paid attention to the control effect of the Cretaceous paleoclimate on the red-bed sand bodies of the Baxigai Formation, and insufficient understanding of the depositional characteristics, depositional environment, and depositional models in the red-bed sand bodies of the Baxigai Formation, resulting in unclear distribution rules and sedimentary boundaries of sand bodies in this area, which seriously restricts the process of oil and gas resource exploration in the Baxigai Formation in the study area (Hong et al., 2016). studied the sedimentary characteristics of the Baxigai Formation in the Xinhe-Sandaoqiao area and concluded that this set of formations is a braided river delta-lake sedimentary system (Wu et al., 2022). studied the Mesozoic sedimentary evolution characteristics of the Tabei Uplift. They concluded that deltas, braided river deltas, alluvial fan or fan delta sedimentary combinations, and beach bar deposits were mainly developed at the end of the Kapusaliang Group (Luo et al., 2021). concluded that the Baxigai formation on the southern slope of the Kuqa Depression developed the inner front-outer front-shallow lake subfacies of a river-controlled shallow water delta (Gao et al., 2014). researched the sedimentary paleoenvironment and model through field outcrops and geochemical analysis. They concluded that the Cretaceous Baxigai formations in the Kuqa Piedmont belt are wide and shallow lakes with large areas in an arid climate. In the Cretaceous Baxigai Formation deposition period, the study area has a hot and dry climate, gentle terrain, and conditions for seasonal delta development, making it an ideal area for the development of seasonal deltas.

This paper takes the red bed deposits of the Cretaceous Baxigai Formation in the western Tabei Uplift as the research object. Through core, well logging, geochemical analysis, and other data, and based on the regional geological background, a systematic study was conducted on the sedimentary environment and sedimentary characteristics of the Baxigai Formation. Based on the principle of historical comparison and combined with the sedimentary characteristics of modern seasonal delta sand bodies in arid climate conditions, the sedimentary types and characteristics, distribution rules, and sedimentary patterns of seasonal deltas of the Cretaceous Baxigai formation in the western Tabei Uplift are discussed. It provides a valuable reference for the reconstruction of paleogeography in the study area.

2 Geological setting

The Tarim Basin is located in northwest China and is the largest petroleum-bearing basin on land in China, covering an area of approximately 560,000 square kilometers (He C. F. et al., 2023; Wu et al., 2019). The basin is rhombus-shaped in plane and is surrounded by the Tianshan Mountains, the Kunlun Mountains, and the Altun Mountains (Figure 1A). It is a large superposition composite basin composed of Paleozoic craton basins and Meso-Cenozoic foreland basins, with a complex tectonic evolution history of ancient continental crust basement and multiple subsidence and Uplift (Du et al., 2023). Proterozoic-Cenozoic

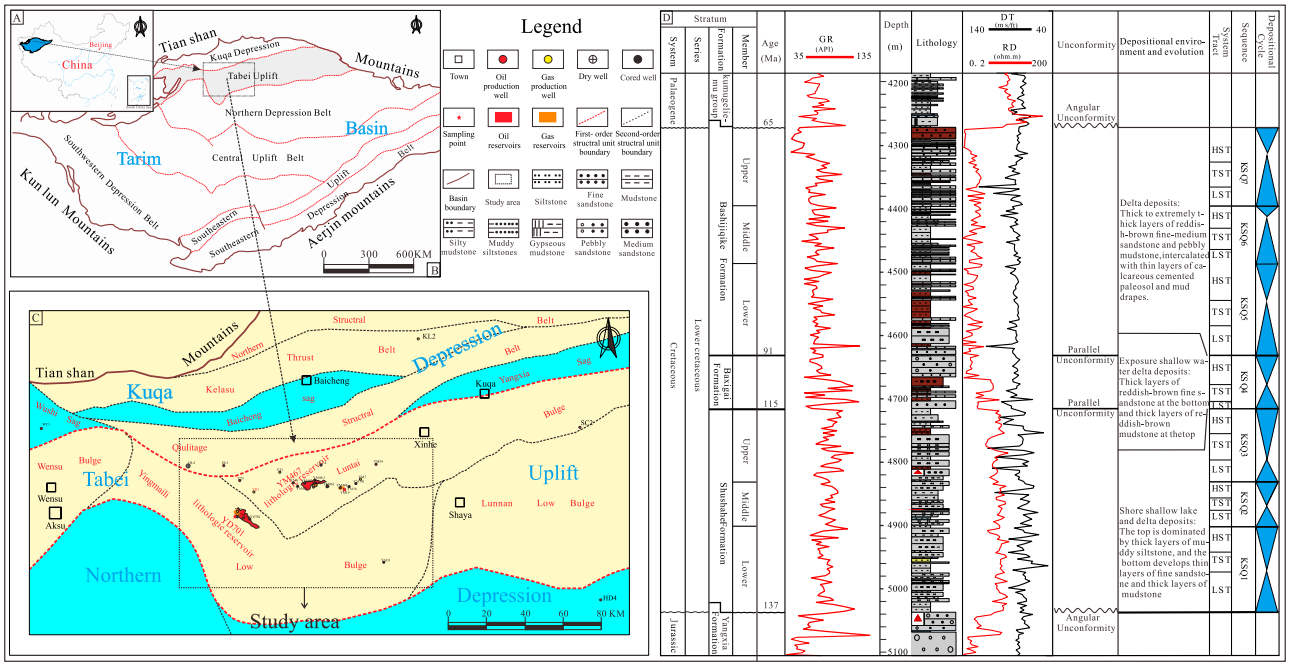

FIGURE 1
Geological background of the western Tabei Uplift **(A)** Location map of the Tarim Basin in NW China (modified from Wang et al., 2023). **(B)** The tectonic location of the study area (modified from Zhao et al., 2022). **(C)** Map showing geological details of the study area, including the location of oil and gas field, cored wells, and partial key wells (modified from Xu et al., 2016). **(D)** Well YM10 Stratigraphic framework and sedimentary background of the interval of interest (modified from Xia et al., 2019; He et al., 2013; Liu Y. F. et al., 2019).

Formation are developed from bottom to top in the basin, with a maximum sedimentary thickness of more than 10.000 m (Tian, 2019). The Tarim Basin can be divided into seven first-level structural units, namely, the Kuqa Depression, the Tabei Uplift, the Northern Depression Belt, the Central Uplift Belt, the Southwestern Depression Belt, the Southeastern Uplift, and the Southeastern Depression Belt, from north to south (Figure 1B) (Jia, 1997). The Tabei Uplift is located in the northern part of the Tarim Basin, spreading in an east-west direction. It is adjacent to the Kuqa Depression in the north and the Northern Depression Belt in the south and consists of the Wensu Bulge, the Yingmaili Low Bulge, the Luntai Bulge, the Lunan Low Bulge, and the Korla Bulge (Li et al., 2012; He et al., 2008; Sun et al., 2020; Li F. J. et al., 2019). The Tabei Uplift is a long-term development of the Paleozoic craton "residual paleo-uplift" with the characteristics of basement uplift (Su et al., 2020). The Uplift was finalized after the late Hercynian movement in the late Paleozoic. At the end of the Permian to the early Triassic, the Tabei uplift was defined as the front Uplift of the foreland basin in the Kuqa depression (Li et al., 2012). Since the Cretaceous period, the Tabei Uplift gradually evolved into a north-dipping gentle slope and was affected by multiple tectonic movements; a concave and convex structural pattern has been formed, and the Tabei Uplift gradually declined (Liu Y. F. et al., 2019; Li J. G. et al., 2015; Xu et al., 2016). Currently, it is mainly covered by the Quaternary strata. The study area is located in the west of Tabei Uplift, which mainly includes the Yingmaili low Uplift, the west of Luntai Uplift, and part of the Lunnan low uplift, and it is a key area for oil and gas exploration in the Tarim Basin at present (Figure 1C).

The Tabei Uplift has superior conditions for the two-way convergence of dual-stage petroleum-bearing systems of Marine Cambrian-Ordovician and continental Triassic-Jurassic and is very rich in oil and gas resources (Zhang et al., 2010). The Triassic, Jurassic, and Cretaceous strata were developed in the study area in the Mesozoic period (Li J. L. et al., 2019). The Cretaceous mainly developed the Lower Cretaceous strata; the Upper Cretaceous strata were denuded and had an angular unconformity contact with the underlying Jurassic and the overlying Palaeogene. The Lower Cretaceous strata are a set of clastic rock depositional systems, and the Kapushaliang Group (Shushanhe Formation and Baxigai Formation) and Bashijiqike Formation developed from bottom to top (Figure 1D). The overall thickness of the Shushanhe Formation is between 50 and 350 m. It is a set of fine-grained clastic rock deposits, the top is dominated by thick layers of muddy siltstone, and the bottom develops thin layers of fine sandstone and thick layers of mudstone, and the development of Shore shallow lake and Delta facies (Xia et al., 2019; He B. Z. et al., 2023). The Bashijiqike Formation is a delta sedimentary system composed of thick to extremely thick layer of reddish-brown fine-medium sandstone and pebbly mudstone, intercalated with thin layers of calcareous cemented paleosol and mud drapes (Liu B. B. et al., 2019). Paleo-uplift were weak in activities, and the accommodation was sustained in the deposition period of the Baxigai Formation (Zhao et al., 2022). Influenced by regional tectonic movement, the

paleogeographic pattern of the southeast high and northwest bottom was formed in the study area, which controlled the distribution of sedimentary facies (Su et al., 2020).

3 Materials and methods

This research was based on cores, well logs, 3D seismic data, and analyzed test (X-ray diffraction whole rock mineral analysis, Particle size analysis, and microelement analysis) data of the Baxigai Formation in the northwestern Tarim Basin (see Figure 1C for cored well location). The data used in this study were obtained from the Institute of Exploration and Development, PetroChina Tarim Oilfield Company. Detailed descriptions, photographs, and sediment particle size analysis from 242 m of core records in 15 cored wells that penetrated the Baxigai Formation were taken for identification of lithofacies and interpretation of sedimentary environments. The core observation and description tasks were conducted in the core library of Tarim Oilfield. Well logs from a total of 160 wells (including exploration wells and oil and gas production wells) and well-logging data were in LAS format in this study. 3D seismic data that cover the central part of the study area (3,174 km^2) were studied for identification Paleogeomorphology in the depositional period of the Baxigai Formation by horizon flatting of a SE—NW direction seismic profile (approximately 71 km long), the 3D seismic surveys were in SEG-Y format. X-ray diffraction whole rock analysis data comes from 66 samples in 7 boreholes and is mainly used to analyze Baxigai formation sandstone types. Identify single-well sedimentary microfacies of cored wells through core observation and description combined with well logs and particle size analysis data. The microelement analysis data samples were from Well YM19 and Well YD704H, with a total of 7 samples (see Figure 1C for sample locations). It is mainly used to analyze the palaeoclimate and palaeoenvironment in the deposition period of the Baxigai Formation. The PerkinElmer inductively coupled plasma mass spectrometer NexION was used as the test instrument for microelement analysis, and the accuracy of over 5 percent adopts the "Methods for Chemical Analysis of silicate Rocks"(GB/T 14506.30–2010). Modern satellite images from Google Earth software were used for Modern analog to improve understanding of the development pattern of the distributary channels in arid climates. Calibration of gamma ray log data with core interpretations was used to establish electro facies that were used to identify sedimentary facies in non-cored wells.

The core depth was corrected based on the GR curve, analyzing the formation color, special minerals, and sedimentary structure characteristics and using the standard chemical parameters from microelement analysis to explain the sedimentary environment of the Baxigai formation. Based on lithology, sedimentary structure, and other related factors, lithofacies classifications of the Baxigai formation were conducted, and by combining the lithofacies classification, well logs, and particle size analysis, single well sedimentary interpretations were conducted in cored wells. Using core interpretation and GR well log curve characteristics, well log facies schemes are established to identify single-well sedimentary microfacies in non-cored wells. By counting the sandstone thickness of 160 wells in the Baxigai Formation, sand body thickness contours are drawn, and combined with the well-tie profile of sedimentary microfacies comparison, the plane distribution of sand body sedimentation microfacies is obtained. Based on the principle of historical comparison method and combined with the comprehensive analysis of the sedimentary characteristics of modern sedimentary high-definition satellite images (including sedimentary background, sedimentary origin, sedimentary morphology, sedimentary scale, etc.) The channel development models in arid climate conditions was extracted from it, and based on this, an accurate sedimentary interpretation of the Baxigai Formation in the study area was performed. Combining paleotopography, provenance, paleoclimate, and hydrodynamic changes and based on the plane distribution of sand body sedimentation microfacies, a two-stage sedimentation model of seasonal delta sand bodies in arid climate conditions was proposed.

4 Results

4.1 Sedimentary environment analysis

4.1.1 Lithology characteristics

The thickness of the Cretaceous Baxigai Formation in the west of Tabei Uplift is between 40 and 60 m, the shaliness gradually increases from bottom to top (Figure 2). Through the statistical analysis of sandstone samples, the results show that The sandstone types of the Baxigai Formation in the study area are mainly lithic feldspar sandstone, followed by feldspar sandstone and feldspar lithic sandstone. The quartz volume fraction is 35%–74%, the average volume fraction is 55%, the feldspar volume fraction is 14%–48.7%, the average volume fraction is 28%, the lithic fragment volume fraction is 6%–35.2%, the average volume fraction is 17% (Figure 3). Overall, the grain size of the red bed sandstone in the Baxigai Formation is mainly medium-fine, well sorted, mainly sub-angular to sub-rounded, with high structural maturity and medium composition maturity.

4.1.2 Formation color and special mineral

Mudstone color is divided into autogenetic color and secondary color. Autogenetic color depends on the color of authigenic minerals during the sedimentary process of clayey deposits and its early diagenetic process, and it is an essential symbol for restoring the ancient depositional environment and reflecting the depth of the water body (Fu et al., 2023; Sun et al., 2015). The colors of the Baxigai Formation mudstone in the study area are mainly brown and reddish-brown. The Phenomena such as mud cracks caused by drought exposure, interbedded between oxidized and reduced colors mudstone, and mutation contact between oxidized and reduced colors mudstone can be seen in the Baxigai Formation (Figures 4A–I), which is because the deposits in this area are caused by seasonal changes in climate and cyclical changes in runoff (flooding and drying periods). In the flood period, the climate was relatively humid, the runoff increased sharply, the water body in the sedimentary area was deep, and mudstone was deposited by the fine-grained suspended matter brought by the flood, showing a gray-green color in a weakly reductive sedimentary environment. In the dry period, the climate was dry, with less rain, the water body in the sedimentary area was shallow or even dry, the mudstone color

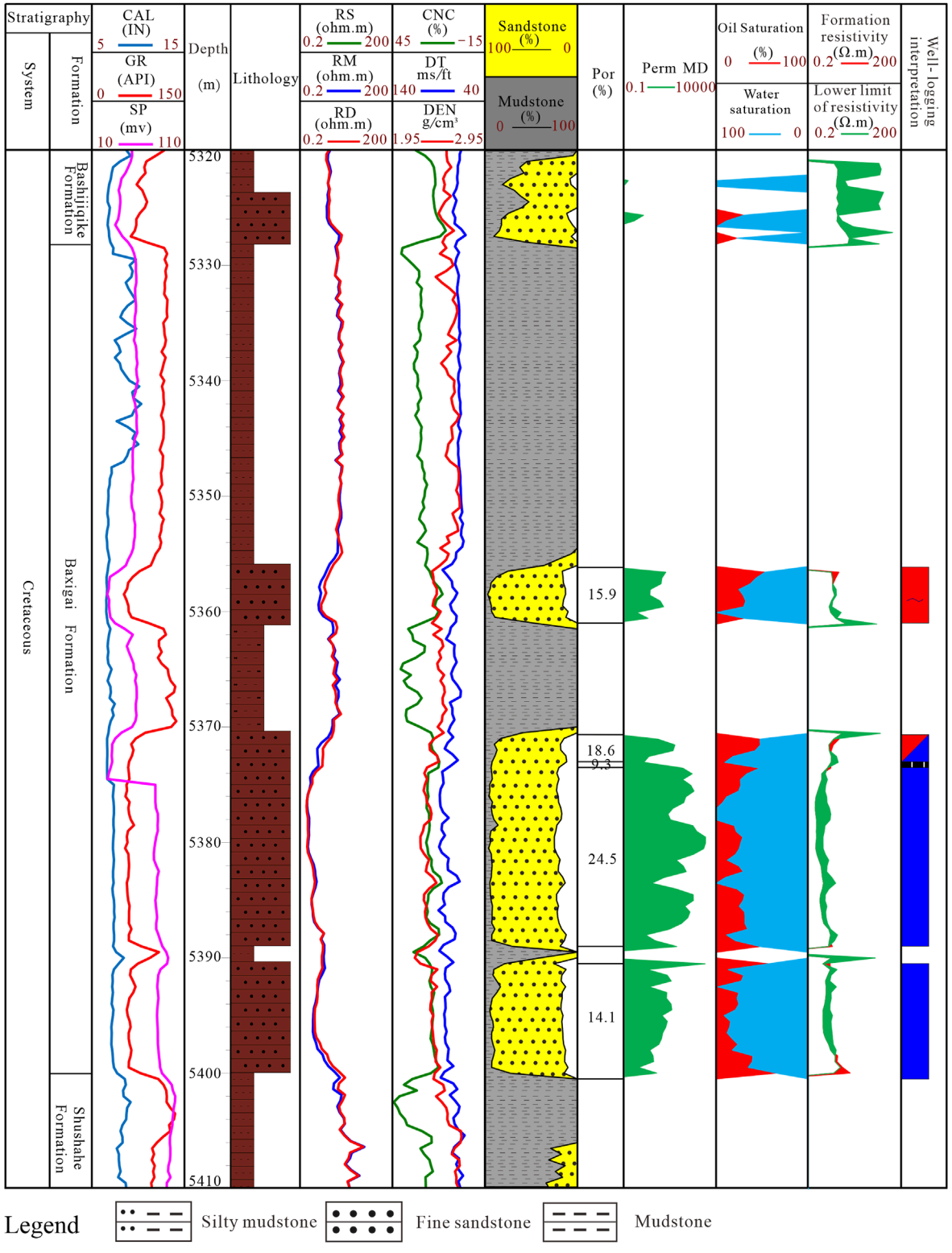

FIGURE 2
Well 469H Well-logging interpretation of Cretaceous Baxigai Formation in the study area.

was reddish brown, and a part of the mudstone was exposed on the earth's surface. From the above mudstone color and bedding plane structure, it is observed that the mudstone is exposed intermittently.

Reduced color sand bodies are commonly found in the oxidized formation (red bed) of the Baxigai Formation in the study area, and the colors of the sandy sediment in the Baxigai

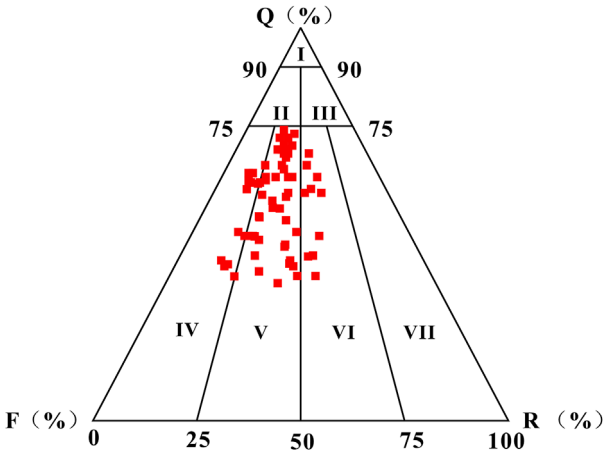

FIGURE 3
Sandstone classification triangle diagram of the Baxigai Formation (66 samples from 7 wells). Classification standard reference (Zhu Xiaomin, 2010). I: quartz sandstone; II: feldspar quartz sandstone; III: lithic quartz sandstone; IV: feldspar sandstone; V: lithic feldspar sandstone; VI: feldspar lithic sandstone; VII: lithic sandstone.

Formation are mainly reddish-brown and gray-green. Reddish-brown sandstone (red bed) does not contain oil and gas, reflecting primary sedimentary characteristics (Figure 4J). The origin of gray-green sandstone is a reduction reaction between oxidizing minerals and hydrocarbon substances caused by oil and gas filling after sandy sediments diagenesis, which makes the mineral autogenetic color transformation. However, due to the low physical properties of calcareous nodules, oil and gas are difficult to invade and retain mineral autogenetic color.

Calcareous nodules are authigenic mineral aggregates composed of calcium carbonate, generally formed by evaporation or leaching in arid-semi-arid regions, and are an essential indicator of paleoclimate analysis (Xing et al., 2019). The calcareous nodules of the Baxigai Formation in the study area are reddish-brown, mainly oval, distributed along the bed, and foam strongly after dropping dilute hydrochloric acid with a concentration of 5%, and they are generally deposited in fine sandstones (Figures 4K, L). These nodules have not cut through the bedding, indicating that they are products of the syngenesis period. Based on the above analyses, it is believed that the study area was in an oxidizing environment with hot and arid paleoclimate conditions during the sedimentary period of the Baxigai Formation.

4.1.3 Sedimentary structure

The primary sedimentary structure type indicates the hydrodynamic mechanisms, deposition rate, and sedimentary environment characteristics in sediment formation. Core observation shows that the Baxigai formation in the study area developed a multi-stage superimposed channels sand body. The deposits are mainly fine sandstone and siltstone, and Sedimentary structures reflecting event sedimentation, such as lag deposit fine conglomerate (Figure 5A), positive graded bedding (Figures 5D, E), and gravel imbricated arrangement (Figure 5F), can be seen locally. Lag deposits: distributed along the scour surface, mainly coarse sandstone and fine conglomerate, with mixed particle sizes and poor sorting, the particles are mainly sub-round, followed by sub-angular, and roundness is medium, reflecting a longer transport distance. Graded bedding: distributed at the bottom of the channels sand bodies, from bottom to top, the particle size changes from coarse to fine. Parallel bedding and massive bedding develops in the upper part of the graded bedding, mainly medium sandstone and fine sandstone, reflected in hydrodynamic conditions with extreme transporting capacity, and the transported clastic particles are rapidly unloaded and deposited in a short time. Gravel imbricated arrangement: gravel is intraclasts (muddy clast) formed by diversion or lateral migration of the river bed to erode muddy deposits at the bottom of the river, landslides, or deposition after short-term transport, which reflects hydrodynamic conditions with strong transporting capacity.

The upper flow regime sedimentary structures are an essential connection between sedimentary records and climate responses and are commonly found in seasonal river deposits (Tan et al., 2018). In the sandstone of the Baxigai Formation, there are not only normal fluvial sedimentary structures but also a series of upper flow regime sedimentary structures. The basic characteristic of upper flow regime is the dynamics of shallow water and rapid flow, which mainly develops after the flow velocity rapidly increases to a certain peak in a short period, and the preservation of upper flow regime sedimentary structures also requires the rapid decline of the flow velocity. The upper flow regime sedimentary structures of the Baxigai Formation mainly include parallel bedding, massive bedding, etc. (Figures 5B, C). Parallel bedding is mainly well developed in fine sandstone, and in hydrodynamic conditions with strong transporting capacity, it is also common in gravelly coarse sandstone and medium sandstone. High deposition rate results in a positive graded of particle size in parallel bedding. Massive bedding is mainly developed in thick layers of fine sandstone, reflecting rapid deposition in high-energy, strong hydrodynamic conditions. The lower flow regime sedimentary structures of the Baxigai Formation mainly include low angle cross-bedding, small trough cross-bedding, oblique bedding, and ripple cross-bedding (Figures 5G–J). They are mostly developed in fine sandstone and represent slow or subcritical flow, a slow-flowing hydrodynamic force dominated by the traction current of one-way water flow, consistent with normal river sedimentary structure characteristics.

The sandstone sedimentation of the Baxigai Formation in the study area is not only affected by the lower flow regime flow mechanism but also develops many distinctive sedimentary structures controlled by the upper flow regime flow mechanism, which reflects the coexistence of seasonal flood events and normal sedimentation in the Baxigai Formation.

4.1.4 Geochemical characteristics

Trace elements in sedimentary rocks are not only controlled by their own physical and chemical properties but also greatly affected by paleoclimate and paleoenvironments. Therefore, the relative content and ratio of trace elements can be used to restore paleoclimate and paleoenvironments (Nesbitt and Young, 1982; Yang et al., 2006). Trace elements such as V, U, Mo, Cr, and Co are redox sensitive elements and are often used as an identification index of the paleooxygen phase (Fan et al., 2019). In this paper, two chemical parameters, V/(V+Ni) and V/Cr, are

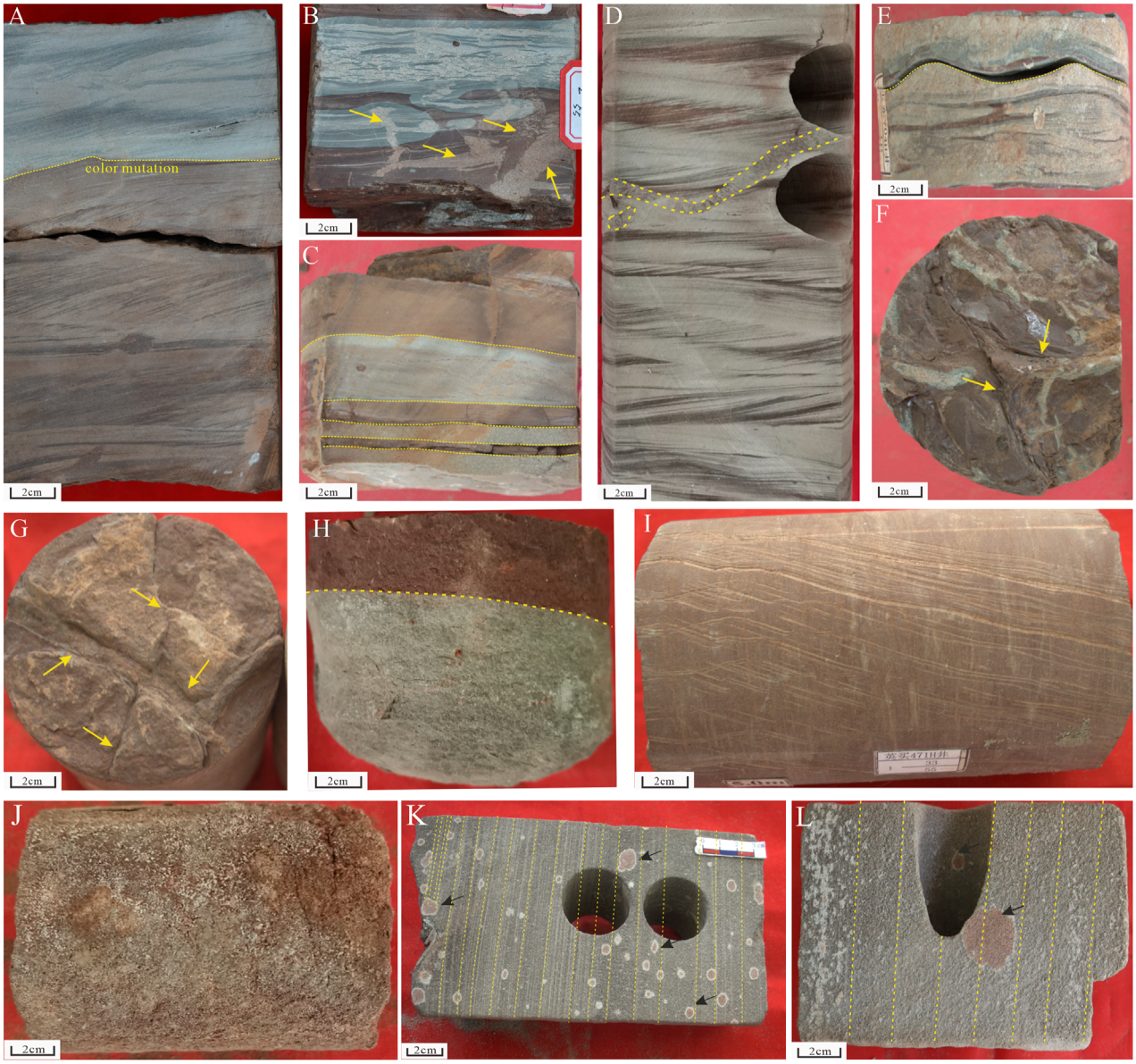

FIGURE 4
Core pictures showing characters in climate-sensitive deposits of the Baxigai Formation. **(A)** WellYD701, 4975.28 m, Ascending cross-bedding silty mudstone with color mutation; (mutation boundary surface mark by yellow arrow) **(B)** WellYD701, 4978.5 m, Reddish brown-grey green mudstone alternating with bioturbation (mark by yellow arrow); **(C)** WellYD704, 4975.63 m, Reddish brown mudstone-gray green siltstone sandstone interbedded; **(D)** WellYD704, 4970.43 m, Ascending cross-bedding muddy siltstone, black lamina at the bottom and brown lamina at the top with bioturbation (mark by yellow lines); **(E)** WellYD704, 4975.30 m, Light red and gray-green muddy siltstone interbedded deposit; **(F)** WellYD704, 4979.18 m, Mud cracks (mark by yellow lines); **(G)** WellYM19, 4999.8 m, Mud cracks (mark by yellow lines); **(H)** WellYM46-1, 5166.7 m, Mudstone color change from gray-green to reddish brown; **(I)** WellYM471, 5201.25 m, reddish brown mudstone; **(J)** WellYM701, 4995 m, Massive bedding, fine sandstone with salt efflorescence; **(K)** WellYM471, 5201.65 m, Calcareous nodules (mark by black arrow) in the parallel bedding very fine sandstone; **(L)** WellYM468, 4998.5 m, Calcareous nodules (mark by black arrow) in the parallel bedding medium sandstone.

selected to distinguish the paleo sedimentary environment of the Baxigai Formation through the analysis, calculation, and statistics of the existing sample data. V/(V+Ni) >0.77, 0.6–0.77, and <0.6 indicate reduction environment, weak oxidation-weak reduction environment and oxidation environment; V/Cr >4.25, 2.0–4.25, and <2 indicate reduction environment, weak oxidation-weak reduction environment and oxidation environment (He et al., 2013; Russell and Morford, 2001; Li F. J. et al., 2019; Jones and Manning, 1994).

In the Baxigai Formation, the value of V/(V+Ni) is 0.02–0.36, and the average value is 0.14; the value of V/Cr is 0.01–0.39, and the average value is 0.13. Based on the results of the above analysis, it can be seen that the sedimentary water body in the study area during the sedimentary period of the Baxigai Formation mainly manifests an oxidation environment.

The Sr/Ba ratio is a commonly used identification index for judging the paleosalinity of water body in sedimentary areas.

FIGURE 5
Typical sedimentary structure characteristics in the Baxigai Formation. **(A)** WellYM467, 5180.2 m, Lag deposit fine conglomerate; **(B)** WellYM468, 5002.45 m, Parallel bedding medium sandstone; **(C)** WellYM16, 5005 m, Massive bedding fine sandstone; **(D)** WellYM463, 5104.5 m, Positive graded bedding (mark by yellow triangle); **(E)** WellYM468, 4998.5 m, Multi-stage lag deposits, The particle size gradually becomes finer from bottom to top and parallel bedding (mark by yellow lines) at the top; **(F)** WellYT4, 5566.6 m, Massive bedding fine sandstone with gray-green muddy clast, gravel imbricated arrangement (mark by yellow lines); **(G)** WellYM468, 4999.7 m, Medium sandstone parallel bedding (mark by yellow lines) and low angle cross-bedding (mark by black lines); **(H)** WellYT4, 5562.42 m, small trough cross-bedding fine sandstone; **(I)** WellYM468, 5000 m, Oblique bedding medium sandstone; **(J)** WellYM8, 5252.1 m, Ripple cross-bedding muddy siltstone.

Sr/Ba <0.6, 0.6–1.0, and >1 indicate freshwater, semi-salt, and saltwater deposition (Wang et al., 1979). The statistical analysis of the Baxigai Formation samples in the study area shows that the Sr/Ba ratio is 1.34–5.00, and the average value is 3.32. It can be inferred that the sedimentary water body of the study area in the Baxigai Formation sedimentary period was a saltwater environment, indicating that the evaporation of water was greater than the rainfall in the sedimentary area, and the climate was dry and hot.

The Sr/Cu ratio responds sensitively to changes in paleoclimate and has a good indication effect. Sr/Cu between 1.3 with 5.0 indicates a warm and humid climate, and Sr/Cu>5.0 indicates a hot and dry climate (Ding et al., 2021). The Sr/Cu ratio of the Baxigai Formation is 2.05–42.32, with an average value of 14.10, and 5 samples are >5.0, indicating that the sedimentary period of Baxigai Formation in the study area was dominated by a hot and dry, with a few periods are humid and warm climate, reflecting the paleoclimate feature of alternating dry and wet.

4.2 Sedimentary facies and their spatial distribution of the Baxigai Formation seasonal delta

4.2.1 Sedimentary facies description and interpretation

Sedimentary facies and their sedimentary characteristics can be identified from core descriptions and particle size analysis to build seasonal delta sedimentary systems in an arid climate. The delta plain and the delta front depositional environments were identified in the seasonal delta sedimentary system.

4.2.1.1 Delta plain

The delta plain is located above the water surface and is mainly controlled by rivers, not affected by lakes, and has been in an oxidizing environment for a long time. The delta plain in the study area can be divided into upper delta and lower delta plain according to the intensity of river action, sand body thickness,

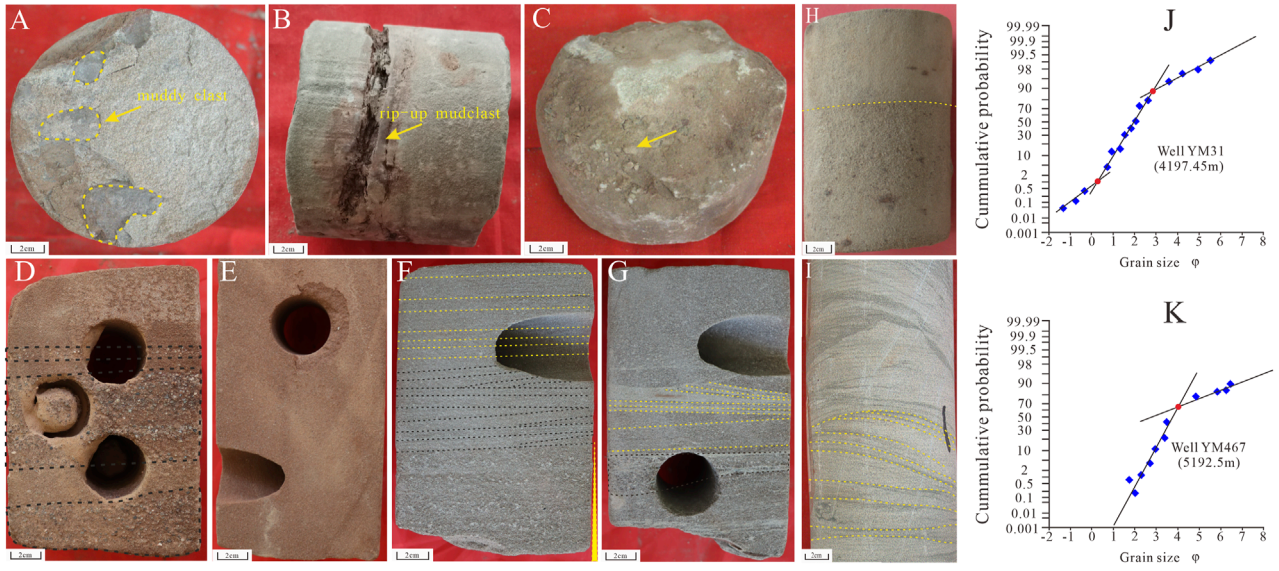

FIGURE 6
Typical sedimentary structure characteristics and cumulative grain-size probability distribution curves of core samples in distributary channels deposits in the Baxigai Formation. **(A)** WellYM31, 4174.25 m, Grayish green muddy clast (mark by yellow lines) in massive bedding medium sandstone; **(B)** WellYM31, 4196.5 m, Brownish rip-up mud clast deposits (arrow) in massive bedding fine sandstone; **(C)** WellYM31, 4197.95 m, Lag deposits (arrow) in medium sandstone; **(D)** WellYM468, 5002.7 m, Multi-stage lag deposits pebbly sandstone layer (mark by black lines); **(E)** WellYM468, 5001.3 m, Massive bedding fine sandstone; **(F)** WellYM468, 4999.8 m, Parallel bedding at the top (mark by yellow lines), low angle cross-bedding (mark by black lines), and positive graded bedding at the bottom (mark by yellow triangle); **(G)** WellYM468, 4998.6 m, Low angle cross-bedding (mark by yellow lines), lag deposits (mark by black lines); **(H)** WellYM46-1, 5173.5 m, Erosional surface between fine sandstone and underlying coarse sandstone; **(I)** WellYM46-1, 5176.1 m, Ripple cross-bedding very fine sandstone; **(J)** Well YM31, 4197.45 m; **(K)** WellYM467, 5192.5 m.

and deposit particle size, mainly developing distributary channels, crevasse channels, Floodplains, and interdistributary bays.

4.2.1.1.1 Distributary channels

There are obvious scour marks at the bottom of the distributary channels sand body, and there is a phenomenon of repeated erosion of multiple stages river channels. The thick layer of massive sandstone is enriched with a large amount of muddy clast and rip-up mud clast, and some of the lag deposit pebbly sandstone layers can be seen (Figures 6A–D). Massive bedding, positive graded bedding, parallel bedding, and low angle cross-bedding are developed above the scour surface (Figures 6E–G). The sediments are mainly medium sandstone and fine sandstone, with a small amount of coarse sandstone and pebbly sandstone. The channels is dominated by vertical aggradation, and multi-stage superimposed channels sand body develops in a positive rhythmic depositional sequence. The thickness of the stage channels sand body is between 4 and 8 m, and the cumulative thickness is up to 45 m.

The cumulative grain-size probability distribution curves are mainly three-stage and two-stage (Figures 6J, K). The deposits are mainly transported by jumps, and the ratio of traction load to suspended load is high. Taking wellYM31 and wellYM467 as examples, wellYM31: the rolling population <2%, the jump population >88%, and the suspended population <10%. YM467: the rolling population is not developed, the jump population >70%, and the suspension population <30%.

In the process of the distributary channels developing forward, the terrain slope gradually slows down, the distributary channels extends and diverts downstream, the density of the channels increases, and the scale decreases. With the increase of provenance distance, the average particle size of distributary channels sediments decreases, and the ratio of traction load to suspended load changes (Figures 6J, K). The sedimentary structure characteristics change accordingly (Figures 6H, I), and the sand body's connectivity gradually worsens. In an arid climate, the hydrodynamic mechanisms of the distributary channels changes periodically with seasonality due to intermittent flood events. In the flood period, distributary channels have extremely high flow intensity, and the upper flow regime is the major sedimentation transport mechanisms. The sediment transported by running water is mainly carried by bed sand load, and the distributary channels sand body is relatively developed. In the dry period, due to the transmission consumption, the runoff decreases, the flow velocity slows down, the channels transport capacity changes and the total sedimentary loading reduces.

4.2.1.1.2 Crevasse channels

Seasonal channels and extreme flood events are easily produced with highly fluctuating discharge in semi-arid climates (Zaman et al., 2012). Hyper-concentrated flows can be generated during flood events (Stuart et al., 2014). Crevasse channels are formed by bifurcation or crevasse processes of delta plain distributary channels during flood periods. The crevasse channels in the Baxigai Formation is controlled by high-energy transient water flow during the flood period, and the crevasse channels are exposed after the flood stage, with mudstone fill deposits in the dry period and turn to red color deposits.

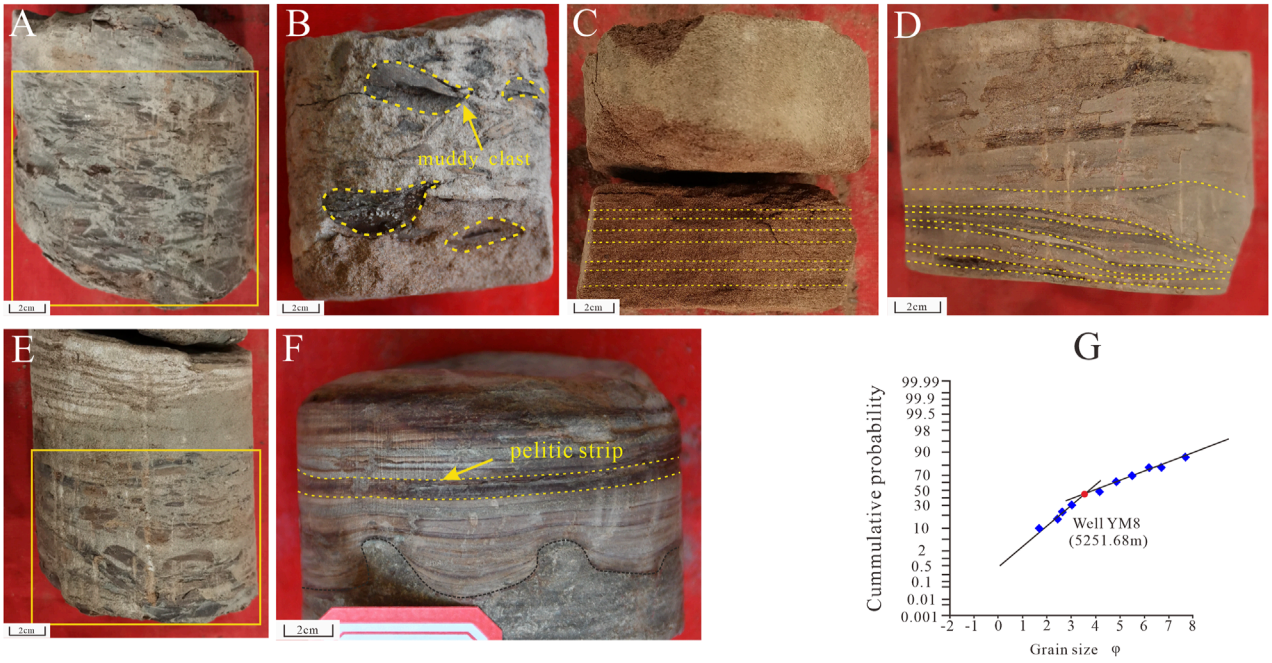

FIGURE 7
Typical sedimentary structure characteristics of the crevasse channels and cumulative grain-size probability distribution curves of the crevasse channels. **(A)** WellYM8, 5250.62 m, Massive bedding Siltstone with rip-up mud clast and muddy clast (marked with rectangle); **(B)** WellYM8, 5250 m, Massive bedding fine sandstone with muddy clast (mark by yellow lines); **(C)** WellYM8, 5248.73 m, Parallel bedding very fine sandstone; **(D)** WellYM8, 5249.24 m, Low angle cross-bedding siltstone; **(E)** WellYM8, 5250.28 m, Siltstone with rip-up mud clast and muddy clast (marked with rectangle); **(F)** WellYM8, 5252.69 m, Drainage structure, fine sandstone at the bottom (mark by black lines) and muddy siltstone at the top with pelitic strip (mark by yellow lines); **(G)** YM8, 5246.2 m, Cumulative grain-size probability distribution curves.

The sediment of the crevasse channels is composed of brown, reddish-brown fine sandstone, very fine sandstone, and siltstone. The sediment developed massive bedding, parallel bedding, low angle cross-bedding, drainage structure, etc (Figures 7A–F). Muddy clast and rip-up mud clast occur at the bottom of crevasse channels succession. The thickness of the sand body in the crevasse channels is mainly 2–4.5 m, and the scale of the sand body is smaller than that of the distributary channels. The cumulative grain-size probability distribution curves are mainly two-stage, and sediments are mainly transported by suspension. Taking wellYM8 as an example, the jump population <40%, and the suspension population >60%. The shaliness in the sandstone is relatively high, and the particle size of the sand body in the crevasse channels is finer than that in the distributary channels (Figure 7G).

4.2.1.1.3 Floodplains

The flood plain is a stagnant depression between distributary channels in the upper delta plain and has weak hydrodynamic forces. Since flood events are often accompanied by channels migration and crevasse diversion, frequent flood events make Floodplains smaller in size. The fine-grained suspended load brought by flowing during the flood period is the most important supply method of Floodplains sediments, mainly composed of reddish-brown mudstone intercalated with thin silty mudstone, and the bedding structure is not developed.

4.2.1.1.4 Interdistributary bays

Interdistributary bays are mainly developed in low-lying areas between distributary channels in the lower delta plain, with weak hydrodynamic, and the sediment are composed of suspended muddy sediments formed during the flood period. The sediment are mainly composed of brown and reddish-brown mudstone and dark brown mudstone with laminated siltstone and silty mudstone. Mud cracks (Figure 4G), plant roots (Figure 8A), salt film (Figure 8B), wave bedding (Figure 8C), and biological fossils of dark brown mudstone (Figure 8D) in periodic wetting-reducing conditions are developed in interdistributary areas. The redox changes in interdistributary bay sediments of the upper delta plain are affected by seasonal runoff. In the flood period, the low-lying areas were small stagnant lakes with dark brown mudstone sediments and preserved biological fossils. Due to sufficient source supply in the flood period, isolated thin sandy sediments are formed. The sediment is mostly siltstone, the thickness of the sand body is generally less than 1 m, and it is often interbedded with mudstone to form a uniform rhythm. In the dry period, the water body shrinks, the sediment is exposed to dry air, and the salt film can be seen in some mudstone, which is an evaporite facies.

4.2.1.2 Delta front

The delta front develops in the transition positions between the delta plain and the shallow lakes and is characterized by dual control

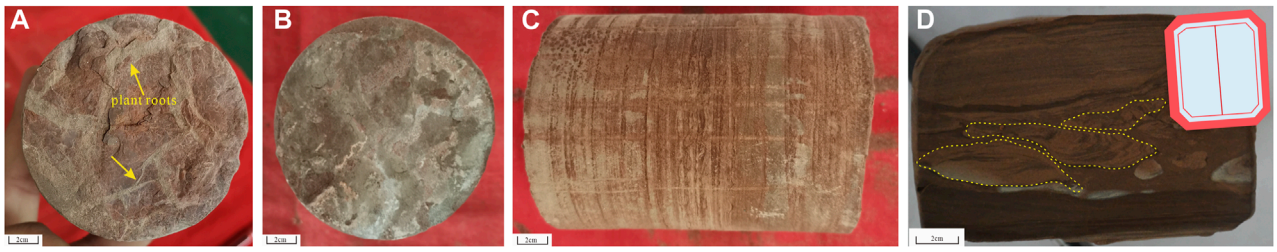

FIGURE 8
Core images showing sedimentary characteristics of interdistributary bays in delta plain **(A)** WellYM8, 5239.13 m, Plant roots (mark by yellow arrow); **(B)** WellYM8, 5237.98 m, Salt film; **(C)** WellYM701, 4998.6 m, Wave bedding silty mudstone; **(D)** WellYD701, 4969.6 m, Biological fossils (mark by yellow lines).

by river and lake interaction. Two types of sedimentary facies were developed in the delta front: terminal distributary channels and subaqueous interdistributary bays.

4.2.1.2.1 Terminal distributary channels

The terminal distributary channels develop as subaqueous extensions of distributary channels on the lower delta plain that are under the influence of high inertia-driven flow passes during flooding periods. In the dry period, due to the consumption of flow percolation and evaporation transfer, most of the river water will disappear along the path above the shoreline of arid lake basins or in the deserts, the terminal distributary channels dry up, and the sediment will be exposed. The hydrodynamic force of the distributary channels is weak, and the sediment is mainly composed of very fine sandstone and siltstone. Pelitic strips and mudstone interlayers are developed in the sandstone. The deposits develop parallel bedding, Ripples, low angle cross-bedding, ripple cross-bedding, etc. (Figures 9A–D). The thickness of the terminal distributary channels sand body is usually less than 2.5 m.

4.2.1.2.2 Subaqueous interdistributary bays

The subaqueous interdistributary bays are relatively developed in the delta front subfacies of the study area, and sedimentation is mainly suspended sedimentation, reflecting a weak hydrodynamic environment. Sediments are deposited between terminal distributary channels consisting of gray-green mudstone and reddish-brown mudstone. Mud cracks (Figure 4F), bioturbation, and lenticular bedding (Figures 9E, F) are common in subaqueous interdistributary bays deposits. The variation of shallow lake water levels controlled by seasonal runoff leads to periodic exposure of sediments in the subaqueous interdistributary bays.

4.2.2 Distribution of different sedimentary facies

From the flattened seismic profile, the paleotopography of the study area was gentle in the sedimentary period of the Baxigai Formation, the average gradient of the study area is low (Figure 10). Determine the type of distributary channels based on the detailed sedimentary interpretation and description in cored wells of the Baxigai Formation. The distributary channels types were identified in non-cored wells mainly through electro facies of gamma ray log curves (Figure 11). From the single-well sedimentary microfacies and the well-tie profile of sedimentary microfacies comparison along the provenance (Figure 12), the boundaries of the upper delta plain, lower delta plain, and delta front were roughly divided. Combined with provenance, paleotopography along the provenance, and sand body thickness contours, the plane distribution of sand body sedimentation microfacies is obtained. In the deposition period of the Baxigai Formation, the study area was in an oxidizing environment of an arid climate. The clastic particle mainly came from the southeast of the study area and entered the study area through several water channels, extended to the northwest, and continued to bifurcate, forming a large fan-shaped accumulation body. The delta plain in the study area extends far to the northwest and mainly develops major distributary channels and crevasse channels. The delta front is relatively underdeveloped and mainly develops terminal distributary channels. The thickness of the sand body in the study area also shows a clear trend of thinning from southeast to northwest (Figure 13).

5 Discussion

5.1 Modern sedimentological demonstration in arid climate

Research on modern arid-semi-arid regions has revealed several basic commonalities: arid and hot environments, flat terrain, extreme flood events, intense evaporation and infiltration, and so on (Zhang et al., 2018; Donselaar et al., 2013). Rivers in arid-semi-arid areas are mostly seasonal rivers, with sedimentary records reflecting oxidation and seasonal river activities (Li et al., 2021; Gao et al., 2015). Today, regions such as Xinjiang and Inner Mongolia in western China have an arid-semi-arid climate environment, with many seasonal rivers (Chen et al., 2020; Zhang et al., 2020). Take the Daihai Lake area of Inner Mongolia as an example; the Bantanzi River is a typical seasonal river sedimentary system in the northern part of the Daihai Lake, and the hydrodynamic mechanism changes periodically with the season. In the flood period, the upper flow regime is the primary sedimentary transport process, and a large amount of deposits can be transported. In the dry period, the lower flow regime is the primary sedimentary transport process, and the river transport capacity is extremely low (Tan et al., 2018). The study area had an arid climate in the Baxigai formation sedimentary

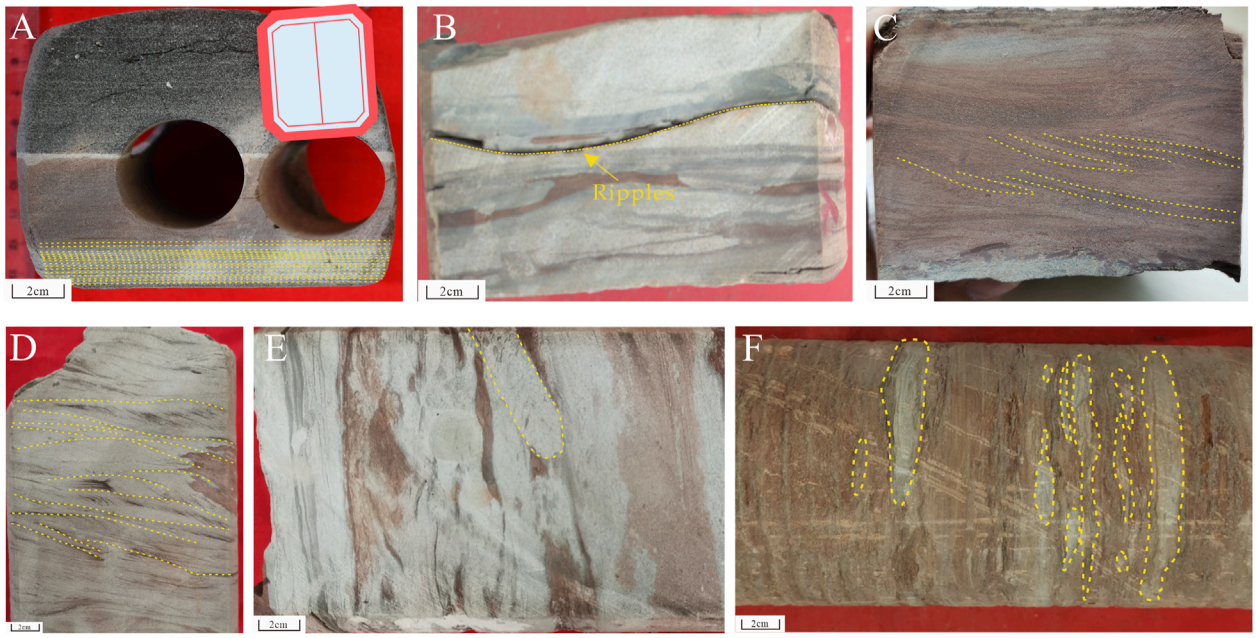

FIGURE 9
(A) WellYM467H, 5180.25 m, Parallel bedding, very fine sandstone (mark by yellow lines); **(B)** WellYD704H, 4977.85 m, Ripples siltstone; **(C)** WellYD704H, 4967.34 m, Low angle cross bedding muddy siltstone (mark by yellow lines); **(D)** WellYD704H, 4970.82 m, Ripple cross-bedding siltstone (mark by yellow lines); **(E)** WellYD704H, 4974 m, Silty mudstone bioturbation (mark by yellow lines); **(F)** WellYD704H, 4972.53 m, Lenticular bedding (mark by yellow lines).

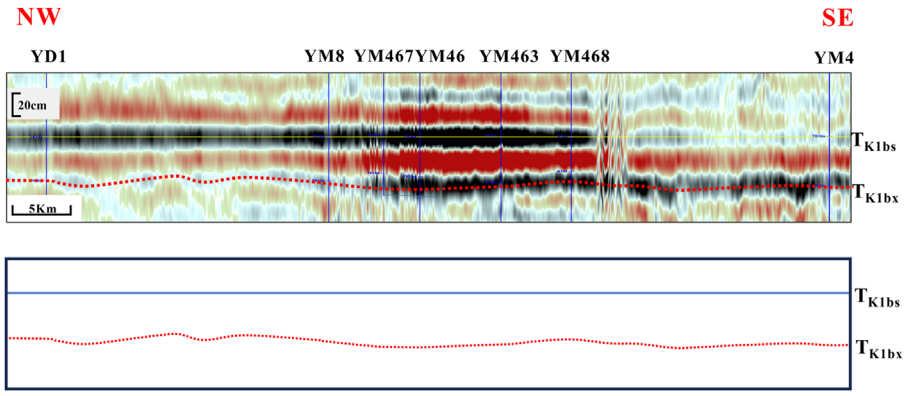

FIGURE 10
Seismic profile (flattened by the bottom of the overlying Bashijiqike formation) showing the paleotopography of the Baxigai Formation from SE to NW in the study area. The average gradient is 0.065%. Note the position of the profile on Figure 13.

period, and combined with the widely developed Supercritical flow sedimentary structures, the authors believes that in the Baxigai sedimentary period, the study area also developed seasonal rivers. Modern examples of seasonal delta deposition can be found in arid-semi-arid sedimentary environments (Li M. et al., 2015; Zan et al., 2022; Gondwe et al., 2021). These sedimentary examples help us to understand the depositional mechanisms and depositional pattern of sand bodies in seasonal delta depositional systems. The Okavango Delta and Amu Darya river Delta are modern examples of seasonal delta deposition in the Baxigai Formation in an arid climate. The Okavango Delta region has an arid-semi-arid climate. Rainfall is mainly concentrated in summer, usually with rainstorms and short duration. The average annual rainfall is 490 mm, and the average annual evaporation is 2,172 mm. The runoff of the Okavango River is controlled by rainfall of the Angola highlands and has seasonal changes, with the maximum runoff occurring in March-April (McCarthy et al., 2005; Tan, 2011). The Amu Darya river Delta has a warm temperate continental climate. The average annual precipitation in the lower reaches of the Amu Darya river is less than 100 mm, and evaporation is about 2000 mm, with the maximum

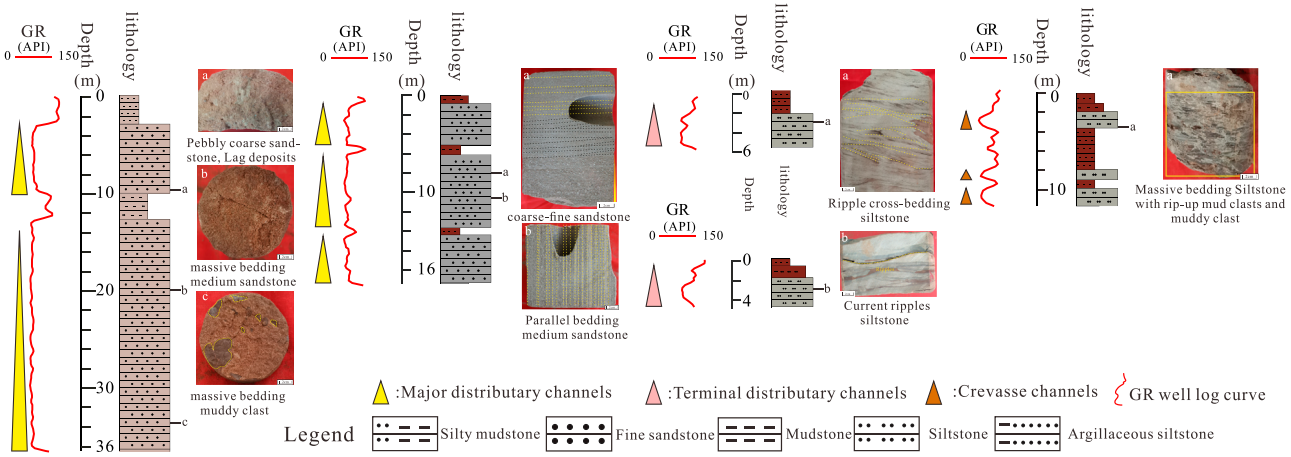

FIGURE 11
Well log facies scheme of the major distributary channels, crevasse channels, and terminal distributary channels deposits of the Baxigai formation in the study area. The box-shaped or Serrate box-shaped with low-amplitude well logs indicate the major distributary channels; The serrate bell-shaped logs with low-amplitude well logs indicate the crevasse channels; finger-shaped logs with low-amplitude or symmetrically serrate-shaped indicate the terminal distributary channels.

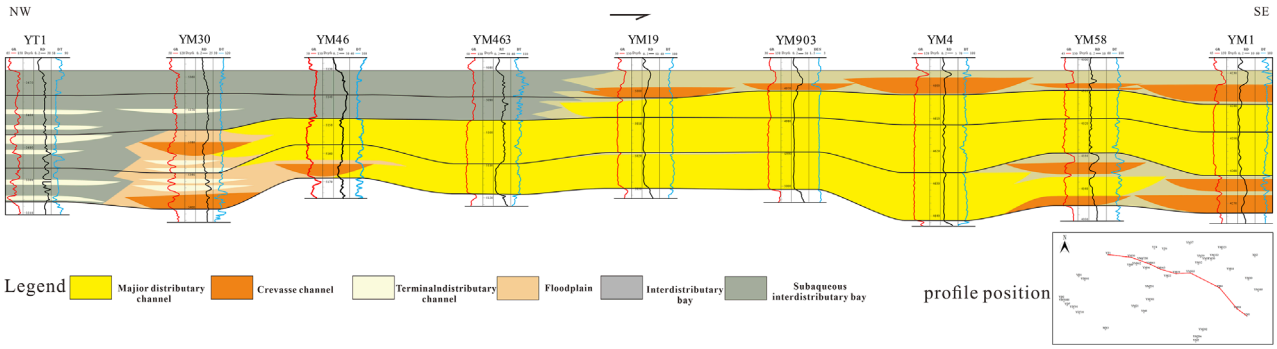

FIGURE 12
Well-tie profile of sedimentary microfacies comparison in the Baxigai Formation. Note the position of the profile on Figure 13.

runoff occurring in July-August. The river water in the Amu Darya river Basin is mainly supplied by melting water from mountain ice and snow and winter and spring rainfall in the upper reaches of the mountains, it is a snow-glacier fed river (Su et al., 2021; Reyisha, 2019; Conrad et al., 2007). Affected by seasonal runoff, the Okavango Delta and Amudarya river Delta areas change during the flood and dry seasons (Figures 14A–D). Seasonal changes in the Okavango Delta and Amu Darya river Delta result in different sedimentary models. In the flood period, the delta area extends, the distributary channels enters a high-flow stage, the total sedimentary loading is high, and the major distributary channels forms crevasse channels by frequent avulsion processes, and terminal distributary channels develop (Figures 14E, G). In the dry period, the total sedimentary loading of the distributary channels decreases with the decrease in runoff, and the river transport capacity is extremely low. The water level of the major distributary channels decreases and the scale decreases. The terminal distributary channels and the crevasse channels dry up, and the deposits are exposed to the dry air (Figures 14F, H).

5.2 Sedimentary model of the seasonal delta in an arid climate

The sand body depositional mechanisms in semi-arid-arid climates with total sedimentary loading variation greatly are quite different from the conventional model (Donselaar et al., 2013; Zhang et al., 2018) The red bed sedimentary sequence of the Baxigai Formation records changes in the total sedimentary loading variation greatly and seasonal flooding events with periodic exposure of sediments in an arid climate. The widely developed supercritical flow sedimentary structures have paleoclimate characteristics indicating strong seasonal changes. In the sedimentary period of the Baxigai Formation, the study area has gentle terrain, and the deposits come from the southeastern part of the basin (Luo et al., 2021; Chen et al., 2012). The climate was hot and arid, and the hydrodynamic mechanisms had seasonal periodic change. Combining regional background geological and based on the sedimentary characteristics and sedimentary facies types of the Baxigai Formation in the study area, considering the

10.3389/feart.2024.1348336

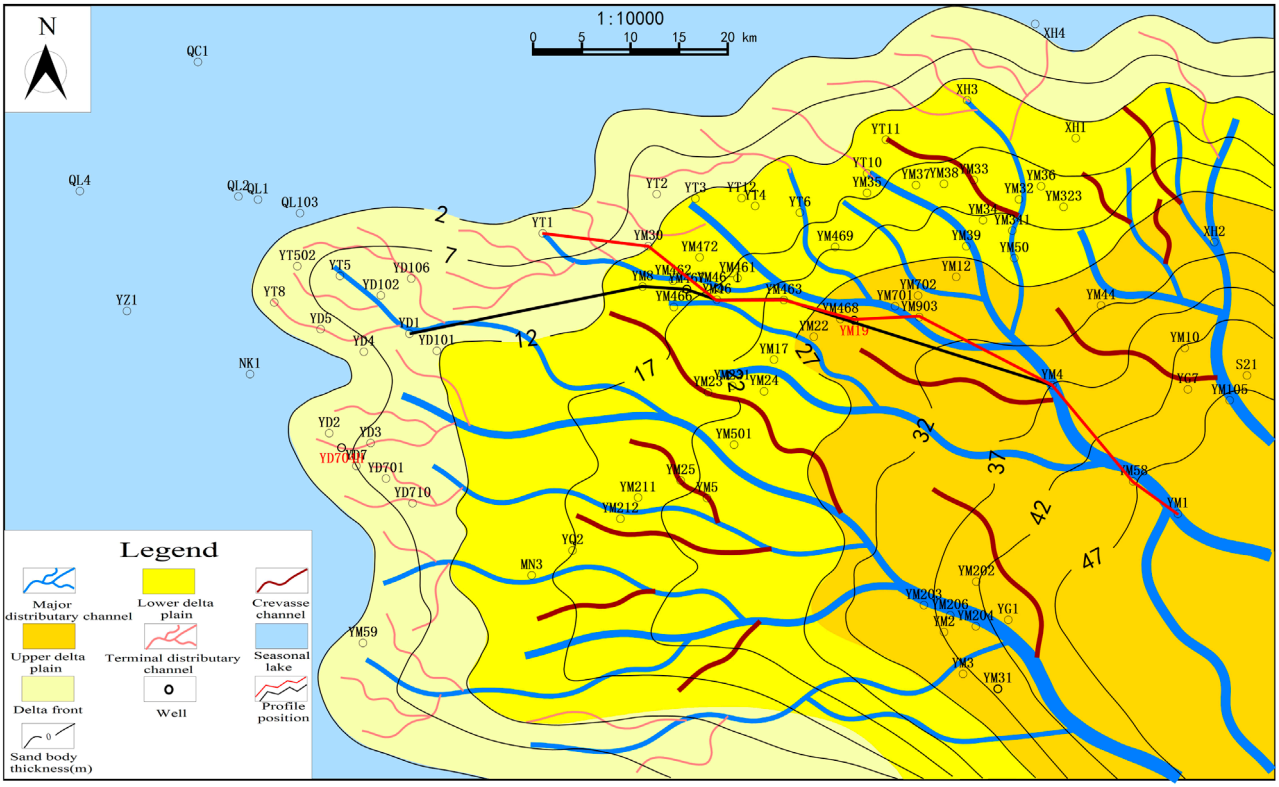

FIGURE 13
Plane distribution of sand body sedimentation microfacies of Cretaceous Baxigai Formation in western Tabei Uplift, (The well locations marked in red are sampling wells).

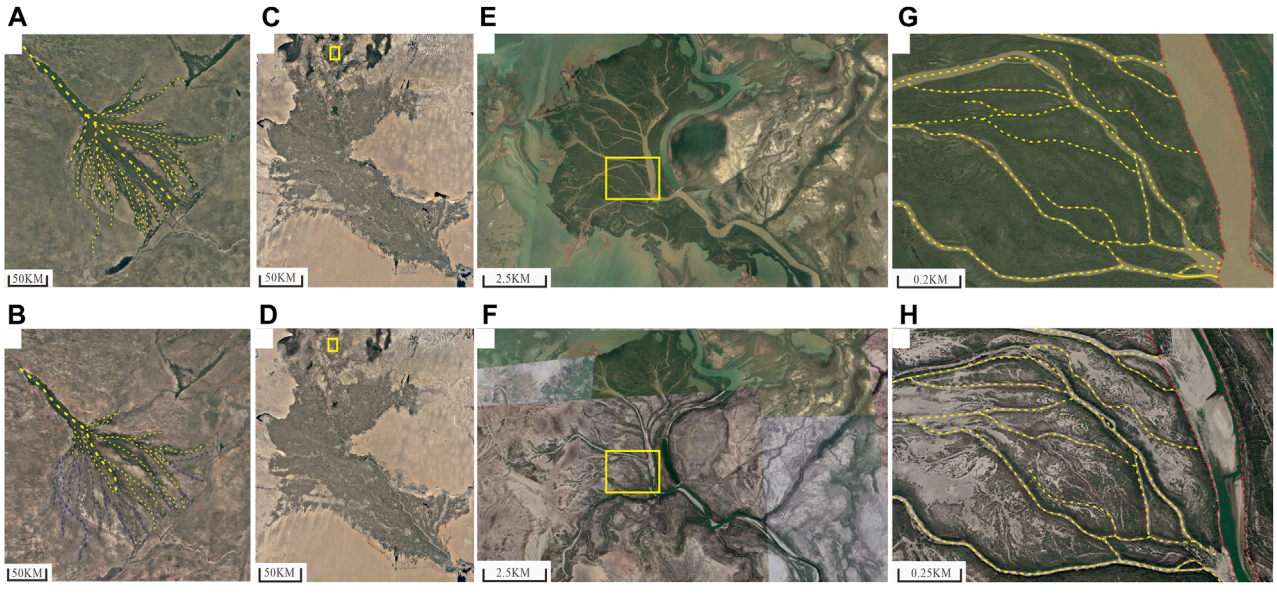

FIGURE 14
Satellite image from the Google Earth software showing seasonal changes of Delta **(A)** Okavango delta. In flood season 17 March 2018; active channels (mark by yellow lines); **(B)** Okavango delta in dry season 25 September 2018; active channels (mark by yellow lines); seasonal channels (mark by blue lines); **(C)** Amu Darya river delta in flood season 1 July 2018; **(D)** Amu Darya river delta in dry season 1 March 2018; **(E)** Part of Amu Darya river delta see location in the yellow rectangle of image **(C)**; **(F)** Part of Amu Darya river delta see location in the yellow rectangle of image **(D)**; **(G)** Major distributary channels and crevasse channels in flood season see location in the yellow rectangle of image **(E)** Major distributary channels (mark by red lines), crevasse channels (mark by yellow lines); **(H)** Major distributary channels and crevasse channels in dry season see location in the yellow rectangle of image **(F)**, major distributary channels (mark by red lines), crevasse channels (mark by yellow lines).

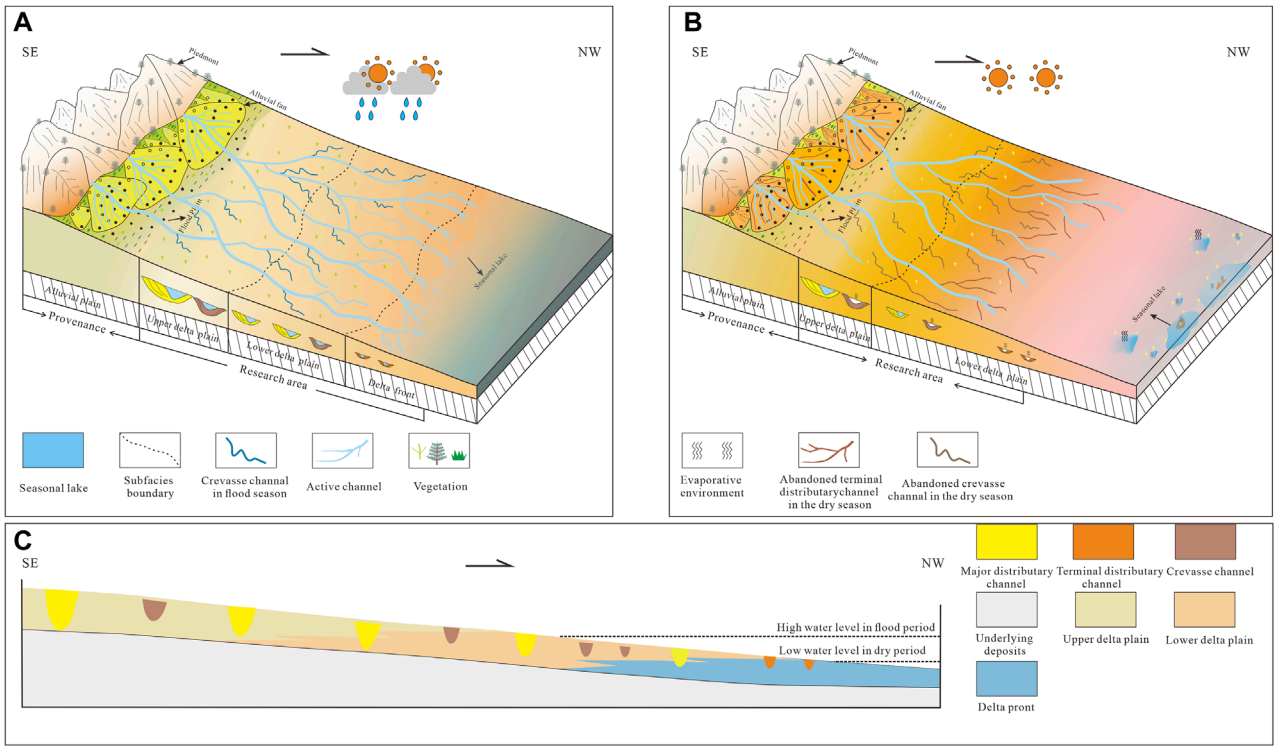

FIGURE 15
Sedimentary models for an arid climate seasonal delta of the Cretaceous Baxigai Formation in the west of the Tabei Uplift. **(A)** Flood period; **(B)** dry period **(C)** showing the sedimentary transition from the delta plain to the delta front.

changes in the hydrodynamic mechanisms of the current seasonal rivers in arid climate and the seasonal periodic changes of the total sedimentary loading and by the morphology and sand body distribution characteristics of current seasonal deltas in an arid climate, the sedimentary model of seasonal deltas of the Baxigai Formation in an arid climate was established (Figure 15). This model explains the depositional process and distribution of seasonal delta sand body in an arid climate. The development of the delta has gone through dual-stage depositional processes, and the depositional characteristics of different stages are obviously different.

In the high discharge stage of the flood period, The delta plain developed a distributary channels network composed of relatively stable major distributary channels and short-lived periodic crevasse channels that are formed by the avulsion process from major distributary channels. Supercritical flow sedimentary structures, such as parallel bedding, massive bedding, rip-up mud clast, etc., are widely developed in the major distributary channels. The major transport mechanism of sediments is the upper flow regime, and the total sedimentary loading is high. The delta progradation towards the basin's center forms terminal distributary channels at the delta front. During severe flood periods, a small amount of terminal distributary channels sand bodies were deposited underwater (Figure 15A). In the low discharge stage of the dry period, the channels takes the lower flow regime as the major transport mechanism, and the lower flow regime sedimentary structure generally exists in the major distributary channels deposits. Due to the consumption of water seepage and evaporation transfer, the terminal distributary channels and crevasse channels are exposed, with mudstone fill deposits, and turn to red color deposits. The density of the distributary channels is reduced, the total sedimentary loading is low, and the major distributary channels in the delta plain becomes the principal sand transport channels (Figure 15B). Controlled by the avulsion, bifurcation process, and influence of climate factors the scale of the major distributary channels and crevasse channels decreased from the upper delta plain to the lower delta plain (Figure 15C).

6 Conclusion

(1) The Cretaceous Baxigai Formation in the west of Tabei Uplift is dominated by red bed deposits. Bioturbation and plant rhizome fossils are developed in the mudstone, and mud cracks can be seen in the mudstone layer. Supercritical flow sedimentary structures such as parallel bedding and massive bedding are developed in the sandstone, and some sandstones develop calcareous nodules. Through the geochemical analysis of the core, it is concluded that the sedimentary environment of the Baxigai Formation in the study area is mainly arid and oxidized, and the sand body deposits have seasonal characteristics.

(2) The red bed sedimentary sequence of the Baxigai Formation records the seasonal delta sedimentary system with total sedimentary loading variation greatly in an arid climate. The

sedimentary process of the seasonal delta sand body in an arid climate is controlled by the dual-stage of the seasonal delta with flood and dry periods. The identification of sedimentary facies characteristic of seasonal river discharge variations is different. In the flood period, The deposits in distributary channels of the delta plain develop supercritical flow sedimentary structures, and the distributary channels migrate and bifurcate frequently. On the delta plain, crevasse channels are formed by the avulsion process of major distributary channels, and the delta progrades toward the center of the basin. In the dry period, The major distributary channels had relatively small scale. Terminal distributary channels and crevasse channels are exposed, with mudstone fill deposits, and turn to red color deposits. The major distributary channels sand bodies in the delta plain area are identified as framework sand bodies of seasonal deltas in arid paleoclimate, and the sedimentary scale of sand bodies is large and relatively thick. The scale of the sand body in the crevasse channels and terminal distributary channels is small, and the thickness of the sand body is thin.

(3) Combining paleotopography, provenance, paleoclimate, and hydrodynamic changes and based on the plane distribution of sand body sedimentation microfacies, combined with the sedimentary characteristics of the Baxigai Formation and referring to modern sedimentary examples, the dual-stage sedimentary model of the seasonal delta sand body with total sedimentary loading variation greatly in an arid climate was established. This dual-stage sedimentary model provides a new perspective on the development patterns of distributary channels in a lacustrine seasonal delta.

Data availability statement

The original contributions presented in the study are included in the article/Supplementary Material, further inquiries can be directed to the corresponding authors.

Author contributions

TW: Conceptualization, Methodology, Writing–original draft. YH: Conceptualization, Methodology, Writing–original draft. BL: Methodology, Writing–review and editing. WH: Project administration, Writing–review and editing. XG: Writing–review and editing, Formal Analysis. LD: Writing–review and editing, Project administration. JW: Formal Analysis, Writing–review and editing.

Funding

The author(s) declare financial support was received for the research, authorship, and/or publication of this article. "This research was funded by (Scientific Research Foundation of Yangtze University), grant number (8021003201)" and "The APC was funded by (8021003201)."

Acknowledgments

The authors wish to thank the Research Institute of Petroleum Exploration and Development, PetroChina Tarim Oilfield Company for providing various data for this study. We are grateful to Li Zhang, Associate Professor, Yangtze University for her constructive feedback that helped improve the quality of this manuscript. We are also greatly appreciate reviewers and editors for their constructive comments for their precious advice.

Conflict of interest

Author BL was employed by PetroChina Tarim Oilfield Company.

The remaining authors declare that the research was conducted in the absence of any commercial or financial relationships that could be construed as a potential conflict of interest.

Publisher's note

All claims expressed in this article are solely those of the authors and do not necessarily represent those of their affiliated organizations, or those of the publisher, the editors and the reviewers. Any product that may be evaluated in this article, or claim that may be made by its manufacturer, is not guaranteed or endorsed by the publisher.

References

Chen, G., Huang, Z. B., Zhang, H. L., Zhang, R. H., and Yan, X. F. (2012). Provenance analysis of clastic rocks in the cretaceous Bashijiqike Formation at Kuqa depression. *Nat. Gas. Geosci.* 23 (6), 1025–1033. Available at: http://www.nggs.ac.cn/CN/Y2012/V23/I6/1025.

Chen, X. J., Wang, X. Q., and Lu, Q. (2020). Soil moisture content and soil water lnfiltration in seasonal watercourse in arid area. *Arid. Zone Res.* 37 (01), 97–104. doi:10.13866/j.azr.2020.01.11

Conrad, C., Dech, S. W., Hafeez, M., Lamers, J., Martius, C., and Strunz, G. (2007). Mapping and assessing water use in a Central Asian irrigation system by utilizing MODIS remote sensing products. *Irrig. Drain. Syst.* 21, 197–218. doi:10.1007/s10795-007-9029-z

Ding, J. H., Zhang, J. C., Shi, G., Shen, B. J., Tang, X., and Yang, Z. X. (2021). Sedimentary environment and organic matter accumulation for the Longtan Formation shale in xuancheng area. *Acta Sedimentol. Sin.* 39 (02), 324–340. doi:10.14027/j.issn.1000-0550.2020.056

Donselaar, M. E., Gozalo, M. C. C., and Moyano, S. (2013). Avulsion processes at the terminus of low-gradient semi-arid fluvial systems: lessons from the Río Colorado, Altiplano endorheic basin, Bolivia. *Sediment. Geol.* 283, 1–14. doi:10.1016/j.sedgeo.2012.10.007

Du, D. D., Li, H. H., Yan, L., Zhou, D. Y., Cao, Y. H., Yang, M., et al. (2023). Deformation migration and three major geological events in Tarim Basin and their geological significance. *Chin. J. Geol.* 58 (02), 379–397. doi:10.12017/dzkx.2023.024

Fan, M. M., Bu, J., Zhao, X. Y., Kang, B., Li, W. H., and Zhang, W. G. (2019). Geochemical characteristics and environmental implications of trace elements of Yanchang Formation in southeastern Ordos Basin. *J. Northwest Univ. Sci. Ed.* 49 (4), 633–642.

Fu, J. H., Li, S. X., and Liu, X. Y. (2013). Geological theory and practice of petroleum exploration in the Ordos Basin. *Nat. Gas. Geosci.* 24 (6), 1091–1101. Available at: http://www.nggs.ac.cn/CN/Y2013/V24/I6/1091.

Fu, W. J., Zhang, C. M., Ji, D. S., Lou, L., Liu, J. L., and Wang, X. L. (2023). Sedimentary characteristics of shallow water delta of middle jurassic toutunhe Formation in southern anjihai river outcrops, junggar basin. *Lithol. Reserv.* 35 (4), 145–160. doi:10.12108/yxyqc.20230414

Gao, Z. Y., Feng, J. R., Zhou, C. M., Cui, J. G., Li, X. P., Zhao, X. S., et al. (2014). Arid climate seasonal rivers deposition: a case of lower cretaceous in kuche river outcrop. *Acta Sedimentol. Sin.* 32 (06), 1060–1071.

Gao, Z. Y., Zhou, C. M., Feng, J. R., Cui, J. G., Guo, M. L., and Wu, H. (2015). Distribution of a large area of sand body formation mechanism:ephemeral streams in arid climate. *Acta Sedimentol. Sin.* 33 (03), 427–438. doi:10.14027/j.cnki.cjxb.2015.03.001

Gondwe, M. J., Murray-Hudson, M., Mazrui, N. M., Moses, O., Mosimanyana, E., and Mogobe, O. (2021). A review of the limnology of the Okavango Delta, Botswana. *Afr. J. Aquat. Sci.* 46 (3), 251–273. doi:10.2989/16085914.2021.1882931

Gugliotta, M., Kurcinka, C. E., Dalrymple, R. W., Flint, S. S., and Hodgson, D. M. (2016). Decoupling seasonal fluctuations in fluvial discharge from the tidal signature in ancient deltaic deposits: an example from the Neuquén Basin, Argentina. *J. Geol. Soc. Lond.* 173 (1), 94–107. doi:10.1144/jgs2015-030

He, B. Z., Jiao, C. L., Liu, R. H., Cao, Z. C., Cai, Z. H., Lan, M. J., et al. (2023). The paleotectonic and paleogeography of Neoproterozoic in the Tarim Basin and the prediction of favorable deep source rock areas. *Earth Sci. Front.* 30 (4), 19–42. doi:10.13745/j.esf.sf.2022.10.18

He, C. F., Zhang, X., Tian, J. C., Xia, Y. T., Yang, Y. R., Chen, J., et al. (2023). Sedimentary facies characteristics and sedimentary model of thin sand bodies of Lower Cretaceous Shushanhe Formation in Xinhe area,northern Tarim Basin. *Lithol. Reserv.* 35 (01), 120–131. doi:10.12108/yxyqc.20230111

He, D. F., Zhou, X. Y., Yang, H. J., Guan, S. W., and Zhao, C. J. (2008). Formation mechanism and tectonic types of intracratonic paleo-uplifts in the Tarim basin. *Earth Sci. Front.* 15 (2), 207–221. doi:10.3321/j.issn:1005-2321.2008.02.024

He, Z. W., Yang, R. D., Gao, J. B., Cheng, W., and Huang, J. G. (2013). Geological and geochemical characteristics of manganese-bearing rock series of yangjiawan manganese deposit, songtao county, guizhou province. *Geoscience* 27 (03), 593–602. Available at: http://www.geoscience.net.cn/CN/Y2013/V27/I3/593.

Hong, C. J., Kang, R. D., Zhou, F. F., Fei, J. W., and Fang, X. L. (2016). Sedimentary characteristics of cretaceous Baxigai Formation in xinhe-sandaoqiao area. *Xinjiang Geol.* 34 (02), 230–234.

Huang, S. Y., Yang, W. J., Lu, Y. H., Zhang, K., Zhao, Q., and Fan, S. (2018). Geological conditions, resource potential and exploration direction of natural gas in Tarim Basin. *Nat. Gas. Geosci.* 29 (10), 1497–1505. doi:10.11764/j.issn.1672-1926.2018.09.012

Jia, C. Z. (1997). *Structural characteristics and oil and gas in Tarim basin*. China. Beijing: Petroleum Industry Press.

Jones, B., and Manning, D. A. C. (1994). Comparison of geochemical indices used for the interpretation of palaeoredox conditions in ancient mudstones. *Chem. Geol.* 111 (1-4), 111–129. doi:10.1016/0009-2541(94)90085-X

Li, F. J., Lei, Y. L., Gong, G. L., Zhang, H., Shen, F., Jing, X. G., et al. (2019). Geochemical characteristics and sedimentary environment analysis from datangpo Formation in neoproterozoic nanhua system, southwestern hunan province-an example from zhaodong manganese ore deposits in jingzhou county, hunan province. China. *Earth Sci.* 44 (10), 3484–3494. doi:10.3799/dqkx.2019.075

Li, J. G., Bristow, C. S., Luthi, S. M., and Donselaar, M. E. (2015). Dryland anabranching river morphodynamics: Río Capilla, Salar de Uyuni, Bolivia. *Geomorphology* 250, 282–297. doi:10.1016/j.geomorph.2015.09.011

Li, J. L., Wu, G. K., Lin, C. S., Liu, Y. F., Liu, J. Y., Sun, Q., et al. (2019). Restriction of unconformity triangle zone on stratigraphic traps in the slope area with paleo-uplift: a case study of the Cretaceous in the West North Tarim Uplift. *J. Northeast Petroleum Univ.* 43 (02), 68–78.

Li, M., Tang, L. J., Qi, L. X., Huang, T. Z., Zhen, S. J., and Tian, Y. J. (2015). Differential tectonic evolution and its controlling on hydrocarbon accumulation in the south slope of Tabei Uplift. *Nat. Gas. Geosci.* 26 (2), 218–228. doi:10.11764/j.issn.1672-1926.2015.02.0218

Li, X. B., Liu, H. Q., Dong, X. Q., Wang, Y. T., Long, L. W., Wen, L. H., et al. (2021). The concept of fluvial fans in an arid environment: a new explanation of the origin of "sand-filled basins" in the yanchang formation, ordos basin. *Acta Sedimentol. Sin.* 39 (05), 1208–1221. doi:10.14027/j.issn.1000-0550.2020.077

Li, Y. J., Yang, H. J., Zhang, G. Y., Zheng, D. M., Liu, Y. X., Zhao, Y., et al. (2012). Redivision of the tectonic units of Tabei rise in Tarim Basin, NW China. *Acta Petrol. Sin.* 28 (8), 2466–2478.

Liu, B. B., Tan, C. P., Yu, X. H., Shan, X., and Li, S. L. (2019). Evolution model of a modern delta fed by a seasonal river in Daihai Lake, North China: determined from ground-penetrating radar and trenches. *Front. Earth Sci-Prc* 13, 262–276. doi:10.1007/s11707-018-0740-x

Liu, Y. F., Xia, H., Sun, Q., Lin, C. S., Zhao, H. T., and Li, H. (2019). Sequence stratigraphy and depositional evolution of the Bashijiqike Formation in the western Tabei uplift, Tarim Basin. *Nat. Gas. Geosci.* 30 (1), 62–73. Available at: http://www.nggs.ac.cn/EN/Y2019/V30/I1/62.

Luo, H. Y., Chen, J., Zhang, X. Q., Meng, X. X., Zhao, F. Q., Wu, S. j., et al. (2021). Sedimentary characteristics of fluvial dominated shallow water delta front and its control lithologic reservoir: a case study of Baxigai Formation in south slope of Kuqa Depression. *Lithol. Reserv.* 33 (5), 70–80. doi:10.12108/yxyqc.20210507

Ma, H. Q., Xia, Y. T., Zhao, Y. Q., Han, Q., and Qiao, G. L. (2022). Reservoir characteristics and controlling factors of cretaceous Baxigai Formation in xinhe-sandaoqiao area. *Xinjiang Geol.* 40 (02), 236–241.

McCarthy, J., Gumbricht, T., and McCarthy, T. S. (2005). Ecoregion classification in the Okavango Delta, Botswana from multitemporal remote sensing. *Int. J. Remote Sens.* 26 (19), 4339–4357. doi:10.1080/01431160500113583

Nesbitt, H. W., and Young, G. M. (1982). Early Proterozoic climates and plate motions inferred from major element chemistry of lutites. *Nature* 299, 715–717. doi:10.1038/299715a0

Reyisha, J. L. L. (2019). Study on the impacts of climate change and human activitieson runoff in the Amu Darya river, Central Asia. dissertation/master's thesis. Urumchi (China): Xinjiang Normal University.

Russell, A. D., and Morford, J. L. (2001). The behavior of redox-sensitive metals across a laminated-massive-laminated transition in Saanich Inlet, British Columbia. *Mar. Geol.* 174 (1-4), 341–354. doi:10.1016/S0025-3227(00)00159-6

Stuart, J. Y., Mountney, N. P., McCaffrey, W. D., Lang, S. C., and Collinson, J. D. (2014). Prediction of channel connectivity and fluvial style in the flood-basin successions of the Upper Permian Rangal coal measures (Queensland). *AAPG Bull.* 98 (2), 191–212. doi:10.1306/06171312088

Su, Y. Y., Li, Y. P., Liu, Y. R., Huang, G. H., Jia, Q. M., and Li Y, F. (2021). An integrated multi-GCMs Bayesian-neural-network hydrological analysis method for quantifying climate change impact on runoff of the Amu Darya River basin. *Int. J. Climatol.* 41 (5), 3411–3424. doi:10.1002/joc.7026

Su, Z., Liu, Y. F., Han, J. F., Yang, S. W., Liu, B., Lai, P., et al. (2020). Application of ultra-deep sandstone reservoirs prediction technology under seismic facies controlled in Yudong Block of Tabei Uplift, Tarim Basin. *Nat. Gas. Geosci.* 31 (2), 295–306. doi:10.11764/j.issn.1672-1926.2019.10.012

Sun, C. Y., Hu, M. Y., Hu, Z. G., Xue, D., and Liu, S. Y. (2015). Sedimentary characteristics of shallow water delta of Quan-4 member in Xingcheng area, Songliao Basin. *Lithol. Reserv.* 27 (03), 66–74. doi:10.3969/j.issn.1673-8926.2015.03.010

Sun, D. Q., Li, W. H., Lu, S. F., Liu, X. P., He, T. H., Zhu, P. F., et al. (2020). Reservoir characteristics and controlling factors of Shushanhe Formation in Yingmaili area of Tabei uplift. *J. Northeast Petroleum Univ.* 44 (06), 82–93. doi:10.3969/j.issn.2095-4107.2020.06.009

Tan, C. P., Yu, X. H., Liu, B. B., Xu, L., Li, S. L., Feng, S. Q., et al. (2018). Sedimentary structures formed under upper-flow-regime in seasonal river system: a case study of Bantanzi River, Daihai Lake, Inner Mongolia. *J. Palaeogeogr.* 20 (06), 929–940.

Tan, T. (2011). Ground water resources exploitation and protection in Okavango delta under the condition of climate change. dissertation/master's thesis. Wuhan (China): China University of Geosciences, Wuhan.

Tian, J. (2019). Petroleum exploration achievements and future targets of Tarim Basin. *XingJiang Pet. Geol.* 40 (01), 1–11. doi:10.7657/XJPG20190101

Wang, C., Yan, C. J., Zhu, Z. J., Li, S. H., Lv, D. C., Wang, X. X., et al. (2023). Interpretation of sand body architecture in complex fault block area of craton basin: case study of TIII in sangtamu area, Tarim Basin. *Energies* 16 (8), 3454. doi:10.3390/en16083454

Wang, Y. Y., Guo, W. Y., and Zhang, G. D. (1979). Application of some geochemical indicators in determining of sedimentary environment of the Funing Group Jinhu depression, Jiangsu Province. *J. Tongji Univ. Nat. Sci.* (2), 51–60.

Wu, G. K., Lin, C. S., Liu, Y. F., Liu, J. Y., Yang, X. Z., and Li, H. (2019). Characteristics of major unconformities and paleo-geomorphology during the Mesozoic key transformation stages in Kuqa-Tabei area. *Oil Gas. Geol.* 40 (04), 763–777. doi:10.11743/ogg20190407

Wu, G. K., Zhang, Z. M., Lin, C. S., Tian, N. X., Zuo, X. J., and Li, H. (2022). Evolution of mesozoic sedimentary fill in the Tabei uplift region, Tarim Basin. *Oil Gas. Geol.* 43 (4), 845–858. doi:10.11743/ogg20220409

Xia, H., Lin, C. S., Liu, Y. F., Li, H., Sun, Q., Zhao, H. T., et al. (2019). A research on relative lacustrine level changes of Cretaceous Shushanhe Formation in the Yingmaili area of Tarim Basin. *Nat. Gas. Geosci.* 30 (11), 1579–1589. doi:10.11764/j.issn.1672-1926.2019.08.001

Xing, Z. F., Lin, J., Zhou, H., Li, D., Qi, Y. A., and Zheng, W. (2019). Palaeoclimate changes revealed by sedimentary records of the upper permian-lower triassic strata in yiyang area, western henan province, China. *Geol. J. China Univ.* 25 (3), 401–411. Available at: https://geology.nju.edu.cn/EN/Y2019/V25/I3/401.

Xu, G. F., Lin, C. S., Liu, Y. F., and Sun, Q. (2016). Evolution of palaeo-uplift and its controlling on sedimentation of Kapushaliang group of early cretaceous in western Tabei uplift. *Earth Sci.* 41 (04), 619–632. doi:10.3799/dqkx.2016.051

Yang, H., Fu, J. H., and Yu, J. (2003). Oil reservoir enrichment models of large delta systems and application of exploration techniques in Shanbei area. *Acta Petrol. Sin.* 24 (03), 6–10. doi:10.7623/syxb200303002

Yang, S. Y., Li, C. X., and Cai, J. G. (2006). Geochemical compositions of core sediments in eastern China: implication for Late Cenozoic palaeo-environmental changes. *Palaeogeogr. Palaeoclimatol. Palaeoecol.* 229 (4), 287–302. doi:10.1016/j.palaeo.2005.06.026

Zaman, M. A., Rahman, A., and Haddad, K. (2012). Regional flood frequency analysis in arid regions: a case study for Australia. *J. Hydrol.* 475, 74–83. doi:10.1016/j.jHydrol.2012.08.054

Zan, C. J., Liu, T., Huang, Y., Bao, A. M., Yan, Y. Y., Ling, Y. N., et al. (2022). Spatial and temporal variation and driving factors of wetland in the Amu Darya River Delta, central asia. *Ecol. Indic.* 139, 108898. doi:10.1016/j.ecolind.2022.108898

Zhang, B., Cui, J., Gu, Q. Y., Zhu, Y. G., and Su, J. (2010). Oil origin classification in composite hydrocarbon accumulation play in the western Tabei Uplift and its geological significance. *Acta Petrol. Sin.* 31 (01), 55–60+67. doi:10.7623/syxb201001009

Zhang, C. M., Zhu, R., Guo, X. G., Wang, X. L., Yin, T. J., and Yuan, R. (2020). Arid fluvial fandelta-fluvial fan transition: implications of huangyangquan fan area. *Earth Sci.* 45 (05), 1791–1806. doi:10.3799/dqkx.2019.165

Zhang, L., Bao, Z. D., Dou, L. X., Zang, D. S., Mao, S. W., Song, J., et al. (2018). Sedimentary characteristics and pattern of distributary channels in shallow water deltaic red bed succession: a case from the Late Cretaceous Yaojia formation, southern Songliao Basin, NE China. *J. Petrol Sci. Eng.* 171, 1171–1190. doi:10.1016/j.petrol.2018.08.006

Zhao, H. T., He, Q. L., Yuan, R., Yi, Z. L., Li, B., Yang, S. W., et al. (2022). Sequence stratigraphic filling model of the cretaceous in the western Tabei uplift, Tarim Basin, NW China. *Open Geosci.* 14 (1), 1137–1146. doi:10.1515/geo-2022-0423

frontiers | Frontiers in Earth Science

TYPE Original Research
PUBLISHED 15 February 2024
DOI 10.3389/feart.2024.1364515

Check for updates

OPEN ACCESS

EDITED BY
Xixin Wang,
Yangtze University, China

REVIEWED BY
Zhishui Liu,
Chang'an University, China
Yuhang Gyo,
Jilin University, China

*CORRESPONDENCE
Zhiqiang Mao,
maozq@cup.edu.cn
Peiqiang Zhao,
pqzhao@cup.edu.cn

RECEIVED 02 January 2024
ACCEPTED 26 January 2024
PUBLISHED 15 February 2024

CITATION
Shi P, Shi P, Bie K, Han C, Ni X, Mao Z and Zhao P (2024), Prediction of permeability in a tight sandstone reservoir using a gated network stacking model driven by data and physical models.
Front. Earth Sci. 12:1364515.
doi: 10.3389/feart.2024.1364515

COPYRIGHT
© 2024 Shi, Shi, Bie, Han, Ni, Mao and Zhao. This is an open-access article distributed under the terms of the Creative Commons Attribution License (CC BY). The use, distribution or reproduction in other forums is permitted, provided the original author(s) and the copyright owner(s) are credited and that the original publication in this journal is cited, in accordance with accepted academic practice. No use, distribution or reproduction is permitted which does not comply with these terms.

Prediction of permeability in a tight sandstone reservoir using a gated network stacking model driven by data and physical models

Pengyu Shi[1,2,3], Pengda Shi[4], Kang Bie[5], Chuang Han[5], Xiaowei Ni[6], Zhiqiang Mao[1,2,3]* and Peiqiang Zhao[1,2,3]*

[1]College of Geophysics, China University of Petroleum, Beijing, China, [2]National Key Laboratory of Petroleum Resources and Engineering, Beijing, China, [3]Beijing Key Laboratory of Earth Prospecting and Information Technology, Beijing, China, [4]School of Software Engineering, Chengdu University of Information Technology, Chengdu, China, [5]Exploration and Production Research Institute, PetroChina Tarim Oilfield Company, Korla, China, [6]Oil & Gas Field Productivity Construction Department, PetroChina Tarim Oilfield Company, Korla, China

Introduction: Permeability is one of the most important parameters for reservoir evaluation. It is commonly measured in laboratories using underground core samples. However, it cannot describe the entire reservoir because of the limited number of cores. Therefore, petrophysicists use well logs to establish empirical equations to estimate permeability. This method has been widely used in conventional sandstone reservoirs, but it is not applicable to tight sandstone reservoirs with low porosity, extremely low permeability, and complex pore structures.

Methods: Machine learning models can identify potential relationships between input features and sample labels, making them a good choice for establishing permeability prediction models. A stacking model is an ensemble learning method that aims to train a meta-learner to learn an optimal combination of expert models. However, the meta-learner does not evaluate or control the experts, making it difficult to interpret the contribution of each model. In this study, we design a gate network stacking (GNS) model, which is an algorithm that combines data and model-driven methods. First, an input log combination is selected for each expert model to ensure the best performance of the expert model and selfoptimization of the hyperparameters. Petrophysical constraints are then added to the inputs of the expert model and meta-learner, and weights are dynamically assigned to the output of the expert model. Finally, the overall performance of the model is evaluated iteratively to enhance its interpretability and robustness.

Results and discussion: The GNS model is then used to predict the permeability of a tight sandstone reservoir in the Jurassic Ahe Formation in the Tarim Basin. The case study shows that the permeability predicted by the GNS model is more accurate than that of other ensemble models. This study provides a new approach for predicting the parameters of tight sandstone reservoirs.

KEYWORDS

machine learning, ensemble model, gate network, tight sandstone reservoir, permeability prediction

1 Introduction

The absolute permeability, k, is a measure of the ability of a porous medium to pass through a certain fluid in the presence of one or more fluid phases. The accurate prediction of permeability plays an important role in the evaluation of reservoir quality, numerical simulations of reservoirs, and estimation of geological reserves. Rock permeability is usually obtained through laboratory core measurements (Wu, 2004). However, this method is time-consuming and costly, and it has problems such as non-random sampling locations and limited quantity, making it impossible to characterize the permeability characteristics of the entire reservoir.

Scholars have performed extensive research on the problem of permeability predictions. The Kozeny-Carman equation (KC equation) based on the tube-like model applies the porosity and Kozeny constant to calculate permeability (Kozeny, 1927; Carman, 1937). However, the formation is not a uniform porous medium; thus, the prediction results are unreliable (Paterson, 1983; Mauran et al., 2001). Timur established a relationship using the porosity, bulk volume irreducible (BVI), and free fluid index (FFI) to predict permeability, but the predicted value was sensitive to the value of BVI, and it generally tended to overestimate permeability (Timur, 1968). Coates and Dumanoir derived a new free fluid model that ensured zero permeability at zero porosity when the irreducible water saturation was 100%. However, this model was only valid for intergranular pores and was not applicable for tight sandstones (Coates and Dumanoir, 1973). Ahmed considered the influence of minerals based on the Timur model and introduced a dual-mineral diffusion water model to estimate the permeability values. However, the irreducible water saturation is related to the shale volume and particle size; therefore, in complex heterogeneous or fractured reservoirs, the results are unreliable (Ahmed et al., 1991). The above research shows that it is very difficult to establish a comprehensive permeability prediction equation for highly heterogeneous reservoirs, and it is necessary to find a nonlinear method that uses well log curves for prediction.

In some cases, the models used in petrophysical calculations are nonlinear and cannot be explained by empirical theory. Machine learning is a data-driven approach that can provide alternative models in the absence of deterministic physical models; therefore, machine learning is a suitable technique for building regression models (Mohaghegh and Ameri, 1995; Saemi et al., 2007; Ahmadi et al., 2013; Saljooghi and Hezarkhani, 2014). Rogers applied a backpropagation neural network (BPNN) to predict the permeability and input the porosity log (Rogers et al., 1995). Jamialahmadi predicted the permeability of typical Iranian oil fields based on radial basis function (RBF) neural networks (Jamialahmadi and Javadpour, 2000), and Nazari applied support vector regression (SVR) to extract data into hyperplane dimensions to avoid overfitting (Nazari et al., 2011). Al–Anazi applied the gamma-ray log (GR), density (DEN), neutron (CN) and compressional slow-ness (DT) to predict permeability; the results showed that SVR was better than artificial neural networks (ANN) (Al-Anazi and Gates, 2012). The above research shows that machine learning methods have significant advantages over empirical models. However, overtraining often occurs in the process of using these models for prediction, resulting in individual models that are not robust and have poor generalization. Zhang constructed a visual prediction model and concluded that ResNet learned the best-fitting nonlinear porosity–permeability relationship from the input feature (Zhang et al., 2021).

To improve the problem of limited performance of a single model, ensemble learning has been developed; this method combines separate machine learning models through different combination strategies to improve the performance of the combined model (Nilsson, 1965; Friedman, 2001; Sammut and Webb, 2011; Zhang et al., 2022; Kalule et al., 2023). Chen and Lin used a committee machine with empirical formulas (CMEF) model to predict permeability using a collection of empirical formulas as experts. The results showed that the proposed model was more accurate than any single empirical formula (Chen and Lin, 2006). Sadegh built a supervised committee machine neural network (SCMNN), and each estimator of the SCMNN was the combination of two simple networks and one gating network; the prediction results were in good agreement with the core experimental results (Karimpouli et al., 2010). Zhu built a hybrid intelligent algorithm that combined the AdaBoost algorithm, adaptive rain forest optimization algorithm, and improved Back Propagation Neural Network (BPNN) with Nuclear Magnetic Resonance (NMR) logging data to improve and reconstruct the original artificial intelligence algorithm (Zhu et al., 2017). Zhang established a regression model based on the fusional temporal convolutional network (FTCN) method that can accurately predict the formation properties when there are major changes (Zhang et al., 2022). Bai established an RCM model to predict reservoir parameters, and the prediction results of the integrated model were more accurate than those of individual expert models (Bai et al., 2020). Morteza combined the social ski-driver (SSD) algorithm with a multilayer perception (MLP) neural network and presented a new hybrid algorithm to predict the value of rock permeability. The results indicated that the hybrid models can predict rock permeability with excellent accuracy (Matinkia et al., 2023).

However, in current ensemble learning training, the input data are mostly well log measured *in situ*, resulting in input features that often lack petrophysical constraints. In log interpretation, the classic petrophysical model is applicable to sandstones with medium and high porosity. However, for tight sandstones, the porosity is low and the pore structure is complex; therefore, the porosity–permeability relationship cannot be explained by a simple linear model. Therefore, we aim to build an improved stacking model in this study.

In this study, we improve a classic stacking model called the gate network stacking (GNS) model. In the methodology section, we introduce the structure of the GNS model, which includes four parts: the input layer, expert layer, meta-learner, and gate network. In the case study section, we apply the GNS model to predict the permeability of tight sandstones in the Jurassic formation of the Tarim Basin and compare its performance with other ensemble learning models. In the discussion section, we discuss the advantages of the GNS model over other models and present the conclusions of the study.

2 Methodology

2.1 Input layer

2.1.1 Data processing

The input layer of the model is the data import port, which is responsible for data standardization and preprocessing. The input data for the gated network stacking model are a variety of well log curves, and the units and orders of magnitude of these log curves are quite different. Data normalization converts raw data into dimension-less and order-of-magnitude standardized values that can be compared between different input indicators. We use Z-value standardization for data preprocessing of the conventional well-logging curves. This method converts the data into a normal distribution with a mean of zero and a standard deviation of one without changing the distribution characteristics. To ensure that the model exhibits the best possible performance, the value of the output variable (core permeability) is considered as a logarithm. The Z-value normalization formula is shown in Eqs 1–3.

$$Z_i = \frac{x_i - \mu}{\sigma} \tag{1}$$

$$\mu = \frac{1}{n}\sum_{i=1}^{n} x_i \tag{2}$$

$$\sigma = \sqrt{\frac{1}{n}\sum_{i=1}^{n}(x_i - \mu)^2} \tag{3}$$

where Z_i is the standardized result of the i-th sample, x_i is the i-th sample data, μ is the mean calculated for all samples, σ is the variance calculated for all samples, and n is the total number of samples in the dataset.

After data preprocessing, based on the game theory proposed by Shapley (1988), we used Shapley values to analyze the contribution of features and evaluate the importance of features in the ensemble learning model. The Shapley value is a method from cooperative game theory used to fairly distribute the total gains or losses among players based on their individual contributions to the collective effort.

The Shapley regression value represents the feature importance of a linear model in the presence of multicollinearity (Lundberg and Lee, 2016). It assigns an important value to each feature, indicating the impact of including the feature in the model prediction. SHAP (SHapley Additive exPlanations) explains the output of a model by attributing the importance of each feature to the prediction, which can be used to identify a new class of additive feature importance measures and show that there is a unique solution and a desirable set of properties in this class (Lundberg and Lee, 2017; Lundberg et al., 2018; Lundberg et al., 2020). The SHAP value is a unified measure of feature importance that combines these conditional expectation functions with the classic Shapley value from game theory to attribute ϕ_i values to each feature, as shown in Eqs 4, 5.

$$f_x(S) = E[f(x)|x_S] \tag{4}$$

$$\phi_i = \sum_{S \subseteq N \setminus \{i\}} \frac{|S|!(|M| - |S| - 1)!}{M!}\left[f_x(S \cup \{i\}) - f_x(S)\right] \tag{5}$$

where S is the subset and $E[f(x)|x_S]$ is the expected value of the function conditioned on a subset S of the input features. ϕ_i is the Shapley value. N is the set of all input features. $S \subseteq N\backslash\{i\}$ comprises all the possible subsets with feature i. $S \cup \{i\}$ is a subset S with added i, and $|S|$ is the size of the subset before the ith feature is added to the interaction. $\frac{|S|!(|M|-|S|-1)!}{M!}$ is the weight of the combination, and $f_x(S \cup \{i\}) - f_x(S)$ is the marginal contribution.

2.1.2 Petrophysical models

In the process of intelligent well-logging interpretation, simply using a data-driven strategy without geological constraints can easily lead to training model prediction results that are significantly different from the objective understanding. Even if the evaluation index of the trained model is good, its prediction results for unknown samples are not convincing. Therefore, we add the results of the petrophysical model as the input.

The volume of clay from the gamma ray log, Vsh, is as follows:

$$SH = \frac{GR - GR_{min}}{GR_{max} - GR_{min}} \tag{6}$$

$$V_{sh} = \frac{2^{GCUR * SH} - 1}{2^{GCUR} - 1} \tag{7}$$

where GR_{min} is the minimum value of GR, which is about approximately 40 API; GR_{max} is the maximum value of GR, which is about approximately 140 API; SH is the relative value of the clay volume, and GCUR is an empirical coefficient that is approximately 2.

For the volume model of shaley sandstone, the density porosity from the density log, ϕ_D, is as follows:

$$\phi_D = \frac{\rho - \rho_{ma}}{\rho_{mf} - \rho_{ma}} - V_{sh}\frac{\rho_{sh} - \rho_{ma}}{\rho_{mf} - \rho_{ma}} \tag{8}$$

where ρ_{ma} is the matrix density of tight sandstone (density of quartz), which is about approximately 2.65 g/cm^3; ρ_{mf} is the density of mud filtrate, which is approximately 1.0 g/cm^3; and ρ_{sh} is the density of shale, which is approximately 2.3 g/cm^3.

In addition, the difference between the neutron porosity and density porosity, ND, is as follows:

$$ND = (\phi_N - \phi_{N\mathrm{ma}}) - \frac{\rho - \rho_{ma}}{\rho_{mf} - \rho_{ma}} \tag{9}$$

where $\phi_{N\mathrm{ma}}$ is the matrix neutron porosity of sandstone, i.e., the neutron porosity of quartz, which is about −0.02, fraction.

2.2 Expert layer

The expert layer in this study has the same structure as the expert layer of the stacking model (Wolpert, 1992). It is an intelligent system composed of multiple algorithms (experts), and all experts handle the same tasks. During the model training process, the data set is divided into k folds, and all of the experts output simulation prediction results through K simulation training and prediction processes as the input data set of the meta-learner. Finally, all data sets are used to complete the training of the expert. In the actual prediction process, the test set is input to each expert, and their prediction results are input to the meta-learner for combination.

Permeability prediction is an important aspect of formation evaluation. In the stacking model, using strong learners as experts

can improve the accuracy and robustness of the model. Therefore, we selected five experts to construct the expert layer: multilayer perceptron (MLP), support vector regression (SVR), ElasticNet (EN), light gradient boosting machine (LightGBM), and category boosting (CatBoost). The characteristics and advantages of the five experts are discussed in detail below:

An MLP is a feed-forward neural network composed of multiple layers of nodes and neurons. It performs nonlinear mapping through activation functions to complete classification and regression tasks. The error between the predicted and actual results is then measured based on the loss function, and a backpropagation algorithm is applied to update the weights and biases of the neural network. The MLP can adapt to different datasets and tasks, has good capabilities for solving complex function-fitting problems, and has certain generalization capabilities.

SVR is a regression algorithm based on a support vector machine (SVM). It maps the original features to a high-dimensional feature space, transforms the regression problem into a convex optimization problem by determining the optimal hyperplane, and solves the optimization problem to determine the best hyperplane. SVR has strong nonlinear modeling capabilities, can solve complex regression tasks involving nonlinear relationships and high-dimensional data, is robust to noise and outliers in the training data, and can effectively avoid overfitting.

ElasticNet regression is an extended form of linear regression. It uses both L1 and L2 regularization terms in the objective function. The L1 regularization term judges the importance of features through the size of the coefficient, such that for unimportant features the coefficient tends to zero, which is suitable for dealing with problems with redundant features. The L2 regularization term controls the complexity of the model and reduces the impact of the correlation between features on the model. The model is more stable when highly correlated features are present. ElasticNet regression has good robustness when dealing with regression problems with redundant features or fewer samples, and it is relatively insensitive to noise and outliers in the data.

LightGBM iteratively trains multiple weak learners using the gradient boosting algorithm and optimizes and adjusts the newly generated weak learners according to the objective function to improve the accuracy of the model. It retains samples with larger gradients to accelerate the training process and uses a leaf-wise growth algorithm with depth restrictions to prevent overfitting. LightGBM sorts features according to their importance and performs feature selection based on thresholds, thereby improving the generalization ability and interpretability of the model. Further, LightGBM is suitable for processing large-scale data sets with uneven feature distributions.

CatBoost is a gradient boosting algorithm that is specially designed to effectively handle categorical features. The impact of most noise and outliers is diluted in the entire tree structure, thereby reducing their impact on individual nodes. CatBoost dynamically adjusts the learning rate according to the distribution of data and the complexity of the model and has strong accuracy and robustness when processing datasets with noise and outliers.

2.3 Meta-learner

In the classic stacking model, the meta-learner is between the expert and output layers. Its main function is to combine the prediction results of different experts in a manner that minimizes errors, as shown in Figure 1. By generalizing the outputs of multiple expert models, the prediction accuracy of the overall model is improved, and the final prediction result is output. When choosing a meta-learner, the capacity and complexity should be considered. Stronger meta-learners may overfit the model, whereas weaker meta-learners may fail to capture complex relationships. Because the meta-learner only learns the combination of expert models, only simple machine learning models (weak learners) can be used; when dealing with high-dimensional feature sets output by multiple expert models, the fitting effect is often poor.

In this study, the AdaBoost model (Freund and Schapire, 1997) is used as the meta-learner, and the weak learner in the model is a linear regression model. During the training process for each learner, the sample weight is adjusted according to the error rate of the previous round, and greater weights are assigned to the misclassified samples to iteratively learn and correct the errors, thereby improving the accuracy of the meta-learner model. The GNS model proposed in this study uses a gate network to assign different weights to the input data of the meta-learner and adds physical model constraints to allow the meta-learner to better find the best combination of expert models while complying with the physical model constraints.

2.4 Gate network

A gate network is a neural network structure that is used to control the flow and processing of information in a model. By adding a gate network mechanism, the input features can be selectively filtered, amplified, or suppressed, thus forming a constraint function for the model. In the classic stacking model, differences in expert performance cause the relationship between the features and learning objectives to become more complex. In addition, the impact of the added experts on the overall model cannot be measured. Therefore, this study introduces gate networks to solve the aforementioned problems, adjust the model architecture, and improve the accuracy and interpretability of the overall model.

In the GNS model, the role of the gate network includes three main aspects.

a. In the input layer, the gate network extracts the input petrophysical model and adds physical constraints to the input data of all expert models and meta-learners to improve the prediction performance and stability of the model and achieve model driving.
b. In the k-fold cross-validation of the expert model, the weight calculated according to the mean squared error (MSE) of each expert model is saved to the gate network, and the features corresponding to each expert model are weighted according to the weight combination saved by the gate network, which reduces the complexity of the meta-learner learning process and improves the robustness. The expert weights of the storage entry network are shown in Eq. 10, and the expert prediction results calculated based on the combination of weights are shown in Eq. 11.

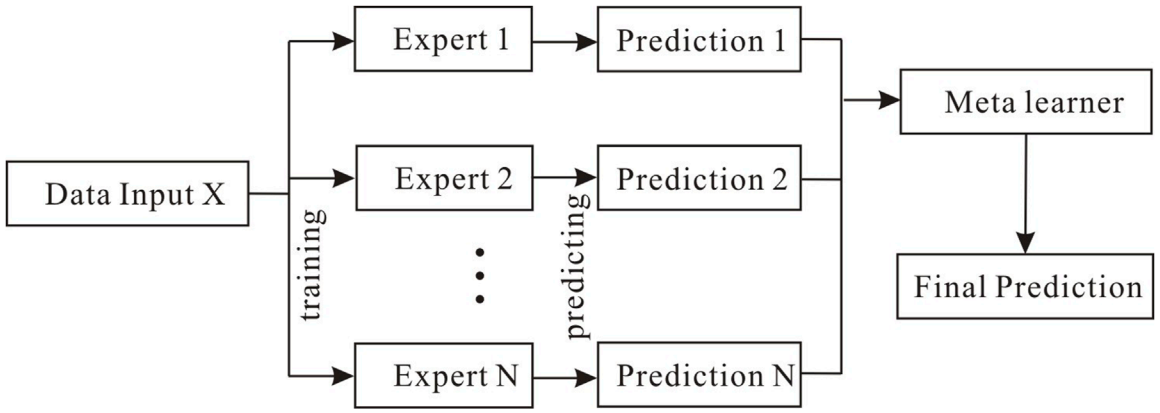

FIGURE 1
Stacking model architecture consisting of an input layer, experts, prediction results, meta-learner, and output layer.

$$w_{t_GN} = \frac{1}{MSE_t} / \sum_{i=1}^{T} \frac{1}{MSE_i} \tag{10}$$

where T is the total number of expert models, and MSE_t is the MSE of the t-th expert.

$$H_t(x) = w_{t_GN} \cdot h_t(x) \tag{11}$$

where $h_t(x)$ is the prediction result of the t-th expert and $H_t(x)$ is the prediction result of the t-th expert after assigning weights through the gate network.

c. When the meta learner outputs results, the accuracy indicators of the expert model combination are evaluated through a gate network. Experts who have a positive impact on the accuracy indicators are retained, abandoning experts who have a negative impact on the accuracy indicators are abandoned to ensure that the overall performance of the model is improved.

2.5 GNS model architecture and workflow

For the formation permeability prediction problem, the aforementioned components are used in this study to form a GNS model. First, a dataset is created and labeled. The logging dataset includes the natural gamma-ray log (GR), spectral gamma-ray log (K-TH-U), compressional slow-ness log (DT), neutron log (CN), and density log (DEN). Lab-measured core permeability data points are used as labels. In addition to the logging data mentioned above, V_{sh}, ND, and ϕ_D, calculated using Eqs 6–9, are also input into the GNS, called petrophysical constraints. Finally, a petrophysical and data-driven intelligent model is developed.

In the input layer, the optimal combination of the corresponding well log curves is selected for each expert model based on the SHAP value, and the petrophysical constraints are input into the gate network. In the expert layer, petrophysical constraints are added to the input data of the expert model through the gate network, and the hyperparameters of the model are self-optimized. The Bayesian optimization method is used in this study to optimize the parameters; it estimates the posterior distribution of the objective function by constructing a Gaussian process (GP) model and determines the hyperparameter value for the next sampling, thereby quickly finding the global optimal solution. Cross-validation partitioning the dataset into multiple subsets, training the model on some of these subsets, and evaluating its performance on the remaining subsets. After model optimization is completed, each expert model is simulated and predicted using a five-fold cross-validation method. The performance of the expert model is evaluated according to the MSE of the model and stored in the gate network. Each expert model is then trained using all of the datasets.

According to the ranking of expert performance indicators, the expert model simulation prediction results are added to the meta-learner and given weights to form the input set of the meta-learner. At the same time, the gate network adds petrophysical constraints.

Finally, the meta-learner is trained. We evaluate the output results, retain the expert models that positively impact the overall model performance, eliminate the expert models that negatively impact the overall model, and finally output the prediction results of the best model combination.

Because the expert model adds dynamic weight constraints, it is more robust and interpretable than the classic stacking algorithm. Figure 2 shows the GNS workflow based on petrophysical and data-driven methods.

2.6 Performance evaluation

To verify the reliability and accuracy of the proposed GNS model, three statistical parameters are introduced as performance

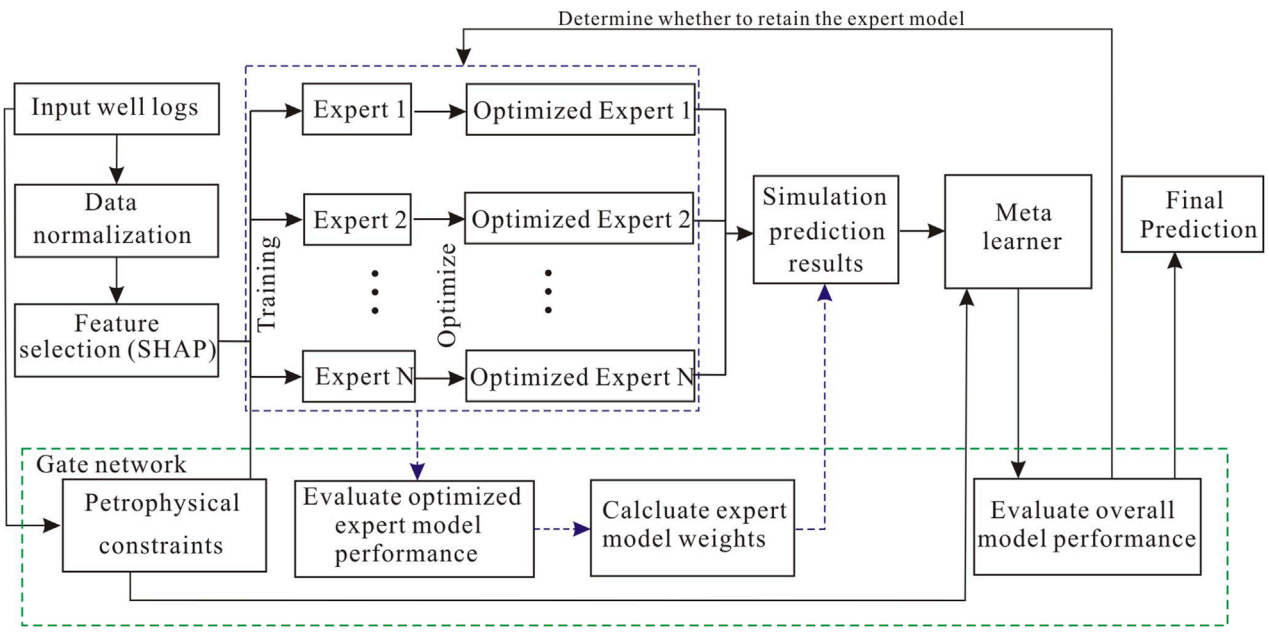

FIGURE 2
GNS model workflow consisting of five parts: the input layer, expert layer, meta-learner, gate network, and output layer.

TABLE 1 Parameters for assessment to evaluate the model performance.

Accuracy measure	Mathematical exp
Coefficient of determination (R^2)	$R^2 = 1 - \frac{\sum_{i=1}^{N}(y_i - \hat{y}_i)^2}{\sum_{i=1}^{N}(y_i - \bar{y}_i)^2}$
Mean square error (MSE)	$MSE = \frac{1}{N}\sum_{i=1}^{N}(y_i - \hat{y}_i)^2$
Maximum absolute error (MAE)	$MAE = \frac{1}{N}\sum_{i=1}^{N}\lvert(y_i - \hat{y}_i)\rvert$

evaluation indicators. The equations used to calculate each parameter are listed in Table 1.

3 Case study

3.1 Geological background

The Dibei tight gas reservoir in the Kuqa Depression of the Tarim Basin has become a key exploration area because of its large gas reserve potential. The main production and storage unit is the Jurassic Ahe formation. The lithology is mainly coarse sandstone, and the sedimentary type is a braided river delta plain channel. The rock type in the sedimentation is mainly lithic sandstone, followed by feldspathic lithic sandstone, with a quartz content of more than 60%. Feldspar, clay minerals, calcite, and dolomite are all developed. The Dibei gas reservoir has low porosity, a complex pore throat structure, and a wide range of permeability changes. Multiple factors jointly control the permeability of the reservoir, and the predictive effect of the empirical model is poor. It is necessary to apply a model that can identify nonlinear characteristics between well logs and core data. Therefore, we apply the GNS model to predict the permeability.

3.2 Data acquisition

The stability and accuracy of the model depend on the reliability of the training data. In this study, 1,088 samples were collected from five wells in the Dibei area. The locations of the core wells are shown in Figure 3. The input variables include seven conventional well logs (GR, K, TH, U, DT, DEN, and CN) and three petrophysical constraints (ND, V_{sh} , and ϕ_D); the permeability value is the desired output. To ensure that the GNS model has the best possible performance, the training data were normalized. Based on the data normalization, we calculated the SHAP value of each input feature, as shown in Figure 4, which reflects the contribution of each feature to the model prediction, further indicating the relative importance of each feature to the prediction results.

The bar chart in Figure 4 shows that the contributions of the SHAP values in descending order are DEN, GR, TH, CN, K, DT, and U. Five different expert models were trained based on the SHAP value contribution of the well log, and the MSE of the training results is shown in the line chart in Figure 4. The MSE reduction is defined as a log that has a positive contribution to the model, while conversely, when it has a negative contribution to the model, the positive contribution log is retained as the input of the expert model, and different log combinations are input for different expert models. Together with the permeability label, these constitute the training set, as summarized in Table 2.

3.3 Model training and performance evaluation

The feature combinations in Table 2 are input into the expert model for training, and the Bayesian optimization method is used to find the optimal hyperparameter values such that the model can

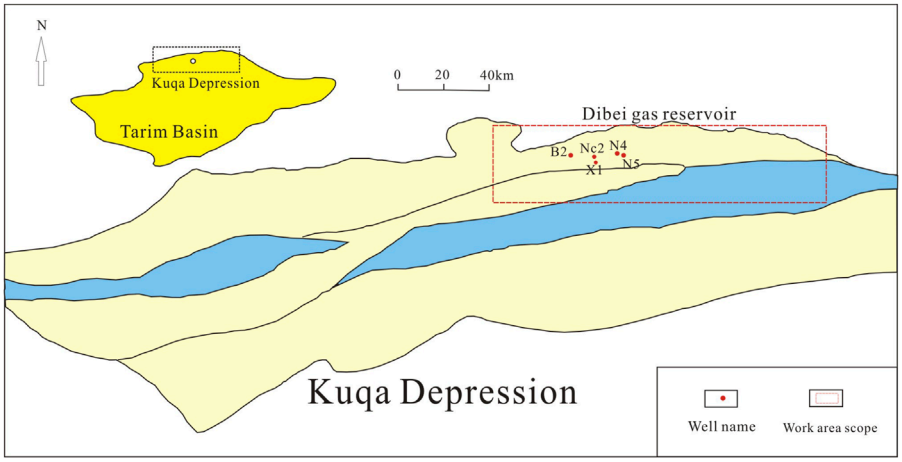

FIGURE 3
The Dibei gas reservoir is located in the northern part of the Kuqa Depression, as indicated by the red box in the thumbnail; the red dot indicates the location of the coring well.

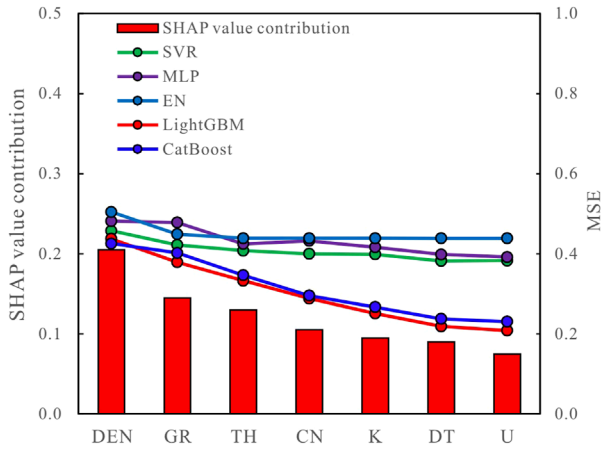

FIGURE 4
SHAP contribution of well logs and changes in the MSE of well log combinations in each expert model.

TABLE 2 Well log input combinations for different experts.

Model	Well logs
SVR	DEN, GR, TH, CN, DT
MLP	DEN, TH, K, DT, U
EN	DEN, GR, TH
LightGBM	DEN, GR, TH, CN, K, DT, U
CatBoost	DEN, GR, TH, CN, K, DT, U

achieve the best performance on the target task. A performance comparison of the expert model using optimal hyperparameter values and the expert model using default parameters is summarized in Table 3.

The petrophysical constraints stored in the gate network are added to the feature combination of each expert to form the input dataset for each expert. Targeting the core permeability, multiple random sampling and no-replacement iterative predictions are conducted on experts to obtain a set of simulation prediction results, record the expert model MSE, save it to the gate network, and use all datasets to train each expert model. The expert combination is formed iteratively based on the MSE of the expert model (from small to large), the weight of each expert in the combination is calculated (Eq. 8), and the corresponding simulation prediction results are weighted (Eq. 9). Next, the weighted prediction results and petrophysical constraints are input into the meta-learner for training to determine the optimal expert model combination strategy. To demonstrate the effectiveness and advantages of the GNS algorithm, a classic stacking model is used for comparison. To ensure consistency, the same experts and meta-learners are used in the models. A performance comparison of the two models is shown in Figure 5.

It can be seen that the addition of the gate network clearly improves the overall model. In contrast, the classic stacking model lacks petrophysical constraints and expert evaluation mechanisms and cannot optimize over-fitting, coupling correlation, and other problems existing in the integration process of experts; as a result, the overall performance of the stacking model is inferior to that of the GNS. For example, in the fourth iteration shown in Figure 5, the MLP model may have problems with dataset misfit or poor coupling with other expert results, resulting in negative improvements to the overall model when an expert is added to the stacking model. In the GNS algorithm, the addition of this expert is judged to be a negative improvement. Therefore, the prediction results of this expert are eliminated from the overall model, ultimately maintaining the quality of the overall expert group.

TABLE 3 Expert performance comparison when applying optimized and default hyperparameters.

	SVR	MLP	EN	LightGBM	CatBoost
MSE of experts using default hyperparameter values	0.38	0.39	0.44	0.21	0.23
MSE of experts using optimal hyperparameter values	0.34	0.36	0.39	0.18	0.21

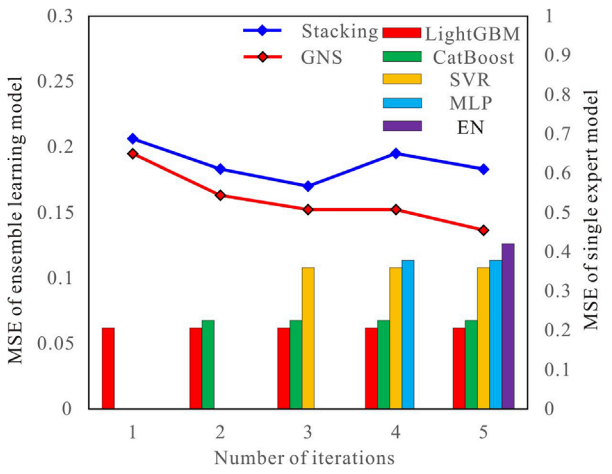

FIGURE 5
MSE of the expert model and changes in the MSE when iteratively inputting the ensemble learning model.

TABLE 4 Performance evaluation parameters of different ensemble learning models.

Model	MSE	MAE	R^2
GNS	0.1364	0.2802	0.7291
RCM	0.1762	0.2941	0.6124
Bagging	0.2230	0.3467	0.5566
Voting	0.2764	0.4005	0.4512

The above analysis shows that the performance of the GNS model is better than that of the stacking model, indicating that the improvement in the gate network is effective. To discuss the superiority of the model architecture, this study conducts a horizontal comparison with other ensemble learning models. We selected three representative integration strategies: two heterogeneous integration models (RCM and Voting) and a bagging integration model constructed using LightGBM. Three evaluation indicators—MSE, MAE, and R2—are used to evaluate the performance of the model. The results are summarized in Table 4. The GNS and RCM models have better prediction performance, and the GNS model achieves the best prediction results.

Figure 6A shows the error between the core permeability measured in the laboratory and that predicted using the GNS model. To compare the prediction effect more intuitively, the permeability is plotted on a cross diagram (Figure 6B), where the 45° diagonal line represents a perfect match between the predicted and true penetration rates. The prediction error of the model conforms to a normal distribution; therefore, the accuracy of the model can be judged based on the variance and MSE (Helle et al., 2001; Zhong et al., 2019). Figures 7–9 show the prediction results of the RCM, bagging, and voting models, respectively.

The GNS model has a variance of 0.0931 and MSE of 0.1364. It has the highest degree of fit with the core permeability values. The error does not exceed one order of magnitude for any of the core samples, showing the best performance (Figure 6). The variance of the RCM model is 0.1109 and the MSE is 0.1762. The prediction results are slightly lower in the high-permeability interval, and the performance is slightly weaker than that of the GNS (Figure 7). The variance of the bagging model is 0.1272, and the MSE is 0.2230. Some sample points exhibit large errors at different permeability intervals. This may be because random sampling will lead to a loss of some useful information (Figure 8). Finally, the voting model has the largest variance and MSE, and the predicted permeability has a larger error than the core permeability (Figure 9). These studies demonstrate that the GNS model is consistent with the measured permeability of the cores.

3.4 Prediction results

Well N4 is a core well in the Dibei gas reservoir in the Tarim Basin. The target reservoir is the Jurassic Ahe Formation. Logging data includes natural gamma ray log (GR), porosity logs (DEN-CN-DT), and natural gamma spectrum logs (K-TH-U). In this study, we selected the above seven well logs and three petrophysical constraints (VSH, PHID, and ND) as inputs, used the core permeability measured in the laboratory as label data, and entered it into the GNS model for prediction. For comparison, the results of several other ensemble learning models were obtained. Figure 10 shows the prediction results for each model in Well N4. The first track is the natural gamma curve, the second track is the natural gamma spectrum curve, the third track is the porosity log curve, and the fourth track is the petrophysical constraints. Tracks 6, 7, 8, and 9 are the comparisons between the prediction results of the GNS model, RCM model, bagging model, and voting model and the true value of the core permeability, respectively. The prediction results of the GNS model exhibit the best agreement with the core measurement results. The RCM and bagging models have certain errors at lower permeabilities. The voting model exhibits the largest difference from the core measurement results. The case study shows that the GNS model has advantages in predicting permeability. Importantly, we applied the gate network to integrate the petrophysical constraints with the model, rather than simply taking the petrophysical constraints as inputs. In addition, we controlled the weight of the model through the gate network, avoiding the influence of weak experts. Thus, the proposed model

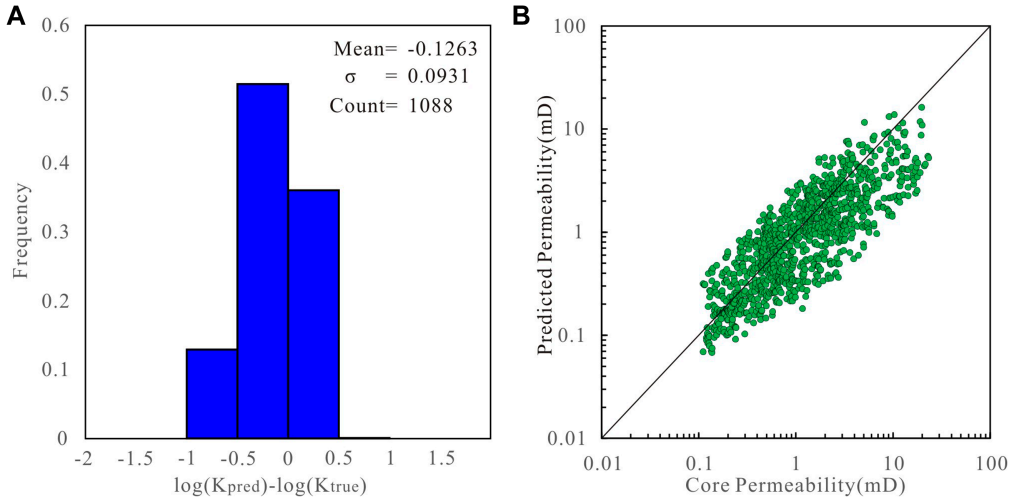

FIGURE 6
(A) Histogram of the error between the core measured permeability value and the permeability predicted by the GNS model. **(B)** Cross plot of the core measured permeability value and permeability predicted by the GNS model.

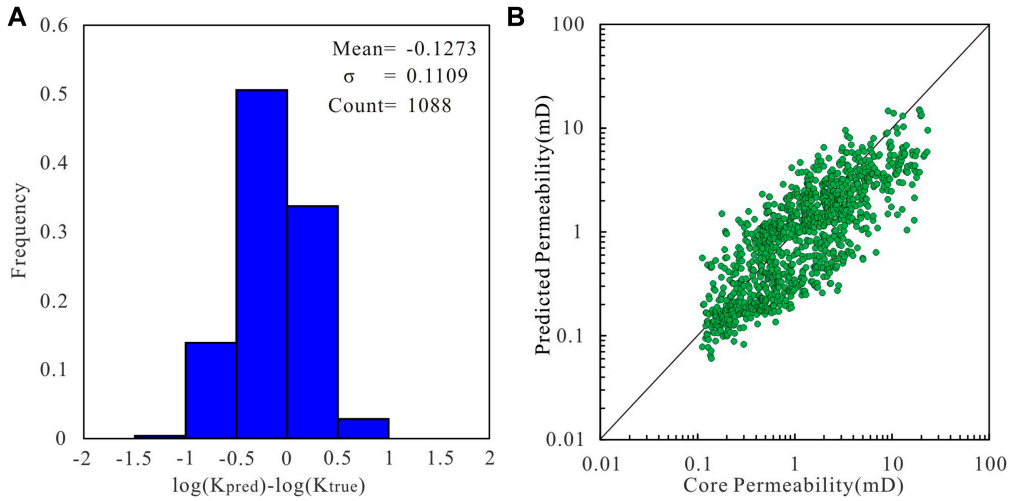

FIGURE 7
(A) Histogram of the error between the core measured permeability value and the permeability predicted by the RCM model. **(B)** Cross plot of the core measured permeability value and permeability predicted by the RCM model.

is more flexible than previously established empirical equations and other machine learning models.

4 Discussion

In recent years, machine learning has promoted the intelligent development of log interpretation. In the process of supervised learning, machine learning automatically adjusts the internal structure to satisfy the mapping relationship between the feature data and label data and establishes a prediction model with certain generalization capabilities. However, data-driven learning is the core of current machine learning. Most studies have only considered the use of indicators such as accuracy and mean square error to evaluate the performance of machine learning models, ignoring the impact of physical constraints on the overall model. Therefore, even a model with superior performance is not convincing in its predictions for unknown samples. It is clear that a single data-driven method cannot meet the requirements of log interpretation tasks. The combination of model- and data-driven methods is a development trend for the future application of machine learning models in the field of log interpretation. This approach considers model performance and interpretability. While ensuring the accuracy of the model, it also ensures that it conforms to the physical laws of the logging interpretation process.

The stacking model typically consists of an expert model layer and a meta-learner, which has better performance than a single model in actual tasks. However, the meta-learner only learns the

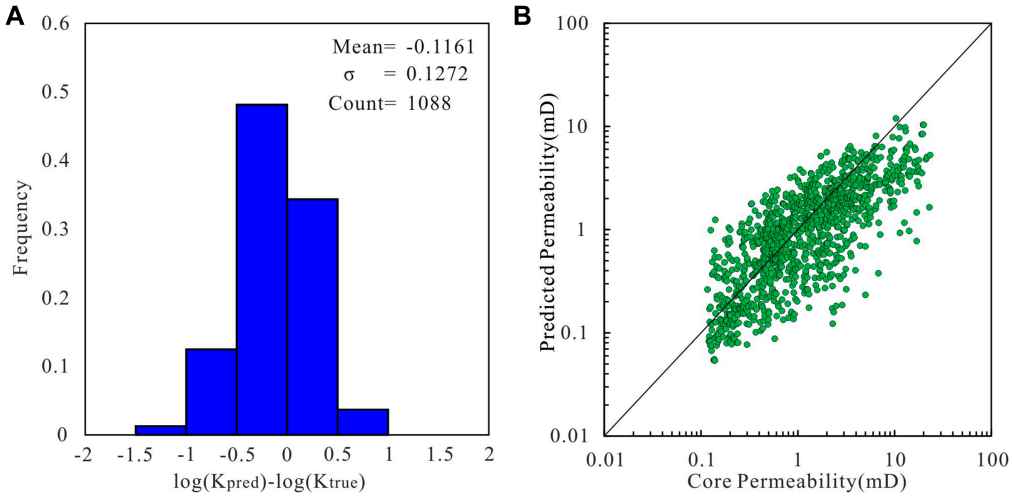

FIGURE 8
(A) Histogram of the error between the core measured permeability value and the permeability predicted by the bagging model. **(B)** Cross plot of the core measured permeability value and permeability predicted by the bagging model.

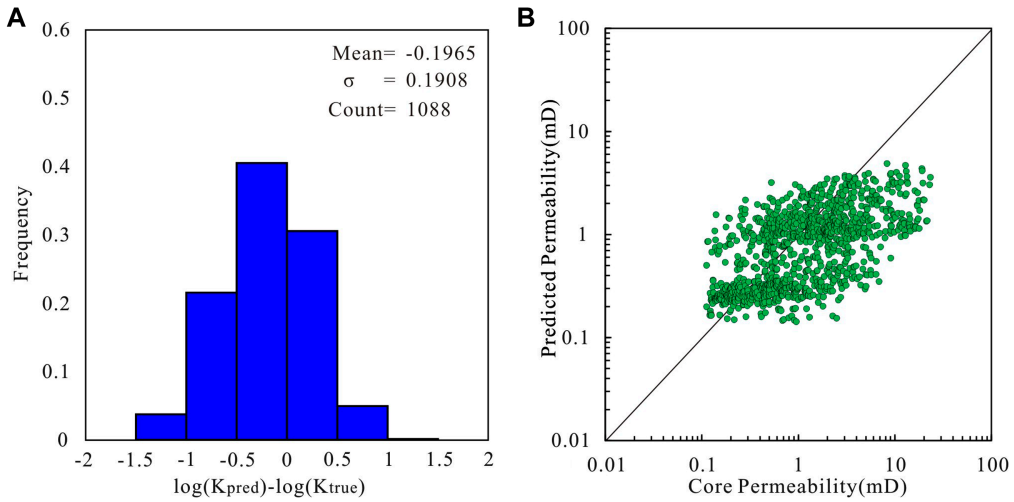

FIGURE 9
(A) Histogram of the error between the core measured permeability value and the permeability predicted by the voting model. **(B)** Cross plot of the core measured permeability value and permeability predicted by the voting model.

combination of experts and does not perform any evaluation or control of the experts, resulting in poor interpretability and difficulty in explaining the contribution of each model. The RCM model relies on the performance of experts, and some weak models may have a greater impact on the results and a weak ability to solve the problem of data imbalance. The bagging model aims to reduce the variance. When the data distribution was uneven, each basic model learned different features from different data subsets. In addition, if the basic model itself has overfitting or underfitting problems, bagging cannot solve them. The voting algorithm relies on the performance of experts. Because the weights are the same, the information obtained by each model may not be fully utilized. The voting model is sensitive to noise. In this study, it is also found that for sample sets with large differences in permeability, noise causes the model to obtain poor results. The GNS model controls the model through the gate network mechanism, adds petrophysical constraints to the inputs of the expert model and meta-learner, dynamically assigns weights to the output of the expert model, and finally iteratively evaluates the overall performance of the model. Connecting each training step of the model and adding constraints uniformly improves the shortcomings of the traditional model and significantly enhances the interpretability and credibility of the overall model.

However, petrophysical constraints are calculated from well logs, and there is still a certain similarity in their features. During the model training process, feature redundancy is

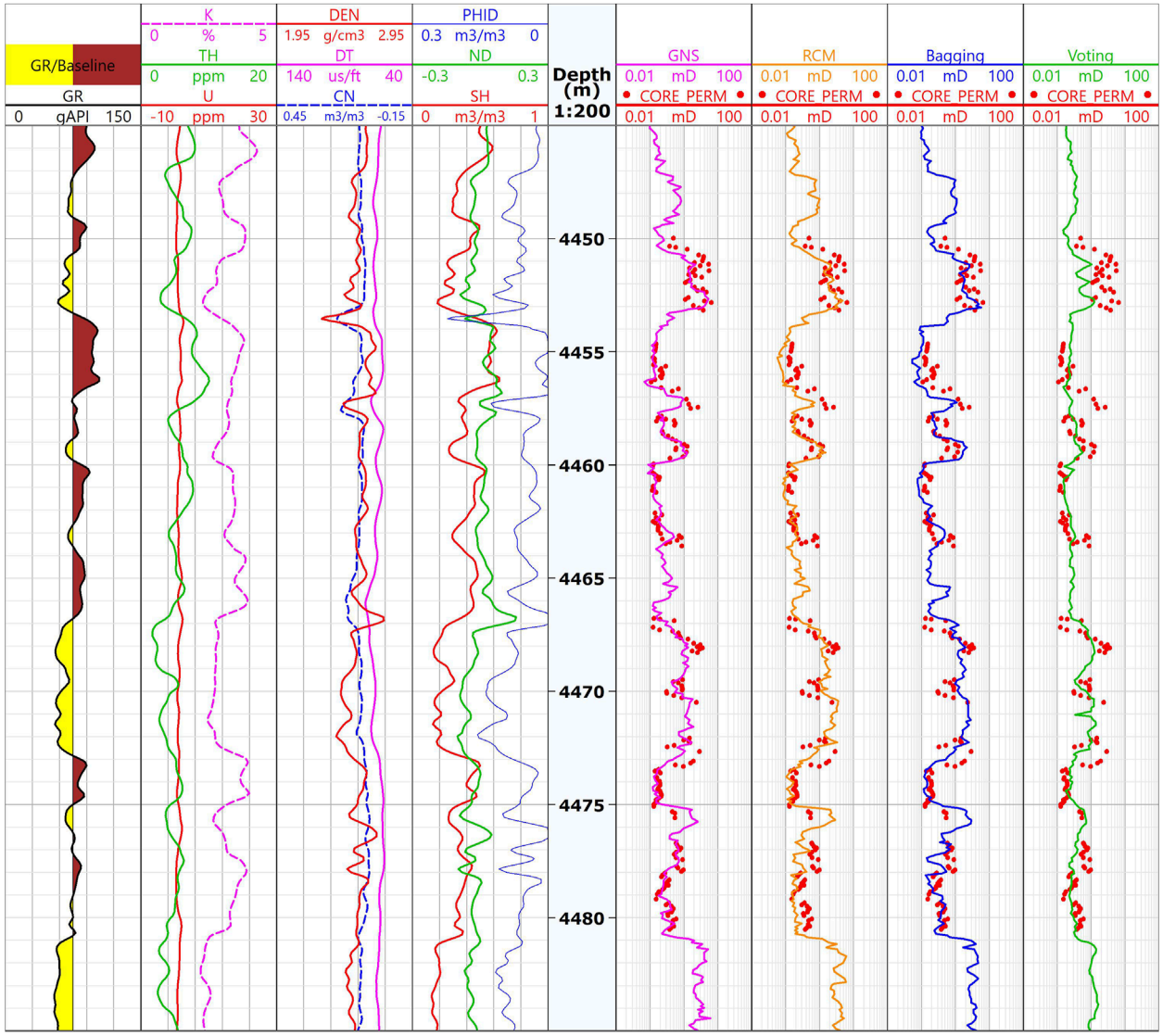

FIGURE 10
Permeability prediction results for Well N4 in the Dibei Gas Reservoir, Tarim Basin.

possible, and the information dimension may not be sufficiently rich. Therefore, the choice of petrophysical constraints is important. In the future research, while applying petrophysical constraints, more logging information can be used as the input or constraint of the model, such as imaging logging to achieve better results.

5 Conclusion

This paper proposes a workflow for reservoir permeability prediction based on the GNS model. The SHAP value is used to analyze the contribution of the feature curve, select the optimal feature combination to build the traditional stacking model, and use the gate network to control and dynamically optimize the overall model. Finally, the results of other models are compared to verify the superior performance of the GNS model. The following conclusions can be drawn from this study.

1) The selection of a well log is crucial for the prediction performance of intelligent algorithms. Intelligent algorithms based on appropriate features can output more accurate results. SHAP contribution analysis is an effective means of evaluating the importance of well logs.
2) Based on the classical stacking model, the GNS model applies gate networks to control and dynamically optimize the overall model. GNS is an algorithm driven by both data and models. It retains the advantages of the stacking model's strong expressive ability and significantly improves the interpretability of the algorithm. Compared with single data-driven algorithms, it is more reliable and superior in practical logging task applications.

3) The GNS model can effectively solve the nonlinear prediction problem of high-dimensional features. In the tight sandstone reservoir permeability prediction example, the results of the GNS model are closer to the laboratory-measured permeability than the results of the RCM, voting, and bagging models, thus verifying that the proposed model is an accurate method.

Data availability statement

The data analyzed in this study is subject to the following licenses/restrictions: exploratory research. Requests to access these datasets should be directed to PS, shipy0410@126.com.

Author contributions

PS: Conceptualization, Investigation, Methodology, Software, Validation, Writing–original draft, Writing–review and editing, Data curation, Formal Analysis. PS: Data curation, Methodology, Software, Validation, Writing–original draft, Writing–review and editing. KB: Validation, Writing–review and editing. CH: Validation, Writing–review and editing. XN: Validation, Writing–review and editing. ZM: Supervision, Validation, Writing–review and editing. PZ: Funding acquisition, Validation, Writing–review and editing, Supervision.

Funding

The author(s) declare financial support was received for the research, authorship, and/or publication of this article. The Science Foundation of China University of Petroleum, Beijing (2462020BJRC001).

Conflict of interest

Authors KB, CH and XN were employed by PetroChina Tarim Oilfield Company.

The remaining authors declare that the research was conducted in the absence of any commercial or financial relationships that could be construed as a potential conflict of interest.

Publisher's note

All claims expressed in this article are solely those of the authors and do not necessarily represent those of their affiliated organizations, or those of the publisher, the editors and the reviewers. Any product that may be evaluated in this article, or claim that may be made by its manufacturer, is not guaranteed or endorsed by the publisher.

References

Ahmadi, M. A., Ebadi, M., Shokrollahi, A., and Majidi, S. M. J. (2013). Evolving artificial neural network and imperialist competitive algorithm for prediction oil flow rate of the reservoir. *Appl. Soft Comput.* 13 (2), 1085–1098. doi:10.1016/j.asoc.2012.10.009

Ahmed, U., Crary, S., and Coates, G. (1991). Permeability estimation: the various sources and their interrelationships. *J. Pet. Technol.* 43 (5), 578–587. doi:10.2118/19604-PA

Al-Anazi, A. F., and Gates, I. D. (2012). Support vector regression to predict porosity and permeability: effect of sample size. *Comput. Geosci.* 39, 64–76. doi:10.1016/j.cageo.2011.06.011

Bai, Y., Tan, M., Shi, Y., Zhang, H., and Li, G. (2020). Regression committee machine and petrophysical model jointly driven parameters prediction from wireline logs in tight sandstone reservoirs. *IEEE Trans. Geosci. Remote Sens.* 60, 1–9. doi:10.1109/TGRS.2020.3041366

Carman, P. C. (1937). Fluid flow through a granular bed. *Trans. Instit. Chem. Eng.* 15, 150–156. doi:10.1016/S0263-8762(97)80003-2

Chen, C. H., and Lin, Z. S. (2006). A committee machine with empirical formulas for permeability prediction. *Comput. Geosci.* 32 (4), 485–496. doi:10.1016/j.cageo.2005.08.003

Coates, G. R., and Dumanoir, J. L. (1973). "A new approach to improved log-derived permeability," in *SPWLA annual logging symposium* (Lafayette, Louisiana: SPWLA).

Freund, Y., and Schapire, R. E. (1997). A decision-theoretic generalization of on-line learning and an application to boosting. *J. Comput. Syst. Sci.* 55 (1), 119–139. doi:10.1006/jcss.1997.1504

Friedman, J. H. (2001). Greedy function approximation: a gradient boosting machine. *Ann. Stat.* 29 (5), 1189–1232. doi:10.1214/aos/1013203451

Helle, H. B., Bhatt, A., and Ursin, B. (2001). Porosity and permeability prediction from wireline logs using artificial neural networks: a North Sea case study. *Geophys. Prospect.* 49 (4), 431–444. doi:10.1046/j.1365-2478.2001.00271.x

Jamialahmadi, M., and Javadpour, F. (2000). Relationship of permeability, porosity and depth using an artificial neural network. *J. Pet. Sci. Eng.* 26 (1-4), 235–239. doi:10.1016/S0920-4105(00)00037-1

Kalule, R., Abderrahmane, H. A., Alameri, W., and Sassi, M. (2023). Stacked ensemble machine learning for porosity and absolute permeability prediction of carbonate rock plugs. *Sci. Rep.* 13 (1), 9855. doi:10.1038/s41598-023-36096-2

Karimpouli, S., Fathianpour, N., and Roohi, J. (2010). A new approach to improve neural networks' algorithm in permeability prediction of petroleum reservoirs using supervised committee machine neural network (SCMNN). *J. Pet. Sci. Eng.* 73 (3-4), 227–232. doi:10.1016/j.petrol.2010.07.003

Kozeny, J. (1927). Uber kapillare leitung der Wasser in boden. *R. Acad. Sci.* 136, 271–306.

Lundberg, S., and Lee, S. I. (2016). An unexpected unity among methods for interpreting model predictions. arXiv Preprint. doi:10.48550/arXiv.1611.07478

Lundberg, S. M., Erion, G., Chen, H., Degrave, A., Prutkin, J. M., Nair, B., et al. (2020). From local explanations to global understanding with explainable AI for trees. *Nat. Mach. Intell.* 2 (1), 56–67. doi:10.1038/s42256-019-0138-9

Lundberg, S. M., Erion, G. G., and Lee, S. I. (2018). Consistent individualized feature attribution for tree ensembles. arXiv Preprint. doi:10.48550/arXiv.1802.03888

Lundberg, S. M., and Lee, S. I. (2017). "A unified approach to interpreting model predictions," in *NIPS'17: proceedings of the 31st international conference on neural information processing systems (ACM)*. Available at: https://www.aap.org/sections/perinatal/NCE08/TheRole2.pdf

Matinkia, M., Hashami, R., Mehrad, M., Hajsaeedi, M. R., and Velayati, A. (2023). Prediction of permeability from well logs using a new hybrid machine learning algorithm. *Petroleum* 9 (1), 108–123. doi:10.1016/j.petlm.2022.03.003

Mauran, S., Rigaud, L., and Coudevylle, O. (2001). Application of the carman–kozeny correlation to a high-porosity and anisotropic consolidated medium: the compressed expanded natural graphite. *Transp. Porous Med.* 43 (2), 355–376. doi:10.1023/a:1010735118136

Mohaghegh, S., and Ameri, S. (1995). Artificial neural network as a valuable tool for petroleum engineers. Paper SPE, 29220, 1–6.

Nazari, S., Kuzma, H. A., and Rector, J. W. (2011). "Predicting permeability from well log data and core measurements using support vector machines," in *SEG technical program expanded abstracts 2011*. Editor S. Fomel (Tulsa, Okla: Society of Exploration Geophysicists). doi:10.1190/1.3627601

Nilsson, N. J. (1965). *Learning machines*. New York: McGraw-Hill.

Paterson, M. (1983). The equivalent channel model for permeability and resistivity in fluid-saturated rock—a re-appraisal. *Mech. Mat.* 2 (4), 345–352. doi:10.1016/0167-6636(83)90025-X

Rogers, S., Chen, H., Kopaska-Merkel, D. T., and Fang, J. (1995). Predicting permeability from porosity using artificial neural networks. *AAPG Bull.* 79 (12), 1786–1797. doi:10.1306/7834DEFE-1721-11D7-8645000102C1865D

Saemi, M., Ahmadi, M., and Varjani, A. Y. (2007). Design of neural networks using genetic algorithm for the permeability estimation of the reservoir. *J. Pet. Sci. Eng.* 59 (1-2), 97–105. doi:10.1016/j.petrol.2007.03.007

Saljooghi, B. S., and Hezarkhani, A. (2014). Comparison of WAVENET and ANN for predicting the porosity obtained from well log data. *J. Pet. Sci. Eng.* 123, 172–182. doi:10.1016/j.petrol.2014.08.025

Sammut, C., and Webb, G. I. (2011). *Encyclopedia of machine learning*. Berlin: Springer Science & Business Media.

Timur, A. (1968). "An investigation of permeability, porosity, and residual water saturation relationships," in *SPWLA 9th annual logging symposium* (New Orleans, Louisiana: SPWLA).

Wolpert, D. H. (1992). Stacked generalization. *Neural Netw.* 5 (2), 241–259. doi:10.1016/S0893-6080(05)80023-1

Wu, T. (2004). Permeability prediction and drainage capillary pressure simulation in sandstone reservoirs. Doctoral thesis. Texas: Texas A&M University.

Zhang, G., Wang, Z., Mohaghegh, S., Lin, C., Sun, Y., and Pei, S. (2021). Pattern visualization and understanding of machine learning models for permeability prediction in tight sandstone reservoirs. *J. Pet. Sci. Eng.* 200, 108142. doi:10.1016/j.petrol.2020.108142

Zhang, H., Fu, K., Lv, Z., Wang, Z., Shi, J., Yu, H., et al. (2022a). FTCN: a reservoir parameter prediction method based on a fusional temporal convolutional network. *Energies* 15 (15), 5680. doi:10.3390/en15155680

Zhang, S., Gu, Y., Gao, Y., Wang, X., Zhang, D., and Zhou, L. (2022b). Petrophysical regression regarding porosity, permeability, and water saturation driven by logging-based ensemble and transfer learnings: a case study of sandy-mud reservoirs. *Geofluids* 2022, 1–31. doi:10.1155/2022/9443955

Zhong, Z., Carr, T. R., Wu, X., and Wang, G. (2019). Application of a convolutional neural network in permeability prediction: a case study in the Jacksonburg-Stringtown oil field, West Virginia, USA. *Geophysics* 84 (6), B363–B373. doi:10.1190/geo2018-0588.1

Zhu, L. Q., Zhang, C., Wei, Y., and Zhang, C. M. (2017). Permeability prediction of the tight sandstone reservoirs using hybrid intelligent algorithm and nuclear magnetic resonance logging data. *Arab. J. Sci. Eng.* 42 (4), 1643–1654. doi:10.1007/s13369-016-2365-2

frontiers | Frontiers in Earth Science

TYPE Original Research
PUBLISHED 15 February 2024
DOI 10.3389/feart.2024.1361052

Check for updates

OPEN ACCESS

EDITED BY
Wenguang Wang,
Northeast Petroleum University, China

REVIEWED BY
Yiming Yan,
China University of Petroleum (East China), China
Pengfei Zhang,
Shandong University of Science and Technology, China
Huaimin Dong,
Chang'an University, China

*CORRESPONDENCE
Weichao Tian,
520044@yangtzeu.edu.cn

RECEIVED 24 December 2023
ACCEPTED 26 January 2024
PUBLISHED 15 February 2024

CITATION
Li Z, Ren Y, Chang R, Zhang Y, Zhang X and Tian W (2024), Clarifying the contribution of multiscale pores to physical properties of Chang 7 tight sandstones: insight from full-scale pore structure and fractal characteristics.
Front. Earth Sci. 12:1361052.
doi: 10.3389/feart.2024.1361052

COPYRIGHT
© 2024 Li, Ren, Chang, Zhang, Zhang and Tian. This is an open-access article distributed under the terms of the Creative Commons Attribution License (CC BY). The use, distribution or reproduction in other forums is permitted, provided the original author(s) and the copyright owner(s) are credited and that the original publication in this journal is cited, in accordance with accepted academic practice. No use, distribution or reproduction is permitted which does not comply with these terms.

Clarifying the contribution of multiscale pores to physical properties of Chang 7 tight sandstones: insight from full-scale pore structure and fractal characteristics

Zhen Li[1,2], Yilin Ren[1], Rui Chang[1], Yuanli Zhang[1], Xuze Zhang[1] and Weichao Tian[3]*

[1]Research Institute of Exploration and Development, PetroChina Changqing Oilfield Company, Xi'an, China, [2]National Engineering Laboratory for Exploration and Development of Low Permeability Oil and Gas Fields, Xi'an, China, [3]Hubei Key Laboratory of Petroleum Geochemistry and Environment, Yangtze University, Wuhan, China

The pore structure and its heterogeneity of tight reservoirs are key factors affecting the storage and percolation of crude oil. The pore system of Chang 7 tight sandstone has multi-scale and multi-type characteristics. However, the contribution of different pore types and pore sizes to the physical properties of Chang 7 tight sandstone is still unclear. In this paper, we collected a suite of Chang 7 tight sandstones to investigate the full-scale pore structure and fractal characteristics by casting thin section, field emission scanning electron microscope, two-dimensional multi-scale backscattered scanning electron microscopy, N_2 adsorption (NA) and NMR. The pore diameters of Chang 7 tight sandstone are usually distributed between 0.001 and 20 μm. Intercrystalline pores are mainly distuibuted <500 nm. Dissolution pores vary from 100 nm to 100 μm. Residual intergranular pores range from 1 μm to 40 μm. Based on the fractal characteristics, pore system is divided into macropores (mainly >300 nm), mesopores (mainly 7–300 nm), and micropores (mainly <7 nm). Micropores are adsorb-fluid pores that do not contribute to the storage and percolation but contribute significantly to contrasting specific surface area. Mesopores represent bound-fluid pores and only contribute to total porosity but not to permeability. Macropores represent movable-fluid pores, contributing to both porosity and permeability. The content and heterogeneity of macropores control the quality of Chang 7 tight sandstone. When macropore volume is $>12\times10^{-3}$ mL/g, the continuous percolation network consists entirely of macropores, resulting in higher porosity and permeability of the reservoir. Moreover, reservoir physical properties show excellent correlation with macropore heterogeneity. These results demonstrate that the content and heterogeneity of macropores are key indicators indicating the quality of the Chang 7 tight sandstones.

KEYWORDS

full-scale pore structure, fractal characteristics, physical properties, NMR, Chang 7 tight sandstone

1 Introduction

Tight oil, as an important unconventional oil and gas resource, is changing the World Energy Pattern. The U.S. is currently the most successful country in tight oil exploration and development. In 2022, U.S. tight oil production will reach 7.5 million barrels per day (IEA, 2023). Influenced by the successful development of tight oil in the U.S., China has vigorously strengthened the evaluation and exploration of tight oil and achieved important breakthroughs in recent years. In 2019, PetroChina Changqing Oilfield Company discovered more than 1 billion tons of shale oil (or tight oil) reserves in the Chang 7 formation of the Longdong area from the Ordos Basin (Fu et al., 2021). The period of the Chang 7 Member was the maximum lake flooding period, and a set of organic-rich mudstone-shale inter-calated with silt/fine sandstone sedimentary combination was deposited. Tight oil (shale oil) occurring in interlayered silt/fine sandstone is the most realistic exploration and development target in the Chang 7 Member (Fu et al., 2020). The porosity of interlayered silt/fine sandstone is mostly less than 11%, and the permeability is mostly less than 0.3 mD, belong to a typical tight reservoir (Lai et al., 2016; Fu et al., 2021; Wen et al., 2022). Characterizing the full-scale pore structure of Chang 7 tight sandstone and clarifying the relationship between different pore sizes and physical properties are important for understanding reservoir quality and seepage mechanism. However, the pore structure of Chang 7 tight sandstone is characterized by wide pore size distribution, diverse types and strong nonuniformity, which increases the difficulty of comprehensively characterizing its pore structure and heterogeneity. Furthermore, the relationships between different pore sizes and the physical properties of Chang 7 tight sandstone is still unclear.

It is of great significance to study the contribution of different pore sizes and different pore types to the physical properties of tight reservoirs. According to the characteristics of the mercury intrusion curve, Sakhaee-Pour and Bryant (2014) divides the pores into intergranular pores and treelike pores, and stated that recovery has a significant positive correlation with treelike pore content. Xi et al. (2016) considered that the permeability is dominated by larger pore-throats. Xiao et al. (2017a) believed that nanopores contribute to both permeability and porosity, micropores mainly control permeability, and mesopores mainly contribute to porosity. Tian et al. (2020) indicated that fluid mobility is controlled by the content of intergranular pores in low-permebility conglomerate. Therefore, the research results of different scholars are quite different. To understand the contribution of different pore sizes to the physical properties of Chang 7 tight sandstone, we must first classify the pore sizes. Many scholars have confirmed that the pore system of rocks has multi-segment fractal characteristics (Lai and Wang, 2015; Zhang L. et al., 2017; Xiao et al., 2017b; Shao et al., 2017; Xu et al., 2018; Wang et al., 2020; Zheng et al., 2023). Therefore, we can utilize the fractal characteristics of full-scale pore structures for pore classification.

Since different experiments have certain limitations in characterizing the pore structure, researchers have tried to combine multiple experiments to characterize the full-scale pore structure of porous media. The full-scale pore-throat structure of tight sandstones was acquired by integrating the rate-controlled mercury injection (RMI) and high-pressure mercury injection (HPMI) experiments (Xi et al., 2016). Zhang et al. (2018) and Zhang et al. (2020) utilized gas adsorption and HPMI experiments to characterize the full-scale pore structure of shale. Zhang et al. (2017b) and Gao et al. (2019) characterized the full-scale pore structure of tight reservoir by combining N_2 adsorption (NA) and HPMI experiments. In addition, NMR is often used in conjunction with other experiments such as mercury intrusion and NA to investigate the full-scale pore structure in tight sandstones (Xiao et al., 2017b; Zhang et al., 2017c; Dong et al., 2019; Tian et al., 2019; Wu et al., 2019). However, different experiments have different pore hypothesis models. NA, HPMI and NMR usually assume that the pores are cylinders, while RMI assumes that the pores are spherical. Meanwhile, the information detected by NA and NMR

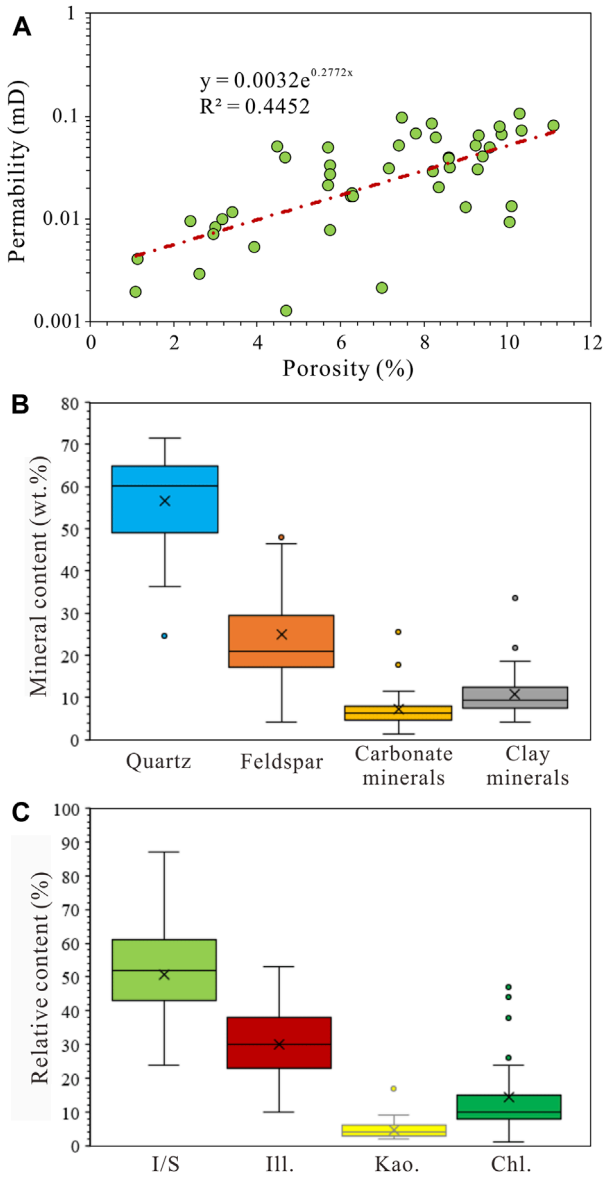

FIGURE 1
(A) the relationship between permeability and porosity, **(B)** whole-rock results, and **(C)** the relative contents of clay minerals.

TABLE 1 Porosity, permeability, and mineral compositions of the Chang 7 tight sandstones (Φ-porosity, K-permeability, PV-pore volume).

Sample ID	Φ (%)	K (mD)	XRD analysis (wt.%)				NA experiments	
			Quartz	Feldspar	Carbonate minerals	Clay minerals	SSA (m^2/g)	PV (mL/100g)
L1	9.433	0.0393	38.1	45.4	7.8	8.7	2.4987	0.6999
L2	6.265	0.0161	57.5	4.1	4.9	33.5	3.5794	1.7288
L3	8.286	0.0606	38.3	46.2	6	9.5	5.7141	0.9477
L4	4.71	0.00126	37.5	43.5	8.4	10.2	3.2173	1.1055
L5	9.87	0.065	68.7	22.4	4.6	4.3	3.7539	1.0631
L6	8.19	0.0832	70.7	14.9	5.2	9.2	3.0414	0.9702
L7	10.317	0.104	62.5	14.2	9.3	13	2.0109	0.7056
L8	3.005	0.00823	51.7	21	7	14.9	1.1067	0.4302
L9	10.071	0.00917	-	-	-	-	-	-
L10	7.494	0.0956	41.5	48	1.3	9.2	1.7405	0.5857
L11	5.771	0.0326	40	46.4	4.5	9.1	1.4645	0.6953
L12	5.756	0.0265	36.9	44.7	8.9	9.5	2.9136	0.9397
L13	3.431	0.0115	36.4	35.6	9.4	18.6	4.7433	1.095
L14	8.237	0.0283	42.2	41.4	6.6	9.8	2.2332	1.0352
L15	2.421	0.00941	24.6	42.9	25.6	6.9	3.0163	0.8536
L16	8.381	0.0197	39	42.1	7	11.9	3.4718	1.1823
L17	3.177	0.00979	62.8	13.5	6.5	14.9	4.2265	1.0912
L18	8.606	0.0391	64.3	21.4	5	9.3	3.4258	1.0545
L19	8.629	0.0309	64.4	20.4	8	7.2	3.9513	1.1448
L20	6.278	0.0172	67.3	17.5	8	6.8	0.9202	0.5769
L21	1.148	0.00402	58.9	16	17.9	7.2	2.4017	0.8422
L22	2.625	0.00285	50.9	17.9	18.7	12.5	1.0811	0.6304
L23	5.721	0.0209	63.1	16.9	6.4	13.6	5.3351	1.4415
L24	9.247	0.0513	70	13.9	5.3	10.4	3.6119	1.3864
L25	2.956	0.00702	70.2	17.1	5.3	7.4	1.6221	0.6342
L26	1.102	0.00192	60.3	20.7	9.1	9.3	0.9631	0.6534
L27	3.942	0.00523	66.7	12.9	8.1	12.3	1.1222	0.7013
L28	9.324	0.0629	57.6	29.4	4.5	6.8	1.8481	0.6114
L29	8.604	0.0384	64.7	22	6.4	6	2.9495	0.863
L30	5.768	0.00768	59.6	19.4	3.7	15.4	6.4345	1.3176
L31	7.168	0.0306	61.7	23.9	4.2	9.4	3.0229	0.9069

(Continued on the following page)

TABLE 1 (*Continued*) Porosity, permeability, and mineral compositions of the Chang 7 tight sandstones (Φ-porosity, K-permeability, PV-pore volume).

Sample ID	Φ (%)	K (mD)	XRD analysis (wt.%)				NA experiments	
			Quartz	Feldspar	Carbonate minerals	Clay minerals	SSA (m^2/g)	PV (mL/100g)
L32	9.021	0.0128	58.8	20.1	6.1	13.6	2.606	0.8519
L33	10.347	0.0712	-	-	-	-	-	-
L34	7.82	0.0668	64.9	25.5	3	6.2	1.51	0.8525
L35	11.115	0.0798	53.9	26.5	11.6	7.6	3.6054	1.1165
L36	4.495	0.0492	69.4	21.5	3.9	5.2	2.8974	0.9649
L37	7.011	0.00208	64.1	18.8	5.6	10.6	5.4696	1.2493
L38	10.113	0.0129	58.8	25.3	6.6	8.7	1.0704	0.694
L39	9.588	0.0486	71.6	16.3	4.3	7.8	3.4211	1.0897
L40	7.409	0.0504	65	21.5	4.3	9.2	4.8561	1.4152
L41	4.688	0.0392	64.2	19.5	7.3	9	5.1325	1.4602
L42	9.834	0.0768	56.2	22.8	5.4	14.6	5.0072	1.2975
L43	6.302	0.0162	49.1	19.8	7.8	21.8	4.602	1.3721
L44	5.721	0.0489	69.2	17.3	3.7	9.8	3.787	1.2966
L45	9.298	0.0298	64.4	20	5.7	9.4	5.035	1.4997

includes both pores and throats, while HPMI only obtains the size of the throat and the corresponding pore volume. Therefore, it is unreasonable to combine NA and HPMI or to combine HPMI and RMI or to combine HPMI and NMR to obtain the full-scale pore structure.

In this work, casting thin section (CTS), field emission scanning electron microscope (FE-SEM), Two-dimensional multi-scale backscattered scanning electron microscopy (2D-MS-BSEM), NA, NMR and physical property were performed on the Chang 7 tight sandstones to reveal the full-scale pore structure and fractal characteristics. Then the multi-scale pores were classified. Moreover, the contribution of different pore scales to physical properties was investigated.

2 Materials and methods

2.1 Samples

We selected 11 typical wells for core observations of Chang 7 Member and collected forty-five fine-grained sandstone samples. Cylindrical cores with a diameter of approximately 2.5 cm were drilled parallel to the lamination for all samples. Prior to the experiments, we clean the cores with distilled water to remove the drilling mud. Then the cores were placed in a Soxhlet extractor for 7 days and a mixed solvent of dichloromethane and methanol (9:1 v/v) was used to remove the residual oil in the cores. Finally, a series of experiments were conducted, including physical properties analysis, X-ray diffraction (XRD) analysis, CTS, FE-SEM, NA and NMR experiments.

2.2 Experimental methods

2.2.1 Porosity and permeability

The helium porosity was measured on a PDP-200 Porosimetry Instrument without a confining pressure. The permeability measurements were performed on a KA-210 permeability instrument under a confining pressure of 200 psi and a gas pressure of 30 psi. The experimental process complies with the Chinese Oil and gas industry standard SY/T 6385-2016.

2.2.2 XRD analysis

XRD analysis was performed using the Bruker AXS D8 Discover X-ray diffractometer according to the Chinese Oil and gas industry standard SY/T 5163–2018. The sample is crushed and ground to obtain a powder for mineral content analysis. The mineral content of the whole rock and the relative contents of clay minerals were determined.

2.2.3 CTS and FE-SEM

Samples were observed using a CIAS-2007 Rock Casting Image Analyzer following the SY/T6103- 2004. Thin sections were impregnated with blue epoxy resin for easy visualization of pores.

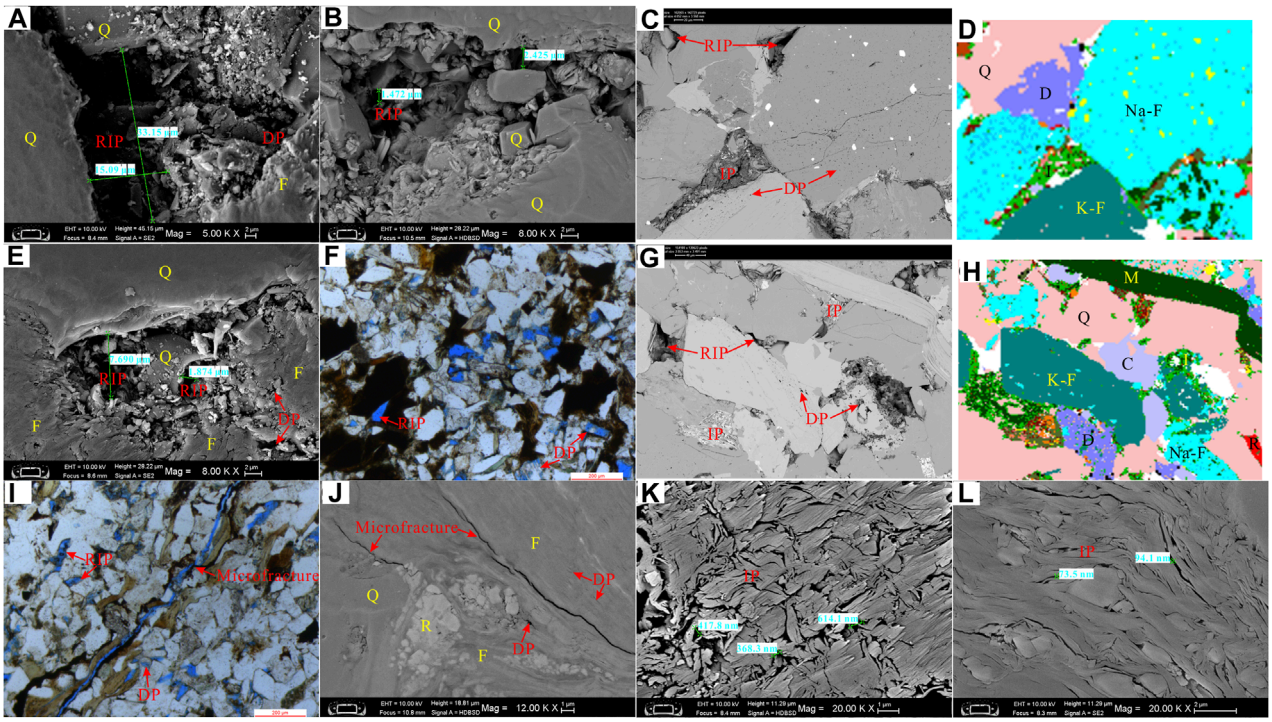

FIGURE 2
The main storage space of Chang 7 tight sandstone in the Longdong area. **(A)** DPs and RIPs, Sample L33, SEM; **(B)** RIPs, Sample L10, SEM; **(C)** RIPs, DPs, and IPs, Sample L5, 2D-MS-BSEM; **(D)** the same view field as photo **(C)**, QEMSCAN; **(E)** RIPs and DPs, Sample L34, SEM; **(F)** RIPs and DPs, Sample L1, Casting thin section; **(G)** RIPs, DPs, and IPs, Sample L7, 2D-MS-BSEM; **(H)** the same view field as photo **(G)**, QEMSCAN; **(I)** RIPs, DPs, and microfracture, Sample L11, Casting thin section; **(J)** Microfracture and DPs, Sample L42, SEM; **(K)** IPs, Sample L40, SEM; **(L)** IPs, Sample L41, SEM. DPs–dissolution pores, RIPs–residual intergranular pores, IPs–intercrystalline pores, Q–quartz, F–feldspar, D–dolomite, C–calcite, I–illite, Na-F–albite, K-F–orthoclase, M–mica.

Before FE-SEM, the samples were prepared with a length, width and height of 1 cm × 1 cm × 0.5 cm, respectively. An argon ion beam was used to polish the observation surface. Then, SEM tests were performed on a Quanta 450 field emission scanning electron microscope following the GB/T 16594-2008. Moreover, the magnification of view field ranges from 100× to 100000×.

2.2.4 NA experiments

4–10 g powdered samples were subjected to N_2 adsorption on an ASAP 2460 physisorption instrument. The relative pressure (P/P0) varies from 0.01 to 0.995. The detail of NA experiments refer to Tian et al. (2019). The pore size distribution (PSD) and specific surface area (SSA) of pore in the range of 1–200 nm can be quantitatively analyzed using the data from adsorption branch based on BJH and BET models.

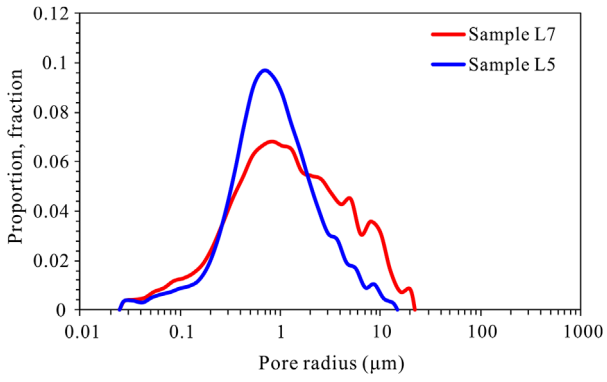

FIGURE 3
The PSD derived from 2D-MS-BSEM.

2.2.5 NMR experiments

Transverse relaxation (T_2) analyses were carried out on a MesoMR23-060H-1 instrument manufactured by Suzhou Niumag Analytical Instrument Corporation (China). Moreover, two sets of T_2 analysis were measured on the tight sandstones: (1) dried state, (2) water-saturated state. The T_2 spectra of the dried state are used as the background signal, and the T_2 spectra of the water-saturated state are used to analyze the full-scale PSD. The corresponding parameters were set as: T_w, 4000 ms; T_E, 0.08 ms; NECH, 10000; NS, 32.

2.2.6 2D-MS-BSEM and Qemscan

Two-dimensional multi-scale backscattered scanning electron microscopy (2D-MS-BSEM) was carried out using Helios NanoLab 650. The 2D-MS-BSEM has a resolution of 25 nm. Quantitative evaluation of minerals by scanning electron microscopy (Qemscan)

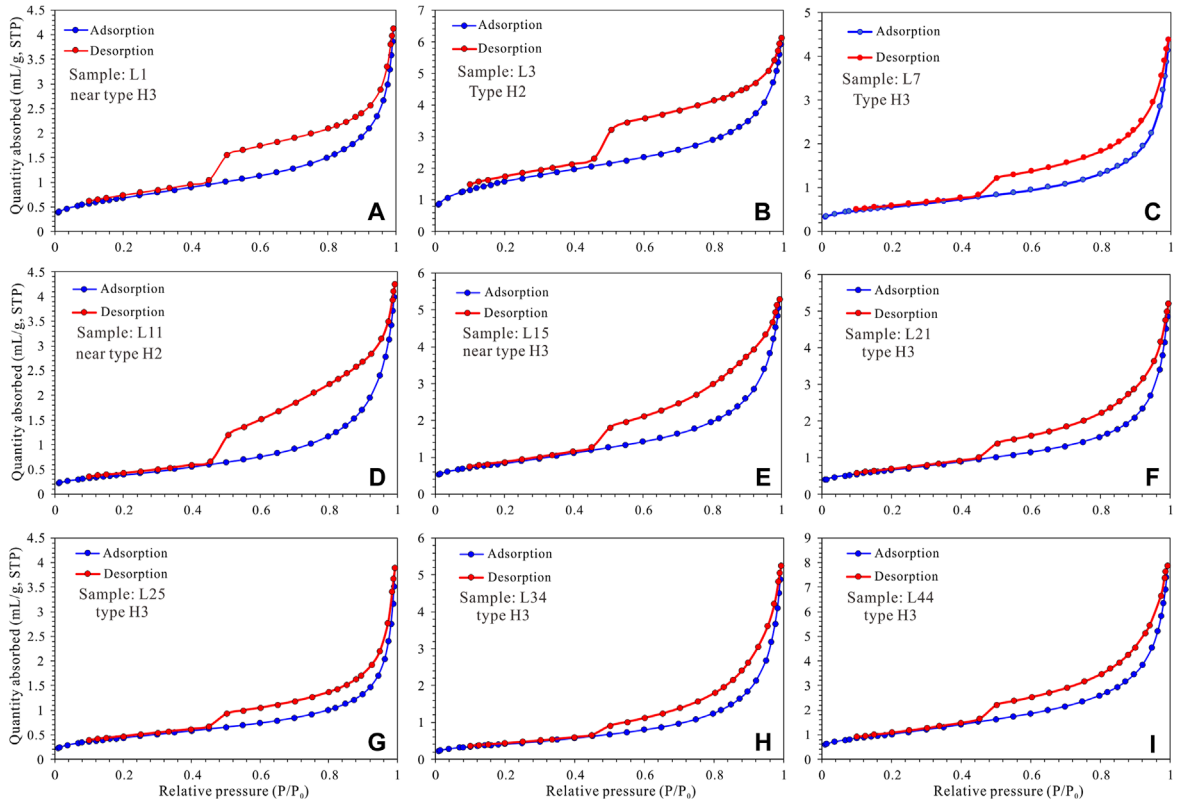

FIGURE 4
The N_2 adsorption/desorption isotherms of Chang 7 tight sandstones. **(A)** is from Sample L1, **(B)** is from Sample L3, **(C)** is from Sample L7, **(D)** is from Sample L11, **(E)** is from Sample L15, **(F)** is from Sample L21, **(G)** is from Sample L25, **(H)** is from Sample L34, and **(I)** is from Sample L44.

was performed on an Qemscan 650F. Qemscan has a resolution of 2 μm. The scanning areas of 2D-MS-BSEM and Qemscan are about 4 mm × 4 mm.

3 Results

3.1 Porosity, permeability and mineral compositions

The reservoir quality of Chang 7 sandstone is quite poor, showing the characteristics of tight reservoirs (Zou et al., 2012). Helium porosity of 45 selected samples varies from 1.10% to 11.12% (average of 6.86%). Permeability is in the range of 0.0013–0.1040 mD. There is a weak positive relationship between permeability and porosity, with a correlation coefficient (R^2) of 0.45 (Figure 1A; Table 1).

The XRD analysis showed that Chang 7 tight sandstones are dominated by quartz and feldspar, with the contents of 24.6%–71.6% (average of 56.7%) and 4.1%–48.0% (average of 24.9%), respectively. The carbonate minerals content ranges from 1.3% to 25.6%, with an average of 7.2%, including calcite, dolomite, Fe-dolomite and very small amount of siderite. The clay minerals content varies from 4.3% to 33.5%, with a mean value of 10.7% (Figure 1B; Table 1). Among clay minerals, illite/smecite mixed layer (I/S), illite and chlorite are the dominated compositions, with relative contents of 24.0%–87.0% (mean of 56.8%), 10.0%–53.0% (mean of 30.2%), and 1.0%–47.0% (mean of 14.3%), respectively (Figure 1C; Table 1).

3.2 Pore types

Based on the CTS and SEM images, four types of storage spaces were observed, including residual intergranular pores (RIPs), dissolution pores (DPs), intercrystalline pores (IPs) and microfracture (Figure 2). RIPs only developed in the tight sandstones with better grain sorting and rich in rigid grains. Due to the effects of compaction and cementation, the shape of RIPs becomes extremely irregular. The pore size of RIPs mainly ranges from 1 to 40 μm (Figures 2A, B, E). DPs are the most important storage spaces of Chang 7 tight sandstones. DPs are mainly formed by feldspar dissolution, followed by rock fragments dissolution, while DPs of carbonate are relatively rare (Lai et al., 2016). DPs have a wide PSD, varying from 100 nm to 100 μm (Figures 2A, C, E–G, I, J). Slit-shaped clay IPs are usually observed in Chang 7 tight sandstone, most of which are below 500 nm in diameter (Figures 2C, G, K, L). Microfractures in this work can be classified into two types: structural fractures and diagenetic fractures. Structural fractures generally extend far, and the width is mostly at the micron level. Diagenetic fractures generally have a short extension distance, and the width is mostly at the nano-scale (Figures 2I, J).

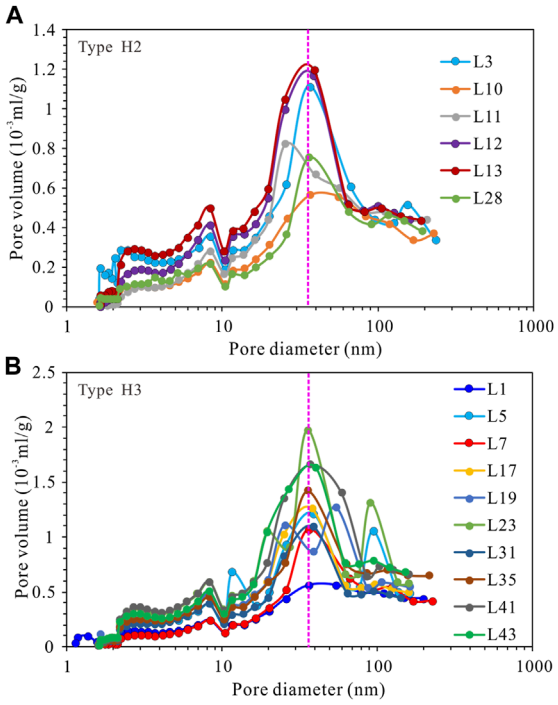

FIGURE 5
The pore size distributions derived from the NA experiments. **(A)** is from the type H2 samples, **(B)** is from the type H3 samples.

The field of view area is large enough that the pores extracted from 2D-MS-BSEM are representative. Based on 2D-MS-BSEM, we can obtain the PSD of pores >25 nm. The gray value of pores is larger than that of minerals. Therefore, pores in 2D-MS-BSEM images can be extracted and quantified using ImageJ software. The pore size distribution derived from 2D-MS-BSEM range from 25 nm to 20 μm with a unimodal distribution, and the peak position is around 700 nm (Figure 3).

3.3 Pore structure characteristics by NA experiments

NA experiment can characterize the pores of 1.5–200 nm. The N2 adsorption/desorption isotherms were shown in Figure 4. When P/P0 > 0.45, there is an obvious hysteresis loop in the adsorption/desorption isotherm. The type of hysteresis loop can reveal the morphology of pores. The hysteresis loops of Chang 7 tight sandstones are dominated by H3 and near-H3 types, accounting for about 86% (Figure 4), indicating that slit-shaped pores are the dominated pore shapes. Under SEM observation, IPs are mainly slit-shaped pores, while DPs and RIPs are mostly ink bottle-shaped pores (Figure 2). These results illustrate that the pores below 200 nm are mainly IPs.

The SSA calculated by the BET method varies from 0.92 to 6.43 m^2/g (average 3.17 m^2/g). The average pore size calculated by the BJH method is in the range of 6.44–20.65 nm, with an average of 11.03 nm. Based on BJH model, the pore volume derived from NA data ranges from 0.4302 mL/100g to 1.7288 mL/100g, with a mean of 1.0012 mL/100g (Table 1). The porosity (Φ_{NA}) characterized by N_2 adsorption can be determined by the equation: $\Phi_{NA} = V_{NA} \times \rho_{rock} \times 100\%$, where, V_{NA} is the pore volume derived from NA experiments, mL/g; ρ_{rock} is the rock density, g/mL. Φ_{NA} is in the range of 1.41%–4.18% (average 2.53%), suggesting that the Chang 7 tight sandstone develops a large number of IPs.

The PSDs obtained from the NA experiments are present in Figure 5. The H3 type samples have the same pore size distribution characteristics as the type H2 samples. The pore size distributions have a unimodal distribution, with a peak ranging from 30 to 40 nm.

3.4 Pore structure characteristics by NMR experiments

The NMR T_2 spectra under water-saturated state are presented in Figure 6. The T_2 spectra of all samples show bimodal shape, with peaks at 0.01–2 ms (P1) and 2–300 ms (P2). According to the amplitude and shape of the T_2 spectra, Chang 7 tight sandstone samples can be classified into three types. The T_2 spectra of type I samples exhibit a higher P2 peak and a lower P1 peak (Figure 6A), reflecting that their pore system is dominated by larger pores. Taking sample L7 as an example, abundant micron-sized RIPs and DPs were observed under the CTS and SEM images (Figures 6B, C). The T_2 spectra of type II samples show unimodal shape (Figure 6D). This phenomenon may be attributed to the close pore size of DPs and IPs, resulting in the merger of P1 and P2 into one peak. This interpretation is supported by microscopic photographs (Figures 6E, F). The T_2 spectra of type III samples exhibit a higher P1 peak and a lower P2 peak (Figure 6G), reflecting that their pore system is dominated by smaller pores. In sample L30, we only observed significant amounts of nanoscale IPs while microscale DP or RIP were lacking (Figures 6H, I). Therefore, we can infer that the P2 peak mainly reflects RIPs and DPs, while the P1 peak mainly reflects IPs.

4 Discussion

4.1 The full-scale PSD combining the NMR and NA experiments

At low T_E (0.08 ms), the T_2 spectra of tight sandstone saturated with low-viscosity fluid can reflect its full-scale PSD. In the case of uniform magnetic field intensity and short T_E, the T_2 spectra of tight sandstone saturated with low-viscosity fluid is controlled by the surface relaxation (Kleinberg and Horsfield, 1990; Morriss et al., 1997; Coates et al., 1999). In other words, the larger the T_2 value, the larger the corresponding pore diameter. The expression between T_2 and pore diameter can be described as:

$$\frac{1}{T_2} \approx \left(\frac{1}{T_2}\right)_s = \rho_2 \frac{S}{V} = \rho_2 \frac{F_s}{D} \quad (1)$$

where $\left(\frac{1}{T_2}\right)_s$ is the surface relaxation; ρ_2 denotes the transverse surface relaxivity, μm/s; S is the pore surface area, μm^2; V denotes

10.3389/feart.2024.1361052

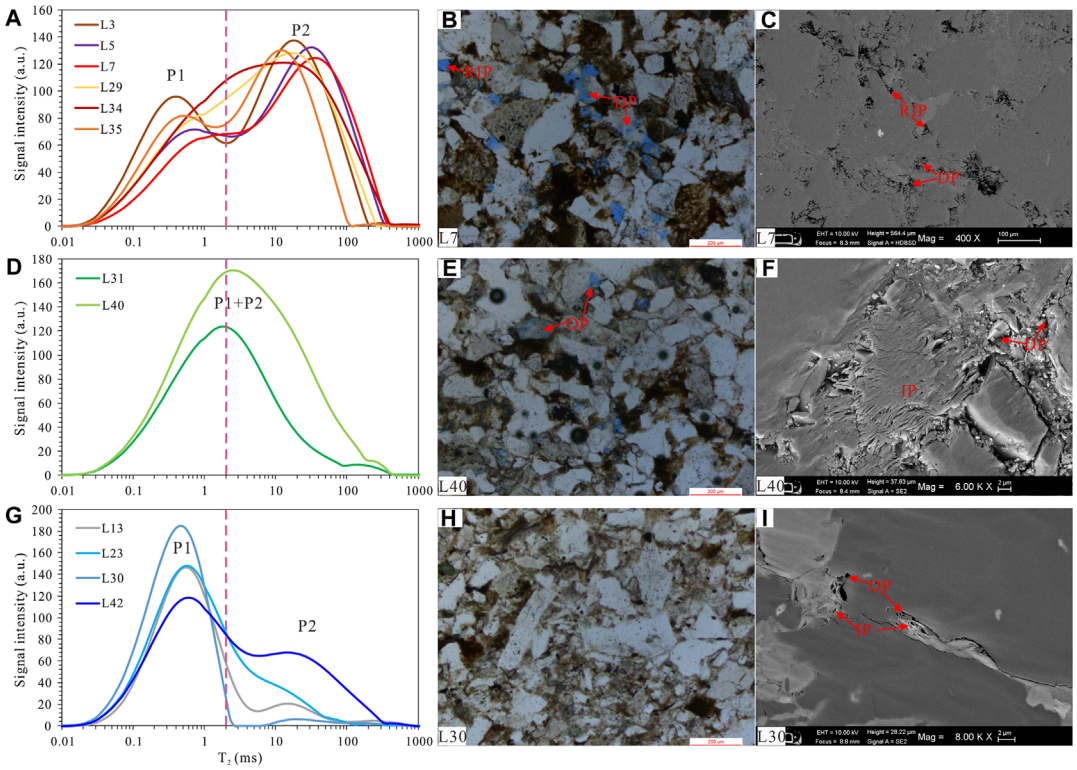

FIGURE 6
Three types of T_2 spectra of Chang 7 tight sandstone under water-saturated state and microscopic evidence of typical samples. **(A)** T_2 spectra of type I samples; **(B)** RIPs and DPs in sample L7, Casting thin section; **(C)** RIPs and DPs in sample L7, SEM; **(D)** T_2 spectra of type II samples; **(E)** DPs in sample L40, Casting thin section; **(F)** DPs and IPs in sample L40, SEM; **(G)** T_2 spectra of type III samples; **(H)** No pores can be observed in sample L30, Casting thin section; **(I)** IPs and DPs in sample L30, SEM.

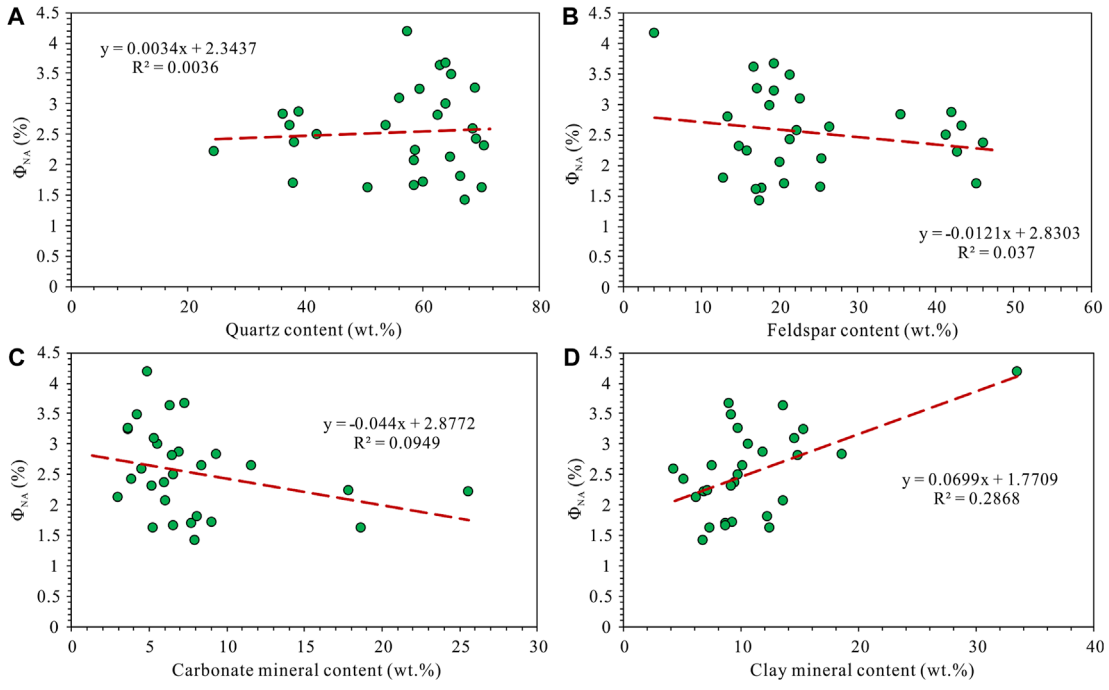

FIGURE 7
The relationships between Φ_{NA} and mineral contents. **(A)** Φ_{NA} versus quartz content, **(B)** Φ_{NA} versus feldspar content, **(C)** Φ_{NA} versus carbonate mineral content, and **(D)** Φ_{NA} versus clay mineral content.

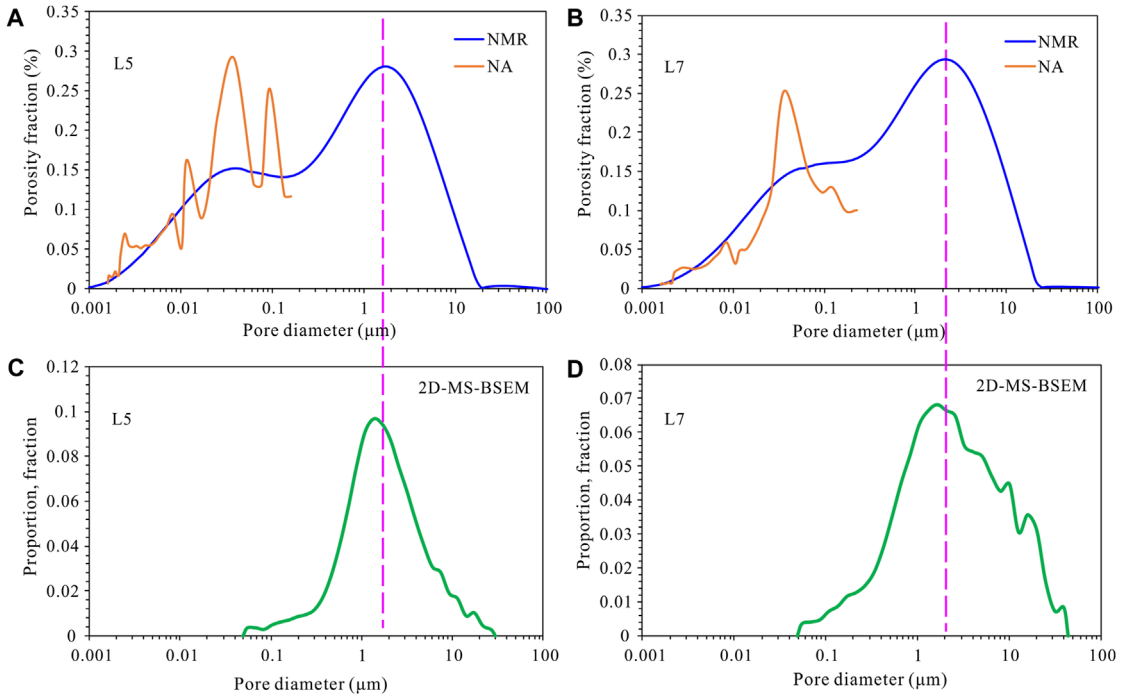

FIGURE 8
Comparison of PSDs by NA, NMR, and 2D-MS-SEM. **(A)** Comparison of PSDs by NA and NMR from Sample L5, **(B)** Comparison of PSDs by NA and NMR from Sample L7, **(C)** PSD by 2D-MS-SEM from Sample L5, and **(D)** PSD by 2D-MS-SEM from Sample L7.

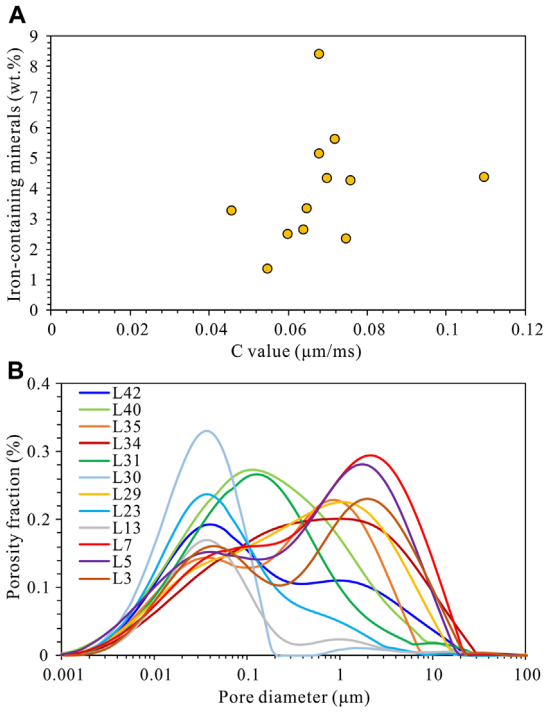

FIGURE 9
(A) Relationship between iron-containing minerals and C values, **(B)** NMR PSD of the selected samples.

the pore volume, μm^3; F_s denotes the geometry morphologic factor; and D is the pore diameter, μm.

Based on the Eq. 1, another expression between T_2 and pore diameter can be depicted as:

$$D = \rho_2 F_s T_2 = C T_2 \quad (2)$$

where C denotes the conversion coefficient, μm/s.

The relationships between Φ_{NA} and mineral contents are displayed in Figure 7. The Φ_{NA} presents a remarkable positive relationship with clay mineral content, but it shows no obvious correlation with other mineral contents (Figure 7). These relationships demonstrate that the pores revealed by NA experiments are dominated by IPs in clay minerals. Simultaneously, the P1 peak of T_2 spectrum mainly reflects IPs. Thus, the PSD obtained from the NA experiment should be comparable in morphology and amplitude to the P1 peak of the T_2 spectrum. Therefore, we can calibrate the T_2 spectra to the PSDs based on this similarity.

The calibrated NMR PSD is displayed in Figure 8, ranging from 1 nm to 20 μm. The NMR results show good consistency with the 2D-MS-BSEM results, suggesting that it is feasible to calibrate NMR T_2 spectra by using NA data. The calculated C values are in the range of 0.046–0.11 μm/ms (average of 0.069 μm/ms). C values show an obvious positive correlation with the content of iron-containing minerals (i.e., Fe-dolomite, Siderite, pyrite and chlorite) (Figure 9A), which is consistent with the studies of Saidian and Prasad (2015) and Tian et al. (2019). The full-scale PSDs of the selected samples

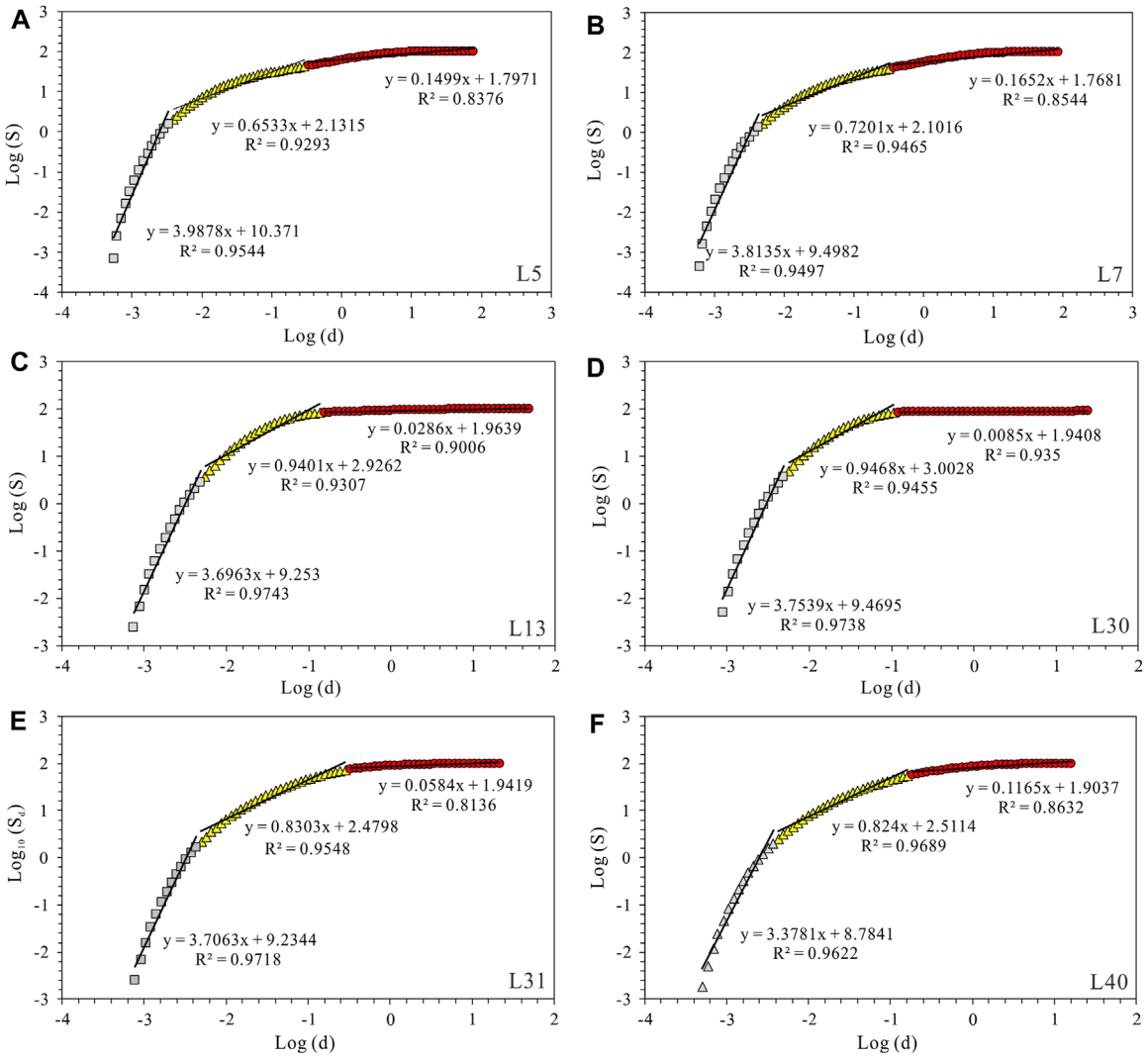

FIGURE 10
Fractal characteristics of full-scale pore structure from NMR data. **(A)** is from Sample L5, **(B)** is from Sample L7, **(C)** is from Sample L13, **(D)** is from Sample L30, **(E)** is from Sample L31, and **(F)** is from Sample L40.

are displayed in Figure 9B. The maximum pore diameter of Chang 7 tight sandstone is about 30 μm, and the minimum pore diameter is about 1 nm.

4.2 Pore classification based on fractal characteristics

Shao et al. (2017) developed fractal dimension by using NMR data [20]. The corresponding expression is as follows:

$$\log_{10}\left(S_{T_2}\right) = (3-D)\log_{10}(T_2) + (D-3)\log_{10}\left(T_{2max}\right) \quad (3)$$

where S_{T_2} is the cumulative pore volume percentage with pore diameter < T_2, %; D de-notes the fractal dimension; T_{2max} is the maximum T_2, ms.

The relationship between $\log_{10}(S_d)$ (cumulative pore volume with pore diameter < d) and $\log_{10}(d)$ can be obtained by substituting Eq. 2 into the Eq. 3.

$$\log_{10}(S_d) = (3-D)\log_{10}(d) + (D-3)\log_{10}(d_{max}) \quad (4)$$

where d_{max} is the maximum pore diameter, μm.

Based on the Eq. 4, a scatter plot of $\log_{10}(S_d)$ and $\log_{10}(d)$ was used to illustrate the fractal characteristics of Chang 7 tight sandstone (Figure 10). Chang 7 tight sandstone exhibits three-stage fractal characteristics. The two cut-off points are named d1 and d2 from left to right, and are in the range of 3.6~7.2 nm (average of 5.0 nm) and 29.8~344.3 nm (average of 169.9 nm) respectively. Therefore, using d1 and d2 as the cut-off points, the pores are classified into macropores, mesopores and micropores. The fractal dimensions of micropores, mesopores and macropores are named D1, D2 and D3. D1 is in the range of −1.00~-0.37, with an average of −0.68, which is smaller than the lower limit of fractal dimension of three-dimensional pore structure. This result indicates that micropores do not have fractal characteristics. D2 varies from

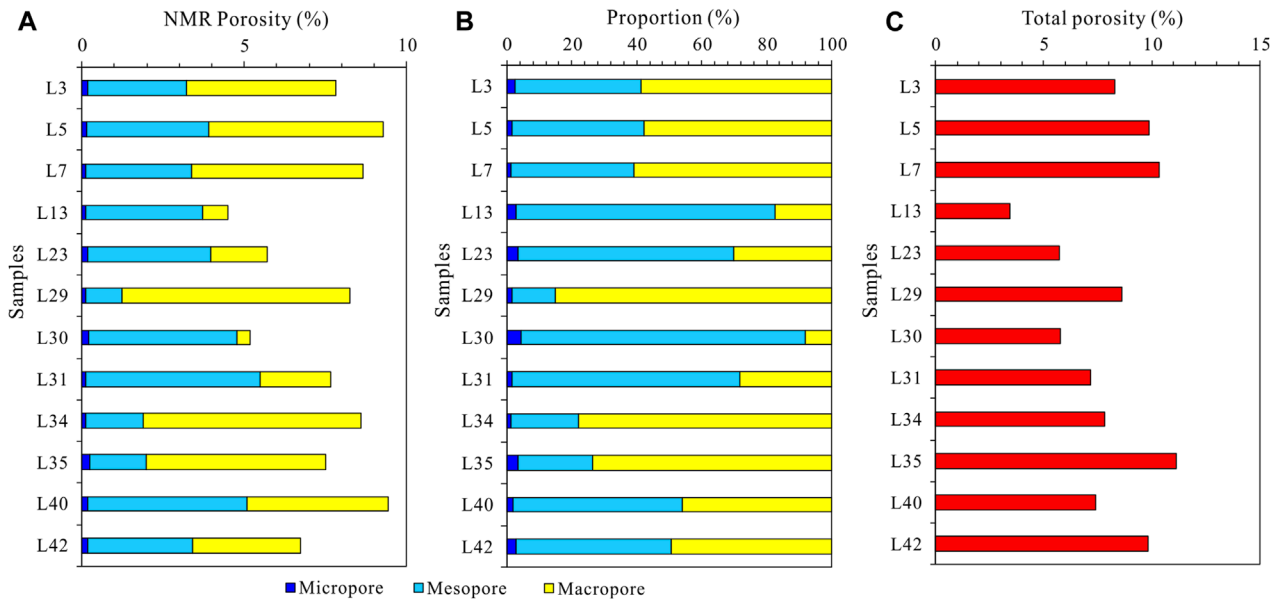

FIGURE 11
(A) NMR Porosity, **(B)** proportion of different types of pores, and **(C)** total porosity.

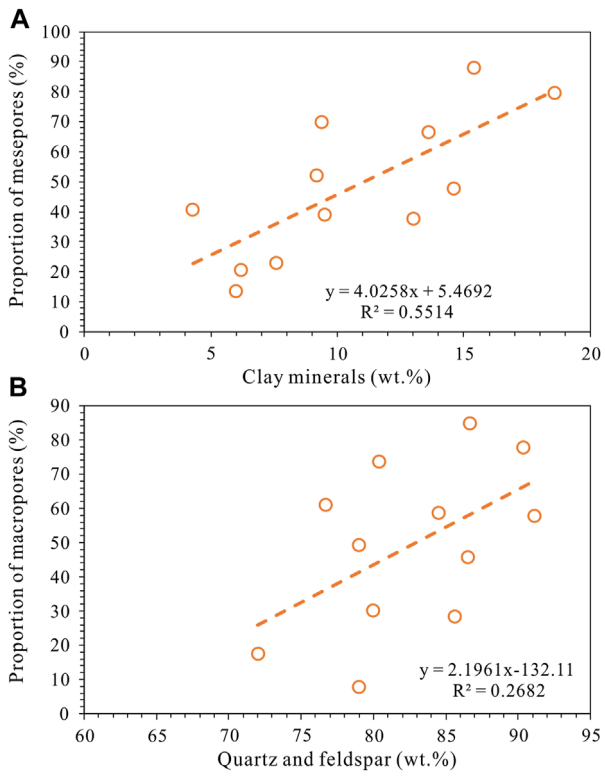

FIGURE 12
(A) Relationship between the proportion of mesopores and the content of clay minerals, and **(B)** relationship between the proportion of macropores and the content of quartz and feldspar.

1.86~2.35, with a mean of 2.13. D3 ranges from 2.70~2.99, with an average of 2.87. The value of D3 is much larger than the value of D2, demonstrating that macropores are more heterogeneous than mesopores.

4.3 Relationship between different types of pores and physical properties

The porosity and proportion of different types of pores were determined based on NMR PSD. Mesopres and macropores are predominant in Chang 7 tight sandstone, and the content of micropores is very small. Porosity of macropores varies from 0.41% to 7.00%, accounting for 7.92%~84.95%. Porosity of mesopores varies from 1.12% to 5.37%, ac-counting for 13.59%~87.84%. Porosity of micropores varies from 0.11% to 0.25%, accounting for 1.27%~4.25% (Figure 11). The content of mesopores displays a distinctly positive relationship with the content of clay minerals (Figure 12A), indicating that mesopores are dominated by clay IPs. The proportion of macropores shows a positive correlation with the contents of quartz and feldspar (Figure 11B), implying that macropores are composed of RIPs and DPs associated with quartz and feldspar. These understandings are consistent with observations under the microscope (Figure 2; Figure 6). Total porosity has a significant positive relationship with the content of macropores, and a significant negative relationship with the proportion of mesopores. (Figures 11B, C), suggesting that an increased content of mesopores compromises total porosity. Clay minerals have two origins: non-authigenic origin and authigenic origin (Rushing et al., 2008; Xiao et al., 2018). Non-authigenic clay exists in the form of

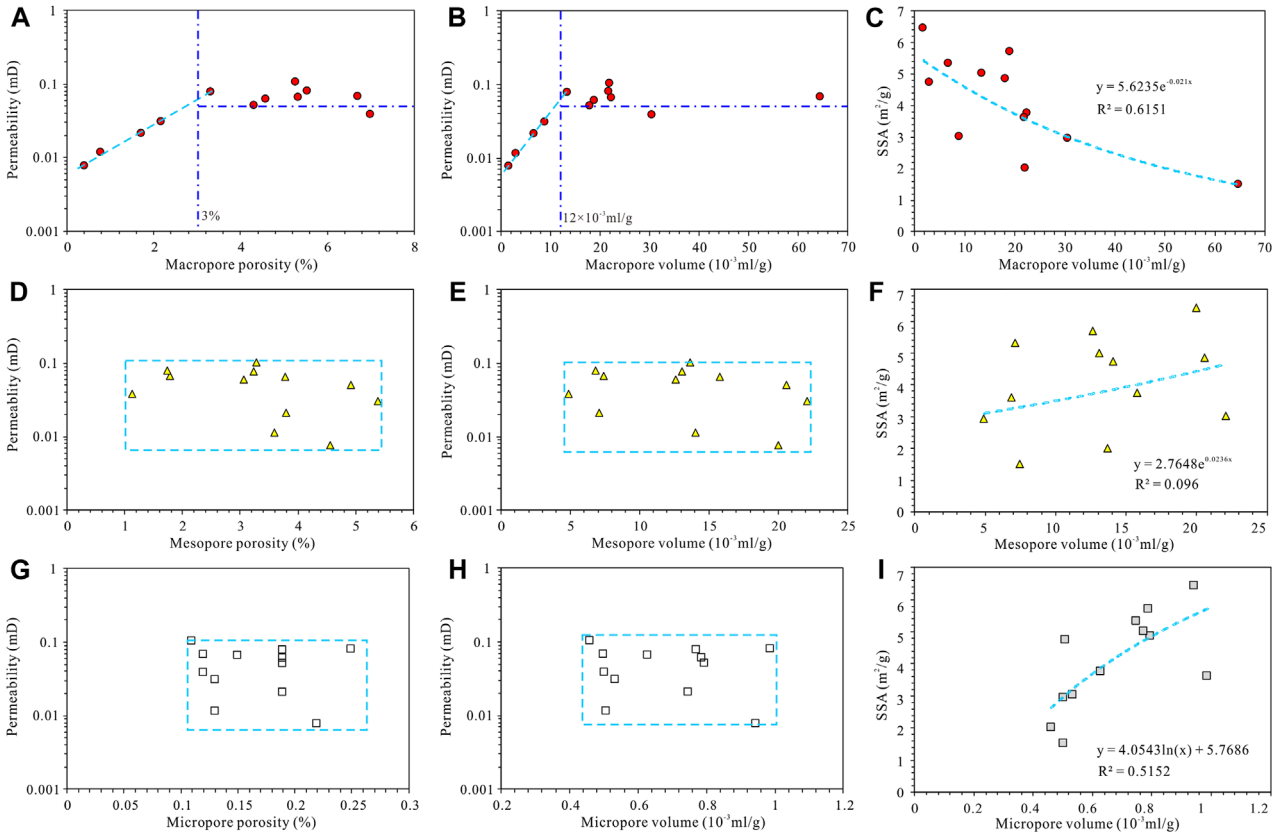

FIGURE 13
Relationships between permeability and the porosity **(A, D, G)** and volume **(B, E, H)** of macropores, mesopores and micropores and relationships between specific surface area (SSA) and the volume of macropores **(C)**, mesopores **(F)** and micropores **(I)**.

argillaceous matrix. A higher content of non-authentic clay minerals will reduce the rock's ability to resist compaction, resulting in a lower porosity. Authigenic clay exists in the form of cement that block pores and throats, resulting in a reduction in porosity and permeability.

Daigle and Johnson (2016) believed that fluid can flow through the porous media only when the continuous percolation network (CPN) reaches a certain volume. The experimental results of Li et al. (2017) showed that pores below 6~7 nm was completely blocked by water. Meanwhile, the volume and porosity of micropores have no obvious relationship with permeability (Figures 13G, H). Moreover, micropore volume and SSA exhibit an excellent positive correlation (R^2=0.5152) (Figure 13I). Thus, micropores are adsorb-fluid pores and do not contribute to the storage and percolation of oil and gas. Mesopore porosity and mesopore volume have no obvious correlation with permeability and SSA, indicating that mesopores only contribute to total porosity but not to permeability (Figures 13D–F). Thus, mesopores represent bound-fluid pores.

The permeability shows a two-stage change relationship with the increase of macropore porosity and volume: 1) when macropore porosity exceeds 3% or macropore volume exceeds 12×10^{-3} mL/g, the permeability is a stable and high value, mostly higher than 0.05 mD. According to the classification and evaluation scheme of Chang 7 reservoir established by Gao et al. (2021), samples with permeability >0.05 mD belong to high quality reservoirs; 2) When the macropore porosity is less than 3% or the macropore volume is less than 12×10^{-3} mL/g, the permeability shows an obvious upward trend (Figures 13A, B). We believe that when the macropore volume exceeds 12×10^{-3} mL/g, the CPN is completely composed of macropores. When the macropore volume is less than 12×10^{-3}mL/g, the CPN is composed of macropores and mesopores. Mesopores are mainly composed of clay IPs. The higher the proportion of mesopores in the CPN, the tortuosity of the CPN will increase, resulting in lower permeability. In addition, macropore volume and SSA exhibit an excellent negative correlation (R^2=0.6151) (Figure 13C). These results confirm that macropores represent movable-fluid pores and contribute to both porosity and permeability.

Both permeability and porosity have a significant negative correlation with D3, with R^2 of 0.5416 and 0.5715, respectively (Figures 14A, B), suggesting that the stronger the heterogeneity of macropores, the worse the quality of the sample is. This is due to the strong compaction and cementation effects that increase the heterogeneity of macropores. Permeability and porosity display almost no relationships with D2, with R^2 of only 0.1842 and 0.0899 (Figures 14C, D), showing that the strength of mesopore heterogeneity does not affect the quality of the reservoir.

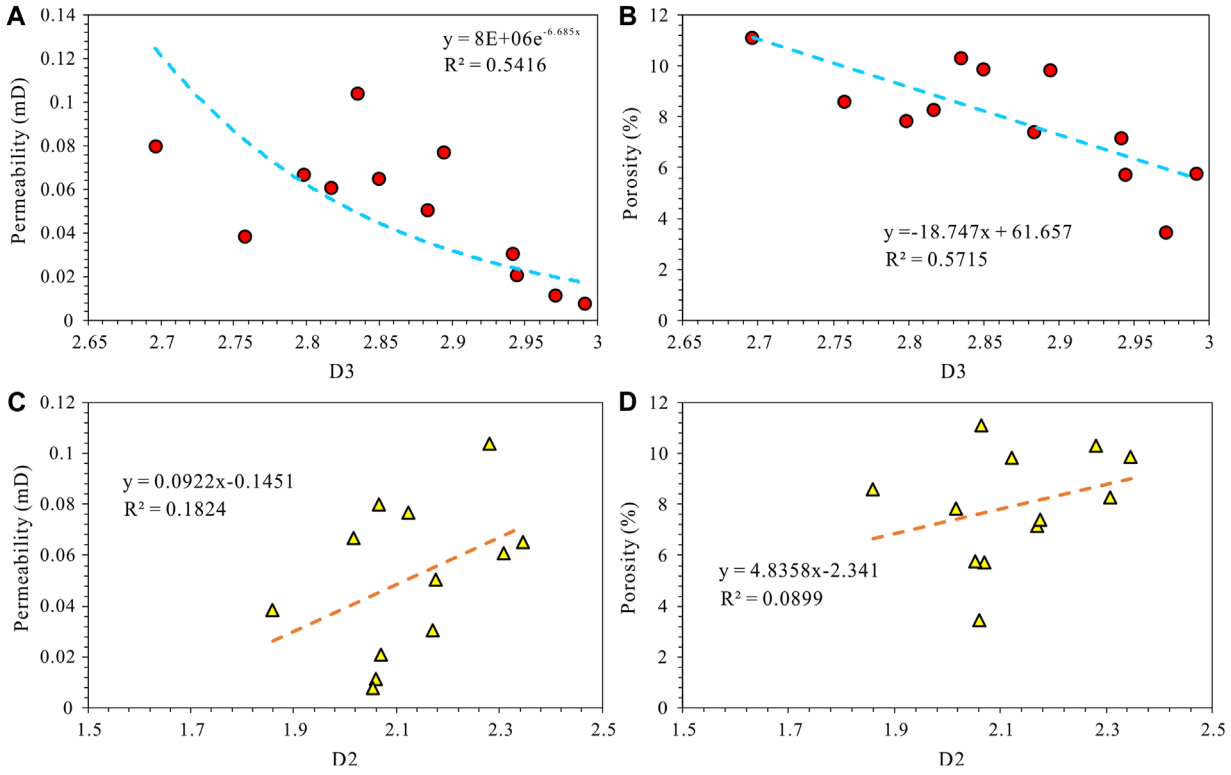

FIGURE 14
Relationship between physical properties and the fractal dimensions of macropores and mesopores. **(A)** Permeability versus D3, **(B)** porosity versus D3, **(C)** permeability versus D2, and **(D)** porosity versus D2.

5 Conclusion

The Chang 7 tight sandstones were measured by CTS, FE-SEM, 2D-MS-BSEM, NA, and NMR experiments to quantify the full-scale PSD and fractal characteristics. Furthermore, the relationship between pores of different sizes and physical properties is further discussed. The primary conclusions are as follows.

(1) NA experiments can be used to calibrate NMR T_2 spectra to obtain full-scale PSD. According to the fractal inflection point of full-scale PSD, pore system was divided into macropores, mesopores, and micropores. The critical values of mesopores and micropores are between 3.6 and 7.2 nm, while the critical values of mesopores and macropores are in the range of 29.8~344.3 nm.

(2) Micropores, mesopores and macropores have different contributions to porosity and permeability. Permeability is dominated by macropores, and porosity is contributed by both macropores and mesopores. Micropores only contributed to SSA. In addition, strong heterogeneity in large pores leads to poor reservoir quality.

(3) Macropore content and heterogeneity can be used as good indicators to judge quality of Chang 7 tight sandstone. The macropore volume of 12×10^{-3} mL/g can be used as the lower limit of high-quality reservoirs. High quartz-feldspar content and low clay mineral content are necessary conditions for the development of macropores.

Data availability statement

The original contributions presented in the study are included in the article/supplementary material, further inquiries can be directed to the corresponding author.

Author contributions

ZL: Conceptualization, Project administration, Writing–original draft. YR: Formal Analysis, Writing–original draft. RC: Investigation, Writing–original draft. YZ: Resources, Writing–original draft. XZ: Data curation, Writing–original draft. WT: Conceptualization, Funding acquisition, Methodology, Supervision, Writing–review and editing.

Funding

The author(s) declare financial support was received for the research, authorship, and/or publication of this article. This

research was financially supported by the National Natural Science Foundation of China (Grant No. 42202187 and 42272160) and key applied science and technology project of China National Petroleum Corporation "Research and testing of Continental Shale Oil Development Optimization Technology" (Grant No. 2023ZZ15YJ03).

Conflict of interest

Authors ZL, YR, RC, YZ, and XZ were employed by PetroChina Changqing Oilfield Company.

The remaining author declares that the research was conducted in the absence of any commercial or financial relationships that could be construed as a potential conflict of interest.

The authors declare that this study received funding from the key applied science and technology project of China National Petroleum Corporation. The funder had the following involvement in the study: design, collection, analysis, interpretation of data, the writing of this article or the decision to submit it for publication.

Publisher's note

All claims expressed in this article are solely those of the authors and do not necessarily represent those of their affiliated organizations, or those of the publisher, the editors and the reviewers. Any product that may be evaluated in this article, or claim that may be made by its manufacturer, is not guaranteed or endorsed by the publisher.

References

Coates, G. R., Xiao, L., and Prammer, M. G. (1999). *NMR logging: principles and applications*. Houston, TX, USA: Halliburton Energy Services.

Daigle, H., and Johnson, A. (2016). Combining mercury intrusion and nuclear magnetic resonance measurements using percolation theory. *Transp. Porous Med.* 111, 669–679. doi:10.1007/s11242-015-0619-1

Dong, H., Sun, J., Zhu, J., Lin, Z., Cui, L., Yan, W., et al. (2019). Quantitative characterization and characteristic analysis of pore structure of shale-gas reservoir in the Sichuan Basin, China. *Interpretation* 7 (4), 23–32. doi:10.1190/INT-2018-0169.1

Fu, J., Li, S., Niu, X., Deng, X., and Zhou, X. (2020). Geological characteristics and exploration practice of the self-sourced reservoir in Chang 7 member of triassic yanchang formation Ordos Basin NW China. *Petrol. explor. Dev.* 47 (5), 1–14. doi:10.11698/PED.2020.05.03

Fu, J., Liu, X., Li, S., Guo, Q., Zhou, X., and Yang, W. (2021). Discovery and resource potential of shale oil of Chang 7 member, triassic yanchang formation, Ordos Basin. *China Pet. explor.* 26, 1–11. doi:10.3969/j.issn.1672-7703.2021.05.001

Gao, H., Zhou, X., Wen, Z., Guo, W., Tian, W., Li, S., et al. (2022). Classification and evaluation of shale oil reservoirs of the Chang 71-2 Sub-Member in the Longdong area. *Energies* 15 (15), 5364. doi:10.3390/en15155364

Gao, Z., Yang, X., Hu, C., Wei, L., Jiang, Z., Yang, S., et al. (2019). Characterizing the pore structure of low permeability eocene liushagang formation reservoir rocks from beibuwan basin in northern south China sea. *Mar. Petrol. Geol.* 99, 107–121. doi:10.1016/j.marpetgeo.2018.10.005

IEA (2023). *World energy outlook 2023*. Paris, France: International Energy Agency, 130–135.

Kleinberg, R. L., and Horsfield, M. A. (1990). Transverse relaxation processes in porous sedimentary rock. *J. Magn. Reson.* 88 (1), 9–19. doi:10.1016/0022-2364(90)90104-H

Lai, J., and Wang, G. (2015). Fractal analysis of tight gas sandstones using high-pressure mercury intrusion techniques. *J. Nat. Gas. Sci. Eng.* 24, 185–196. doi:10.1016/j.jngse.2015.03.027

Lai, J., Wang, G., Ran, Y., Zhou, Z., and Cui, Y. (2016). Impact of diagenesis on the reservoir quality of tight oil sandstones: the case of Upper Triassic Yanchang Formation Chang 7 oil layers in Ordos Basin, China. *J. Pet. Sci. Eng.* 145, 54–65. doi:10.1016/j.petrol.2016.03.009

Li, J., Li, X., Wu, K., Feng, D., Zhang, T., and Zhang, Y. (2017). Thickness and stability of water film confined inside nanoslits and nanocapillaries of shale and clay. *Int. J. Coal Geol.* 179, 253–268. doi:10.1016/j.coal.2017.06.008

Morriss, C., Rossini, D., Straley, C., Tutunjian, P., and Vinegar, H. (1997). Core analysis by low-field NMR. *Log. Anal.* 38 (2), 84–93.

Rushing, J. A., Newsham, K. E., and Blasingame, T. A. (2008). "Rock typing—keys to understanding productivity in tight gas sands," in SPE Unconventional Resources Conference/Gas Technology Symposium, Keystone, Colorado, USA, February, 2008.

Saidian, M., and Prasad, M. (2015). Effect of mineralogy on nuclear magnetic resonance surface relaxivity: a case study of Middle Bakken and Three Forks formations. *Fuel* 161, 197–206. doi:10.1016/j.fuel.2015.08.014

Sakhaee-Pour, A., and Bryant, S. L. (2014). Effect of pore structure on the producibility of tight-gas sandstones. *Am. Assoc. Petrol. Geol. Bull.* 98 (4), 663–694. doi:10.1306/08011312078

Shao, X., Pang, X., Li, H., and Zhang, X. (2017). Fractal analysis of pore network in tight gas sandstones using NMR method: a case study from the Ordos Basin, China. *Energy fuels.*, 31 (10), 10358–10368. doi:10.1021/acs.energyfuels.7b01007

Tian, W., Lu, S., Huang, W., Wang, S., Gao, Y., Wang, W., et al. (2019). Study on the full-range pore size distribution and the movable oil distribution in glutenite. *Energy fuels.*, 33 (8), 7028–7042. doi:10.1021/acs.energyfuels.9b00999

Tian, W., Lu, S., Huang, W., Wang, W., Li, J., Gao, Y., et al. (2020). Quantifying the control of pore types on fluid mobility in low-permeability conglomerates by integrating various experiments. *Fuel* 275, 117835. doi:10.1016/j.fuel.2020.117835

Tian, W., Lu, S., Li, J., Wang, W., Li, J., and Wen, Z. (2022). Insights into the pore structure and pore development pattern of subaqueous volcanic rocks in the Santanghu Basin, western China. *Mar. Petrol. Geol.* 135, 105387. doi:10.1016/j.marpetgeo.2021.105387

Wang, X., Hou, J., Li, S., Dou, L., Song, S., Kang, Q., et al. (2020). Insight into the nanoscale pore structure of organic-rich shales in the Bakken Formation, USA. *J. Pet. Sci. Eng.* 191, 107182. doi:10.1016/j.petrol.2020.107182

Wen, Z., Luo, Y., Liu, J., Zhao, C., Li, S., Tian, W., et al. (2022). Pore structure characteristics and genetic mechanism of Triassic Chang 7 shale oil reservoir in Longdong area. *Lithol. Reserv.* 34 (6), 47–59. doi:10.12108/yxyqc.20220604

Wu, Y., Tahmasebi, P., Lin, C., Zahid, M. A., Dong, C., Golab, A. N., et al. (2019). A comprehensive study on geometric, topological and fractal characterizations of pore systems in low-permeability reservoirs based on SEM, MICP, NMR, and X-ray CT experiments. *Mar. Petrol. Geol.* 103, 12–28. doi:10.1016/j.marpetgeo.2019.02.003

Xi, K., Cao, Y., Haile, B. G., Zhu, R., Jahren, J., Bjørlykke, K., et al. (2016). How does the pore-throat size control the reservoir quality and oiliness of tight sandstones? The case of the Lower Cretaceous Quantou Formation in the southern Songliao Basin, China. *Mar. Pet. Geol.* 76, 1–15. doi:10.1016/j.marpetgeo.2016.05.001

Xiao, D., Jiang, S., Thul, D., Huang, W., Lu, Z., and Lu, S. (2017a). Combining rate-controlled porosimetry and NMR to probe full-range pore throat structures and their evolution features in tight sands: a case study in the Songliao Basin, China. *Mar. Petrol. Geol.* 83, 111–123. doi:10.1016/j.marpetgeo.2017.03.003

Xiao, D., Jiang, S., Thul, D., Lu, S., Zhang, L., and Li, B. (2018). Impacts of clay on pore structure, storage and percolation of tight sand-stones from the Songliao Basin, China: implications for genetic classification of tight sandstone reservoirs. *Fuel* 211, 390–404. doi:10.1016/j.fuel.2017.09.084

Xiao, D., Lu, S., Yang, J., Zhang, L., and Li, B. (2017b). Classifying multiscale pores and investigating their relationship with porosity and permeability in tight sandstone gas reservoirs. *Energy fuels.*, 31 (9), 9188–9200. doi:10.1021/acs.energyfuels.7b01487

Xu, Q., Ma, Y., Liu, B., Song, X., Li, L., Xu, J., et al. (2018). Fractal characteristics of lacustrine tight carbonate na-noscale reservoirs. *Energy fuels.*, 32 (1), 107–118. doi:10.1021/acs.energyfuels.7b02625

Zhang, J., Li, X., Xie, Z., Li, J., Zhang, X., Sun, K., et al. (2018). Characterization of microscopic pore types and structures in ma-rine shale: examples from the upper permian dalong formation, northern sichuan basin, south China. *J. Nat. Gas. Sci. Eng.* 59, 326–342. doi:10.1016/j.jngse.2018.09.012

Zhang, J., Tang, Y., He, D., Sun, P., and Zou, X. (2020). Full-scale nanopore system and fractal characteristics of clay-rich lacustrine shale combining FE-SEM, nano-CT, gas adsorption and mercury intrusion porosimetry. *Appl. Clay Sci.* 196, 105758. doi:10.1016/j.clay.2020.105758

Zhang, L., Lu, S., Xiao, D., and Gu, M. (2017a). Characterization of full pore size distribution and its significance to macroscopic phys-ical parameters in tight glutenites. *J. Nat. Gas. Sci. Eng.* 38, 434–449. doi:10.1016/j.jngse.2016.12.026

Zhang, P., Lu, S., Li, J., Xue, H., Li, W., and Zhang, P. (2017b). Characterization of shale pore system: a case study of Paleogene Xin'gouzui Formation in the Jianghan basin, China. *Mar. Petrol. Geol.* 79, 321–334. doi:10.1016/j.marpetgeo.2016.10.014

Zhang, P., Lu, S., Li, J., Zhang, J., Xue, H., and Chen, C. (2017c). Comparisons of SEM, low-field NMR, and mercury intrusion capillary pressure in characterization of the pore size distribution of lacustrine shale: a case study on the Dongying Depression, Bo-hai Bay Basin, China. *Energy fuels.*, 31 (9), 9232–9239. doi:10.1021/acs.energyfuels.7b01625

Zheng, J., Tian, W., Gao, Y., Wen, Z., Fan, Y., Gao, H., et al. (2023). Multi-scale fractal characteristics of the pore system in low-permeability conglomerates from the junggar basin. *Processes* 11 (9), 2667. doi:10.3390/pr11092667

Zou, C., Zhu, R., Wu, S., Yang, Z., Tao, S., Yuan, X., et al. (2012). Types, characteristics, genesis and prospects of conventional and unconventional hydrocarbon accumulations: taking tight oil and tight gas in China as an instance. *Acta Pet. Sin.* 33 (2), 173–187. doi:10.7623/syxb20120200

frontiers | Frontiers in Earth Science

TYPE Original Research
PUBLISHED 23 February 2024
DOI 10.3389/feart.2024.1371219

Check for updates

OPEN ACCESS

EDITED BY
Xixin Wang,
Yangtze University, China

REVIEWED BY
Yadong Chen,
Southwest Petroleum University, China
Yunfeng Xu,
Yangtze University, China

*CORRESPONDENCE
Feng He,
1264485659@qq.com

RECEIVED 16 January 2024
ACCEPTED 06 February 2024
PUBLISHED 23 February 2024

CITATION
He F, Yue M, Zhou Y, He H, Jiang W, Liu L, Qian C and Shu P (2024), Research on the data-driven inter-well fracture channeling identification method for shale gas reservoirs. *Front. Earth Sci.* 12:1371219.
doi: 10.3389/feart.2024.1371219

COPYRIGHT
© 2024 He, Yue, Zhou, He, Jiang, Liu, Qian and Shu. This is an open-access article distributed under the terms of the Creative Commons Attribution License (CC BY). The use, distribution or reproduction in other forums is permitted, provided the original author(s) and the copyright owner(s) are credited and that the original publication in this journal is cited, in accordance with accepted academic practice. No use, distribution or reproduction is permitted which does not comply with these terms.

Research on the data-driven inter-well fracture channeling identification method for shale gas reservoirs

Feng He*, Ming Yue, Yibo Zhou, Huaiying He, Wei Jiang, Long Liu, Chao Qian and Pinghua Shu

Shale Gas Exploration and Development Department, CNPC Chuanqing Drilling Engineering Co., Ltd., Chengdu, China

The issue of inter-well fracture channeling in shale reservoirs is becoming increasingly prominent, significantly impacting the production of nearby wells. Therefore, it is crucial to accurately determine the location of fracture channeling in order to effectively design anti-channeling measures and optimize reservoir fracturing. In this paper, a data-driven fracture propagation model and fracture channeling identification method are established. In the model, the fracture morphology is fitted by the bottom-hole flowing pressure constraint. The bottom-hole flowing pressure (p_{wp}) calculated by the construction pump pressure and the fluid wellbore flow is mainly considered as the real solution. The bottom-hole flowing pressure (p_{wf}) calculated by the construction displacement and the fracture morphology is used as the constraint variable, and the fracture parameters are changed using the SPSA optimization algorithm to realize the dynamic fitting of the fracture morphology. In order to accurately describe the position of fracture channeling, the seepage radius of the fracture boundary is introduced to calculate the volume of fracture reconstruction. The volume coefficient of repeated reconstruction is used as the quantitative evaluation index of fracture channeling. This approach enables an accurate depiction of the position of fracture channeling. Finally, the model method is applied to the actual fracture channeling well. The study shows that the fracture length of the well inversion is greater than the well spacing, and there is a possibility of inter-well fracture channeling. The volume coefficient of repeated reconstruction is 8%, similar to the critical fracture channeling index. There are nine fracturing sections with fracture channeling, and the maximum fracture channeling coefficient is 14.2%. This paper successfully explains the reason for cross-well fracture channeling, and its conclusion aligns with the actual monitoring results. The proposed method in this paper effectively identifies the location of fracture channeling and offers guidance for optimizing channeling prevention in subsequent designs.

KEYWORDS

shale reservoir, fracture propagation, data-driven, dynamic fitting, fracture channeling identification, numerical simulation

1 Introduction

Fracturing is a crucial technology for the commercial development of shale reservoirs (Wang et al., 2012; Du et al., 2014; Huang et al., 2022). However, the fracturing of infill wells in the later stage can often result in fracture communication between new and old wells, leading to fracture channeling. This communication issue significantly impacts the production of parent or adjacent wells, causing substantial economic losses (He et al., 2020). Hence, there is an urgent need to implement new technologies that enable the quantitative identification of reservoir inter-well fracture channeling.

The current methods for identifying fracture channeling can be categorized into three types: microseismic monitoring technology, tracer monitoring technology, and the dynamic analysis method (Zhang et al., 2019; Zhao B. et al., 2020; Fu and Dehghanpour, 2020; Escobar et al., 2021). Microseismic monitoring technology is a crucial tool used in oilfield exploration and development processes. It involves locating fractures by detecting induced microseismic events that occur during fracturing. This method is primarily used for dynamically imaging fracturing fractures in low-permeability reservoirs, enabling the tracking of the fracturing range and providing an objective evaluation of the location of fracture channeling (Zhang et al., 2019). Aleksandrov et al. (2018) and Wu et al. (2017) used this method for fracture analysis. However, with the advancement of technology, it has been found that the error of microseismic monitoring technology is large, and the actual fractures are only between 30% and 70% of the monitoring results (Huang et al., 2021a). The credibility of evaluating fracture channeling using microseismic monitoring can be greatly reduced. Tracer monitoring technology is a direct method for determining reservoir communication (Meng et al., 2022). This method reflects the flow of reservoir fluid and inter-well communication information through the breakthrough curve of tracer concentration monitored in the production well. Brigham and Smith (1965) were the first to apply chemical tracers to the evaluation of reservoir fracturing and achieved positive results. Over time, the types of tracers have become more diverse, allowing for the evaluation of various pieces of information, such as fracture type, reservoir seepage capacity, and fracture channeling (Geng et al., 2017). However, tracer monitoring technology is time-consuming and requires a long cycle to draw the tracer concentration curve. Additionally, the economic cost of using tracers is high. As a result, this method is less commonly used in the evaluation of inter-well fracture channeling. Instead, the dynamic analysis method relies on the dynamic data of production wells or fracturing wells to analyze the degree of fracture channeling. This includes examining the changes in parent-well productivity and child-well construction pressure (Puneet et al., 2021). Ajani and Kelkar (2012) used the productivity change of the parent well to evaluate the influence of the well spacing and the production time of the parent well on fracture channeling and provided a reference for the well location deployment. King et al. (2017) analyzed the influence of fracturing parameters on fracture channeling according to the change in child-well construction pressure. With the advantages of low cost and simple operation, the dynamic analysis method is widely used in the analysis of inter-well fracture channeling. However, this method also has the disadvantage of being time-consuming and being affected by multi-well interference and external factors, resulting in a large analysis error. Furthermore, all three methods mentioned above are qualitative evaluations of fracture channeling, which cannot accurately determine the location of fracture channeling or propose specific solutions to address this phenomenon. The main cause of inter-well fracture channeling is the dominant fracture channel formed by child-well fracturing to connect with the fractures of the parent well. Therefore, the most effective approach to determine the position of pressure channeling is to accurately describe the fracture morphology and quantitatively identify the fracture communication position.

The simulation methods of fracture propagation are mainly divided into the finite element method (FEM), extended finite element method (XFEM), boundary element method (BEM), and unconventional fracture propagation model (UFM) (Li and Wang, 2005; Olson, 2008; Zhou et al., 2020; Huang et al., 2021b). Dali Taleghani (2010) used the XFEM to simulate the fracture propagation of hydraulic fracturing vertical wells in shale reservoirs. The BEM can transform the problem into a boundary integral equation, and the approximate solution can be found discretely on the boundary. The BEM is more suitable for cases with a complex fracture network, but its applicability in simulating fluid–solid coupling problems is poor (Olson, 2008). The UFM adopts the 2D displacement discontinuity method to solve the interaction between reservoir stress field and fractures. Meanwhile, the fracture width and proppant concentration can be calculated using a 3D fracture height equation and proppant sedimentation equation (Weng et al., 2011; Kresse and Weng, 2018). However, these types of fracture propagation simulation methods have their own advantages in solving the calculation of fracture parameters and reservoir stress parameters, but the fracture morphology described is mostly a single fracture. The fractures in the reservoir are mostly staggered branch fractures, and fracture channeling is also formed by the intersection of fracture branches. Therefore, a single fracture cannot effectively describe the channeling fracture. Zhao et al. (2021), Zhao H. et al. (2020), and Sheng et al. (2023) proposed a reservoir fracturing model based on lightning simulation, which can simulate the fracture morphology of complex induced fractures. In this paper, the method proposed by Zhao H. et al. (2020) is used to establish a fracture channeling identification model based on the connection element method. In the method, the fluid flow in the wellbore and fracture is considered, and the fracture boundary seepage radius is introduced to calculate the fracture reconstruction volume. Taking the volume coefficient of repeated stimulation as the quantitative evaluation index of fracture channeling, the accurate description of the location of fracture channeling is realized, and it is analyzed and applied in the actual fracture channeling wells.

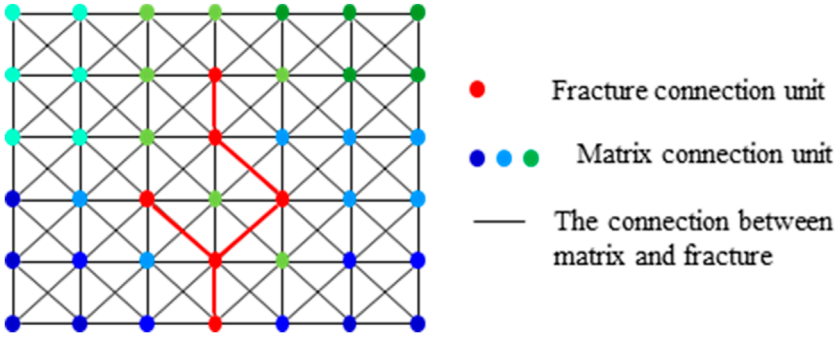

FIGURE 1
Reservoir and fracture node division of the connection element method.

2 Mathematical model of shale reservoir channeling identification based on the connection element method

2.1 Fracture propagation model based on the connection element method

In order to simulate accurately and quickly, we simplify the reservoir and use the connection element method to characterize the reservoir model. In the model, the reservoir and rock are discretized into continuous connection nodes, and the communication relationship between the nodes and the adjacent nodes is established by a connection, as shown in Figure 1. In the acquisition of connection unit data, the reservoir is first divided into unevenly distributed grids according to the geological model, and the center of each grid is considered the initial node. The initial node parameters are obtained from the actual geological model obtained using the interpolation algorithm. In the simulation process, the nodes can be increased or decreased. Second, when the special medium (such as natural fractures) is distributed into the reservoir, a new node is added to describe the special lithology medium. On the basis of the node connection system, flexible meshless nodes can be used to replace the traditional mesh topology. Figure 1 shows that the blue to green nodes represent reservoir nodes of different parameters, and the red nodes represent fracture nodes.

2.1.1 Mechanical model of fractures

In the model, considering that the rock is a porous elastic medium, the principal stress parameters of the rock can be obtained by combining the logging data, which are expressed as

$$\begin{cases} \sigma_h = \dfrac{v}{1-v}\sigma_v - \dfrac{v}{1-v}\alpha_{vert}P_p + \alpha_{hor}P_p + \dfrac{E}{1-(v)^2}\xi_h + \dfrac{vE}{1-(v)^2}\xi_H \\ \sigma_H = \dfrac{v}{1-v}\sigma_v - \dfrac{v}{1-v}\alpha_{vert}P_p + \alpha_{hor}P_p + \dfrac{E}{1-(v)^2}\xi_H + \dfrac{vE}{1-(v)^2}\xi_h \end{cases}, \tag{1}$$

where σ_h represents the minimum horizontal principal stress, MPa; σ_H represents the maximum horizontal principal stress, MPa; α_{vert} and α_{hor} represent the vertical and horizontal Biot coefficient; ξ_H and ξ_h represent the strain coefficient of the maximum principal stress and the minimum principal stress, respectively; v represents Poisson's ratio; E represents the elastic modulus, GPa; and P_p represents the pore pressure, MPa. In this paper, it is considered that rock fracturing is affected by opening and shearing, which is I–II composite fractures (Feng and Kang, 2013). Rock failure is affected by the combined action of horizontal principal stress σ_h, σ_H, and fluid pressure in the fracture, as shown in Figure 2A. According to the superposition principle, the composite model can be decomposed into two independent models. Figure 2B shows that the fracture is subjected to far-field stress; Figure 2C shows that the fracture is affected by the fluid pressure in the fracture.

For model (b), the stress intensity factor at the crack tip is expressed as

$$\begin{cases} K_{Ib} = \sigma_y\sqrt{\pi a} = \sqrt{\pi a}\cdot\left(\sigma_H \sin^2\beta + \sigma_h \cos^2\beta\right) \\ K_{\Pi b} = \tau_{xy}\sqrt{\pi a} = \sqrt{\pi a}\cdot\left(\sigma_H - \sigma_h\right)\sin\beta\cos\beta \end{cases}. \tag{2}$$

For model (c), the stress intensity factor at the fracture tip is expressed as

$$\begin{cases} K_{Ic} = p\sqrt{\pi a} \\ K_{\Pi c} = 0 \end{cases}. \tag{3}$$

After superposition, the final stress intensity factor at the fracture tip can be obtained. Since the pressure in the fracture and the far-field stress have opposite effects on the fracture, it is necessary to pay attention to the direction of the force, which is finally expressed as

$$\begin{cases} K_{\mathrm{I}} = \sqrt{\pi a}\cdot\left(p - \sigma_H \sin^2\beta - \sigma_h \cos^2\beta\right) \\ K_{\Pi} = \tau_{xy}\sqrt{\pi a} = -\sqrt{\pi a}\cdot\left(\sigma_H - \sigma_h\right)\sin\beta\cos\beta \end{cases}, \tag{4}$$

where K_{Ib} represents the type I stress intensity factor of the b model, MPa $m^{0.5}$; K_{Ib} represents the type II stress intensity factor of the b model, MPa $m^{0.5}$; σ_y represents the y-axis principal stress, MPa; τ_{xy} represents the shear stress, MPa; a represents the half length of the fracture, m; β represents the angle between the fracture and x-axis; and p represents the net fracture pressure, MPa.

The critical initiation stress of fracture is related to the fracture toughness of rock. Combined with Eq. 1–Eq. 4, the fracture propagation conditions are expressed as (Weng et al., 2011)

$$\sigma_{fr} = \frac{1}{\sqrt{2\pi r}}\cos\frac{\theta}{2}\left(K_1\cos^2\frac{\theta}{2} - \frac{3}{2}K_2\sin\theta\right) - \sigma_{cr} \geq 0, \tag{5}$$

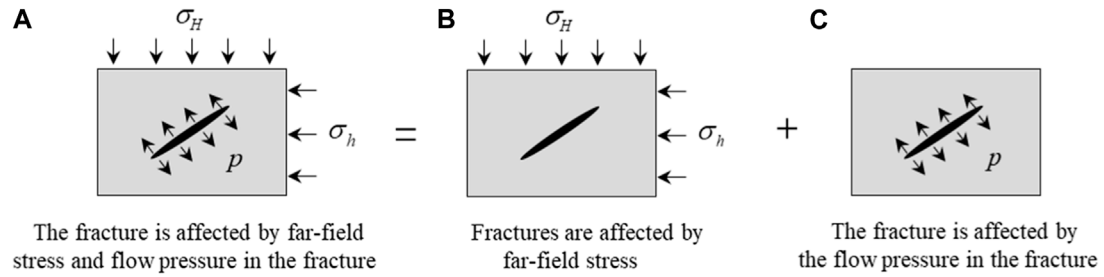

FIGURE 2
Fracture stress decomposition.

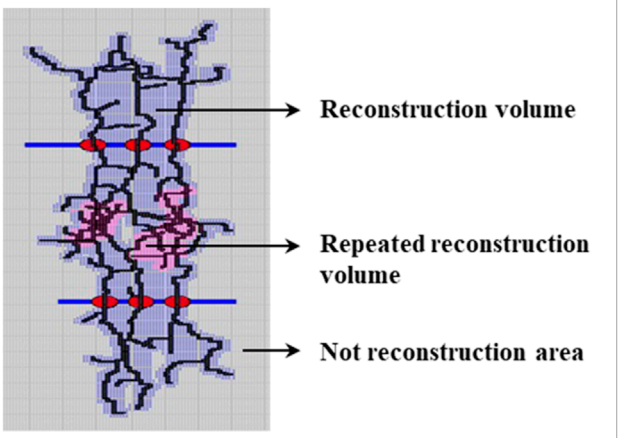

FIGURE 3
Fracture repeated reconstruction area.

where σ_{fr} represents the residual initiation stress, MPa; σ_{cr} represents the critical initiation stress, MPa.

2.1.2 Data-driven fitting calculation of fluid parameters in fractures

The purpose of this section is to calculate the appropriate fracture morphology according to the determined construction displacement data at a certain time step and to calculate the flow pressure in the fracture, so as to fit the actual construction pump pressure. The model mainly includes two operation processes. The positive calculation process considers the actual construction pressure, fracturing fluid viscosity, and related friction factors to calculate the bottom-hole flow pressure. The reverse calculation process is the fitting stage. Considering the fracture morphology, construction displacement, fracturing fluid filtration, and friction effect, the bottom-hole flow pressure is fitted by an iterative calculation of the fracture control range.

(a) Bottom-hole flow pressure calculation based on pump pressure

According to the principle of force balance, when the pump pressure is known, combined with the net liquid column pressure and tubing friction, the bottom-hole flow pressure can be obtained, which is expressed as

$$p_{wp} = p_s + p_H - p_{pf}, \tag{6}$$

where p_{wp} represents the bottom-hole flow pressure calculated based on pump pressure, MPa; p_s represents the pump pressure of fracturing construction, MPa; p_H represents the net liquid column pressure, MPa; and p_{pf} represents the tubing friction, MPa.

The pump pressure in Eq. 6 is the actual construction data, which can be obtained directly. Assuming that the wellbore is fully filled with fluid, the net liquid column pressure is calculated according to the fluid density and wellbore depth. The friction in the tubing is calculated according to the empirical formula and is expressed as

$$p_{pf} = \frac{5.1 \times 10^{-6} l_p v^2 f \rho_1}{d}, \tag{7}$$

where l_p represents the length of the fracturing string, m; v represents the flow velocity of the fracturing fluid in the tubing, m/s; ρ_1 represents the density of the fracturing fluid, kg/m^3; d represents the inner diameter of the fracturing string, m; and f represents the dimensionless friction coefficient.

(b) Bottom-hole flowing pressure calculation based on displacement

The reverse calculation of bottom-hole flowing pressure from the fracture structure is expressed as

$$p_{wf} = p_f + p_c + p_{ff}, \tag{8}$$

where p_{wf} represents the bottom-hole flowing pressure calculated based on the displacement, MPa; p_f represents the net pressure of the fracture, MPa; p_c represents the closure pressure of rock, MPa, which can be measured by a compressibility experiment; and p_{ff} represents the friction generated by the fluid in the rock, MPa.

Using the construction displacement data in the actual fracturing construction process and then according to the fracture morphology under time t, the fluid pressure in the fracture can be calculated. Taking into account the fluid loss on the rock, the actual flow rate of the fluid injected into the fracture is expressed as

$$q(t) = Q - 2\left(\frac{C}{\sqrt{t_{frac}}}\right) HL(t - t^*), \tag{9}$$

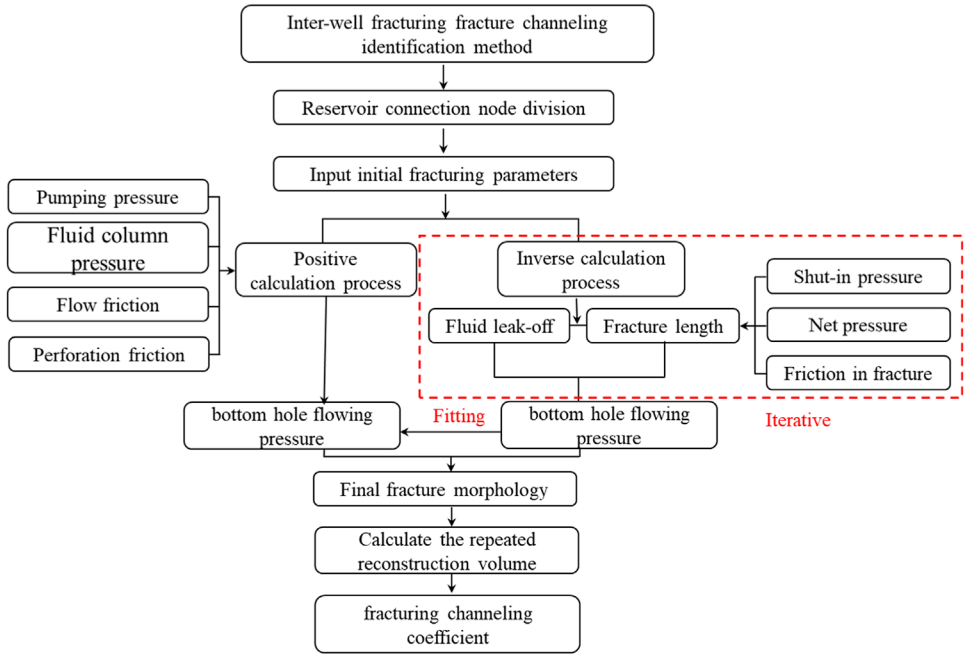

FIGURE 4
Inter-well fracture channeling identification calculation process.

where $q(t)$ represents the injection flow rate of the fracturing fluid under reduced conditions, m^3/min; Q represents the injection flow of the fracturing fluid under actual conditions, m^3/min; C represents the filter loss coefficient, m/$min^{0.5}$; t represents the current time, min; t^* represents the time under the previous time step, min; H represents the height of the fracture, m; and $L(t-t^*)$ represents the total length of fractures generated at the current time step, m.

According to the reduced flow q at the current time step, the fracture pressure of the fracture is calculated and expressed as

$$\begin{cases} p_f(t) = \alpha^{\frac{1}{2n+2}} \left(\frac{\pi}{2}\right)^{\frac{2n+1}{2n+2}} \left[KE^{2n+1} \frac{q^n(t)}{H^n L^{2n}(t)} \right]^{\frac{1}{2n+2}} \\ \alpha = 2\left[\frac{2(2n+1)}{n}\right]^n \end{cases}, \quad (10)$$

where p_f represents the fracture pressure of the fracture at time t, MPa; K represents the consistency coefficient, MPa/min; n represents the rheological index; and E represents Young's modulus, MPa.

Taking into account the flow friction generated by the fluid contacting the fracture surface in the fracture and assuming that the fluid friction in the fracture does not change with the fracture position, the friction p_{ff} is expressed as

$$\begin{cases} p_{ff}(t) = aL(t^*) + bL(t-t^*) \\ L_f(t) = L(t^*) + L(t-t^*) \end{cases}, \quad (11)$$

where $p_{ff}(t)$ represents the flow resistance at time t, MPa; a and b represent the friction coefficients in different states, MPa, respectively; and $L_f(t)$ represents the total length of the fracture, m.

TABLE 1 Basic parameters of the model.

Parameter/unit	Value	Parameter/unit	Value
Maximum principal stress/MPa	67	Injection value/m^3·min^{-1}	12
Minimum principal stress/MPa	50.6	Maximum pump pressure/MPa	70
Formation pressure/MPa	32–42	Rock density/g/cm^3	2.3
Young's modulus/GPa	42.7	Porosity/%	5.3
Poisson's ratio	0.2	Permeability/nD	15–28

2.2 Inter-well fracture channeling identification method

2.2.1 Methodology

The inter-well fracture channeling is related to the fracture distribution and the seepage intersection area between the fractures. Therefore, based on the fracture distribution pattern between wells obtained by fracture propagation simulation, the irregular fracture reconstruction volume is calculated. Considering the intersection between the fractures of the child and parent wells, the repeated reconstruction volume coefficient is used to evaluate the degree of fracture channeling, and the identification method of fracture channeling in shale gas reservoirs is formed, as shown in Figure 3.

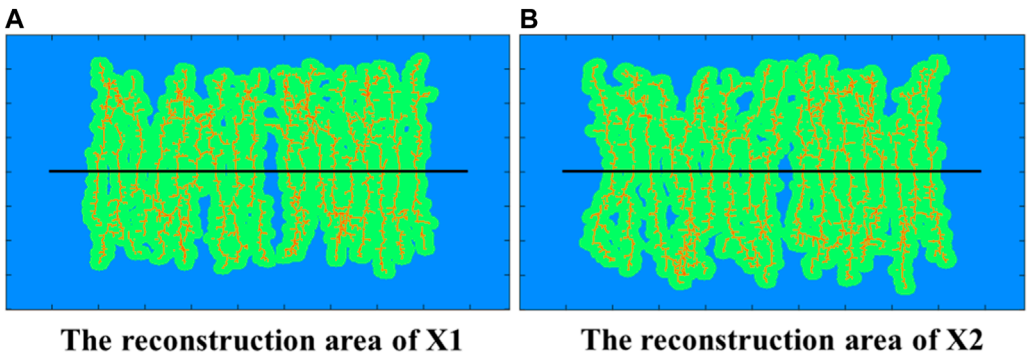

FIGURE 5
Fracture morphology and reconstruction area.

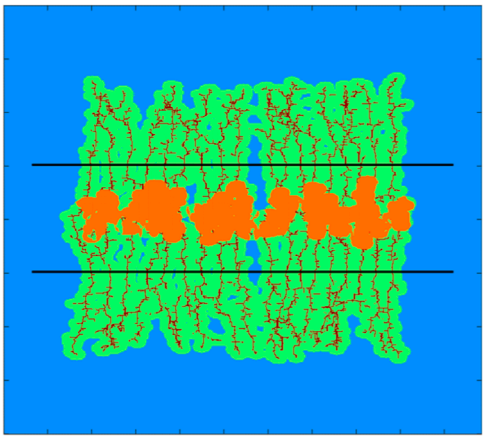

FIGURE 6
Fracturing channeling area between two wells.

In the case of known fracture morphology and fracture permeability, the seepage radius of the fracture facing the reservoir can be obtained, which is expressed as

$$r = \sqrt{\frac{kt}{\pi\mu}}, \tag{12}$$

where r represents the flow radius, m; k represents the permeability of the fracture, mD; t represents time, s; and μ represents the viscosity of the fluid, MPa.

Through the seepage radius of the fracture, the volume of the fracture can be calculated, and the volume coefficient of the repeated reconstruction between the fractures is expressed as

$$R = \frac{V_c}{\sum_{i=1}^{N} V_i}, \tag{13}$$

where R represents the volume coefficient of repeated reconstruction; N represents the number of fracture sections; V_c represents the repeated reconstruction volume, m^3; and V_i represents the reconstruction volume of the fracture section, m^3.

2.2.2 Fracture channeling identification simulation process

The calculation process of the identification method of fracture channeling is shown in Figure 4. The specific calculation steps are as follows: a) According to the actual reservoir size, the connection nodes are divided, and the connection nodes are used for subsequent calculation. b) Combined with geological data, the value of the connection node can be obtained by the interpolation of the existing geological model, including physical parameters and mechanical parameters. c) According to the actual fracturing scale, the perforation data and initial fracture parameters are set. d) The bottom-hole flow pressure at the next time step is calculated according to the construction pump pressure parameters (Eq. 6 and Eq. 7). e) Comparing the bottom-hole flow pressure values of forward calculation and reverse calculation, if not equal, new fracture connection nodes are added (Eq. 8–Eq. 11). f) Steps d ~ e are repeated until the fitting error is less than the specified error value, and the fracture morphology is output. g) The fracture seepage radius is calculated. h) The repeated reconstruction volume of the parent well is calculated. i) The volume coefficient of repeated reconstruction (fracture channeling coefficient) is calculated, and the quantitative identification of inter-well fracture channeling position is finally realized.

3 Identification and application of fracture channeling in shale reservoirs

3.1 Conceptual model of fracture channeling identification

Based on the identification method of inter-well fracture channeling, a two-well opposite staggered perforation fracturing model is established to quantitatively analyze the location of fracture channeling. The model sets the distance between two wells to be 200 m, and nine clusters of perforations are performed. The cluster spacing is 10 m. The relevant calculated parameters are shown in Table 1.

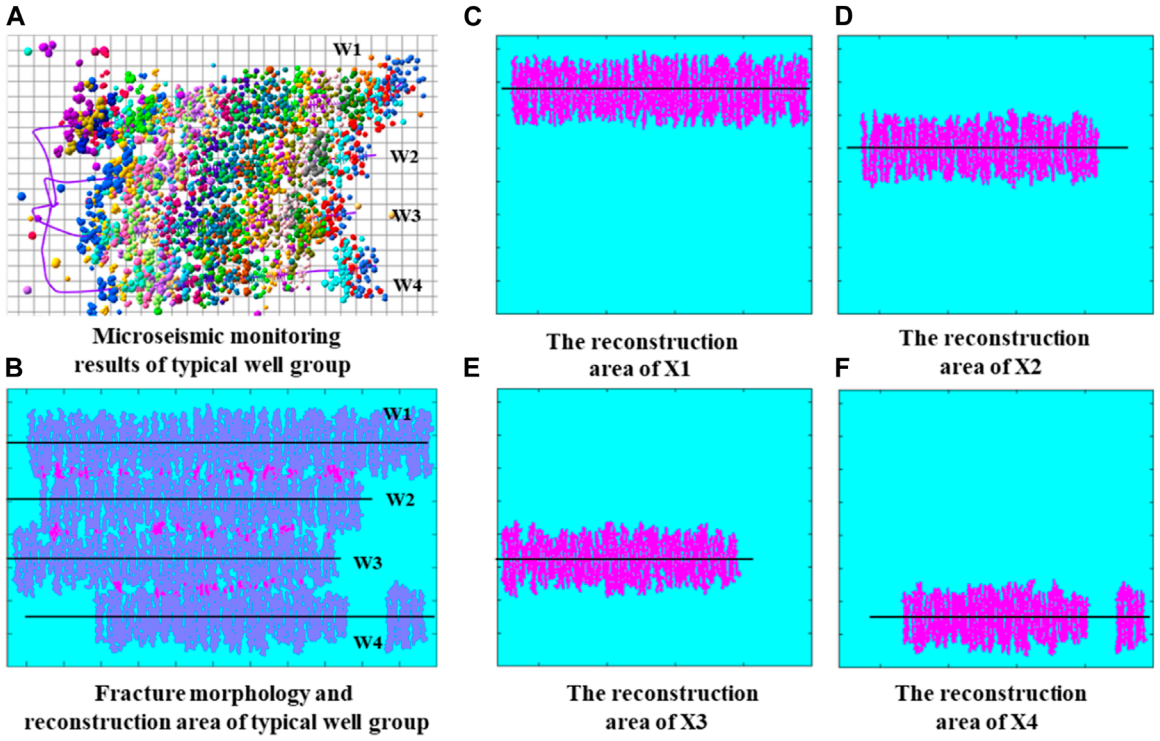

FIGURE 7
Fracture morphology and channeling identification of typical well groups.

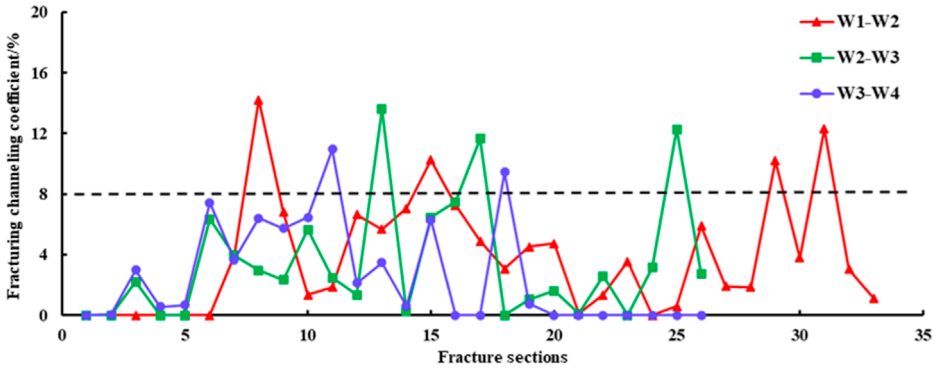

FIGURE 8
Distribution of fracture channeling coefficient in each well section.

Figure 5 shows the fracture morphology of the two wells after fracturing. The simulation results show that the fracture length of the X1 well is approximately 290 m, and the reconstruction area is 47962 m^2. The fracture length of the X2 well is approximately 300 m, and the reconstruction area is 52686 m^2. The repeated reconstruction area of the two wells is 8469 m^2, and the fracture channeling coefficient of the child well is 16.1%. Figure 6 shows that the fracture channeling area of the two wells occupies nearly half of the seepage intersection area between the two wells, and there is a great risk of fracture channeling.

3.2 Fracture morphology simulation and channeling analysis in actual blocks

The fractured channeling well in the Weiyuan area is selected as the research object. The reservoir porosity, permeability, and formation pressure coefficient of this well group are low, and the energy supply is insufficient. After fracturing, the reservoir's physical properties have been improved, but the inter-well fracture channeling is more serious, resulting in great economic losses. According to the existing production dynamic data, the source of fracture channeling in this typical well group has been qualitatively

analyzed. At present, it is preliminarily determined that W1, W2, and W3 wells are affected by W4 well fracture channeling, and the specific location is not clear.

According to the method in this paper, the fracturing model of the typical well group is constructed. The actual geological model parameters are the same as those in Table 1, and the simulated fracture morphology is shown in Figures 7B–F.

The fracture morphology of W1 ~ W4 wells is shown in Figures 7C–F; Figure 7B shows the reconstruction area after fracturing of the whole well group. A total of 108 sections and 347 clusters of fractures are inverted in the model. The fracture length is between 353 m and 380 m, and the average fracture length exceeds the well spacing (360 m). The simulated fracture length is 87% of the fracture length interpreted by microseismic monitoring. The simulation results are in good agreement with the microseismic monitoring results (Figure 7A).

From the simulation results shown in Figure 7B, there is a certain fracture channeling between wells. In order to further quantify the fracture channeling position, Figure 8 shows the channeling coefficient between each well section. When the channeling coefficient is 8%, it is used as the critical fracturing channeling index, which can be given according to the actual situation. The location of fracture channeling between W1 and W2 wells is mainly distributed in the 8–9, 15, and 29–31 sections. The fracture channeling positions between W2 and W3 wells are mainly distributed in 13, 17, and 25 sections. The location of fracture channeling between wells W3 and W4 is mainly distributed in 11 and 18 sections. It can be analyzed that the W4 well is channeled to the W3 well through 11 and 18 sections and the W3 well is channeled to W2 through 13 and 17 sections and then channeled to W1 through 8 and 15 sections of W2, thus affecting the whole well group, which is consistent with the actual results.

It is worth noting that in this paper, the actual fracturing data fitting method is used to constrain the fracture morphology, which depends on the accuracy of the pressure calculation in the fracture. However, the calculation of fracture pressure and fracture filtration used in this paper does not take into account the fluid–solid coupling effect of the reservoir. Therefore, in the follow-up study, the influence of fluid–solid coupling on fracture morphology needs to be further considered.

4 Conclusion

In this paper, a fracture inversion model based on the connection element method is established, which takes into account the fitting of actual fracturing parameters and fracture parameters. In addition, the pressure channeling index is established to quantitatively describe the location of fracture channeling. At the same time, conceptual cases and actual cases are established to verify the accuracy of the model. The main conclusions are as follows:

(1) In the model, the bottom-hole flowing pressure (p_{wp}) calculated by considering the construction pump pressure and the wellbore flow is used to constrain the bottom-hole flowing pressure (p_{wf}) calculated by the construction displacement and fracture morphology, so as to realize the dynamic fitting of the fracture morphology.

(2) Based on the fracture inversion model, the seepage radius of the fracture is considered, and the volume coefficient of repeated reconstruction is used as the quantitative evaluation index of fracture channeling, so as to establish the quantitative identification model of fracture channeling. Through the calculation of the conceptual model, the model can accurately identify the location of channeling.

(3) The actual fracture channeling well group was used for the quantitative analysis of fracture channeling. A total of 108 fractures were simulated. The fracture channeling well section was quantitatively identified by combining the fracture repeated reconstruction volume, and the reason of cross-well fracture channeling is analyzed. The conclusion is consistent with the actual result.

Data availability statement

The original contributions presented in the study are included in the article/Supplementary Material; further inquiries can be directed to the corresponding author.

Author contributions

FH: data curation, methodology, writing–original draft, and writing–review and editing. MY: data curation, methodology, writing–original draft, and writing–review and editing. YZ: data curation, methodology, writing–original draft, and writing–review and editing. HH: data curation and writing–review and editing. WJ: software and writing–review and editing. LL: software and writing–review and editing. CQ: methodology and writing–review and editing. PS: validation and writing–review and editing.

Funding

The authors declare that no financial support was received for the research, authorship, and/or publication of this article.

Conflict of interest

Authors FH, MY, YZ, HH, WJ, LL, CQ, and PS were employed by CNPC Chuanqing Drilling Engineering Co., Ltd.

Publisher's note

All claims expressed in this article are solely those of the authors and do not necessarily represent those of their affiliated organizations, or those of the publisher, the editors, and the reviewers. Any product that may be evaluated in this article, or claim that may be made by its manufacturer, is not guaranteed or endorsed by the publisher.

References

Ajani, A., and Kelkar, M. "Interference study in shale plays," in Proceedings of the SPE Hydraulic Fracturing Technology Conference and Exhibition, Woodlands, TX, USA, February 2012.

Aleksandrov, V., Kadyrov, m, Ponomarev, A., Drugov, D., and Bulgakova, I. (2018). Microseismic multistage formation hydraulic fracturing (MFHF) monitoring analysis results. *Key Eng. Mater.* 785, 107–117. doi:10.4028/www.scientific.net/kem.785.107

Brigham, W., and Smith, D. "Prediction of tracer behavior in fivespot flow," in Proceedings of the Conference on Production Research and Engineering, Tulsa, Oklahoma, May 1965.

Dali Taleghani, A. (2010). *Fracture re-initiation as a possible branching mechanism during hydraulic fracturing*. Salt Lake City, Utah: Omnipress.

Du, J., Liu, H., Ma, D., Fu, J., Wang, Y., and Zhou, T. (2014). Discussion on effective development techniques for continental tight oil in China. *Petroleum Explor. Dev.* 41 (2), 217–224. doi:10.1016/s1876-3804(14)60025-2

Escobar, F. H., Prada, E. F., and Suescún-Díaz, D. (2021). Interpretation of pressure interference tests for wells connected by a large hydraulic fracture. *J. Petroleum Explor. Prod. Technol.* 11 (8), 3255–3265. doi:10.1007/s13202-021-01249-4

Feng, Y., and Kang, H. (2013). The initiation of I-II mixed mode crack subjected to hydraulic pressure in brittle rock under compression. *J. China Coal Soc.* (2), 226–232. doi:10.13225/j.cnki.jccs.2013.02.003

Fu, Y., (2020). How far can hydraulic fractures go? A comparative analysis of water flowback, tracer, and microseismic data from the Horn River Basin. *Mar. Petroleum Geol.* 115, 104259. doi:10.1016/j.marpetgeo.2020.104259

Geng, Y., Song, Z., Yan, Y., Chen, D., and Wang, L. (2017). Research and application of productivity monitoring technology using new tracer. *J. Yangtze Univ. Nat. Sci. Ed.* 14 (23), 83–86+7. doi:10.16772/j.cnki.1673-1409.2017.23.017

He, L., Yuan, S., and Gong, W. (2020). Influencing factors and preventing measures of intra-well frac hit in shale gas. *Petroleum Reserv. Eval. Dev.* 10 (05), 63–69. doi:10.13809/j.cnki.cn32-1825/te.2020.05.009

Huang, L., Lu, M., Sheng, G., Gong, J., and Ruan, J. (2021b). Research advance on prediction and optimization for fracture propagation in stimulated unconventional reservoirs. *Lithosphere* 2021. doi:10.2113/2022/4442001

Huang, L., Sheng, G., Chen, Y., Zhao, H., Luo, B., and Ren, T. (2022). A new calculation approach of heterogeneous fractal dimensions in complex hydraulic fractures and its application. *J. Petroleum Sci. Eng.* 219, 111106. doi:10.1016/j.petrol.2022.111106

Huang, L., Sheng, G., Li, S., Tong, G., Wang, S., Peng, X., et al. (2021a). A review of flow mechanism and inversion methods of fracture network in shale gas reservoirs. *Geofluids* 2021, 1–10. doi:10.1155/2021/6689698

King, G. E., Rainbolt, M. F., and Swanson, C. "Frac hit induced production losses: evaluating root causes, damage location, possible prevention methods and success of remedial treatments," in Proceedings of the SPE Annual Technical Conference and Exhibition?, San Antonio, TX, USA, October 2017.

Kresse, O., and Weng, X. (2018). Numerical modeling of 3D hydraulic fractures interaction in complex naturally fractured formations. *Rock Mech. Rock Eng.* 51 (12), 3863–3881. doi:10.1007/s00603-018-1539-5

Li, L., and Wang, T. (2005). Extended finite element method (XFEM) and its application. *Adv. Mech.* (1), 5–20. doi:10.3321/j.issn:1000-0992.2005.01.002

Meng, L., Bao, W., Guo, B., Shen, J. W., and Sun, H. (2022). Research progress of tracer technology in fracturing effect evaluation. *Petrochem. Ind. Appl.* 41 (3), 1–4. doi:10.3969/j.issn.1673-5285.2022.03.001

Olson, J. E. "Multi-fracture propagation modeling: applications to hydraulic fracturing in shales and tight gas sands," in Proceedings of the the 42nd U.S. Rock Mechanics Symposium (USRMS), San Francisco, CA, USA, June 2008.

Puneet, S., Ripudaman, M., Ashish, K., and Sharma, M. M. (2021). Analyzing pressure interference between horizontal wells during fracturing. *J. Petroleum Sci. Eng.* 204, 108696. doi:10.1016/j.petrol.2021.108696

Sheng, G., Zhao, H., Ma, J., Huang, H., Deng, H. Y., Zhan, W. T., et al. (2023). A new approach for flow simulation in complex hydraulic fracture morphology and its application: fracture connection element method. *Petroleum Sci.* 20, 3002–3012. doi:10.1016/j.petsci.2023.03.026

Wang, Y., Lu, Y., Li, Y., Wang, X., Yan, X., and Zhang, Z. (2012). Progress and application of hydraulic fracturing technology in unconventional reservoir. *Acta Pet. Sin.* 33 (S1), 149.

Weng, X., Kresse, O., Cohen, C., Wu, R., and Gu, H. (2011). Modeling of hydraulic-fracture-network propagation in a naturally fractured formation. *SPE Prod. Operations* 26 (4), 368–380. doi:10.2118/140253-pa

Wu, F., Yan, Y., and Yi, C. (2017). Real-time microseismic monitoring technology for hydraulic fracturing in shale gas reservoirs: a case study from the Southern Sichuan Basin. *Nat. Gas. Ind. B* 4 (1), 68–71. doi:10.1016/j.ngib.2017.07.010

Zhang, B., Tian, X., Ji, B., Zhao, J., Zhu, Z., and Yin, S. (2019). Study on microseismic mechanism of hydro-fracture propagation in shale. *J. Petroleum Sci. Eng.* 178, 711–722. doi:10.1016/j.petrol.2019.03.085

Zhao, B., Panthi, K., and Mohanty, K. K. (2020a). Tracer eluting proppants for hydraulic fracture characterization. *J. Petroleum Sci. Eng.* 190, 107048. doi:10.1016/j.petrol.2020.107048

Zhao, H., Sheng, G., Huang, L., Ma, J., Ye, Y., and Leng, R. (2020b). Calculation of reservoir fracture network propagation based on lightning breakdown path simulation. *Sci-entia Sin. Technol.* 52, 499–510. doi:10.1360/sst-2020-0406

Zhao, H., Sheng, G., Huang, L., Zhong, X., Fu, J., Zhou, Y., et al. (2021). "Application of lightning breakdown simulation in inversion of induced fracture network morphology in stimulated reservoirs," in Proceedings of the International Petroleum Technology Conference, San Francisco, CA, USA, March 2021. doi:10.2523/IPTC21157-MS

Zhou, T., Wang, H., Li, F., Li, Y., Zou, Y., and Zhang, C. (2020). Numerical simulation of hydraulic fracture propagation in laminated shale reservoirs. *Petroleum Explor. Dev.* 47 (5), 1117–1130. doi:10.1016/s1876-3804(20)60122-7

frontiers | Frontiers in Earth Science

TYPE Original Research
PUBLISHED 11 March 2024
DOI 10.3389/feart.2024.1377738

Check for updates

OPEN ACCESS

EDITED BY
Xixin Wang,
Yangtze University, China

REVIEWED BY
Luxing Dou,
Yangtze University, China
Long Luo,
Chongqing University of Science and Technology, China

*CORRESPONDENCE
Zhuang Liang,
13206822011@163.com

RECEIVED 28 January 2024
ACCEPTED 23 February 2024
PUBLISHED 11 March 2024

CITATION
Li G, Li C, Zhang B, Zhang L, Liang Z and Chen Q (2024), Characterization of reservoir quality in tight sandstones from the Benxi Formation, eastern Ordos Basin, China. *Front. Earth Sci.* 12:1377738. doi: 10.3389/feart.2024.1377738

COPYRIGHT
© 2024 Li, Li, Zhang, Zhang, Liang and Chen. This is an open-access article distributed under the terms of the Creative Commons Attribution License (CC BY). The use, distribution or reproduction in other forums is permitted, provided the original author(s) and the copyright owner(s) are credited and that the original publication in this journal is cited, in accordance with accepted academic practice. No use, distribution or reproduction is permitted which does not comply with these terms.

Characterization of reservoir quality in tight sandstones from the Benxi Formation, eastern Ordos Basin, China

Guoyong Li[1], Cong Li[1], Boming Zhang[1], Lei Zhang[2], Zhuang Liang[3,4]* and Qi Chen[3,4]

[1]China National Petroleum Corp, JiDong Oilfield, Tangshan, Hebei, China, [2]Luliang Oilfield Operation Area of Xinjiang Oilfield Branch Company, PetroChina, Karamay, China, [3]State Key Laboratory of Petroleum Resources and Prospecting, China University of Petroleum (Beijing), Beijing, China, [4]College of Geoscience, China University of Petroleum (Beijing), Beijing, China

The Benxi Formation in the eastern Ordos Basin harbors abundant natural gas resources and shows promising exploration and development potential. However, the reservoir characteristics are complex, and the primary controlling factors are unclear, presenting significant challenges for reservoir characterization. In response to these challenges, we conducted a systematic study on the characteristics of tight sandstone reservoirs in the Benxi Formation by integrating thin section analysis, scanning electron microscopy, high-pressure mercury injection, and conventional petrophysical analysis alongside well log data analysis. By applying empirical calculation formulas of a porosity evolution quantitative model, we elucidated the primary controlling factors of reservoir heterogeneity. Our research identified that the reservoirs in the eastern Ordos Basin, Benxi Formation, are predominantly composed of quartz sandstone and lithic quartz sandstone, with pore-filling cementation as the dominant cement type and the main storage spaces being intergranular pores and dissolved pores. The homogenization temperatures of fluid inclusions in authigenic quartz range from 92.8 to 185.7°C, indicating that the target layer is in the mesodiagenesis phase B. The main reasons for the differences in reservoir quality in the Benxi Formation are attributed to both sedimentation and diagenesis. In terms of sedimentation, two distinct sedimentary microfacies control the distribution of reservoir quality differences based on variations in quartz content and soluble components. Regarding diagenesis, the Benxi Formation underwent compaction, cementation, and dissolution, with compaction being the fundamental cause of widespread reservoir compaction.

KEYWORDS

Ordos Basin, Benxi Formation, reservoir quality, tight sandstone reservoirs, diagenesis

1 Introduction

The Benxi Formation in the Ordos Basin is a deep-buried reservoir of the Paleozoic era, with high natural gas reserves and an unobstructed flow rate exceeding 50 × 104 m^3/day (Jia et al., 2019a; Jia et al., 2019b; Li et al., 2021; Wang et al., 2021a). Therefore, the Benxi Formation is an important potential alternative area for increasing oil and gas reserves and

production. However, due to the complex composition, high quartz content, and strong diagenesis of the Benxi Formation, the reservoir exhibits strong heterogeneity and complex pore structures, thus limiting the exploration and development of natural gas (Li et al., 2021; Wang et al., 2021b).The rigid compressive strength of quartz inhibits compaction and leads to a significant amount of residual intergranular pores. These pore spaces are conducive to the entry of acidic fluids and the development of dissolution processes. Acidic fluids dissolve quartz and other detrital particles (Colo n et al., 2004; Crundwell, F, 2014; Wang et al., 2020a), connecting isolated pores and increasing the secondary porosity of the rock. This is a key factor affecting the overall porosity and permeability of tight sandstones (Li et al., 2020; Panagiotopoulou et al., 2007; Pokrovsky et al., 2009).

During a specific period, the Benxi Formation exhibits significant variations in unstable mineral composition and diagenetic fluid properties. Unstable components in feldspar and rock fragments are commonly dissolved in an acidic environment, leading to the formation of dissolution pores and casting pores within the grains, typically during the early to middle diagenetic stages. In contrast, quartz and other silicate minerals dissolve mainly during the late to post-diagenetic stages (Crundwell, 2014; Panagiotopoulou et al., 2007). Compaction, dissolution, and cementation processes interact with each other. The residual intergranular pores formed as a result of mechanical compaction provide favorable pathways for acidic fluids, while the unstable components in early sediments serve as the material basis for dissolution processes, thereby improving reservoir quality. Conversely, clay minerals (such as illite, kaolinite, and quartz cement) resulting from dissolution remain in the pores of tight sandstone reservoirs, hindering the flow of diagenetic fluids (Zhong et al., 2007; Gao et al., 2020; Hong et al., 2020; Wang et al., 2022; Morad et al., 2010; Taylor et al., 2010). Due to the fact that the tight sandstone reservoirs within the Benxi Formation are situated in a high-acidity environment formed within coal-bearing strata from source rocks (Li et al., 2021; Wang et al., 2021c), it is crucial to clarify the diagenetic evolution sequence, the contributions of various diagenetic processes to reservoir quality, and the controlling factors in order to promote efficient exploration in the Benxi Formation oil and gas development area.

This study combines experimental and theoretical approaches to investigate the quality characteristics of the Benxi Formation reservoir and the controlling factors of quality variations in tight sandstone reservoirs in the eastern Ordos Basin. Thin section analysis, core petrophysical analysis, and scanning electron microscopy (SEM) were used to conduct in-depth investigations into the reservoir types, structural features, composition of detrital particles, and cementation of the rocks. Based on the Scherer initial porosity recovery model (Scherer, 1987) and the Paxton and Ehrenberg compaction porosity loss formula, the primary controlling factors of diagenetic processes were determined by calculating the decrease in porosity based on compaction and cementation processes (Scherer, 1987; Ehrenberg, 1990; Ehrenberg et al., 2009; Paxton et al., 2002). The aim was to clarify the characteristics of sandstone reservoirs, describe the process of reservoir densification, and elucidate the evolution of primary and secondary porosity based on consideration of both sedimentation and diagenesis. Moreover, the study analyzed the influence of geological factors (such as grain size, mineral content, and diagenetic processes) on the reservoir quality of the Benxi Formation. The findings of this research can provide a basis for the prediction of favorable reservoirs in the eastern Ordos Basin.

2 Geological background

The Ordos Basin is located in the western part of the North China Block (Figure 1A). It is a poly-cycle cratonic basin with a north-south uplift, a long and gentle eastern flank, and a short and steep western flank. It can be divided into six tectonic units: the Yimeng Uplift, the Jinxi Tectonic Zone, the Weibei Uplift, the Western Thrust Zone, the Tianhuan Depression, and the Yishan Slope (Lin et al., 2013; Wang et al., 2017) (Figure 1B).

The research area is located in the northeastern part of the Yishan Slope in the Ordos Basin, located between 37° 41′47″ ~ 38° 23′34″N, 110° 0′45" ~ 110° 45′10″E. Administratively, it is within the boundaries of Shenmu County, Jia County, and Mizhi County in Yulin City, Shanxi Province. The stratigraphic formation in this area is the tight sandstone reservoir of the Benxi Formation in the Carboniferous (Figures 1C, D; Wang et al., 2017).

The top coal seams of the Benxi Formation are in conformable contact with the sandstone or mudstone of the Taiyuan Formation and are unconformably in contact with the lower Ordovician Majiagou Formation limestone (Wang et al., 2017). The thickness of the formation ranges from 27.8 to 82.8 m, with an average of 51.9 m (Figure 2). During the sedimentation period of the Benxi Formation, the tectonic stability was high, and the topography was relatively flat. The predominant sedimentary environment was tidal flat depositional with minor influences of shoreline, tidal channel, sand flat, mud flat, and swamp microfacies types (Jia et al., 2019a; Jia et al., 2019b; Lin et al., 2013). Among them, the tidal channel and sand flat are favorable for the development of tight sandstone reservoirs within the Benxi Formation. The mud flat and swamp, including the coal seams, serve as good hydrocarbon source rocks and are the primary contributors to the tight sandstone gas in the Benxi Formation.

3 Data and experiments

3.1 Data

A total of 22 cylindrical sandstone samples were collected from the target formation in 65 wells in the Jiaxian Block. Each sample had a diameter of 2.5 cm and a length of 8 cm, obtained by vertically drilling fresh core plugs from the wellbore. Additionally, pore volume and permeability data were collected for 134 samples from the Jidong branch of PetroChina, CTS analysis for 205 samples, SEM data for 20 samples, and cathodoluminescence (CL) data for 17 samples.

Prior to experiments, the 22 samples underwent washing to remove residual hydrocarbons and were subsequently dried at 120°C for 48 h. Initially, the samples were tested for pore volume and permeability. Then, a 0.5 cm length was cut from the top of each sample for CTS observation to investigate the lithological characteristics, pore morphology, and genetic types of different samples. Based on the physical properties and CTS assessment,

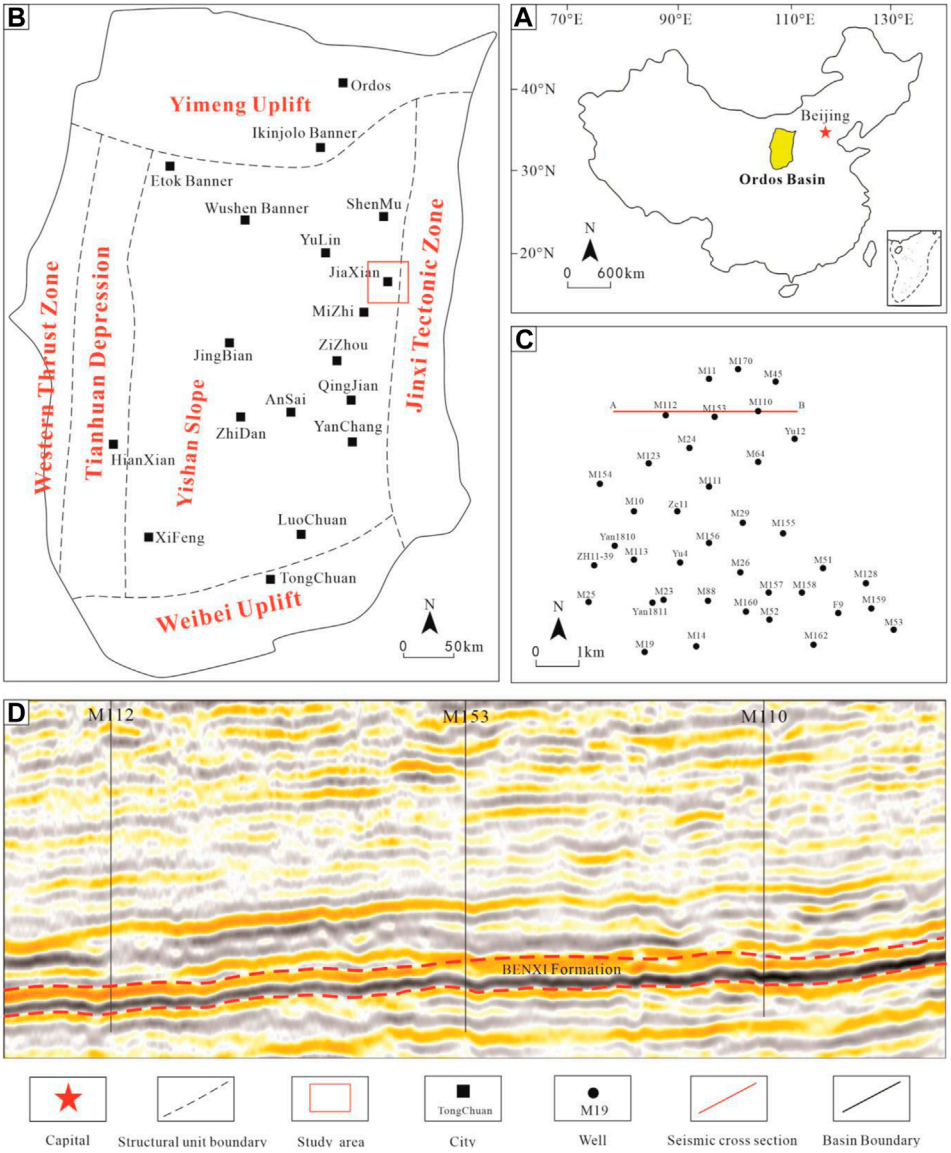

FIGURE 1
(A) Geographical location map of Ordos Basin **(B)** Structural location map of Ordos Basin (Lin, J et al., 2013) **(C)** Well location in the study area **(D)** Seismic cross section of AB connection in Figure 1C.

eight representative samples were selected and sliced into 2.5 cm and 5 cm sections. The SEM observation was conducted on the 2.5 cm sections of the eight samples. Subsequently, fluid inclusion tests were conducted on the 5 cm sections of the same eight samples. Detailed information for each experiment is described as follows.

3.2 Experiments

3.2.1 Well-logging data analysis

The log curves of the development wells in the study area were systematically analyzed using Petrel 2018 software and Resforrm V3.5 software. Firstly, the GR, RT and AC log curves were normalized to ensure consistency among the different units. Next, these three log curves were utilized to distinguish lithological formations such as sandstone, mudstone, coal, and limestone. Sandstone exhibits low GR, low RT, and low AC values, while coal displays low GR, high RT, and high AC values. Limestone is characterized by low GR, low RT, and high AC values, while other formations are identified as mudstone. After distinguishing the lithological formations, the rhythmic patterns of the GR curve and sandstone thickness were used to determine the sedimentary facies type, providing fundamental data for subsequent reservoir quality studies.

3.2.2 Core physical property test

A CMS~300 apparatus was used to test porosity and permeability at the State Key Laboratory of China University of Petroleum-Beijing (CUPB). The helium dilation method and the

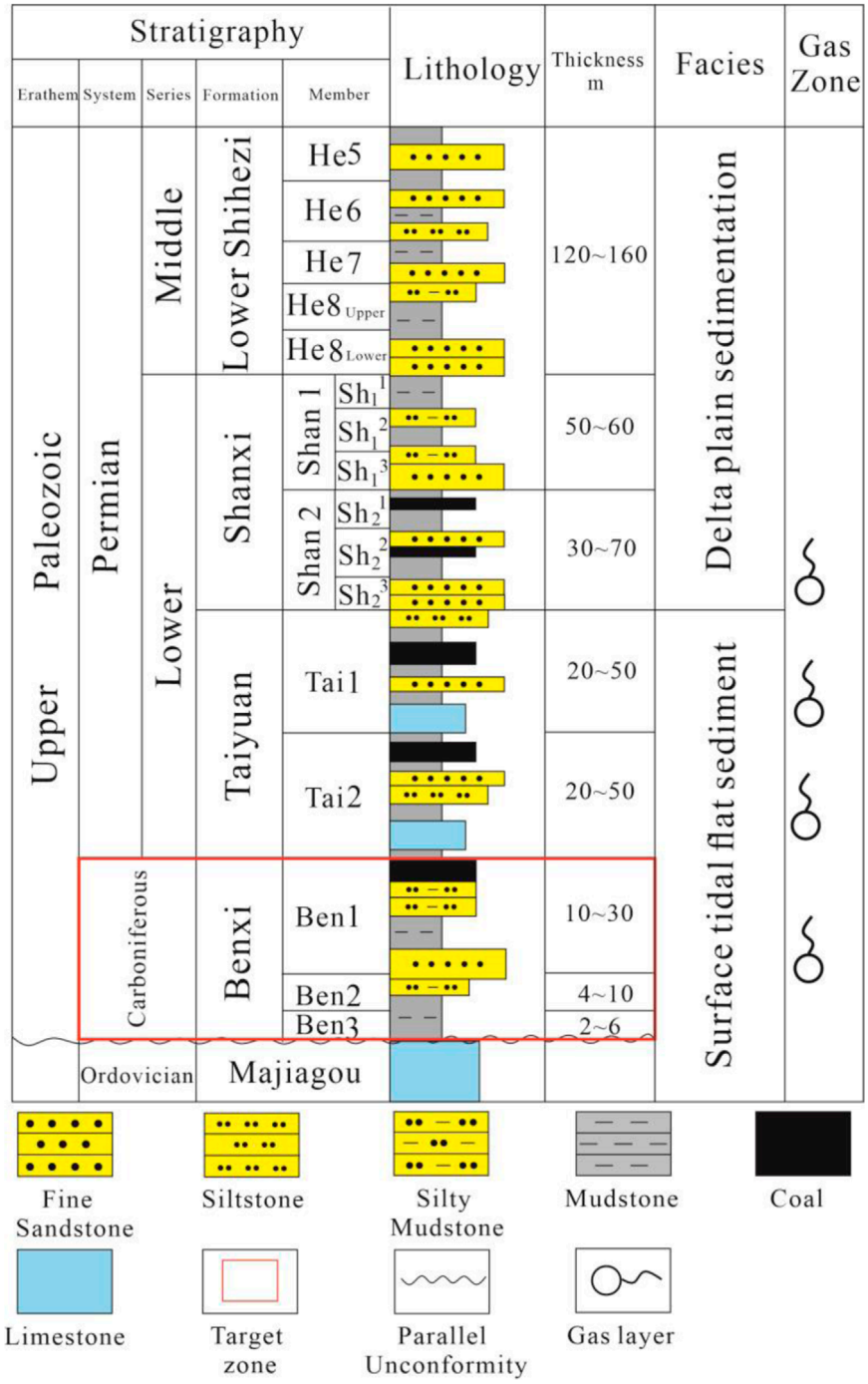

FIGURE 2
Stratigraphic overview map of the study area (Wang, F et al., 2017).

dynamic pressure method were used to measure porosity and permeability, respectively, Klinkenberg calibration was performed during the permeability measurement, which was performed at the ambient temperature of 23°C, the humidity of 61% and the conffning pressure of 97.2 kPa by SY/T 5336–1996. Through core porosity and penetration rate testing, understand the core physical property and reservoir properties in the study area.

3.2.3 CTS and SEM

Polished thin sections with a thickness of 0.3 mm were impregnated with blue resin and analyzed using a polarizing microscope (ikLV100nPOL) to examine the rock composition, pore and throat types, morphology, particle sorting, abrasion, and fracturing. The point counting method was employed to study the rock composition, pore and throat types, morphology, particle

classification, abrasion, and cementation of the sandstone samples. Generally, a minimum of 200 points were quantified for each sample. The statistical error for each microphotograph was less than 2%. Testing was done according to the SY/T 5368~2016 standard. Scanning electron microscope (SEM) analysis was performed using a Quanta~200 FESEM with a maximum resolution of 1.2 nm. SEM analysis provided high-resolution micrographs, including high-resolution microimages of pores and throats, intercrystalline micropores of authigenic and clay minerals, and further insights into mineral paragenetic sequences, clay mineral morphological sequences, clay mineral morphologies, pore sizes, and connectivity.

3.2.4 Fluid inclusions

Polished thin sections with a diameter smaller than 20 mm were placed on the stage of the microscope for microscopic observation of fluid inclusions in quartz. The main observations focused on the occurrence state, inclusion types, size and shape, distribution characteristics, and gas phase percentage within the inclusions. This allowed for the selection of suitable fluid inclusion samples for subsequent testing and analysis.

Microthermal analysis was conducted on the selected fluid inclusion samples using a Linkam TH600 stage. By measuring the low-temperature phase transition temperature and homogenization temperature of the inclusions, information on fluid salinity and the minimum trapping temperature of the inclusions was obtained. The testing was conducted in accordance with the SY/T 6010~2011 standard.

Homogenization temperature analysis of fluid inclusions provides insights into determining the main mineralization period or mineralization stage and their chronological sequence. Additionally, it aids in further studying the diagenetic stages and diagenetic processes.

3.2.5 HPMI

The HPMI experiment was conducted with an AutoPore IV9505 mercury porosimeter at the Analysis and Test Center of Exploration and Development Research Institute of China Changqing Oilfield Company.

The test standard is according to Chinese standard SY/T 5346–2005. The eight cylindrical samples had a diameter of 2.5 cm and a length of 3.0 cm. The highest mercury intrusion pressure was set to 200 MPa, and the corresponding pore radius was 0.0037 μm, which was the smallest pore radius obtained in the test. After the mercury injection pressure reaches the maximum, the pressure progressively declines and the mercury is withdrawn from the sample. The HPMI test can acquire the capillary pressure vs mercury saturation curve during mercury intrusion and extrusion. The equivalent pore throat radius of capillary pressure can be computed using the Washburn equation. Finally, multiple characteristic parameters representing pore size distribution can be obtained.

4 Results

4.1 Reservoir lithological

Based on the identification of cast thin sections and whole-rock X-ray diffraction, the Benxi Formation tight sandstone reservoir consists of three types: quartz sandstone, lithic quartz sandstone, and lithic sandstone (Li et al., 2021; Wang et al., 2021c; Hu et al., 2019). Lithic quartz sandstone and lithic sandstone are the predominant types, accounting for 50.9% and 33.5% of the total samples, respectively. Quartz sandstone is less abundant, accounting for only 15.6% (Figure 3). The composition of sandstone clasts is primarily quartz, with an average content of 70.9%. The content of lithic clasts is relatively low, at 29.05%. Feldspar content is minimal or absent (Table 1). There are various types of lithic clasts, mainly including schist clasts and quartzite clasts, followed by phyllite, slate, and metamorphic sandstone, with occasional occurrences of pyrite, siderite, and other minerals. The overall sandstone is mainly composed of medium to fine sandstone, showing moderate to good sorting, particle support, linear-convex contacts, and predominantly pore-filling cementation. The sandstone exhibits a high level of compositional maturity and structural maturity.

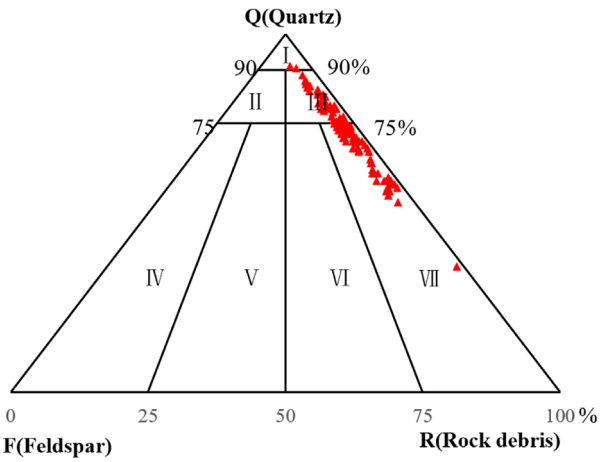

FIGURE 3
Triangular diagram of sandstone composition of Benxi Formation. Number of samples = 110. I-Quartz sandstone; II-Feldspar quartz sandstone; III-Lithic quartz sandstone; IV-Feldspar sandstone; V-Lithic feldspar sandstone; VI-Feldspar lithic sandstone; VII-Lithic sandstone.

The main cementing material in the tight sandstone is clay minerals, with kaolinite having the highest average content at 46.1%, followed by illite at 31.2%. The interlayered illite/smectite and chlorite have contents of 17.8% and 4.9%, respectively (Figure 4). As the Benxi Formation was deposited in a marine environment, abundant Ca^{2+} and Mg^{2+} ions provided by seawater promoted the development of various types of carbonate cements, such as calcite and dolomite (Hu et al., 2019; Wang et al., 2021). Through the observation of cast thin sections and scanning electron microscope analysis, worm-like kaolinite (Figure 5A) and needle-like chlorite, as clay minerals, were identified as authigenic fills in the pores. Iron-bearing calcite (Figure 5B) and iron-bearing dolomite (Figure 5C) are the main carbonate cements, with iron-bearing calcite replacing clasts and iron-bearing dolomite filling the pores in a pseudomorphic manner (Figures 5D, E). Sporadic occurrences of pyrite are found between intergranular pores (Figure 5F).

10.3389/feart.2024.1377738

TABLE 1 Composition table of sandstone clastic particles in Benxi Formation.

Well	Sample numbers	Quartz (%)	Feldspar (%)	Rock debris (%)	Quartzite (%)	Phyllite (%)	Metasandstone (%)	Slate (%)
M46	202,308,006	53	0	47	12	2	0	0
F9	202,308,007	64	0	36	4.5	1.5	2	0.5
M51	202,308,008	72	0	28	6	2	1	1
M51	202,308,009	74	0	26	7	0	0	0.5
M158	202,308,010	81	0	19	3	0	0.5	0
M161	202,308,011	71	0	29	17	0	0.5	0

4.2 Reservoir pore structure

The pore types in the Benxi Formation sandstone include primary pores (intergranular pores), secondary pores (intergranular dissolution pores, feldspar dissolution pores, lithic clasts dissolution pores, miscellaneous substance dissolution pores), intercrystalline pores, and microfractures, totaling five types (Figure 6). Intergranular pores generally range from 0.2% to 3.5%, with an average of 1.2%. Secondary pores are distributed between 0.1% and 4.8%, with an average of 1.27%, mainly consisting of intergranular dissolution pores and lithic clasts dissolution pores (Hu et al., 2019). Intercrystalline pores and microfractures are less abundant, accounting for an average of 0.3%. Intergranular pores and dissolution pores serve as the primary reservoir spaces in the tight sandstone reservoir of the Benxi Formation.

4.3 Porosity and permeability

Based on the core analysis test data from 404 core samples taken from 14 wells, the porosity of the Benxi Formation sandstone ranges from 0.23% to 13.77%, with an average of 6.2%. The permeability ranges from 0.002 to 12.56 × 10^3 μm^2, with an average of 1.35 × 10^3 μm^2, indicating that it belongs to low porosity and extremely low permeability reservoirs (Figure 7A). Additionally, there is a significant positive correlation between porosity and permeability (Figure 7B), indicating that the reservoir in the Benxi Formation has a simple pore-throat structure, and its reservoir properties are mainly determined by the size of the pore space.

Based on the analysis of high-pressure mercury intrusion pore-throat parameters, the Benxi Formation tight sandstone reservoir exhibits relatively large median pore-throat radius, close to unity sorting coefficient, indicating moderate to good pore-throat sorting and a concentrated distribution (Table 2). Overall, the reservoir shows good homogeneity. The skewness of the throats is not significant, suggesting that the throat sizes are biased towards larger throats compared to the average throat radius. The displacement pressure is relatively low, indicating the presence of larger maximum connected pore-throat radius and good reservoir permeability. The maximum mercury saturation is relatively high, reflecting the reservoir's good storage capacity.

4.4 Fluid inclusions

Based on fluid inclusion test data, it is observed that fluid inclusions are mainly distributed within dissolution pores or fractures within quartz grains, often appearing as irregular gas-liquid two-phase inclusions. Inclusions in the cementing material are rarely encountered. The quantity of fluid inclusions is moderate, with well-developed quartz triple junctions. There are two main stages: early-stage inclusions are found within early-stage fractures of quartz grains, which are narrow and contain relatively smaller individual inclusions. Late-stage inclusions are distributed within dissolution pores or late-stage fractures within quartz grains, showing a good fluorescent response.

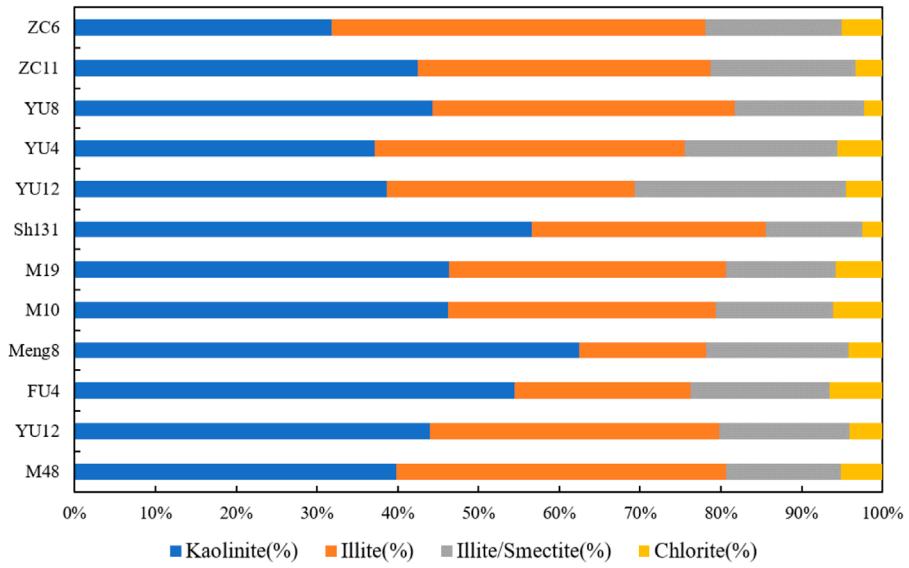

FIGURE 4
Microscopic characteristics of Benxi Formation reservoirs in JiaXian area.

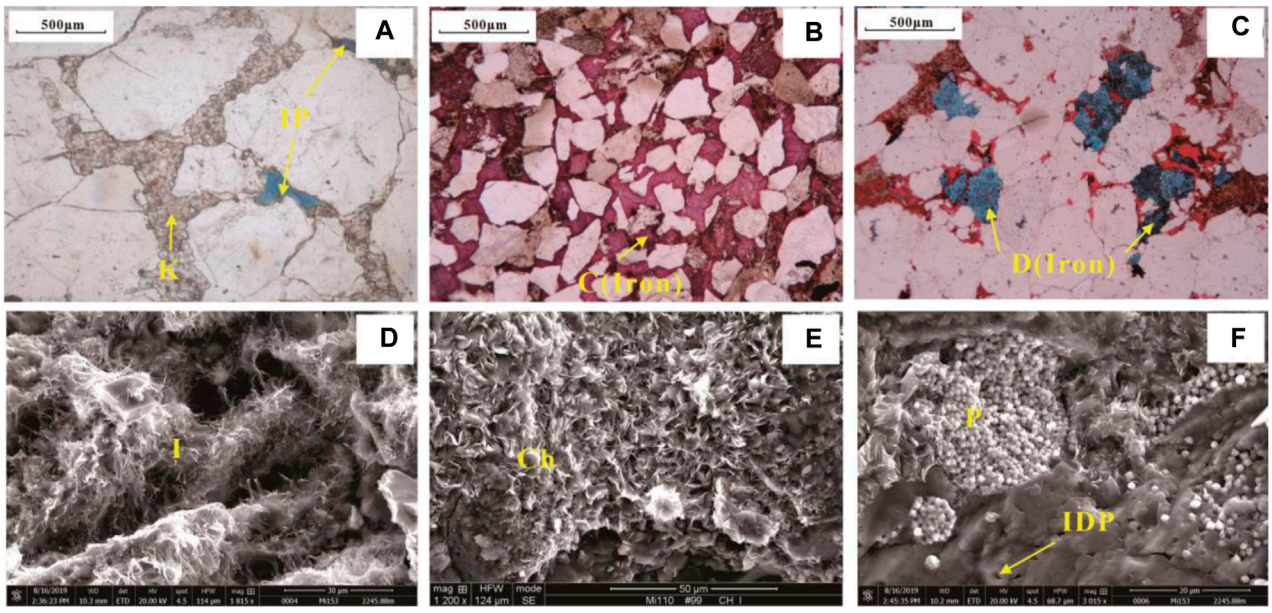

FIGURE 5
Microscopic characteristics of Benxi Formation reservoirs in JiaXian area **(A)** Sub-angular-sub-circular quartz grains, intergranular filling with worm-like kaolinite, Well M51, 2158 m, (–); **(B)** Iron-bearing calcite cementation, Well M112, 2091 m, (–); **(C)** Iron-bearing dolomite, Well M128, 2006 m, (–); **(D)** Filamentous illite, Well M157, 2060 m, (–); **(E)** Scaly chlorite, Well M110, 2105 m, SEM; **(F)** Pyrite filling and intergranular dissolution, Well M158, 2110 m, SEM. IP=Intergranular pore, C (Iron)=Iron-bearing calcite, D (Iron)= Iron-bearing dolomite, I= illite, Ch= chlorite, P= Pyrite, IDP= Intergranular dissolution pore, K= Kaolinite.

Experimental results demonstrate that the fluid inclusions in the reservoir sandstone exhibit a uniform temperature distribution, ranging from 92.8°C to 185.7°C (Figure 8). The reservoir in this area has undergone two distinct peaks at around 120 ~ 130°C and 150 ~ 160°C, indicating two hydrocarbon charging events in the evolution from early diagenesis to mesodiagenesis (Wang et al., 2021).

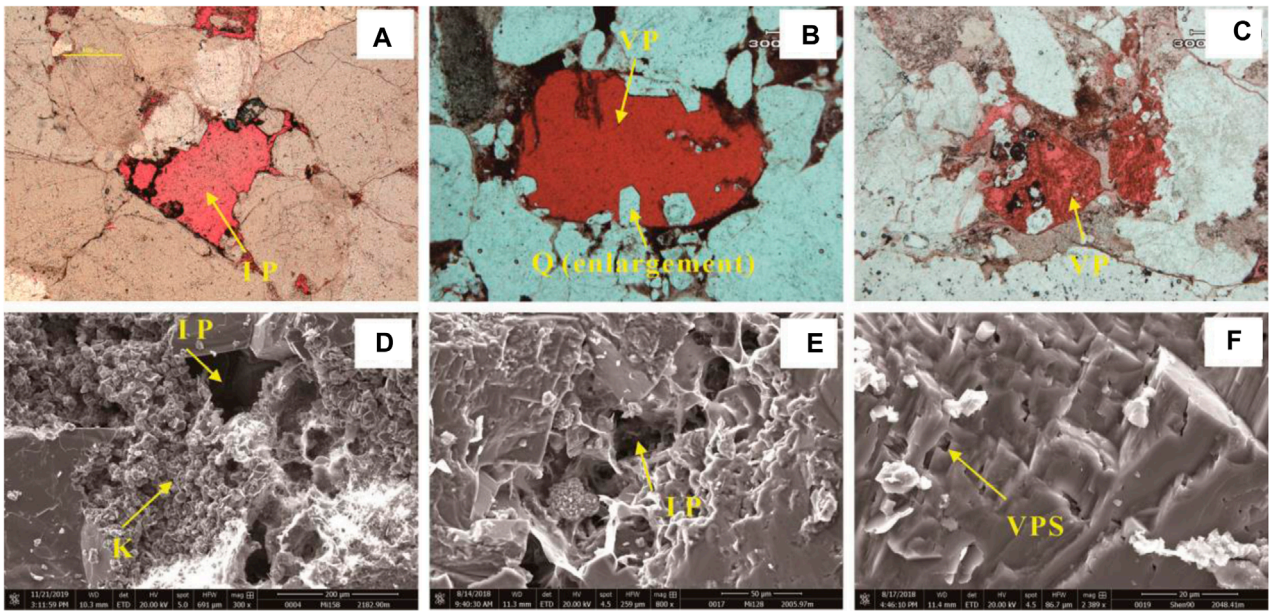

FIGURE 6
Microscopic Characteristics of Pore Structure of Benxi Formation Sandstone **(A)** Residual Intergranular Pores, Well M52, 2018 m, (–); **(B)** Rock debris dissolution pores, Well M7, 2168 m, (–); **(C)** Rock debris dissolution pores, Well M26, 2136 m, (–); **(D)** Residual Intergranular Pores, Well M158, 2182 m, SEM; **(E)** Kaolinite dissolution, Residual Intergranular Pores, Well M23, 2115 m, SEM; **(F)** Iron-bearing calcite dissolution pores, Well S90, 2048 m, SEM. IP= Intergranular Pores, VPS=Vugular pore space, Q (enlargement)= Quartz enlargement, K= Kaolinite.

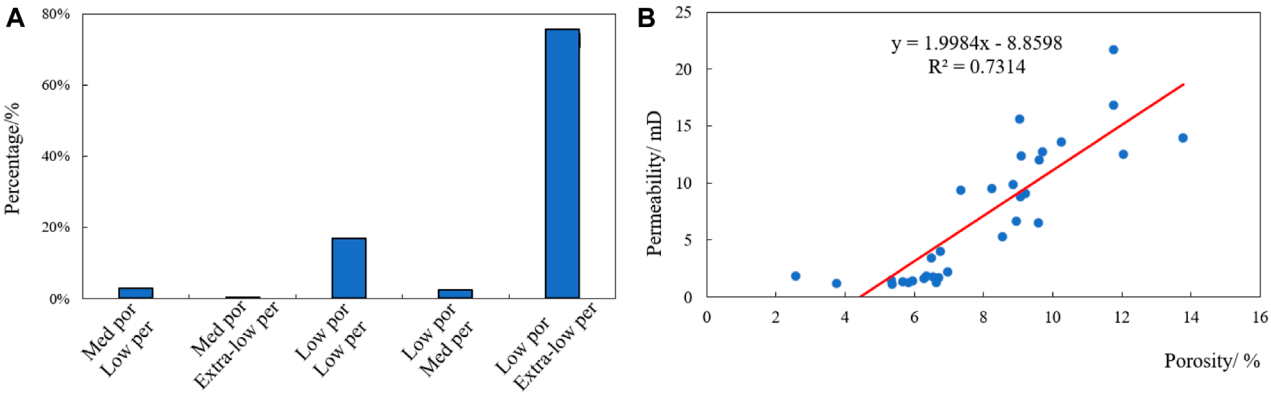

FIGURE 7
Statistical chart of reservoir characteristics and pore types. **(A)** Histogram of reservoir type; **(B)** Histogram of porosity and permeability.

5 Discussion

5.1 Sedimentation controls the material composition of the reservoir

Sedimentation processes do not directly impact reservoir quality. They influence reservoir quality through the macroscopic control of rock grain size and composition, which further affects the diagenetic processes of sediment and ultimately influences reservoir quality. In general, diagenetic processes are the direct factors that impact reservoir quality.

5.1.1 Rock grain size controls reservoir physical properties

Sedimentary processes have an inherent control on reservoirs. Sediments possess numerous primary pores, and their size and distribution are controlled by sedimentary facies. Coarser-grained rocks with lower mud content generally exhibit better original porosity and permeability (Wang et al., 2021c). Experimental studies on reservoir properties of different rock facies provide values for porosity and permeability. Among these facies, coarse sandstone exhibits the highest porosity and permeability, with average values of 9% and 1.01 mD, respectively. Fine sandstone, on the other

TABLE 2 High pressure mercury injection curve parameter table.

Well	Depth (m)	Displaceme pressure (MPa)	Median radius (μm)	Maximum mercury saturation (%)	Mercury removal efficiency (%)	Mean value	Skewness	Sorting coefficient
S90	2048.41	1.42	0.18	86.72	37.33	11.89	1.25	1.25
S90	2051.20	0.31	0.89	94.31	36.54	9.89	1.74	1.15
M128	2003.04	0.35	0.90	89.62	20.96	10.04	1.88	1.38
M128	2014.01	0.42	0.76	87.73	24.58	10.25	1.81	1.32
M51	2149.48	0.27	0.13	93.30	30.59	11.95	2.68	1.28
M51	2157.86	0.40	0.17	90.56	31.29	11.41	2.48	1.49
M46	2252.30	0.05	1.09	87.97	40.10	9.52	2.49	1.49
M26	2311.10	8.13	0.09	78.78	38.89	9.71	1.51	1.27

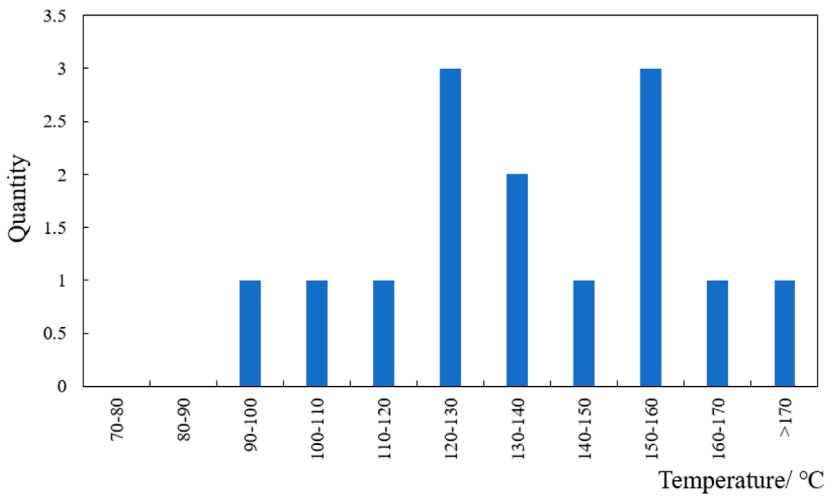

FIGURE 8
Fluid inclusion homogeneous temperature histogram.

hand, has the lowest original porosity, with an average of 2.3% (Figures 9A, B).

Furthermore, grain size also influences diagenetic processes. Coarse sandstone is formed in high-energy water environments with strong transportation capacity and good continuity, making it difficult for some weakly compactable detrital or plastic minerals to be preserved. Thus, the original sediment of coarse sandstone exhibits strong compaction resistance (Figure 9C). As a result, the remaining original porosity is relatively high, facilitating dissolution and cementation processes. Conversely, fine-grained sandstones have weak compaction resistance, resulting in very limited residual pore space after compaction, which hinders fluid flow during diagenesis, leading to relatively weaker cementation and dissolution processes (Figure 9D).

5.1.2 Sedimentary facies determine the material composition of rocks

The overall development of lagoonal tidal flat sedimentation is observed in the study area, but the reservoir performance of various microfacies within it shows some variations. Quartz sandstone exhibits relatively good reservoir performance, followed by lithic quartz sandstone, and lithic sandstone has the poorest performance (Table 3). The development and distribution of these rock types are clearly controlled by sedimentary microfacies (Wang et al., 2021a; Hu et al., 2019; Dutton and Loucks, 2010).

Two main types of microfacies are developed in the reservoir interval within the study area, and they exhibit distinct reservoir characteristics (Figure 10). The first type is the tidal channel microfacies of the subtidal zone, characterized by thicker channel sand bodies that are laterally limited and only developed in the

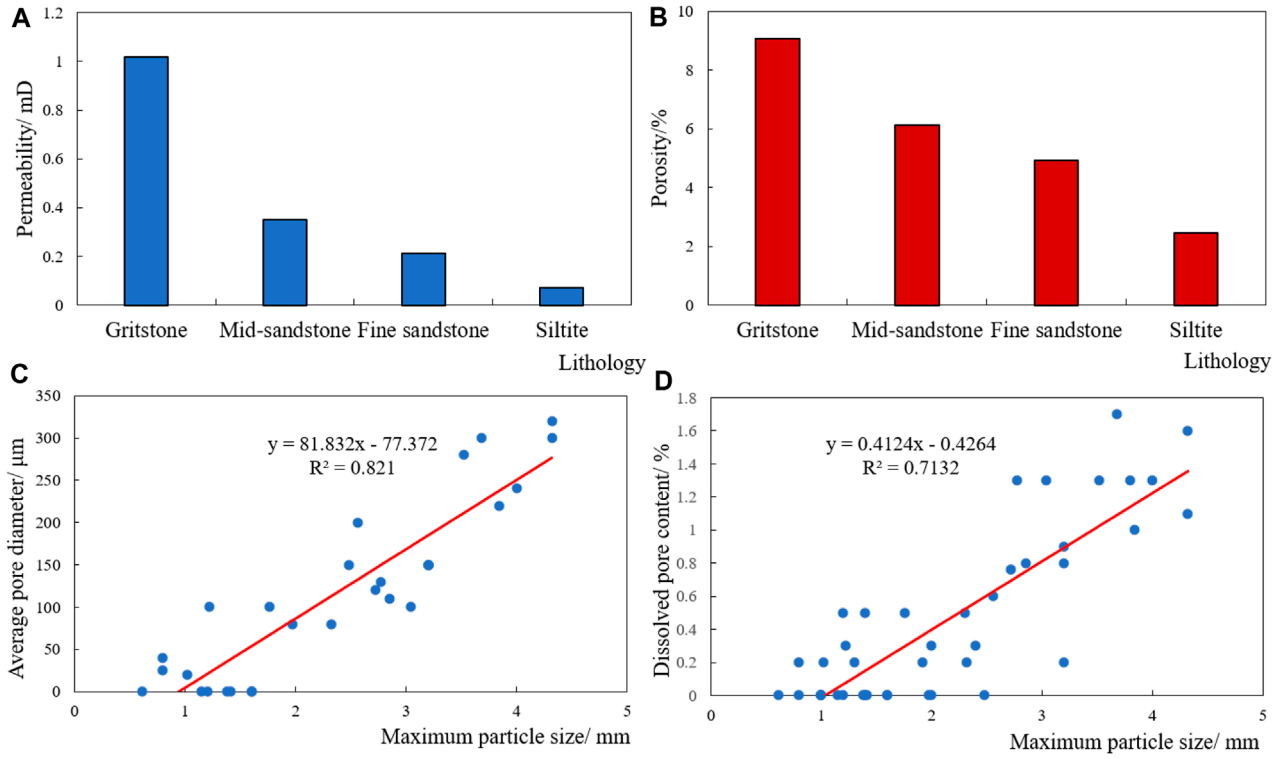

FIGURE 9
Physical properties of reservoirs of different lithologies in the Benxi Formation. **(A)** Histogram of lithology and permeability; **(B)** Histogram of lithology and porosity; **(C)** Relationship between maximum particle size and average pore size; **(D)** Relationship between maximum particle size and dissolved pore content.

TABLE 3 Rock type reservoir quality difference table.

Sedimentary facies type	Sandstone type	Porosity (%)	Permeability (10^{-3} μm^2)	Media radius (μm)	Sorting coefficient	Variable coefficient	Displacemen pressure (MPa)	Maximum mercury saturation (%)
Tidal channel microfacies	Quartz sandstone	9.6	1.95	0.67	2.21	0.22	0.27	86.85
Sand flat microfacies	Lithic Quartz Sandstone	7.1	1.27	0.45	2.38	0.21	0.35	78.35
Sand flat microfacies	Lithic Sandstone	5.02	0.59	0.2	1.85	0.15	0.79	83.1

southern part of the study area. The bottom of the channel shows evidence of finer gravel lag deposits, transitioning upward to medium to coarse sandstone, with a sharp top, exhibiting a well-defined box-shaped log response. The tidal channel microfacies experience turbulent water flow and strong hydraulic energy, as the clastic particles have undergone prolonged scouring, resulting in a relatively low content of unstable rock fragments. The dominant lithology is quartz sandstone, with abundant intergranular volume, facilitating the entry of acidic fluids and exhibiting good porosity and permeability. It is considered the highest-quality reservoir in the area.

The second type is the sand flat microfacies of the intertidal zone, characterized by thinner sand bodies and interbedded sand and mud. They are laterally extensive and widespread throughout the study area. Similar to the tidal channel microfacies, the bottom of the sand flat microfacies shows evidence of lag deposits, transitioning upward to medium to fine sandstone, with a gradual top and log response exhibiting a box-shaped or bell-shaped curve with significant notching. The sand flat microfacies are located in the intertidal zone, where the water is relatively stable compared to the subtidal zone, allowing for ample deposition of clastic material. The dominant lithologies are lithic quartz sandstone and quartz

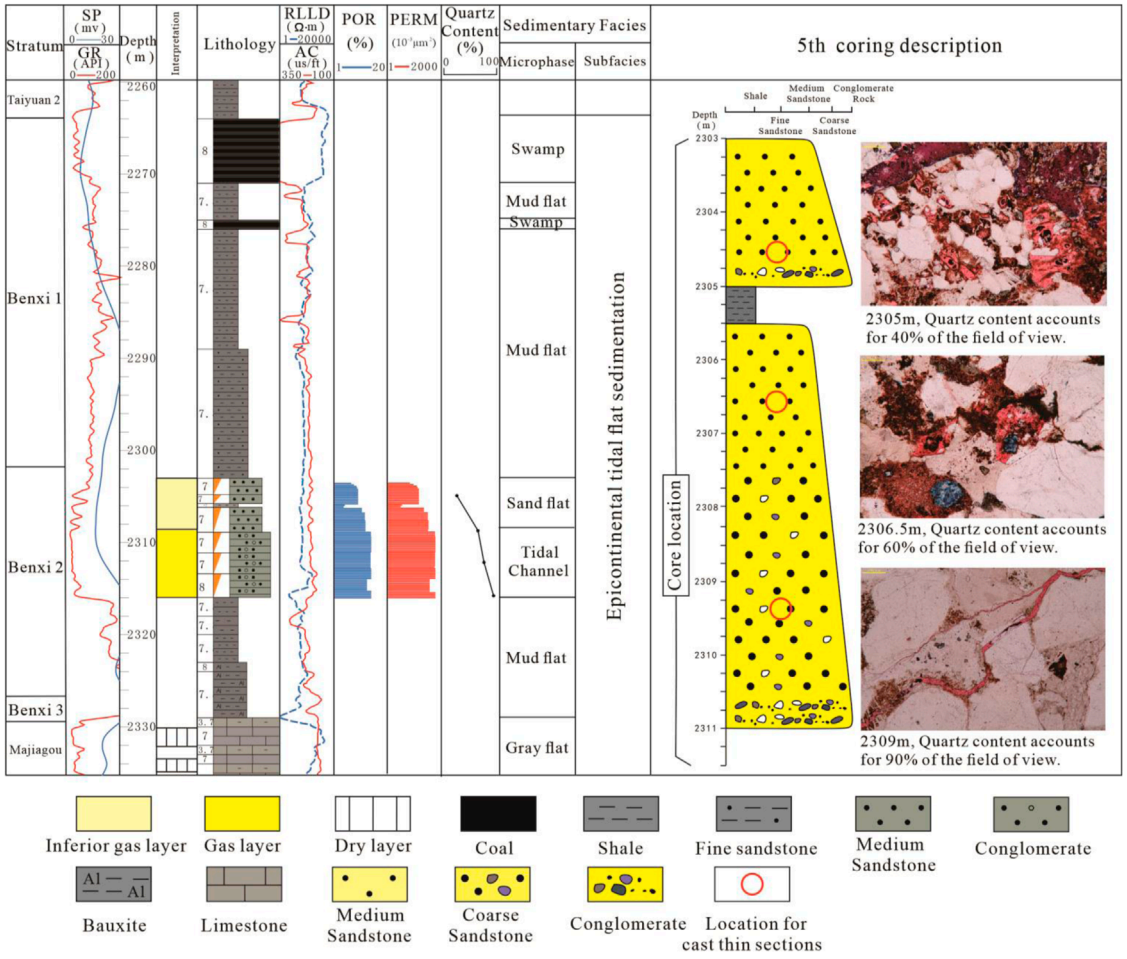

FIGURE 10
Columnar diagram of core from Benxi Formation, Well M26.

sandstone, with moderate porosity and permeability, making them the most well-developed reservoirs in the area.

5.2 Diagenesis controls the differential characteristics of reservoirs

5.2.1 Diagenetic stage of reservoir

In the study area, the burial depth of the Benxi Formation ranges from 2300 to 3400 m (Wang et al., 2021b; Hu et al., 2019). The vitrinite reflectance (Ro) of the samples is between 1.3% and 2.0% (Li et al., 2021) The ratio of I/S is less than 10%. The fluid inclusions in authigenic quartz exhibit a uniform temperature range of 100°C–170°C. According to the SYT5477-2003 petroleum industry standard, the target interval is in the mesodiagenesis B (Figure 11). A comprehensive study has been conducted on the diagenetic characteristics and diagenetic stages of different lithologies within the Benxi Formation sandstone in the study area.

5.2.1.1 Eodiagenesis A

During the Late Carboniferous (310~240 million years ago), the sandstone reservoirs of the Benxi Formation in the study area were in the early diagenesis stage A. During this period, the basin underwent a phase of stable subsidence, with a burial depth generally less than 900 m and paleogeothermal temperatures below 65°C. The vitrinite reflectance (Ro) was below 0.35%, indicating the organic matter was in an immature stage (Hu et al., 2019). The presence of biotite and volcanic rock fragments in the sandstone underwent illitization and chloritization, resulting in an increase in reservoir alkalinity (Li et al., 2016). The decomposition of these minerals released Mg^{2+} and Fe^{2+} ions, facilitating the formation of thin films of chlorite along the grain boundaries.

During this stage, sedimentary materials underwent initial compaction, leading to a gradual increase in particle packing, while ductile lithic fragments deformed and filled the pore space. Primary intergranular pores were well-developed. At this stage, the reservoir had sufficient pore space, providing ample room for subsequent diagenetic processes.

5.2.1.2 Eodiagenesis B

During the Mid-Permian to Middle Jurassic period (240~210 million years ago), the sandstone of the Benxi Formation was in the early diagenesis stage B. During this period, the basin experienced

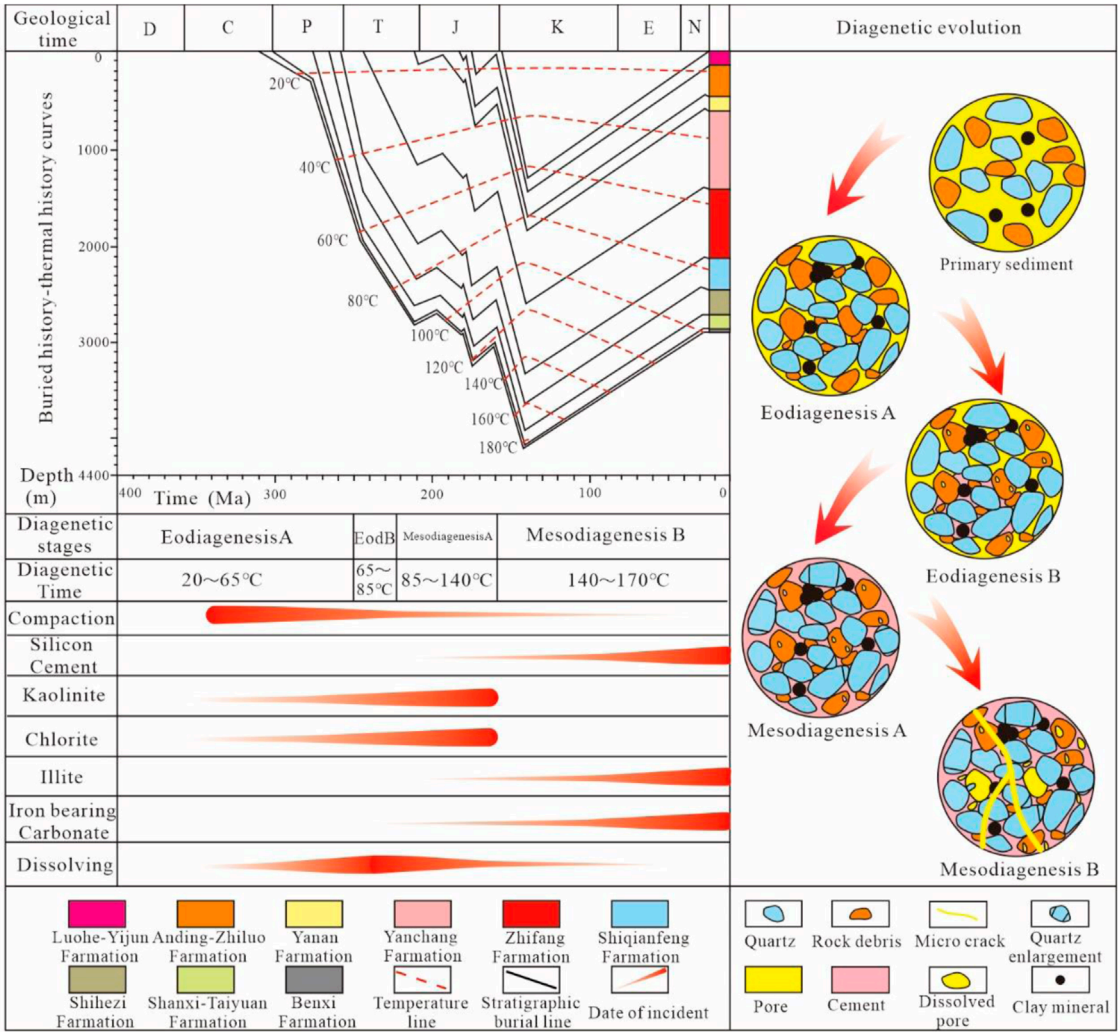

FIGURE 11
Diagram of rock~forming stages in the study area.

fluctuating subsidence, with burial depths ranging from 900 to 1800 m and paleogeothermal temperatures ranging from 65°C to 85°C. The vitrinite reflectance (Ro) values ranged from 0.35% to 0.5%, indicating the organic matter was in an immature to semi-mature stage (Hu et al., 2019). The primary diagenetic processes during this stage were compaction and the formation of siliceous and kaolinite cements. Due to the generation of organic acids, the pore fluids in the sandstone were acidic. Unstable components such as feldspar and lithic fragments underwent silicate mineral alteration, resulting in the precipitation of SiO_2 and the production of a small amount of HCO^{3-}. Under such acidic conditions, well-formed kaolinite cements precipitated and filled the intergranular pores (Li et al., 2016). Since fluid activity during this period was relatively weak, no corresponding hydrocarbon inclusions were captured in the sandstone.

During this period, sediment continued to settle, and compaction intensified, resulting in a continuous reduction of primary pores. Additionally, there was a short-term cementation process during this period, whereby some of the original intergranular pores were filled with cement, leading to a deterioration in reservoir quality.

5.2.1.3 Mesodiagenesis A

During the Late Jurassic to Early Cretaceous period (210~140 million years ago), the sandstone reservoir of the Benxi Formation entered the intermediate diagenesis phase A. At this time, the basin was still experiencing fluctuating subsidence, with burial depths ranging from 1800 to 4,100 m and paleogeothermal temperatures ranging from 85°C to 140°C. The vitrinite reflectance (Ro) values ranged from 0.5% to 1.3%, indicating the organic matter was in a low mature to mature stage (Hu et al., 2019). The main diagenetic processes during this period were kaolinite and siliceous cementation in the sandstone. Additionally, a first-stage oil and gas charging event occurred between 165 and 100 million years ago, corresponding to relatively low homogenization temperatures (120~130°C) of hydrocarbon inclusions. This event resulted in a large-scale distribution of oil and gas in primary fractures such as grain cracks, cleavage fractures, and various types of dissolution

pores and fractures in high-plastic rock debris sandstone, lithic quartz sandstone, and quartz sandstone.

This period was characterized by the most active organic-inorganic reactions between source rocks and reservoirs. The abundant organic and inorganic acid fluids formed during this time dissolved the unstable aluminosilicate minerals, clay minerals, and early cements in the Benxi sandstone, creating secondary porosity (Li et al., 2016). With increasing temperature and pressure conditions, the solubility of SiO_2 in the pore fluid increased, leading to the precipitation of siliceous cement within intergranular pores. Simultaneously, under acidic conditions, the dissolved kaolinite cement, derived from the dissolution of feldspar, filled the dissolution pores within the feldspar grains. As temperature and pressure continued to rise and organic acids were consumed, extensive dehydration of clay minerals occurred, resulting in the release of alkaline cations such as Na^+ and K^+ during the process of mineral dissolution and ion exchange. This increased the pH of the pore fluid, transitioning the diagenetic environment to a weak alkaline state. It also led to the transformation of illite/montmorillonite mixed layers and part of the kaolinite into illite. Additionally, a small amount of late-stage carbonate cementation occurred (Li et al., 2016).

During this period, the sediment was influenced by various diagenetic processes. The most significant influence was from compaction, which intensified with increasing depth. As a result, pore space was compressed, and the reservoir quality tended to become more tight. The period also experienced the first stage of acid leaching, where unstable components in the original sediment were dissolved by organic acids, creating a significant number of secondary pores. However, in the later stages of this period, the diagenetic environment transitioned to a weak alkaline condition, leading to the generation of a small amount of cement. This material filled the previously formed secondary pores, causing a deterioration in reservoir quality.

5.2.1.4 Mesodiagenesis B

During the Late Cretaceous (140~65 million years ago), the sandstone reservoir of the Benxi Formation entered the intermediate diagenesis phase B. At this time, the basin was undergoing tectonic uplift, with burial depths exceeding 3,100 m. The maximum burial depth was reached at the end of the Early Cretaceous, reaching 4,100 m. Paleogeothermal temperatures ranged from 140°C to 175°C, and vitrinite reflectance (Ro) values ranged from 1.3% to 2.0%, indicating the organic matter was in a highly mature stage (Hu et al., 2019). Due to the organic matter being highly mature, the kerogen had transformed into hydrocarbons, releasing a significant amount of organic acids and resulting in an acidic diagenetic environment. Late-stage carbonate cementation, formed during intermediate diagenesis phase A, was dissolved, leading to the occurrence of secondary dissolution during this period. Additionally, under high temperature, high pressure, and acidic conditions, illite transformed into kaolinite. A second-stage oil and gas charging event occurred between 90 and 70 million years ago, corresponding to relatively high homogenization temperatures (150~160°C) of hydrocarbon inclusions mentioned earlier.

During this period, there was structural uplift, and the effect of compaction weakened. As a result, some microfractures opened up, creating reservoir space. Additionally, the diagenetic environment transitioned to an acidic condition, causing the dissolution of later-formed carbonate cement, which resulted in the formation of numerous secondary dissolution pores. This led to an improvement in reservoir quality.

5.2.2 Mechanical compaction is the main cause of reservoir density

The Benxi Formation is in the middle stage of diagenesis, characterized by a prolonged period of mechanical compaction. The impact of compaction on reservoir quality can be attributed to the following factors:

(1) Compaction leads to the compression and densification of particles, resulting in a significant reduction in primary intergranular pores due to the particles' concave-convex contact.
(2) The presence of abundant ductile minerals, such as mica and shale fragments, within the lithic clasts can cause bending and deformation under pressure, filling the primary pore spaces and greatly reducing porosity and permeability.
(3) Intense compaction reduces the pore space, leading to complex pore-throat structures that hinder fluid entry, thereby inhibiting other diagenetic processes.

The outcome of diagenesis is the alteration of reservoir rock structure, composition, and storage capacity to some extent. The original porosity of reservoirs can be quantitatively estimated using empirical formulas based on porosity evolution models (Beard and Weyl, 1973). The calculation formula is as Eqs 1, 2:

$$\Phi = 20.91 + 22.9/S0 \quad (1)$$

$$S0 = P75/P25\% \quad (2)$$

The percentage of original porosity eliminated can be determined by Eqs 3, 4 (Huoseknecht, 1987):

$$\Phi ys = (\Phi - \Phi yy)/\Phi \quad (3)$$

$$\Phi jj = ((Vjjw)/\Phi) \times 100\% \quad (4)$$

Φ—Original pore volume; S0—Sorting coefficient; Φys—Compaction porosity loss rate; Φjj—Cementation porosity loss rate; Φyy—Core porosity; Vjjw—Cementation content.

By utilizing thin section identification data and petrophysical analysis data, parameters such as compacted porosity loss rate and cemented porosity loss rate can be calculated using appropriate formulas. These calculations help in assessing the extent to which different diagenetic processes affect reservoir properties (Figure 12A). In the studied area, compaction leads to a porosity loss of up to 80%, while cementation causes a porosity loss of approximately 10%. Therefore, mechanical compaction is the most significant diagenetic process affecting the quality of sandstone reservoirs in the study area and is also one of the primary reasons for their tightness.

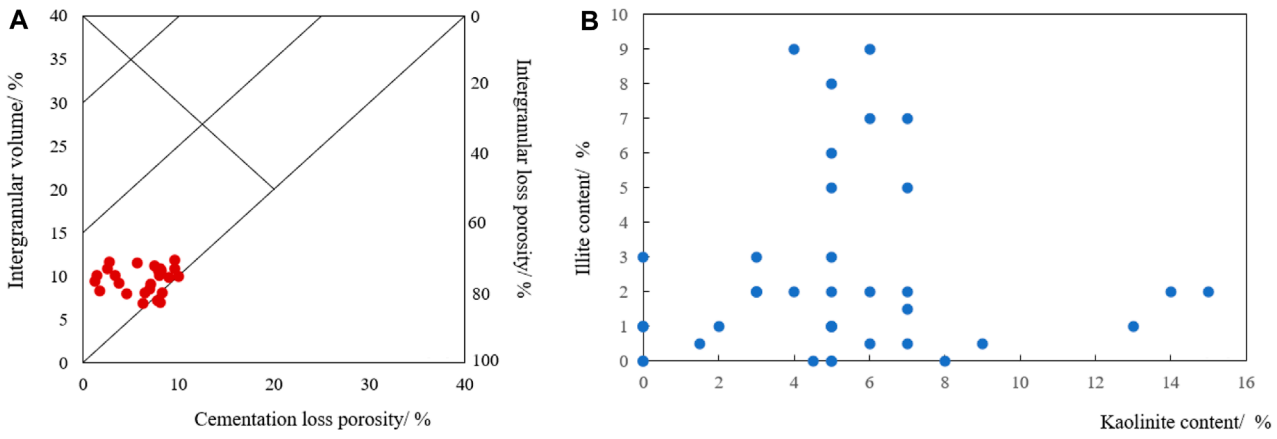

FIGURE 12
(A) Evaluation of the effect of cementation and compaction on porosity; **(B)** Correlation diagram between kaolinite and illite.

5.2.3 Silica cementation is the root cause of blocked pore throats

During the eodiagenesis to the mesodiagenesis stages of the Benxi Formation, sub-stances such as montmorillonite, kaolinite, and feldspar in the original sediments un-dergo mineral transformation and quartz grain dissolution due to increasing temper-ature and pressure (Hu et al., 2019). This process generates a certain amount of silica cement. The silica cements are relatively stable and, after their formation, they fill pores and block channels, resulting in a reduction in the size of the original wide and elongated pore structures and a change in pore structure type, thereby reducing the reservoir's storage capacity (Li et al., 2016). The silica cements primarily originate from the following two sources:

5.2.3.1 Mineral transformation process

The Benxi Formation belongs to terrestrial-marine tidal flat deposits, predominantly occurring in immersion areas such as the intertidal zone and subtidal zone (Peng et al., 2023). During the eodiagenesis, feldspar minerals experience increased burial depth which leads to gradual elevation in temperature and pressure. The initial hydrocarbon generation takes place at the top of the Benxi Formation, resulting in the production of abundant organic acids, thereby causing a shift towards an acidic diagenetic environment. Feldspar minerals combine with hydrogen ions to generate kaolinite, siliceous components, and sodium-potassium ions. Consequently, the content of silicates increases, culminating in the formation of siliceous cement after saturation. The chemical formula for the conversion of orthoclase feldspar into kaolinite is depicted as Eq. 5 (Li, Y et al., 2020):

$$2KAlSi_3O_8(F) + 2H^+ + H_2O \rightarrow Al_2Si_2O_5(OH)_4(K) + 4SiO_2 + 2K^+ \quad (5)$$

Significant dissolution of orthoclase feldspar only occurs when the temperature exceeds 90°C. At temperatures above 130°C, reaction between kaolinite and orthoclase feldspar takes place, resulting in the release of SiO_2, which aligns with the results obtained from fluid inclusion thermometry. The reaction can be described as Eq. 6 (Li et al., 2020):

$$Al_2Si_2O_5(OH)_4(K) + KAlSi_3O_8(F) \rightarrow KAlSi_3O_{10}(OH)_2(I) + 2SiO_2 + H_2O \quad (6)$$

In this reaction, kaolinite and orthoclase feldspar convert into illite and free SiO_2. The phenomenon of kaolinite illitization, accompanied by the presence of authigenic quartz grains, can be observed in Figure 13A, B. Moreover, the negative correlation between kaolinite and illite (Figure 12B), as well as the presence of data points exceeding 130°C in fluid inclusion thermometry results, provide evidence for this outcome.

During the mesodiagenesis, the second phase of hydrocarbon generation takes place in the upper coal layers of the Benxi Formation, resulting in the abundant release of organic acids. Illite is unstable and under high temperature and pressure conditions, it undergoes reverse transformation to become kaolinite. This phenomenon explains the higher content of kaolinite and lower content of feldspar minerals and illite in the Benxi Formation strata within the study area (Table 4).

5.2.3.2 Pressure dissolution of quartz particles

Pressure-solution provides a significant supply of silica for siliceous cementation, serving as a primary factor in secondary quartz overgrowth and interpenetration between particles (Figure 14A). In the study area, the burial depth of the Benxi Formation ranges from 2300 to 3400 m. With increasing temperature and pressure conditions, the pressure exerted on quartz grain contacts by overlying layers or laterally by tectonic stress exceeds the normal pore fluid pressure (Figure 14B). As a result, the solubility of quartz grain contacts increases, leading to lattice deformation and dissolution. The dissolved silica migrates with the pore water flow. When the pore water flows through low-pressure zones (Figure 14C), the reduced solubility of silica promotes crystal precipitation, resulting in the deposition of siliceous cement in intergranular pores.

10.3389/feart.2024.1377738

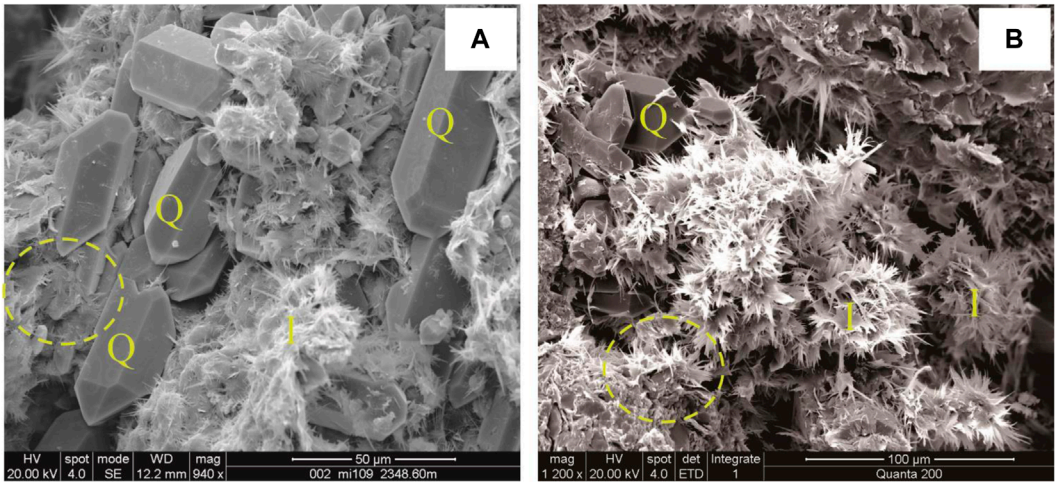

FIGURE 13
Kaolinite converts to illite and produces authigenic quartz. **(A)** Well M109, 2342m, SEM; **(B)** Well M128, 2042m, SEM. Q=Quartz, I=Illite.

TABLE 4 Clay mineral content table of different layers in the study area.

Stratum	Kaolinite	Illite	Chlorite	Reticulated clay	Total	Sample number
He 8	1.97	6.99	1.71	0.07	10.74	970
Shan 1	2.27	7.13	1.19	0.004	10.59	262
Shan 2	2.03	6.23	0.27	0.2	8.73	380
Taiyuan	1.03	9.77	0.36	0.04	11.2	142
Benxi	4.6	2.17	0.08	0	6.85	124

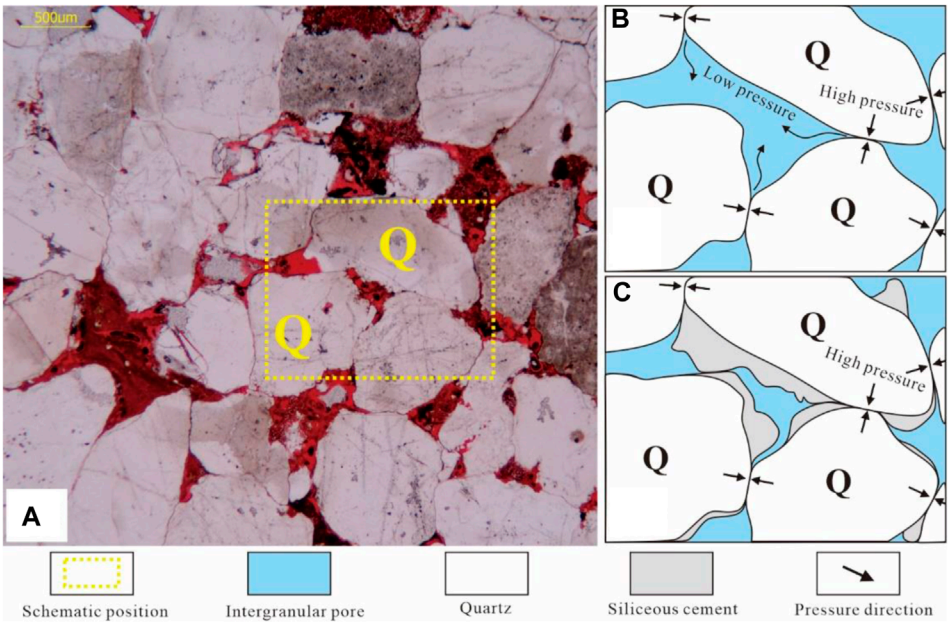

FIGURE 14
Micrographs showing compaction of quartz grains from the Benxi Formation. **(A)** Residual Intergranular Pores, Well M52, 2018m, (~); **(B)** Original contact state of quartz particles; **(C)** The current state of quartz particles. Q=Quartz.

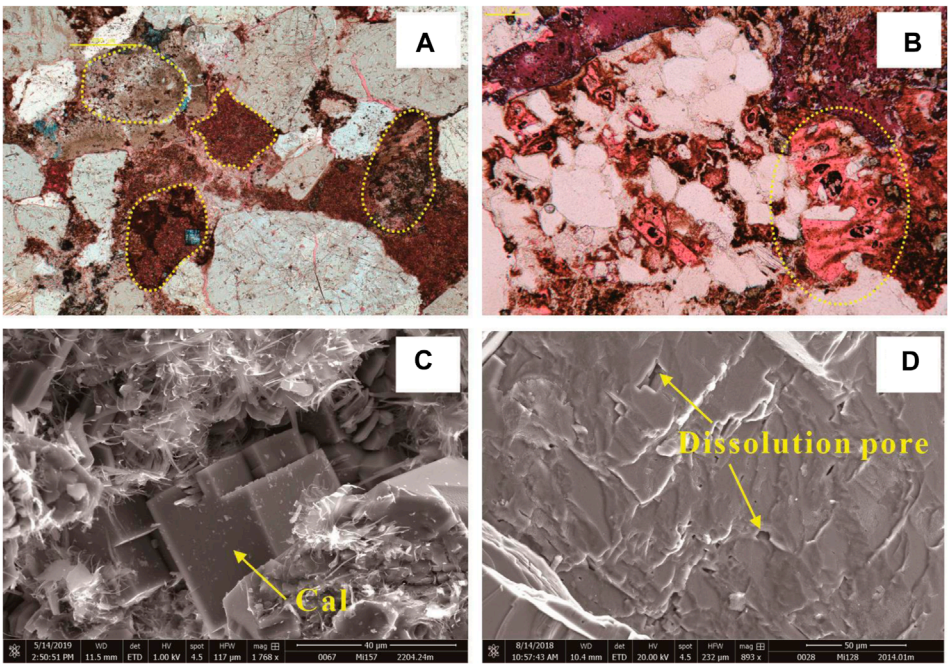

FIGURE 15
Micrographs showing compaction of quartz grains from the Benxi Formation. **(A)** Debris dissolution and cementation filling, Visible particle boundary morphology, Well M157, 2201 m, (~); **(B)** Late cementation is eroded, Well M110, 2101 m, (~); **(C)** The filling of calcite from pig iron can be seen in some pores, Well M157, 2204.24 m, SEM; **(D)** Residual Intergranular Pores, Well M128, 2014 m, SEM. Cal=Calcite.

5.2.4 Multi-phase dissolution is an important factor in reservoir porosity enhancement

For the majority of reservoirs, dissolution plays a crucial role in improving reservoir properties, and the secondary pores generated by dissolution are an important component of the rock storage space (Yuan et al., 2015). In the Benxi Formation, the thick coal rocks at the top act as the primary source of natural gas. During the process of coal generation and hydrocarbon expulsion, the organic acids produced infiltrate into the reservoir, creating a significant number of secondary pores. Fluid inclusion data from quartz overgrowths in the Benxi Formation indicate that the reservoir underwent two periods of gas charging, occurring at temperatures of 120~130°C and 150~160°C, respectively (Figure 8).

During the early stage of diagenesis, when the paleotemperature ranged from 120 to 130°C, the Benxi Formation experienced compaction to a lesser extent due to the high quartz content in the detrital materials, thereby preserving residual intergranular pores. Organic acids generated during this period entered the reservoir through these residual intergranular pores, causing dissolution of unstable feldspar and lithic fragments, resulting in the formation of secondary pores. Some of these secondary pores were later filled by subsequent mud or carbonate cementation (Figures 15A–C).

During the middle stage of diagenesis, when the paleotemperature reached 150~160°C, the Benxi Formation entered the B-stage of mesodiagenesis. The detrital materials underwent early mechanical compaction, followed by siliceous cementation in the intermediate stage, and late mud and iron carbonate cementation, leading to reservoir densification. During this period, the organic acids produced by coal rocks dissolved the later cements, creating a significant number of secondary pores, thus providing favorable storage space for natural gas accumulation (Figure 15D).

By using the dissolution porosity calculation formula Eqs 7, 8, it is estimated that the increased porosity due to dissolution in the Benxi Formation in the study area accounts for approximately 30%–40% of the total pore volume. Meanwhile, the primary intergranular porosity in the Benxi Formation accounts for only about 10%–20% of the total pore volume (Figure 16). This indicates that dissolution pores are the main reservoir space in the pore system of the Benxi Formation.

$$Vkx = Vrs + Vlj + Vqt \tag{7}$$

$$\Phi rs = ((Vrs)/Vkx) \times 100\% \tag{8}$$

Φ—Original pore volume; Φrs—Dissolution porosity; Vrs—Dissolution pore volume; Vlj—Intergranular pore volume; Vqt—Other pore volume; Vkx—total pore volume.

5.3 Comparative analysis

The reservoir quality of tight sandstone formations exhibits significant variations, as observed through a comparative analysis of different basins. It has been observed that the larger the grain size of tight sandstone reservoirs, the better their reservoir

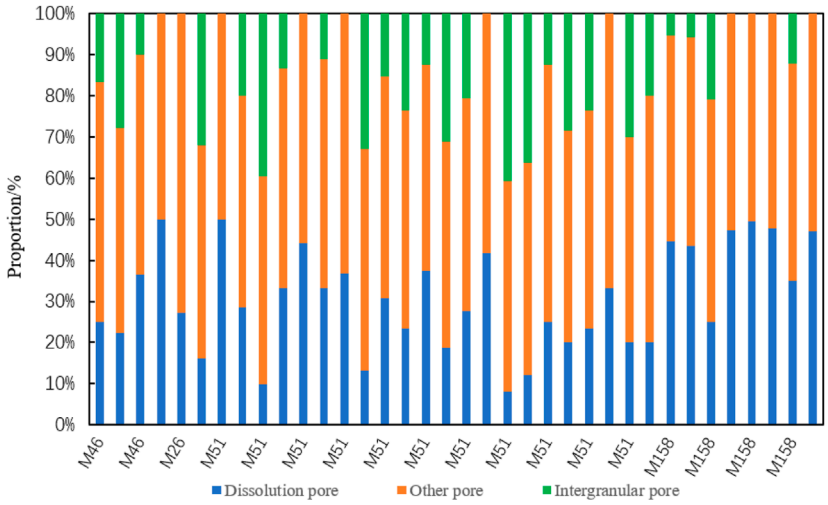

FIGURE 16
Percentage diagram of dissolved pore and intergranular pore.

TABLE 5 Reservoir quality differences of tight sandstone gas reservoirs in different basins.

Area	Reservoir type	Reservoir quality		Source
		Porosity (%)	Permeability ($\times10^{-3}$ μm^2)	
SichuanBasin, China	Fine and coarse grains	0.79~10.53	0.1	Huang et al. (2022)
Ordos Basin, China	Medium and coarse grains	0.23~13.77	1.35	This study
Tarim Basin, China	Fractured reservoir	2~8	0.1	Wang, J. P et al. (2023)
Yinggehai Basin, China	Medium grain	1.97~14.51	1.79	Zhao, X. B et al. (2022)
Songliao Basin, China	Argillaceous siltstone and sandstone	1.40~8.90	0.22	Xu, Z. J et al. (2020)

quality (Figures 9A, B). Additionally, if fractures form within the reservoir, the reservoir quality further improves. Fractures serve as favorable natural storage spaces for natural gas, with higher porosity and permeability compared to other types of reservoirs (Table 5).

5.4 Limitations

Although various methods and approaches were employed in this study, there are some limitations to be acknowledged. In the discussion of dissolution processes, the lack of experiments specifically focusing on organic acids was due to experimental constraints. Hence, only macroscopic descriptions of the dissolution effects from the two stages of acid leaching were provided, without quantitative characterization. Furthermore, the inclusion of experimental results from CT scans in the description of pore space types would have provided a clearer representation of the types and quantities of pore space within the reservoir, leading to more accurate research conclusions.

6 Conclusion

(1) Benxi Formation is mainly in the middle diagenetic B stage, which mainly undergoes compaction, cementation and dissolution. The two-stage acid discharge shown by fluid inclusions proves that there is two-stage dissolution, which is the fundamental reason for the increase of reservoir porosity.
(2) Based on the initial porosity recovery model and empirical formulas for compaction-induced porosity loss from the literature, thin section porosity analysis was used to determine that the original porosity of the Benxi Formation sandstone

is 39.8%, and compaction has led to a reduction in porosity of up to 80%. Cementation has caused a porosity decrease of 1.0%–5.4%, with an average of 4.1%. Compaction is the main reason for the widespread compactness in the study area's Benxi Formation.

(3) The rock type and source rock macroscopically influence pore evolution in the study area. Coarser-grained rocks with lower mud content have better original porosity and permeability. Compared to quartz sandstone, immature lithic sandstone and lithic quartz sandstone show stronger dissolution properties.

(4) Different diagenetic processes microscopically affect pore evolution in the study area. Stronger compaction leads to fewer pore spaces, limiting the modification of reservoirs by diagenetic fluids. Acidic cements formed by calcareous cement (such as illite) promote dissolution. Additionally, alkaline cements during late diagenesis also dissolve siliceous cements. Organic acids have a positive impact on dissolution, controlled by hydrocarbon expulsion. In conclusion, diagenesis has practical significance in predicting and exploring favorable areas for natural gas in the tight sandstones of the Benxi Formation.

Data availability statement

The original contributions presented in the study are included in the article/Supplementary material, further inquiries can be directed to the corresponding author.

Author contributions

GL: Conceptualization, Methodology, Writing–original draft, Writing–review and editing. CL: Investigation, Writing–original draft. Boming Zhang: Data curation, Writing–original draft. LZ: Writing–review and editing. ZL: Data curation, Writing–review and editing. QC: Writing–review and editing.

Funding

The author(s) declare that financial support was received for the research, authorship, and/or publication of this article. This work was supported by National Natural Science Foundation of China (No. 42172154).

Conflict of interest

Authors GL, CL, and BZ were employed by China National Petroleum Corp. Author LZ was employed by Luliang Oilfield Operation Area of Xinjiang Oilfield Branch Company.

The remaining authors declare that the research was conducted in the absence of any commercial or financial relationships that could be construed as a potential conflict of interest.

Publisher's note

All claims expressed in this article are solely those of the authors and do not necessarily represent those of their affiliated organizations, or those of the publisher, the editors and the reviewers. Any product that may be evaluated in this article, or claim that may be made by its manufacturer, is not guaranteed or endorsed by the publisher.

References

Beard, D. C., and Weyl, P. K. (1973). Influence of texture on porosity and permeability of unconsolidated sand. *AAPG Bull.* 57 (2), 349–369. doi:10.1306/819A4272-16C5-11D7-8645000102C1865D

Colo n, C. F. J., Oelkers, E. H., and Schott, J. (2004). Experimental investigation of the effect of dissolution on sandstone permeability, porosity, and reactive surface area. *Geochem Cosmochim. Acta* 68 (4), 805–817. doi:10.1016/j.gca.2003.06.002

Crundwell, F. (2014). The mechanism of dissolution of minerals in acidic and alkaline solutions: Part II Application of a new theory to silicates, aluminosilicates and quartz. *Hydrometallurgy* 149 (11), 265–275. doi:10.1016/j.hydromet.2014.07.003

Dutton, S. P., and Loucks, R. G. (2010). Diagenetic controls on evolution of porosity and permeability in lower Tertiary Wilcox sandstones from shallow to ultradeep (200–6700 m) burial, Gulf of Mexico Basin, USA. *Mar. Petroleum Geol.* 27 (1), 69–81. doi:10.1016/j.marpetgeo.2009.08.008

Ehrenberg, S. (1990). Relationship between diagenesis and reservoir quality in sandstones of the Garn Formation, Haltenbanken, mid-Norwegian continental shelf. *AAPG Bull.* 74 (10), 1538–1558. doi:10.1306/0c9b2515-1710-11d7-8645000102c1865d

Ehrenberg, S., Nadeau, P., and Steen, Ø. (2009). Petroleum reservoir porosity versus depth: influence of geological age. *AAPG Bull.* 93 (10), 1281–1296. doi:10.1306/06120908163

Folk, W. (1957). A study in the significance of grain size parameters. *J. Sediment. Petrol.* 27, 3–27. doi:10.1306/74D70646-2B21-11D7-8648000102C1865D

Gao, Z. D. (2020). *Provenance analysis of Benxi Formation of upper carboniferous in Ordos Basin and distribution regularity of favorable sand bodies.* Chengdu: Chengdu University of Technology.

Hong, D. D., Cao, J., Wu, T., Dang, S. S., Hu, W. X., and Yao, S. P. (2020). Authigenic clay minerals and calcite dissolution influence reservoir quality in tight sandstones: insights from the central Junggar Basin, NW China. *Energy Geosci.* 1 (1-2), 8–19. doi:10.1016/j.engeos.2020.03.001

Hu, P., Yu, X. H., Chen, H. L., Zhao, C. F., Zhou, J. S., Han, X. Q., et al. (2019). Characteristics and a quantitative diagenetic porosity evolution mode of barrier bar sandstone reservoirs: a case study of the Benxi Formation, Yanchang exploration block, Ordos Basin. *Acta Sedimentol. Sin.* 37 (02), 390–402. doi:10.14027/j.issn.1000-0550.2018.121

Huang, Y., Wang, A., Xiao, K., Lin, T., and Jin, W. (2022). Types and genesis of sweet spots in the tight sandstone gas reservoirs: insights from the Xujiahe Formation, northern Sichuan Basin, China. *Energy Geosci.* 3 (3), 270–281. doi:10.1016/j.engeos.2022.03.007

Huoseknecht, D. W. (1987). Assessing the relative importance of compaction processes and cementation to reduction of porosity in sandstone. *AAPG Bull.* 71 (3), 633–642. doi:10.1306/9488787F-1704-11D7-8645000102C1865D

Jia, L. B., Zhong, D. K., Ji, Y. L., Zhou, Y., Liu, J. L., Mi, L. J., et al. (2019a). Architecture of tectonic sequences, depositional systems, and tectonic controls of the sedimentary fills of the riftrelated Wenchang Formation in the Lufeng Depression, Pearl River Mouth Basin, China. *Geol. J.* 54 (4), 1950–1975. doi:10.1002/gj.3272

Jia, L. B., Zhong, D. K., Sun, H. T., Zhang, C., Mo, W., Qiu, C., et al. (2019b). Sediment provenance analysis and tectonic implication of the Benxi Formation, Ordos Basin. *Acta Sedimentol. Sin.* 37 (5), 1087–1103. doi:10.14027/j.issn.1000-0550.2019.014

Li, J., Zhang, C. L., Jiang, F. J., Pei, Y., Wang, J. Y., Wang, X. R., et al. (2021). Main factors controlling the enrichment of upper caiboniferous Benxi Formation tight gas in the Ordos Basin. *Nat. Gas. Ind.* 41 (04), 30–40. doi:10.3787/j.issn.1000-0976.2021.04.004

Li, M., Hou, Y. D., Luo, J. L., Chen, J. P., Luo, X. R., and Jia, Y. N. (2016). Quantitative analysis of burial-diagenesis-hydrocarbon charging evolution process and pore evolution of tight sandstone reservoirs - a case study of natural gas reservoirs in the Upper Paleozoic He 8 Member in the eastern Ordos Basin. *Oil Gas Geol.* 37 (06), 882–892. doi:10.11743/ogg20160610

Li, Y., Xu, W. K., Wu, P., and Meng, S. Z. (2020). Dissolution versus cementation and its role in determining tight sandstone quality: a case study from the Upper Paleozoic in northeastern Ordos Basin, China. *J. Nat. Gas Sci. Eng.* 78, 103324. doi:10.1016/j.jngse.2020.103324

Lin, J., Li, Y., and He, J. (2013). An analysis of the source and the sedimentary system of the carboniferous Benxi Formation in yanchang area of Ordos Basin. *Geol. China* 40 (5), 1542–1551.

Morad, S., Al-Ramadan, K., Ketzer, J. M., and De Ros, L. (2010). The impact of diagenesis on the heterogeneity of sandstone reservoirs: a review of the role of depositional facies and sequence stratigraphy. *AAPG Bull.* 94, 1267–1309. doi:10.1306/04211009178

Panagiotopoulou, C., Kontori, E., Perraki, T., and Kakali, G. (2007). Dissolution of aluminosilicate minerals and by-products in alkaline media. *Mat. Sci.* 42 (9), 2967–2973. doi:10.1007/s10853-006-0531-8

Paxton, S., Szabo, J., Ajdukiewicz, J., and Klimentidis, R. (2002). Construction of an intergranular volume compaction curve for evaluating and predicting compaction and porosity loss in rigid-grain sandstone reservoirs. *AAPG Bull.* 86 (0), 2047–2067. doi:10.1306/61eeddfa-173e-11d7-8645000102c1865d

Peng, Z. X., Yu, X. H., Li, S. L., Qi, R., Fu, C., and Jiang, L. Y. (2023). Barrier migration patterns and controlling factors of Benxi Formation in southeastern Ordos Basin. *J. Palaeogeogr.* 25 (06), 1330–1346. doi:10.7605/gdlxb.2023.06.092

Pokrovsky, O. S., Golubev, S. V., Schott, J., and Castillo, A. (2009). Calcite, dolomite and magnesite dissolution kinetics in aqueous solutions at acid to circumneutral pH, 25 to 150 °C and 1 to 55 atm pCO2: new constraints on CO2 sequestration in sedimentary basins. *Chem. Geol.* 265 (1-2), 20–32. doi:10.1016/j.chemgeo.2009.01.013

Scherer, M. (1987). Parameters influencing porosity in sandstones: a model for sandstone porosity prediction. *AAPG Bull.* 71 (5), 485–491. doi:10.1306/94886ed9-1704-11d7-8645000102c1865d

Taylor, T. R., Giles, M. R., Hathon, L. A., Diggs, T. N., Braunsdorf, N. R., Birbiglia, G. V., et al. (2010). Sandstone diagenesis and reservoir quality prediction: models, myths, and reality. *AAPG Bull.* 94 (8), 1093–1132. doi:10.1306/04211009123

Wang, F., Liu, X. C., Deng, X. Q., Li, Y. H., Tian, J. C., Li, S. Y., et al. (2017). Geochemical characteristics and environmental implications of trace elements of Zhifang Formation in Ordos Basin. *Acta Sedimentol. Sin.* 35 (6), 1265–1273. doi:10.14027/j.cnki.cjxb.2017.06.017

Wang, J., Zhang, C. L., and Li, J. (2021a). Tight sandstone gas reservoirs in the Sulige gas field: development understandings and stable production proposals. *Nat. Gas. Ind.* 41 (02), 100–110. doi:10.3787/j.issn.1000-0976.2021.02.012

Wang, J. P., Wang, H. Y., Zhang, R. H., Li, D., Wang, K., and Zhang, Z. Y. (2023). Improvement of reservoir quality of ultra-deep tight sandstones by tectonism and fluid: a case study of Keshen gas field in Tarim Basin, western China. *Petroleum* 9 (1), 124–134. doi:10.1016/j.petlm.2023.01.002

Wang, J. Y., Jiang, F. J., Zhang, C. L., Song, Z. Z., and Mo, W. L. (2021b). Study on the pore structure and fractal dimension of tight sandstone in coal measures. *Energy Fuel* 35, 3887–3898. doi:10.1021/acs.energyfuels.0c03991

Wang, X., Hou, J., Li, S., Dou, L., Song, S., Kang, Q., et al. (2020a). Insight into the nanoscale pore structure of organic-rich shales in the Bakken Formation, USA. *J. Petroleum Sci. Eng.* 176, 107182–107320. doi:10.1016/j.petrol.2020.107182

Wang, X., Liu, Y., Hou, J., Li, S., Kang, Q., Sun, S., et al. (2020b). The relationship between synsedimentary fault activity and reservoir quality — a case study of the Ek1 formation in the Wang Guantun area, China. *China. Interpret.* 8, sm15–sm24. doi:10.1190/INT-2019-0131.1

Wang, X., Yu, S., Li, S., and Zhang, N. (2022). Two parameter optimization methods of multi-point geostatistics. *J. Petroleum Sci. Eng.* 208, 109724. doi:10.1016/j.petrol.2021.109724

Wang, X., Zhang, F., Li, S., Dou, L., Liu, Y., Ren, X., et al. (2021c). The architectural surfaces characteristics of sandy braided river reservoirs, case study in gudong oil field, China. *Geofluids* 2021, 1–12. doi:10.1155/2021/8821711

Xu, Z. J., Jiang, S., Liu, L. F., Wu, K. J., Li, R., Liu, Z. Y., et al. (2020). Natural gas accumulation processes of tight sandstone reservoirs in deep formations of Songliao Basin, NE China. *J. Nat. Gas Sci. Eng.* 83, 103610. doi:10.1016/j.jngse.2020.103610

Yuan, G. H., Cao, Y. C., Gluyas, J., Li, X. Y., Xi, K. L., Wang, Y. Z., et al. (2015). Feldspar dissolution, authigenic clays, and quartz cements in open and closed sandstone geochemical systems during diagenesis: typical examples from two sags in Bohai Bay Basin, East China. *AAPG Bull.* 99 (11), 2121–2154. doi:10.1306/07101514004

Zhang, C. L., Sun, W., Gao, H., Xi, T. D., He, Q. Y., Shi, J. C., et al. (2014). Quantitative calculation of sandstone porosity evolution based on thin section data: a case study from Chang 8 reservoir of Huanjiang Area, Ordos Basin. *Acta Sedimentol. Sin.* 32 (02), 365–375. doi:10.14027/j.cnki.cjxb.2014.02.021

Zhao, X. B., Yao, G. Q., Chen, X. J., Zhang, R. X., Lan, Z. J., and Wang, G. C. (2022). Diagenetic facies classification and characterization of a high-temperature and high-pressure tight gas sandstone reservoir: a case study in the Ledong area, Yinggehai Basin. *Mar. Petroleum Geol.* 140, 105665. doi:10.1016/j.marpetgeo.2022.105665

Zhong, D. K., Zhu, X. M., Zhou, X. Y., and Wang, Z. M. (2007). An approach to categories and mechanisms of SiO2 dissolution in sandstone reservoirs in the Tarim Basin. *Chin. J. Geol. Geol. Sinica* 42 (02), 403–414.

frontiers | Frontiers in Earth Science

TYPE Original Research
PUBLISHED 13 March 2024
DOI 10.3389/feart.2024.1371358

Check for updates

OPEN ACCESS

EDITED BY
Xixin Wang,
Yangtze University, China

REVIEWED BY
Lei Gong,
Northeast Petroleum University, China
Yu Liu,
China University of Mining and Technology, Beijing, China

*CORRESPONDENCE
Xiaodong Lan,
lansecup@163.com

RECEIVED 16 January 2024
ACCEPTED 15 February 2024
PUBLISHED 13 March 2024

CITATION
Lan X, Bai Z, Yang Y, Jiang Z and Zhang J (2024), Source and geological significance of Jurassic asphalt in the Ruoqiang Sag of Southeast Depression, Tarim Basin, Northwestern China.
Front. Earth Sci. 12:1371358.
doi: 10.3389/feart.2024.1371358

COPYRIGHT
© 2024 Lan, Bai, Yang, Jiang and Zhang. This is an open-access article distributed under the terms of the Creative Commons Attribution License (CC BY). The use, distribution or reproduction in other forums is permitted, provided the original author(s) and the copyright owner(s) are credited and that the original publication in this journal is cited, in accordance with accepted academic practice. No use, distribution or reproduction is permitted which does not comply with these terms.

Source and geological significance of Jurassic asphalt in the Ruoqiang Sag of Southeast Depression, Tarim Basin, Northwestern China

Xiaodong Lan[1]*, Zhongkai Bai[2], Youxing Yang[2], Zhenglong Jiang[1] and Jile Zhang[1]

[1]School of Ocean Sciences, China University of Geosciences, Beijing, China, [2]Oil and Gas Survey, China Geological Survey, Beijing, China

The Southeast Depression of the Tarim Basin has a very low petroleum exploration degree, and currently, no industrial oil and gas have been discovered. Many hydrocarbon shows exist in the Ruoqiang Sag, where hydrocarbon sources and accumulation processes are unclear. Only two potential Jurassic hydrocarbon source rocks developed in the Ruoqiang Sag, the Yangye (J_2y) lacustrine mudstone of the Middle Jurassic and the Kangsu (J_1k) coal-bearing mudstone of the Lower Jurassic. In this study, the Jurassic asphalt found in the QD1 well, combined with the source rocks of drilling cores and outcrops, was used to explore the possible hydrocarbon source and forming process in the Ruoqiang Sag using oil-source correlation and hydrocarbon accumulation geochronology methods. The asphalts have lower light and heavy rare earth fractionation than the J_2y mudstone, and the total rare earth element (ΣREE) content, chondrite-normalized curves, and δEu and Y/Ho values are similar to those of the J_1k mudstone, especially for the J_1k coal. The *n*-alkane ratios of the carbon preference index and the odd-to-even preference (OEP) of Jurassic asphalts are greater than 1.0, indicating that its source rock has experienced low thermal evolution. All Jurassic samples have similar source-related biomarkers but different maturity-related parameters, and the thermal evolution degree of asphalt is close to the J_1k mudstone and coal but slightly higher than the J_2y mudstone. Meanwhile, rhenium–osmium isotopes show the asphalts are formed in 192+30/−45 Ma, which is similar to the J_1k sedimentation time. The asphalts contain coal macerals and probably derived from the asphaltene precipitated by the J_1k coal during the early coalification. The low abundance of 25-norbornanes with a non- or slight petroleum biodegradation degree indicates the asphalt was generated relatively late and migrated into the J_2y formation along the faults, possibly accompanied by the striking activities of the Altyn Tagh Fault during the Neotectonics movement. This study provides evidence for the J_1k coal-bearing strata serving as the effective source rock in the Ruoqiang Sag and increases confidence for Jurassic petroleum exploration in the Southeast Depression of the Tarim Basin. The structural and lithological traps near hydrocarbon source stoves, where Jurassic strata were

deeply buried and far from the Altyn Tagh Range, are favorable oil and gas exploration targets.

KEYWORDS

Ruoqiang Sag, Jurassic source rock, asphalt, hydrocarbon accumulation, Re-Os isotopic dating

1 Introduction

The Tarim Basin (Figure 1A) is the largest inland hydrocarbon-bearing basin in China, and it has great potential for petroleum exploration. The Southeast Depression of the Tarim Basin is located in the southeast of the Tarim Basin, covering an area of approximately 100,000 km^2, and has no industrial oil and gas accumulations. Up to now, only eight wells have been drilled, and two wells have obtained oil and gas, both in the Jurassic strata. A 30-m gas logging anomaly was found in the Jurassic of the RC1 well, and the QD1 well drilled Jurassic asphalt in 2016. Meanwhile, the Ruoqiang Sag has active hydrocarbon shows in the Jurassic outcrops, such as Qiemo Coalmine, Qigeleke, Ashahantuohai, and Jianggelesayi, which are oil seeds, oil traces, and asphalt veins (Chen and Hu, 1996). Previous studies on the Jurassic strata mainly focused on sedimentary characteristics, stratigraphic sequences, tectonic evolution, and petroleum geological conditions (Wang et al., 2000). The oil-source correlation was analyzed with Jurassic oil seeds and oil sands found in the Ruoqiang Sag (Xu et al., 1994; Chen and Hu, 1996). However, the few studies carried out on the regional source rock and hydrocarbon accumulation, which suggested that the source rock was from the Ordovician or directly from the J_2y lacustrine mudstone (Huang et al., 2013), were controversial. With the investment in regional petroleum exploration in recent years, the seismic work and drilling wells have revealed that the Jurassic is thick with a maximum sedimentary thickness of more than 1500 m, and Jurassic source rocks of J_1k and J_2y formations are good quality and well-developed in the outcrops and drilling wells. Many Jurassic asphalts were drilled in the QD1 well and are evidence of oil and gas generation, migration, and hydrocarbon accumulation, and can provide important research materials for regional petroleum geology.

The asphalt contains a large amount of heavy organic matter that can be analyzed for oil and source comparison and hydrocarbon accumulation by organic and inorganic geochemical methods, such as carbon isotopes, biomarkers, and main and trace elements (Moldowan et al., 1985; Curiale, 1986; Jacob, 1989; Hwang et al., 1998; Guckert and Mossman, 2003; Liao et al., 2015). The asphaltene of crude oils has over 90% of Re and Os elements due to their organophilic characteristics (Mahdaoui et al., 2013) and almost represents the entire crude oil isotopic composition of Re and Os (Selby et al., 2007). The organic-rich geological samples related to hydrocarbon accumulation, such as source rocks and asphalt, can be directly tested and analyzed by Re and Os isotope dating for petroleum accumulation geochronology (Selby and Creaser, 2005; Liu et al., 2018; Ge et al., 2020; Wu et al., 2021). In this study, the asphalts were researched to explore the possible hydrocarbon sources and accumulation processes in the Ruoqiang Sag, combined with the source rocks of the drilling core and outcrops.

2 Regional geology

The Southeast Depression of the Tarim Basin is distributed in a northeast-to-southwest direction (Figure 1A), adjacent to the Tadong Low Rise and Tangguzibas Sag bounded in the north by the Cherchen Fault (Figure 1B). It borders the Tiekelike Upfaulted Zone, the Altyn Tagh Range, and the Qaidam Basin by the left-lateral Altyn Fault in the south. The depression is divided into four secondary tectonic units, which are Minfeng Sag, Jiemo High, Ruoqiang Sag, and Luobuzhuang High from west to east. The Ruoqiang Sag is located in the central-eastern section of the depression and bounded by the Cherchen Fault in the north and the Altyn Tagh Range in the south. The sag is nearly diamond shaped, with an area of approximately 0.255 million square kilometers.

The three QD1, RC1, and RC2 wells are drilled in the Ruoqiang Sag (Figure 1B), and all encounter the Jurassic strata. From bottom to top, the regional strata exposed by outcrops and drilling wells are the Proterozoic, Jurassic, Cretaceous, Paleocene, Neoproterozoic, and Quaternary, with a large number of strata missing from Cambrian to Triassic. The Proterozoic has the main lithology of the variegated granite and dark gray gabbro. The Jurassic deposited above the Paleozoic basement with a set of coal-bearing sediments, including the fluvial and lacustrine facies, and is divided into Shalitash (J_1s) and Kangsu (J_1k) formations of the Lower Jurassic, Yangye (J_2y) and Targa (J_2t) formations of the Middle Jurassic (Figure 2), and a Kuzigongsu (J_3k) Formation of the Upper Jurassic from bottom to top.

During the strong faulting period of the Early Jurassic (Wang et al., 2005), the J_1s strata rapidly deposited along the marginal faults NE toward the Ruoqiang Sag as an alluvial fan or braided-river delta and have the lithology of gray conglomerate and sandstone sandwiched with gray siltstone. In the late Early Jurassic, the J_1k strata deposited a set of coal-bearing sediments with the sedimentary facies of braided-river delta and shallow coastal lakes (Ritts and Biffi, 2000; Yue et al., 2004). The J_1k lithology is characterized by conglomerate, coarse to fine sandstone, gray-black carbonaceous mudstone, and coal. During the Middle Jurassic, the paleo-lacustrine basin continued to expand, and the J_2y strata were deposited under a hemi-deep or deep lake environment (Cheng et al., 2008). The J_2y lithology is sandstone and mudstone interbedded with varying thicknesses, interbedded with dark mudstone and carbonaceous mudstone. However, the climate became hot and arid in the late Middle Jurassic, and the J_2t developed fluvial or fan-deltaic facies sediments (Li, 1998), mainly composed of purple-red sandstone and conglomerate with a thickness of 277–302.7 m. As the Upper Jurassic, the J_3k strata have been eroded, and the residual thickness is relatively thin with the lithology of purple-red or brownish-red sandstone and mudstone. In the Late Jurassic, the Lhasa terrane collided with

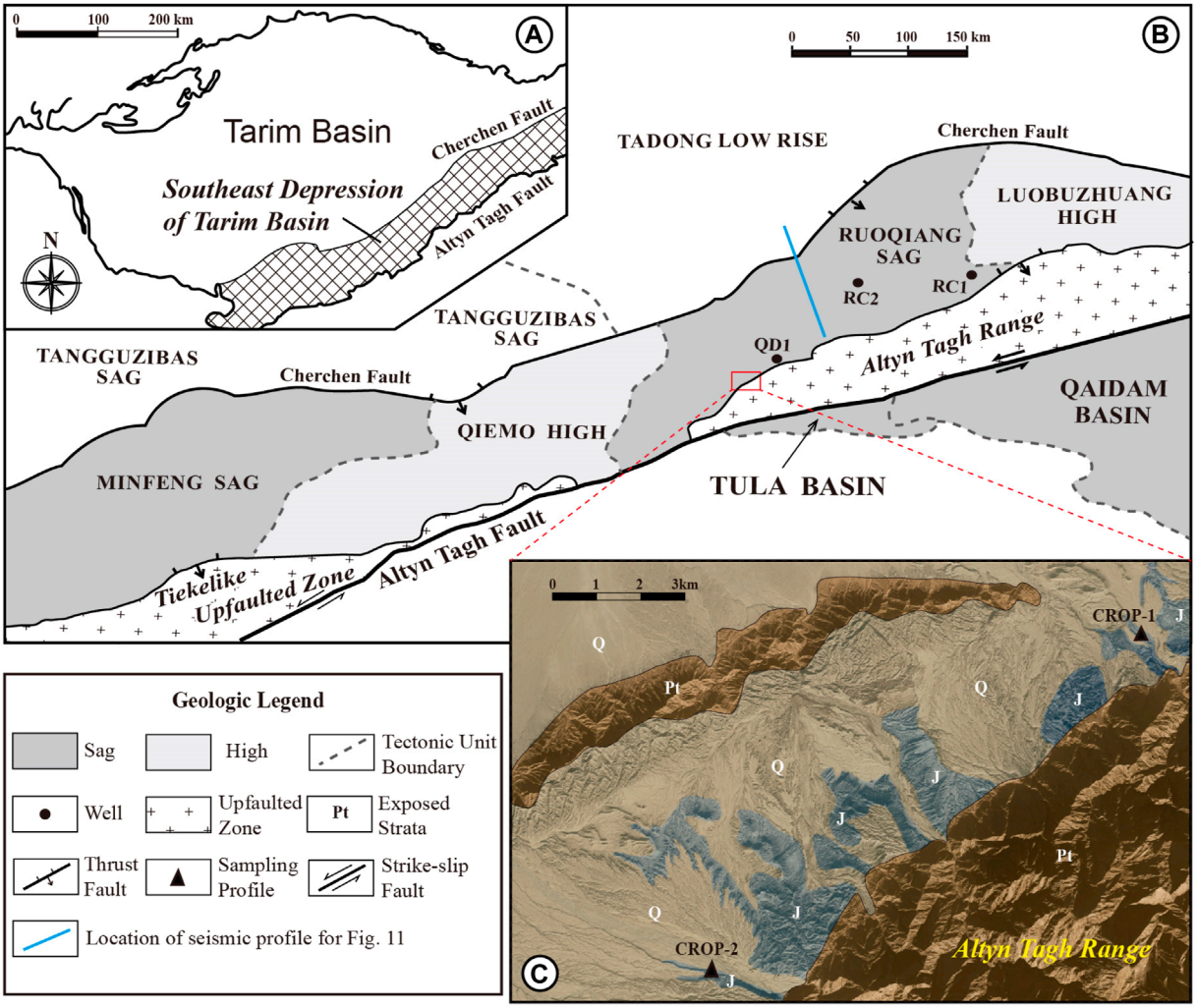

FIGURE 1
Map of the study area showing the location of Ruoqiang Sag, outcrops, and strata. **(A)** Location of the Southeast Depression of the Tarim Basin; **(B)** tectonic units of the Southeast Depression of the Tarim Basin and wells in the Ruoqiang Sag; **(C)** location of three outcrops in this study.

the Qiangtang terrane (Li et al., 2002; Liu et al., 2003), resulting in the overall Southeast Depression of the Tarim Basin uplifting with extensive absence of syn-depositional sediments. The Lower Cretaceous has a restricted distribution and is composed of red medium-coarse-grained clasolite. The Cenozoic strata are a set of sandstone and mudstone deposits of braided fluvial facies (Cheng et al., 2008) and in angular unconformable contact with the underlying strata, with a thickness of less than 3,914 m. The Quaternary is mainly composed of thin aeolian sediments. From the perspective of lithology and burial depth, the regional hydrocarbon sources can only come from the J_1k and J_2y formations.

3 Samples and methods

Twenty-five source rock samples and five asphalt samples shown in Figure 2 were collected and marked. The source rock samples include 16 drilling cores (marked from QD-1 to QD-16) and nine outcrop samples, six from Outcrop-1 (marked from C1-1 to C1-6) and three from Outcrop-2 (marked from C2-1 to C2-3), among which the C1-6 is only J_1k coal sample collected from Outcrop-1 (Figure 1C). The others were mudstone, including the 15 J_2y and 9 J_1k samples. In order to ensure the purity of the asphalt, the asphalt samples were selected from the fractures of the Yangye Formation in the QD1 well and marked from SA-1 to SA-5.

Four experiments were completed in the State Key Laboratory of Oil and Gas Resources and Prospecting of China University of Petroleum (Beijing). Two asphalt samples were polished and analyzed for macerals and vitrinite reflectance using DM4P-Leica DM 4 P& MSP9000C polarization microscopes. Organic carbon content and rock pyrolysis experiments on 25 samples were done with a Leco CS230 analyzer and an OGE-II oil and gas pyrolyzer, respectively. A 20-g powdered sample was slowly mixed with excess HCl; heated to 80°C to remove the inorganic carbon;

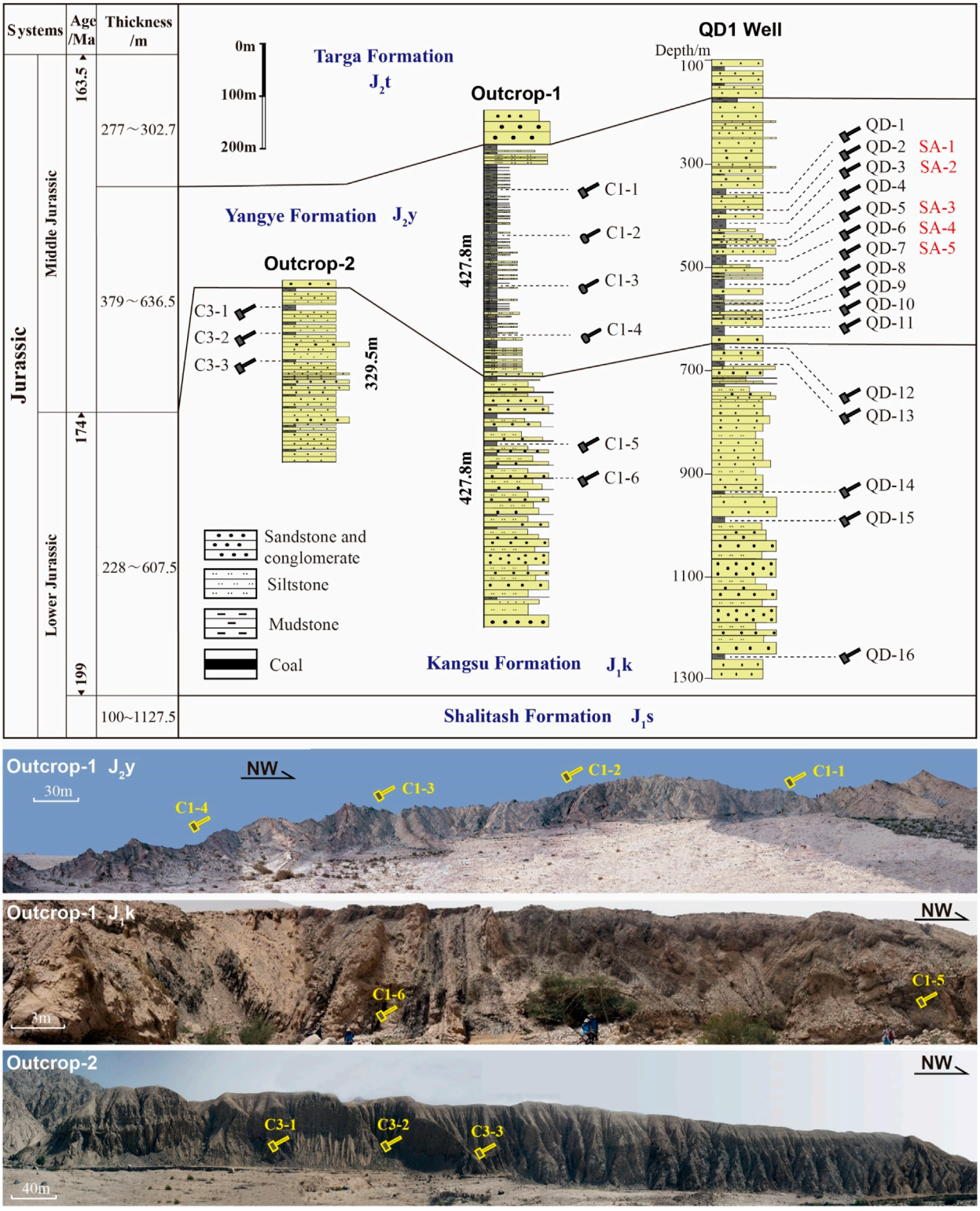

FIGURE 2
Jurassic lithology histogram and samples in the QD1 well and two outcrops. Source rock samples are marked with black and yellow in the outcrop photos, while asphalt samples are marked in red with the same depths as the source rock samples in front of them.

and then washed, dried, and placed in the carbon and sulfur analyzer for organic carbon determination. The rock pyrolysis experiments were completed in the OGE-II oil and gas evaluator. The hydrocarbons emitted from the powdered samples during the pyrolysis process were detected in the carrier gas stream using a hydrogen flame ionization detector. Six samples were

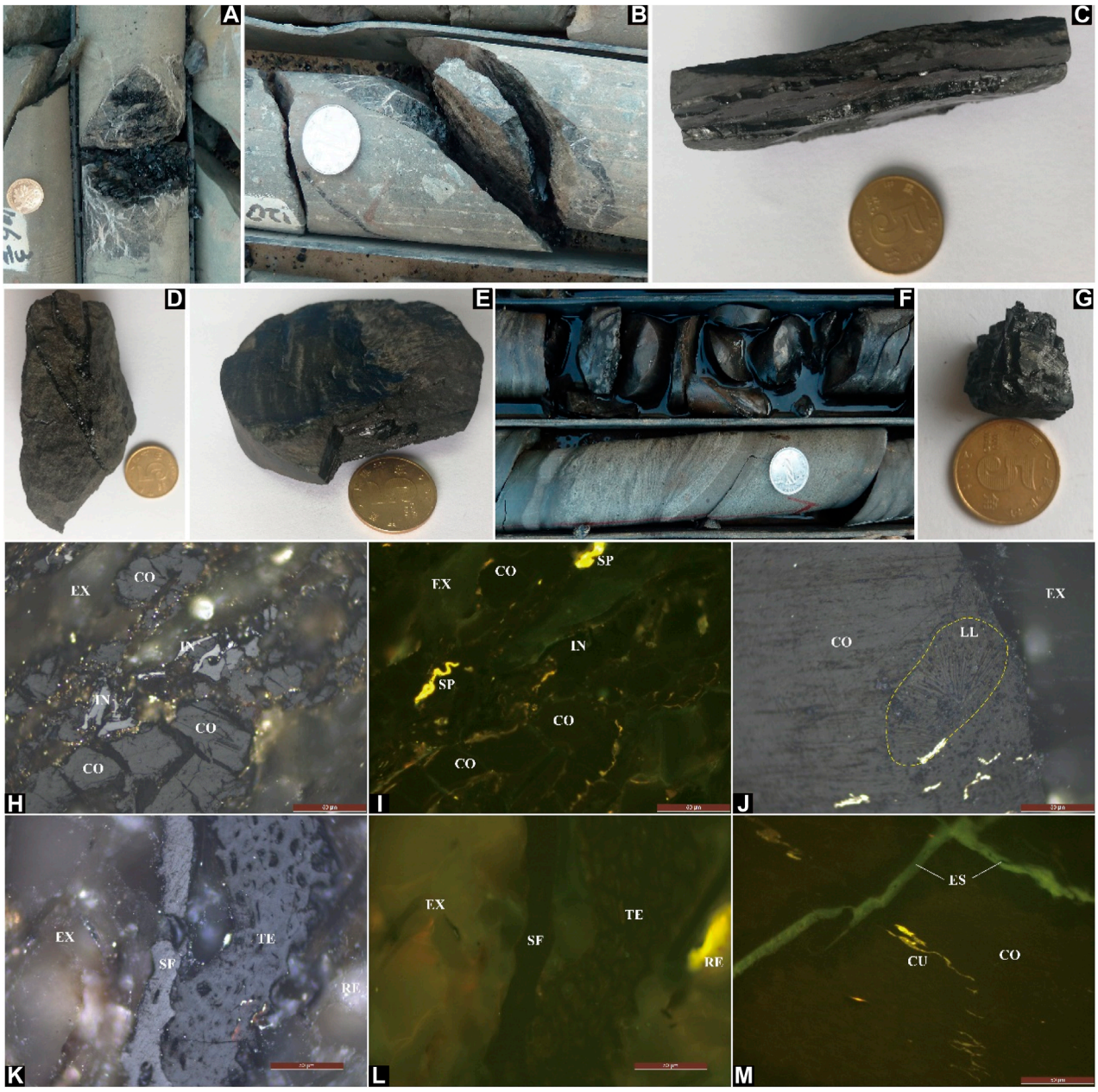

FIGURE 3
Jurassic asphalt photographs in the cores and under the microscope. The core photographs of **(A–G)** are from QD1 depth sections of 229.4 m, 363.7 m, 431.0 m, 425.7 m, 496.3 m, 459.5 m, and 366.0 m, respectively. Photographs of **(H, J, K)** are taken under oil-immersed reflected light, while ultraviolet light is used to take the photographs of **(I, L, M)**. The **(J–M)** are from Sample SA-3, while **(H, I)** are from Sample SA-4. The shown maceral components include exinite (EX), collinite (CO), sporophyte (SP), leaf lobes (LL), semifusinite (SF), telinite (TE), cutinite (CU), exsudatinite (ES), and resinite (RE).

subjected to a gas chromatography-mass spectroscopy (GC-MS) experiment, including one J_1k coal and one J_1k mudstone, two J_2y mudstones, and two J_2y asphalt samples. The saturate fraction was performed on a Thermo Fisher Trace-DSQII instrument with an HP-5MS fused silica column (60 m × 0.25 mm × 0.25 μm). The initial temperature was held at 50°C for 1 min, programmed to increase to 100°C at 15°C/min, then to 200°C at 2°C/min, 315°C at 1°C/min, and held for 20 min. The flow rate of carrier gas was 1 mL/min.

Rare earth element analyses of eight samples, including two asphalts of 1 J_2y and 1 J_1k, one J_1k coal, three J_2y mudstone, and two J_1k mudstone samples, were done in the Beijing Institute of Nuclear Industry Geology. A 0.05 g powdered sample was placed in a closed sampler, and 1 mL HF and 0.5 mL HNO_3 were added, allowed to dissolve, and heated to 185°C. The mixed solution was placed on an electric heating plate for evaporation and then sealed with nitric acid for dissolution after removing hydrofluoric acid. Finally, the diluted solution was analyzed on a Thermo Scientific

10.3389/feart.2024.1371358

TABLE 1 TOC, rock-eval pyrolysis, and vitrinite reflectance data on Jurassic samples in the Ruoqiang Sag.

Sample	Lithology	Location	Depth (m)	Formation	TOC (%)	S_1 (mg/g)	S_2 (mg/g)	S_3 (mg/g)	T_{max} °C	OI	HI	S_1+S_2 (mg/g)	Ro (%)
QD-1	Mudstone	QD1 well	312.8	J_2y	4.02	0.86	10.77	2.04	422	50.77	268.04	11.63	0.34
QD-2	Mudstone	QD1 well	366.0	J_2y	2.88	1.81	21.10	4.56	424	158.61	734.02	22.91	0.33
QD-3	Mudstone	QD1 well	385.0	J_2y	4.02	1.81	21.10	4.47	424	111.25	525.21	22.91	0.37
QD-4	Mudstone	QD1 well	417.0	J_2y	5.35	0.17	25.30	1.32	416	24.69	473.25	25.47	0.36
QD-5	Mudstone	QD1 well	425.0	J_2y	9.20	2.93	15.99	1.06	408	11.52	173.85	18.92	0.38
QD-6	Mudstone	QD1 well	459.5	J_2y	3.50	0.10	14.57	0.99	425	28.33	416.88	14.67	0.37
QD-7	Mudstone	QD1 well	502.8	J_2y	4.19	0.16	27.78	1.03	412	24.58	662.85	27.94	0.37
QD-8	Mudstone	QD1 well	534.9	J_2y	7.20	0.15	28.40	1.25	425	17.36	394.44	28.55	0.33
QD-9	Mudstone	QD1 well	556.0	J_2y	4.06	0.17	25.65	1.30	410	31.99	631.15	25.82	0.38
QD-10	Mudstone	QD1 well	564.9	J_2y	1.71	0.05	3.40	1.08	420	63.16	198.83	3.45	0.34
QD-11	Mudstone	QD1 well	582.0	J_2y	4.60	0.25	33.83	1.40	413	30.43	735.43	34.08	0.41
QD-12	Mudstone	QD1 well	608.4	J_1k	1.17	0.40	6.80	0.86	430	73.50	581.20	7.20	0.39
QD-13	Mudstone	QD1 well	643.3	J_1k	4.94	0.16	21.90	1.38	425	27.92	443.14	22.06	0.42
QD-14	Mudstone	QD1 well	880.0	J_1k	1.97	0.90	6.20	0.80	433	40.69	315.36	7.10	0.45
QD-15	Mudstone	QD1 well	923.1	J_1k	11.15	0.79	43.47	2.48	413	22.24	389.87	44.26	0.42
QD-16	Mudstone	QD1 well	1,211.0	J_1k	2.97	0.03	4.15	3.58	436	120.46	139.64	4.18	0.57
C2-1	Mudstone	Outcrop-2	-	J_1k	4.67	0.03	3.32	3.28	430	70.24	71.13	3.35	0.42
C2-2	Mudstone	Outcrop-2	-	J_1k	1.12	0.10	3.38	3.16	438	282.14	301.61	3.48	0.43
C2-3	Mudstone	Outcrop-2	-	J_1k	1.11	0.05	3.20	2.78	420	251.58	289.14	3.24	0.45
C1-1	Mudstone	Outcrop-1	-	J_2y	4.42	0.06	4.71	4.00	436	90.44	106.50	4.77	0.37
C1-2	Mudstone	Outcrop-1	-	J_2y	4.58	0.07	6.22	4.86	435	106.06	135.75	6.29	0.36
C1-3	Mudstone	Outcrop-1	-	J_2y	3.97	0.04	3.83	3.73	435	93.89	96.41	3.87	0.37

(Continued on the following page)

TABLE 1 (*Continued*) TOC, rock-eval pyrolysis, and vitrinite reflectance data on Jurassic samples in the Ruoqiang Sag.

Sample	Lithology	Location	Depth (m)	Formation	TOC (%)	S_1 (mg/g)	S_2 (mg/g)	S_3 (mg/g)	T_{max} °C	OI	HI	S_1+S_2 (mg/g)	Ro (%)
C1-4	Mudstone	Outcrop-1	-	J_2y	3.83	0.05	4.79	3.22	434	84.04	125.02	4.84	0.41
C1-5	Mudstone	Outcrop-1	-	J_1k	1.25	7.78	2.25	1.48	430	118.68	180.19	10.02	0.38
C1-6	Coal	Outcrop-1	-	J_1k	23.00	1.35	71.25	4.73	423	20.57	309.78	72.60	0.49
SA-3	Asphalt	QD1 well	425.0	J_2y	-	-	-	-	-	-	-	-	0.41
SA-4	Asphalt	QD1 well	459.5	J_2y	-	-	-	-	-	-	-	-	0.54

S_1-free hydrocarbons; S_2-hydrocarbons from pyrolysis of kerogen; S_3-release of trapped CO_2; Ro is the average vitrinite reflectance from 40 measurement points; OI, $S_3\times100$/TOC; HI, $S_2\times100$/TOC.

high-resolution inductively coupled plasma mass spectrometer of ELEMENT XR, and the rare earth element content was calculated with the external standard method.

The rhenium–osmium isotopes of asphalt were tested using the same five samples (SA-1 to SA-5) in two laboratories. Five samples (marked from SA-1_d to SA-5_d) were tested at Durham University, United Kingdom, and six samples (marked from SA-1_c to SA-5_c; SA-3_c was further divided into two parts and labeled as SA-3_{c1} and SA-3_{c2}) were tested in the National Geological Experimental Test Center of the Chinese Academy of Geological Sciences. The asphalt samples were ground into a 4~5 mm powder, 0.1–0.2 g was weighed into a Carlos tube, and reverse aqua regia (HNO_3+3 HCl) and 2 mL of 30% H_2O_2 solution were added as the dissolution reagent. After adding a certain amount of diluent, the tube was sealed. Then, the samples were dissolved with a stage heating method (first, heated to 120°C, stabilized for about 1 h; then heated to 160°C, stabilized for about 2 h; and finally raised to 200°C and stabilized for 24 h). Then, the tube was opened after freezing, and Os was separated and purified by *in situ* direct distillation and microdistillation. After that, 5 mol/L NaOH solution was added, and acetone was used to extract Re. The acetone was evaporated to dryness at low temperature, and then, HNO_3 and H_2O_2 were added to destroy the organic phase to separate the Re. The separated and purified Re and Os were measured by a Thermo Fisher Triton Plus Negative Ion Thermal Ionization Mass Spectrometer (N-TIMS).

4 Results

4.1 Maceral composition of asphalt

In the QD1 drilling core, the asphalts are filled in the fractures (Figures 3A,B) or as thin layers in the Jurassic mudstone (Figures 3C–E), and an oil slick occurs when soaked in water (Figure 3F). The fresh asphalt is bright black with visible conchoidal fractures (Figure 3G). Under the microscope, the asphalt contains three obvious groups of macerals—vitrinite, exinite, and inertinite. Overall, the macerals are mainly composed of vitrinite, especially the collinite (Figure 3H) and telinite (Figure 3K), which appear dark gray under oil-immersed reflected light and brownish-black under fluorescence. The exinite components are rich and show grayish black under oil-immersed reflected light (Figures 3H,J,K) and orange to bright yellow under fluorescence. The exinites are dominated by sporophyte (Figure 3I), cutinite (Figure 3M), and resinite (Figure 3L). The inertinite components are less abundant with fusinite and semifusinite (Figure 3K) and show grayish-white under oil-immersed reflected light (Figure 3H) and black under fluorescence (Figure 3I). Some exsudatinites are visible in cracks and residual pore cavities of the microcomponent (Figure 3M), and even fossilized plant leaf lobes (Figure 3J) and flow morphology of macerals are visible (Figures 3J,L). Therefore, the Jurassic asphalt retains the coal macerals and is related to the Jurassic coal.

4.2 Rock-eval pyrolysis

In the 25 samples (Table 1), the total organic carbon (TOC) of J_1k and J_2y are both greater than 1.0% (1.17–23.00%), making them

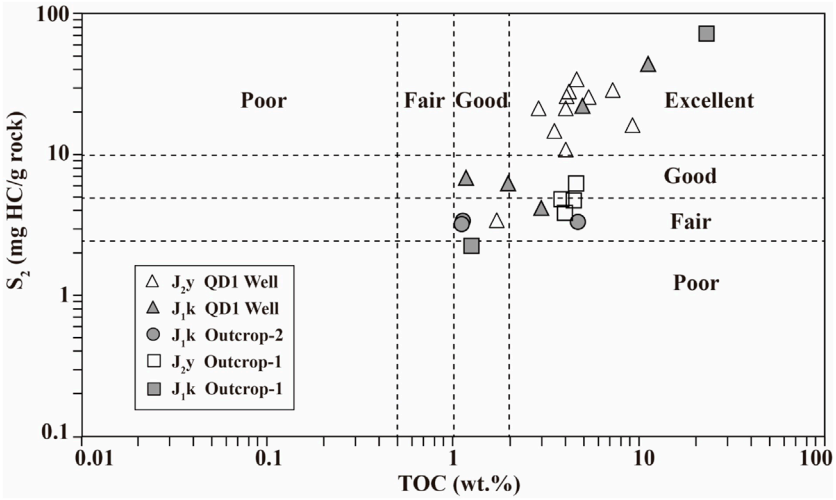

FIGURE 4
TOC vs. S_2 crossplot (Dembicki, 2009) for quality of the Jurassic source rock in the QD1 well and outcrops (for location, see Figure 1B).

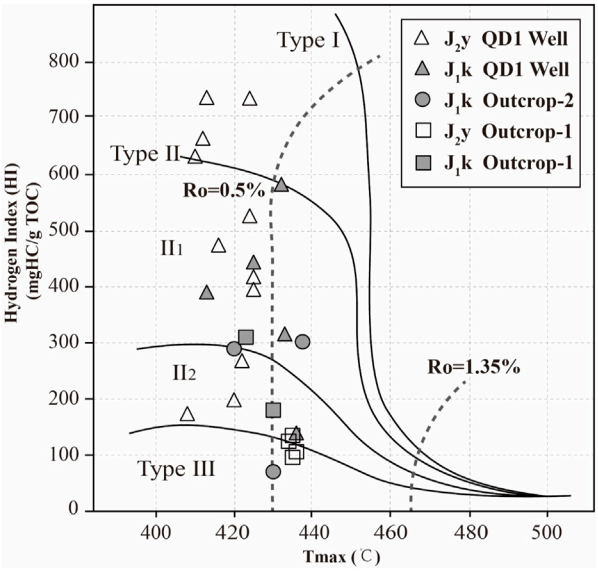

FIGURE 5
T_{max} vs. hydrogen index crossplot for quality evaluation of the Jurassic source rock in the Ruoqiang Sag.

good to excellent source rocks (Figure 4). The J_1k samples are poor to excellent source rocks with a pyrolysis parameter (S_2) ranging from 2.25 to 71.25 mg HC/g rock. The J_2y samples have higher quality than the J_1k source rock with an S_2 ranging from 3.40 to 33.83 mg HC/g Rock. From the T_{max} vs. HI crossplot (Figure 5), J_2y source rocks have three kerogen types while J_1k has kerogen of the II and III types. Based on the comprehensive pyrolysis parameters, the J_2y source rocks have better quality than J_1k. The testing samples have an Ro from 0.33% to 0.57%, which indicates an immature to low maturity stage. Two Ro values of asphalt are 0.41% and 0.54%, close to the J_1k Ro values (Ro = 0.38%–0.57%, average = 0.44%) and above the J_2y Ro values, which range from 0.33% to 0.41% with an average of 0.37%.

4.3 Rare earth element characteristics

The total rare earth element (REE) concentrations of J_2y mudstone are the highest, from 275.59 to 317.45 μg/g (Table 2), followed by those of the J_1k mudstone at 139.20–143.77 μg/g. J_1k coal has an REE concentration of 68.71 μg/g, which is slightly higher than the asphalt (35.88–41.92 μg/g). Light rare earth elements (LREEs) are more enriched in all samples than heavy rare earth elements (HREE), and the LREE/HREE ratios of J_2y mudstone are from 9.27 to 9.70, which is higher than the 6.37–6.95 of J_1k mudstone, higher than the 4.73 of J_1k coal, and higher than the 1.45–2.04 of the asphalt. The chondrite normalization values are after Boynton (1984), and all of the chondrite-normalized REE curves show the right-sloping characteristics with LREE enrichment. However, the curves gradually flatten from the J_2y mudstone to J_1k mudstone to J_1k coal and then to asphalt (Figure 6). All the samples show pronounced negative Eu anomalies. The δEu values of asphalt value vary from 0.84 to 0.92, close to those of J_1k mudstone and coal, ranging from 0.83 to 0.89, much higher than J_2y values of 0.70–0.80. The Ce anomalies are weak and relatively close, with slightly lower δCe values of asphalt, ranging from 0.90 to 0.98.

The J_2y/Ho ratios vary from 23.80 to 27.50, which is lower than those of J_1k mudstones (30.67–31.50) and asphalt Y/Ho ratios of 30.04–44.69, which are close to the 36.3 of J_1k coal (Table 2). The $(Ce/Yb)_N$, $(La/Yb)_N$, $(La/Sm)_N$, and $(Gd/Yb)_N$ ratios of J_2y mudstone are 8.84–9.11, 11.39–11.95, 3.32–3.47, and 2.22–2.39, much higher than those of J_1k samples, which are 3.18–5.96, 4.49–7.63, 2.90–3.57, and 1.00–1.78, respectively. The corresponding ratios of asphalt samples were 0.75–0.95, 1.15–1.17, 1.08–1.15, and 0.77–1.07, respectively.

TABLE 2 Rare earth elements of the Jurassic samples in the Ruoqiang Sag.

Sample	ΣREE	LREE	HREE	LREE/HREE	$(Ce/Yb)_N$	$(La/Yb)_N$	δEu	$(La/Sm)_N$	$(Gd/Yb)_N$	δCe	Y/Ho
SA-3	35.88	24.09	11.79	2.04	0.95	1.17	0.92	1.15	0.77	0.91	30.04
SA-4	41.92	24.78	17.14	1.45	0.75	1.15	0.84	1.08	1.07	0.90	44.69
QD-3	275.59	249.83	25.76	9.70	9.11	11.95	0.70	3.47	2.31	0.97	27.50
QD-6	317.45	286.53	30.92	9.27	8.85	11.61	0.80	3.32	2.39	0.96	24.93
QD-8	297.29	269.21	28.08	9.59	8.84	11.39	0.77	3.42	2.22	0.98	23.80
C1-6	68.71	56.73	11.98	4.73	3.18	4.49	0.83	3.57	1.00	0.96	36.25
QD-13	139.20	120.32	18.88	6.37	5.14	6.72	0.89	3.02	1.62	0.98	31.50
QD-14	143.77	125.69	18.08	6.95	5.96	7.63	0.84	2.90	1.78	0.98	30.67

$\delta Eu = Eu_N/(Sm_N \times Gd_N)^{1/2}$; $\delta Ce = Ce_N/(La_N \times Pr_N)^{1/2}$.

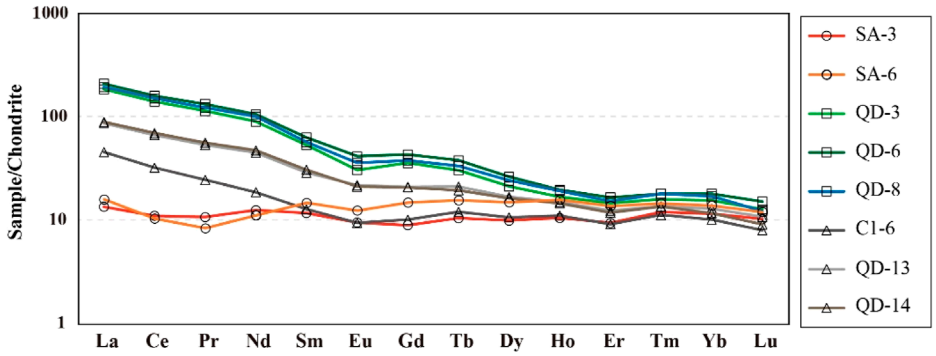

FIGURE 6
Chondrite-normalized REE patterns of the Jurassic samples in the Ruoqiang Sag.

4.4 Organic geochemistry characterization

The Jurassic alkanes are primarily distributed from *n*-C_{12} to *n*-C_{35}, with *n*-C_{25} as the single dominant *n*-alkane on the *m/z* 85 fragmentation diagram (Figure 7). The *n*-alkane composition has a distinct odd-even dominance with the odd *n*-alkane abundance higher than the even ones. The J_1k samples have an OEP (2.22–2.47) and CPI (1.38–1.75) similar to those of asphalt samples (OEP: 2.78–4.09; CPI: 1.84–2.30) and significantly lower than those of J_2y samples, which have OEP values of 5.02 and 5.19 and CPI values of 3.04 and 3.10, respectively (Table 3). The Pr/Ph ratios of Jurassic samples are all higher than 2.5, and the Pr/Ph values of the two J_2y mudstones are 3.01 and 3.62, slightly higher than that of the J_1k mudstone (2.85). However, the Jurassic mudstone Pr/Ph values are significantly lower than those of J_1k coal (5.12) and asphalt (5.09–5.85).

Quantified using *m/z* 191, the relative abundances of tricyclic and tetracyclic terpenoids are generally low, while the pentacyclic triterpenes are abundant, especially the C_{29} to C_{32} hopanes (Figure 7). The Ga/C_{30}H ratios range from 0.03 to 0.09 for all Jurassic samples (Table 3). The Ts/(Ts+Tm) values of the J_1k coal and mudstone are 0.78 and 0.90, respectively, significantly higher than those of the two J_2y mudstones (0.44 and 0.56). The asphalt extracts also have high Ts/(Ts+Tm) ratios, 0.52 and 0.56 for the two samples, respectively.

From the *m/z* 217 sterane compounds (Figure 7; Table 3), C_{27}, C_{28}, and C_{29} conventional steranes are distributed in a "V" shape with the abundance of C_{29}ααR sterane higher than C_{27}ααR and C_{28}ααR steranes. The asphalt extracts have a slightly higher proportion of C_{29} steranes and a lower proportion of C_{28} steranes, distinguished from the similar sterane compositions of the J_1k and J_2y. Meanwhile, the Jurassic extract values from the two maturity indexes of C_{27} (DSt/St) and C_{29} 20s/(20s+20r) are close. The J_1k C_{29} ββ/(αα+ββ) values are 0.51 and 0.46, higher than two J_2y extracts (0.27 and 0.38) and close to two asphalt values of 0.52 and 0.50.

4.5 Rhenium–osmium isotopes

The Jurassic asphalts have low Re and Os contents (Table 4). The Re content is between 0.82 and 11.36 ppb, with Os content varying from 26.82 to 131.85 ppt (Table 4), which is different from the Re and Os composition of the continental crust (Re content less than 1 ppb, and Os content less than 50 ppt). The $^{187}Re/^{188}Os$

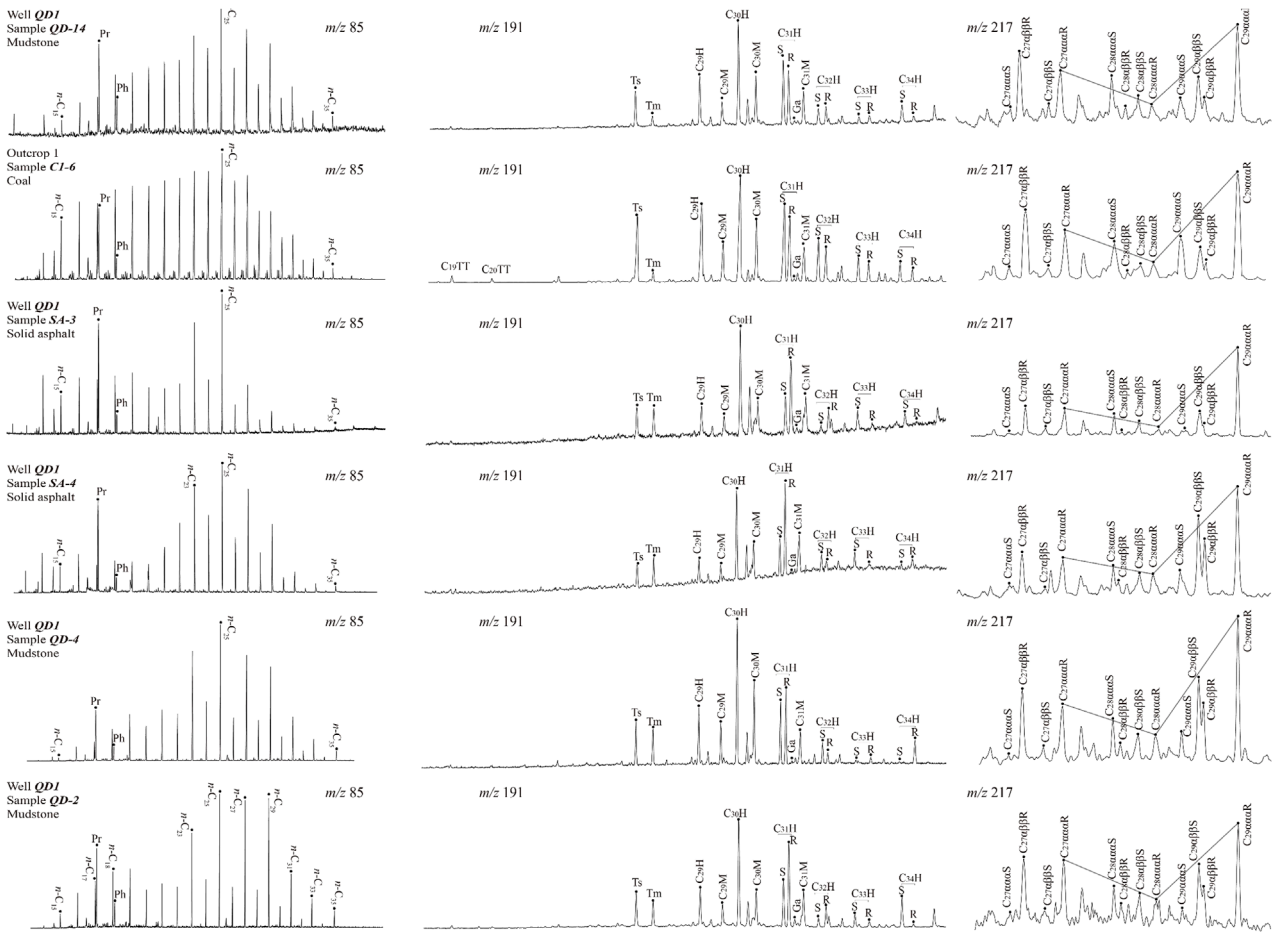

FIGURE 7
GC-MS characteristics of the Jurassic extracts in the Ruoqiang Sag.

values of asphalt vary from 58.7 to 576.1, while the $^{187}Os/^{188}Os$ ratio is in the range of 1.56–3.09 (Table 4). The linear fitting between $^{187}Re/^{188}Os$ and $^{187}Os/^{188}Os$ is relatively high with an R^2 of 91.8%, and the asphalt forming age is calculated to be 192 +30/−45 Ma with the isochrone slopes (Figure 8).

5 Discussion

5.1 Oil–source correlation

The rare earth elements have very similar and highly stable chemical properties that are not easily affected by metamorphism and can be used to determine the depositional environment, type, and origin of source rock (Condie, 1991; Tribovillard et al., 2006). The J_2y mudstones have significantly higher REE content and $(La/Sm)_N$ and $(Gd/Yb)_N$ ratios than the J_1k, indicating that the J_2y deposited with higher LREE and HREE fractionation under a warmer and wetter environment (Fleet, 1984). The J_1k coal and asphalt have similar REE content, reflecting a similar sedimentary environment. The J_2y REE curves appear to have steeper right-sloping characteristics than the J_1k ones (Figure 6) and have higher ratios of $(La/Yb)_N$ and $(Ce/Yb)_N$, with the LREE higher than HREE. Compared to braided-river delta and shallow coastal lakes of J_1k sedimentary environment close to the sediment source (Cheng et al., 2008), the J_2y distal sediments have fine particles and strong adsorption with the REE characteristics mentioned above. The δCe values of all samples are relatively close, with similar oxidizing properties of depositional environments (Elderfield and Pagett, 1986). However, the δEu values of asphalt and J_1k samples are significantly higher than the J_2y ones, reflecting the differences in sedimentary waters (Hass et al., 1995). The rare earth elements Y and Ho have very similar geochemical properties, but Y has an unusually low affinity for Fe oxides compared to Ho (Gong et al., 2021). It is clear that the J_2y Y/Ho values are higher than those of the asphalt and J_1k samples, indicating the J_2y depositional environment was more reduced. Therefore, combined with the REE partition curves and ratio relationships (Figure 6; Table 2), the asphalts have a closer relationship with the J_1k, especially the J_1k coal, suggesting that they are more closely related.

The Jurassic biomarker compounds show the characteristics of high Pr/Ph, high C_{29} steroid, and low abundance of tricyclic terpene alkanes, highly consistent with the Jurassic source rocks studied by previous researchers (Hendrix et al., 1995). The asphalt extracts have

10.3389/feart.2024.1371358

TABLE 3 Summary biomarker parameters for Jurassic sample extracts in the Ruoqiang Sag.

Sample	QD-2	QD-4	QD-14	C1-6	SA-3	SA-4
	J_2y mudstone	J_2y mudstone	J_1k mudstone	J_1k coal	J_2y asphalt	J_2y asphalt
Dominant *n*-alkane	25	25	25	25	25	25
CPI	3.10	3.04	1.75	1.38	2.30	1.84
OEP	5.19	5.02	2.47	2.22	4.09	2.78
Pr/Ph	3.62	3.01	2.85	5.12	5.09	5.85
Ts/(Ts+Tm)	0.56	0.44	0.78	0.9	0.52	0.53
G/C_{30}H	0.09	0.19	0.04	0.07	0.07	0.06
C_{31} 22S/(22S+22R)	0.36	0.33	0.54	0.58	0.34	0.45
C_{32} 22S/(22S+22R)	0.32	0.54	0.49	0.55	0.32	0.33
C_{27} (DSt/St)	0.10	0.36	0.22	0.17	0.20	0.25
C_{29} 20s/(20s+20r)	0.32	0.28	0.25	0.28	0.29	0.29
C_{29} ββ/(αα+ββ)	0.27	0.38	0.51	0.46	0.52	0.50
C_{27} *	0.32	0.28	0.31	0.28	0.25	0.24
C_{28} *	0.21	0.23	0.24	0.23	0.17	0.16
C_{29} *	0.47	0.50	0.45	0.48	0.57	0.60
C_{27}/C_{29}	0.68	0.56	0.70	0.59	0.44	0.40
C_{28}/C_{29}	0.45	0.45	0.54	0.49	0.30	0.27

CPI, $0.5 * (n\text{-}C_{25}+n\text{-}C_{27}+n\text{-}C_{29}+n\text{-}C_{31}+n\text{-}C_{33}) * [1/(n\text{-}C_{24}+n\text{-}C_{26}+n\text{-}C_{28}+n\text{-}C_{30}+n\text{-}C_{32})+ 1/(n\text{-}C_{26}+n\text{-}C_{28}+n\text{-}C_{30}+n\text{-}C_{32}+n\text{-}C_{34})]$; TAR = $(n\text{-}C_{27}+n\text{-}C_{29}+n\text{-}C_{31})/(n\text{-}C_{15}+n\text{-}C_{17}+n\text{-}C_{19})$; OEP = $(n\text{-}C_{(Nmax-2)}+6 * n\text{-}C_{Nmax}+ n\text{-}C_{(Nmax+2)})/(4 * n\text{-}C_{(Nmax-1)}+ n\text{-}C_{(Nmax+1)})$; Pr/Ph, pristine/phytane; Ts/(Ts+Tm) = 18a(H)-22,29,30-trisnorneohopane/(18a(H)-22,29,30-trisnorneohopane +17a(H)-22,29,30-trisnorhopane); G/C_{30}H, gammacerane to C_{30} hopane; C_{31} 22S/(22S+22R) = 22S to (22S + 22R) ratios for C_{31} 17α-hopanes; C_{32} 22S/(22S+22R) = 22S to (22S + 22R) ratios for C_{32} 17α-hopanes; C_{27} (DSt/St) = 13β, 17α(H) - diasteranes 20S+20R] to 20S+20R isomers of C_{27} isosterane and C27 regular steranes; C_{29} ββ/(αα+ββ) = ββ to (αα+ββ) isomerization of C_{29} 20S and 20R regular steranes; C_{29} 20s/(20s+20r) = C_{29} 5a(H), 14a(H), and 17a(H) sterane 20S/(20S + 20R); C_{27} * , C_{28} * , and C_{29} * , relative percentages of C_{27}, C_{28}, and C_{29} regular steranes, respectively; C_{27}/C_{29}, regular sterane ratio of C_{27} to C_{29}; C_{28}/C_{29}, regular sterane ratio of C_{28} to C_{29}.

similar Pr/Ph ratios with J_1k coal, which suggests they have similar depositional environment oxidizing properties and closer affinities. The peak alkane is *n*-C_{25} for all samples (Figure 7; Table 3), reflecting that the regional Jurassic organic matter sources are highly related to terrestrial sources. In terms of the *m/z* 217 sterane compounds (Table 3), the J_2y extracts have similar C_{27} regular sterane content with the J_1k and slightly higher C_{27}/C_{29} regular sterane ratio and slightly lower C_{28}/C_{29} regular sterane ratio, indicating that the origins of J_2y organic matter have more algae (Volkman, 1986). The CPI and OEP of the Jurassic source rocks and asphalt are all greater than 1.0, suggesting that their thermal maturity is low. In contrast, the J_1k CPI and OEP values are lower than those of the J_2y (Table 3) and close to those of asphalt, indicating that the asphalts have similar thermal maturity to the J_1k. By the maturity-related biomarker parameters of Ts/(Ts+Tm), C_{31}22S/(22S+22R), and C_{32}22S/(22S+22R), the J_1k and asphalt have proximate maturity with biomarker parameters higher than those of the J_2y. By the C_{29} ββ/(αα+ββ) ratio, the J_1k has similar thermal maturity with asphalt but slightly higher than the J_2y extracts. Therefore, the Jurassic asphalts are more closely related to the J_1k.

Even if the source rock underwent hydrocarbon generation and expulsion processes, the Re-Os system can still remain closed and record its sedimentary age (Creaser et al., 2002). However, the isochronous age of asphalt Re-Os isotopes may reflect the sedimentary age of source rock or hydrocarbon migration/accumulation age, which mainly depends on the closure of the Re-Os isotopic system. If the Re-Os isotopic system is not closed with different Re and Os isotopes evenly mixed, then the asphalt Re-Os isochronous age represents the migration/accumulation age (Selby and Creaser, 2005). Using the plots of $^{187}Os/^{188}Os$ *versus* $^{187}Re/^{188}Os$, the age of the Jurassic asphalt is 192+30/−45 Ma, similar to the J_1k deposition time, suggesting that the asphalt is closely related to J_1k strata. It is obvious that the J_2y asphalt retains the Re-Os characteristics of J_1k coal, and the Re-Os isotope system is closed during the entire hydrocarbon generation and migration process.

TABLE 4 Rhenium–osmium data synopsis for Jurassic samples in the Ruoqiang Sag.

Sample	Re (ppb)	2σ	Os (ppt)	2σ	^{187}Os	2σ	$^{187}Re/^{188}Os$	2σ	$^{187}Os/^{188}Os$	2σ
$SA\text{-}1_d$	0.82	0.01	80.0	0.7	27.8	0.3	58.7	1.0	1.563	0.023
$SA\text{-}2_d$	2.85	0.01	79.5	0.7	25.5	0.3	222.3	2.8	2.317	0.034
$SA\text{-}3_d$	2.48	0.01	35.7	0.5	10.8	0.2	457.8	9.7	2.927	0.066
$SA\text{-}4_d$	11.36	0.03	131.8	1.2	39.2	0.4	576.1	6.0	3.093	0.042
$SA\text{-}5_d$	2.06	0.01	65.9	0.6	22.6	20.3	181.4	2.5	1.702	0.026
$SA\text{-}1_c$	1.56	0.01	32.9	0.1	8.5	0.1	229.1	2.9	1.984	0.013
$SA\text{-}2_c$	2.19	0.02	48.0	0.1	14.5	0.1	220.5	2.3	2.308	0.005
$SA\text{-}3_{c1}$	3.28	0.02	35.4	0.1	13.3	0.1	448.3	4.6	2.886	0.006
$SA\text{-}3_{c2}$	3.99	0.03	43.5	0.1	16.4	0.1	442.1	4.5	2.895	0.006
$SA\text{-}4_c$	3.66	0.03	43.6	0.1	15.6	0.1	405.9	4.2	2.761	0.007
$SA\text{-}5_c$	1.88	0.01	26.8	0.1	8.9	0.1	338.1	3.5	2.534	0.007

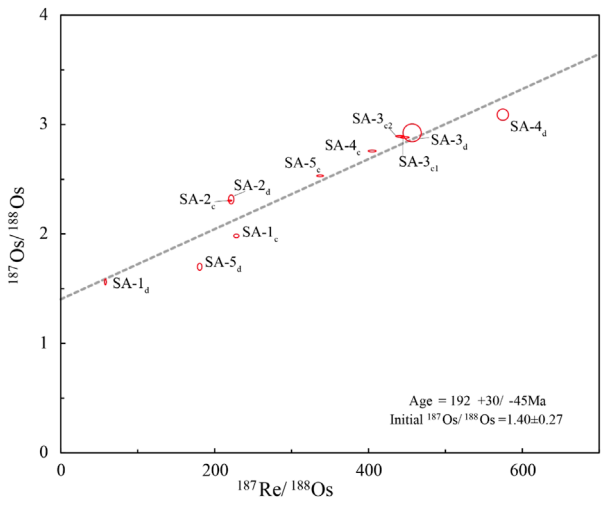

FIGURE 8
$^{187}Re/^{188}Os$ *versus* $^{187}Os/^{188}Os$ plots for the Jurassic solid asphalts.

More importantly, from the macerals, the Jurassic asphalt is mainly precipitated from exinite-rich components such as sporophytes, alginate, and resinite during the coalification. The asphalt precursor was mixed with vitrinite, inertinite, and other coal macerals and sometimes, flow traces are visible under the microscope (Figures 3I,M). They were formed during the early coalification equivalent to the oil window (Stach et al., 1982) and then filled in Jurassic pores and fractures.

Coal is not only an important gas-source rock but also an oil-source rock, which has been confirmed by the petroleum exploration practices in western Chinese basins, such as the Tuha Basin (Zhao and Cheng, 1998). Generally, these coals were deposited in a deltaic inter-bay swamp (Shao et al., 2003). The J_1k sedimentary facies were braided-river delta and shallow coastal lakes, where ferns and other herbaceous plants flourished (Vakhrameev, 1991). Undecomposed hydrogen-rich components carried by the river accumulated here. The enrichment of detrital exinite, coupled with the strong microbiolysis of peat swamps, resulted in coals with high hydrogen content, which laid a good environmental foundation for coal-derived hydrocarbons.

5.2 Asphalt-forming process

The Jurassic has an unconformable contact relationship with the Paleozoic basement and steadily developed in the Early and Middle Jurassic. Overall uplifting occurred in the Late Jurassic, which resulted in the absence of the Middle and Upper Jurassic in the Ruoqiang Sag. In the Jurassic, the paleo-temperature gradient was not high, 2.8°C/100 m (Li et al., 2005), and the J_1k source rock does not reach the Ro 0.5% with a maximum burial depth of only 1840 m in the QD1 well (Figure 9).

The Cretaceous in the Ruoqiang Sag is only a localized remnant even though it is 100 m thick in the Tadong and Tangguzibas Depression due to the uplifting in the study area and strong denudation of the pre-deposited strata in the late Cretaceous (Yang et al., 2001; Arnaud et al., 2003). During the Cretaceous, the J_1k source rock underwent continued subsidence and uplifting. Its maximum burial depth of 2029 m did not meet the hydrocarbon threshold. The J_1k source rock did not mature with a paleo-temperature gradient of 2.7°C/100 m (Li et al., 2005).

The regional Paleogene exhibits weakly extensional sedimentation of sandstone and mudstone (Li, 1998), while the Himalayan movement that occurred at the end of the Paleogene resulted in a large-scale withdrawal of the lake water in the Ruoqiang Sag (Li et al., 2002), and the Paleogene near the QD1 well

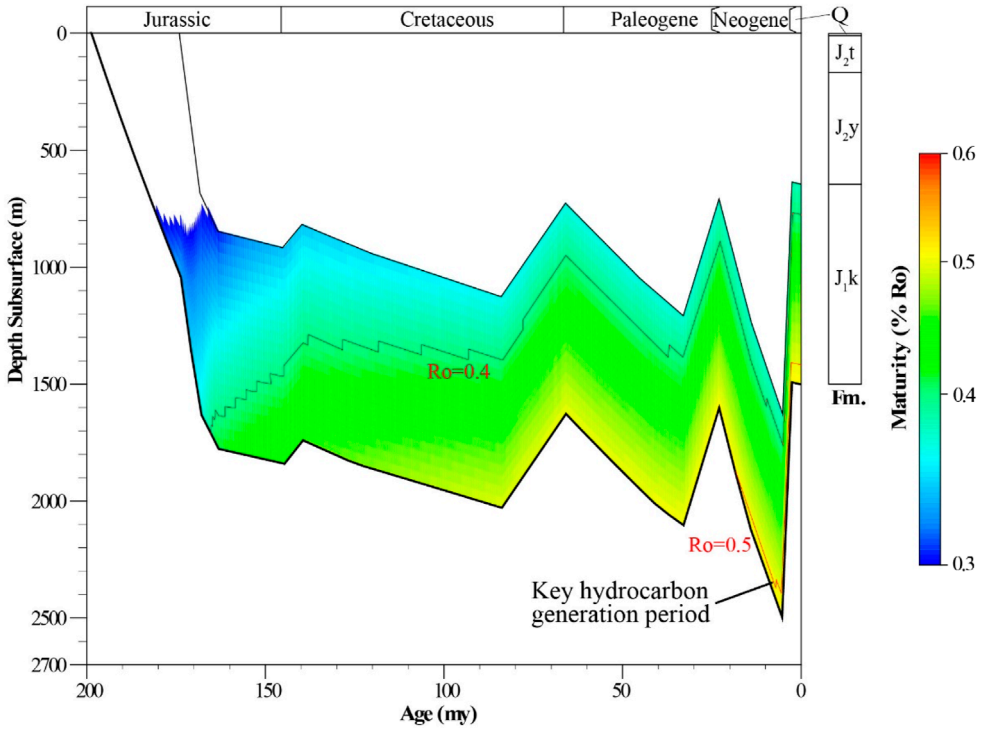

FIGURE 9
Burial and maturity evolution of the J_1k strata in the QD1 well.

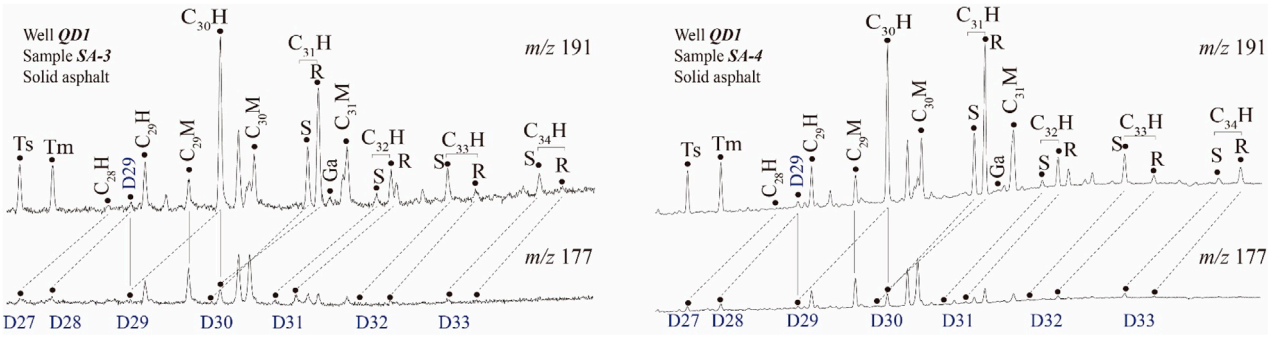

FIGURE 10
Mass chromatograms at *m/z* 191 and *m/z* 177 indicate that 25-norhopanes (indicated by a D-carbon number) occur in the Jurassic asphalt. Vertical lines indicate some peaks that yield both m/z 191 and m/z 177 ions. The C_{31}–C_{35} 17α-hopane (22S + 22R) corresponds to two C_{30}–C_{34} 25-norhopane epimers.

was also completely eroded. In the Miocene, affected by large-scale thrusting activities in the West Kunlun tectonic belt, the Ruoqiang Sag underwent flexural subsidence and deposited a thick Neogene (Tian et al., 2023). With a low paleo-temperature gradient of 2.1°C/100 m (Li et al., 2005), the J_1k burial depth met the hydrocarbon threshold with a maximum burial depth of 2500 m and Ro 0.5%, and J_1k coal began early hydrocarbon generation evolution (Figure 9). The coal macerals began the asphaltenization stage of coalification, and the exsudatinites filled in the fractures and pores, or were preserved *in situ*, or were transported to the overlying J_2y mudstone under the presence of faults, where they were accumulated, were preserved, and formed an asphalt-like appearance. After that, the Altyn Tagh Fault underwent a large-scale strike-slip activity, and the deposited Neoproterozoic was completely denuded. With the rapid rise of the Tibetan Plateau after the Pleistocene, the Quaternary was deposited only several meters thick near the QD1 well.

After the J_1k hydrocarbon evolution, the asphalt was formed from the Miocene and maintained a similar REE composition as the J_1k coal. The rhenium–osmium isotopes in the asphalt had not been sufficiently fractionated, so the ages of asphalt were consistent with the J_1k. Meanwhile, the rhenium and osmium contents indicated that they

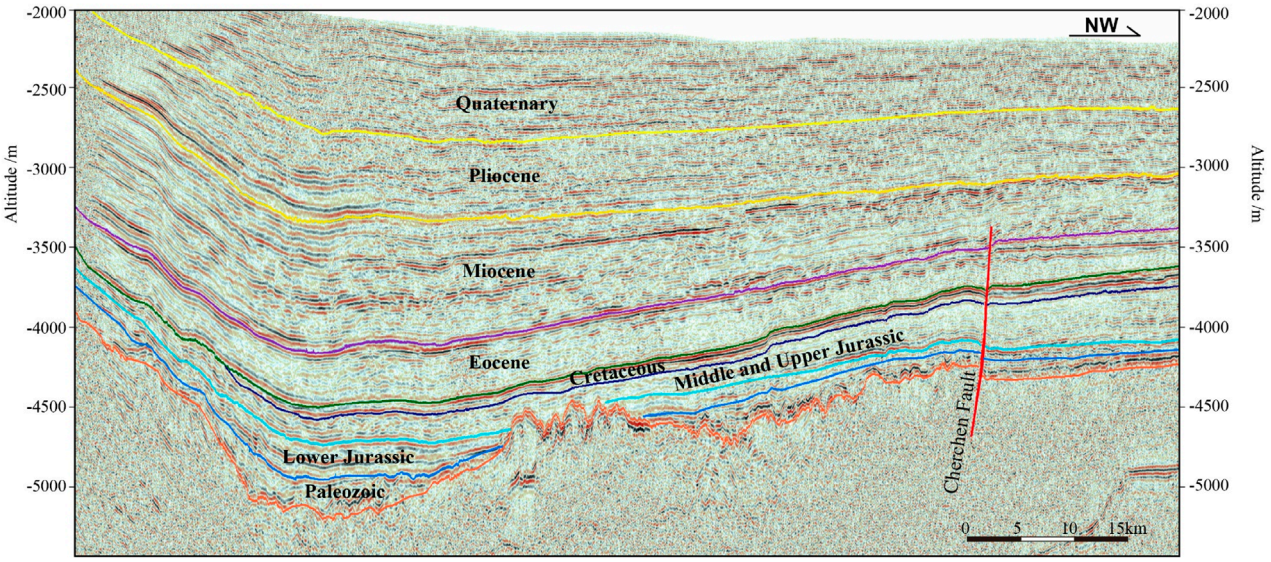

FIGURE 11
Northwest-southeast oriented seismic section of the Ruoqiang Sag. The profile is marked in Figure 1B.

came from a source rich in organic matter rather than crustal mixing during the transport process (Sun et al., 2003; Selby et al., 2007). Due to the late formation of asphalt, the 25-norbornanes were rarely detected or not detected in the *m/z* 191 composition (Figure 10). The 25-norhopanes are believed to originate from the loss of a methyl group from C-10 in hopanes and have a high abundance of biodegradation (Volkman et al., 1983). C_{29} 25-nor-17α-hopane (D29) from the C_{30} hopane has very low content of both *m/z* 191 and *m/z* 177 ions, and the ion content values of D30 and D31 from C_{31}–C_{32} 17α-hopane (22S + 22R) are only slightly higher (Figure 10). The asphalt did not undergo many secondary changes, such as oxidization and biodegradation, during its formation process.

5.3 Insights for regional petroleum exploration

Relying on samples of the QD1 well and outcrops in the Ruoqiang Sag, the Jurassic asphalt is confirmed to be derived from the J_1k coal and serves as the product of hydrocarbon generation and evolution in the early maturity of J_1k coal. The current understanding diverges considerably from the previous understanding of regional oil sources (Xu et al., 1994; Chen and Hu, 1996; Huang et al., 2013), but the current evidence is much stronger and more robust. Meanwhile, in the Tula Basin (Figure 1B), which is faulted by the Altyn Tagh Fault with Ruoqiang Sag, oil sandstones more than 100 m thick with a large amount of asphalt veins were found in the Upper Jurassic (Guo et al., 1998; Robinson et al., 2003) and were considered to be similar to the Jurassic oils in the Qaidam Basin by previous researchers, whose source rocks are also from the Middle and Lower Jurassic (Zeng et al., 2022). This undoubtedly increases the confidence in the Jurassic oil and gas exploration in the Ruoqiang Sag.

Although the understanding of the low maturity evolution degree of J_1k source rock is unfavorable for the regional Jurassic petroleum exploration, it confirms that the J_1k coal-bearing source rock has a very good hydrocarbon generation potential. Furthermore, the sampling study area is located in the premontane area at the southern margin of the Ruoqiang Sag (Figure 1). The current morphology of the Ruoqiang Sag is generally characterized by a northeast-oriented belt that is higher in the south and lower in the north (Figure 11). The Jurassic has a greater burial depth away from the premontane area and develops with a large area of J_1k and J_2y lacustrine deposits (Cheng et al., 2008; Jiang et al., 2014). From the seismic section (Figure 11), the Lower Jurassic strata are buried more than 3000 m deep and are hundreds of meters thick. Therefore, the J_1k coal-bearing source rock has matured and could provide hydrocarbons for the Ruoqiang Sag. The J_1k and J_2y have developed sedimentary facies such as deltas and shallow coastal lakes, which are favorable for the sandstone reservoirs, while the J_2y mudstone has pure lithology and large thickness and could be a very good caprock. From the analysis of the Jurassic lithological assemblage, the Ruoqiang Sag has developed a good reservoir-seal assemblage. Therefore, fault-related tectonic and lithologic traps near the hydrocarbon stove are targets for regional Jurassic petroleum exploration.

6 Conclusion

(1) According to the studies of biomarker compounds, rare earth elements, and rhenium–osmium isotopes, it is believed that the Jurassic asphalt of the QD1 well originates from the J_1k coal, which addresses the regional source rocks, responds to oil-source divergence, and confirms that the J_1k coal-bearing source rock has great hydrocarbon potential for petroleum exploration in the Ruoqiang Sag.

(2) The forming age of asphalt is determined as 192+30/−45 Ma by rhenium–osmium isotope isochrones, which is consistent

with the J_1k deposition time. The asphalt is formed late as the exsudatinite of the asphaltenization stage of coalification from the Miocene and is derived from the J_1k coal.

Data availability statement

The original contributions presented in the study are included in the article/Supplementary Material; further inquiries can be directed to the corresponding author.

Author contributions

XL: funding acquisition, methodology, and writing–original draft. ZB: investigation, resources, and writing–review and editing. YY: conceptualization, formal analysis, and writing–review and editing. ZJ: investigation, project administration, and writing–review and editing. JZ: data curation, formal analysis, and writing–review and editing.

Funding

The author(s) declare that financial support was received for the research, authorship, and/or publication of this article. The study was funded by the National Natural Science Foundation (41802169).

Acknowledgments

The authors thank Chao Li of the National Center for Geological Experimental Testing, the Chinese Academy of Geological Sciences, and Professor Dave Selby of Durham University, United Kingdom, for conducting the rhenium-osmium isotope testing work. They would also like to thank the National Natural Science Foundation (41802169) for its support of this study.

Conflict of interest

The authors declare that the research was conducted in the absence of any commercial or financial relationships that could be construed as a potential conflict of interest.

Publisher's note

All claims expressed in this article are solely those of the authors and do not necessarily represent those of their affiliated organizations, or those of the publisher, the editors, and the reviewers. Any product that may be evaluated in this article, or claim that may be made by its manufacturer, is not guaranteed or endorsed by the publisher.

References

Arnaud, N., Tapponnier, P., Roger, F., Brunel, M., Scharer, U., Chen, W., et al. (2003). Evidence for mesozoic shear along the western Kunlun and altyn-tagh fault, northern tibet (China). *J. Geophys. Res. - Sol. Ea.* 108, 1–27. doi:10.1029/2001jb000904

Boynton, W. V. (1984). "Geochemistry of the rare earth elements: meteorite studies," in *Rare earth element Geochemistry*. Editor P. Henderson (Amsterdam: Elsevier), 63–114.

Chen, R. L., and Hu, M. (1996). Discovery of jurassic oil-bearing sandstone and its oil source in the Southeast Tarim Basin. *Chin. Sci. Bull.* 41 (18), 1685–1688. doi:10.1360/csb1996-41-18-1685

Cheng, X. G., Liao, L., Chen, X. A., Guo, Q. Y., Wang, D. E., Chen, H. L., et al. (2008). Jurassic sedimentary facies and paleoenvironmental reconstruction of southeastern Tarim Basin, northwestern China. *J. China Univ. Min. Technol.* 37 (04), 519–525.

Condie, K. C. (1991). Another look at rare earth elements in shales. *Geochim. Cosmochim. Acta* 55, 2527–2531. doi:10.1016/0016-7037(91)90370-k

Creaser, R. A., Sannigrahi, P., Chacko, T., and Selby, D. (2002). Further evaluation of the Re-Os geochronometer in organic-rich sedimentary rocks: a test of hydrocarbon maturation effects in the Exshaw Formation, Western Canada Sedimentary Basin. *Geochim. Cosmochim. Acta* 66 (19), 3441–3452. doi:10.1016/s0016-7037(02)00939-0

Curiale, J. A. (1986). Origin of solid bitumens, with emphasis on biological marker results. *Org. Geochem.* 10 (1–3), 559–580. doi:10.1016/0146-6380(86)90054-9

Dembicki, H., Jr. (2009). Three common source rock evaluation errors made by geologists during prospect or play appraisals. *AAPG Bull.* 93 (3), 341–356. doi:10.1306/10230808076

Elderfield, H., and Pagett, R. (1986). Rare earth elements in ichthyoliths: variations with redox conditions and depositional environment. *Sci. Total Environ.* 49, 175–197. doi:10.1016/0048-9697(86)90239-1

Fleet, A. J. (1984). Chapter 10 - aqueous and sedimentary geochemistry of the rare earth elements. *Dev. Geochem.* 2, 343–373. doi:10.1016/B978-0-444-42148-7.50015-0

Ge, X., Shen, C. B., Selby, D., Feely, M., and Zhu, G. Y. (2020). Petroleum evolution within the Tarim Basin, northwestern China: insights from organic geochemistry, fluid inclusions, and rhenium-osmiumgeochronology of the Halahatang oil field. *AAPG Bull.* 104 (2), 329–355. doi:10.1306/05091917253

Gong, Q. L., Li, F., Lu, C. J., Wang, H. Z., and Tang, H. (2021). Tracing seawater- and terrestrial-sourced REE signatures in detritally contaminated, diagenetically altered carbonate rocks. *Chem. Geol.* 570, 120169. doi:10.1016/j.chemgeo.2021.120169

Guckert, K. D., and Mossman, D. J. (2003). Pennsylvanian coal and associated bitumen at johnson mills, shepody bay, new brunswick, Canada. *Int. J. Coal Geol.* 53 (3), 137–152. doi:10.1016/s0166-5162(02)00181-7

Guo, Z. J., Zhang, Z. C., and Zeng, F. G. (1998). Discovery of mega-thick oil sandstone and asphalt in the Jurassic System in the Tula Basin and its significance. *Chin. Sci. Bull.* 43 (22), 1898–1901. doi:10.1007/bf02883468

Hass, J. R., Shock, E. L., and Sassani, D. C. (1995). Rare earth elements in hydrothermal systems: estimates of standard partial molal thermodynamic properties of aqueous complexes of the rare earth elements at high pressures and temperatures. *Geochim. Cosmochim. Acta* 59 (21), 4329–4350. doi:10.1016/0016-7037(95)00314-p

Hendrix, M. S., Brassell, S. C., Carroll, A. R., and Graham, S. A. (1995). Sedimentology, organic geochemistry, and petroleum potential of jurassic coal measures: Tarim, junggar, and turpan basins, northwest China. *AAPG Bull.* 79 (7), 929–959. doi:10.1306/8d2b2187-171e-11d7-8645000102c1865d

Huang, Y. P., Jiang, Z. L., Luo, X., Liu, M. Y., and Duan, C. (2013). Comparison and hydrocarbon accumulation model of oil source rocks in Jianggalesayi structural belt in Tadongnan Depression of Southeastern Tarim Basin. *Xinjiang Pet. Geol.* 34 (3), 287–290.

Hwang, R. J., Teerman, S. C., and Carlson, R. M. (1998). Geochemical comparison of reservoir solid bitumens with diverse origins. *Org. Geochem.* 29 (1-3), 505–517. doi:10.1016/s0146-6380(98)00078-3

Jacob, H. (1989). Classification, structure, genesis and practical importance of natural solid oil bitumen ("migrabitumen"). *Int. J. Coal Geol.* 11 (1), 65–79. doi:10.1016/0166-5162(89)90113-4

Jiang, Z. L., Qiu, H. J., Huang, Y. P., Fu, W. K., Jiang, K. P., and Chen, J. (2014). Jurassic lacustrine source rock characteristics and its petroleum geological significance in the Southeast Depression of Tarim Basin, China. *Arab. J. Geosci.* 7, 5093–5106. doi:10.1007/s12517-013-1187-8

Li, H. B., Yang, J. S., Xu, Z. Q., Wu, C. L., Wan, Y. S., Shi, R. D., et al. (2002). Geological and chronological evidence of Indo-Chinese strike-slip movement in the Altyn Tagh fault zone. *Chin. Sci. Bull.* 47 (1), 27–32. doi:10.1360/02tb9005

Li, H. L., Qiu, N. S., Jin, Z. J., and He, Z. L. (2005). Geothermal history of Tarin basin. *Oil Gas Geol.* 26 (5), 613–617. *(in Chinese)*.

Li, W. H. (1998). Jurassic sedimentary system of fault depression in Southeast Tarim and its hydrocarbon significance. *Oil Gas Geol* 9 (2), 110–l14.

Liao, Y. H., Fang, Y. X., Wu, L. L., Cao, Q. G., and Geng, A. S. (2015). The source of highly overmature solid bitumens in the Permian coral reef paleo-reservoirs of the Nanpanjiang Depression. *Mar. Petrol. Geol.* 59, 527–534. doi:10.1016/j.marpetgeo.2014.10.008

Liu, J. J., Selby, D., Obermajer, M., and Mort, A. (2018). Rhenium–osmium geochronology and oil–source correlation of the Duvernay petroleum system, Western Canada sedimentary basin: implications for the application of the rhenium–osmium geochronometer to petroleum systems. *AAPG Bull.* 102 (08), 1627–1657. doi:10.1306/12081717105

Liu, Y. J., Genser, J., Ge, X. H., Neubauer, F., Friedl, G., Chang, L. H., et al. (2003). $^{40}Ar/^{39}Ar$ age evidence for Altyn fault tectonic activities in western China. *Chin. Sci. Bull.* 48 (18), 2024–2030. doi:10.1007/bf03183998

Mahdaoui, F., Reisberg, L., Michels, R., Hautevelle, Y., Poirier, Y., and Girard, J.-P. (2013). Effect of the progressive precipitation of petroleum asphaltenes on the Re▪Os radioisotope system. *Chem. Geol.* 358, 90–100. doi:10.1016/j.chemgeo.2013.08.038

Moldowan, J. M., Seifert, W. K., and Gallegos, E. J. (1985). Relationship between petroleum composition and depositional environment of petroleum source rocks. *AAPG Bull.* 69 (8), 1255–1268. doi:10.1306/ad462bc8-16f7-11d7-8645000102c1865d

Ritts, B. D., and Biffi, U. (2000). Magnitude of post-Middle Jurassic (Bajocian) displacement on the central Altyn Tagh fault system, northwest China. *GSA Bull.* 112 (1), 61–74. doi:10.1130/0016-7606(2000)112<61:mopjbd>2.0.co;2

Robinson, D. M., Dupont-Nivet, G., Gehrels, G. E., and Zhang, Y. Q. (2003). The Tula uplift, northwestern China: evidence for regional tectonism of the northern Tibetan Plateau during late Mesozoic–early Cenozoic time. *GSA Bull.* 115 (1), 35–47. doi:10.1130/0016-7606(2003)115<0035:ttunce>2.0.co;2

Selby, D., and Creaser, R. A. (2005). Direct radiometric dating of hydrocarbon deposits using rhenium-osmium isotopes. *Science* 308 (5726), 1293–1295. doi:10.1126/science.1111081

Selby, D., Creaser, R. A., and Fowler, M. G. (2007). Re-Os elemental and isotopic systematics in crude oils. *Geochim. Cosmochim. Acta* 71 (2), 378–386. doi:10.1016/j.gca.2006.09.005

Shao, L. Y., Zhang, P. F., Hilton, J., Gayer, R., Wang, Y. B., Zhao, C. Y., et al. (2003). Paleoenvironments and paleogeography of the Lower and lower Middle Jurassic coal measures in the Turpan-Hami oil-prone coal basin, northwestern China. *AAPG Bull.* 87 (2), 335–355. doi:10.1306/09160200936

Stach, E. M., Mackowsky, M. T., Teichmüller, M., Taylor, G. H., and Teichmüller, R. (1982). *Stach's text book of coal petrolog*. Berlin: Gebruder Borntraeger.

Sun, W. D., Bennett, V. C., Eggins, S. M., Kamenetsky, V. S., and Arculus, R. J. (2003). Enhanced mantle-tocrust rhenium transfer in undegassed arc magmas. *Nature* 422 (6929), 294–297. doi:10.1038/nature01482

Tian, H. F., Chen, H. L., Cheng, X. G., Wu, L., Lin, X. B., Gao, S. B., et al. (2023). Limited northward expansion of the Tibetan plateau in the late cenozoic: insights from the Cherchen Fault in the southeastern Tarim Basin. *Tectonics* 42 (7), e2022TC007694. doi:10.1029/2022tc007694

Tribovillard, N., Algeo, T. J., Lyons, T., and Riboulleau, A. (2006). Trace metals as paleoredox and paleoproductivity proxies: an update. *Chem. Geol.* 232 (1/2), 12–32. doi:10.1016/j.chemgeo.2006.02.012

Vakhrameev, V. A. (1991). *Jurassic and cretaceous floras and climates of the earth*. Cambridge: Cambridge University Press.

Volkman, J. K. (1986). A review of sterol markers for marine and terrigenous organic matter. *Org. Geochem.* 9 (2), 83–99. doi:10.1016/0146-6380(86)90089-6

Volkman, J. K., Alexander, R., Kagi, R. I., and Woodhouse, G. W. (1983). Demethylated hopanes in crude oils and their applications in petroleum geochemistry. *Geochim. Cosmochim. Acta* 47 (4), 785–794. doi:10.1016/0016-7037(83)90112-6

Wang, J. G., Wang, L. F., and Zhou, Q. (2000). Prospects of jurassic hydrocarbon exploration in southeast Tarim Basin. *Oil Gas Geol.* 21 (3), 259–263.

Wang, Y., Zhang, X. M., Zhang, J. F., Wang, E. C., Li, Q., and Sun, G. H. (2005). $^{40}Ar/^{39}Ar$ thermoch ronological evidence for formation and Mesozoic evolution of the northern-central segment of the Altyn Tagh fault system in the northern Tibetan plateau. *GSA Bull.* 117, 1336–1346. doi:10.1130/b25685.1

Wu, L. Y., Jin, Z. J., Liu, K. Y., Chu, Z. Y., and Yang, P. (2021). Evolution of a deeply-buried oil reservoir in the north Shuntuoguole Low Uplift, Tarim Basin, western China: insights from molecular geochemistry and Re–Os geochronology. *Mar. Petrol. Geol.* 134, 105365. doi:10.1016/j.marpetgeo.2021.105365

Xu, X., Hu, M., Zhang, Q., and Bai, S. (1994). Geochemical characteristics of the Jurassic oil-bearing sandstones in the fault depression, the SE Tarim Basin. *Exp. Pet. Geol.* 16 (4), 345–352.

Yang, J. S., Meng, F. C., Zhang, J. X., and Li, H. B. (2001). The shoshonitic volcanic rocks at hongliuxia: pulses of the Altyn Tagh Fault in cretaceous? *Sci. China* 44, 94–102. doi:10.1007/bf02911976

Yue, Y. J., Ritts, B. D., Hanson, A. D., and Graham, S. A. (2004). Sedimentary evidence against large strike-slip translation on the Northern Altyn Tagh fault, NW China. *Earth Planet. Sci. Lett.* 228 (3-4), 311–323. doi:10.1016/j.epsl.2004.10.008

Zeng, X., Wang, B., Cao, Q., Wang, A., Jia, P., Zhang, P., et al. (2022). Characteristics of Jurassic source rocks and oil and gas exploration direction in the piedmont zone between the south-western Qaidam Basin and Altun Mountain. *Geol. J.* 57 (10), 4152–4166. doi:10.1002/gj.4535

Zhao, C. Y., and Cheng, K. M. (1998). Expulsion and primary migration of the oil derived from coal. *Sci. China* 41 (04), 345–353. doi:10.1007/bf02932684

frontiers | Frontiers in Earth Science

TYPE Original Research
PUBLISHED 18 March 2024
DOI 10.3389/feart.2024.1375590

Check for updates

OPEN ACCESS

EDITED BY
Xixin Wang,
Yangtze University, China

REVIEWED BY
Wentong Zhang,
Xi'an Shiyou University, China
Gang Yan,
Yangtze University, China

*CORRESPONDENCE
Min Wang,
wangm@upc.edu.cn
Jinbu Li,
lijinbu@gig.ac.cn

RECEIVED 24 January 2024
ACCEPTED 01 March 2024
PUBLISHED 18 March 2024

CITATION
Zhang J, Wang M, Li J, Liu Z and Xu L (2024), Research on loss rules of oil and gas in preserved shale cores after open air exposure. *Front. Earth Sci.* 12:1375590. doi: 10.3389/feart.2024.1375590

COPYRIGHT
© 2024 Zhang, Wang, Li, Liu and Xu. This is an open-access article distributed under the terms of the Creative Commons Attribution License (CC BY). The use, distribution or reproduction in other forums is permitted, provided the original author(s) and the copyright owner(s) are credited and that the original publication in this journal is cited, in accordance with accepted academic practice. No use, distribution or reproduction is permitted which does not comply with these terms.

Research on loss rules of oil and gas in preserved shale cores after open air exposure

Jinyou Zhang[1,2], Min Wang[3]*, Jinbu Li[4]*, Zhao Liu[2] and Liang Xu[2]

[1]School of Earth Sciences, Northeast Petroleum University, Daqing, China, [2]Exploration and Development Research Institute of PetroChina Daqing Oilfield Company, Daqing, China, [3]National Key Laboratory of Deep Oil & Gas, China University of Petroleum (East China), Qingdao, China, [4]State Key Laboratory of Organic Geochemistry, Guangzhou Institute of Geochemistry, Chinese Academy of Sciences, Guangzhou, China

There is a large amount of oil and gas loss in traditional conventional core samples. Revealing the rules of oil and gas loss is of great significance for restore the pristine oil content and oil component in the shale. In this study, four preserved shale cores with different thermal maturity (R_o = 1.01–1.53%) and different total organic carbon content (TOC = 1.69–5.48 *wt*.%) were selected. The samples are obtained from the first member of the Qingshankou Formation in the Gulong Sag. Nuclear magnetic resonance (NMR) T_1–T_2 mapping and thermal desorption gas chromatography (TD–GC, at a constant temperature of 300°C for 3 min) were performed on the preserved cores and their replicas that were exposed in open air for different times, to study dynamic loss process and the molecular composition changes of shale oil. The results show that during exposure, shale experiences a large amount of oil loss, with a loss ratio of about 42%–78%, and the higher the maturity, the greater the loss ratio. The oil loss is mainly contributed by free oil, with a loss ratio as high as 88%. The adsorbed oil content, however, remains basically unchanged and has a good positive correlation with the TOC of shale. Once the cores were crushed, the gaseous hydrocarbon in oil was basically evaporated in just 5 min. After long-term storage, 90% of the C_{14-} light hydrocarbon is lost, while the C_{14+} heavy hydrocarbon experiences basically no loss. Therefore, effective and timely analysis of preserved shales is extremely important. The oil content of uncrushed shale cores characterized by NMR T_1–T_2 mapping is much greater than that of the crushed sample measured by TD-GC, which means that NMR T_1–T_2 mapping can be important method to evaluate the original fluid saturation of shale.

KEYWORDS

shale oil, light hydrocarbon loss, NMR T1-T2 mapping, preserved shale, Gulong Sag

1 Introduction

In 2021, Daqing Oilfield reported 1.268 billion tons reserves of Gulong shale oil, which greatly boosting confidence in shale oil exploration (Sun et al., 2021). The key parameter for the evaluation of shale oil reserves and resource potential is the pristine oil content (Wang et al., 2022). However, due to the loss of light components in oil and gas, the oil content obtained from conventional coring samples (core samples that have long exposed to the open environment) is much lower than the *in situ* underground pristine oil content.

The lost component has the highest mobility and is exactly the most meaningful part for production, especially for medium-to high-thermal matured shale oil composed of high proportion of light hydrocarbons. Loss of light hydrocarbon (including gaseous hydrocarbons C_1-C_5 and liquid hydrocarbons C_6-C_{14}) would lead to underestimation of resource potential and misjudgment of sweet spots (Jarvie, 2014). Therefore, there is an urgent need to conduct research on the loss patterns of shale light hydrocarbons, which is crucial for objective evaluation of shale oil resource potential, reserve scale, and sweet spot.

Under the influence of storage condition and pretreatment, and crucible waiting time (about 5 min) before Rock-Eval six pyrolysis experiments, the S1 value of shale sample measured in laboratory does not contain small molecular hydrocarbons, and thus is much lower than *in situ* S1 in shale oil reservoir when further considering the heavy hydrocarbons in S2 peak (Jarvie, 2014; Jiang et al., 2016; Romero-Sarmiento, 2019; Yan et al., 2023). The loss of light hydrocarbons is mainly caused by two aspects. On one hand, when the shale is brought from the underground to the surface, small molecular hydrocarbons will release due to sudden changes in temperature and pressure (Chen and Jiang, 2020). On the other hand, sample storage, pretreatment such as crushing, and Rock–Eval crucible waiting process also lead to evaporation of light components (Jarvie, 2014; Li et al., 2022a). Generally speaking, the loss of light hydrocarbons is related to its their proportion in shale oil, and the higher the proportion, the greater the loss (Noble et al., 1997; Ma et al., 2024). The proportion of light hydrocarbons is further controlled the organic matter type and thermal maturity of shale. For example, compared with Type I organic matter, Type II organic matter is more likely to generate gas and thus contribute a higher proportion of light hydrocarbons (Ma et al., 2020). In addition, highly matured organic matter will experience intense thermal cracking, generating more light hydrocarbons. Jarvie (2014) pointed out that the evaporation of light hydrocarbons (up to C_{10}) in shale oil depends to a large extent on the richness of organic matter, lithofacies, oil properties, whether the sample is crushed or not, and storage conditions. The evaporation loss ratio ranges from 33% to 85%.

In previous studies, there have developed several methods to evaluate hydrocarbon loss, including empirical approach (Cooles et al., 1986), calculation the proportion of light hydrocarbon in oil/extracts (Michael et al., 2013; Jarvie, 2014; Wang et al., 2014), mass balance approach (Chen and Jiang, 2020), and sealing and pressure coring techniques (Jiang et al., 2016), etc. The ratio of hydrocarbon loss reported by different scholars varies a lot, ranging from 35% to 80% (Cooles et al., 1986; Jarvie, 2014). When assessing resource potential of shale, especially the target areas with a large maturity range, it is inappropriate to simply use a fixed light hydrocarbon loss ratio. Based on the difference in hydrocarbon content between thermal desorption-gas chromatography (TD-GC) of shale powder and GC of the crude oil from the shale, the light hydrocarbon loss can be calculated, and the corrected pristine hydrocarbon content is S1 × (hydrocarbon content in crude oil/hydrocarbon content in shale extracts) (Jarvie and Breyer, 2012). Song et al. (2013) assumed that the C_{14-} component in the saturates are all lost, and then calculated the correction coefficient of the light hydrocarbon loss of shale extracts (by chloroform) from the same strata and at near depth with the crude oil, by using GC chromatography of the crude oil. They found that correction coefficient of light hydrocarbon evaporative losses increases with thermal maturity. When the maturity of shale increases from 0.5% to 0.7%, 0.9%, 1.1%, and 1.3%, the corresponding correction coefficients are 1.09, 1.16, 1.30, 1.41, and 1.52, respectively. In the work of Michael et al. (2013), they assumed that all the C_{15-} component is lost, and the amount of loss is positively related to API gravity of crude oil, that is, the amount of loss increases with the increase of API gravity. On the basis of this, it is proposed to use the relationship between API gravity of crude oil and C_{15-} content to estimate the loss of light hydrocarbons (API = 0.412 × C_{15-} + 20.799). Results showed that when the API is 50, the maximum C_{15-} loss ratio can reach 70%. In order to reduce light hydrocarbon fluid loss and contamination in the samples before experimental analysis, sealed coring technology was developed. Liquid nitrogen freezing was performed at the well site before the shale cores being transported back to the laboratory for analysis. The fresh samples obtained by this method can retain as much as light hydrocarbons and are closer to the *in situ* geological conditions. By using the light hydrocarbon logging technology of fresh samples, or comparing the difference in oil content between fresh samples and long-term exposed/conventional coring samples, the loss of light hydrocarbons can be obtained (Jarvie, 2014; Zhu et al., 2015; Jiang et al., 2016). For example, for the shale from Shahejie Formation of Jiyang Depression, eastern China, it is found that, the Rock-Eval S1 value of the preserved samples is 1.5–2.0 times that of the conventional samples stored in open air for 30 days, and the difference in S1 is related to thermal maturity.

Previous studies have focused primarily on the amount of light hydrocarbon loss using shale samples obtained through seal coring techniques, lacking attention to the dynamic loss process, component change during loss, and the influencing factors. Therefore, in this study, preserved shale samples of different thermal maturity and organic matter richness were collected. The fresh shales and their replicas with different exposure time were subjected to nuclear magnetic resonance (NMR) T_1–T_2 mapping, TD–GC, and Rock–Eval analysis. By dynamically monitoring changes in oil content and its chemical composition, the pattern of light hydrocarbon loss of shale oil is revealed.

2 Samples and methods

2.1 Samples

The samples were collected from the shale oil Well in the Qing1 Member of the Gulong Sag in Daqing Oilfield that was drilled in 2020. All samples were obtained through sealed coring technology that preserves the original fluid components in shale. Preserved cores were sprayed with liquid nitrogen while cutting. When full-diameter cores were brought to the surface, they were immediately frozen in liquid nitrogen bucket at −196°C. Liquid nitrogen freezing can effectively retain the fluid components in shale, ensuring that the oil content analyzed in the experiment is closer to the *in situ* oil content. The thermal maturity, total organic carbon content, and mineral composition is shown in Table 1.

TABLE 1 Basic geochemical characteristics and mineral composition of the sample.

Sample no.	Well	Depth (m)	R_o (%)	TOC (*wt.*%)	S1 (mg/g)	S2 (mg/g)	Tmax (°C)	Main mineral composition (%)					
								Quartz	Plagiocla	Calcite	Dolomite	Pyrite	Clay
A	FX1603	1943.66	1.01	5.48	6.27	41.32	450	27.9	12.3		15.2	4.9	39.7
B	GLB544	2266.39	1.29	3.88	4.7	9.82	450	32	9.8			2.9	36.2
C	GY8	2409.1	1.44	1.69	—	—	—	32.7	25	17.4			20.8
D	GY8	2497.1	1.53	3.01	—	—	—	29.2	9.7	4.1			57

Note: represent no data analysis.

2.2 Experiments

The preserved core samples were subjected to NMR T_1–T_2 mapping to quantify the oil content in shale and TD-GC experiments to characterize the molecular composition in oil. One sample was divided into two categories based on sample size and experimental purpose. One part of blocks with 3–5 cm size was used for NMR T_1-T_2 map experiments. The other part of blocks was crushed to 60–80 mesh powders and subjected to TD–GC analysis. Both NMR and TD-GC do not require resampling. After sample was exposed to open air for different time intervals (such as 10 min, 20 min, 30 min, 1 h, 2 h, 8 h, 24 h, 48 h, etc.), block sample was resubmitted to NMR experiment while a small proportion of powder sample (30–50 mg) was taken out to perform TD-GC analysis each time. In this work, four preserved samples were subjected to NMR experiment while only sample A were subjected to TD-GC analysis at different time intervals due to material limited.

2.2.1 NMR T_1–T_2 mapping

H^1-NMR spectroscopy was performed using an instrument produced by Core Laboratories, USA, with a frequency of 22 MHz, and the magnet temperature is 35°C. The nuclear magnetic probe has a diameter of 30 mm and dead time of signal acquisition to 15 μs, to measure short relaxation components such as solid organic matter (OM) and nanoporous fluid in shale. Compared with mainstream 2 MHz and 12 MHz nuclear magnetic equipment, the instrument used in this experiment emit a greater frequency, and its T_1–T_2 map can clearly distinguish oil, water and solid organic matter signals. The main testing parameters are: echo time (TE), 70 μs; recycle delays (RD), 1,000 ms; number of echos, 4,000; number of inverse times, 31; and target signal-to-noise ratio (SNR), 200. The number of scans and gain values was automatically optimized by the instrument based on the hydrogen contents of the samples (Liu et al., 2019; Li et al., 2022b).

During the test, the magnetic field excites the protons of hydrogen nuclei, which will cause the sample to self-heat up. This may cause the fluid to evaporate from the preserved sample. In order to avoid fluid evaporation, during test, the samples should be kept rich in total hydrogen content (which can be achieved by increasing the sample mass) and the number of scans should be low. In this study, the NMR T_1–T_2 test for preserved samples were all controlled within 5 min, and the signal-to-noise ratio maintained above 200. The detailed test process for preserved shale has been shown in Li et al. (2022b).

2.2.2 Thermal desorption-gas chromatography (TD-GC)

TD-GC combines pyrolysis device and gas chromatography. The chromatograph is Shimadzu GC-14B, and the chromatographic column is HP-5. Before test, the preserved shale with block shape was quickly crushed to about 60 mesh. Then, about 30–50 mg was put in to the pyrolysis oven and pyrolyzed at preset temperature program. The pyrolysis products were carried by carrier gas into a liquid nitrogen-frozen trap for collection. After collection, the trap was quickly heated to allow the organic compounds to be fully released and then enter the chromatographic column for analysis. The detector is hydrogen ion flame detector (FID) and the products were quantified by external standard method. The GC oven temperature was initially held at 30°C for 3 min, and then increased to the final temperature of 315°C at a heating rate of 3°C/min. The flame ionization detector (FID) temperature was maintained at 315°C until no components flowed out. The carrier gas was helium with flow rate of 1 mL/min, and the split ratio was 1:25. The TD-GC detected the P1 peak, corresponding to the S1 peak of the Rock-Eval pyrolysis, of which the pyrolysis temperature was 300°C and maintenance time was 3 min (Jiang et al., 2016; Beti et al., 2020). Compound identification was based on comparison of GC retention time with those in literature.

Previous scholars have demonstrated that the sample size will affect the pyrolysis results (Sun et al., 2023). In this work, the reason for using a 60 mesh sample is that the experimental object is sealed coring sample with large amount hydrocarbons. If the sample is crushed too finely (such as 100 mesh), the crushed sample will be very sticky, and the loss of hydrocarbons is too fast in a short period of time, making more difficult to detect process of hydrocarbon loss.

3 Results and discussion

3.1 Pristine oil content in shale and molecular composition of oil

Our previous study revealed that sample crush caused large amount of light hydrocarbon and water loss in preserved shale (Li et al., 2022a). In order to avoid evaporation loss and accurately quantify the pristine fluid content in shale, the preserved cores were not crushed in this study, and the NMR tests were conducted on regularly rectangular rock pieces. Figure 1 showed T_1–T_2 maps of the four preserved shales. In the maps, five regions are divided

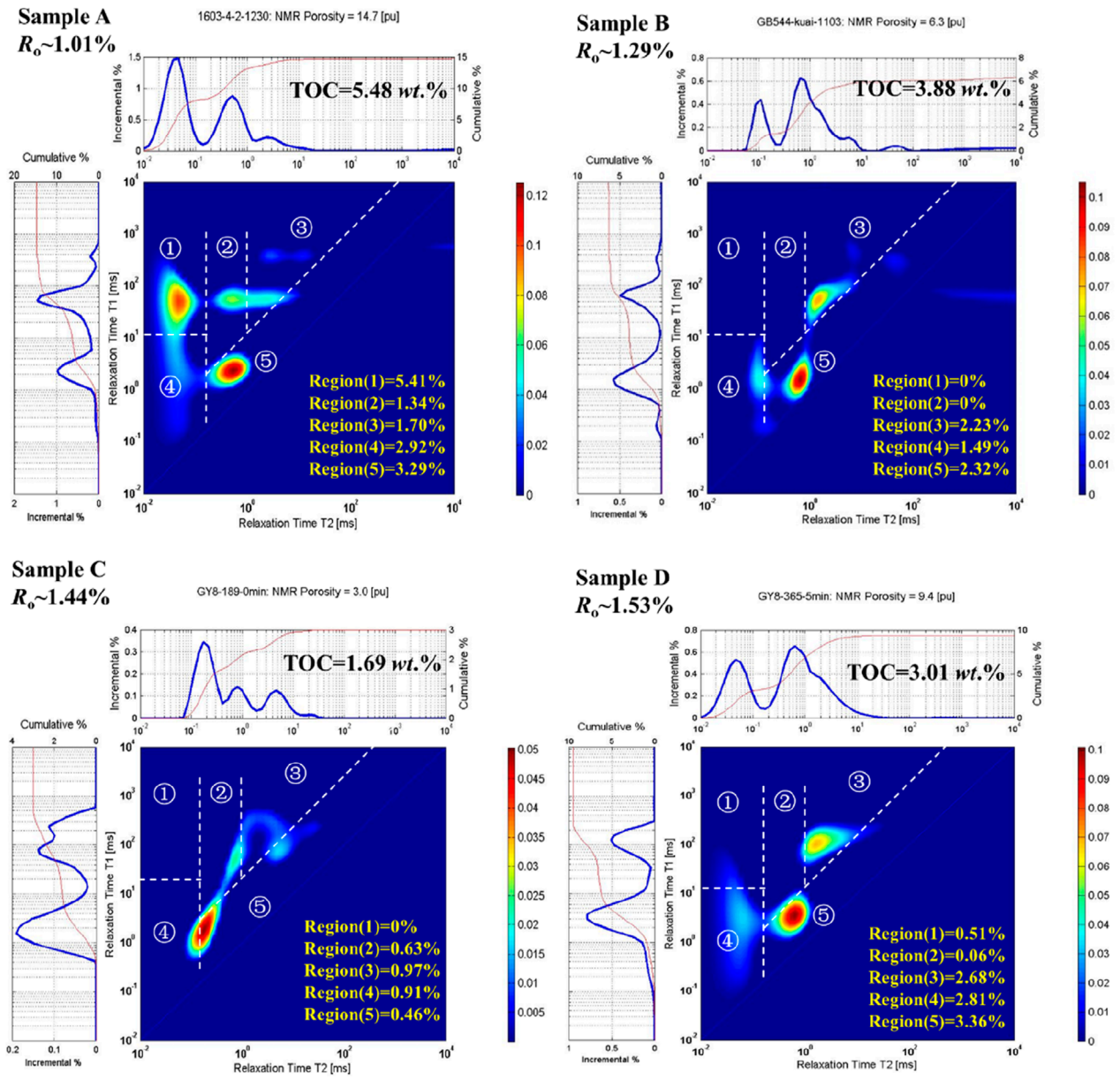

FIGURE 1
The NMR T_1-T_2 maps of the four preserved shale samples.

by white dashed lines, and the components represented by each region are based on our previous reported scheme (Li et al., 2018; Li et al., 2020; Mukhametdinova et al., 2021). Region 1 (T_2 < 0.2 ms, T_1 > 10 ms) represents solid organic matter (OM), Region 2 (0.2 ms < T_2 < 1 ms, T_1/T_2 > 10) corresponds to adsorbed/heavy hydrocarbon; region 3 (T_2 > 1 ms, T_1/T_2 > 10) refers to free/light hydrocarbon; Region 4 (T_2 < 0.2 ms, T_1 < 10 ms) is adsorbed water and hydroxyl/structured water, and region 5 (T_2 > 0.2 ms, T_1/T_2 < 10) represents pore water.

In general, the signals of the T_1–T_2 map of the four samples are relatively strong in region 3 and 5, indicating that the pores of the sample are mainly composed of shale oil and water. There are differences in T_1–T_2 maps of different samples. For sample A with relatively low thermal maturity and high TOC content, due to its high oil density, the oil adsorption ability of organic matter is high, resulting strong signal in region 2. In comparison, for samples with high thermal maturity and low TOC content, the strong signal mainly distributes in region 3, and the shale oil is mainly free oil. In addition, Sample A has strong signal in region 1, while other samples have basically no signal in region 1. The reasons may be lie in two aspects. On one hand, the NMR signal intensity of solid organic matter is related to its content. Obviously, sample A have highest TOC value of 5.48%, and their T1-T2 map showing the strong signal in Region 1, while no signals in Region 1was shown in sample C with TOC value of only 1.69% (Table 1). Organic matter is characterized by fast relaxation rate and short relaxation time. Although the NMR

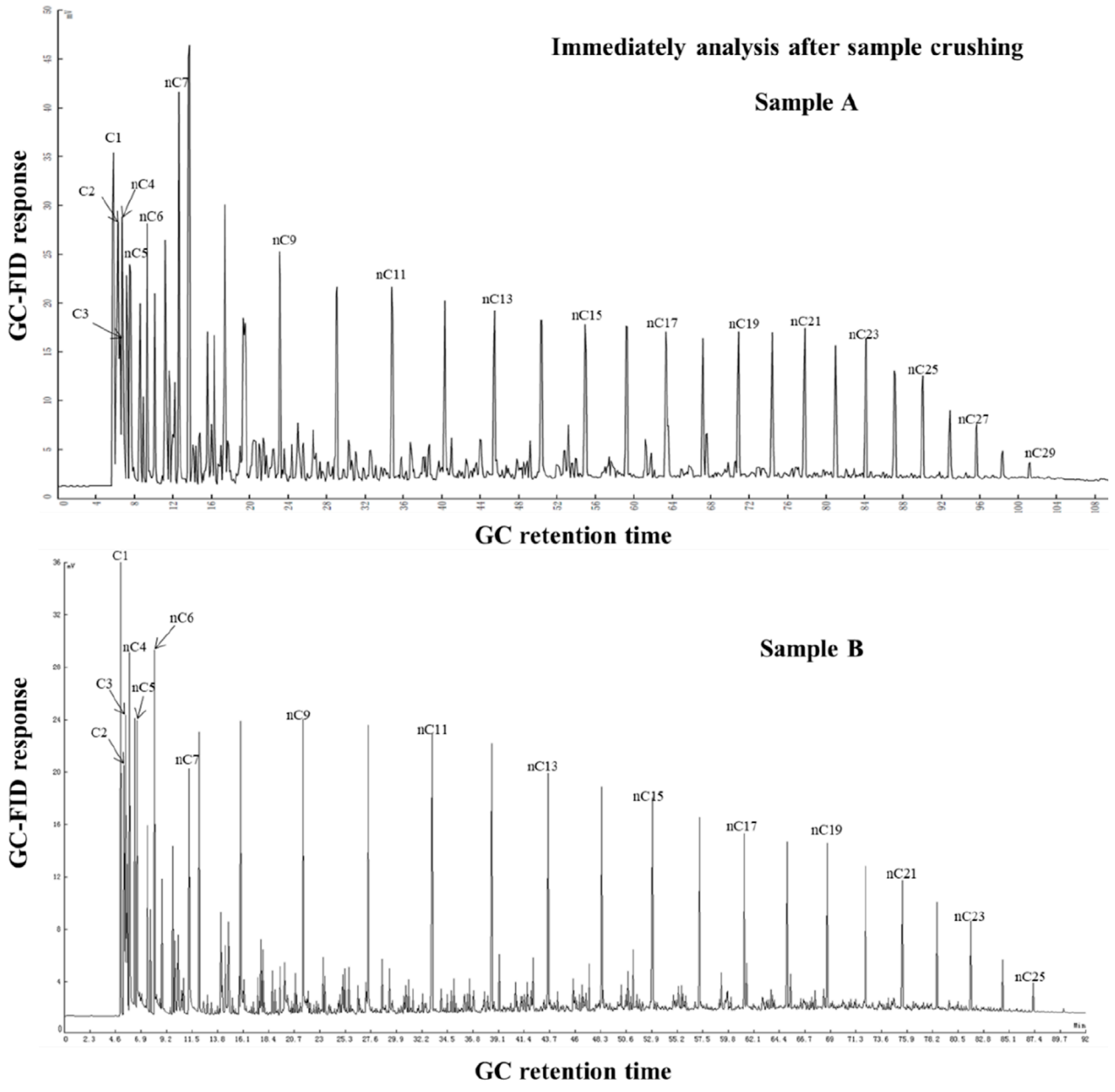

FIGURE 2
The S1 fingerprints of preserved shale samples **(A, B)**.

tests adopted the solid echo sequence (Washburn and Birdwell, 2013), unlike detecting pore fluid, it is still difficult to detect all solid organic matter signals (Fleury, 2016). On the other hand, affected by the high fluid content of the preserved shale, the signal of organic matter may be masked. The signal in region four reflects mineral structure water and adsorbed water. The signal intensity is related to the clay mineral content. It is obvious that sample D with clay content of up to 57% shows intense signal in region 4, while sample C with relatively lower clay content shows basically no signal in area 4.

Based on our previously calibrated coefficient between the signal intensity of shale oil and its content (Li et al., 2022b), the pristine oil content of the four samples was estimated to be 33.15 mg/g, 19.82 mg/g, 10.61 mg/g, and 22.62 mg/g, respectively. Obviously, the oil content in preserved shale is much higher than that in conventional coring sample.

Figure 2 shows the S1 chromatograph of TD-GC products of preserved shale samples A and B. GC fingerprints present distinct gaseous hydrocarbon components (C_1—C_5), with methane accounting for the most proportion. This indicates that the oil content measured by NMR T_1–T_2 mapping includes gaseous hydrocarbons. In addition, there seems no loss of C_6-C_{14} component in oil. The S1 value was quantified by external standard method. For sample A, the total amount of S1 is 11.43 mg/g, of which the gaseous hydrocarbons C_1-C_5 is 1.85 mg/g and the hydrocarbons

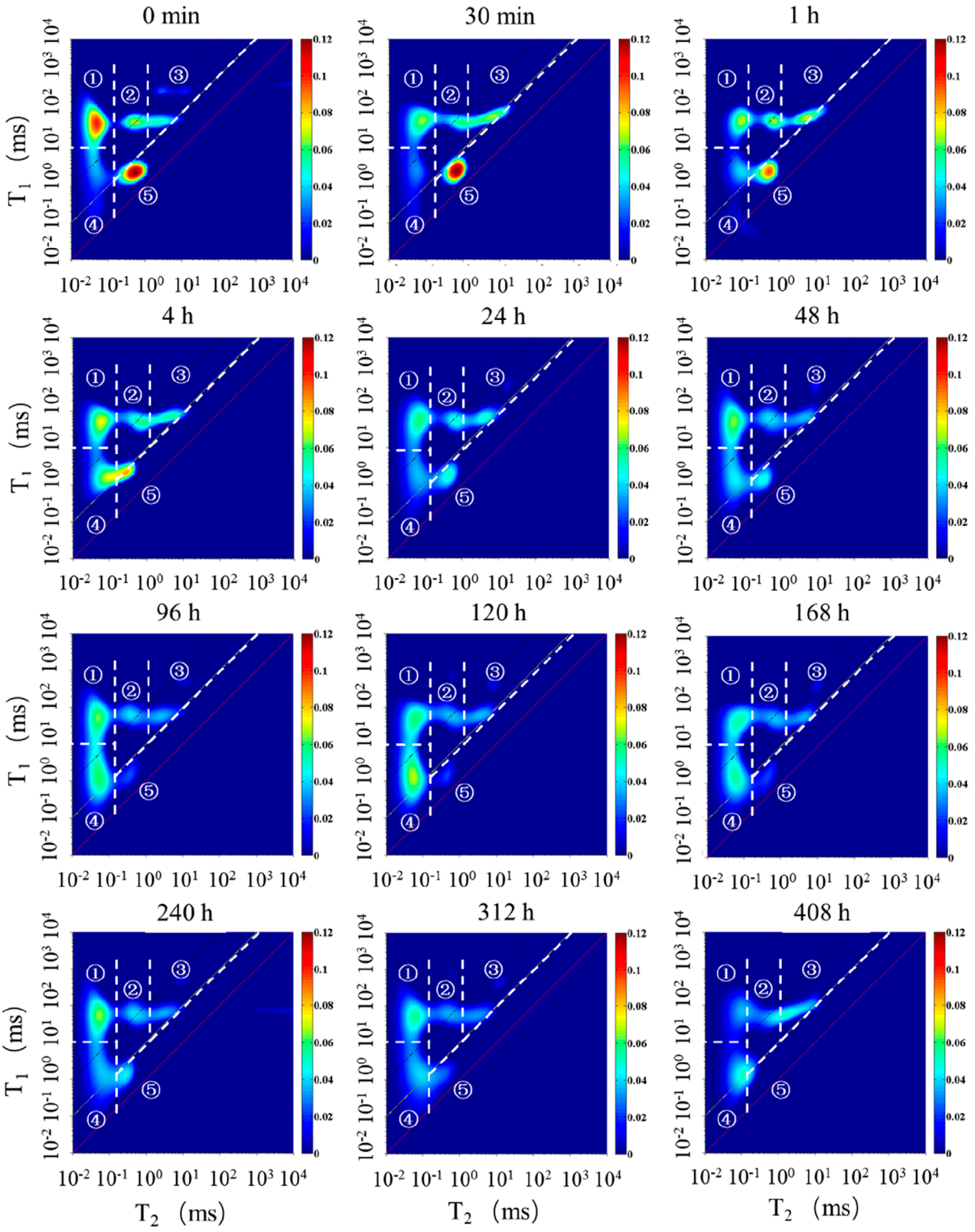

FIGURE 3
NMR T_1–T_2 maps of sample A (R_o = 1.0%, TOC = 5.48%) analyzed immediately and exposed to the open air at different time intervals. The NMR signals of each state were normalized to per Gram rock. The same color bar is used in each figure for ease of comparison.

C_6-C_{14} is 6.25 mg/g. For sample B, the total amount of S1 is 9.12 mg/g, of which the gaseous hydrocarbons C_1-C_5 is 0.56 mg/g and the hydrocarbons C_6-C_{14} is 5.44 mg/g. The proportions of C_{14-} component in S1 of sample A and B are similar, 71% and 66% respectively. However, the S1 value is much lower than the oil content measured by NMR T_1–T_2 mapping method (Figure 1).

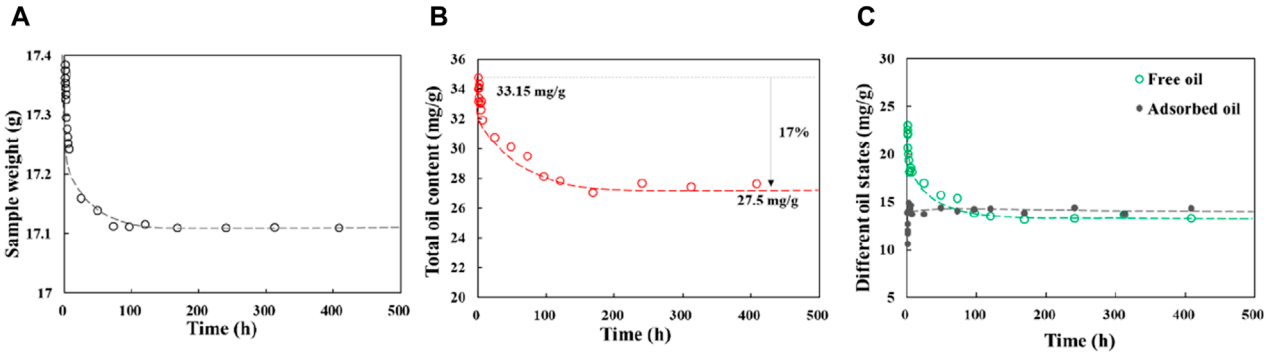

FIGURE 4
Variation diagram of each content of No. A sample after being placed for different times. **(A)** Total mass change diagram; **(B)** Oil content change diagram; **(C)** Variation diagram of free oil rate and adsorbed oil rate.

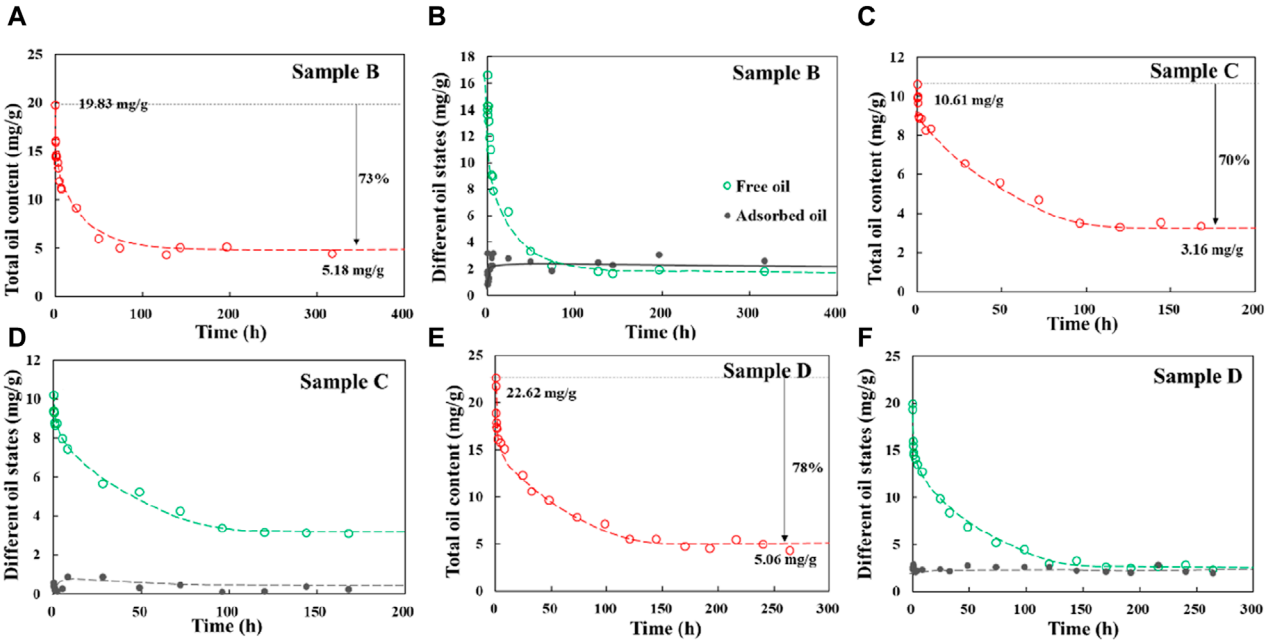

FIGURE 5
Changes of oil content, free oil, and adsorbed oil of preserved shales after different exposure times.

Reasons may lie in two aspects. Firstly, sample crushing before the TD-GC experiment resulted in hydrocarbon loss (Li et al., 2022a). Secondly, some heavy hydrocarbons had boiling points higher than 300°C and therefore could not be detected by TD-GC (Jarvie and Breyer, 2012).

3.2 Changes in shale oil content during exposure

The preserved shale cores (in rock pieces of 3–5 cm) were exposed in open air for 30 min, 1 h, 4 h, 8 h, 24 h, 48 h, etc. After different exposure time, shale pieces were resubjected to 2D NMR experiments to measure the mass of the shale pieces and the changes of T_1–T_2 maps. Figure 3 exhibits the changes of NMR T_1–T_2 maps of the sample A after different exposure times (for comparison, the colors in each map adopt a unified color scale). With the increase in exposure time, both the signals of shale oil (regions 2 and 3) and water (region 5) show a decreasing trend, indicating the loss of both oil and water when the preserved shale is exposed to air. Therefore, the assumption of only oil loss occurs is incorrect when using conventional cores to restore the *in situ* fluid saturation. This will overestimate the pristine oil content (Ali et al., 2020; Nikitin et al., 2019).

Figure 4A shows the weight changes in preserved shale core sample A after exposure to open air at different time intervals. The initial weight of the sample is 17.385 g, and it shows a linear decline in the first 8 h of exposure. As the exposure time increases,

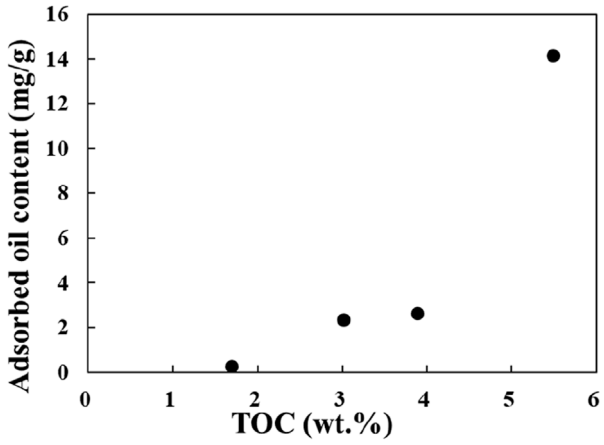

FIGURE 6
The relationship between adsorbed oil content and TOC of shale samples after long-term exposure.

the sample shows an exponential decrease, and the rate of decline progressively slows down. After 200–300 h, the trend levels off and the weight is stabled at 17.11 g, indicating no more fluid loss in shale pores. During the whole exposure process, about 0.275 g fluid was lost, accounting for 1.6% of the original weight of the shale. The change of oil content is similar to that of shale weight (Figure 4B), which decreased from 33.15 mg/g to 27.5 mg/g, with an oil loss rate of 17%.

The changes of adsorbed oil and free oil during sample A exposure is shown in Figure 4C. During oil loss, the adsorbed oil remains basically unchanged while a large amount of free oil is lost. With the increase of exposure time, the content of shale oil or free oil in large pores (T_2 > 1 ms) decreased from 23.06 mg/g to 13.3 mg/g, with a loss rate of 42%. In comparison, the adsorbed oil showed a different trend. In the early stage of storage (<100 h), which corresponds to the time period when free oil decreases rapidly, the adsorbed oil content shows an increasing trend. There maybe two reasons for the increase. First, the adsorbed oil generally exists in a solid-like state on the pore surface (Wang et al., 2015). In the early stage of the NMR test, controlled by the accuracy of the instrument, the adsorbed oil under freezing conditions may not be fully detected. As the exposure time increases, the sample was gradually thawed, and thus adsorbed oil was gradually detected. Second, as the free oil in the center of the pore gradually evaporates, the NMR T_2 map of the fluid in the pore generally shows a left-shifting trend, leading signal intensity increases at T_2 < 1 ms. The adsorbed oil content of sample A remains unchanged during the entire exposure process and was stable at 14.17 mg/g.

The losses of adsorbed oil, free oil at different exposure time in preserved shale samples B, C, and D were also calculated according to the changes of NMR T_1–T_2 maps, and the results are shown in Figure 5. For sample B, the total oil content reaches equilibrium after 100–150 h. The oil content decreases from 19.83 mg/g to 5.18 mg/g, and the loss rate is as high as 73%. Compared with sample A with lower maturity and higher TOC content, it takes shorter time for oil in sample B to reach loss equilibrium. The main reason maybe that sample B contains more light hydrocarbons than Sample A. For sample B, the free oil in large pores (T_2 > 1 ms) drops from 16.64 mg/g to 1.9 mg/g and the loss rate is 88%, which is much greater than sample A. The adsorbed oil of sample B changes the same with sample A, which first increases and then levels off and finally remains at 2.5 mg/g. Similarly, the shale oil loss rates of samples C and D are 70% and 78%, respectively after long-term storage. The decrease in shale oil is mainly attributed to free oil, while the adsorbed oil content remains basically unchanged. The hydrocarbon loss ratio shows a negative trend with TOC data (Table 1), which similar to the phenomenon found by Jiang et al. (2016).

Comparing the amounts of adsorbed oil and free oil in the four samples after long-term storage, it is found that for samples A, B, and D with relatively high TOC content, the adsorbed oil and free oil contents are basically the same, each account for about 50%. For sample C with low TOC and clay mineral content, however, the shale oil is still dominated by free oil after long-term storage, and the adsorbed oil content is extremely low. It is been concluded that shale oil adsorption is mainly controlled by organic matter richness, thermal maturity and clay mineral (Li et al., 2022c). In the present work, the adsorption oil content measured by 2D NMR is positively correlated with TOC content (Figure 6). Therefore, shale with low TOC content and clay mineral, especially for interbedded layers between organic-rich shale strata, may be favorable areas for shale oil exploration.

3.3 Changes in molecular composition of shale oil during exposure

The preserved shale samples (in powder) were exposed in open air environment, and were subjected to TD-GC experiments after different exposure times (e.g., 30 min, 1 h, 4 h, 8 h, 24 h, 48 h) to dynamically reveal molecular changes of shale oil. Figure 7 shows the TD–GC S1 fingerprints of sample A at different exposure times. When the preserved core is initially pulverized and the experiment conducted immediately, the thermal desorption products contain high proportion of C_1-C_5 gaseous components. As the exposure time increases, the gaseous components are evaporated first. After 5–10 min, the gaseous hydrocarbon components have volatilized in large quantities. During this period, the C_6-C_{10} components also decrease. The gaseous components are almost disappeared after 2 h. As the storage time further increases, the C_{12-} components continue to be lost. After 4–6 d, the C_{12-} components basically disappear completely. From the TD–GC S1 fingerprints, the exposure process exerts basically no impact on the C_{14+} components.

The contents of C_1-C_5 gaseous hydrocarbon, C_6-C_{14} light hydrocarbon and C_{14+} heavy hydrocarbon were calibrated according to the peak areas of the GC–FID traces, and the results are listed in Table 2. The S1 total hydrocarbon of shale powder analyzed immediately after pulverization (0 min) is 11.43 mg/g. After just 2 min, the value drops to 9.67 mg/g. The lost components are mainly gaseous and light hydrocarbons in oil. Therefore, for preserved shales, especially for crushed preserved shales, effective and timely analysis is extremely important due to rapid loss of hydrocarbons. After 2 h exposure, the S1 value is 5.94 mg/g, a decrease of about

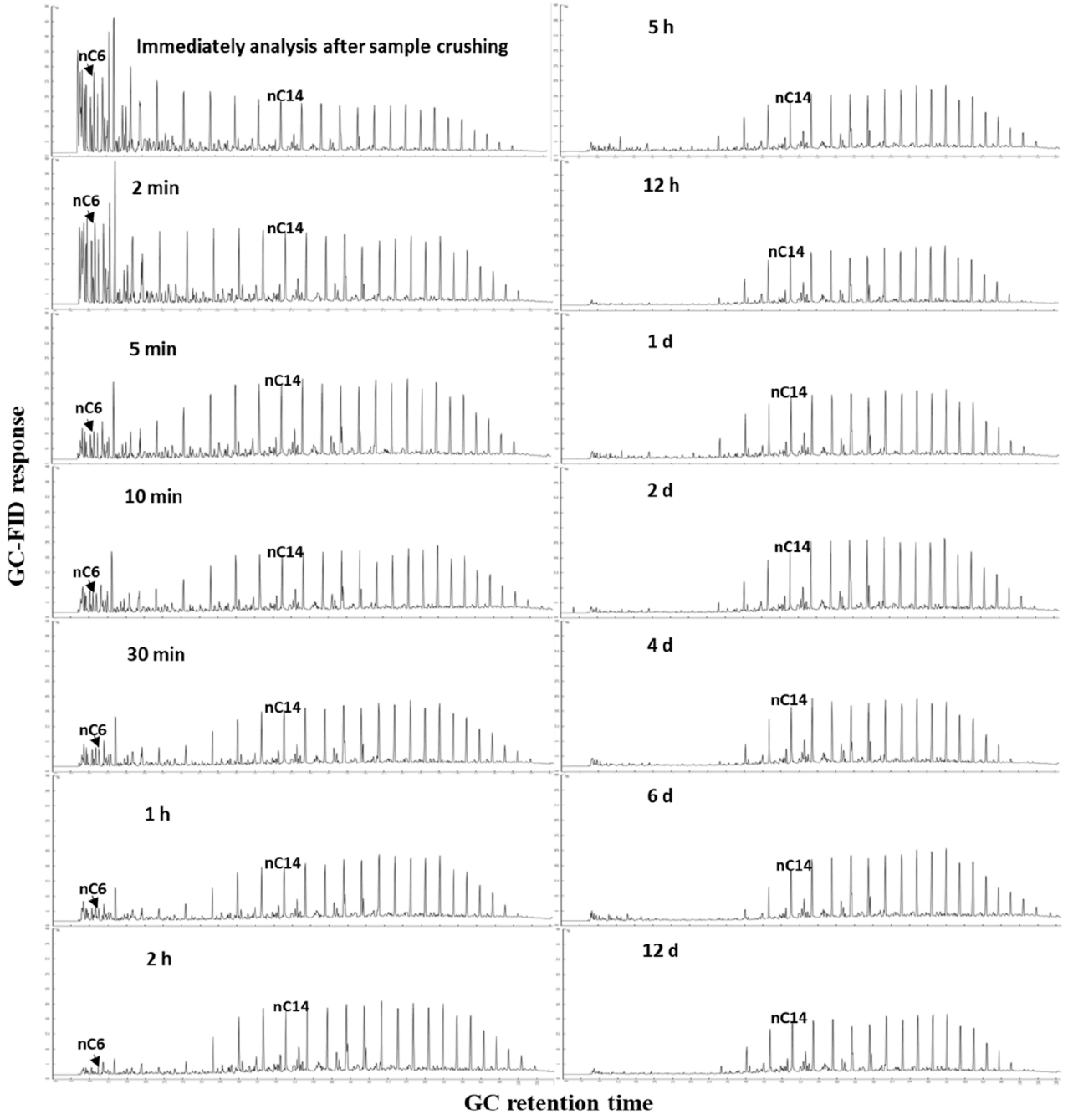

FIGURE 7
Thermal desorption chromatogram of preserved sample A at different exposure times.

50% compared with the initial moment. Furthermore, after long-term exposure for 6 d or 12 d, the hydrocarbon content of the shale is only about 4.6 mg/g, which means that 60% of the hydrocarbons in the initial S1 have been lost.

After 1–2 h, the C_1-C_5 gaseous hydrocarbon has basically disappeared, and the value fluctuates between 0.04 and 0.07 mg/g. The remaining gaseous hydrocarbon maybe due to adsorption or the measurement error of the instrument. The original content of the C_6-C_{14} light hydrocarbon is 6.25 mg/g. After long-term storage it decreases to 0.68 mg/g, which means that 90% is lost during the storage process. During the entire process, the C_{14+} heavy hydrocarbon of shale oil remained basically unchanged, fluctuating between 3.33 and 4.2 mg/g.

The content of *n*-alkanes in saturated fractions of oil was also calculated, and the results are shown in Figure 8. It is obvious that methane (C_1) evaporates the fastest, with loss rates of 94.77% after 2 min and 99.39% after 20 min. As the carbon chain length of hydrocarbon molecules increases, the overall loss rate shows a decreasing trend. The loss rate of pentane (C_5) is 83.93% after 2 min, and reaches 93.72% after 20 min. The loss rate of C_{10} is

TABLE 2 Calibrated C_1–C_5, C_6–C_{14}, and C_{14+} contents of sample A at different exposure times based on the peak areas of the GC–FID traces.

Time interval	C_1-C_5 (mg/g)	C_6-C_{14} (mg/g)	C_{14+} (mg/g)	Total oil (mg/g)
Analyzed immediately	1.85	6.25	3.33	11.43
2 min	1.05	4.92	3.7	9.67
5 min	0.23	3.03	4.2	7.47
10 min	0.23	2.64	4.01	6.88
30 min	0.2	2.28	3.91	6.39
1 h	0.2	2.01	3.8	6.01
2 h	0.05	1.74	4.15	5.94
5 h	0.06	1.27	3.86	5.2
12 h	0.04	1.06	3.85	4.95
1 d	0.06	1.27	3.57	4.89
2 d	0.04	0.94	3.8	4.78
4 d	0.06	0.98	3.62	4.65
6 d	0.07	0.76	3.86	4.69
12 d	0.06	0.68	3.85	4.6

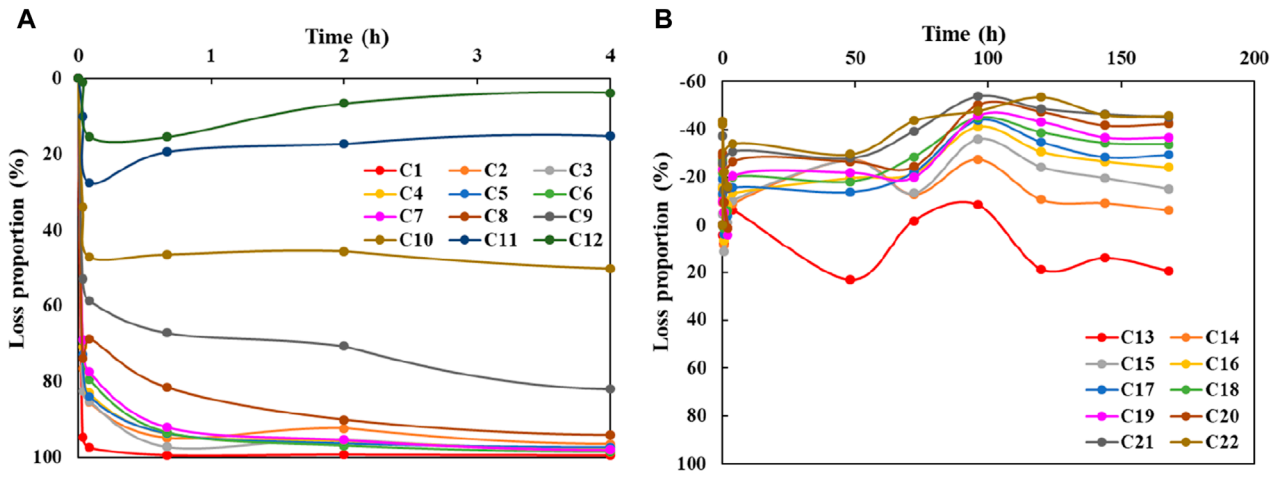

FIGURE 8
Changes of *n*-alkanes in thermal desorption products of sample A during exposure. **(A)** Hydrocarbons before C12; **(B)** Hydrocarbons after C12.

33.75% after 2 min, and reaches 91.81% after 48 h. Different from small molecular n-alkanes, the heavy molecular *n*-alkanes (n > 14) are not lost as the storage time increases, but fluctuates. The reason may be related to the weak diffusion/mobility ability of heavy hydrocarbons. Another possibility is that the TOC content of sample A is relatively high, and the organic matter has a strong ability to absorb heavy hydrocarbons, making it difficult for heavy components to volatilize.

4 Conclusion

In this work, four preserved shale cores with different thermal maturity and organic matter richness were selected. NMR T_1–T_2 mapping and TD-GC experiments were performed on preserved/fresh cores and their replicas that had been long-term exposed to ambient conditions to study the hydrocarbon loss rules. The main conclusions are as follows:

(1) The four preserved shale cores have relatively high pristine oil content. The 2D NMR quantified oil content of crushing the cores ranges from 10.61 mg/g to 33.15 mg/g and averages at 21.3 mg/g, which is much higher than the value obtained by geochemical methods.
(2) During storage, the preserved shale cores experienced large amount of oil loss, with a loss rate of approximately 42%–78%. The higher the maturity, the greater the loss rate. The shale oil loss is mainly contributed by free oil, while the adsorbed oil remains basically unchanged during exposure. The remaining content of adsorbed oil is positively correlated with TOC of the shale.
(3) Thermal desorption products at different time periods show that for powdered samples, the gaseous hydrocarbons in the shale have basically evaporated in just 5 min, indicating the necessity of timely and effective analysis of preserved cores. After long-term storage, 90% of the C_{14-} light hydrocarbon of shale oil is lost, while the C_{14+} heavy hydrocarbon remains basically unchanged.
(4) During the exposure process of preserved cores, in addition to shale oil loss, water will also decrease. There remain challenges in how to use conventional core samples to restore the original fluid occurrence and original fluid saturation of shale.

Data availability statement

The raw data supporting the conclusion of this article will be made available by the authors, without undue reservation.

Author contributions

JZ: Data curation, Investigation, Resources, Writing–original draft, Writing–review and editing. MW: Conceptualization, Funding acquisition, Supervision, Writing–review and editing. JL: Data curation, Funding acquisition, Methodology, Writing–review and editing. ZL: Data curation, Methodology, Writing–review and editing. LX: Data curation, Methodology, Writing–review and editing.

Funding

The author(s) declare that financial support was received for the research, authorship, and/or publication of this article. This study was funded by the National Natural Science Foundation of China (42102154, 41922015, 42072147).

Conflict of interest

Authors JZ, ZL, and LX were employed by Exploration and Development Research Institute of PetroChina Daqing Oilfield Company.

The remaining authors declare that the research was conducted in the absence of any commercial or financial relationships that could be construed as a potential conflict of interest.

Publisher's note

All claims expressed in this article are solely those of the authors and do not necessarily represent those of their affiliated organizations, or those of the publisher, the editors and the reviewers. Any product that may be evaluated in this article, or claim that may be made by its manufacturer, is not guaranteed or endorsed by the publisher.

References

Ali, M., Ali, S., Mathur, A., and Belanger, C. (2020). Organic shale spontaneous imbibition and monitoring with NMR to evaluate *in-situ* saturations, wettability and molecular sieving, unconventional resources technology conference, 20–22 july 2020. *Unconv. Resour. Technol. Conf. (URTEC)*, 3104–3117. doi:10.15530/urtec-2020-3096

Chen, Z., and Jiang, C. (2020). An integrated mass balance approach for assessing hydrocarbon resources in a liquid-rich shale resource play: an example from Upper Devonian Duvernay Formation, Western Canada Sedimentary Basin. *J. Earth Sci.* 31 (06), 1259–1272. doi:10.1007/s12583-020-1088-1

Cooles, G. P., Mackenzie, A. S., Quigley, T. M., et al. (1986). Calculation of petroleum masses generated and expelled from source rocks. *Org. Geochem.* 10 (1-3), 235–245. doi:10.1016/0146-6380(86)90026-4

Jarvie, D. M. (2014). Components and processes affecting producibility and commerciality of shale resource systems. *Geol. Acta Int. Earth Sci.* 12 (4), 307–325.

Jarvie, D. M., and Breyer, J. A. (2012). Shale resource systems for oil and gas; Part 2, Shale-oil resource systems. *AAPG Mem.* 97, 89–119. doi:10.1306/13321447m973489

Jiang, C., Chen, Z., Mort, A., Milovic, M., Robinson, R., Stewart, R., et al. (2016). Hydrocarbon evaporative loss from shale core samples as revealed by Rock-Eval and thermal desorption-gas chromatography analysis: its geochemical and geological implications. *Mar. Petroleum Geol.* 70, 294–303. doi:10.1016/j.marpetgeo.2015.11.021

Li, J., Huang, W., Lu, S., Wang, M., Chen, G., Tian, W., et al. (2018). Nuclear magnetic resonance T 1–T 2 map division method for hydrogen-bearing components in continental shale. *Energy and Fuels* 32 (9), 9043–9054. doi:10.1021/acs.energyfuels.8b01541

Li, J., Jiang, C., Wang, M., Lu, S., Chen, Z., Chen, G., et al. (2020). Adsorbed and free hydrocarbons in unconventional shale reservoir: a new insight from NMR T1-T2 maps. *Mar. Petroleum Geol.* 116, 104311. doi:10.1016/j.marpetgeo.2020.104311

Li, J., Jiang, C., Wang, M., Xu, L., Li, M., Yu, C., et al. (2022a). Determination of *in situ* hydrocarbon contents in shale oil plays. Part 1: is routine Rock–Eval analysis reliable for quantifying the hydrocarbon contents of preserved shale cores? *Org. Geochem.* 170, 104449. doi:10.1016/j.orggeochem.2022.104449

Li, J., Wang, M., Fei, J., Xu, L., Shao, H., Li, M., et al. (2022b). Determination of *in situ* hydrocarbon contents in shale oil plays. Part 2: two-dimensional nuclear magnetic resonance (2D NMR) as a potential approach to characterize preserved cores. *Mar. Petroleum Geol.* 145, 105890. doi:10.1016/j.marpetgeo.2022.105890

Li, J., Wang, M., Jiang, C., Lu, S., and Li, Z. (2022c). Sorption model of lacustrine shale oil: insights from the contribution of organic matter and clay minerals. *Energy* 260, 125011. doi:10.1016/j.energy.2022.125011

Liu, B., Bai, L., Chi, Y., Jia, R., Fu, X., and Yang, L. (2019). Geochemical characterization and quantitative evaluation of shale oil reservoir by two-dimensional nuclear magnetic resonance and quantitative grain fluorescence on extract: a case study from the Qingshankou Formation in Southern Songliao Basin, northeast China. *Mar. Petroleum Geol.* 109, 561–573. doi:10.1016/j.marpetgeo.2019.06.046

Ma, W., Hou, L., Luo, X., Liu, J., Tao, S., Guan, P., et al. (2020). Generation and expulsion process of the Chang 7 oil shale in the Ordos Basin based on temperature-based semi-open pyrolysis: implications for *in-situ* conversion process. *J. Petroleum Sci. Eng.* 190, 107035. doi:10.1016/j.petrol.2020.107035

Ma, W., Li, J., and Wang, M. (2024). Determination of *in situ* hydrocarbon contents in shale oil plays: Part 3: quantification of light hydrocarbon evaporative loss in old cores based on preserved shales. *Mar. Petroleum Geol.* 160, 106574. doi:10.1016/j.marpetgeo.2023.106574

Michael, G. E., Packwood, J., and Holba, A. (2013). *Determination of in-situ hydrocarbon volumes in liquid rich shale plays*. SPE168695.

Mukhametdinova, A., Habina-Skrzyniarz, I., and Krzyzak, A. (2021). NMR relaxometry interpretation of source rock liquid saturation—a holistic approach. *Mar. Petrol. Geol.* 132, 105165. doi:10.1016/j.marpetgeo.2021.105165

Nikitin, A., Durand, M., McMullen, A., Blount, A., Driskill, B., and Hows, A. (2019). Crushed rock analysis workflow based on advanced fluid characterization for improved interpretation of core data. *Petrophysics-The SPWLA J. Format. Eval. Reserv. Descript.* 60, 755–769. doi:10.30632/pjv60n6-2019a4

Noble, R. A., Kaldi, J. G., and Atkinson, C. D. (1997). *AAPG memoir 67: seals, traps, and the petroleum system*. Chapter 2: Oil Saturation in Shales: Applications in Seal Evaluation.

Romero-Sarmiento, M. F. (2019). A quick analytical approach to estimate both free versus sorbed hydrocarbon contents in liquid-rich source rocks. *AAPG Bull.* 103 (9), 2031–2043. doi:10.1306/02151918152

Song, G., Zhang, L., Lu, S., et al. (2013). Resource evaluation method for shale oil and its application. *Earth Sci. Front.* 20 (4), 221–228.

Sun, L., Liu, H., He, W., Li, G., Zhang, S., Zhu, R., et al. (2021). An analysis of major scientific problems and research paths of Gulong shale oil in Daqing Oilfield, NE China. *Petroleum Explor. Dev.* 48 (3), 527–540. doi:10.1016/s1876-3804(21)60043-5

Sun, Y., Wang, Y., Liao, L., Shi, S., and Liu, J. (2023). How grain size influences hydrocarbon generation and expulsion of shale based on Rock-Eval pyrolysis and kinetics? . *Mar. Petroleum Geol.* 155, 106369. doi:10.1016/j.marpetgeo.2023.106369

Wang, M., Li, M., Li, J. B., Xu, L., and Zhang, J. X. (2022). The key parameter of shale oil resource evaluation: oil content. *Petroleum Sci.* 19 (4), 1443–1459. doi:10.1016/j.petsci.2022.03.006

Wang, M., Tian, S., Chen, G., Xue, H., Huang, A., and Wang, W. (2014). Correction method of light hydrocarbons losing and heavy hydrocarbon handling for residual hydrocarbon (S1) from shale. *Acta Geol. Sin. (Beijing)* 88 (06), 1792–1797. doi:10.1111/1755-6724.12345

Washburn, K. E., and Birdwell, J. E. (2013). Updated methodology for nuclear magnetic resonance characterization of shales. *J. Magnetic Reson.* 233, 17–28. doi:10.1016/j.jmr.2013.04.014

Yan, G., Xu, Y. H., Xu, W. L., Bai, B., Bai, Y., Fan, Y. P., et al. (2023). Shale oil resource evaluation with an improved understanding of free hydrocarbons: insights from three-step hydrocarbon thermal desorption. *Geosci. Front.* 14 (6), 101677. doi:10.1016/j.gsf.2023.101677

Zhu, R., Zhang, L., Li, J., et al. (2015). Quantitative evaluation of residual liquid hydrocarbons in shale. *Acta Pet. Sin.* 36 (1), 13–18.

frontiers | Frontiers in Earth Science

TYPE Original Research
PUBLISHED 20 March 2024
DOI 10.3389/feart.2024.1375637

Check for updates

OPEN ACCESS

EDITED BY
Wenguang Wang,
Northeast Petroleum University, China

REVIEWED BY
Weichao Tian,
Yangtze University, China
Zhihao Jiang,
Xi'an Shiyou University, China
Haitao Wang,
Chongqing University of Science and Technology, China
Elham Bakhshi,
University of Talca, Chile

*CORRESPONDENCE
Huaimin Dong,
sdsddhm@chd.edu.cn
Peng Chi,
b21010024@s.upc.edu.cn

RECEIVED 24 January 2024
ACCEPTED 05 March 2024
PUBLISHED 20 March 2024

CITATION
Dong H, Luo B, Dang C, Xu S, Wang F and Chi P (2024), Quantitative characterization of the carbonate rock microstructure considering topological features: a case study from the Gaoshiti–Moxi block of the Sichuan Basin.
Front. Earth Sci. 12:1375637.
doi: 10.3389/feart.2024.1375637

COPYRIGHT
© 2024 Dong, Luo, Dang, Xu, Wang and Chi. This is an open-access article distributed under the terms of the Creative Commons Attribution License (CC BY). The use, distribution or reproduction in other forums is permitted, provided the original author(s) and the copyright owner(s) are credited and that the original publication in this journal is cited, in accordance with accepted academic practice. No use, distribution or reproduction is permitted which does not comply with these terms.

Quantitative characterization of the carbonate rock microstructure considering topological features: a case study from the Gaoshiti–Moxi block of the Sichuan Basin

Huaimin Dong[1,2]*, Bin Luo[3], Chenyue Dang[4], Shuang Xu[5], Feng Wang[5] and Peng Chi[6]*

[1]School of Geological Engineering and Geomatics, Chang'an University, Xi'an, China, [2]Key Laboratory of Western China's Mineral Resources and Geological Engineering, Xi'an, China, [3]Research Institute of Petroleum Exploration and Development, Changqing Oilfield Company, Xi'an, China, [4]Department of Geology, Northwest University, Xi'an, China, [5]No.1 Oil Production Plant, Changqing Oilfield Company, Yan'an, China, [6]School of Geosciences, China University of Petroleum, Qingdao, China

The precise characterization of the rock microstructure is crucial for predicting the physical characteristics, flow behavior, and mechanical properties of rocks. This is particularly important for carbonate rocks, which depict a complex microstructure with multimodal pore radius distribution and natural fractures. Here, topological features that are typically ignored are taken into account to quantify the carbonate microstructure. Carbonate samples used are obtained from the Gaoshiti–Moxi block of the Sichuan Basin, which showed remarkable potential for oil and gas. Specifically, nuclear magnetic resonance (NMR), X-ray micro-computed tomography (micro-CT), and mercury injection capillary pressure (MICP) techniques are performed to describe the topological and geometric characteristics. The results indicate that NMR and MICP techniques can describe more rock pores than micro-CT. However, due to the presence of pore shielding in MICP tests, the pore radius obtained by MICP is smaller than that obtained by micro-CT and NMR. Furthermore, the effective method used for characterizing the pore structure is NMR technology. The hardest part is that the coefficient between the pore radius and T_2 relaxation time is difficult to calculate. Therefore, a better calculation method must be found. In addition, micro-CT is an irreplaceable technique for obtaining a large number of topological and geometric features, and multi-phase or single-phase flow simulations can be conducted via digital rock models. However, for carbonates, micro-CT is not sufficient to describe the complete pore systems because macropores cannot be fully represented and sub-resolution micropores cannot be described. Those macropores and micropores have a very important effect on their seepage properties. Therefore, multi-scale digital rock modeling involving small and large pores is essential for complex rocks, which

is of great significance for the analysis of pore systems and the simulation of rock physical properties.

KEYWORDS

carbonates, geometric features, topological structure, fractal dimension, petrophysics experiments

1 Introduction

The microstructure characterization of subsurface systems is crucial for determining the permeable regions, petrophysical properties, and associated reservoir quality (Tahmasebi, 2017; Dong et al., 2023). These microstructural petrophysical properties of the rocks control the macroscopic properties and flow behavior (Daigle et al., 2017; Fagbemi et al., 2018; Tahmasebi and Kamrava, 2018), which include the topological and geometrical characteristics (Dong et al., 2017; Abro et al., 2019). In this context, carbonate rocks offer a relatively complex microstructure, which is attributed to a range of factors, including but not limited to multimodal pore radius distribution (e.g., micro-porosity and vugs) and mineral heterogeneity (e.g., the classic case of the Arab-D reservoir, where dolomitization leads to massive heterogeneous lithologies) (Arif et al., 2020; Chandra et al., 2021; Li et al., 2022).

A range of techniques have been applied to investigate the carbonate microstructure (Kibria et al., 2018; Gao et al., 2019), which can be categorized into direct imaging techniques, such as X-ray micro-computed tomography (micro-CT), scanning electron microscopy (SEM), and laser confocal scanning (Van Geet et al., 2001; Romero and Simms, 2008; Norbisrath et al., 2015; Zhang et al., 2021), and indirect techniques, such as nuclear magnetic resonance (NMR), mercury injection capillary pressure (MICP), small-angle neutron scattering (SANS), and gas adsorption (Yao et al., 2010; Okolo et al., 2015; Radlinski and Mastalerz, 2017; Yu et al., 2020; Hosseini et al., 2021). There are scores of previous studies that have characterized the carbonate microstructure using one or a combination of the techniques mentioned above; however, a majority of those typically aimed at the pores' geometric characteristics only (Zhang et al., 2016; Sarkar et al., 2018), while the analysis of the pore systems' topological characteristics is frequently ignored, although these parameters have important effects on the transport properties.

In this paper, for the sake of comprehensively characterizing the topological and geometrical characteristics of carbonate rocks, MICP, NMR, and micro-CT tests are performed on six carbonate samples. These samples were acquired from the Longwangmiao and Dengying formations in the Gaoshiti–Moxi field, Sichuan Basin, China, which is a significant discovery made in terms of hydrocarbon potential as evidenced in recent years (Otiede and Wu, 2011; Zhou et al., 2020). The samples' preparation and experimentation are performed, followed by the fractal dimension calculation to examine the topological features.

2 Geological setting

The Gaoshiti–Moxi block is located in the middle of the gentle tectonic belt in the middle Sichuan area and the eastern part of the axis of the Leshan–Longnvsi ancient uplift in the Sichuan Basin, which included the Cambrian Longwangmiao Formation and Sinian Dengying Formation (Wei et al., 2015a; Zeng et al., 2023), and the structural map of the Sinian top in the study area is shown in Figure 1. The Gaoshiti–Moxi latent tectonic belt has experienced synsedimentation and denudation uplift from multi-cycle tectonic movement. It was controlled by the basement uplift of the middle Sichuan and Longmenshan mountains and represents a paleo-uplift with a certain inheritance (Du et al., 2014; Lai et al., 2023). During the Sinian period, the carbonate-striped platform was developed in the Sichuan Basin and its periphery, and the carbonate-slope-type platform was developed during the deposition period of the Longwangmiao Formation of Cambrian (Zou et al., 2014), forming complex fracture-cavity and pore-type carbonate reservoirs. The reservoir and percolation space of the Longwangmiao Formation are mainly fracture-pore/cave type, followed by pore type, which is well-matched with pore, cave, and fracture. The reservoir and percolation space of the Dengying Formation are fracture-pore/cave type and pore/cave type (Li et al., 2017; Yang et al., 2023). The average porosity of carbonate reservoirs in the second and fourth members of the Dengying Formation and the Longwangmiao Formation is 3.35%, 3.22%, and 4.28%, respectively, and the average permeability is 1.160×10^{-3} μm^2, 0.593×10^{-3} μm^2, and 0.966×10^{-3} μm^2. The purpose of this study is to examine the deep carbonate rock fracture-cave reservoirs of the Sinian Dengying Formation and the Cambrian Longwangmiao Formation in the Gaoshiti–Moxi block of the Sichuan Basin.

3 Experiments and methods

3.1 Sample preprocessing and experiment preparation

Six carbonate samples are collected from the Longwangmiao Formation and Dengying Formation in the Gaoshiti–Moxi block, Sichuan Basin. All samples were tested by NMR, MICP, and micro-CT. After sample preprocessing, the samples were processed into cylinders with a length of 50 mm and a diameter of 25 mm. Subsequently, for NMR tests, these samples were processed into subsamples, and the length of the two cylinders is 30 mm and 18 mm. These cylinders with a length of 30 mm were used for MICP experiments, and the other tiny samples were prepared in cylinders

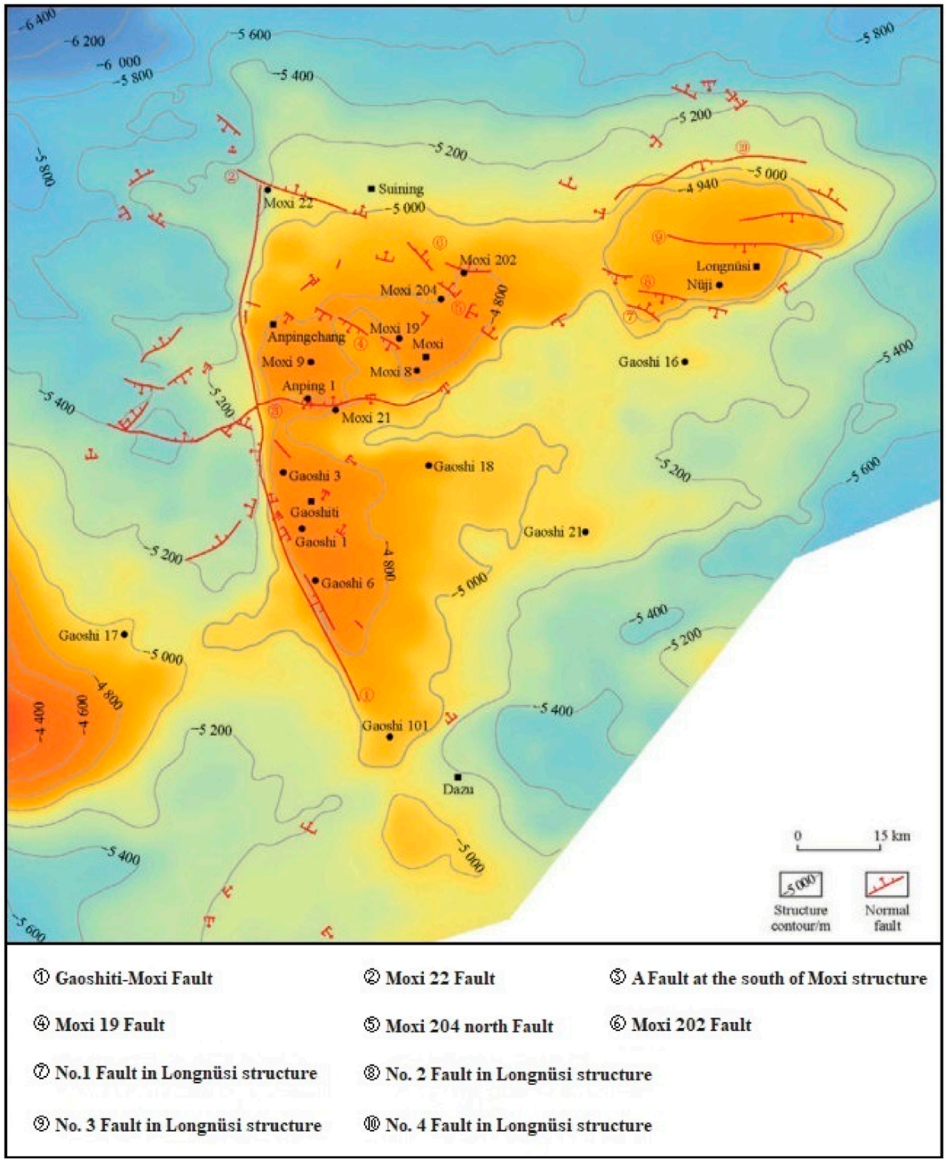

FIGURE 1
Geological map of the Sinian top in the Sichuan Basin (modified from Wei et al., 2015b).

with a length of 10 mm and a diameter of 3 mm for micro-CT experiments.

3.2 NMR measurements

The NMR technique is widely applied to the analysis of pore structures (Golsanami et al., 2019; Yan et al., 2019; Ouyang et al., 2023) and is especially useful for analyzing rock/fluid interactions (Ali et al., 2022; Isah et al., 2022; Wang et al., 2023), despite its limitations. The experiments were conducted at the China University of Petroleum (East China). First, six samples were dried for 48 h at 369.15 K. Next, the samples prepared were saturated with distilled water and centrifuged to achieve the state with different irreducible water. Simultaneously, the transverse relaxation time was measured using the MesoMR23-060H-1 nuclear magnetic instrument.

Regarding low-field NMR, there is a relationship, as expressed in Eq. 1.

$$\frac{1}{T_2} = \frac{1}{T_{2B}} + \frac{1}{T_{2D}} + \frac{1}{T_{2S}}, \tag{1}$$

where T_2 is the transverse relaxation time; T_{2S}, T_{2B}, and T_{2D} are the surface relaxation time, transverse relaxation time, bulk relaxation time, and diffusion relaxation time, respectively.

The bulk relaxation time is usually much larger than the transverse relaxation time, which can be ignored. Therefore, Eq. 1 is simplified to Eq. 2 as follows:

$$\frac{1}{T_2} = \frac{1}{T_{2S}} = \rho\frac{S}{V}, \tag{2}$$

where ρ is the transversal surface relaxivity, μm/ms; V is the pore volume, μm^3; and S is the pore surface area, μm^2.

The correlation of the pore surface area and pore volume is expressed in Eq. 3.

$$\frac{S}{V} = \frac{m}{r}, \tag{3}$$

where m is a constant, which is related to the pore's shape; r is the pore radius. Thus, the correlation of the pore radius and transverse relaxation time is expressed in Eq. 4.

$$r = nT_2, \tag{4}$$

where n is a coefficient, which is related to ρ and m, μm/ms.

In addition, the conversion coefficient can be determined by comparing the cumulative probability curve of the pore radius in MICP experiments and that of the T_2 spectrum in NMR tests when it is tangent, and finally, the purpose of characterizing the rock pore structure based on NMR technology can be realized (Dong et al., 2019).

3.3 MICP tests

The MICP method can measure the radius distribution of pores and throats (Okolo et al., 2015; Zhang et al., 2020; Yang et al., 2022), which was conducted at Shengli Oilfield using the Auto Pore 9500 automatic mercury injection instrument. First, the samples were washed to remove salt and oil, then dried for 48 h at 96°C, and stored in a vacuum. Then, mercury was injected into the pore systems at pressures ranging from 0 to 207 MPa, and relevant data were recorded. Finally, the pore radius can be obtained in Eq. 5 as follows:

$$r = \frac{2\sigma \cos\theta}{P_c\left(S_{Hg}\right)}, \tag{5}$$

where S_{Hg} is the mercury saturation; r is the pore radius; θ is the contact angle, °; σ is the interfacial tension, N/m; and P_c is the capillary pressure. Then, Eq. 6 can be obtained as follows:

$$PDF = R\frac{dS_{Hg}}{dR} = -P_c\frac{dS_{Hg}}{dP_c} = -\frac{dS_{Hg}}{d\ln P_c}, \tag{6}$$

where PDF represents the probability distribution function of the pore radius.

3.4 Micro-CT experiments

The micro-CT technique can perform non-destructive imaging, three-dimensional imaging, and so on (Mathews et al., 2017; Qi et al., 2023). The advancement in computational power and imaging analysis has led to the growth of digital rock analysis. In this investigation, all carbonate samples were scanned using the XTH high-resolution micro-CT imaging system. In the process of scanning, a series of X-ray photographs were uniformly recorded along the trajectory, with a resolution of 26.6 μm/voxel.

In micro-CT experiments, once the resolution is set, the micropores and ultra-micropores with a pore radius smaller than this value will not be covered. The representative elementary volume (REV) is an important parameter that needs to be determined in advance when using micro-CT for pore space analysis. During CT image processing, the REV is first extracted from the original gray-scale CT images; then, a median filter is applied, followed by combining with a threshold value to separate solid and pore space for interactive threshold segmentation. Then, smoothed pore space was obtained by using the closing algorithm. In the end, REV's porosity was obtained. According to whether the pore space is connected, the pore space can be divided into isolated and connected pore spaces. The connected pore space refers to the connection between the pore bodies and other pore bodies through the throats. After separating the pore space, the maximal sphere algorithm was used to distinguish the pore and throat. Furthermore, the pore network model was extracted.

The specific Euler number and coordination number can characterize the topological features more clearly, which can help describe the connectivity of specific components. The maximal sphere algorithm is used to calculate the distribution of the coordination number. The specific Euler number was proposed by Vogel and Roth (2001), as expressed in Eq. 7.

$$\chi_V = \frac{\chi}{V}, \tag{7}$$

where χ represents the conventional Euler number for a porous medium with volume V.

In addition, a two-point correlation function was applied to characterize the probability of selecting two voxels in the 3D pore space, and this parameter is defined in Eq. 8.

$$S(x, x+\boldsymbol{h}) = I(x)I(x+\boldsymbol{h}), \tag{8}$$

where $I(x)$ is an indicator function, $\boldsymbol{h}$ is the magnitude of the vector, and x and $x+\boldsymbol{h}$ are two voxels; when x and $x+\boldsymbol{h}$ are in the void space, $I(x+\boldsymbol{h})=1$; conversely, $I(x+\boldsymbol{h})=0$, and $I(x)I(x+\boldsymbol{h})$ represents the average of the multiplication of two indicator functions.

Assuming that the pores are an equivalent circle, the pore radius is calculated using Eq. 9 as follows:

$$r = \sqrt{\frac{A}{\pi}}, \tag{9}$$

where A is the pore surface area and r is the pore radius.

Indeed, many pores are not circular, and therefore, in order to obtain a more realistic result, the pore radius can be computed through the shape factor. Pore space can be obtained using the thresholding method. Then, the median filter is used for denoising, and the watershed algorithm is used to separate the connected pores. The pore and throat shape factors are the important parameters utilized for characterizing the morphology of the pore and throat. The shape factor of the pore can be calculated using Eq. 10 as follows:

$$G = \frac{A}{P^2}, \tag{10}$$

where G is the shape factor, A is the area of the pore, and P is the perimeter of the pore. The shape factors of the equilateral circle, square, and triangle are 0.0796, 0.071, and 0.0481, respectively.

3.5 Fractal dimension calculation

For pores with fractal characteristics, the fragmentation and regularity of the pore system can be described by the fractal dimension (Han et al., 2023; Jiang et al., 2023). The relationship between pore radius and fractal dimension is expressed in Eq. 11 as follows (Li et al., 2017):

$$N(r) \propto r^{-D_f}, \tag{11}$$

where r is the pore radius, D_f is the fractal dimension, and $N(r)$ is the number of pores with the pore radius greater than r. According to Eq. 11, the pore radius distribution function can be obtained, as expressed in Eq. 12.

$$f(r) = \frac{dN(r)}{dr} \propto r^{-D_f-1}. \tag{12}$$

Assuming that the pore volume and pore radius can be descripted in Eq. 13 as follows:

$$v \propto r^3. \tag{13}$$

Thus, the cumulative pore volume of the pore with the radius greater than r can be calculated, as expressed in Eq. 14.

$$V(r) = \int_r^{r_{\max}} f(r)v dr = \int_r^{r_{\max}} a r^{2-D_f} dr = b \cdot \left(r_{\max}^{3-D_f} - r^{3-D_f}\right), \tag{14}$$

where a and b are constants related to the pores' shape; $r_{\max}$ is the maximum pore radius. When r is equal to $r_{\min}$, the entire pore volume can be obtained using Eq. 15 as follows:

$$V(> r_{\min}) = b \cdot \left(r_{\max}^{3-D_f} - r_{\min}^{3-D_f}\right). \tag{15}$$

Then, the pore volume accumulative frequency $F(>r)$ can be calculated, as expressed in Eq. 16.

$$F(> r) = \frac{V(> r)}{V(> r_{\min})} = \frac{r_{\max}^{3-D_f} - r^{3-D_f}}{r_{\max}^{3-D_f} - r_{\min}^{3-D_f}}. \tag{16}$$

Since $r_{\min} \ll r_{\max}$, Eq. 16 can be converted to Eq. 17.

$$F(> r) = \frac{r_{\max}^{3-D_f} - r^{3-D_f}}{r_{\max}^{3-D_f}} = 1 - \left(\frac{r}{r_{\max}}\right)^{3-D_f}. \tag{17}$$

Therefore, the pore radius is less than r, and the pore volume accumulation frequency is $F(<r)$, as shown in Eq. 18.

$$F(< r) = 1 - F(> r) = \left(\frac{r}{r_{\max}}\right)^{3-D_f}. \tag{18}$$

In MICP experiments, when the pore radius is less than r, the pore volume accumulation frequency can be expressed as Eq. 19.

$$F(< r) = 1 - S_{Hg}. \tag{19}$$

So, the following formula can be obtained:

$$\log\left(1 - S_{Hg}\right) = \left(D_f - 3\right)\log P_c - \left(D_f - 3\right)\log P_{\min}. \tag{20}$$

D_f can be determined by the slope of the $\log(1\text{-}S_{\text{Hg}})$ and $\log P_c$ in double-log plots. The fractal dimensions of pores with different radii were computed using Eq. 20.

$$D_f = \frac{D_{f1} \cdot \phi_1 + D_{f2} \cdot \phi_2 + D_{f3} \cdot \phi_3 + D_{f4} \cdot \phi_4}{\phi}, \tag{21}$$

where ϕ_1, ϕ_2, ϕ_3, and ϕ_4 are the porosity of the pores in descending order of radius, ϕ is the porosity of the entire pores, and D_{f1}, D_{f2} D_{f3}, D_{f4}, and D_f are the fractal dimensions of corresponding pores.

As for NMR tests, from Eqs 4 and 18, Eq. 22 can be obtained as follows:

$$\log\left(F(< r)\right) = \left(3 - D_f\right)\log T_2 - \left(3 - D_f\right)\log T_{2\,\max}. \tag{22}$$

Equation 22 is similar to Eq. 20, allowing for the calculation of the fractal dimension of NMR.

As for micro-CT experiments, the pores from this experiment cannot cover all pore types. Hence, the fractal dimensions of the images are calculated, which can be realized using commercial software Avizo (Mathews et al., 2011).

4 Results and discussion

4.1 Pore space features and pore radius distribution

4.1.1 MICP results

The MICP curves of the six carbonate samples showed that mercury began to be injected into the pores when the pressure reached 0.01 MPa. When the pressure reaches 1 MPa, the mercury content in samples S2 and S4 increases, which means that there are many large pores in these samples (Figure 2A). The pore radius distribution of each sample can be calculated using Eq. 6. Figure 2B shows that the pore radius distribution characteristics of S1, S2, S4, and S6 are similar, whose peak pore volume fraction is all greater than 0.04, while the peak pore volume fraction of S3 is approximately 0.12 and that of S5 is approximately 0.16. The main pore radius of S2, S4, and S6 is 0.008 ~ 0.3, 0.4 ~ 1.0, and 50.0 ~ 200 μm, respectively. In addition, the median saturation radius of each sample is 0.15, 0.03, 0.51, 0.08, 1.52, and 0.23 μm, and the maximum throat radius is 3.81, 0.89, 3.81, 0.53, 21.32, and 1.52 μm.

The pores can be divided into ultra-micropores, micropores, mesopores, and macropores, and the radius ranges are less than 0.1, 0.1 ~ 1, and 1 ~ 10 μm and greater than 10 μm, respectively. The porosity of these groups was calculated and shown in Table 1, which indicates that the proportion of macropores in S2 and S5 is higher than that of S1, S3, S4, and S6, which are all greater than 30%. The proportion of mesopores in S1, S3, and S5 is all greater than 10%, indicating that there are more mesopores in the pores. In addition, there are many ultra-micropores in S1, S2, and S4, which account for up to 25%, effectively connecting the pores and improving permeability.

4.1.2 NMR results

The results of NMR experiments are shown in Figure 3. It can be seen that S2, S4, and S6 are bimodal, and S3 is unimodal, and S1 and S5 are trimodal. The variation in porosity increment with relaxation time is similar for S1 and S5 and S2 and S6.

One of the difficulties in the NMR characterization of the pore structure is the determination of the coefficient. The coefficient values of each sample are determined, as shown in Figure 4. The results are shown in Table 2, indicating that there is a large gap in the cumulative probability curve of the pore

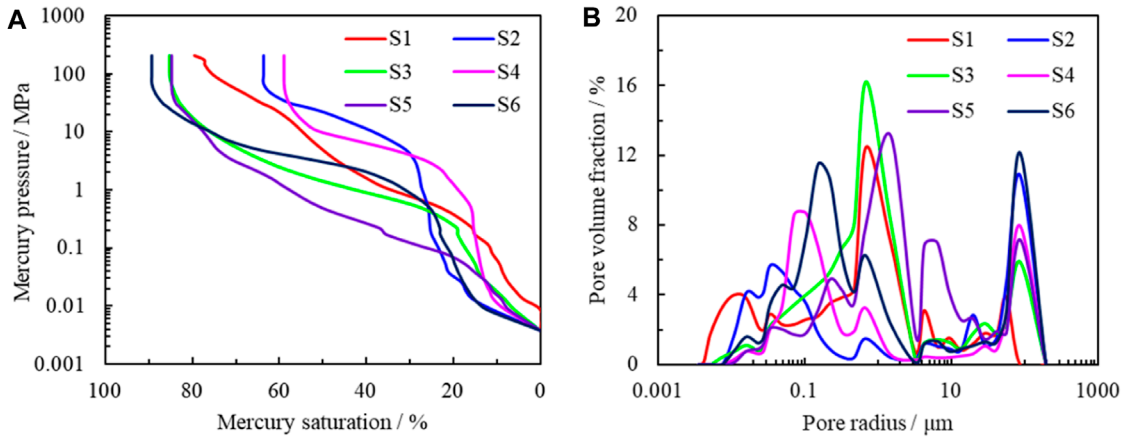

FIGURE 2
Test results of MICP. **(A)** MICP curves, and **(B)** pore radius distribution curves.

TABLE 1 Porosity of different pores in MICP tests.

Sample no.	ϕ	Macropore		Mesopore		Micropore		Ultra-micropore	
		φ_1	ϕ_1	φ_2	ϕ_2	φ_3	ϕ_3	φ_4	ϕ_4
S1	4.19	15.61	0.65	14.07	0.59	38.31	1.61	32.01	1.34
S2	3.17	37.50	1.19	3.10	0.10	13.40	0.42	46.00	1.46
S3	5.92	20.90	1.24	11.80	0.70	52.60	3.11	14.70	0.87
S4	4.67	24.88	1.16	2.26	0.11	44.89	2.10	27.97	1.30
S5	7.36	33.90	2.50	25.30	1.86	30.30	2.23	10.50	0.77
S6	4.50	24.49	1.11	4.10	0.18	51.60	2.32	19.81	0.89

ϕ, ϕ_1, ϕ_2, ϕ_3, and ϕ_4 are the porosity of sample, macropores, mesopores, micropores, and ultra-micropores; φ_1, φ_2, φ_3, and φ_4 are the proportion of macropores, mesopores, micropores, and ultra-micropores in the total pores, respectively.

TABLE 2 Coefficient values for the six carbonate samples.

Sample no.	S1	S2	S3	S4	S5	S6
Coefficient value/μm·ms^{-1}	0.00096	0.0014	0.001	0.001	0.004	0.0025

radius for NMR and MICP, which represents the heterogeneity characteristics, among which S2 and S4 have the strongest heterogeneity.

The pore radius distribution of each sample can be obtained through Eq. 4, as shown in Figure 5, demonstrating that the curve of S3 is unimodal, the curves of S2, S4, and S6 are bimodal, and those of S1 and S5 are trimodal. The main pore radius of S2, S4, and S6 ranges from 7 μm to 50 μm, and the secondary peak ranges from 0.3 μm to 2 μm. Some pores with a pore radius up to 100 μm appeared in S5, which may be the cause of small fractures. Moreover, the pore radius corresponding to the peaks of S1~S6 is 17.21, 17.23, 29.45, 20.13, and 2.06 μm. In addition, the proportions of pores with different radii are shown in Table 3.

The parameters in this table are consistent with those observed in Table 1.

4.1.3 Micro-CT results

In this investigation, based on the variation of sub-volume porosity with its volume, as shown in Figure 6, a sample (500 × 500 × 500 voxels) is selected as the representative basic volume size. Taking samples S4, S5, and S6 as examples, the separated solids and pore space are as shown in Figure 7A, Figures 7B, D, Figures 7E, G, and Figure 7H, which indicates that the connectivity between S4 and S6 is poor. The reason is that ultra-micropores and micropores may connect mesopores and macropores, respectively, and micropores are not tested by micro-CT. After separating the pore space, the

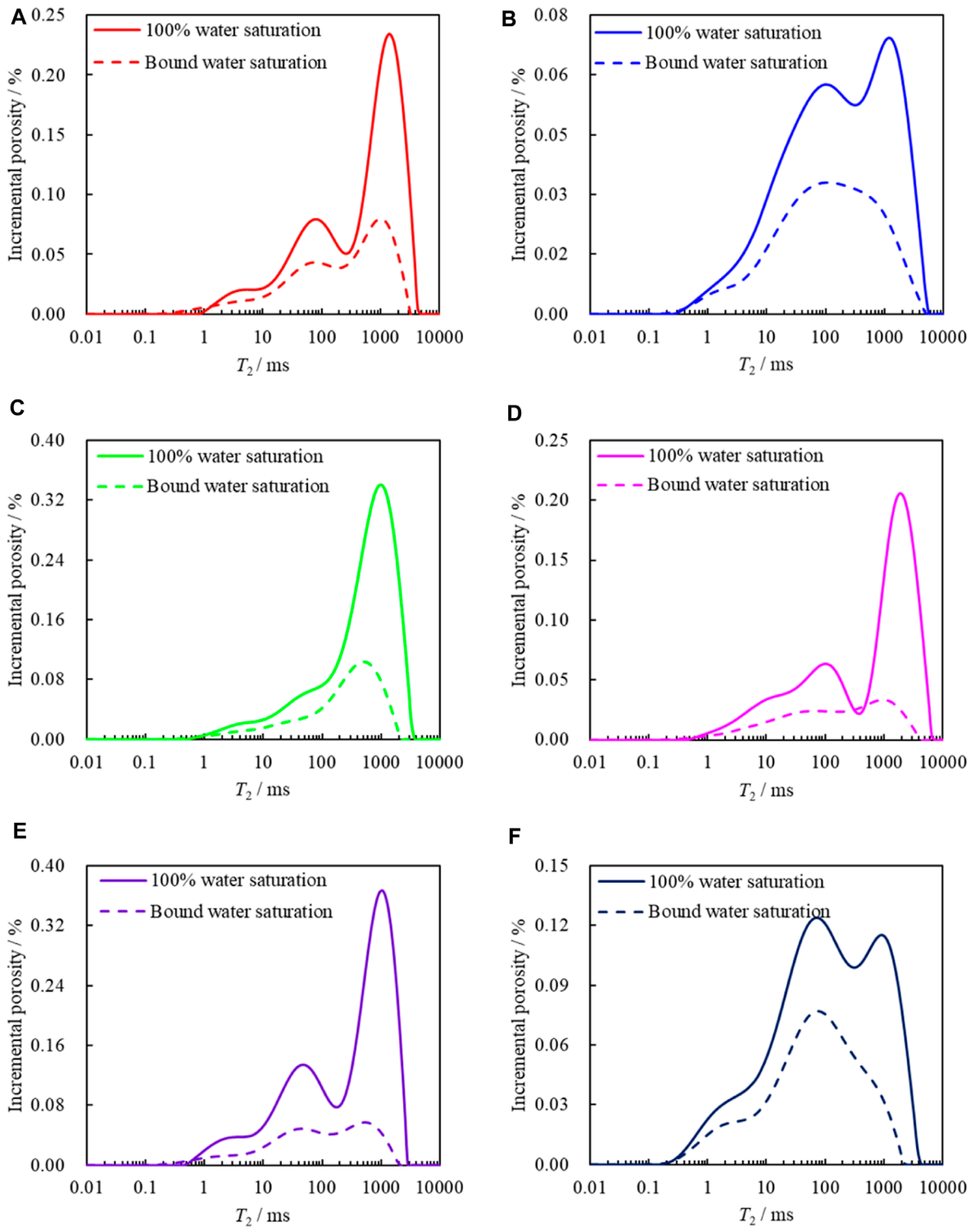

FIGURE 3
NMR relaxation time of samples with different states. **(A–F)** Porosity increment in samples S1 to S6.

throats and pores were extracted, and then the pore network models were extracted, as shown in Figures 7C, F and Figure 7I.

The maximal ball algorithm was used to calculate the coordination number distribution, and the results are shown in Figure 8A. It can be inferred from the coordination distribution that most of the pores are connected by the number of throats, ranging from 1 to 6. The maximum coordination number is 24, confirming the presence of many small throats around the pores.

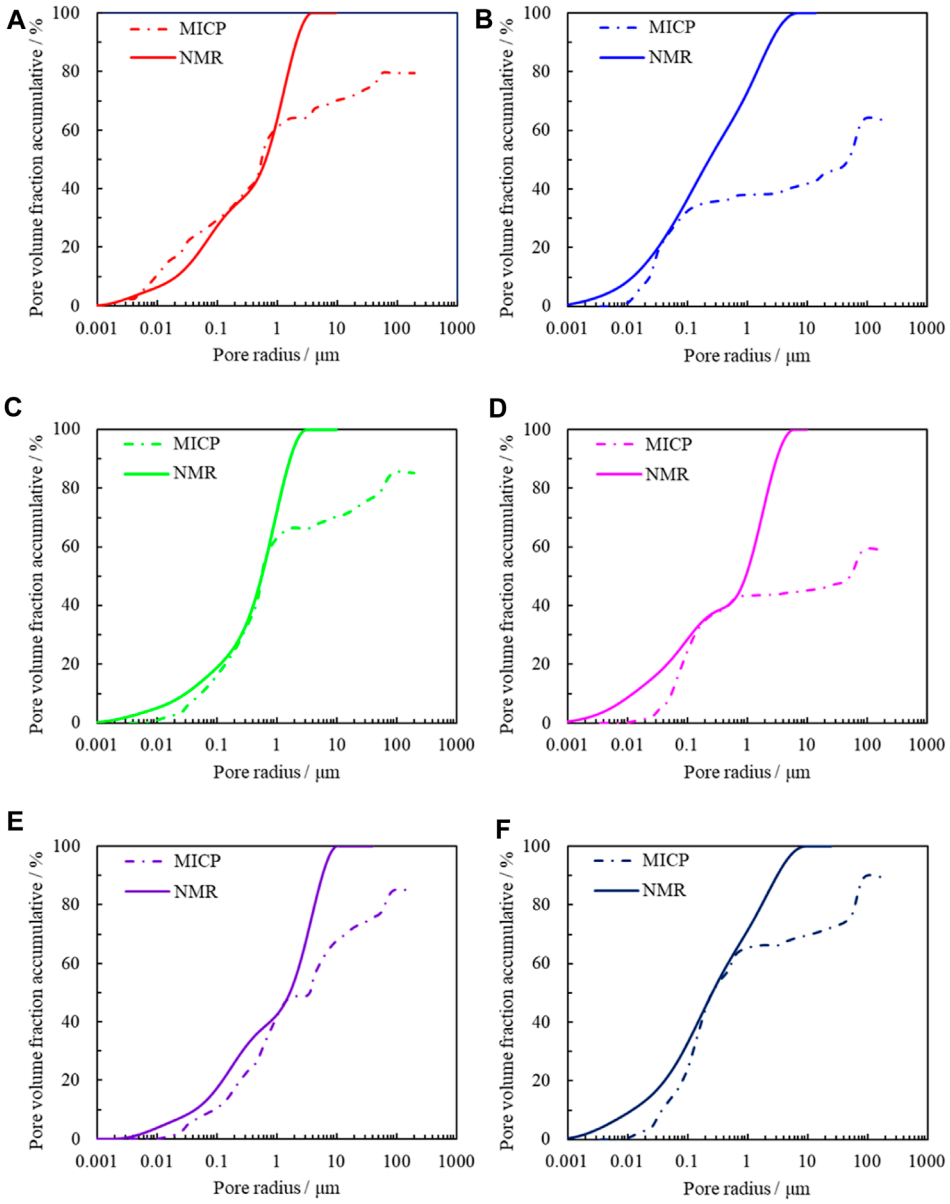

FIGURE 4
Cumulative probability curves of T_2 relaxation time. **(A–F)** Distribution curves of pore volume fraction accumulative for S1 to S6.

TABLE 3 Porosity of different types of pores obtained from NMR tests.

Sample no.	ϕ	Macropore		Mesopore		Micropore		Ultra-micropore	
		φ_1	ϕ_1	φ_2	ϕ_2	φ_3	ϕ_3	φ_4	ϕ_4
S1	3.91	6.36	0.25	20.71	0.81	37.49	1.46	35.44	1.39
S2	1.99	7.33	0.14	27.06	0.54	45.16	0.90	20.45	0.41
S3	5.98	3.34	0.20	7.51	0.45	23.67	1.41	65.48	3.92
S4	3.57	8.95	0.32	22.15	0.79	23.05	0.82	45.85	1.64
S5	6.82	3.54	0.24	8.45	0.58	33.64	2.29	54.37	3.71
S6	4.16	7.90	0.33	20.14	0.84	46.55	1.93	25.41	1.06

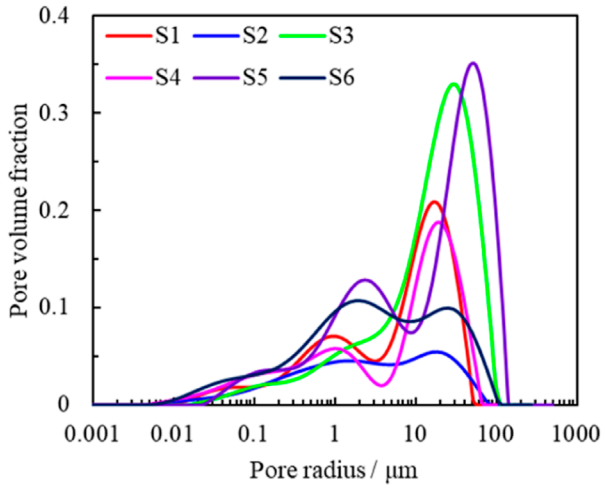

FIGURE 5
Pore radius distribution of all samples from NMR tests.

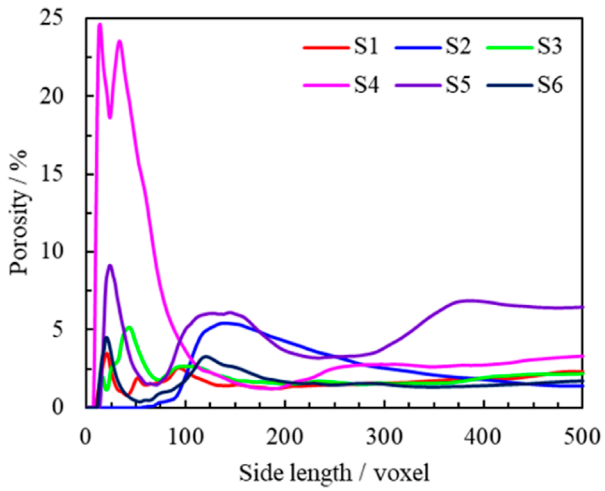

FIGURE 6
Petrophysical porosity of sub-volume varies with the volume.

The specific Euler number curves are shown in Figure 8B, showing that pore connectivity changes with the number of layers. In addition, the two-point correlation function was calculated, as shown in Figure 8C, which shows that the correlation between the two voxels decreases as the distance between the two voxels increases. In particular, when the distance between the two voxels is greater than 200 μm, the two-point correlation function stabilizes at 0.0006.

Figure 8D ~ Figure 8H show that the pore radius mostly ranges from 4 to 30 μm, and approximately 60.34% of throat radius distribution was between 3 and 6 μm. In addition, most of the pore shape factor and throat shape factor are less than 0.04, indicating that the shape of the throats and pores on the sections is non-circular. The relative ratio of the aspect ratio in the range of 1–5 is 75.36%, and the maximum aspect ratio is 53.98.

4.1.4 Comparison of MICP, NMR, and micro-CT results

The comparison between the results of MICP, NMR, and micro-CT and the pore radius distribution is shown in Figure 9, which shows that the pore radius characterized by MICP and NMR is larger than that characterized by micro-CT, as the experimental sample size of MICP and NMR (25.0 mm) is larger than that of micro-CT (approximately 2.0 mm). If there is a larger micro-CT, a more accurate pore radius distribution can be obtained. In addition, more pore and throat features can be obtained through micro-CT scanning images. Additionally, NMR can obtain more information about small pores than MICP, as water can enter the small pores more easily than mercury for water-wet rocks. The similarity among those different methods is that they can effectively describe the macropores.

For the same carbonate sample, the porosity measured by NMR is greater than that tested through MICP. In addition, the pore radius tested through NMR is larger than that measured by MICP. As a result, the pore volume and throat radius, tested via MICP, are interconnected through the throats, leading to a relationship between S_{Hg} and P_c. In MICP tests, the volume of mercury injected is the total volume, including the pores and throats. NMR is a good technique for measuring pore radius distribution. Nevertheless, the coefficient between the pore or throat radius and the transverse relaxation time varies from sample to sample, which makes it a lot of trouble to figure out the coefficients for each sample. Therefore, a good calculation method must be found. Compared with the previous three methods, micro-CT can obtain more pore structure parameters and simulate rock physical properties, such as multi-phase or single-phase flow.

4.2 Fractal dimension analysis

4.2.1 Fractal dimension from MICP

The fractal dimension of the pore system can be calculated using Eq. 21. The detailed parameters of the various fractal dimensions are listed in Table 4 and presented in Figure 10, which show that for the same carbonate sample, D_{f1}, D_{f2} D_{f3}, and D_{f4} gradually decrease, indicating that the macropores are more irregular, owing to D_{f1} being the largest among the four fractal dimensions. In general, the surface of pore space is rough, and the fractal dimensions are greater than 2.6.

4.2.2 Fractal dimension from NMR

The fractal dimensions of different types of pores in carbonate samples are shown in Figure 11A, and the values are shown in Table 5, in which the larger values are the fractal dimensions of macropores. However, the fractal dimensions of S2 and S6 are similar to those of the mesopores. In addition, the fractal dimension of the overall pore system in the NMR experiments of the same carbonate sample is smaller than that of MICP, which may be because NMR can capture more ultra-micropores and smooth the surface of the pore system.

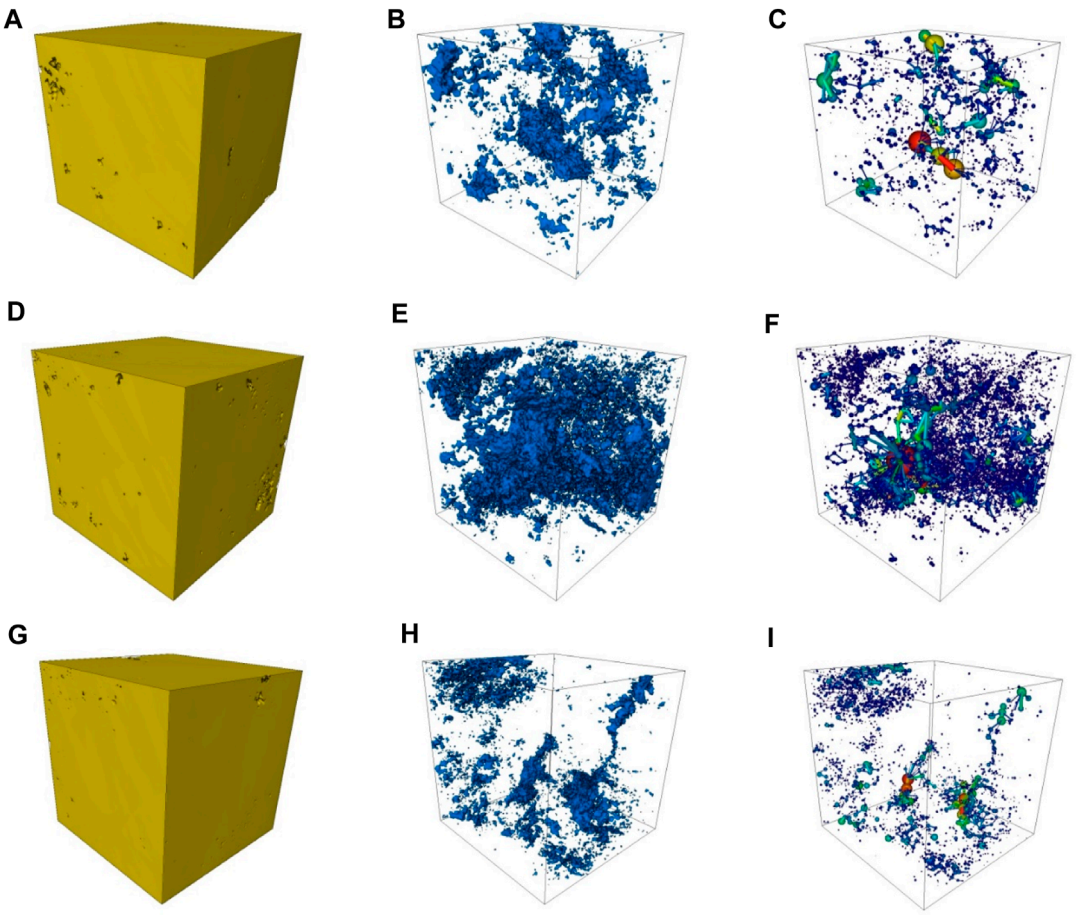

FIGURE 7
Digital rock models and structural analysis of S4, S5, and S6. **(A**, **D**, and, **G)** solid space; **(B**, **E**, and, **H)** pore space; and **(C**, **F**, and, **I)** pore network model.

TABLE 4 Fractal dimension values of the six carbonate samples in MICP tests.

Sample no.	D_f	Macropore		Mesopore		Micropore		Ultra-micropore	
		D_{f1}	φ_1	D_{f2}	φ_2	D_{f3}	φ_3	D_{f4}	φ_4
S1	2.83	2.96	15.17	2.90	13.67	2.84	37.21	2.73	33.95
S2	2.84	2.95	37.52	2.99	3.07	2.95	13.44	2.70	45.97
S3	2.74	2.95	21.00	2.89	11.81	2.62	52.88	2.76	14.31
S4	2.84	2.98	14.13	2.99	2.85	2.77	48.93	2.89	34.09
S5	2.78	2.93	25.69	2.75	33.64	2.69	30.34	2.74	10.33
S6	2.65	2.96	24.49	2.97	4.10	2.52	51.61	2.56	19.80

4.2.3 Fractal dimension from micro-CT

The fractal dimensions of 3D pore space are 2.08, 2.00, 2.10, 2.05, 2.30, and 2.04, indicating that the surface of the pore space is not smooth. As shown in Figure 12A, the fractal dimensions of 2D images are all greater than 0.8 and the fractal dimensions of S5 are all greater than 1.2, which means that the pore boundaries demonstrate stronger regularity than other samples. In addition, the heterogeneity of the pore space can be expressed by calculating the porosity of each layer (Figure 12B). The pore spaces of S4, S5, and S6 are heterogeneous, while those of S1, S2, and S3 are relatively

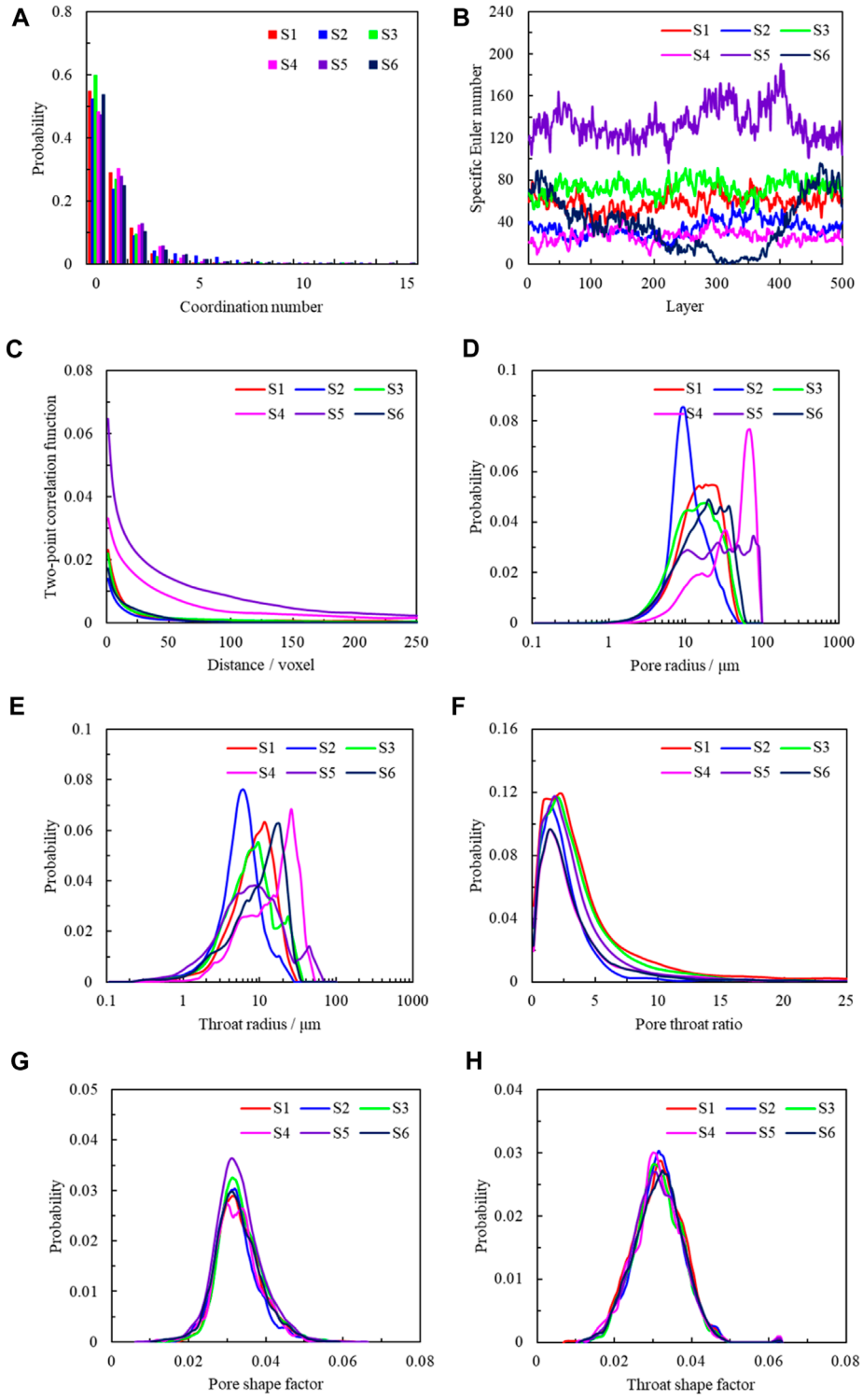

FIGURE 8
Geometric and topological characteristics of pores via micro-CT. **(A)** Coordination number, **(B)** specific Euler number, **(C)** two-point correlation function, **(D)** pore radius, **(E)** throat radius, **(F)** aspect ratio, **(G)** pore shape factor, and **(H)** throat shape factor.

homogeneous, and the porosity of each layer changes within a certain small range.

In summary, by comparing the fractal dimensions acquired by NMR and MICP techniques, it can be found that the fractal dimension calculated by MICP is larger than that obtained by NMR, and the reason may be that NMR can cover all types of pores, including ineffective ones containing formation fluids. However, MICP has a very limited ability to detect ineffective pores. Moreover,

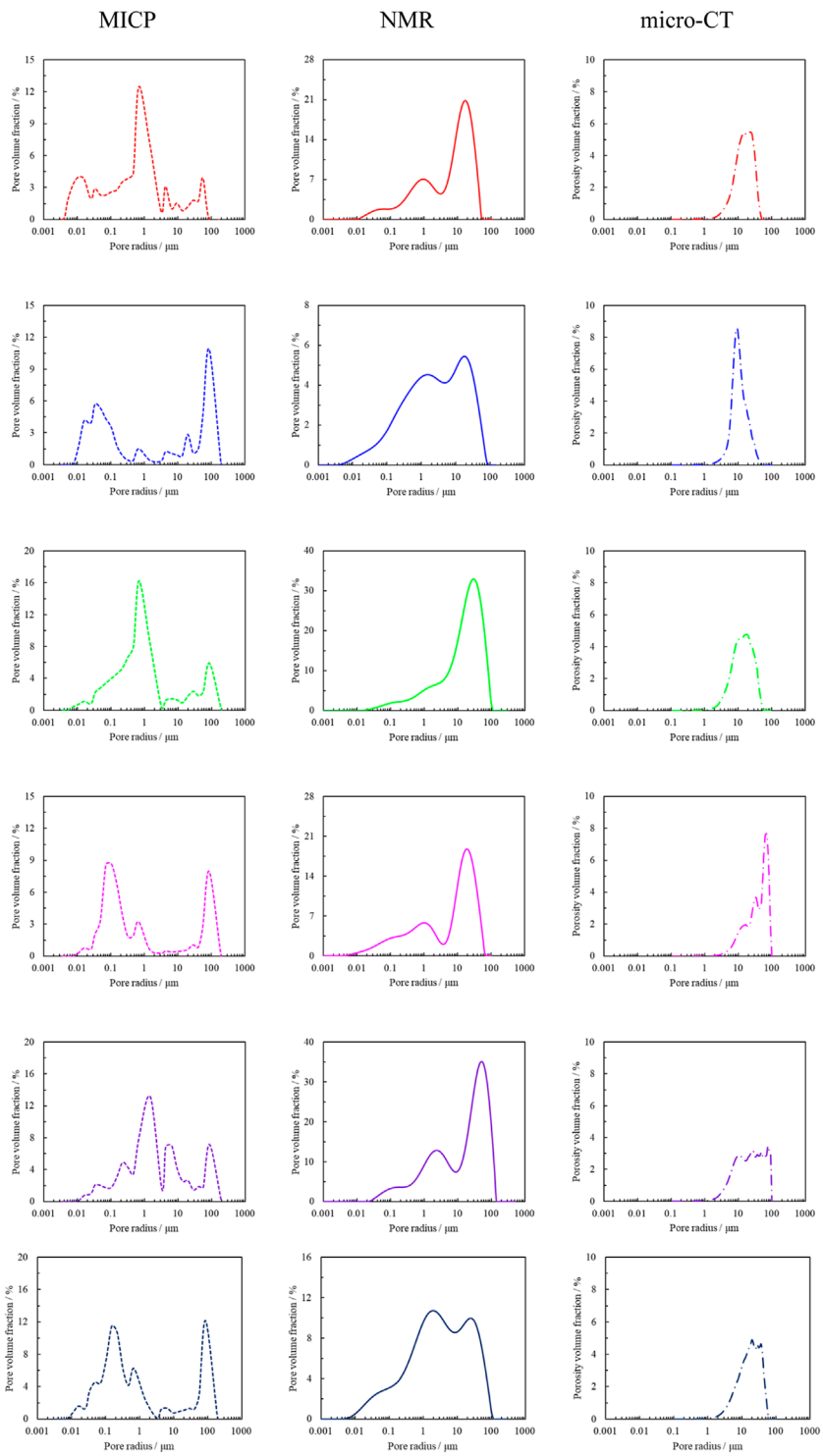

FIGURE 9
Comparison of the pore radius distribution in different experiments.

for the measurement results of micro-CT, the fractal dimensions and the pores of each layer showed the same change trend in 2D images, and the fractal dimensions are the smallest among the three techniques, which is essentially due to the limitation of scanning resolution and affects the acquisition of complete information of macropores and ultra-micropores at low-scanning resolution. As

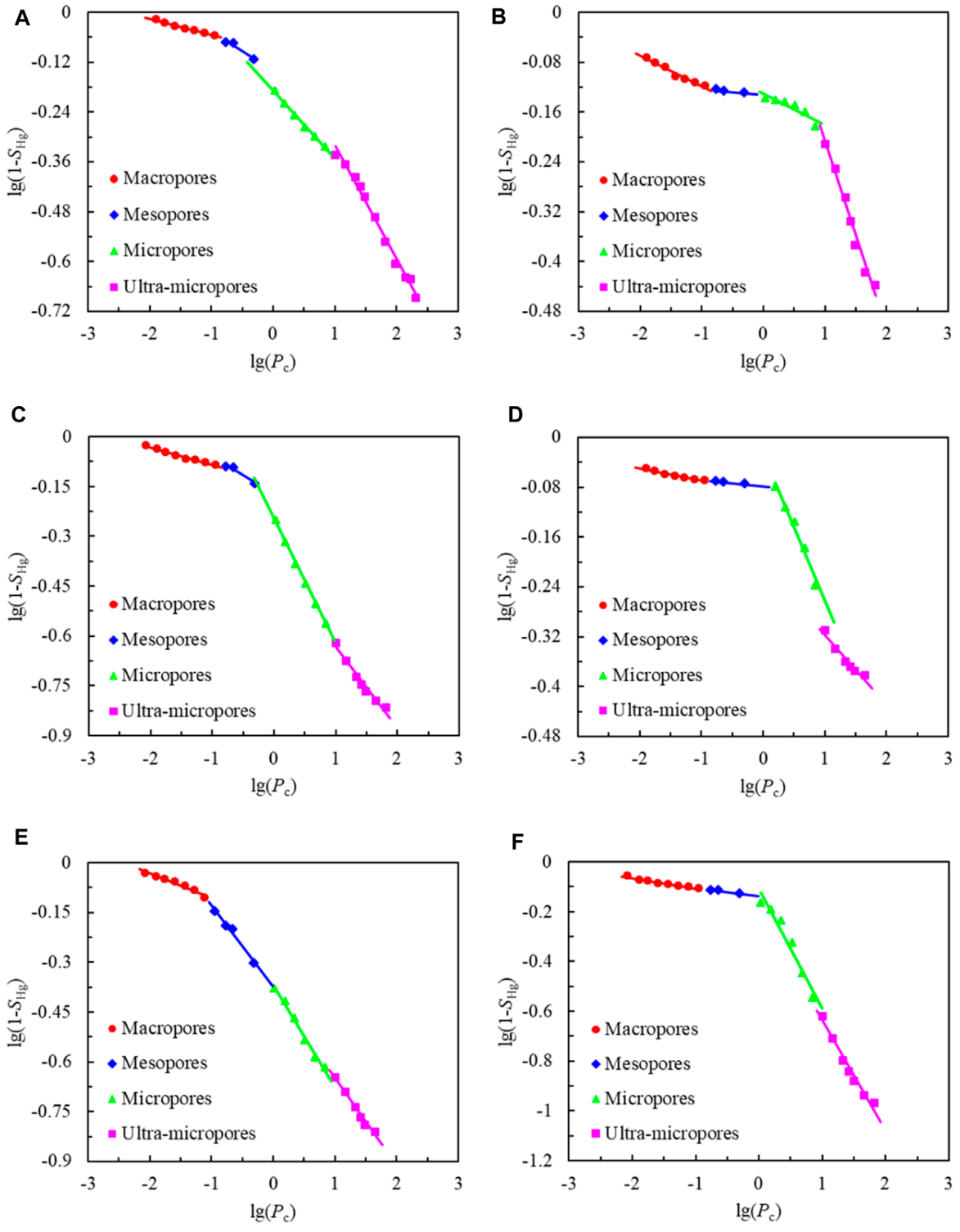

FIGURE 10
(A–F) Fractal dimensions of the six carbonate samples obtained from MICP experiments.

for the carbonate samples used in this experiment, they exhibit fractal characteristics from the nanometer scale to the millimeter scale. In addition, in the case of carbonate reservoirs that develop karst caves, there should also be fractal characteristics on the meter scale.

4.3 Transport properties, formation factor, and fractal dimension

The permeability and formation factors of six carbonate samples were measured by laboratory petrophysical experiments,

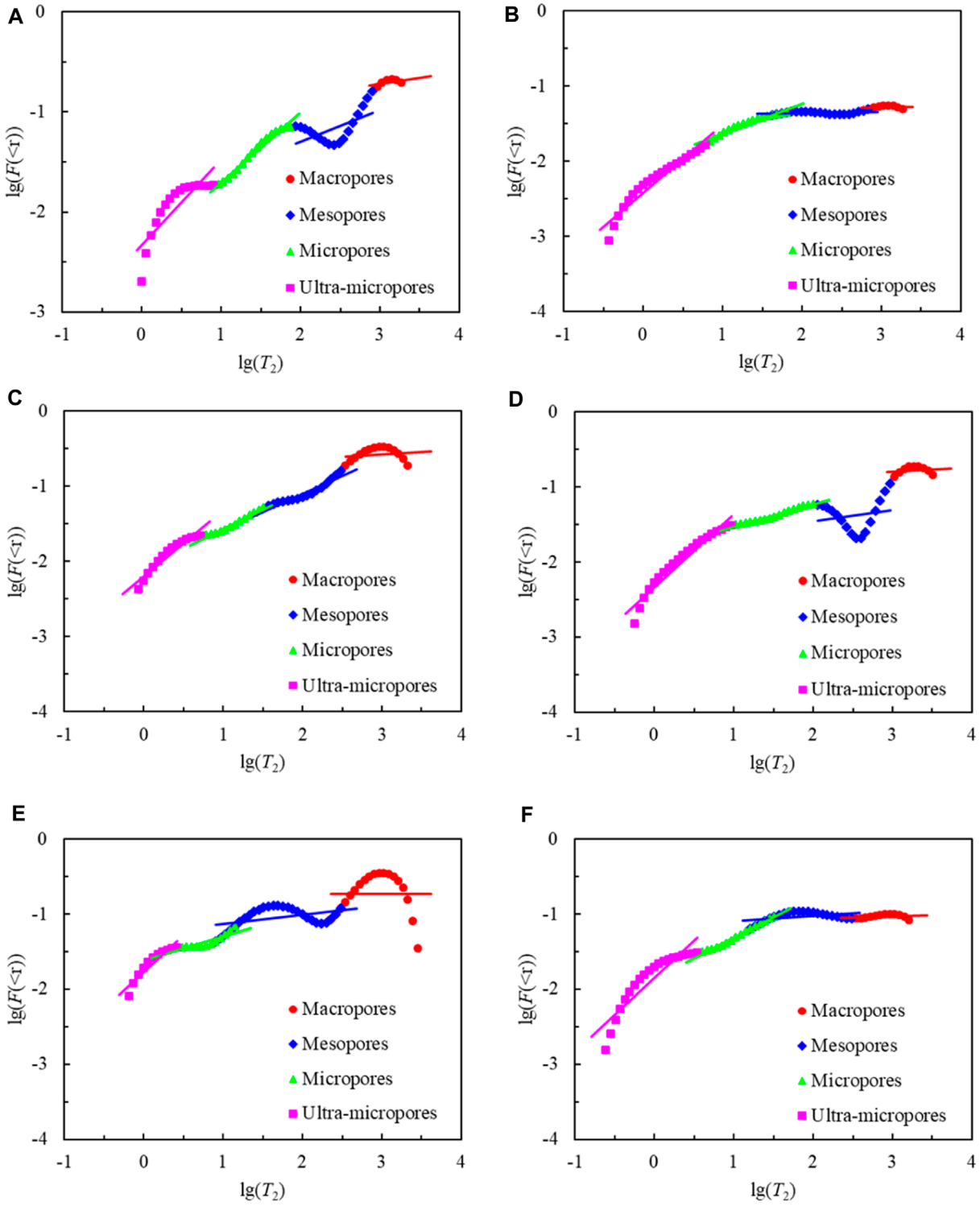

FIGURE 11
(A–F) Fractal dimensions of all carbonate samples obtained from NMR experiments.

representing the transport properties of fluids and electrical current. Figure 13 illustrates the relationship between transport properties and fractal dimensions and compares the relationship between fractal dimensions calculated by three different methods with permeability and formation factors. There are substantial discrepancies between the different methods used for calculating fractal dimensions, particularly the results of micro-CT, which exhibits an opposite trend to the other two experimental results.

TABLE 5 Fractal dimension parameters of all samples obtained from NMR experiments.

Sample no.	D_f	Macropore		Mesopore		Micropore		Ultra-micropore	
		D_{f1}	φ_1	D_{f2}	φ_2	D_{f3}	φ_3	D_{f4}	φ_4
S1	2.36	2.87	6.36	2.68	20.71	2.29	37.49	2.15	35.44
S2	2.63	2.99	7.33	2.98	27.06	2.61	45.16	2.10	20.45
S3	2.25	2.94	3.34	2.52	7.51	2.47	23.67	2.11	65.48
S4	2.45	2.95	8.95	2.86	22.15	2.70	23.05	2.03	45.85
S5	2.34	2.99	3.54	2.88	8.45	2.68	33.64	2.01	54.37
S6	2.48	2.98	7.90	2.93	20.14	2.45	46.55	2.01	25.41

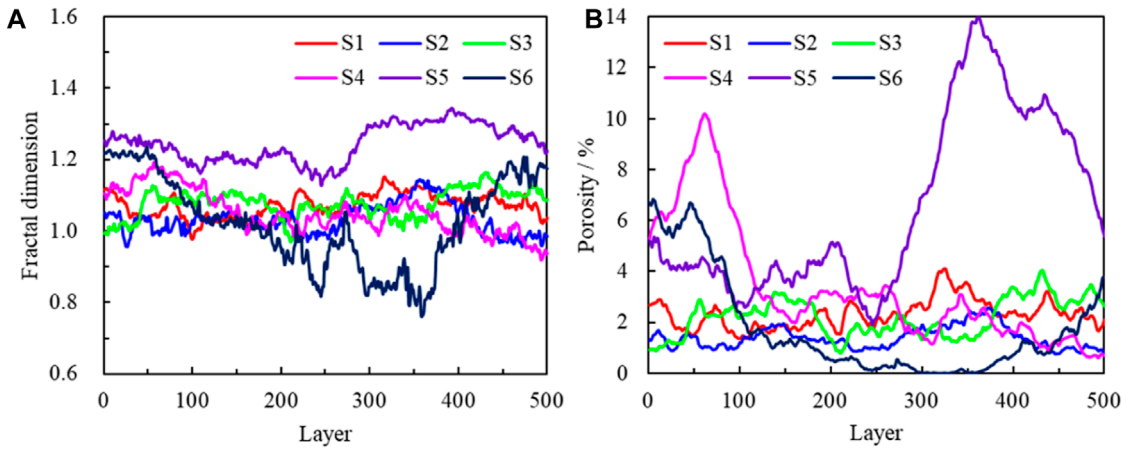

FIGURE 12
Change in vital parameters in each layer via micro-CT images. **(A)** Fractal dimension and **(B)** porosity varies with layers.

Generally, under the same measurement method, the larger the fractal dimension, the more complex the pore structure, hindering the transport in the pore. Therefore, the fractal dimensions calculated by MICP and NMR yield results that are consistent with the general understanding of fractal theory. The larger the fractal dimension, the lower the permeability, the higher the formation factors, the lower the fluid flow capacity, and the higher the rock resistivity. Moreover, compared with MICP, NMR can better reflect the relationship between transport properties and fractal dimensions, demonstrating a stronger correlation, which further highlights the ability of NMR to more comprehensively characterize the pore structure of rocks.

Due to the limited scanning resolution, micro-CT measurements cannot capture all types of pores. Consequently, the calculated fractal dimension can only represent the characteristics of large pores. In other words, in this context, the pore types exhibit relative homogeneity, and with the increase in porosity, the pore structure becomes progressively more complex, leading to an increase in fractal dimension. Consequently, the fractal dimension calculated using micro-CT yields an incomplete representation of the pore structure, rendering the relationship between transport capacity and fractal dimension unreliable. In summary, we prefer utilizing the NMR fractal dimension to represent the transport properties of rocks, in which the transport capacity exhibits a negative dimension correlated with the fractal dimension.

5 Conclusion

The topological, fractal, and geometric characteristics of the pore structure of carbonate samples from the Longwangmiao Formation and Dengying Formation of the Gaoshiti–Moxi block, Sichuan Basin, were analyzed using micro-CT, NMR, and MICP experiments, respectively. According to the pore radius distribution tested via different techniques, their disadvantages and advantages are summarized. NMR and MICP techniques can describe more pores than micro-CT. However, due to the presence of pore shielding in MICP tests, the pore radius obtained by MICP is smaller than that obtained by micro-CT and NMR. Furthermore, the most effective method for characterizing the pore structure is NMR technology. The hardest part is that the coefficient between the pore

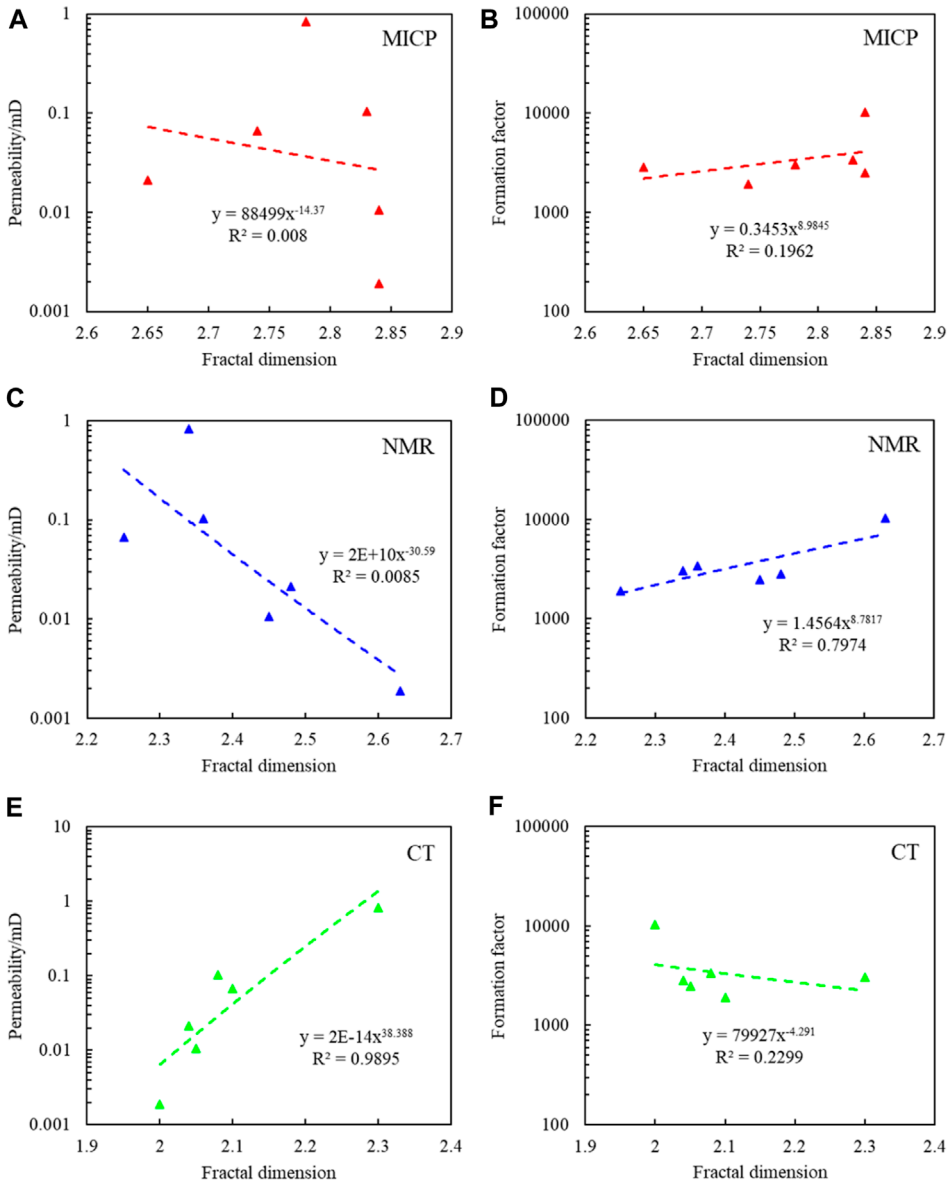

FIGURE 13
(A–F) Relationship between permeability and formation factors with the fractal dimension.

radius and T_2 relaxation time is difficult to calculate. Therefore, a better calculation method must be found. In addition, micro-CT is an irreplaceable technique for obtaining a large number of topological and geometric features, and multi-phase or single-phase flow simulations can be conducted via digital rock models. However, for carbonates, micro-CT is not sufficient to describe the complete pore space because macropores cannot be fully represented and sub-resolution micropores cannot be described. Those macropores and micropores have a very important effect on their seepage properties. Therefore, multi-scale digital rock modeling involving small and large pores is essential for complex rocks, which is of great significance for the analysis of pore systems and the simulation of rock physical properties. Moreover, the fractal dimension was calculated through different techniques, and the values of all types of pores, from macropores to ultra-micropores, can be analyzed using NMR and MICP techniques. Compared with ultra-micropores and micropores, macropores have irregularity and heterogeneity. The fractal dimension of samples from NMR is smaller than that of MICP. In addition, micro-CT images can be used to acquire the fractal dimensions of the 3D and 2D pore spaces. Nevertheless, due to the low resolution of this method, the fractal dimension of micropores and ultra-micropores cannot be acquired, which can prove that the fractal dimension in 2D micro-CT images changes with the variation in the pore space area. Therefore, the fractal theory is an efficient means for pore type classification and reservoir quality evaluation.

Data availability statement

The original contributions presented in the study are included in the article/Supplementary Materials; further inquiries can be directed to the corresponding authors.

Author contributions

HD: funding acquisition, investigation, methodology, and writing–original draft. BL: writing–review and editing. CD: writing–review and editing. SX: data curation, software, visualization, and writing–original draft. FW: data curation and writing–original draft. PC: writing–review and editing.

Funding

The author(s) declare that financial support was received for the research, authorship, and/or publication of this article. This work was supported by the Youth Program of National Natural Science Foundation of China (grant no. 42204105), the China Postdoctoral Science Foundation (grant no. 2021M700525), the High-level Innovation and Entrepreneurship Talent Program of Qinchuangyuan, China (grant no. QCYRCXM-2022-24), the Fundamental Research Funds for the Central Universities, CHD (grant no. 300102263103), and the Young Talent Fund of Association for Science and Technology in Shaanxi, China (grant no. 20230703).

Conflict of interest

Author BL was employed by Changqing Oilfield Company. Authors SX and FW were employed by Changqing Oilfield Company.

The remaining authors declare that the research was conducted in the absence of any commercial or financial relationships that could be construed as a potential conflict of interest.

Publisher's note

All claims expressed in this article are solely those of the authors and do not necessarily represent those of their affiliated organizations, or those of the publisher, the editors, and the reviewers. Any product that may be evaluated in this article, or claim that may be made by its manufacturer, is not guaranteed or endorsed by the publisher.

References

Abro, W. A., Shar, A. M., Lee, K. S., and Narejo, A. A. (2019). An integrated analysis of mineralogical and microstructural characteristics and petrophysical properties of carbonate rocks in the lower Indus Basin, Pakistan. *Open Geosci.* 11 (1), 1151–1167. doi:10.1515/geo-2019-0088

Ali, M., Al-Yaseri, A., Awan, F. U. R., Arif, M., Keshavarz, A., and Iglauer, S. (2022). Effect of water-soluble organic acids on wettability of sandstone formations using streaming zeta potential and NMR techniques: implications for CO_2 geo-sequestration. *Fuel* 329, 125449. doi:10.1016/j.fuel.2022.125449

Arif, M., Abu-Khamsin, S. A., Zhang, Y., and Iglauer, S. (2020). Experimental investigation of carbonate wettability as a function of mineralogical and thermo-physical conditions. *Fuel* 264, 116846. doi:10.1016/j.fuel.2019.116846

Chandra, V., Petrovic, A., Khanna, P., Ramdani, A. I., Yalcin, B., Vahrenkamp, V., et al. (2021). Impact of depositional and diagenetic features on petrophysical and rock mechanical properties in Arab-D reservoir equivalent upper Jubaila Formation, Saudi Arabia. *Mar. Petroleum Geol.* 129, 105076. doi:10.1016/j.marpetgeo.2021.105076

Daigle, H., Hayman, N. W., Jiang, H., Tian, X., and Jiang, C. (2017). Multiscale pore networks and their effect on deformation and transport property alteration associated with hydraulic fracturing. *Energy Procedia* 125, 71–79. doi:10.1016/j.egypro.2017.08.067

Dong, H., Sun, J., Li, Y., Cui, L., Yan, W., and Zhang, J. (2017). Verification of the carbonate double-porosity conductivity model based on digital cores. *Interpretation* 5 (2), 173–183. doi:10.1190/INT-2016-0071.1

Dong, H., Sun, J., Zhu, J., Lin, Z., Cui, L., Yan, W., et al. (2019). Quantitative characterization and characteristic analysis of pore structure of shale-gas reservoir in the Sichuan Basin, China. *Interpretation-A J. Subsurf. Charact.* 7 (4), 23–32. doi:10.1190/INT-2018-0169.1

Dong, H., Zeng, X., Zhou, D., Zhu, J., Golsanami, N., Sun, J., et al. (2023). Insights into the multiscale conductivity mechanism of marine shales from Wufeng-Longmaxi formation in the Southern Sichuan Basin of China. *J. Energy Eng.* 149 (3), 04023008. doi:10.1061/JLEED9.EYENG-4667

Du, J., Zou, C., Xu, C., He, H., Shen, P., Yang, Y., et al. (2014). Theoretical and technical innovations in strategic discovery of a giant gas field in Cambrian Longwangmiao Formation of central Sichuan paleo-uplift, Sichuan Basin. *Petroleum Explor. Dev.* 41 (3), 294–305. doi:10.1016/S1876-3804(14)60035-5

Fagbemi, S., Tahmasebi, P., and Piri, M. (2018). Interaction between fluid and porous media with complex geometries: a direct pore-scale study. *Water Resour. Res.* 54 (9), 6336–6356. doi:10.1029/2017WR022242

Gao, Z., Yang, X., Hu, C., Wei, L., Jiang, Z., Yang, S., et al. (2019). Characterizing the pore structure of low permeability eocene liushagang formation reservoir rocks from beibuwan basin in northern south China sea. *Mar. Petroleum Geol.* 99, 107–121. doi:10.1016/j.marpetgeo.2018.10.005

Golsanami, N., Sun, J., Liu, Y., Yan, W., Chen, L., Jiang, L., et al. (2019). Distinguishing fractures from matrix pores based on the practical application of rock physics inversion and NMR data: a case study from an unconventional coal reservoir in China. *J. Nat. Gas Sci. Eng.* 65, 145–167. doi:10.1016/j.jngse.2019.03.006

Han, X., Shan, S., Xu, G., Han, Y., Guo, Y., Yang, B., et al. (2023). Single- and multifractal dimension variation of the pore-fracture system in tight sandstone by using high-pressure mercury intrusive tests and its influence on porosity-permeability variation. *Energy fuels.* 37 (16), 11969–11981. doi:10.1021/acs.energyfuels.3c01622

Hosseini, M., Arif, M., Keshavarz, A., and Iglauer, S. (2021). Neutron scattering: a subsurface application review. *Earth-Science Rev.* 221, 103755. doi:10.1016/j.earscirev.2021.103755

Isah, A., Arif, M., Hassan, A., Mahmoud, M., and Iglauer, S. (2022). Fluid-rock interactions and its implications on EOR: critical analysis, experimental techniques and knowledge gaps. *Energy Rep.* 8, 6355–6395. doi:10.1016/j.egyr.2022.04.071

Jiang, W., Zhou, Y., Wu, C., and Du, M. (2023). Fractal characteristics and theirs influence on methane adsorption in high-rank coals with NMR. *Front. Earth Sci.* 10, 1047557. doi:10.3389/feart.2022.1047557

Kibria, M. G., Hu, Q., Liu, H., Zhang, Y., and Kang, J. (2018). Pore structure, wettability, and spontaneous imbibition of woodford shale, permian basin, west Texas. *Mar. Petroleum Geol.* 91, 735–748. doi:10.1016/j.marpetgeo.2018.02.001

Lai, Q., Qi, L., Chen, S., Ma, S., Zhou, Y., Fang, P., et al. (2023). Resercoir space characteristics and pore structure of Jurassic Lianggaoshan Formation lacustrine shale reservoir in Sichuan Basin, China: insights into controlling factors. *Front. Earth Sci.* 11, 1133413. doi:10.3389/feart.2023.1133413

Li, C., Li, X., Gao, S., Liu, H., You, S., Fang, F., et al. (2017). Experiment on gas-water two-phase seepage and inflow performance curves of gas wells in carbonate reservoirs: a case study of Longwangmiao Formation and Dengying Formation in Gaoshiti-Moxi block, Sichuan Basin, SW China. *Petroleum Explor. Dev.* 44 (6), 983–992. doi:10.1016/S1876-3804(17)30110-6

Li, C., Pan, J., Wang, H., Li, H., Feng, C., and Zhou, J. (2022). Study on seismic petrophysics and dispersion characteristics of carbonate rocks with deep ultra-deep complex pore structure in Tarim Basin. *Appl. Geophys.* 19 (2), 1–15. doi:10.1007/s11770-022-0974-y

Mathews, J. P., Campbell, Q. P., Xu, H., and Halleck, P. (2017). A review of the application of X-ray computed tomography to the study of coal. *Fuel* 209, 10–24. doi:10.1016/j.fuel.2017.07.079

Mathews, J. P., Pone, J. D. N., Mitchell, G. D., and Halleck, P. (2011). High-resolution X-ray computed tomography observations of the thermal drying of lump-sized subbituminous coal. *Fuel Process. Technol.* 92 (1), 58–64. doi:10.1016/j.fuproc.2010.08.020

Norbisrath, J. H., Eberli, G. P., Laurich, B., Desbois, G., Weger, R. J., and Urai, J. L. (2015). Electrical and fluid flow properties of carbonate microporosity types from multiscale digital image analysis and mercury injection. *AAPG Bull.* 99 (11), 2077–2098. doi:10.1306/07061514205

Okolo, G. N., Everson, R. C., Neomagus, H. W. J. P., Roberts, M. J., and Sakurovs, R. (2015). Comparing the porosity and surface areas of coal as measured by gas adsorption, mercury intrusion and SAXS techniques. *Fuel* 141, 293–304. doi:10.1016/j.fuel.2014.10.046

Otiede, D., and Wu, K. (2011). The effect of image resolution on the geometry and topological characteristics of 3-D reconstructed images of reservoir rock samples. *Int. J. Eng. Res. Afr.* 6, 37–44. doi:10.4028/www.scientific.net/JERA.6.37

Ouyang, S., Lu, X., Zhang, Y., Chen, L., Qu, Y., and Sun, W. (2023). Impacts of the pore-throat structure on fluid mobility in tight sandstone: insight from an improved method based on rate-controlled porosimetry and nuclear magnetic resonance. *Energy & Fuels* 37 (1), 273–290. doi:10.1021/acs.energyfuels.2c03285

Qi, A., Huang, H., Li, K., Li, J., and Zhang, F. (2023). Study on pressure sensitive pore structure of the hole-type carbonate based on situ CT. *Chin. J. Undergr. Space Eng.* 19 (1), 173–182.

Radlinski, A. P., and Mastalerz, M. (2017). Neutron scattering study of vitrinite: insights into sub-micrometer inclusions in North American Carboniferous coals of bituminous rank. *Int. J. Coal Geol.* 186, 145–154. doi:10.1016/j.coal.2017.10.012

Romero, E., and Simms, P. H. (2008). Microstructure investigation in unsaturated soils: a review with special attention to contribution of mercury intrusion porosimetry and environmental scanning electron microscopy. *Geotech. Geol. Eng.* 26 (6), 705–727. doi:10.1007/s10706-008-9204-5

Sarkar, P., Kumar, A., Singh, K. H., Ghosh, R., and Singh, T. N. (2018). Pore system, microstructure and porosity characterization of Gondwana shale of Eastern India using laboratory experiment and watershed image segmentation algorithm. *Mar. Petroleum Geol.* 94, 246–260. doi:10.1016/j.marpetgeo.2018.04.006

Tahmasebi, P. (2017). HYPPS: a hybrid geostatistical modeling algorithm for subsurface modeling. *Water Resour. Res.* 53 (7), 5980–5997. doi:10.1002/2017WR021078

Tahmasebi, P., and Kamrava, S. (2018). Rapid multiscale modeling of flow in porous media. *Phys. Rev. E* 98 (5), 052901. doi:10.1103/PhysRevE.98.052901

Van Geet, M., Swennen, R., and David, P. (2001). Quantitative coal characterisation by means of microfocus X-ray computer tomography, colour image analysis and back-scattered scanning electron microscopy. *Int. J. Coal Geol.* 46 (1), 11–25. doi:10.1016/s0166-5162(01)00006-4

Vogel, H. J., and Roth, K. (2001). Quantitative morphology and network representation of soil pore structure. *Adv. Water Resour.* 24 (3), 233–242. doi:10.1016/S0309-1708(00)00055-5

Wang, N., Du, Y., Fu, C., Ma, X., Zhang, X., Wang, J., et al. (2023). Experimental study on spontaneous imbibition of coal samples of different ranks based on the NMR relaxation spectrum. *ACS Omega* 8 (37), 33526–33542. doi:10.1021/acsomega.3c03534

Wei, G., Du, J., Xu, C., Zou, C., Yang, W., Shen, P., et al. (2015a). Characteristics and accumulation modes of large gas reservoirs in Sinian-Cambrian of Gaoshiti-Moxi region, Sichuan Basin. *Acta Pet. Sin.* 36 (1), 1–12. doi:10.7623/syxb201501001

Wei, G., Yang, W., Du, J., Xu, C., Zou, C., Xie, W., et al. (2015b). Tectonic features of Gaoshiti-Moxi paleo-uplift and its controls on the formation of a giant gas field, Sichuan Basin, SW China. *Petroleum Explor. Dev.* 42 (3), 283–292. doi:10.1016/S1876-3804(15)30018-5

Yan, W., Sun, J., Golsanami, N., Li, M., Cui, L., Dong, H., et al. (2019). Evaluation of wettabilities and pores in tight oil reservoirs by a new experimental design. *Fuel* 252, 272–280. doi:10.1016/j.fuel.2019.04.130

Yang, J., Zhang, J., Ji, Y., Lv, W., Wu, H., He, Z., et al. (2022). Pore structure characteristics and controlling factors of a tight sandstone reservoir in the paleogene shahejie formation, nanpu sag, bohai bay basin, China. *ACS Omega* 7 (2), 1740–1756. doi:10.1021/acsomega.1c04573

Yang, S., Yang, H., Peng, X., Lan, X., Yang, Y., Zhao, Y., et al. (2023). Research of influencing factors on permeability for carbonate rocks based on LBM simulation: a case study of low-permeability gas reservoir of Sinian Dengying Formation in Sichuan Basin. *Front. Earth Sci.* 11, 1091431. doi:10.3389/feart.2023.1091431

Yao, Y., Liu, D., Che, Y., Tang, D., Tang, S., and Huang, W. (2010). Petrophysical characterization of coals by low-field nuclear magnetic resonance (NMR). *Fuel* 89 (7), 1371–1380. doi:10.1016/j.fuel.2009.11.005

Yu, H., Wang, Z., Wen, F., Rezaee, R., Lebedev, M., Li, X., et al. (2020). Reservoir and lithofacies shale classification based on NMR logging. *Petroleum Res.* 5 (3), 202–209. doi:10.1016/j.ptlrs.2020.04.005

Zeng, F., Yang, W., Wei, G., Yi, H., Zeng, Y., Zhou, G., et al. (2023). Structural features and exploration targets of platform margins in sinian Dengying Formation in deyang-anyue rift, Sichuan Basin, SW China. *Petroleum Explor. Dev.* 50 (2), 306–320. doi:10.1016/S1876-3804(23)60389-1

Zhang, W., Shi, Z., and Tian, Y. (2020). An improved method to characterize the pore-throat structures in tight sandstone reservoirs: combined high-pressure and rate-controlled mercury injection techniques. *Energy Explor. Exploitation* 38 (2), 2389–2412. doi:10.1177/0144598720920729

Zhang, Y., Bijeljic, B., Gao, Y., Lin, Q., and Blunt, M. J. (2021). Quantification of nonlinear multiphase flow in porous media. *Geophys. Res. Lett.* 48 (5), e2020GL090477. doi:10.1029/2020GL090477

Zhang, Y., Xu, X., Lebedev, M., Sarmadivaleh, M., Barifcani, A., and Iglauer, S. (2016). Multi-scale x-ray computed tomography analysis of coal microstructure and permeability changes as a function of effective stress. *Int. J. Coal Geol.* 165, 149–156. doi:10.1016/j.coal.2016.08.016

Zhou, B., Ku, Q., Wang, H., and Wang, J. (2020). Particle classification and intra-particle pore structure of carbonate sands. *Eng. Geol.* 279, 105889. doi:10.1016/j.enggeo.2020.105889

Zou, C., Du, J., Xu, C., Wang, Z., Zhang, B., Wei, G., et al. (2014). Formation, distribution, resource potential, and discovery of Sinian-Cambrian giant gas field, Sichuan Basin, SW China. *Petroleum Explor. Dev.* 41 (3), 306–325. doi:10.1016/S1876-3804(14)60036-7

frontiers | Frontiers in Earth Science

TYPE Original Research
PUBLISHED 21 March 2024
DOI 10.3389/feart.2024.1375713

Check for updates

OPEN ACCESS

EDITED BY
Wenguang Wang,
Northeast Petroleum University, China

REVIEWED BY
Zhipeng Huo,
Northeastern University at Qinhuangdao, China
Jijun Li,
China University of Petroleum (East China), China
Xuan Tang,
China University of Geosciences, China

*CORRESPONDENCE
Fujie Jiang,
jfjhtb@163.com
Qiang Zhang,
904836105@qq.com

RECEIVED 24 January 2024
ACCEPTED 05 March 2024
PUBLISHED 21 March 2024

CITATION
Zhao G, Jiang F, Zhang Q, Pang H, Liu X and Chen D (2024), Key factors controlling the accumulation of oil reservoir in the Gaosheng area of Western Depression, Liaohe Basin, Northeastern China.
Front. Earth Sci. 12:1375713.
doi: 10.3389/feart.2024.1375713

COPYRIGHT
© 2024 Zhao, Jiang, Zhang, Pang, Liu and Chen. This is an open-access article distributed under the terms of the Creative Commons Attribution License (CC BY). The use, distribution or reproduction in other forums is permitted, provided the original author(s) and the copyright owner(s) are credited and that the original publication in this journal is cited, in accordance with accepted academic practice. No use, distribution or reproduction is permitted which does not comply with these terms.

Key factors controlling the accumulation of oil reservoir in the Gaosheng area of Western Depression, Liaohe Basin, Northeastern China

Guangjie Zhao[1,2], Fujie Jiang[2]*, Qiang Zhang[3]*, Hong Pang[1,2], Xingzhou Liu[4] and Di Chen[1,2]

[1]College of Geoscience, China University of Petroleum, Beijing, China, [2]State Key Laboratory of Petroleum Resource and Prospecting, China University of Petroleum, Beijing, China, [3]No.7 Exploration Institute of Geology and Mineral Resources in Shandong Province, Linyi, China, [4]PetroChina Liaohe Oilfield Exploration and Development Research Institute, Panjin, China

The Proterozoic oil in Gaosheng area of the Western Depression of Liaohe Basin has great potential and is an important exploration field. However, the study about control factors of Gaosheng reservoir needs to be improved. The source rocks are characterized by using geochemical techniques and the structural evolution history is restored by using 2D-Move software. The characteristics of reservoirs and caps are clarified, and the controlling factors of reservoir formation are summarized. The oil generation intensity of Es4 and Es3 is generally 5×10^6–10×10^6 t/km^2, indicating that the oil source is sufficient. The sandstone reservoir has fracture and dissolution porosity, which provide storage space for oil accumulation. Faults and unconformities provide pathways for oil migration. The dense Fangshenpao and Mesozoic basalt is a good cap layer to preserve the reservoir, which effectively prevents the upward migration of oil. According to the comprehensive analysis of main controlling factors, the favorable exploration areas are pointed out. The research results are of great significance to guide the future oil and gas exploration in Liaohe Basin.

KEYWORDS

controlling factors, buried-hill reservoir, hydrocarbon accumulation, favorable zones, Gaosheng oilfield, Liaohe Basin

Highlights

- The characteristics of source rocks and tectonic evolution are revealed.
- The condition of sandstone reservoir and cap rock are clearly clarified.
- The factors controlling oil reservoir accumulation were summarized systematically.

1 Introduction

Unconventional oil and gas attract wide attention in the world due to its success of exploration and development in North America (Hein et al., 2019). According to the statistics of relevant scholars, the amount of unconventional oil resources in the world is

about 4495 × 10^8t, which is roughly equivalent to that of conventional oil resources (IEA, 2013). By 2030, global oil production is expected to increase by 16.1 million barrels per day compared to today, with nearly half of that coming from tight oil, which will meet nearly 10% of global energy demand by then (IEA, 2012).

The distribution of tight oil in China is characterized by a wide range, multiple blocks, and large series span. In addition, tight sandstone in the Quang 4th member Formation in Songliao Basin (Huang et al., 2017), Jurassic Formation of the Tuha Basin (Feng et al., 2021), Yanchang Formation in Ordos Basin (Xu et al., 2017), Cretaceous tight limestone of the Jiuquan Basin (Chen et al., 2018) and the dolomites of Permian Lucaogou Formation in Junggar Basin (Liu et al., 2023) all have geological conditions for forming tight oil reservoir. In terms of geological background, source rock quality, reservoir quality, formation overpressure, source-reservoir communication and crude oil quality, the Bakken oil formation in Williston Basin in North America is comparable to the Bakken and Eagle Ford tight oil in North America. Even in terms of source-reservoir combination, the Bakken oil formation in Williston Basin in North America is inferior to the tight oil of Yanchang Formation in Ordos Basin (Zou et al., 2012; Zhang et al., 2013). Previous studies mainly focused on geochemical characteristics (El Diasty et al., 2016; Kobraei et al., 2019; Wu et al., 2021), accumulation conditions (Xu et al., 2021; Szatmari and Schaffer, 2023), physical properties (Busch et al., 2019; Zhao et al., 2021; Odrzygóźdź et al., 2023), diagenesis (Higgs et al., 2007; Alsuwaidi et al., 2022; Er et al., 2022), charging period (Han et al., 2022; Liu et al., 2022), fractures (Chen et al., 2022; Zhao et al., 2022; Panara et al., 2023) and so on. However, due to the rare research literature on tight gas reservoir control, the comprehensive understanding of control factors still needs to be further improved.

The exploration and development of the buried hill reservoir in Liaohe Basin is early, and the buried hill reservoir accounts for a major proportion of the reserves and production of Liaohe oilfield, which is the important oil exploration field (Luo et al., 2005). After oil test, a high oil flow rate of 22.47 tons per day was obtained in the well section of 2680 m–2714.07 m in Proterozoic in Gaogu (GG) 2 well, thus the Gaosheng Proterozoic buried hill reservoir was discovered. Gaosheng oilfield has shown great potential in the process of exploration (Yu, 2016).

In recent years, we have a consensus view of the formation conditions of tight oil reservoirs in Gaosheng area. Reservoir formation is influenced by fractures, high quality source rocks and good preservation conditions of volcanic cover in Gaosheng area (Yu, 2016). It is also basically clear that the structure is the main migration channel of reservoir formation (You et al., 2006). However, the systematic summary of reservoir controlling factors and the prediction of favorable areas are relatively scarce and there is still room for improvement in the in-depth understanding of reservoir controlling factors. Lack of understanding of control factors has limited exploration progress. Therefore, it is significant to explore the main controlling factors of Gaosheng reservoir.

The main goals of the study are: 1) describe the characteristics of Es3 (Shahejie Member 3) and Es4 (Shahejie Member 4) source rocks and sandstone reservoirs; 2) reveal the characteristics of tectonic evolution and cover layer in Gaosheng area; 3) discuss the controlling factors of reservoir formation. The results can be used for reference to guide oil and gas exploration, and have practical application value in areas similar to the Western Depression in the world. In addition, it also has reference value for the exploration of other similar reservoirs.

2 Geological setting

Gaosheng area is in the northeast of the Western Depression of Liaohe Basin, Bohai Bay Basin. Liaohe Depression is a Cenozoic continental rift basin developed over the Mesozoic Basin, including several secondary structural units, such as the Eastern Depression, Western Depression, Damintun Depression, Shenbei Depression, Eastern Bulge, Western Bulge and Central Bulge (Hu et al., 2005). In the Paleogene, the Western Depression was a long and narrow half graben-like fault depression with a northeastward distribution and a steep slope in the east and a gentle slope in the west (Figure 1). The Western Depression is rich in oil and gas and the exploration degree of conventional oil and gas is high. The target strata studied in this paper are Proterozoic strata.

The Liaohe Basin was a part of the North China platform before the Early Triassic, and was uplifted for a long time after the Paleozoic, resulting in the loss of some strata. During the Mesocenozoic period, under the influence of the Pacific plate subduction to the northwest, several depressions spread north and east, and thick Mesozoic-Cenozoic sand-mudstone strata were deposited. Most of the Western Depression is based on Archeozoic strata, and the Shuguang area is based on Proterozoic and Paleozoic strata. The maximum thickness of the Cenozoic cap layer is thousands of meters and it is relatively widely distributed (Figure 2).

In terms of regional structure, Liaohe Basin is a part of the Bohai Bay oil and gas belt, belonging to the Middle and Cenozoic rift basin and located in the northeast of the North China platform, bordering the Liaodong Platform anticline to the east, the Yanshantai fold to the west and the eastern edge of the Inner Mongolia axis to the north (Zhang et al., 2014). The Liaohe Depression is characterized by a high geothermal field, regional shallow gravity negative anomalies, narrow geological features, frequent volcanic activity, and a fault system dominated by normal faults. It is a product of the uplift of the upper mantle and the extension of the upper crust. Its formation and development can be divided into three periods: the expansion period, the deep sag stage, and the suture period (convergence period) (Ge, 2018).

The source rocks in the Western Depression are mainly Es3 and Es4 strata and they have excellent oil generation potential to form large oil reservoir (Yu, 2016). The reservoirs are mainly Es3, Es4, Pz, Pt and Ar. The reservoir of Gaosheng oilfield is mainly concentrated in Pt.

3 Samples and methods

3.1 Samples

The samples of 4 wells were obtained to clarify the characteristic of source rocks and sandstone reservoir (Table 1). The source

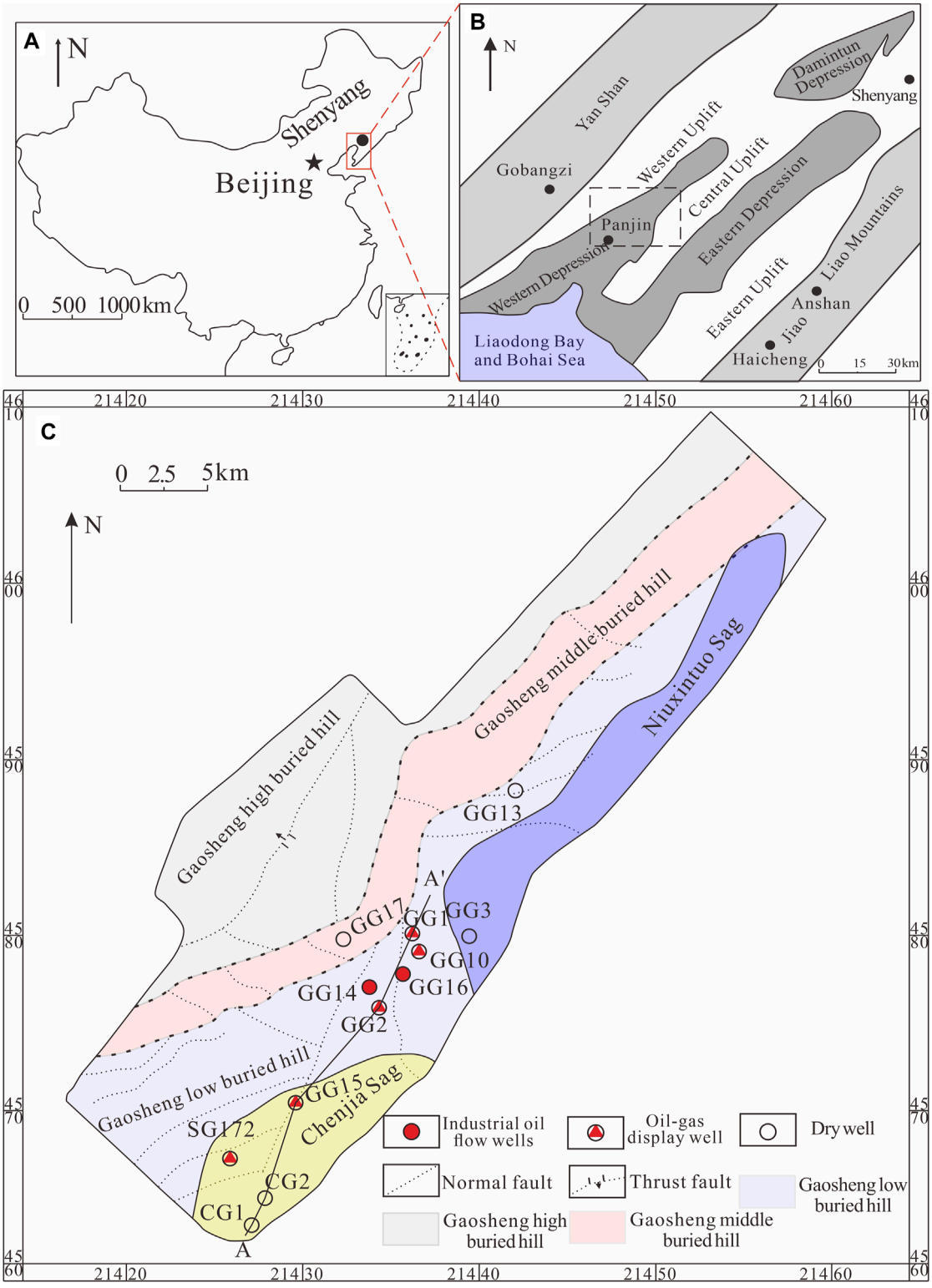

FIGURE 1
Location map of Gaosheng area in Western Depression of Liaohe Basin (modified from Hu et al., 2005). **(A)** Location of the Liaohe Basin in eastern China; **(B)** Location of the Gaosheng area in the Liaohe Basin; **(C)** The geological map the Gaosheng structural belt.

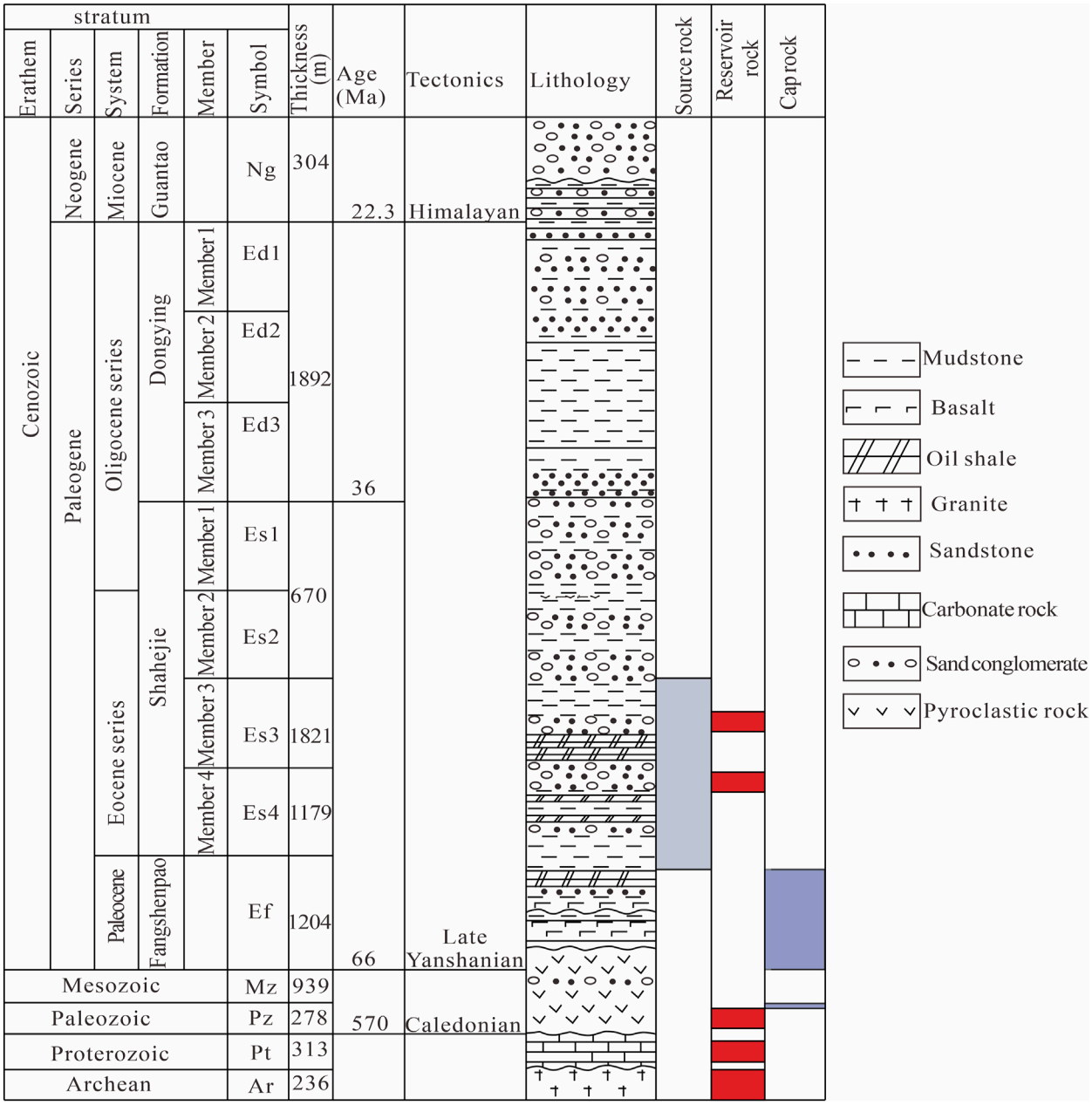

FIGURE 2
Comprehensive column chart of Gaosheng area in Western Depression of Liaohe Oilfield (modified from Leng et al., 2008).

rock samples were tested for geochemical characteristics. And the sandstones were for physical properties of reservoir.

3.2 Methods

3.2.1 2D-move was used to make structural evolution profile

According to 2D seismic profiles, geological and drilling data, the evolution history of a typical profile is recovered using 2D-Move software, which is implemented by the balanced profile method. The restoration of profile evolution provides a basis for explaining the evolution of structure and sedimentation in the study area. At the same time, these data are comprehensively utilized to establish the hydrocarbon accumulation model in the Gaosheng area.

3.2.2 Analysis of geochemical characteristics

The pyrolysis analysis method is to crush the sample to about 100 mesh, and the instrument used is YY3000A comprehensive evaluation instrument for source rocks. The analysis method is referred to GB/T 18602-2012 (Rock Pyrolysis Analysis). The organic geochemical parameters are mainly total organic carbon content (TOC), maturity (*Ro*), generation potential (S_1+S_2) and so on.

TABLE 1 Data of the obtained samples.

Well	Layer	Depth (m)	Lithology	Type of sample
GG2	Es3	1259.2	Mudstone	Source rock
GG2	Es4	1318.5		
GG14	Es3	1247.9		
GG14	Es4	1458.3		
GG15	Es3	1274.7		
GG15	Es4	1468.4		
GG16	Es3	1327.6		
GG16	Es4	1489.8		
GG2	Pt	3049.2	Sandstone	Sandstone reservoir
GG14	Pt	2941.88		
GG15	Pt	2869.26		
GG16	Pt	2656.5		

3.2.3 Experiment of reservoir

The porosity was measured by JS100007 helium porosity meter, and the permeability was measured by A-10133 gas permeability meter, utilizing standard industrial methods (Li et al., 2019). The resin or liquid glue dyed blue is poured into the pore space of the rock under a vacuum to solidify the resin or liquid glue, and then the rock is ground into thin slices, and finally the pore structure is observed under a polarizing microscope. The pore types and measurement parameters of reservoir rock can be clearly shown in the scanning electron microscopy (SEM). The SEM images were produced by China University of Petroleum (Beijing). The diameter of the sample is 0.5–3.0 cm, and the thickness is 0.2–1.0 cm. The observation instrument was Zeiss SUPRA 55 sapphire scanning electron microscope. Samples of quartz sandstone are cut into thin slices and then viewed through instruments.

4 Results

4.1 Characteristics of source rock

The source rocks of Es4 developed in the initial rifting stage of the rift valley, mainly in the western slope of the northern and southern parts of the depression, with a thickness of 0–700 m, generally about 300 m. The dark mudstone and sandy mudstone account for the majority. The contour map of source rocks (Figure 3A) indicates that the source rocks in Niuxintuo Sag in the northeast of Gaosheng area are the most developed, with a thickness of up to 700 m. According to the evaluation criteria of source rocks, the TOC of source rocks in Es4 Member ranges from 0.14% to 8.02% (average 2.35%), and the organic matter is mainly II_1 and II_2 types. The *Ro* ranged from 0.3% to 1.26% (average 0.76%).

The source rock of Es3 member is dark mudstone rich in organic matter, which is widely distributed and produced in the deep depression period. The isocontour map of source rock thickness (Figure 3B) indicates that the source rocks of Niuxintuo Sag, Chenjia-Panshan Sag and Qingshui Sag are relatively developed, and the most developed is Qingshui Sag with the maximum thickness of 1,500 m, followed by Chenjia Sag and Panshan Sag with the thickness of source rock up to 1,200 m, and the thickness of Niuxintuo Sag source rock is only 700 m. Generally speaking, this set of source rocks is the best source rock with the widest distribution and the largest thickness in the Western Depression. The TOC of the source rocks in Es4 ranges from 0.03% to 1.19% (average 0.19%). The organic matter is dominated by types II_1 and II_2, and the *Ro* ranges from 0.28% to 1.29% (average 0.68%).

4.2 Tectonic evolution

According to the structural development history, this area is mainly composed of three major structural layers: Paleogene pre-structural layer, Paleogene structural layer and Neogene structural layer. In the Mesozoic to early and middle Paleogene, fault activity was intense and frequent, showing obvious inheritance and neogenesis (Figure 4). In the middle and late Paleogene, fault activity gradually weakened, and there was basically no new fault development in the Neogene, showing stages of tectonic evolution. The reservoir formation model of the established Gaosheng reservoir is shown in Figure 5, which is conducive to revealing the formation mechanism of the reservoir.

4.3 Characteristics of the reservoir

The reservoirs include siliceous quartz sandstone, quartzite sandstone, glauconitic quartz sandstone, generally greyish-gray and dark gray, widely distributed in this area. The debris consists of fine particles, coarse and medium particles, sorting is generally good, roundness is mainly subroundness. The clastic composition is mainly monocrystalline quartz and feldspar and siltstone debris are occasionally seen. The content of quartz is generally 95%–99% of the detritus (Figure 6).

According to the porosity experiment, the porosity of quartz sandstone ranges from 0.4% to 22.1%, the porosity of less than 10% accounts for about 50%, the permeability ranges from 0.03 to 10.2 mD, and the permeability of less than 0.1 mD accounts for about 32% (Figure 7). It indicates that the quartz sandstone in Pt formation has a certain degree of density, but the heterogeneity is obvious.

Based on the data of core observation and cast thin sections, the pore types of Proterozoic reservoir rocks in this area are mainly secondary pores and fractures. Among them, the pore types mainly include: residual intergranular pores, intergranular dissolved pores, and intragranular dissolved pores.

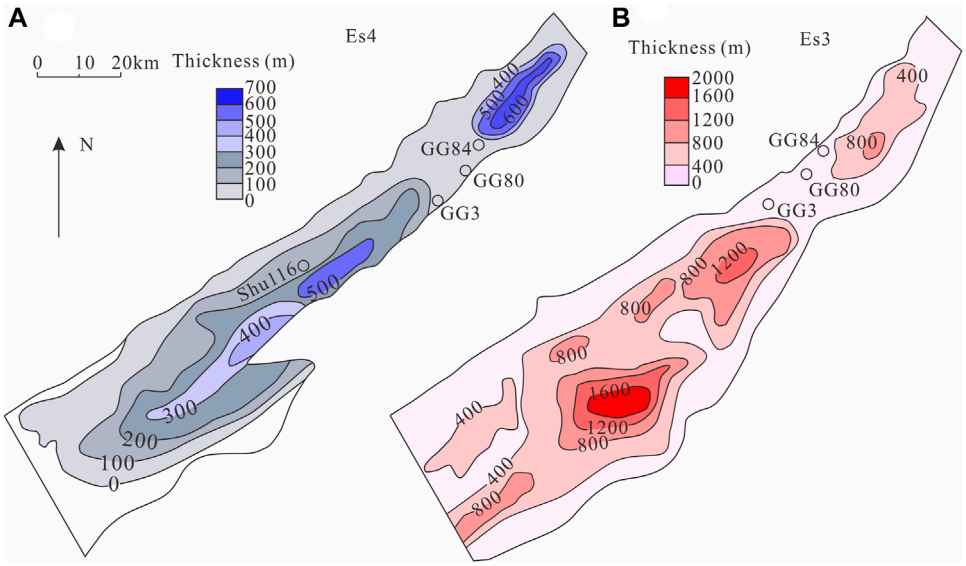

FIGURE 3
Isopach map of source rocks in the Western Depression of Liaohe Basin (The data are from Liaohe Oilfield). **(A)** Es4 source rocks; **(B)** Es3 source rocks.

Most of the fractures are open fractures, and the fracture surface extends longer, and most of them cut the whole core. Multiple groups of fractures develop and are distributed in a macroscopic network, so the core is often broken into small pieces. The presence of a lot of fractures in the core indicates that microfractures in the quartz sandstone are well developed (Figure 8).

4.4 Characteristics of the cap rock

This map is based on data collected from drilling Wells. Since Cenozoic, the subduction of the Pacific plate to the Eurasian plate led to the influence of Tanlu fault activity in the early stage of Liaohe Depression. During the Paleocene period, under the action of regional tensile stress, the fault activity was extremely strong, represented by the deep fault activity. The Tai' an major fault was strongly active and broke off the upper mantle. Then mantle materials poured out along the fracture and erupted to the surface, forming a thick basalt blanket in the Gaosheng—Leijia area (Figure 9).

The Fangshenpao Formation and the Mesozoic basalts are strongly controlled by the main fault and have a large thickness near the fault. It is analyzed that the eruption center is formed in the Gaosheng area, the thickness is larger in the main part of the buried hill, and it is thinner toward the low part of the buried hill (Figure 9). The basalt of this group has the characteristics of large single-layer thickness, multiple layers and large cumulative thickness. And the lithology is dense, which is a good cap layer. For example, the cumulative thickness of basalt in GG 2 well is 632 m, the cumulative thickness of basalt in GG 1 well is 1199 m, and the cumulative thickness of basalt in GG 1 well is 1189 m (Wu, 2012).

5 Discussion

5.1 The influence of source rock on accumulation

Proximity to the hydrocarbon generating center is conducive to oil migration and accumulation, which is the basic guarantee of reservoir formation (Zhao et al., 2019). The isocontour thickness maps of Es3 and Es4 in the Western Depression indicate the source rocks are thick (Figure 3). According to Section 4.1 of the results, the Es3 and Es4 source rocks have high abundance, good types, and their *Ro* are at the oil generation window, indicating that the source rocks have the potential to provide a large amount of crude oil and thus form large reservoirs. High hydrocarbon generation intensity is conducive to reservoir formation and the value of large reservoirs is generally greater than 350×10^4 t/km^2 (Hu et al., 2017; Feng et al., 2021; Song et al., 2021). The hydrocarbon generating intensity of Es4 is generally 5×10^6–10×10^6 t/km^2, and that of Es3 is generally greater than 5×10^6–15×10^6 t/km^2, which also indicates that the hydrocarbon generating potential of source rocks is good (Wu, 2012). It should be pointed out that proximity to the hydrocarbon generating depression is not a sufficient condition for hydrocarbon accumulation. The possibility of accumulation increases only in the dominant direction of oil and gas migration (Guo et al., 2017) and Gaosheng Oilfield meets this requirement (Figure 5).

5.2 Palaeouplift controls the direction of hydrocarbon migration

Palaeouplift area is the location of oil and gas accumulation, which is beneficial for the formation of various reservoir traps, such as structure, lithology-stratigraphy. The systematic analysis of

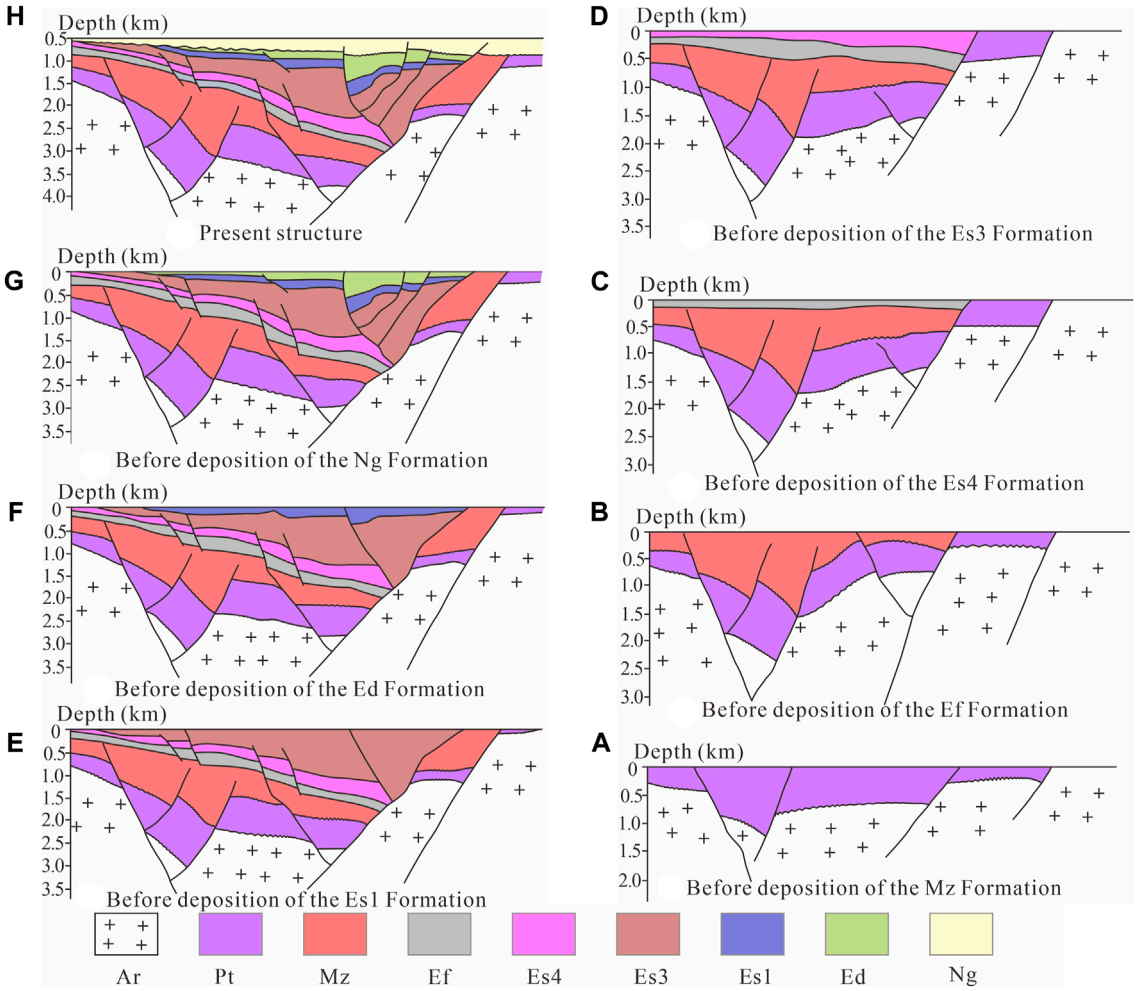

FIGURE 4
Structural evolution history of typical profiles in Gaosheng area of Liaohe Basin. (**A**–**H**) respectively indicate the sedimentary periods of Pt, Mz, Ef, Es4, Es3, Es1, Ed, and Ng strata.

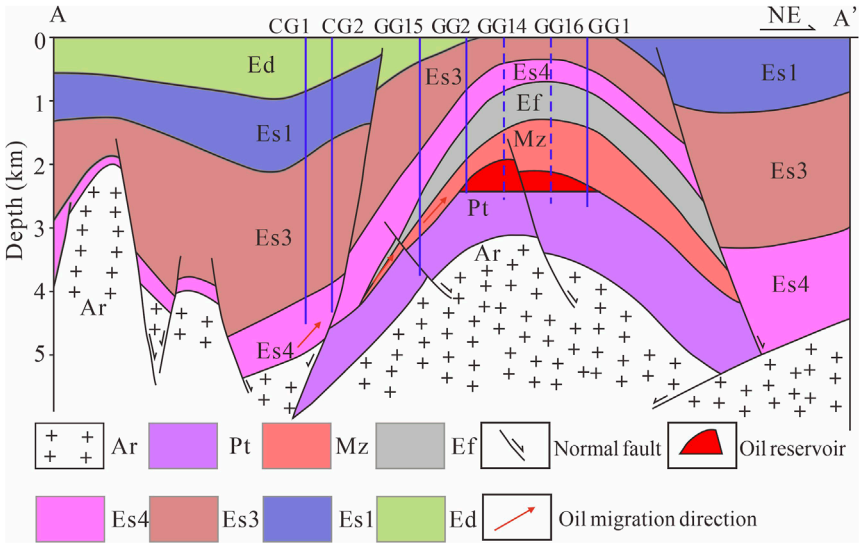

FIGURE 5
Accumulation model of Gaosheng area in Liaohe Basin.

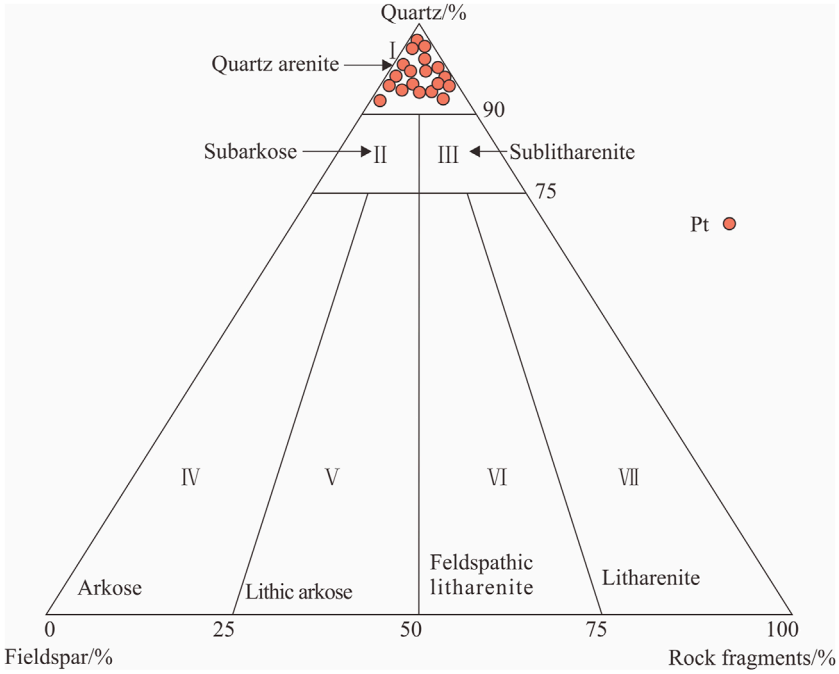

FIGURE 6
Compositional classification of Pt sandstone in Gaosheng area of Liaohe Basin.

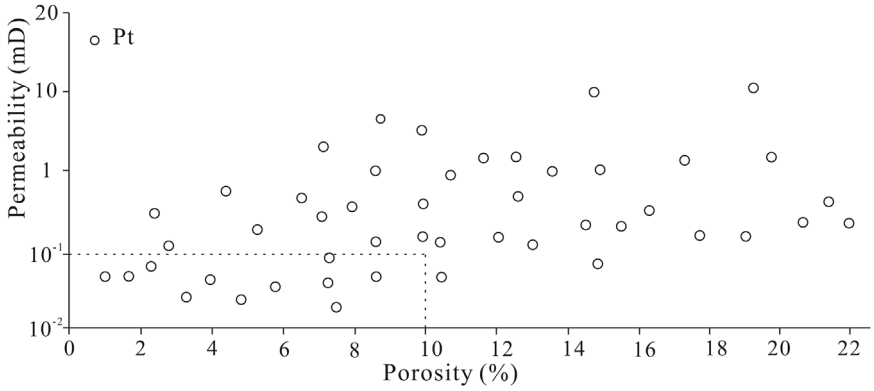

FIGURE 7
Pore permeability relationship of Pt reservoir in Gaosheng area of Liaohe Basin.

reservoir development characteristics in palaeouplift area is of great significance for oil and gas exploration. If the palaeouplift is in the dominant direction of oil and gas migration, it is conducive to accumulation (Jiang et al., 2023).

The archetype of Gaosheng buried-hill palaeouplift was formed at the end of Mesozoic, and it was basically formed in the middle of Eocene (late sedimentation of Es3 Member) (Wu, 2012).

Uplift is a positive tectonic unit (Jin, 2012). In the oil-gas accumulation unit, uplift is located in the low potential area of hydrocarbon fluid migration, which is a favorable place for oil-gas accumulation. At the same time, the traps formed during the formation and evolution of uplift are mainly anticlinal traps. The migration of oil and gas in such traps is more affected by buoyancy and tends to converge to the apex. Therefore, this type of reservoir is formed by the movement of oil from the deep to the shallow layer through faults and unconformities under the action of buoyancy. The oil migrated to the direction of regional uplift and accumulated in the suitable trap (Figure 5) (Liu et al., 2015).

5.3 The influence of reservoir on hydrocarbon accumulation

Reservoir physical property is an important factor affecting the formation of oil and gas reservoirs, especially for tight sandstone reservoirs. The development degree of reservoir

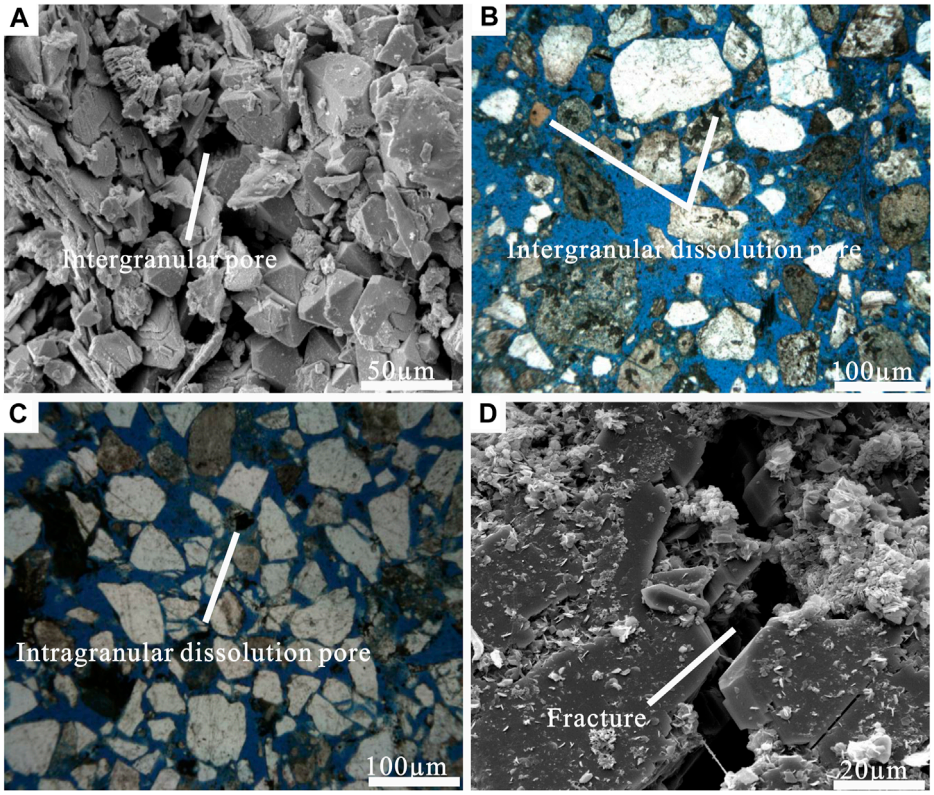

FIGURE 8
Pore structure characteristics of quartz sandstone in Gaosheng area. **(A)** Intergranular pore, SEM, GG2, 3049.2 m (Pt quartz sandstone); **(B)** Intergranular dissolution pore, cast thin section, GG14, 2941.88 m (Pt quartz sandstone); **(C)** Intragranular dissolution pore, cast thin section, GG15, 2869.26 m (Pt quartz sandstone); **(D)** Fracture, SEM, GG16, 2656.5 m (Pt quartz sandstone).

porosity, permeability and fracture have an influence on the formation of hydrocarbon reservoirs (Liu et al., 2017; Liu and Xiong, 2021).

The main reservoir in the study area is the sandstone of Pt formation. The pore types mainly include residual intergranular pores, intergranular dissolved pores, intra-granular dissolved pores and fractures (Figure 8), which provide sufficient space for the accumulation of crude oil.

Fracture can improve the permeability and the physical properties of the reservoir, and also seriously influence on the distribution of the reservoir (Jiang et al., 2015; Zhao et al., 2022)

From the analysis of failed wells in and around this area, it can be concluded that undeveloped reservoir or poor reservoir physical properties are the main factors leading to failure, accounting for the largest proportion. In the favorable sand body distribution area, good exploration results have been obtained in recent years. This is also evidenced by the high oil flow rates of wells GG14, SG169, and SG158. On the contrary, good result was not achieved due to poor reservoir conditions in the wells GG1 and GG15.

The distribution of sand body and the physical properties of reservoir restrict the enrichment and high production of oil and gas, so the comprehensive study on the distribution of reservoir and sand body should be strengthened.

5.4 Cap rock influence the preservation of reservoir

The formation of a large number of reservoirs requires an overlying layer as a good preservation condition (Guo et al., 2017; Liu et al., 2017; Jiang et al., 2022). The thickness of cap layer is positively correlated with oil and gas reserves (Liu et al., 2017). The basalt cap layer with large thickness is developed in the Gaosheng area, and the largest area can reach 2100 m. For example, the cumulative thickness of basalt in GG 2 is 1903 m, and the cumulative thickness of basalt in GG 1 is 1189 m. The cap layer has large thickness and stable distribution, so it is a regional cap layer to preserve the reservoir. In addition, the reservoir and overlying basalt constitute a good reservoir-cap combination.

5.5 Favorable zones and belts

On the basis of comprehensive analysis of main controlling factors of accumulation in Gaosheng area, favorable exploration

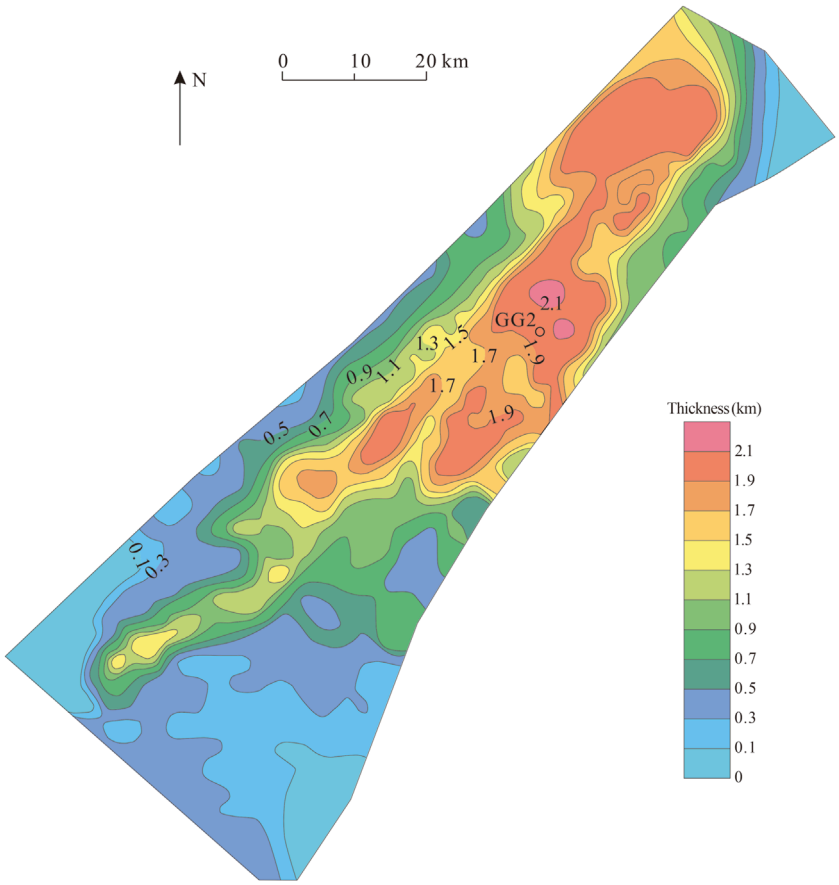

FIGURE 9
Ef+Mz basalt isopach map in the Western Depression of Liaohe Basin (The data are from Liaohe Oilfield).

zones are pointed out. According to the evaluation ideas and indicators, the reservoir forming factors such as structural conditions, source rock conditions, reservoir development, preservation conditions and trap development in Gaosheng area are evaluated. Combined with previous studies (You et al., 2006; Yu, 2016), it is considered that the formation conditions of the Gaosheng area are superior and the Proterozoic and Mesozoic oil-gas accumulation associations are the most promising in the Gaosheng area. Due to the small number of drilled wells, the low degree of exploration and the poor quality of seismic data, the development of fault system and the connection between reservoir and source rock are not fully evaluated. The Proterozoic and Mesozoic oil and gas accumulation associations in the middle-buried hill belt are the direction of oil and gas migration, and are potential exploration fields with great potential, which must be paid sufficient attention to.

In addition, the formation high pressure caused by hydrocarbon generation may also be one of the main controlling factors of oil and gas accumulation, but there is a lack of related research, so this should be one of the future research focuses.

6 Conclusion

Buried-hill reservoir is a reservoir different from conventional reservoirs. This kind of oil and gas reservoir needs the accumulation conditions of conventional reservoirs. In addition, the reservoir with abundant dissolved pores and fractures and the special migration channels formed by faults and unconformities are also critical. The source rock, reservoir and structure were analysed by geochemical method, reservoir experiment and 2D move software. Buried-hill reservoirs are mainly controlled by the following factors: 1) hydrocarbon generating depressions control the overall distribution of buried-hill reservoirs, 2) paleo-uplift and paleo-slope control the direction of oil and gas migration, 3) faults and unconformity constitute the system of oil and gas migration channels, and 4) reservoirs with dissolved holes and fractures control hydrocarbon enrichment.

The reservoir is close to the main hydrocarbon-generating depression. These areas have paleouplift background, deep faults and unconformities formed migration channels, and reservoirs with solution holes and fractures developed and suitable cap beds. The hydrocarbon accumulation association of Proterozoic and

Mesozoic in the middle buried-hill belt is the direction of hydrocarbon migration.

Data availability statement

The data analyzed in this study is subject to the following licenses/restrictions: None. Requests to access these datasets should be directed to QZ; 904836105@qq.com.

Author contributions

GZ: Conceptualization, Writing–original draft, Writing–review and editing. FJ: Writing–original draft. QZ: Project administration, Writing–review and editing. HP: Conceptualization, Writing–review and editing. XL: Software, Writing–original draft. DC: Funding acquisition, Writing–review and editing.

Funding

The author(s) declare that financial support was received for the research, authorship, and/or publication of this article. This research was financially funded by Science Foundation of China University of Petroleum, Beijing (2462022XKBH005) and China Postdoctoral Science Foundation (2022M723487).

Acknowledgments

Thanks to engineers Zhi Tian and Yanmin Guo for their guidance and help. Many thanks to the staff of the Exploration and Development Research Institute of Liaohe Oilfield of PetroChina for their assistance in collecting samples and providing some data.

Conflict of interest

The authors declare that the research was conducted in the absence of any commercial or financial relationships that could be construed as a potential conflict of interest.

Publisher's note

All claims expressed in this article are solely those of the authors and do not necessarily represent those of their affiliated organizations, or those of the publisher, the editors and the reviewers. Any product that may be evaluated in this article, or claim that may be made by its manufacturer, is not guaranteed or endorsed by the publisher.

References

Alsuwaidi, M., Mansurbeg, H., Alsuwaidi, A., Morad, S., Mohamed, A. A. I., Amao, A. O., et al. (2022). Comparison of diagenesis and reservoir quality of microporous lime mudstones (Aptian) between anticline crest and flanks: abu Dhabi, United Arab Emirates. *Mar. Pet. Geol.* 145, 105915. doi:10.1016/j.marpetgeo.2022.105915

Busch, B., Becker, I., Koehrer, B., Adelmann, D., and Hilgers, C. (2019). Porosity evolution of two Upper Carboniferous tight-gas-fluvial sandstone reservoirs: impact of fractures and total cement volumes on reservoir quality. *Mar. Pet. Geol.* 100, 376–390. doi:10.1016/j.marpetgeo.2018.10.051

Chen, J., Xu, Z., and Leung, J. Y. (2022). Analysis of fracture interference – coupling of flow and geomechanical computations with discrete fracture modeling using mrst. *J. Pet. Sci. Eng.* 219, 111134. doi:10.1016/j.petrol.2022.111134

Chen, Q., Deng, Y., Wei, J., Ma, G., Long, L., Xiao, W., et al. (2018). Types, distribution and play targets of lower cretaceous tight oil in Jiuquan basin, NW China. *Pet. Explor. Dev.* 45, 227–238. doi:10.1016/S1876-3804(18)30026-0

El Diasty, W. S., El Beialy, S. Y., Littke, R., and Farag, F. A. (2016). Source rock evaluation and nature of hydrocarbons in the khalda concession, shushan basin, Egypt's western desert. *Int. J. Coal. Geol.* 162, 45–60. doi:10.1016/j.coal.2016.05.015

Er, C., Zhao, J., Li, Y., Si, S., Bai, Y., Wu, W., et al. (2022). Relationship between tight reservoir diagenesis and hydrocarbon accumulation: an example from the early cretaceous Fuyu reservoir in the Daqing oil field, Songliao basin, China. *J. Pet. Sci. Eng.* 208, 109422. doi:10.1016/j.petrol.2021.109422

Feng, Y., Huang, Z., Wang, E., Zhang, H., Li, T., and Liang, Y. (2021). The hydrocarbon generation and expulsion features of source rocks and tight oil potential of the second member of the Qiketai formation, Shengbei area in the Turpan–hami basin, NW China. *Geol. J.* 56, 337–358. doi:10.1002/gj.3963

Ge, W. (2018). *Study on tight oil accumulation characteristics of the fourth member of Shahejie formation in western Liaohe depression*. Chengdu: Southwest Petroleum University.

Guo, Z., Ma, Y., Liu, W., Wang, L., Tian, J., Zeng, X., et al. (2017). Main factors controlling the formation of basement hydrocarbon reservoirs in the Qaidam basin, western China. *J. Pet. Sci. Eng.* 149, 244–255. doi:10.1016/j.petrol.2016.10.029

Han, Y., Noah, M., Lüders, V., Hartwig, A., Rinna, J., Skeie, J. E., et al. (2022). Geochemical characteristics of inclusion oils from the Skarv field a segment and their implications for the oil charge and leakage history. *Mar. Pet. Geol.* 137, 105506. doi:10.1016/j.marpetgeo.2021.105506

Hein, F. J., Ambrose, W. A., Hackley, P., and Mead, J. S. (2019). Unconventional energy resources: 2017 review. *Nat. Resour. Res.* 28, 1661–1751. doi:10.1007/s11053-018-9432-1

Higgs, K. E., Zwingmann, H., Reyes, A. G., and Funnell, R. H. (2007). Diagenesis, porosity evolution, and petroleum emplacement in tight gas reservoirs, taranaki basin, New Zealand. *J. Sediment. Res.* 77, 1003–1025. doi:10.2110/jsr.2007.095

Hu, L., Fuhrmann, A., Poelchau, H., Horsfield, B., Zhang, Z., Wu, T., et al. (2005). Numerical simulation of petroleum generation and migration in the Qingshui sag, western depression of the Liaohe basin, northeast China. *AAPG Bull.* 89, 1629–1649. doi:10.1306/07280504069

Hu, T., Pang, X., Wang, X., Pang, H., Tang, L., Pan, Z., et al. (2017). Source rock characteristics of Permian Lucaogou formation in the Jimusar sag, Junggar basin, northwest China, and its significance on tight oil source and occurrence. *Geol. J.* 52, 624–645. doi:10.1002/gj.2818

Huang, W., Salad Hersi, O., Lu, S., and Deng, S. (2017). Quantitative modelling of hydrocarbon expulsion and quality grading of tight oil lacustrine source rocks: case study of Qingshankou 1-member, central depression, southern Songliao basin, China. *Mar. Pet. Geol.* 84, 34–48. doi:10.1016/j.marpetgeo.2017.03.021

Iea (2012). *World energy outlook 2009*. https://iea.blob.core.windows.net/assets/ac80b701-bdfc-48cf-ac4c-00e60e1246a0/weo2009.

Iea (2013). *Short-term energy outlook supplement: constraints in new England likely to affect regional energy prices this winter*.

Jiang, H., Zhang, B., Liu, S., Wang, W., Zhou, G., and He, Y. (2023). Discovery of Guangan-shizhu Palaeouplift in Sichuan basin and its petroleum geological significance. *Acta Pet. Sin.* 44, 270–284. doi:10.7623/syxb202302004

Jiang, Y., Liu, J., Su, S., Liu, J., and Hu, H. (2022). Discussion on preservation conditions of buried hill oil and gas reservoirs in Bohai bay basin. *J. China Univ. Petroleum Nat. Sci. Ed.* 46, 1–11. doi:10.3969/j.issn.1673-5005.2022.04.001

Jiang, Z., Li, F., Yang, H., Li, Z., Liu, L., and Chen, L. (2015). Fracture development characteristics and reservoir control model of Jurassic tight reservoir in Dibei area, Kuqa Depression. *Acta Pet. Sin.* 36, 102–111. doi:10.7623/syxb2015S2009

Jin, Z. (2012). Formation and accumulation of oil and gas in marine carbonate sequences in Chinese sedimentary basins. *Sci. China Earth Sci.* 55, 368–385. doi:10.1007/s11430-011-4264-4

Kobraei, M., Sadouni, J., and Rabbani, A. R. (2019). Organic geochemical characteristics of Jurassic petroleum system in Abadan plain and north Dezful zones of the Zagros basin, southwest Iran. *J. Earth Syst. Sci.* 128, 50–18. doi:10.1007/s12040-019-1082-0

Leng, J., Pang, X., Li, X., Gao, X., Cui, L., and Su, D. (2008). Main controlling factors of hydrocarbon accumulation in the western depression of Liaohe fault depression. *J. Paleogeogr.* 10, 473–480.

Li, Y., Chang, X., Yin, W., Wang, G., Zhang, J., Shi, B., et al. (2019). Quantitative identification of diagenetic facies and controls on reservoir quality for tight sandstones: a case study of the Triassic Chang 9 oil layer, Zhenjing area, Ordos Basin. *Mar. Pet. Geol.* 102, 680–694. doi:10.1016/j.marpetgeo.2019.01.025

Liu, J., and Liu, G. (2017). Types, evolution of fractures, and their relationship with oil and gas migration of Permian Changxing formation in Yuanba gas field of Sichuan basin, China. *Energy fuels.* 31, 9345–9355. doi:10.1021/acs.energyfuels.7b01893

Liu, L., Li, H., Peng, H., Wang, W., Jiang, D., and Xiao, S. (2015). Quantitative prediction and evaluation of favorable development zones of uplift controlled reservoirs in Zhuyi Depression, pearl river estuary basin. *Acta Pet. Sin.* 36, 134–144. doi:10.7623/syxb2015S2012

Liu, M., and Xiong, C. (2021). Diagenesis and reservoir quality of deep-lacustrine sandy-debris-flow tight sandstones in upper Triassic Yanchang formation, ordos basin, China: implications for reservoir heterogeneity and hydrocarbon accumulation. *J. Pet. Sci. Eng.* 202, 108548. doi:10.1016/j.petrol.2021.108548

Liu, S., Misch, D., Gang, W., Li, J., Jin, J., Duan, Y., et al. (2023). Evaluation of the tight oil "sweet spot" in the middle Permian Lucaogou formation (Jimusaer sag, Junggar basin, NW China): insights from organic petrology and geochemistry. *Org. Geochem.* 177, 104570. doi:10.1016/j.orggeochem.2023.104570

Liu, X., Jin, Z., Bai, G., Guan, M., Liu, J., Pan, Q., et al. (2017). Formation and distribution characteristics of Proterozoic–lower Paleozoic marine giant oil and gas fields worldwide. *Pet. Sci.* 14, 237–260. doi:10.1007/s12182-017-0154-5

Liu, Y., Ye, J., Zong, J., Wang, D., Cao, Q., Yang, B., et al. (2022). Analysis of forces during tight oil charging and implications for the oiliness of the tight reservoir: a case study of the third member of the Palaeogene Shahejie Formation, Qibei slope, Qikou sag. *Mar. Pet. Geol.* 144, 105819. doi:10.1016/j.marpetgeo.2022.105819

Luo, J., Morad, S., Liang, Z., and Zhu, Y. (2005). Controls on the quality of Archean metamorphic and Jurassic volcanic reservoir rocks from the Xinglongtai buried hill, western depression of Liaohe basin, China. *AAPG Bull.* 89, 1319–1346. doi:10.1306/05230503113

Odrzygóźdź, O., Machowski, G., Szczerba, M., Filipek, A., Więcław, D., Perotta, I. D., et al. (2023). Spatial distribution of micro- and Nanoporosity in Oligocene menilite and cretaceous Lgota mudstones (outer Carpathians): organic porosity development as a key to understanding unconventional hydrocarbon reservoirs? *Mar. Pet. Geol.* 148, 106028. doi:10.1016/j.marpetgeo.2022.106028

Panara, Y., Chandra, V., Finkbeiner, T., Petrovic, A., Zühlke, R., Khanna, P., et al. (2023). Fracture intensity and associated variability: a new methodology for 3d digital outcrop model analysis of carbonate reservoirs. *Mar. Pet. Geol.* 158, 106532. doi:10.1016/j.marpetgeo.2023.106532

Song, Y., Wang, E., Peng, Y., Xing, H., Wu, K., Zheng, Y., et al. (2021). Conventional and unconventional hydrocarbon resource potential evaluation of source rocks and reservoirs: a case study of the upper Xiaganchaigou formation, western Qaidam basin, northwest China. *Nat. Resour. Res.* 30, 4355–4377. doi:10.1007/s11053-021-09953-y

Szatmari, P., and Schäffer, R. (2023). Accumulation and removal of world's largest hydrocarbon resources with changing hydrology and climate in the Cenozoic. *Mar. Pet. Geol.* 152, 106213. doi:10.1016/j.marpetgeo.2023.106213

Wu, C. (2012). *Analysis of hydrocarbon accumulation conditions and evaluation of favorable targets in Gaosheng buried hill*. Daqing: Northeast Petroleum University.

Wu, H., Hu, W., Wang, Y., Tao, K., Tang, Y., Cao, J., et al. (2021). Depositional conditions and accumulation models of tight oils in the middle Permian Lucaogou formation in Junggar basin, northwestern China: new insights from geochemical analysis. *AAPG Bull.* 105, 2477–2518. doi:10.1306/06222118094

Xu, W., Li, J., Liu, X., Li, N., Zhang, C., Zhang, Y., et al. (2021). Accumulation conditions and exploration directions of Ordovician lower assemblage natural gas, ordos basin, NW China. *Pet. Explor. Dev.* 48, 641–654. doi:10.1016/S1876-3804(21)60051-4

Xu, Z., Liu, L., Wang, T., Wu, K., Dou, W., Song, X., et al. (2017). Characteristics and controlling factors of lacustrine tight oil reservoirs of the Triassic Yanchang formation Chang 7 in the Ordos basin, China. *Mar. Pet. Geol.* 82, 265–296. doi:10.1016/j.marpetgeo.2017.02.012

You, G., Pan, J., Zhang, K., Liu, B., and Xiao, K. (2006). Analysis on hydrocarbon accumulation conditions of Paleogene in the northern Gaosheng area of the western sag of Liaohe depression. *Acta Geosci. Sin.* 27, 241–246. doi:10.3321/j.issn:1006-3021.2006.03.008

Yu, J. (2016). *Main controlling factors and objective evaluation of hydrocarbon accumulation in Gaosheng Proterozoic buried hill*. Daqing: Northeast Petroleum University.

Zhang, J., Wu, Z., Lv, M., and Yu, Q. (2014). The difference of tectonic activity in the eastern and western depressions of Liaohe depression controls the hydrocarbon accumulation of volcanic rocks. *Geoscience* 28, 1032–1040.

Zhang, N., Liu, L., Su, T., Wu, K., and Zhao, Y. (2013). Comparison of tight oil formation conditions between Chang 7 member of Yanchang formation in ordos basin and Bakken formation in Williston basin and its significance. *Geoscience* 27, 1120–1130.

Zhao, G., Li, X., Liu, M., Li, J., Liu, Y., Zhang, X., et al. (2022). Accumulation characteristics and controlling factors of the Tugeerming gas reservoir in the eastern Kuqa Depression of the Tarim basin, northwest China. *J. Pet. Sci. Eng.* 217, 110881. doi:10.1016/j.petrol.2022.110881

Zhao, J., Li, J., Cao, Q., Bai, Y., Wu, W., and Ma, Y. (2019). Quasi-continuous hydrocarbon accumulation: an alternative model for the formation of large tight oil and gas accumulations. *J. Pet. Sci. Eng.* 174, 25–39. doi:10.1016/j.petrol.2018.10.076

Zhao, W., Hu, S., Deng, X., Bai, B., Tao, S., Sun, B., et al. (2021). Physical property and hydrocarbon enrichment characteristics of tight oil reservoir in Chang 7 division of Yanchang formation, xin'anbian oilfield, ordos basin, China. *Pet. Sci.* 18, 1294–1304. doi:10.1016/j.petsci.2020.07.001

Zou, C., Zhu, R., Wu, S., Yang, Z., Tao, S., and Yuan, X. (2012). Types, characteristics, mechanisms and prospects of conventional and unconventional hydrocarbon accumulation: a case study of tight oil and tight gas in China. *Acta Pet. Sin.* 33, 173–187. doi:10.7623/syxb201202001

Frontiers in Earth Science

Investigates the processes operating within the major spheres of our planet

Advances our understanding across the earth sciences, providing a theoretical background for better use of our planet's resources and equipping us to face major environmental challenges.

Discover the latest Research Topics

See more →

Frontiers

Avenue du Tribunal-Fédéral 34
1005 Lausanne, Switzerland
frontiersin.org

Contact us

+41 (0)21 510 17 00
frontiersin.org/about/contact